

VOLUME 100 Nos. 2,3
JUNE (I) 1995

NIMBEU 100 (2,3) 209-450 (1995)
ISSN 0168-583X

Nuclear Instruments & Methods in Physics Research

Editor-in-Chief: Kai Siegbahn

Section B

Beam Interactions with Materials and Atoms

DISTRIBUTION STATEMENT A

Approved for public release;
Distribution Unlimited

19970324 052

Editors: H. H. Andersen & L. E. Rehn

Proceedings of the Tenth International Workshop on
Inelastic Ion-Surface Collisions (IISC-10)
Grand Targhee Resort, Wyoming, USA, August 8-12, 1994

North-Holland

NUCLEAR INSTRUMENTS AND METHODS IN PHYSICS RESEARCH

Editor-in-Chief: Kai Siegbahn

SECTION B: BEAM INTERACTIONS WITH MATERIALS AND ATOMS

Editors: H.H. Andersen & L.E. Rehn

Editorial Board:

R.S. AVERBACK (Urbana)
P. BAUER (Linz)
K. BETHGE (Frankfurt)
G. FOTI (Catania)
K.S. JONES (Gainesville)
G.J.F. LEGGE (Melbourne)
W.N. LENNARD (Ontario)

M. MANNAMI (Kyoto)
F. PÁSZTI (Budapest)
S.T. PICRAUX (Albuquerque)
D.B. POKER (Oak Ridge)
H.L. RAVN (Geneva)
J.P. RIVIERE (Poitiers)
B. STRITZKER (Augsburg)

M. SZYMONSKI (Cracow)
T. TOMBRELLO (Pasadena)
E. UGGERHØJ (Aarhus)
F. VAN DER VEEN (Amsterdam)
A.E. WHITE (Murray Hill)
I. YAMADA (Kyoto)
ZHU Jieqing (Shanghai)

Information for Authors

Section B of Nuclear Instruments and Methods in Physics Research (NIM B) has been formed to provide a special forum for the discussion of all aspects of the interaction of energetic beams with atoms, molecules and aggregate forms of matter. This includes ion beam analysis and ion beam modification of materials as well as studies of the basic interaction mechanisms of importance for this work. The Editors invite submission of both theoretical and experimental papers of original research in this area.

Contributions should be in English and should be submitted in duplicate directly to the Editors. Together with the hard copies an exactly identical electronic version on diskette can be submitted. To assist in minimizing publication time, it is suggested that manuscripts originating from Europe, India, The Middle East and Africa be sent to Prof. Andersen, and manuscripts from The Americas, The Far East (China and Japan) and Australasia to Dr. Rehn.

Prof. H.H. Andersen
The Niels Bohr Institute, Ørsted Laboratory
Universitetsparken 5
DK-2100 Copenhagen Ø, Denmark
Tel. +45 35320482 FAX: +45 35320460
e-mail: nimb@meyer.fys.ku.dk

Dr. L.E. Rehn
Materials Science Division, Bldg 223, Rm S231
Argonne National Laboratory, 9700 South Cass Avenue
Argonne, IL 60439, USA
Tel. +1 708 2529297 FAX +1 708 2523308
e-mail: lynn_rehn@qmgate.anl.gov

Short contributions of less than 1500 words and not subdivided into sections may be published as Letters to the Editor in a shorter time than regular articles as the proofs will normally be corrected by the Publisher.

Correspondence with the Publisher regarding articles accepted for publication or the return of corrected proofs should be addressed to:

NIM B Editors, Elsevier Science B.V., P.O. Box 103, 1000 AC Amsterdam, The Netherlands
FAX: +31 20 4852 775 telex: 10704 ESP OM tel. +31 20 4852 500 e-mail: nimb-j@elsevier.nl

There are no page charges to individuals or institutions for publication of an article in this journal. 50 reprints of each article will be supplied free of charge. Further reprints can be ordered from the Publisher on the Order Form sent out with the proofs.

Subscriptions

Nuclear Instruments and Methods in Physics Research - B (ISSN 0168-583X). For 1995, volumes 95–107 are scheduled for publication. Subscription prices are available upon request from the Publisher. A combined subscription to NIM A volumes 352–366 and NIM B volumes 95–107 is available at a reduced rate.

Subscriptions are accepted on a prepaid basis only and are entered on a calendar year basis. Issues are sent by surface mail except to the following countries where air delivery via SAL is ensured: Argentina, Australia, Brazil, Canada, China, Hong Kong, India, Israel, Japan, Malaysia, Mexico, New Zealand, Pakistan, Singapore, South Africa, South Korea, Taiwan, Thailand, USA. For all other countries airmail rates are available upon request.

Please address all requests regarding orders and subscription queries to: Elsevier Science, Journal Department, P.O. Box 211, 1000 AE Amsterdam, The Netherlands, tel. +31 20 4853642, FAX: +31 20 4853598. Claims for issues not received should be made within six months of our publication (mailing) date.

Information for Advertisers

Advertising orders and enquiries can be sent to the Advertising Department, Elsevier Science B.V., P.O. Box 211, 1000 AE Amsterdam, The Netherlands, tel. +31 20 485 3796, FAX: +31 20 485 3810. (Courier shipments to street address: Molenwerf 1, 1014 AG Amsterdam, The Netherlands.)
UK: T.G. Scott & Son, Vanessa Bird, Portland House, 21 Narborough Rd, Cosby, Leicestershire LE9 5TA, tel. +44 116 2750521/2753333; FAX: +44 116 2750522. USA, Canada: Weston Media Associates, Daniel Lipner, P.O. Box 1110, Greens Farms, CT 06436-1110, USA, tel. +1 203 261 2500, FAX: +1 203 261 0101.

Elsevier Science B.V.: All rights reserved. No part of this publication may be reproduced, stored in a retrieval system or transmitted in any form or by any means, electronic, mechanical, photocopying, recording or otherwise, without the written permission of the Publisher, Elsevier Science B.V., Copyright & Permissions Dept., P.O. Box 521, 1000 AM Amsterdam, The Netherlands.

Special regulations for authors – Upon acceptance of an article by the journal, the Author(s) will be asked to transfer copyright of the article to the Publisher. This transfer will ensure the widest possible dissemination of information.

Special regulations for readers in the USA – This journal has been registered with the Copyright Clearance Center, Inc. Consent is given for copying articles for personal or internal use, or for the personal use of specific clients. This consent is given on the condition that the copier pays through the Center the per copy fee stated on the first page of each article for copying beyond that permitted by Sections 107 or 108 of the US Copyright Law. The appropriate fee should be forwarded with a copy of the first page of the article to the Copyright Clearance Center, Inc., 222 Rosewood Drive, Danvers, MA 01923, USA. If no code appears on an article, the Author has not given consent to copy and permission to copy must be obtained directly from the Author. The fee indicated on the first page of an article in this issue will apply retroactively to all articles published in the journal, regardless of the year of publication. This consent does not extend to other kinds of copying, such as for general distribution, resale, advertising and promotion purposes, or for creating new collective works. Special written permission must be obtained from the publisher for such copying.

US mailing notice – Nuclear Instruments and Methods in Physics Research - B (ISSN 0168-583X) is published monthly (for five months of the year), semi-monthly in March, July, October and December, three times a month in April and June, and five times in May by Elsevier Science, Molenwerf 1, P.O. Box 211, 1000 AE Amsterdam, The Netherlands. Annual subscription price in the USA is US \$4899 (US \$ price valid in North, Central and South America only), including air speed delivery. Second class postage paid at Jamaica NY 11431.

USA POSTMASTERS: Send address changes to Nuclear Instruments and Methods in Physics Research - B, Publications Expediting, Inc., 200 Meacham Avenue, Elmont NY 11003. Airfreight and mailing in the USA by Publications Expediting.

No responsibility is assumed by the Publisher for any injury and/or damage to persons or property as a matter of products liability, negligence or otherwise, or from any use or operation of any methods, products, instructions or ideas contained in the materials herein. Although all advertising material is expected to conform to ethical standards, inclusion in this publication does not constitute a guarantee or endorsement of the quality or value of such product or of the claims made of it by its manufacturer.

Published monthly

Printed in The Netherlands

REPORT DOCUMENTATION PAGE

Form Approved
OMB No. 070-0188

Public reporting burden for this collection of information is estimated to average 1 hour per response, including the time for reviewing instructions, searching existing data sources, gathering and maintaining the data needed, and completing and reviewing the collection of information. Send comments regarding this burden estimate or any other aspect of this collection of information, including suggestions for reducing this burden, to Washington Headquarters Services, Directorate for Information Operations and Reports, 1215 Jefferson Davis Highway, Suite 1204, Arlington, VA 22202-4302, and to the Office of Management and Budget, Paperwork Reduction Project (070-0188), Washington, DC 20503.

1. AGENCY USE ONLY (Leave blank)		2. REPORT DATE		3. REPORT TYPE AND DATES COVERED	
4. TITLE AND SUBTITLE "Inelastic Ion-Surface Collisions"				5. FUNDING NUMBERS G N00014-94-1-0953	
6. AUTHOR(S) Alan V. Barnes, Norman H. Tolk, and Peter Norlander					
7. PERFORMING ORGANIZATION NAME(S) AND ADDRESS(ES) Center for Molecular and Atomic Studies at Surfaces Department of Physics and Astronomy Vanderbilt University Nashville, TN 37235				8. PERFORMING ORGANIZATION REPORT NUMBER	
9. SPONSORING/MONITORING AGENCY NAME(S) AND ADDRESS(ES) Office of Naval Research Attn: ONR 251:JWK Ballston Tower One 800 North Quincy Street Arlington, VA 22217-5660				10. SPONSORING/MONITORING AGENCY REPORT NUMBER	
11. SUPPLEMENTARY NOTES					
12a. DISTRIBUTION/AVAILABILITY STATEMENT APPROVED FOR PUBLIC RELEASE; DISTRIBUTION IS UNLIMITED.				12b. DISTRIBUTION CODE	
13. ABSTRACT (Maximum 200 words) The Tenth International Workshop on Inelastic Surface Collisions took place August 8 to 12, 1994 at the Grand Targhee Ski & Summer Resort, Wyoming (USA), a mountain retreat located near the Wyoming-Idaho border, just west of the Grand Teton National Park. It was chaired by Alan V. Barnes, Peter Norlander, and Norman H. Tolk. This extraordinarily beautiful and isolated setting contributed significantly to bring together most of the leading workers in the field, as well as many workers in related fields. Consequently, the conference covered experimental and theoretical research on various aspects of inelastic particle-surface interactions and related topics, including inelastic particle scattering from surfaces, sputtering, electronically-induced desorption, laser-induced desorption, secondary particle emission, collision-induced surface chemistry, and collision-induced defect formation. The meeting provided an informal workshop atmosphere with ample time for discussions. Some contributions selected among the submitted abstracts were presented orally. The remaining contributions were presented in poster sessions. There were no parallel sessions. The workshop was attended by approximately 90 scientists. The program included 9 invited lectures and 28 oral presentations of selected abstracts.					
14. SUBJECT TERMS Inelastic-Particle Interactions Laser-Induced Desorption Surface Chemistry				15. NUMBER OF PAGES	
				16. PRICE CODE	
DTIC QUALITY INSPECTED 8					
17. SECURITY CLASSIFICATION OF REPORT Unclassified	18. SECURITY CLASSIFICATION OF THIS PAGE Unclassified	19. SECURITY CLASSIFICATION OF ABSTRACT Unclassified	20. LIMITATION OF ABSTRACT Unlimited		

FOR ADVERTISING INFORMATION PLEASE CONTACT OUR ADVERTISING REPRESENTATIVES

USA/CANADA

Weston Media Associates

Mr. Daniel S. Lipner

P.O. Box 1110, GREENS FARMS, CT 06436-1110

Tel: (203) 261-2500, Fax: (203) 261-0101

GREAT BRITAIN

T.G. Scott & Son Ltd.

Vanessa Bird

Portland House, 21 Narborough Road

COSBY, Leicestershire LE9 5TA

Tel: (0116) 2750.521, Fax: (0116) 2750.522

JAPAN

ES - Tokyo Branch

Ms. Noriko Kodama

20-12 Yushima, 3 chome, Bunkyo-Ku

TOKYO 113

Tel: (03) 3836 0810, Fax: (03) 3839-4344

Telex: 02657617



REST OF WORLD

ELSEVIER SCIENCE

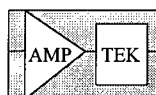
Ms. W. van Cattenburch

Advertising Department

P.O.Box 211, 1000 AE AMSTERDAM

The Netherlands

Tel: (20) 485.3796, Fax: 485.3810



**X-RAY
DETECTOR**

XR-100T

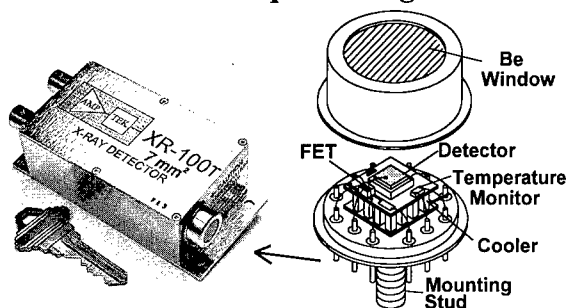
200 eV RESOLUTION

NEW!

Technology Breakthrough

All Solid State Design

No More Liquid Nitrogen !!



FEATURES

- Si-PIN Photodiode
- Peltier Cooler
- Cooled FET
- Amptek A250 Preamp
- Temperature Monitor
- Beryllium Window
- Hermetic Package (TO-8)
- PX2T Amplifier and Power Supply

APPLICATIONS

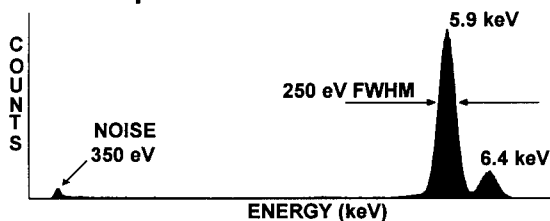
- X-Ray Fluorescence
- Medical X-Ray Detectors
- X-Ray Lithography
- Portable X-Ray Instruments
- X-Ray Teaching & Research
- Mössbauer Spectrometers
- X-Ray Space and Astronomy
- Environmental Monitoring
- Nuclear Plant Monitoring
- Toxic Dump Site Monitoring
- PIXE

Model **XR-100T** is a new high performance X-Ray Detector, Preamplifier, and Cooler system using a Si-PIN Photodiode as an X-Ray detector mounted on a thermoelectric cooler. On the cooler are also mounted the input FET and the feedback components to the Amptek A250 charge sensitive preamp. The internal components are kept at approximately -30°C , and can be monitored by a temperature sensitive integrated circuit. The hermetic TO-8 package of the detector has a light tight, vacuum tight 1 mil (25 μm) Beryllium window to permit soft X-Ray detection.

Power to the XR-100T is provided by the PX2T Power Supply. The PX2T is AC powered and also includes a spectroscopy grade Shaping Amplifier. The XR-100T/PX2T system ensures quick, reliable operation in less than one minute from power turn-on.

The system resolution with a test pulser and the detector connected is 200 eV FWHM. The resolution for the 5.9 keV peak of ^{55}Fe is 250 eV FWHM.

^{55}Fe Spectrum with the XR-100T



AMPTEK INC.

6 De ANGELO DRIVE, BEDFORD, MA 01730-2204 U.S.A.

TEL: + 1 (617) 275-2242 FAX: + 1 (617) 275-3470

e-mail: sales@amptek.com

WORLD-WIDE SALES DIRECT FROM THE FACTORY

543B

Handbook on Semiconductors, Volume 3 Completely Revised and Enlarged Edition Materials, Properties and Preparation

Edited by S. Mahajan

The availability of various novel materials, such as semiconductors, tailor-made polymers and ceramics, has revolutionized information processing and transmission. Since the early fifties, semiconductors have formed the backbone of different information age technologies.

The fabrication of state-of-the-art semiconducting devices requires either substrates or composite structures consisting of thin epitaxial layers. Over the years, great strides have been made both in growing bulk crystals and in controlled deposition of thin homo- and hetero-epitaxial layers.

Understanding of the deformation behaviour of semiconductors has facilitated the growth of high-quality crystals. Heterostructures consisting of extremely thin layers and chemically and structurally sharp interfaces can be deposited. To tailor bandgaps and electronic properties, silicon-germanium/silicon heterojunctions, mixed III-V epitaxial layers that are ordered and phase separated and quantum-well structures have been grown. Also, to improve the optical, electrical and structural quality of as-grown bulk and thin film materials, a variety of interdisciplinary studies have been carried out that has resulted in a number of sophisticated techniques to evaluate semiconductors.

In this volume, scientific issues relevant to these topics and others are discussed in detail. The coverage is in-depth and broad. The resulting volume should serve as a major reference source for education and research on semiconducting materials.

Contents: 1. Growth and evaluation of bulk crystals (*J.-I. Chikawa and J. Matui*). 2. Mechanical behaviour of semiconductors (*K. Sumino*). 3. MOCVD technology and its applications (*M. Razeghi*). 4. Growth mechanisms in MBE and CBE of III-V compounds (*B.A. Joyce, D.D. Vvedensky, C.T. Foxon*). 5. Growth of narrow bandgap semiconductors (*D.L. Partin, J. Heremans*). 6. Growth, characterization and device developments in large bandgap semiconductor thin films (*R.F. Davis*). 7. HgTe-CdTe superlattices (*J.R. Meyer et al.*). 8. Si/Ge and Si/SiGe heterostructures and superlattices (*K. Eberl, W. Wegscheider*). 9. Amorphous semiconductors (*M. Stutzmann*). 10. Characterization and properties of semiconductors (*G.E. Stillman et al.*). 11. Characterization of compound semiconductors by etching (*J.L. Weyhes*). 12. X-ray topography (*P. Franzosi*). 13. Evaluation of semiconductors using scanning microscopy (*C.A. Warwick*). 14. High resolution electron microscopy for semiconducting materials (*J. Van Landuyt, J. Vanhellemont*). 15. Dislocations in heteroepitaxial films (*R. Beanland, C.J. Kiely, R. C. Pond*). 16. Diffusion in semiconductors (*A.F.W. Willoughby*). 17. (Diluted) magnetic semiconductors (*T. Dietl*). 18. Impurity- and defect-centers in compound semiconductors (*M. Skowronski*). 19. Atomic ordering and phase separation in epitaxial III-V alloys (*A. Zunger, S. Mahajan*). 20. Hydrogen in crystalline semiconductors (*E.E. Haller*). 21. Carbon in mono-crystalline silicon (*G. Davies, R.C. Newman*). 22. Oxygen in silicon (*H. Bender,*

J. Vanhellemont). 23. Chalcogen-related defects in silicon (*H.G. Grimmeiss, E. Janzén*). 24. Silicon crystals for giga-bit scale integration (*T. Abe*). 25. Epitaxial silicides (*R.T. Tung*). 26. Metal-compound semiconductor interactions (*T. Sands, V.G. Keramidis*). 27. Ion implantation of silicon and gallium arsenide (*J.P. de Souza, D.K. Sadana*). 28. Passivation and dielectrics (*K.V. Srikrishnan, G.E. Schwartz*).

©1994 2398 pages (in 2 vols.)
Price: Dfl. 1190.00 (US\$680.00)
Set price: Dfl. 2495.00 (US\$1425.50)
ISBN 0-444-88835-7

TO ORDER

Contact your regular supplier or:

ELSEVIER SCIENCE B.V.

attn. C. Ryan
P.O. Box 103
1000 AC Amsterdam
The Netherlands
Fax: (+31) 20 5862580

Customers in the USA and Canada:

ELSEVIER SCIENCE B.V.

attn. J. Weislogel
P.O. Box 882
New York, NY 10159-0945 USA
Fax: (212) 633 3680

No postage will be added to prepaid book orders.
Dutch Guilder price(s) quoted applies worldwide. US Dollar price(s) quoted may be subject to exchange rate fluctuations. Customers in the European Union should add the appropriate VAT rate applicable in their country to the price(s). In New York State please add applicable sales tax. All prices are subject to change without prior notice.



NORTH-HOLLAND

(AN IMPRINT OF ELSEVIER SCIENCE)

MATERIALS SCIENCE JOURNALS AND HANDBOOKS... MATERIALS SCIENCE JOURNALS AND HANDBOOKS... MATERIALS SCIENCE

COMPUTATIONAL MATERIALS SCIENCE

Editors: **U. Landman**, *School of Physics, Georgia Institute of Technology, Atlanta, GA 30332, USA* and **R.M. Nieminen**, *Laboratory of Physics, Helsinki Institute of Technology, 02150 Espoo, Finland*

AIMS AND SCOPE

Publishes articles of interest to physicists, chemists and materials researchers and engineers and to other scientists involved with materials phenomena and computational modelling.

The journal covers computational modelling of materials properties and phenomena, ranging from the synthesis, characterisation and processing of materials, structures and devices to the numerical methodology of materials simulations. Computer videos and a Free Program Database are offered to subscribers.

1995 SUBSCRIPTION DATA

Volumes 3-4 (in 8 issues)
Price: Dfl. 850.00 (US\$447.00)
ISSN 0927-0256

For more information contact :

ELSEVIER SCIENCE B.V.

attn. C. Ryan
P.O. Box 103
1000 AC Amsterdam
The Netherlands
Fax: (+31) 20 5862580

Customers in the USA and Canada:

ELSEVIER SCIENCE INC.

attn. J. Weislogel
P.O. Box 882
New York, NY 10159-0945
Fax: (212) 633 3680

OPTICAL MATERIALS

An International Journal on the Physics and Chemistry of Optical Materials and their Applications, including Devices

Editor-in-Chief: **R.C. Powell**, *Center for Laser Research, Noble Research Center 413, Oklahoma State University, Stillwater, OK 74078, USA*

AIMS AND SCOPE

The purpose of *Optical Materials* is to provide a means of communication and technology transfer between researchers who are interested in materials for potential device applications. The journal publishes original papers and review articles on the design, synthesis, characterisation and applications of optical materials.

1995 SUBSCRIPTION DATA

Volume 4 (in 6 issues)
Price: Dfl 580.00 (US\$305.00)
ISSN 0925-3467

PLEASE VISIT OUR BOOTH AT
THE MRS FALL MEETING
WHERE THESE AND OTHER
MAJOR PUBLICATIONS WILL
BE ON DISPLAY



ELSEVIER

An imprint of Elsevier Science

HANDBOOK OF CRYSTAL GROWTH

Edited by **D.T.J. Hurle**

Volume 1

Fundamentals

- A. Thermodynamics and Kinetics
- B. Transport Processes and Stability

Volume 2

Bulk Crystal Growth

- A. Basic Techniques
- B. Growth Mechanisms and Dynamics

Volume 3

Thin Films and Epitaxy

- A. Basic Techniques
- B. Growth and Dynamics

HANDBOOK ON SEMICONDUCTORS

Completely Revised and Enlarged Edition

Edited by **T.S. Moss**

Volume 1

Basic Properties of Semiconductors

edited by **P.T. Landsberg**

Volume 2

Optical Properties of Solids

edited by **M. Balkanski**

Volume 3

Materials, Properties and Preparation

edited by **S. Mahajan**

Volume 4

Device Physics

edited by **C. Hilsum**

FOR COMPLETE DETAILS ON THESE HANDBOOKS PLEASE CONTACT THE PUBLISHER.



Electronic manuscripts

ELSEVIER SCIENCE B.V.

invites the submission of electronic manuscripts for this journal

Electronic manuscripts offer the possibility of avoiding rekeying the full text of articles and consequently the possibility of improving the speed of delivery and the reliability of proofs.

The preferred storage medium is a 5¼ or 3½ inch disk in MS-DOS or Macintosh format, although other systems are also welcome.

There is little restriction on the word processor used for preparing articles with few and/or uncomplicated equations. The word-processed text should be in a single column format, with no space reserved within the body of the text for figures or tables. Figure captions and tables should be placed at the end of the main text.

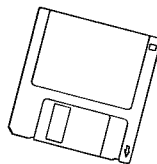
Articles containing many equations are more likely to be processed from authors' files if encoded in LaTeX. Either standard LaTeX (with document style "article") or Elsevier Science style LaTeX are preferred. Further information concerning the latter is available from the Publisher.

Authors are asked to refer to a recent issue of the journal for guidelines concerning the general presentation of article opening and reference list style, etc. Please note: **The Publisher reserves the right to decide whether to process a manuscript from authors' files or not.**

The disk containing the electronic version of a manuscript should be submitted (or resubmitted, in the case of a revised manuscript), together with the usual number of hard copies of the text and figures, as well as a set of original figures, to one of the journal Editors. **It is the responsibility of the author to ensure that the version on disk exactly matches the paper copies.** Upon acceptance of the article for publication, both the disk and a paper copy will be sent by the journal Editor to the Publisher.

For further details, please contact the Publisher:
Elsevier Science B.V.

Desk Editors Nuclear Instruments and Methods B
P.O. Box 103, 1000 AC Amsterdam, The Netherlands
Fax: +31 20 4852 775. E-mail: NIMB-J@ELSEVIER.NL



INELASTIC ION–SURFACE COLLISIONS

Proceedings of the Tenth International Workshop on
Inelastic Ion–Surface Collisions (IISC-10)
Grand Targhee Resort, Wyoming, USA, August 8–12, 1994

Editors

ALAN V. BARNES
NORMAN H. TOLK
Vanderbilt University

PETER NORDLANDER
Rice University



ELSEVIER

1995

NORTH-HOLLAND

The Manuscript of the Proceedings
was received by the Publisher: December 1994–March 1995

Preface

The Tenth International Workshop on Inelastic Ion Surface Collisions took place August 8 to 12, 1994 at the Grand Targhee Ski & Summer Resort, Wyoming (USA), a mountain retreat located near the Wyoming–Idaho border, just west of the Grand Teton National Park. This extraordinarily beautiful and isolated setting contributed significantly to the meeting's success. As in previous workshops, it was the intent of the international and local committees to bring together most of the leading workers in the field, as well as many workers in related fields. Consequently, the conference covered experimental and theoretical research on various aspects of inelastic particle–surface interactions and related topics, including inelastic particle scattering from surfaces, sputtering, electronically-induced desorption, laser-induced desorption, secondary particle emission, collision-induced surface chemistry, and collision-induced defect formation. The meeting provided an informal workshop atmosphere with ample time for discussions. For this purpose, the program contained a limited number of invited lectures on the main conference topics and some of more general interest. Some contributions selected among the submitted abstracts were presented orally. The remaining contributions were presented in poster sessions. There were no parallel sessions. The workshop was attended by approximately 90 scientists. The program included 9 invited lectures and 28 oral presentations of selected abstracts. The manuscripts in these proceedings were refereed anonymously by two referees. Referees were selected both from the conferees as well as externally.

We take this opportunity to thank the members of the international committee for their helpful suggestions regarding the scientific program, and the members of the local committee R. Albridge, R. Baragiola, B. Cooper, J. McKinley, and J.W. Rabalais, for their tireless support during and preceding the workshop. We are grateful for the generous financial support provided by Elsevier, and by the Office of Naval Research through Dr. L.R. Cooper.

Alan V. Barnes
Peter Nordlander
Norman H. Tolk
Guest Editors



International Scientific Committee

Bernheim, M.	Université Paris-Sud, France
Betz, G.	Technische Universität Wien, Austria
Gauyacq, J.P.	Université Paris-Sud, France
Gruen, D.	Argonne National Laboratory, Argonne, IL, USA
Heiland, W.	Universität Osnabrück, Germany
Kelly, R.	Università di Trento, Trento, Italy
MacDonald, R.J.	University of Newcastle, N.S. Wales, Australia
Nordlander, P.	Rice University, Houston, TX, USA
Sroubek, Z.	Acad. of Science Praha, Czech Republic
Szymonski, M.	Jagellonian University, Krakow, Poland
Taglauer, E.	Max-Planck-Inst. für Plasmaphysik, Garching, Germany
Tolk, N.	Vanderbilt University, Nashville, TN, USA
Urazgil'din, I.	Moscow State University, Moscow, Russia
Yamamura, Y.	Okayama University of Science, Okayama, Japan

Local Committee*Co-chairs*

Norman H. Tolk, Vanderbilt University
Peter Nordlander, Rice University

Royal Albridge, Vanderbilt University
Raul Baragiola, University of Virginia
Alan Barnes, Vanderbilt University
Barbara Cooper, Cornell University
James McKinley, Vanderbilt University
J. Wayne Rabalais, University of Houston

Contents

Preface	ix
Conference Photograph	x
Committees	xi
Angular, energy, and population distributions of neutral atoms desorbed by keV ion beam bombardment of Ni{001}	
C. He, S.W. Rosencrance, Z. Postawa, C. Xu, R. Chatterjee, D.E. Riederer, B.J. Garrison and N. Winograd	209
Secondary molecular ion emission from aliphatic polymers bombarded with low energy ions: Effects of the molecular structure and the ion beam induced surface degradation	
A. Delcorte, L.T. Weng and P. Bertrand	213
Sputtering of the most volatile solids: the solid hydrogens	
J. Schou, B. Stenum, O. Ellegaard, R. Pedrys and L. Dutkiewicz	217
Defects induced by ion bombardment of alkali halides	
Q. Yan, A.V. Barnes, N. Seifert, R. Albridge and N. Tolks	224
ESD of nonthermal halogen atoms from In-doped (001)KBr	
Z. Postawa, J. Kolodziej, G. Baran, P. Czuba, P. Piatkowski, M. Szymonski, I. Plavina and A. Popov	228
Inelastic inert gas ion collisions with metal targets. Rearrangement and adsorbate effects	
V.A. Esaulov, L. Guillemot, S. Lacombe and Vu Ngoc Tuan	232
Auger deexcitation of Na(2p ⁻¹) near alkali-halide surfaces	
R.A. Baragiola	242
Spin-dependent studies of the dynamics of He(2 ³ S) atom deexcitation at surfaces	
F.B. Dunning and P. Nordlander	245
Electronic structure of collision cascades in semiconductors	
Z. Šroubek and J. Fine	253
Z ₁ oscillations in yields of doubly and singly charged ions emitted from a germanium surface when bombarded by light ions	
B. Hird, R. Armstrong and P. Gauthier	256
Non-adiabatic effects in charge transfer caused by electron correlation	
H. Shao, P. Nordlander and D.C. Langreth	260
Evidence for electron correlations in secondary ion formation	
A.B. Popov, B.N. Makarenko and A.P. Shergin	267
Resonant coherent excitation of N ⁶⁺ and Mg ¹¹⁺ in planar channeling: anisotropies in ionization probabilities and X-ray emission	
S. Datz, P.F. Dittner, H.F. Krause, C.R. Vane, O.H. Crawford, J.S. Forster, G.S. Ball, W.G. Davies and J.S. Geiger	272
Nonlinear screening effects in the interaction of slow multicharged ions with metal surfaces	
A. Arnau, P.A. Zeijlmans van Emmichoven, J.I. Juaristi and E. Zaremba	279
Electron emission from polycrystalline lithium fluoride bombarded by slow multicharged ions	
M. Vana, F. Aumayr, P. Varga and H.P. Winter	284
Electron emission in the neutralization of multiply-charged ions at low velocities on metal surfaces: the effect of secondary-electron cascades	
N. Lorente, R. Monreal and M. Maravall	290

Multi-electron and multi-state effects in the charge transfer processes between oxygen and metal surfaces D. Teillet-Billy, B. Bahrim and J.P. Gauyacq	296
Resonant electron transfer in ion-metal-surface interactions: The case of large quantum numbers U. Wille	303
Depth of origin of ions in desorption induced by electronic transitions (DIET): ion transmission through ultrathin films T.E. Madey, N.J. Sack and M. Akbulut	309
Velocity dependence of ionization probability of secondary ions emitted from metal surfaces D.V. Klushin, M.Yu. Gusev and I.F. Urazgil'din	316
Line shifts in mass spectra of secondary ions ejected from solids by MeV-ion impact K. Wien, Ch. Koch and Nguyen van Tan	322
Time-of-flight elastic recoil analysis of ion beam modified nitrocellulose thin films J.H. Arps and R.A. Weller	331
Accurate calculation of atomic resonances near surfaces S.A. Deutscher, X. Yang and J. Burgdörfer	336
Singlet levels of an He atom interacting with an Al surface: Interaction between quasi stationary states in the $n = 2-6$ manifolds G.E. Makhmetov, A.G. Borisov, D. Teillet-Billy and J.P. Gauyacq	342
Isotope effects in the formation of MCs^+ molecular secondary ions H. Gnaser	347
Charge exchange of swift molecules H_2^+ , H_2 , CO_2^+ and CO_2 , at Pd(111) surfaces T. Schlathöller and W. Heiland	352
Energy loss straggling of 0.5-MeV protons specularly reflected from a SnTe(001) surface K. Kimura, H. Kuroda, M. Fritz and M.-h. Mannami	356
Sputtering of tin and gallium-tin clusters T. Lill, W.F. Calaway and M.J. Pellin	361
Angular and charge state distributions of highly charged ions scattered during low energy surface-channeling interactions with Au(110) F.W. Meyer, L. Folkerts and S. Schippers	366
MeV He ion impact desorption of hydrogen isotopes from an InP(001)-p(1×1) surface K. Morita, H. Ikegami and M. Ueshima	373
Simulation of fast electron emission from surfaces C.O. Reinhold, J. Burgdörfer, K. Kimura and M.-h. Mannami	378
Luminescence of self-trapped excitons induced by single keV ion bombardment R.G. Kaercher, E.F. da Silveira, J.F. Blankenship and E.A. Schweikert	383
Charge exchange in low-energy D^+ scattering from O-, CO-, and CsCl-adsorbed Pt(111) surfaces R. Souda, K. Yamamoto, W. Hayami, T. Aizawa and Y. Ishizawa	389
Energy loss of fast protons scattered from an Al(111)-surface under grazing incidence M. Wilke, R. Zimny and H. Winter	396
Potential and kinetic electron emission from clean gold induced by multicharged nitrogen ions M. Vana, H. Kurz, HP. Winter and F. Aumayr	402
TPD and ESD of hydrogen from disilane covered Si(100) J. Lozano, J.H. Craig Jr., J.H. Campbell and M.V. Ascherl	407
Growth of ultrathin alumina films on W(110) J. Günster, M. Brause, Th. Mayer, A. Hitzke and V. Kempter	411
H^- formation in proton (Ba)/Ag(111) collisions: effects of the surface structure W.R. Koppers, B. Berenbak, D. Vlachos, U. van Slooten and A.W. Kleyn	417
Inelastic collisions as the source of circumlunar sodium M. Marconi	423

Wavelength-selective laser ablation of diamond using hydrogen-impurity vibration modes	
A. Ueda, R.G. Albridge, A.V. Barnes, A. Burger, W.E. Collins, J.L. Davidson, M.A. George, Z. Hu, M.L. Languell, J.T. McKinley, J. Tribble and N.H. Tolk	427
Statistical treatment of adsorbate effects on charge transfer in ion-surface collisions	
Z.L. Mišković, S.G. Davison and F.O. Goodman	431
CN* desorption from potassium-metal surfaces under electron bombardment	
S. Vijayalakshmi, A.V. Barnes, R.G. Albridge and N.H. Tolk	438
Loss of material from Ga-In liquid surface during bombardment by hyperthermal Ta, Pt and Au atoms	
M.R. Weller and R.A. Weller	444



ELSEVIER

Angular, energy, and population distributions of neutral atoms desorbed by keV ion beam bombardment of Ni{001}

Chun He ^{*}, S.W. Rosencrance, Z. Postawa ¹, C. Xu, R. Chatterjee, D.E. Riederer, B.J. Garrison, N. Winograd

Department of Chemistry, The Pennsylvania State University, University Park, PA 16802, USA

Abstract

Multi-photon resonance ionization, time-of-flight mass spectrometry and imaging techniques have been employed to measure the polar-angle, kinetic energy, and population distributions of Ni atoms desorbed from 5 keV Ar ion bombarded Ni{001}. The measured angle- and energy-resolved intensity maps of the sputtering yield provide a set of data that can be used to examine the detailed interactions between the particles of the solid surface during the sputtering event. The results show a considerable degree of anisotropy associated with both the ejection angle as well as the crystallographic direction. In order to have an understanding of the interactions of the desorbed particles with the surface, molecular dynamics simulations of the ion-induced sputtering event are performed. The agreement between experimental and computer simulation results is excellent. Measurements performed on excited states of sputtered Ni show that the valence electron shell structure is an important factor in determining the angle-integrated kinetic energy distribution while the magnitude of the excitation energy is of secondary importance. Population distribution among different electronic states is obtained through two sets of measurements performed on different instruments. Both measurements employ the same resonant ionization schemes and laser fluences. The results show that the a^3D_3 and a^3D_2 states are more heavily populated than is predicted by a Boltzmann-type distribution.

1. Introduction

Energetic ion impact on a solid initiates a complex dynamical chain of events which include atomic motion, electronic excitation, ionization, and desorption of atomic and molecular species. Measurements on the desorbed particles during the ion–solid interaction process provide a valuable opportunity to examine this complex many-body interaction system [1]. Numerous experiments have been performed by different means to measure various parameters, such as yield, kinetic energy and charged fraction of the ejected particles [2–4]. Since an appreciable portion of the ejected particles are populated in electronic excited states, measurement of the above quantities as a function of each state should provide information about the excitation and de-excitation processes [5–8]. However, after more than two decades of research, many fundamental questions have not yet been answered. This is due to both the extreme complexity of the events which result from

keV ion bombardment and the lack of detailed and reliable experimental data. The situation has been greatly improved with the development of new experimental techniques. Doppler-shifted laser-induced fluorescence (DSLIF) spectroscopy [2,5,9–11] and energy- and angle-resolved neutral (EARN) spectrometry [6–8,12–14] are capable of obtaining state-resolved kinetic energy distribution.

We report experiments on Ni atoms ejected from a Ni{001} single crystal due to 5 keV Ar ion bombardment. The measurements are state-selected, kinetic energy and angle-resolved. In order to fully understand the anisotropic spatial distributions of the ejected Ni atoms from the Ni{001}, a molecular dynamics (MD) computer simulation has been performed on a model single crystal. This simulation employs a MD/MC-CEM interaction potential to describe the forces between Ni atoms during the collision cascade [15]. Experiments were performed on the excited, metastable states of Ni. The ejected Ni atoms are selectively ionized from fine structure states a^3F_j and a^3D_j which have valence electron configurations of $3d^84s^2$ and $3d^94s^1$, respectively. Angular distributions of excited state Ni atoms show basically the same angular anisotropy regardless of excitation energy and electron configuration,

^{*} Corresponding author.

¹ Permanent address: Institute of Physics, Jagellonian University, 30-059 Krakow, ul. Reymonta 4, Poland.

indicating the interactions between nuclei and the solid crystal are mainly responsible for the observed angular anisotropy. However there is a clear evidence that valence electron shell structure is an important factor in determining the angle-integrated kinetic energy distribution while the magnitude of the excitation energy seems to be less significant.

A few years ago, Craig et al. proposed an orbital deexcitation model to account for the lack of $a^2P_{3/2}$ excited state in atoms sputtered from an In foil [16]. The model suggests that the factors which are important in determining whether an atom in an excited state will relax as it departs from the surface depend on the electronic character of its fine-structure states. When the s-orbital is filled, the s-electrons can effectively shield the d-electrons from interaction with the metal, therefore, relaxation processes are minimal and the velocity distribution of the excited atoms is independent of atomic state. On the other hand, when the d-electrons are not completely being shielded or are exposed, the atoms are partially or completely deexcited to the ground state.

The present study shows conclusive experimental evidence that electronic structure rather than the excitation energy is the primary factor in determining kinetic energy distributions of sputtered neutral species. Nickel atoms ionized from the closed s-shell states a^3F_4 , and a^3F_3 show a general profile predicted by an analytical model [17]. Nickel atoms ionized from the open s-shell states a^3D_3 and a^3D_2 show a distinctly different distribution.

The population distribution among different electronic states is obtained through two sets of measurements performed on two experiment instruments: one which measures the energy- and angle-integrated resonance ionization signal intensities of the sputtered Ni; and the other which measures the resonance ionization signal intensities of thermally evaporated Ni atoms with a known temperature. Both measurements employ the same resonant ionization schemes and laser fluences. The results show that the population distribution is distinct from a Boltzmann-type distribution with the a^3D_3 and a^3D_2 states heavily populated.

2. Experimental

The experimental setup and measurement of energy-, and angle-resolved neutrals (EARN) have been described in detail previously [8,12]. The population distribution among different electronic states is obtained by combining data measured on the EARN apparatus and data measured on a high vacuum cell capable of producing gas phase Ni atoms through thermal evaporation. Laser-power-dependence studies have been performed for each of the involved transitions on both experiments. In all cases the photoion signals show a linear dependence on the laser power from 50 to 300 MW/cm².

3. Results and discussion

3.1. Energy-resolved angular distribution of sputtered Ni atoms

The experimentally obtained EARN distributions of Ni atoms in the ground electronic state are shown in Fig. 1. There is considerable anisotropy associated with both the polar-angle distribution as well as the crystallographic directions. This behavior was also reported for Rh{001} and explained on the basis of MD computer simulations of the ion bombardment event [18]. It was concluded that these angular anisotropies result from the specific geometrical structure of the top surface layers of the single crystal. It was shown that the polar-angle distribution is mainly determined by the relative position of surface atoms which influence the trajectories of exiting atoms via channelling and blocking mechanisms.

We performed MD computer simulations for 3 keV Ar ions impacting at normal incidence on a Ni{001} model crystal composed of 9 layers with 200 atoms per layer. The potential function used in the present simulation is the MD/MC-CEM potential [15]. The MD/MC-CEM potential has been chosen in this study since recent studies

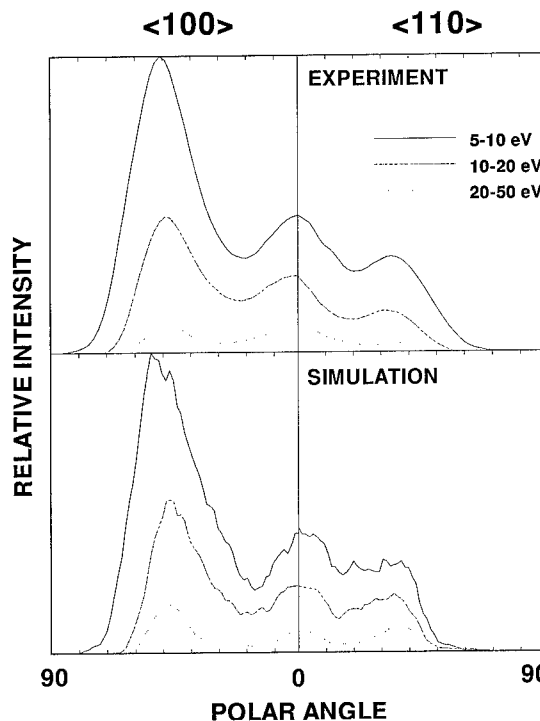


Fig. 1. Energy-resolved polar angle distributions of sputtered Ni atoms in the ground state along $\langle 100 \rangle$ and $\langle 110 \rangle$ azimuthal directions. The top graphs are measured experimentally and the bottom graphs are obtained by integrating 1200 trajectories from the molecular dynamics computer simulations.

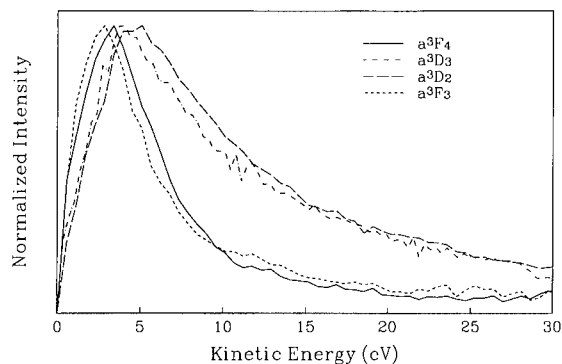


Fig. 2. Angle-integrated kinetic energy distributions of the measured Ni atoms in the four metastable states which belong to the closed s-shell structure, a^3F_4 (ground state) and a^3F_3 (third-excited state, 0.165 eV), and to the open d-shell structure, a^3D_3 , (first-excited state, 0.025 eV) and a^3D_2 , (second-excited state, 0.109 eV), for the $\langle 100 \rangle$ azimuthal direction.

suggest it more accurately reflects the surface binding energy [15].

Results of the MD simulations are presented in the bottom part of Fig. 1. Note that all of the important features of the experimental data are well-reproduced by the calculation. The success of the present simulation demonstrates the validity of applying the MD/MC-CEM potential to accurately describe the energetic ion-solid interaction event. The MD simulation can reveal more information which cannot be accessed experimentally. For example, it shows that 86% of the total ejected atoms originate from the first layer of the crystal, and 12% from the second layer. The remaining 2% of the total yield arises from third and deeper layers.

3.2. Influence of the valence shell electron configuration

The kinetic energy distributions of the measured Ni atoms in the metastable, open s-shell states a^3D_3 , and a^3D_2 , and closed s-shell states a^3F_4 , and a^3F_3 , are presented in Fig. 2 for the $\langle 100 \rangle$ azimuthal direction. From these plots it is evident that the velocity distributions of Ni atoms from different electronic states with different excitation energies but the same electronic shell structure look similar. Velocity distributions of Ni atoms with different electron-shell structures are remarkably different, even when they have almost similar excitation energies. The kinetic energy distributions along the $\langle 110 \rangle$ azimuth show the same character as those along the $\langle 100 \rangle$ direction.

There are two important, and quite different features between these two groups of states. First, the velocity distributions from a closed s-shell are all peaked at the same value of 3.2 eV, which is about 1 eV smaller than those from the open s-shell structure, all of which are peaked at 4.4 eV. In the language of Thompson [19], the open s-shell states have a larger effective 'surface binding energy'. The result is consistent with the electron shell

structure model discussed in the introduction. These atoms are effectively shielded by the filled s-orbital and do not interact as strongly with the metal electrons while departing from the surface. That is, the effective surface binding energy is smaller for atoms having a closed outer shell orbital and is larger for atoms having an open outer shell orbital. Secondly, the atoms ejected from states of open s-shell configuration have broader kinetic energy distributions than those from states of closed s-shell configuration. As these plots are all normalized to their peak intensities, and the ejected particles of high kinetic energy are less likely to be influenced from the interaction with the surface, this observation implies excited Ni atoms with an open s-shell electron configuration are more likely to de-excite than atoms with a closed s-shell configuration.

3.3. Population partitioning among different electronic states

The interpretation of the relationship between the number density of sputtered atoms and the one-color MPRI photoion signal has been a long standing issue [20]. Although there are many studies, both theoretically and spectroscopically devoted to this field, an unambiguous population distribution can not be obtained from the measured photo-ion signal. This is largely due to the complex spectroscopic structure of an atom above its ionization limit [20]. In the present study a new approach is adopted to overcome this obstacle. The solution is to perform another experiment with the same MPRI scheme which has a known population distribution among different states. For example, a Boltzmann distribution for thermally excited particles.

For an initial state i , the MPRI signal via an intermediate state u can be expressed as

$$I_{iu}^S = N_i^S \Phi_{iu}(g_i, g_u, f_{iu}, A_u, \sigma_u, P) \eta^S, \quad (1)$$

$$I_{iu}^T = N_i^T \Phi_{iu}(g_i, g_u, f_{iu}, A_u, \sigma_u, P) \eta^T, \quad (2)$$

where, with superscript "S" representing quantities measured in the sputtering experiment and "T" representing thermal evaporation experiment, I_{iu} is signal intensity, N_i is the population, and η is the detection efficiency. Φ_{iu} is a function which depends on the laser fluence P ; the degeneracies of initial state i and intermediate state u , g_i and g_u , respectively; the oscillator strength of transition $i \rightarrow u$, f_{iu} ; and the lifetime, A_u , and ionization cross section, σ_u , of state u . In most of the cases Φ_{iu} is unknown.

For initial states i and j ionized via a single upper state u , we have

$$N_i^S/N_j^S = N_i^T/N_j^T \{I_{iu}^S/I_{ju}^S\} \{I_{ju}^T/I_{iu}^T\}. \quad (3)$$

Therefore, the relative population of the sputtered Ni at different electronic states can be obtained from the known population in the thermal evaporation experiment, assuming that it exhibits a Boltzmann distribution.

Table 1
Relative population of sputtered Ni in different electronic states

Ni atom initial state	Energy [eV]	Popul. dist. sputtering	Boltzmann dist. at 956°C
a^3F_4	0	1	1
a^3D_3	0.025	5.71	0.79
a^3D_2	0.109	7.42	0.36
a^3F_3	0.165	0.96	0.21

The relative population of the sputtered Ni atoms at different states are listed in Table 1, along with a calculated Boltzmann distribution at the temperature of Ni in the thermal evaporation experiment. The most striking feature is the non-Boltzmann-type distribution observed in the sputtering experiment with the a^3D_3 and a^3D_2 states more heavily populated than the ground state a^3F_4 . Although discrepancies from the Boltzmann-type distribution have been observed by several research groups [5,8,21], this is the first time population inversions in the sputtered particles have been observed. At present we do not understand the mechanisms which cause preferential population of these two states.

4. Conclusion

State-selected, angle- and energy-resolved intensity distributions of Ni atoms desorbed from a 5 keV Ar ion bombarded Ni{001} surface have been measured. The energy-resolved angular distributions show a considerable degree of anisotropy associated with both the polar ejection angle and the crystallographic direction. These intensity distribution anisotropies are reproduced by a molecular dynamics computer simulation, which emulates the energetic ion-solid interaction event, with remarkable resemblance.

Experiments performed on the excited states of sputtered Ni atoms reveal very interesting results which may lead to further understanding of excitation and deexcitation mechanisms during the ion-solid interaction event. Angular distributions of excited state Ni atoms show basically the same angular anisotropy regardless of their excitation energy and electron configuration, indicating the interactions between nuclei and the solid crystal are mainly responsible for the observed angular anisotropy. However there is evidence that valence electron shell structure is the dominant factor in determine the angle-integrated kinetic energy distribution while the potential energy effect is less important. The population of the sputtered Ni atoms in different states is found not to obey the Boltzmann distribution with

a^3D_3 and a^3D_2 states more heavily populated than the ground state.

Acknowledgements

The authors appreciate the financial support from the Department of Energy, the Office of Naval Research, the National Science Foundation and the M. Sklodowska-Curie Fund MEN/NSF-93-144. The authors thank Drs. W. Ernst, D. Shirley and D. Sanders for useful discussions about this work.

References

- [1] N. Winograd, Prog. Solid State Chem. 13, (1982) 285.
- [2] G. Betz, Nucl. Instr. and Meth. B 27 (1987) 104, and references cited therein.
- [3] W.O. Hofer, Topics Appl. Phys. 64 (1991) 15.
- [4] M.L. Yu, Topics Appl. Phys. 64 (1991) 91.
- [5] M.L. Yu, D. Grischkowsky and A.C. Balant, Phys. Rev. Lett. 48 (1982) 427.
- [6] M. El-Maazawi, R. Maboudian, Z. Postawa and N. Winograd, Phys. Rev. B 43 (1991) 12078.
- [7] N. Winograd, M. El-Maazawi, R. Maboudian, Z. Postawa, D.N. Bernardo and B.J. Garrison, J. Chem. Phys. 96 (1992) 6314.
- [8] Chun He, Z. Postawa, M. El-Maazawi, S. Rosencrance, B.J. Garrison and N. Winograd, J. Chem. Phys. 101 (1994) 6226.
- [9] B. Schweer and H.L. Bay, Appl. Phys. A 29 (1982) 53.
- [10] C.E. Young, M.F. Calaway, M.J. Pellin and D.M. Gruen, J. Vac. Sci. Technol. A 2 (1984) 693, and references cited therein.
- [11] E. Dullini, Appl. Phys. A 38 (1985) 131.
- [12] P.H. Kobrin, G.A. Schick, J.P. Baxter and N. Winograd, Rev. Sci. Instr. 57 (1986) 1354.
- [13] N. Winograd, M. El-Maazawi, R. Maboudian, Z. Postawa, D.N. Bernardo and B.J. Garrison, J. Chem. Phys. 96 (1992) 3846.
- [14] D.N. Bernardo, M. El-Maazawi, R. Maboudian, Z. Postawa, N. Winograd and B.J. Garrison, J. Chem. Phys. 97 (1992) 3846.
- [15] T.J. Racker and A.E. DePristo, Int. Rev. Phys. Chem. 10 (1991) 1, and references cited therein.
- [16] B.I. Craig, J.P. Baxter, J. Singh, G.A. Schick, P.H. Kobrin, B.J. Garrison and N. Winograd, Phys. Rev. Lett. 57 (1986) 1351.
- [17] R. Kelly, Phys. Rev. B 25 (1982) 700.
- [18] R. Maboudian, Z. Postawa, M. El-Maazawi, B.J. Garrison and N. Winograd, Phys. Rev. B 42 (1990) 7311.
- [19] M.W. Thompson, Philos. Mag. 18 (1968) 377.
- [20] see, for example, G.S. Hurst, M.G. Payne, S.D. Kramer and J.P. Young, Rev. Mod. Phys. 51 (1979) 767.
- [21] T.J. Whitaker, Anjun Li, P.L. Jones and R.O. Watts, J. Chem. Phys. 98 (1993) 5887.



ELSEVIER

Secondary molecular ion emission from aliphatic polymers bombarded with low energy ions: Effects of the molecular structure and the ion beam induced surface degradation

A. Delcorte, L.T. Weng, P. Bertrand *

Catholic University of Louvain, PCPM, 1 Place Croix du Sud, B-1348 Louvain-la-Neuve, Belgium

Abstract

The influence of the molecular structure on the secondary ion production is studied for three saturated aliphatic polymers (low-density polyethylene, polypropylene and polyisobutylene) bombarded with low energy ions. These polymers differ only by the presence and nature of the pendant group. The intensities of the most characteristic secondary molecular ions are followed as a function of the primary ion dose in the (10^{12} ions/cm²– 10^{14} ions/cm²) range for two primary ion bombardment conditions (4 keV Xe⁺ and 15 keV Ga⁺). The results show that there is a direct relationship between the polymer degradation and the emission of molecular fragments. No truly “static” conditions are found, rather, the polymer surface undergoes a continuous transformation under ion beam bombardment. The most spectacular effect is its dehydrogenation. By rationalizing the competition between the two related processes, surface degradation and molecular ion production, a kinetic model is proposed in order to explain the behavior of molecular fragments belonging to the C8 cluster.

1. Introduction

Large molecular ions are emitted when a polymer is bombarded with low energy ions in the low fluence regime. These ions are characteristic of the polymer molecular structure and their detection (after mass discrimination) constitutes the basis of the Static SIMS technique for polymer surface analysis [1,2]. However, the mechanisms of the molecular ion emission are not yet fully understood. Several models have been invoked to explain the origin of secondary molecular ions in polymers [3,4]. In the precursor model, large molecular ions are believed to be produced only at some distance from the primary ion impact point, where the deposited energy from the collision cascade is limited [5]. However, the inelastic contribution to the ion sputtering is unclear. Part of the primary ion energy deposition is transformed into electronic and vibrational excitations leading to bond breaking and polymer chains fragmentation with the production of radicals and ions. The polymer molecular structure is modified during SIMS analysis even when using low dose levels ($< 10^{13}$ ions/cm²) as evidenced by several authors [6–14].

In this work, a detailed study of the surface degradation mechanisms related to the molecular structure of the poly-

mer chains is presented in order to (i) gain a better understanding of the secondary ion formation in these systems; (ii) look at upper limit of the ion dose for which the molecular information can still be obtained with the SIMS technique. A series of saturated aliphatic polymers only differing by the pendant group (polyethylene, polypropylene, polyisobutylene) is investigated.

2. Experimental

2.1. Samples

Three saturated aliphatic polymers have been studied: low-density polyethylene (LDPE), polypropylene (PP) and polyisobutylene (PIB). LDPE and PP were in the form of films provided by Shell-Louvain-la-Neuve (B) and were analysed as received. PIB was purchased from Aldrich

Table 1
Polymer structure

Polyethylene, PE	Polypropylene, PP	Polyisobutylene, PIB
$(-\text{CH}_2-\text{CH}_2-)_n$	$(-\text{CH}-\text{CH}_2-)_n$ CH ₃	$(-\text{C}-\text{CH}_2-)_n$ CH ₃

* Corresponding author, tel. +32 10 4735 81 or 63, fax +32 10 473452, E-mail: bertrand@pcpm.ucl.ac.be.

Chemie, dissolved in a solution containing 2% of polymer and then spin-coated on Si wafers to produce thin films. The polymer molecular structures are given in Table 1. The samples' cleanliness and purity was tested by XPS (SSI-X-Probe) analysis and contamination was not detected except in the case of LDPE which showed ~ 1 at.% of oxygen on the surface.

2.2. SIMS analyses

The samples were bombarded and analyzed in two different systems. The first system consists of a time-of-flight SIMS microprobe-microscope (Charles Evans & assoc.) using a (5 kHz) pulsed Ga^+ beam (15 kV, 400 pA dc) [15]. The ion dose (D) for one spectrum acquisition is $\leq 10^{12}$ ions/cm². A pulsed electron beam and a stainless steel grid are used for charge compensation. For polymer surface degradation studies, alternated sequences of ToF-SIMS analysis periods (pulsed beam, $D = 10^{12}$ ions/cm²) and continuous bombardment ($5 \times 10^{12} \leq D \leq 2 \times 10^{14}$ ions/cm²) are utilized. In the second system, a Xe^+ (4 keV, 10 nA) ion beam is used and rastered on a 0.3 cm² surface area and the secondary ions are mass analyzed by means of a quadrupole spectrometer (Riber-Q156). For SIMS spectrum acquisition, the ion dose D is kept lower than 10^{13} ions/cm². Charge compensation is achieved by the use of an electron flood gun (2 A, 150 eV).

3. Results and discussion

3.1. Molecular structure

Fig. 1 shows the positive ToF SIMS spectra obtained with 1.1×10^{12} Ga^+ ions/cm² on pristine PE, PP and PIB samples (see their molecular structures in Table 1). These spectra are similar to those reported in the literature [1,2]. Although the molecular structures of the monomers differ only by the presence of methyl pendant groups, the spectra are clearly different in the relative intensities of some ions in the different carbon clusters (a cluster " C_x " refers to the ions having the same number (x) of carbon atoms, the number of hydrogen atoms varying from 0 to $2x + 1$). The maximum intensity is observed for the deprotonated monomer $(\text{M}-\text{H})^+$ at 27 amu for PE, 41 amu for PP and 55 amu for PIB. The pendant methyl group contributes to the high relative intensities of the characteristic fragments at masses 55 and 69 amu for PP and PIB, and the double pendant methyl group of PIB accounts for the peaks at 83 and 97 amu. Their molecular structures have been previously discussed by Van Ooij and Briggs [16,17]. Another significant difference between these spectra is the contribution of the C8 cluster which increases with the branching level: the mean values of the normalized intensities $I(\Sigma \text{C}_8 \text{H}_y)/I_{\text{Tot}}^*$ are respectively 0.42×10^{-2} for PE, 1.05×10^{-2} for PP, and 2.47×10^{-2} for PIB (the stan-

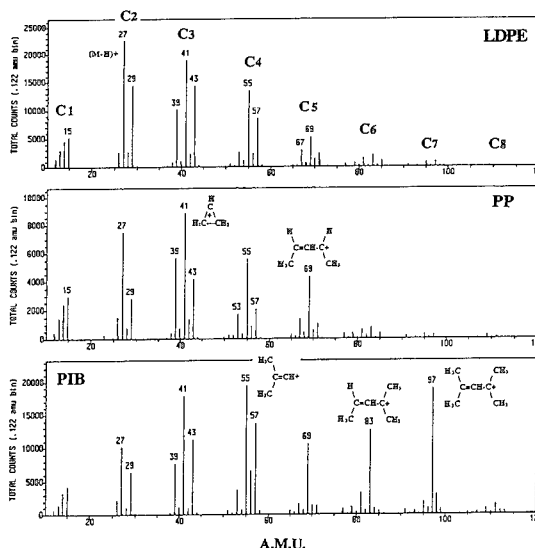


Fig. 1. Positive ToF SIMS spectra obtained with 1.1×10^{12} Ga^+ ions/cm² on pristine PE, PP and PIB samples.

dard deviation is about 1×10^{-3}). I_{Tot}^* is the total integrated intensity minus the hydrogen intensity which is barely reproducible. The explanation for this effect is related to the higher stability of branched ions as compared to the linear ones [16].

3.2. Surface degradation

The influence of the ion dose on the spectrum is stressed in Fig. 2 where a PP spectrum obtained with

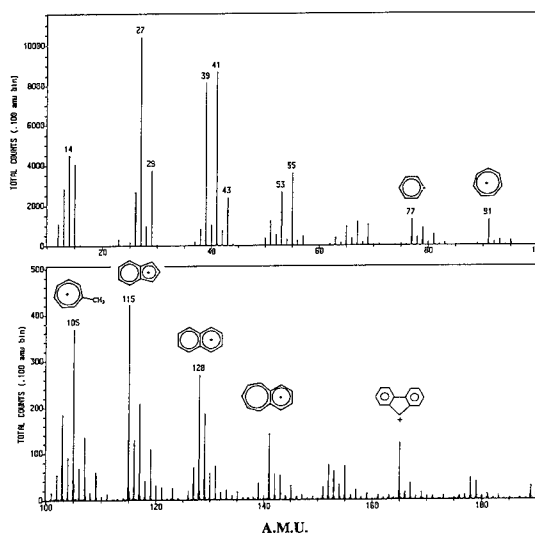


Fig. 2. Positive ToF SIMS spectrum obtained with 1.1×10^{12} Ga^+ ions/cm² on a PP sample previously bombarded with 2×10^{14} Ga^+ ions/cm² ion dose.

2×10^{14} Ga⁺ ions/cm² is shown. Increasing the ion dose gives rise to several differences: (i) the intensity of the peak at 69 amu, which is the most characteristic of the PP structure, decreases strongly; (ii) the cluster C_n with the maximum intensity is shifted to a lower value, the cluster C₂ is becoming predominant; (iii) in every C_n cluster, unsaturated peak intensities increase at the expense of the more saturated ones; and (iv) new peaks of ions with an aromatic structure (at 77, 91, 105, 115, 128 amu [16]) become very intense (similar peaks are observed in polystyrene). The same trends are also observed on the other polymers. The decrease in the intensity of the most characteristic peaks of PP and PIB is shown in Fig. 3 as a function of the cumulated ion dose as described in the experimental section. For PIB, the decrease with the ion dose of characteristic fragments at 83 and 97 amu is already initiated at the first point of measurement while for PP, the peak at 69 amu increases first to a maximum before decreasing. These results show the close relationship between the secondary molecular ion production and the polymer degradation under ion beam bombardment [13]. The direct loss of intensity for the most characteristic ions observed in the investigated ion dose is related to the degradation of the precursor. The maximum observed for the 69 amu peak in PP indicates the competition between two processes: the degradation and the ion formation which may be induced by a previous degradation. Looking at the intensity variation of the less characteristic peaks in the different C_n clusters, a direct loss is always observed for the most saturated fragments and this cannot result from a previous degradation of the surface. In order to investigate more deeply this effect, continuous bombardment and secondary ion intensity measurements were done on PP for specific ions using a quadrupole mass spectrometer and a Xe⁺ (4 keV, 10 nA) ion beam. The results obtained for the different ions of the C₈ cluster are shown in Fig. 4. Special attention was paid to this cluster because

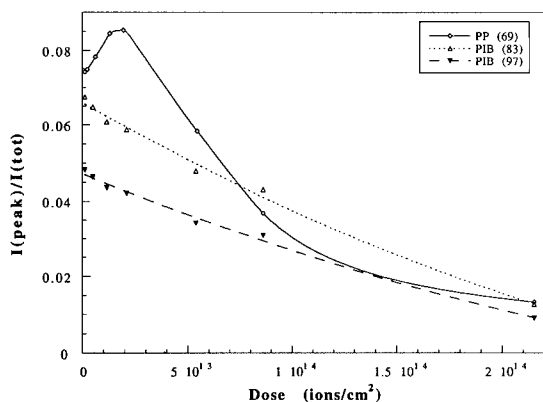


Fig. 3. ToF-SIMS intensity dependence of the most characteristic peaks of PP (69 amu) and PIB (83 and 97 amu) as a function of the cumulated Ga⁺ (15 keV) ion dose.

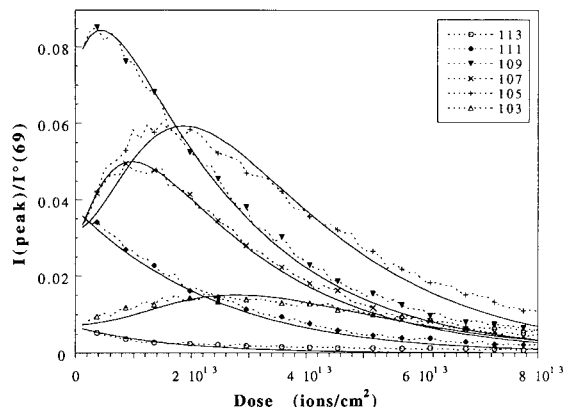


Fig. 4. Quad-SIMS intensities of C₈ cluster (C₈H₇⁺) as a function of the cumulated Xe⁺ (4 keV) ion dose for PP. The intensities are normalized to the initial value of the peak at 69 amu.

it does not contain fragments highly characteristic of the polymer structure. It is striking to see in Fig. 4, the regularity of the (SIMS intensity versus ion dose) curves succession, from the most saturated ion (C₈H₁₇⁺ at 113 amu) to the less saturated one (C₈H₇⁺ at 103 amu). This shows that the degradation is always greater for saturated peaks than for unsaturated ones. Moreover, the curves show a variation in shape and intensity which suggests a dehydrogenation reaction affecting the surface of the polymer. Indeed, only dehydrogenation is able to produce such a continuous transformation into fragments of increasing unsaturation.

We developed a kinetic model able to account for this intra-cluster phenomenon. It is related to the observation that decay of fragments with a given H content contributes to the production of fragments with lower H content. The model is based on the assumption of existence at the polymer surface of precursors for the given molecular ions. Then the intensity of a given ion *i*, *I_i*, is proportional to the surface concentration of its precursors *C_i^{*}*,

$$I_i = \varepsilon_i C_i^*, \quad (1)$$

where ε_i is a sensitivity factor related to the physics of the interaction and to the experimental conditions. The effect of ion beam degradation is to modify the precursor concentrations *C_i^{*}* with a decrease rate α_i and this contributes to the increase of the *C_{i+x}^{*}* concentration with a probability factor γ_{i+x} so that we obtain a set of coupled differential equations for the *C_i^{*}*:

$$dC_i^* = -\alpha_i C_i^* + \alpha_{i-1} \gamma_{i-1} C_{i-1}^* + \alpha_{i-2} \gamma_{i-2} C_{i-2}^* + \dots \quad (2)$$

If we assume that only the first two terms are dominant in the second part of Eq. (2), then

$$dI_i = -\alpha_i I_i + \alpha_{i-1} \gamma_{i-1} (\varepsilon_i / \varepsilon_{i-1}) I_{i-1}, \quad (3)$$

Table 2
Parameters for $C_8H_y^+$ intensity dose dependence

Mass [amu]	y	i	α_i [$10^{-13} \text{ cm}^2/\text{ions}$]	β_i
113	17	1	0.58	0
111	15	2	0.50	1.0
109	13	3	2.0	10.5
107	11	4	2.23	0.7
105	9	5	1.0	0.63
103	7	6	1.0	0.28

or applied to the dehydrogenation of the C8 cluster:

$$dI(C_8H_y) = -\alpha_i I(C_8H_y) + \alpha_{i-1} \beta_{i-1} I(C_8H_{y+2}), \quad (4)$$

where $y = 2x + 1$, $4 \leq x \leq 8$ and $i = 9 - x$ (see Table 2) and

$$\beta_i = \gamma_i \varepsilon_{i+1} / \varepsilon_i. \quad (5)$$

The α_i and β_i values giving the best fit between the model and the experimental results are presented in Table 2 and the calculated dependence of $I(C_8H_y)$ with the ion dose are represented by the full lines in Fig. 4. It is observed that the model describes correctly the experimental behavior and confirms the continuous loss of hydrogen from polymer surfaces bombarded with ions in the experimental conditions of the SIMS analysis. This transformation is already begun at the first point of measurement.

The $1/\alpha_i$ values give the characteristic ion doses for degradation and are in the $\sim 10^{13} \text{ ions/cm}^2$ range. They represent the upper limit for molecular SIMS analyses. The interpretations of the β_i values are not straightforward because they include the probability factors γ_i (≤ 1) and also the ratio of the SIMS sensitivity factors $\varepsilon_{i+1}/\varepsilon_i$ which can be greater than 1. Indeed, the information given by SIMS is not a direct image of molecules lying on the polymer surface. Several parameters, depending on exact physics and chemistry of the phenomenon, influence strongly the fragment intensities. First of all, the detected ions only represent a little fraction of emitted species and this fraction could depend on the mass and structure of the fragments and on their chemical stability. For example, aromatic or branched ions are favored compared to linear aliphatic fragments [16].

4. Conclusion

The degradation study shows that when bombarded with ion beams (Xe^+ , Ga^+), saturated aliphatic polymer surfaces undergo a continuous transformation already initiated at very low doses. This transformation affects the whole spectrum and not only the highly characteristic SIMS peaks which are however the most sensitive to

degradation. This leads to the conclusion that there does not exist a real “static” regime for these polymers and that ion formation is intrinsically related to the degradation process. On the other hand, this study shows clearly, especially the $1/\alpha$ values in Table 2, that reproducible molecular information can be obtained from these polymers when analyzed with ion doses $< 10^{+13} \text{ ions/cm}^2$. One key phenomenon inducing polymer degradation has been identified: the dehydrogenation. But there is still work to be done to understand the modifications of the molecular structures leading to other phenomena such as segmentation, cross-linking and aromatic ion formation. A better understanding of secondary ions formation in polymers is also very desirable and would directly enlight such degradation mechanisms.

Acknowledgements

This work is supported by the Interuniversity Poles of Attraction program initiated by the Belgian federal state. The ToF-SIMS equipment was acquired thanks to the financial support of the FRFC and the “Region Wallonne” of Belgium.

References

- [1] D. Briggs, A. Brown, J.C. Vickerman, Handbook of Static Secondary Ion Mass Spectrometry (SIMS) (Wiley, Chichester, 1989).
- [2] J.G. Newman, B.A. Carlson, R.S. Michael, J.F. Moulder, T.A. Hohl, Static SIMS Handbook of Polymer Analysis, ed. T.A. Hohl (Perkin-Elmer, Minnesota, 1991).
- [3] G.J. Leggett and J.C. Vickerman, Int. J. Mass Spectrom. Ion Proc. 122 (1992) 281.
- [4] S.J. Pachuta and R.J. Cooks, Chem. Rev. 87 (1987) 647.
- [5] A. Benninghoven, in: Ion Formation from Organic Solids, ed. A. Benninghoven, Springer Series in Chemical Physics 25 (Springer, Berlin, 1982) p. 77.
- [6] A. Brown, J.A. van den Berg and J.C. Vickerman, Spectrochim. Acta 40 B (1985) 871.
- [7] J.A. van den Berg, Vacuum 36 (1986) 981.
- [8] D. Briggs and A.B. Wootton, Surf. Interface Anal. 4 (1982) 109.
- [9] D. Briggs and M.J. Hearn, Vacuum 36 (1986) 1005.
- [10] G.J. Leggett and J.C. Vickerman, Anal. Chem. 63 (1991) 561.
- [11] G.J. Leggett and J.C. Vickerman, Appl. Surf. Sci. 55 (1992) 105.
- [12] G. Marletta, Nucl. Instr. and Meth. B 46 (1990) 295.
- [13] S. Pignataro, Surf. Interface Anal. 19 (1992) 275.
- [14] A. Licciardello, S. Pignataro, A. Leute and A. Benninghoven, Surf. Interface Anal. 20 (1993) 549.
- [15] B.W. Schueler, Microsc. Microanal. Microstruct. 3 (1992) 119.
- [16] W.J. van Ooij and R.H.G. Brinkhuis, Surf. Interface Anal. 11 (1988) 430.
- [17] D. Briggs, Surf. Interface Anal. 15 (1990) 734.



ELSEVIER

Sputtering of the most volatile solids: the solid hydrogens

Jørgen Schou ^{a,*}, Bjarne Stenum ^a, Ole Ellegaard ^b, Roman Pedrys ^c, Lukasz Dutkiewicz ^c

^a Department of Optics and Fluid Dynamics, Risø National Laboratory, DK-4000 Roskilde, Denmark

^b Doc. Department, Odense University Library, Odense University, DK-5230 Odense M, Denmark

^c Institute of Physics, Jagellonian University, PL-30 059 Krakow, Poland

Abstract

Electronic sputtering of the three stable hydrogenic solids, H₂, HD and D₂ by keV hydrogen and deuterium ions has been studied at the low-temperature setup at Risø. The yield of the sputtered particles has been determined for hydrogenic films of thicknesses ranging from 0.1×10^{18} up to 10×10^{18} molecules/cm² and for 4–10 keV H⁺, H₂⁺, H₃⁺ and D₃⁺ ions. The yield increases with decreasing film thickness for solid hydrogen as well as for deuterium. This behavior agrees with the trend observed for other volatile gases. For thick films the yield decreases to a constant value. This thick-film yield can be approximated fairly well by a quadratic function of the stopping power except for a somewhat steeper dependence for proton-bombarded deuterium. The yield increases strongly with decreasing sublimation energy from one isotope to another. No existing theory can account for the dependence of the yield on the electronic stopping power as well as the sublimation energy.

1. Introduction

The solid hydrogen isotopes are the most volatile materials that exist in equilibrium with laboratory vacuum. Therefore, sputtering experiments with these solids must be carried out at such a low beam power and temperature that the mass loss from beam-induced evaporation is small compared with that from sputtering processes. Sputtering is characterized as the erosion of surfaces by individual particle impact rather than macroscopic heating from incident beams or external heat sources [1–4].

The sublimation energy *U* (Table 1) ranges from 8.65 meV/H₂ for solid H₂ up to 14.8 meV/T₂ for solid T₂ [5]. These extremely low values mean that the sputtering yield becomes large even for small stopping powers. For the most volatile isotope, solid hydrogen, we observed a sputtering yield of about 800 H₂/H⁺ for 10 keV proton bombardment.

Sputtering of condensed gases by light ions takes place predominantly via *electronic* transitions. This type of erosion, i.e. electronic sputtering, follows a sequence of events initiated by a primary ion. The incident ion generates excited and ionized target particles along its path. Many of these excited states de-excite to repulsive states which transfer energy to atomic motion, e.g. by dissociation of molecules. The energy liberated in this manner initiates a

low-energy collision cascade from which atoms close to the surface may pass the surface barrier and be ejected. Although the overall pattern described here is similar for electronic sputtering of other condensed gases, the surface binding and the electronic deexcitations vary strongly from one gas to another [2,6–10].

A particular property of the most volatile gases is that a pronounced enhancement of the electronic sputtering yield occurs for thin films [2,4,11]. This effect has been observed by other authors as well [12,13] and also with incident electrons [13–16]. The reason for this enhancement is not known, but it seems to be largest for the most volatile condensed gases.

Table 1
Selected properties of the stable hydrogenic solids (evaluated from Ref. [5])

	H ₂	HD	D ₂
Molecular weight [amu]	2.016	3.021	4.028
Sublimation energy per molecule [meV]	8.65	10.8	12.65
Sublimation pressure at 2.7 K [Torr]	1.5×10^{-12}	4.5×10^{-16}	1.3×10^{-19}
Particle density [10 ²² molecules/cm ³]	2.65	2.81	3.03
Mass density [g/cm ³]	0.0887	0.141	0.203

* Corresponding author, tel. +45 4677 4755, fax +45 4237 0115, E-mail: fys-josc@risoe.dk.

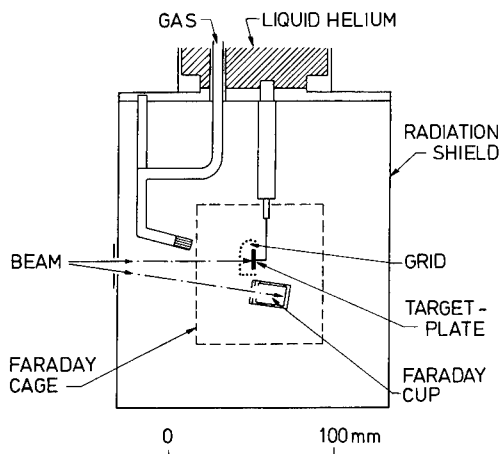


Fig. 1. A schematic view of the experimental setup.

With these volatile hydrogenic solids we have reached an extreme case of sputtering. Most of the less volatile condensed gases exist as parts of icy grains in the interstellar and interplanetary space, in which these grains are targets for energetic cosmic particles. This is not possible for solid H_2 . The vapor pressure of this solid even at the background temperature of the universe, 2.7 K, is 1.5×10^{-12} Torr (Table 1). This value is so high that a surface of solid H_2 cannot exist in equilibrium with interplanetary vacuum. Most of the free hydrogen molecules at grains are typically adsorbed as fractions of monolayers on grain surfaces rather than as multilayers [17].

In the present work we have measured the sputtering yield from the stable hydrogenic solids, H_2 , HD and D_2 for thin and thick films bombarded by hydrogen and deuterium ions with an energy up to 10 keV. Some of the results have been included in a previous publication [1].

2. Experimental

The absolute sputtering yield has been determined by a standard weight-loss method with the setup in Risø. The setup as well as the quartz crystal microbalance have been described elsewhere [1,8] (Fig. 1).

Hydrogenic films of $(0.1\text{--}10) \times 10^{18}$ molecules/ cm^2 are produced by letting a jet of cooled gas impinge on the silver electrode of an oscillating quartz crystal suspended below a liquid-helium cryostat. With this system it is possible to make films of known thickness and to measure the mass loss during irradiation. No detectable evaporation from the films took place before the beam was directed onto the hydrogenic target.

Beams of 4.5–10 keV H^+ , H_2^+ , H_3^+ and D_3^+ are extracted from a duoplasmatron ion source and selected by a 45° magnet. Since the magnet does not allow us to distinguish between H_2^+ and D^+ beams, all comparisons

between hydrogen and deuterium ions were made with D_3^+ and H_3^+ ions. In order to ensure a homogeneously irradiated area on the target, the beam was swept both horizontally and vertically over an aperture in front of the target. The current was measured before and after irradiation by deflecting the beam into a Faraday cup. An open repeller ring (biased at -90 V) in front of the target suppresses the secondary electron emission, and charge-up problems are largely reduced.

During the measurements the pumped helium bath of the cryostat reached a temperature of 2.0 K. The 4000 Å thick electrode was connected thermally to the crystal holder and the cryostat bottom via a low-temperature-solder point directly on the electrode. The precise temperature of the substrate electrode cannot be measured during operation because of the high-frequency oscillations.

In Ref. [1] it was shown that sputtering rather than beam-induced evaporation took place for currents less than 5 nA for solid H_2 . Above this threshold the yield increased strongly. This behavior is a clear indication of beam-induced evaporation at high currents [18]. Consequently, only beam currents less than 5 nA were utilized for the present sputtering measurements on solid H_2 and HD. For the least volatile material, solid D_2 , no dependence on the beam current up to 15 nA was observed.

3. Thin films: results and discussion

As mentioned in the introduction, the sputtering yield decreases strongly with film thickness for thin hydrogenic films. A typical example is shown in Fig. 2. The yield reaches a “thick-film” value of $640 \text{ H}_2/\text{H}$ for thicknesses larger than $1.5 \times 10^{18} \text{ H}_2/\text{cm}^2$. (Here and in the following the yields are given in molecules/atom, since any polyatomic ion dissociates upon impact with an equal sharing of energy among the atoms of the ion.) One notes that the yield for the thinnest films is about 3 times larger than the bulk value. Unfortunately, it was not possible to determine the yield for films of thicknesses below $1.2 \times 10^{17} \text{ H}_2/\text{cm}^2$.

The points shown in Fig. 2 represent the only data series of the complete thickness dependence measured for solid hydrogen. The curves previously determined for solid deuterium [4] look very similar except for the relatively slow fall-off of the points in Fig. 2 at thicknesses around $1.0 \times 10^{18} \text{ H}_2/\text{cm}^2$. A straight line composed of the data points for the thin films of thickness below $0.6 \times 10^{18} \text{ H}_2/\text{cm}^2$ intercepts the asymptotic yield at a thickness of about $0.45 \times 10^{17} \text{ H}_2/\text{cm}^2$. This corresponds to one-half of the average projected range R_p for 4 keV H^+ incident on hydrogen, $R_p = 0.94 \times 10^{17} \text{ H}_2/\text{cm}^2$ [19].

The strong yield enhancement is a common behavior for thin films of the most volatile gases deposited on conductive substrates. Stenum et al. [4] and Ellegaard et al. [11] showed that the yield of the thin films may exceed

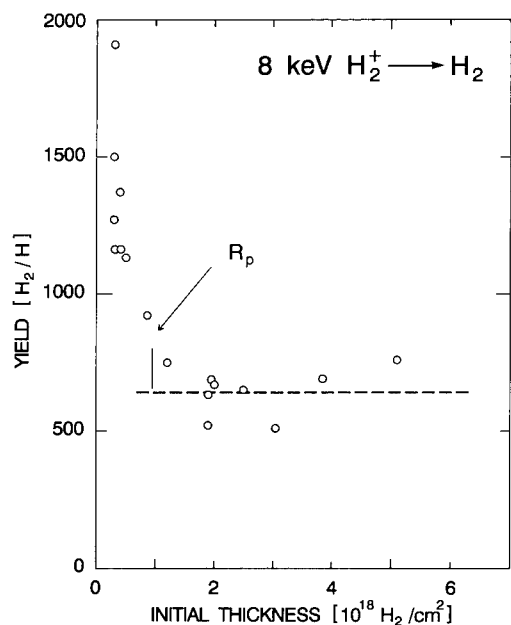


Fig. 2. The sputtering yield per atom as a function of film thickness for bombardment of solid H_2 by 8 keV H_2^+ ions. R_p is the projected range of the primary ions in hydrogen calculated in Ref. [19].

that for thick films by more than a factor of 5. In general, the enhancement is characterized by the following features:

- (i) the effect is most pronounced for the most volatile gases,
- (ii) the enhancement occurs for electron as well as ion bombardment, and
- (iii) the choice of conductive substrate does not seem to play any role.

The effect is a clear thin-film effect since the energy of the primary particle largely is deposited in the substrate. The enhancement is clearly correlated to the electronic energy deposition and has not yet been observed in a convincing manner for combinations of beam particles and film material, for which the erosion process largely is (ordinary) knockon sputtering rather than electronic sputtering. Stenum et al. [4] pointed out that the yield enhancement for solid deuterium did not depend on the magnitude of the current for values up to 20 nA. This observation means that the enhancement is not caused by beam-induced evaporation.

On the other hand, backscattering of the primary particles does not seem to play a significant role either. Schou et al. [16] estimated that electrons backscattered from the silver substrate at most would increase the yield by a factor of 2. Nevertheless, the contribution from backscattered electrons is easily distinguishable from the thin film enhancement because of the linear dependence on film thickness. This contribution appears in the most distinct

manner for condensed gases with no intrinsic thickness dependence and has been observed by Ellegaard et al. [20] for electron sputtering of solid oxygen. For primary hydrogen ions incident on solid nitrogen Ellegaard et al. [8] estimated a contribution of about one-third of the bulk yield from the reflected primaries alone. This value turned out to agree well with the experimental data and is far below the magnitude of the enhancement observed in the present work. These arguments corroborate the point of view that the effect is not caused by particle reflection.

The range of the effect is apparently strongly correlated to the volatility of the solidified gas. For *electron* bombardment the yield decreases with thickness up a value that corresponds to twice the average projected range [2,15]. As discussed above the yield decreases up to thicknesses somewhat smaller or comparable to the particle range for *hydrogen ion* bombardment of hydrogen or deuterium. It means that the enhancement effect contributes even for thicknesses exceeding 10^{18} molecules/ cm^2 for these two solids for electron and ion bombardment. A similar observation was made for He^+ ions incident on solid deuterium as well [21]. For solid neon the effect extends up to thicknesses of about $(5-7) \times 10^{16}$ Ne-atoms/ cm^2 for 2 keV electrons [16] as well as for ions [11]. A slight enhancement may have been observed for the less volatile solid argon up to a thickness of 2×10^{16} Ar-atoms/ cm^2 by Schou et al. [10] and by Hudel et al. [22] up to 5×10^{15} Ar-atoms/ cm^2 .

The thin-film enhancement of the yield has been observed by Erents and McCracken [12,23] for hydrogen, deuterium, argon, nitrogen and carbon monoxide, all solids bombarded by keV electrons or hydrogen ions. Almost all observations of the enhancement have been made at Risø or by these two authors, since the thickness dependence of the sputtering yield from the most volatile condensed gases has been studied in relatively few cases.

The results obtained at Risø have demonstrated that the enhancement takes place on gold, silver and carbon substrates [2,4,14,15,18], whereas Erents and McCracken utilized a copper substrate [12,23]. The effect shows the same trend for all substrates, but the absolute magnitude varies considerably from one substrate to another [2,21]. The measurements of the yield indicate that the enhancement depends on the purity of the substrate as well, and that the effect is less pronounced for slightly contaminated substrates [21].

The large thicknesses, 10^{18} mole./ cm^2 for the hydrogenic solids and 5×10^{16} Ne-atoms/ cm^2 for solid neon, up to which the enhancement occurs, mean that it is not a surface effect. In addition, the results for deuterium have demonstrated that the range of the effect unambiguously is related to the particle range. It means that the enhancement is a clear beam-induced feature rather than a structural interface effect.

One possible reason for the effect is reflection of low-energy cascades on a heavy substrate. Therefore, the

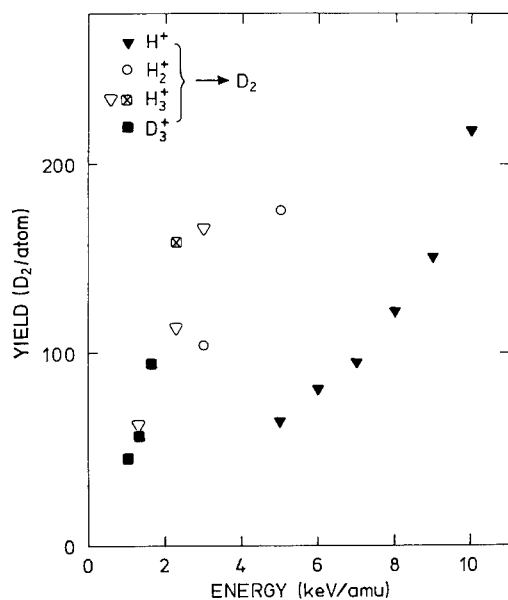


Fig. 3. The sputtering yield (in molecules per atoms) from solid D_2 as function of primary energy. Old data point indicated with crossed square.

range of the collision sequences has been studied with a molecular dynamics simulation code for solid neon. It turned out that even for an initial energy transfer of about 1 eV as a result of the electronic deexcitation, i.e. 50 times larger than the sublimation energy, the low-energy cascades did not contribute to any particle ejection over distances larger than about 10 monolayers [24].

Hudel et al. [22] ascribe the effect to an extended Antoniewicz mechanism of desorption, but no predictions of the range of the effect are available.

In summary, a number of trends that characterize the thin film enhancement have been explored. However, the nature of the effect has not yet been identified.

4. Thick films: results and discussion

The existing measurements as a function of film thickness for all stable hydrogenic solids bombarded by hydrogen ions show a constant yield at sufficiently large film thicknesses. The results for solid deuterium were presented in Ref. [4], whereas an example for solid hydrogen is shown in Fig. 2.

The sputtering yield depicted as a function of energy per ion mass is shown in Fig. 3 for solid deuterium bombarded by hydrogen and deuterium ions. Usually each data point consists of at least three individual measurements. One of the two data sets for 7 keV H_3^+ ions was obtained in a special series measured 4 years earlier than most of the other points. This demonstrates the absolute

uncertainty of the data. However, in subsequent runs the reproducibility is usually better than 15%.

Obviously, the data points lie on three different branches depending on the number of atoms of the ion. This indicates that the sputtering yield per incident atom is enhanced for molecular ions relative to primary protons and for triatomic relative to diatomic ions, but this apparent increase will be discussed in the following. The three points obtained with D_3^+ ions lie clearly on the curve composed of the points from the triatomic ions, and ions of the same velocity produce practically identical yields. All data points are collected in Table 2.

A similar plot of the sputtering yield for thick hydrogen films for molecular hydrogen and deuterium ions is shown in Fig. 4. One notes that also the hydrogen yield lies on two separate branches, the upper one for the triatomic and the lower one for the diatomic ones. The two points obtained with D_3^+ ions lie clearly on the curve composed of the points from the triatomic ions similar to the data for solid deuterium. The results from both hydrogenic solids demonstrate that the yield is determined solely by the electronic stopping power, and that the erosion is dominantly electronic sputtering.

Table 2

Average sputtering yield as a function of the energy. For the accuracy, see text. Note that the *total* yield for the molecular ions is obtained by multiplying the yield in the table with the number of atoms in the ion

Energy [keV]	Average sputtering yield [molecules/atom]		
	H_2	HD	D_2
H^+			
5	386	—	64
6	493	304	81
7	568	262	95
8	607	332	122
9	778	399	151
10	831	471	220
H_2^+			
6	433	—	105
8	635	—	170
10	620	—	176
H_3^+			
4	—	—	72
4.5	312	—	—
7	539	—	113 ^a
8.5	625	—	—
9	—	—	165
10	721	—	—
D_3^+			
6	256	—	46
8	—	—	58
9	300	—	—
10	—	—	96

^a The old data are not included.

The total yield as a function of the sum of the stopping power for the individual atoms in the molecule is shown in Fig. 5 for all hydrogenic solids and for all primary hydrogen ions applied in the present work. One notes that the data points for each solid approximately lie on a single curve. Even though the molecular ions break up at the impact on the surface, each atom deposits the electronic energy so close to the others that one may consider the impact of the molecule as one event. In this manner, a molecular ion corresponds to an ion with an electronic stopping power 2 or 3 times larger than the proton stopping power for the same velocity.

The general dependence of the yield on the primary energy indicates as well that the electronic sputtering is the dominant erosion mechanism for all three isotopes. The nuclear stopping power decreases significantly in this energy interval, and the magnitude of the knockon sputtering yield predicted from linear collision-cascade theory [25] is typically about or below one hydrogenic molecule per ion. Knockon sputtering from either a cylindrical spike or nonoverlapping subspikes leads to an energy dependence [6] that disagrees completely with that observed experimentally. It means that contributions from these mechanisms are relatively unimportant. For solid hydrogen and hydrogen deuteride the yield dependence on the stopping power can be approximated well by the electronic stopping power squared times a constant that depends on the specific isotope. However, for solid deuterium the yield induced by proton bombardment is almost proportional to the cube of the electronic stopping power, whereas the yield from solid deuterium induced by molecular ions may be approximated by the square of the stopping power.

Before going into details of how the electronic energy is converted into atomic motion, let us consider the follow-

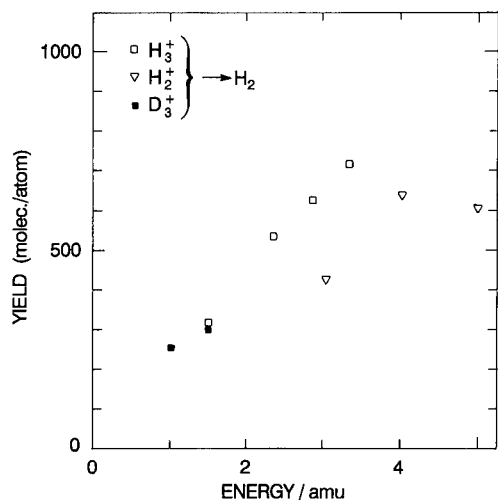


Fig. 4. The sputtering yield (in molecules per atom) as a function of energy per mass unit from solid H_2 induced by molecular hydrogen and deuterium ions.

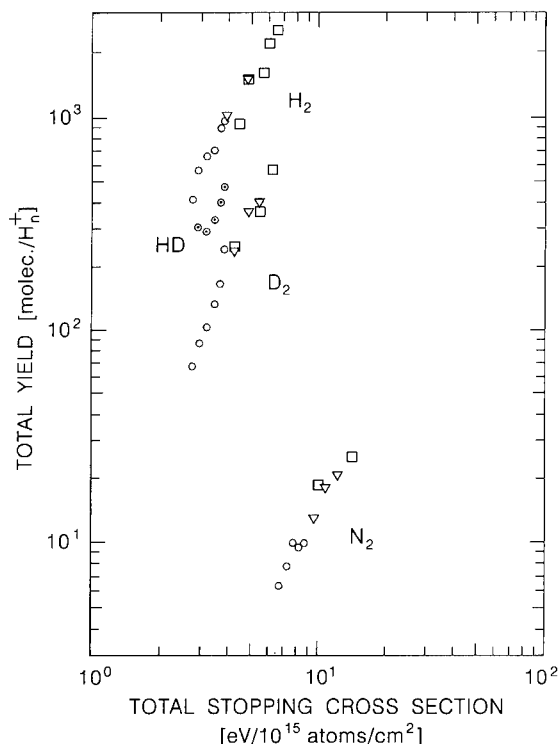


Fig. 5. The total sputtering yield (molecules per ion) as a function of the sum of the electronic stopping power of the atoms of the ion for solid H_2 , HD, D_2 and N_2 bombarded by H^+ (circles, dotted for the HD-points), H_2^+ (triangles) and H_3^+ (squares).

ing picture of the collision dynamics (Fig. 6): the de-excitation processes along the trajectory of the primary ion initiate the motion of repulsing atoms and molecules. The binding of the molecules to the hydrogenic lattice is so weak that the atoms or molecules generate individual subspikes. In such a subspike all target particles are set in motion. These subspikes merge immediately into a cylinder around the ion track, i.e. an electronic, cylindrical spike. If we utilize the picture advocated by Brown et al. [26], the number of atoms set in motion can be estimated by $\Delta E_s/U$, where ΔE_s is the energy converted into atomic motion per electron-ion pair. Even for the least volatile material, solid deuterium, it means that each sphere within which the molecules are set in motion contains at least several other starting points for subspikes. The resulting cylindrical spikes possess an almost perfect cylindrical geometry. The simplest case of electronic sputtering based on linear collision-cascade theory (also shown in Fig. 6) [2,6,21,27] leads to a yield that is much too small compared with the experimental ones. This treatment gives a linear dependence on the electronic stopping power in contrast to what we have observed experimentally. Even though that we here consider electronic sputtering, we have included also the analogous cases for knockon sputtering in Fig. 6.

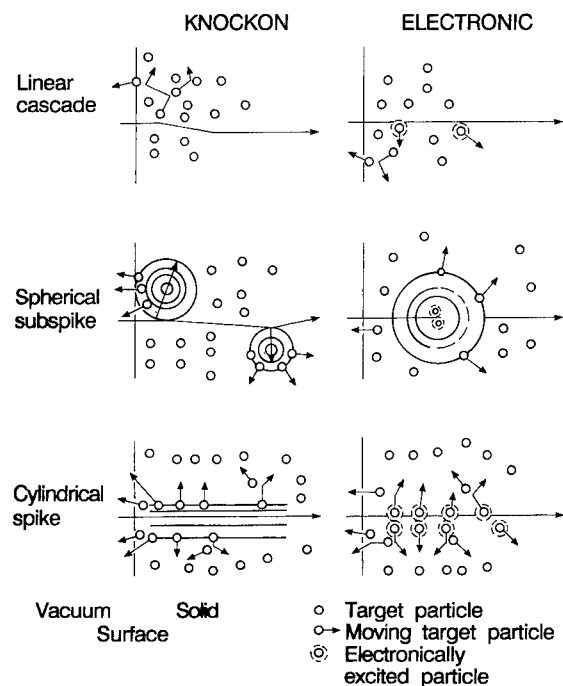


Fig. 6. Schematic survey of the erosion processes for knockon and electronic sputtering. Upper figures: sputtering by linear collision-cascades, middle figures: sputtering by subspike formation, lower figures: sputtering by cylindrical spike formation. Left column: knockon sputtering, right column: electronic sputtering.

There is no satisfactory theory that accounts for the energy release processes leading to sputtering. It is well known that the energy conversion processes vary strongly from one gas to another [6,27]. A process common for molecular solids is dissociative recombination which turned out to be important for the molecular solids, nitrogen and oxygen [7,8,20]. However, the ionization cross section for protons with energies up to 10 keV incident on a hydrogen gas is so small [28] compared with the corresponding electronic stopping power [29] that the average energy loss to produce an electron-ion pair varies from 250 eV at 5 keV to 150 eV at 10 keV. Since this value is far from the asymptotic high-energy value of 37.5 eV per electron-ion pair [30], it means that excitations below the ionization limit are dominant and that the contribution from dissociative recombinations is unimportant for the sputtering yield. Collision spectrometric measurements by Park [31] show that excitations to the $B^1\Sigma_u^+$ -level or to the many close-lying molecular states from the ground state $X^1\Sigma_g^+$ prevail. The distance between two subsequent excitations which according to these results liberate an energy ΔE_s between 5.5 and 11 eV, is so small that the recoils interact [1].

The energy dependence of the yield may be partly explained on the basis of a cylindrical spike model [32,33]. In the comparatively simple treatment of a cylindrical

spike by Sigmund and Szymonski [32] the yield Y is proportional to the square of the deposited energy per unit length:

$$y = c(F_D'^2/U^2) \exp(-U/kT_0), \quad (1)$$

where $c = 0.05525 \text{ \AA}^2$. In this context the energy per unit length F_D' means the part of the electronic stopping power that ends up in electronic excitations below the ionization threshold. T_0 is the initial temperature rise in the core of the spike, and k Boltzmann's constant. The energy spent in ionizations is unavailable for the cylindrical spike except the energy from the triatomic ion formation (D_3^+ , H_3^+ or triatomic combinations of D and H in HD) which takes place simultaneously with the generation of the cylindrical spike [34]. The effective stopping power F_D' is about 0.6 times the electronic stopping power $(dE/dx)_e$. The remaining 40% represent energy loss to ionization, dissociation and kinetic energy of secondary electrons. A minor part of this energy loss leads to energy release from dissociative recombinations of D_3^+ or D_9^+ ions, which may occur on a time scale up to several seconds after the spike generation. This energy leads to sputtering as well, but as mentioned above, the contribution is insignificant compared with the total yield from the cylindrical spike [21]. Considering the large sputtering yields one may expect that many adjacent particles are emitted simultaneously. In that case, a planar barrier of constant magnitude U determined by fixed surface atoms becomes meaningless. Eq. (1) is derived under the assumption that the ejection of particles from a planar surface takes place as an evaporation from a planar surface. Nevertheless, the dependence of the yield is fairly well described by the cylindrical spike except for the data points of deuterium bombarded by protons.

Results for solid nitrogen have been included in Fig. 5. One notes that the hydrogenic results exhibit the same general overall behavior except that the yield for these volatile solids is much higher. The magnitude of the yield for solid deuterium is about 80 times higher than that for solid nitrogen for ions of the same stopping power. This difference reflects the dissimilarity of the energy conversion processes during electronic sputtering, i.e. of ΔE_s , and the large ratio of the sublimation energy for solid nitrogen and that for deuterium. Since this ratio is about a factor of 6, it may indicate that the dependence on the sublimation energy is strongly nonlinear. This point agrees with the tendency observed between the hydrogenic isotopes as well.

5. Conclusion

The first comprehensive measurements for all stable hydrogen isotopes have been presented. We have divided the discussion into two parts, the pronounced thin-film

enhancement and the behavior for thick films. The origin of the high yield for small film thicknesses has not been identified, but the effect is common for all of the most volatile solids, and is induced by protons as well as electrons. The magnitude and the range of the thin-film enhancement for solid hydrogen are similar to the results for solid deuterium. The yields for thick films induced by hydrogen ion bombardment are very high. No existing model can account satisfactorily for both the yield dependence on the primary energy and the sublimation energy as well as the magnitude of the yield. The extreme volatility of the hydrogenic solids does not lead to any yield dependence on the stopping power that contrasts other frozen gases.

Acknowledgements

The authors thank H. Sørensen, P. Sigmund and R. Baragiola for support during the measurements and numerous discussions, and appreciate the competent technical assistance from A. Nordskov and B. Sass. This work was supported by a grant from the Danish Natural Science Research Council.

References

- [1] B. Stenum, J. Schou, O. Ellegaard, H. Sørensen and R. Pedrys, *Phys. Rev. Lett.* 67 (1991) 2842.
- [2] J. Schou, *Dr. scient. Thesis*, Risø-R-591 (EN) (1991).
- [3] B. Stenum, O. Ellegaard, J. Schou, H. Sørensen and R. Pedrys, *Nucl. Instr. and Meth. B* 58 (1991) 399.
- [4] B. Stenum, O. Ellegaard, J. Schou and H. Sørensen, *Nucl. Instr. and Meth. B* 48 (1990) 530.
- [5] P.C. Souers, *Hydrogen properties for fusion energy* (University of California Press, Berkeley, 1986).
- [6] R.E. Johnson and J. Schou, *K. Dan. Vidensk. Selsk. Mat. Fys. Medd.* 43 (1993) 403.
- [7] K.M. Gibbs, W.L. Brown and R.E. Johnson, *Phys. Rev. B* 38 (1988) 11001.
- [8] O. Ellegaard, J. Schou, B. Stenum, H. Sørensen, R. Pedrys, B. Warczak, D.J. Oostra, A. Haring and A.E. de Vries, *Surf. Sci.* 302 (1994) 371.
- [9] C.T. Reimann, W.L. Brown and R.E. Johnson, *Phys. Rev. B* 37 (1988) 1455.
- [10] J. Schou, O. Ellegaard, H. Sørensen and R. Pedrys, *Nucl. Instr. and Meth. B* 33 (1988) 808.
- [11] O. Ellegaard, J. Schou and H. Sørensen, *Nucl. Instr. and Meth. B* 13 (1986) 567.
- [12] S.K. Erents and G.M. McCracken, *J. Appl. Phys.* 44 (1973) 3129.
- [13] P. Børgesen and H. Sørensen, *Phys. Lett. A* 90 (1982) 319.
- [14] P. Børgesen, *Ph.D. Thesis*, Risø R-457 Risø National Laboratory (1982).
- [15] B. Thestrup, W. Svendsen, J. Schou and O. Ellegaard, *Phys. Rev. Lett.* 73 (1994) 1444.
- [16] J. Schou, P. Børgesen, O. Ellegaard, H. Sørensen and C. Claussen, *Phys. Rev. B* 34 (1986) 93.
- [17] V. Pironello, in: *Chemistry in space*, eds. J.M. Greenberg and V. Pironello (Kluwer, Dordrecht, 1991) p. 263.
- [18] J. Schou, H. Sørensen and P. Børgesen, *Nucl. Instr. and Meth. B* 5 (1984) 44.
- [19] P. Børgesen and H. Sørensen, *Nucl. Instr. and Meth.* 200 (1982) 571.
- [20] O. Ellegaard, J. Schou, H. Sørensen and P. Børgesen, *Surf. Sci.* 167 (1986) 474.
- [21] B. Stenum and J. Schou, unpublished.
- [22] E. Hudel, E. Steinacker and P. Feulner, *Phys. Rev. B* 44 (1991) 8972.
- [23] S.K. Erents and G.M. McCracken, in: *Atomic collisions in solids*, eds. S. Datz, B.R. Appleton and C.D. Moak (Plenum, New York, 1975) p. 625.
- [24] L. Dutkiewicz, unpublished.
- [25] P. Sigmund, in: *Sputtering by particle bombardment I*, ed. R. Behrisch (Springer, Heidelberg, 1981) p. 9.
- [26] W.L. Brown, L.J. Lanzerotti, K.J. Marcantonio, R.E. Johnson and C.T. Reimann, *Nucl. Instr. and Meth. B* 14 (1986) 392.
- [27] J. Schou, *Nucl. Instr. and Meth. B* 27 (1988) 188.
- [28] M.E. Rudd, Y.-K. Kim, D.H. Madison and J.W. Gallagher, *Rev. Mod. Phys.* 57 (1985) 965.
- [29] H.H. Andersen and J.F. Ziegler, *Hydrogen stopping powers and ranges in all elements* (Pergamon, New York, 1977).
- [30] ICRU, Rep. 31, Commission on Radiation Units and Measurements, 7910 Woodmont Avenue, Washington D.C. 20014, USA, pp. 1–49.
- [31] J.T. Park, in: *Collision spectroscopy*, ed. R.G. Cooks (Plenum, 1978) p. 19.
- [32] P. Sigmund and M. Szymonski, *Appl. Phys. A* 33 (1984) 141.
- [33] P. Sigmund and C. Claussen, *J. Appl. Phys.* 52 (1981) 990.
- [34] R.L. Brooks and J.L. Hunt, *Phys. Can.* 47 (1991) 132.



ELSEVIER

Defects induced by ion bombardment of alkali halides

Qun Yan ^{a,*}, A.V. Barnes ^a, N. Seifert ^b, R. Albridge ^a, N. Tolk ^a^a *Department of Physics and Astronomy and Center for Molecular and Atomic Studies at Surfaces, Vanderbilt University,
Box 1807 Station B, Nashville, TN 37235, USA*^b *Institut für Allgemeine Physik, Technische Universität Wien, A-1040 Wien, Austria*

Abstract

Defects induced by 20 keV ion bombardment of NaF and LiF crystals have been investigated by optical absorption and photo luminescence measurements. The F center band and F center aggregate bands have been identified in NaF and LiF crystals under argon ion bombardment. We found that the concentration of F centers is proportional to the square root of the ion dose on both samples. A recombination model of interstitial–vacancies is developed to explain this dependence.

1. Introduction

The study of defects induced by ion bombardment of alkali-halides is an interesting field on both the fundamental level and in application, because it is now recognized that analogous processes occur in other non-metallic solids. Typical defects created in alkali halides under ion bombardment are F centers and F center aggregates. These centers are also called color centers because their absorption bands are in the visible region of the spectrum. One importance of studying color centers in insulating crystals is that these crystals may be utilized as high-gain active materials in tunable solid-state lasers [1].

In general, the energy of an incident ion is deposited into a solid by nuclear and electronic collisions. The partitioning of the total stopping power S into an nuclear part S_n (nuclear stopping power) and an electronic part S_e (electronic stopping power) is dependent on the projectiles, the target material, and the ion beam energy. In alkali halides, lifetimes of excited electronic states (excitons and holes, for example) may be comparable to or even longer than the average time for the sputtering process to take place, and these states can interact with a lattice to form localized defects which can subsequently de-excite [2,3]. The displacement energy for an electronically excited lattice may be only a few eV as the lattice relaxes, rather than the approximately 25 eV needed for dynamic events, thus there may also be synergistic effects between the electronic and nuclear collision processes of energy transfer [4]. Therefore defects created by both nuclear stopping and

electronic stopping are possible for alkali halides under 20 keV ion-beam bombardment.

It is well accepted that the first step in the conversion of the energy deposited into the electronic system of the alkali-halide crystal is the creation of an electron–hole pair or an exciton, followed by the formation of a self-trapped exciton (STE), i.e. an electron coulombically bound to the site of a covalently bounded diatomic halogen molecular ion (X_2^-) [5]. It is very possible that after a few ps, the X_2^- ion moves off-center due to a relaxation [6]. These self-trapped excitons may then decay either by means of photon or phonon production, or by means of radiationless transitions that form halogen vacancies (F centers) and interstitial halogen atoms (H centers). Self-trapped excitons exhibit two luminescence bands: the π -polarized luminescence band, emitted from the lowest triplet state and the σ -polarized luminescence band, emitted from the singlet state [6,7]. Since our experiment was carried out at room temperature or above, F center formation is the dominant process [8].

In this paper, we report first measurements of F centers and F center aggregates induced by low energy ion bombardment from 10 to 25 keV, instead of in the MeV range. We have investigated defects in LiF and NaF crystals due to ion bombardment using optical absorption spectroscopy.

2. Experimental

Sodium-fluoride single crystals and lithium-fluoride single crystals were bombarded by 20 keV Ar^+ ions. The ion beam current density was on the order of $10 \mu A/cm^2$. The experiment was conducted in an ultra-high vacuum chamber with a base pressure 1×10^{-9} Torr. The sample temperature, which could be raised to as high as 500°C by

* Corresponding author, tel. +1 615 322 6803, fax +1 615 343 723, E-mail: yang@ctrvax.vanderbilt.edu.

means of a button heater, was monitored by a thermocouple. The ion-beam current was measured by means of a Faraday cup. The photons emitted from the sample were collected by a McPherson scanning Monochromator or a OMA system (2000–8500 Å) from one side of the chamber. A xenon-lamp or deuterium-lamp was used as the light source for our optical absorption measurements. The light was focused by a quartz lens on the crystal with a spot size approximately 1.5 mm in diameter, which was considerably smaller than the spot size of the ion beam (about $\frac{1}{4}$ in. in diameter). The windows on the chamber were made of quartz, which facilitated a wavelength range from 2000 to 8000 Å for study. The transmitted light was focused into a spectrometer/PMT system. A full scan with 20 Å steps took approximately 6 min. Our crystals were acquired from Harshaw and cleaved in air at $\langle 100 \rangle$ surface. Prior to our measurements, samples were annealed in vacuum overnight at 400°C.

3. Results and discussion

In the case of 20 keV argon ion bombardment of a LiF crystal, the changes in optical density are shown in Fig. 1. One can clearly observe the F-center bands centered at 2500 Å and the F₂-center bands centered at 4450 Å. Also when the sample was heavily dosed by the ion beam, F₃-center bands centered at 3150 Å and 3750 Å and F₄-center bands centered at 5300 Å appeared.

Optical absorption spectroscopy is widely used to study defects induced by radiation particularly at high radiation energies. This method is advantageous in dealing with large defects concentrations, because the effective optical path is short. The concentration of absorbing centers N can

be determined by the Smakula formula (as modified by Dexter) [4,9]:

$$Nf = \frac{9cm^*n}{2\pi^2e^2\hbar(n^2+2)^2} \int \mu(E) dE, \quad (1)$$

where f is the oscillator strength of the optical transition and n is the index of refraction of the matrix at the spectral region of the band. m^* is the effective mass of the electron and μ is the absorption coefficient. The oscillator strength for the transition from ground to excited state equals approximately one in the case of the F-centers, whereas it typically equals 0.2 to 0.3 for F₂ centers. The distribution of defects is not homogeneous under ion bombardment due to non-constant energy loss along the ion track. Therefore the concentration of the centers is also a function of depth x , as well as a function of the absorption coefficient. The detailed distribution of defects is still not clear, and the concentration of the centers can not be directly determined from the change of optical density (COD) which is defined as:

$$\begin{aligned} \text{COD}(E) &= \log_{10}(I_0(E)/I(E)) \\ &= \int_0^d \mu(E, x) dx / \ln 10, \end{aligned} \quad (2)$$

where I is the light intensity transmitted through the bombarded sample and I_0 is the light intensity of the beam through the unbombarded sample. d is the effective optical path which is equal to the penetration depth. The integral of Eq. (1) over the penetration depth gives the following form:

$$\int_0^d N(x) dx = \frac{9cm^*n}{2\pi^2e^2\hbar(n^2+2)^2f} \int \int_0^d \mu(E, x) dx dE. \quad (3)$$

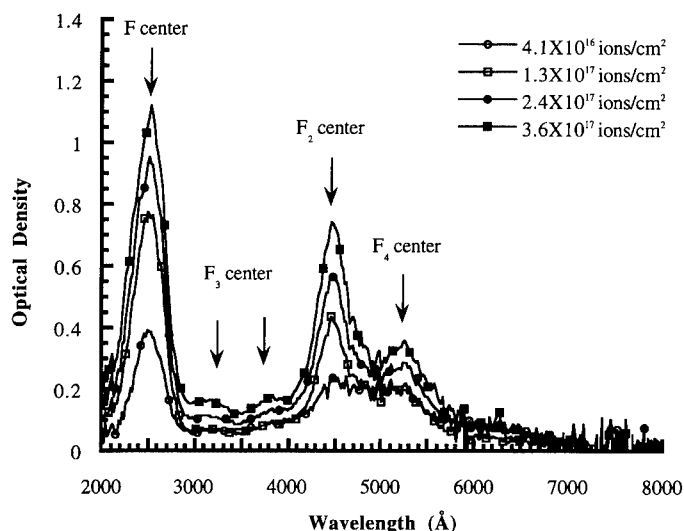


Fig. 1. The change of optical density of LiF crystal under 20 keV Ar⁺ ion bombardment at normal incidence showing defect absorption features.

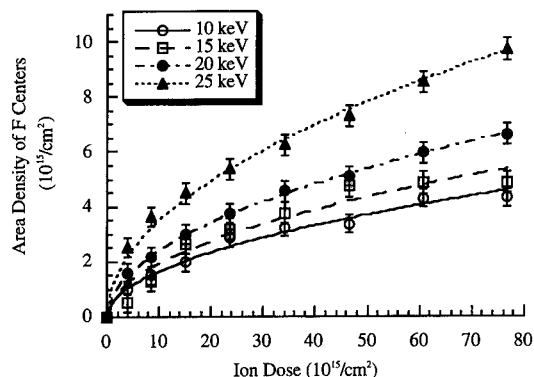


Fig. 2. The area density of F centers of LiF as function of ion dose. Curves represent the fits of square root of dose for different argon ion beam energies.

Therefore the left term of Eq. (3) is the area density of the number of centers which depend on the dose and energy of a given ion beam. We use D to represent this quantity. Substituting Eq. (2) into Eq. (3) and putting into the numerical values of the constants, one can get the following useful form for D :

$$D = \int_0^d N(x) dx$$

$$= 1.89 \times 10^{17} \frac{n}{(n^2 + 2)^2 f} \int \text{COD}(E) dE. \quad (4)$$

The average concentration of the center (\bar{N}) along the ion track can be easily determined by D :

$$\bar{N} = D/d. \quad (5)$$

The area density of F centers as function of ion dose of 10 keV, 15 keV, 20 keV and 25 keV are presented in Fig. 2. Our experimental results clearly show that the area density

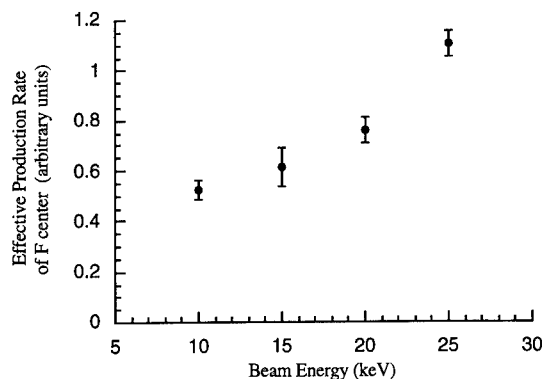


Fig. 3. The effective production rate of F centers, R , as function of argon ion beam energy indicates the rise of R as beam energy increases.

of the number of F centers is proportional to the square root of the ion dose. Durand, Farge and Lambert developed a recombination model of interstitial–vacancies to explain the same dose dependence of the number of F centers induced by X-ray irradiation of LiF samples [10]. Their model was based on the assumption that the KI number of interstitial–vacancy pairs per unit volume per second are created uniformly in the crystal by radiation intensity I and interstitials are captured either by F centers or traps. Their model yielded the result that the concentration of F centers, N , could be represented by the following equation:

$$N = (2KI t K_2 Y / K_1)^{1/2}, \quad (6)$$

where Y is the concentration of traps, and K_1 and K_2 are coefficients which take into account at the same time the mobility of interstitials and the effective capture cross section of interstitials by a vacancy or by a trap. t is

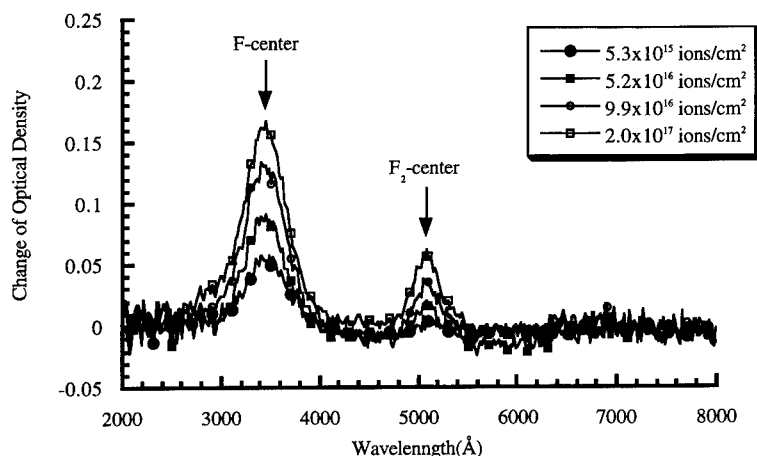


Fig. 4. The change of the optical density of a NaF crystal under 20 keV Ar^+ ion bombardment at normal incidence showing defect absorption features.

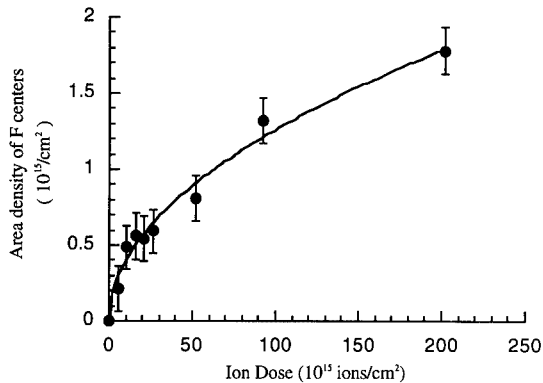


Fig. 5. The area density of F centers of NaF as function of 20 keV Ar^+ ion dose. Curves represent the fits of the square root of the dose.

radiation time. This model can not be applied directly to defects induced by ion bombardment of alkali-halide crystals because of the inhomogeneous distribution of interstitials created by ions bombardment. It is obvious that K is also a function of the distance from the surface. Substituting $N(x)$ given by Eq. (6) into Eq. (4) we get:

$$D = (2ItK_2/K_1)^{1/2} \int_0^d (K(x)Y(x))^{1/2} dx$$

$$= 1.89 \times 10^{17} \frac{n}{(n^2 + 2)^2 f} \int \text{COD}(E) dE. \quad (7)$$

It is clear that the area density of F centers, D , is still proportional to the square root of ion dose (It) according to this modified model. As shown in Fig. 2, our data is well fitted by the following equation:

$$D = R(It)^{1/2}, \quad (8)$$

where R is the assembly of other parameters as shown by Eq. (9):

$$R = (2K_2/K_1)^{1/2} \int_0^d (K(x)Y(x))^{1/2} dx. \quad (9)$$

Since $K(x)$ is the creation rate of interstitial–vacancy pairs, it should be related to ion stopping power which is a function of beam energy. By fitting our data, the beam energy dependence of R is depicted in Fig. 3. The rise of R as beam energy increases is due to the increase of energy deposition of the ion into the material. Basically one can get the energy dependence of R by Eq. (9) if the explicit form of $K(x)Y(x)$ and stopping power are known.

Fig. 4 shows the optical absorption spectrum for different doses of 20 keV argon ion bombardment of NaF

crystal. One can clearly observe the F-center bands centered at 3400 Å, and the F_2 -center bands centered at 5050 Å. The area density of the number of F center as function of ion dose of 20 keV Ar^+ ion is presented in Fig. 5. The data of Fig. 5 bears out the same linear dependence to the square root of the ion dose as seen in LiF crystal. The rate of creation of F centers, R , is 0.128 cm^{-1} as determined from fitting Eq. (8) to our data, which is much smaller than the R (0.76 cm^{-1}) of LiF crystal under same dose and same beam energy. This means that crystalline NaF is a better material than LiF for resisting defects due to ion bombardment.

4. Conclusions

We have investigated the defects induced by 20 keV ion bombardment of LiF and NaF crystals. Optical absorption were used to identify various defects in the crystals, including F centers, F_2 centers, F_3 centers, and F_4 centers of LiF and NaF crystals. An optical absorption technique was applied to determine the area density of defects by using Smakula's formula. We have found that the concentration of F centers is proportional to square root of ion dose in both crystals under Ar^+ ion bombardment. Durand's model is modified to explain this dependence for the case of inhomogeneous distribution of F centers. The beam-energy dependence of the rate R given in Eq. (9) gives additional information about the creation of defects due to ion bombardment.

References

- [1] W. Gellermann, J. Phys. Chem. Solids 52 (1991) 249.
- [2] P. Sigmund, in: Sputtering by Particle Bombardment I, ed. R. Behrisch, Topics in Applied Physics, vol. 47 (Springer, Berlin, 1981).
- [3] K. Kierkegaard, S. Ludvigsen, B. Petterson and E. Veje, Nucl. Instr. and Meth. B 13 (1986) 388.
- [4] F. Agullo-Lopez, C.R.A. Catlow and P.D. Townsend, in: Point Defects In Materials (Academic Press, 1988).
- [5] R.T. Williams, Radiat. Eff. 108 (1989).
- [6] R.T. Williams, K.S. Song, J. Phys. Chem. Solids 51 (1990) 679.
- [7] N. Itoh and K. Tanimura, J. Phys. Chem. Solids 51 (1990) 717.
- [8] N. Itoh, Nucl. Instr. and Meth. B 27 (1987) 155.
- [9] A. Smakula, Z. Phys. 59 (1930) 603.
- [10] P. Durand, Y. Farge and M. Lambert, J. Phys. Chem. Solids 30 (1969) 1353.



ELSEVIER

ESD of nonthermal halogen atoms from In-doped (001)KBr

Z. Postawa^{a,*}, J. Kolodziej^a, G. Baran^a, P. Czuba^a, P. Piatkowski^a, M. Szymonski^a,
I. Plavina^b, A. Popov^b

^a Institute of Physics, Jagiellonian University, 30-059 Kraków 16, ul. Reymonta 4, Poland

^b Institute of Solid State Physics, University of Latvia, 8 Kengaraga St., LV-1063 Riga, Latvia

Abstract

We have measured the kinetic energy distributions of neutral halogen atoms emitted due to electron-stimulated desorption (ESD) from In-doped (001)KBr single crystals. The concentration of In⁺ in investigated samples varied between 10¹⁷ and 10²⁰ particles/cm³. The measurements were performed at target temperature of 150°C. In all cases the energy spectra consist of two peaks. The distribution of low-energy particles can be described by the thermal (Maxwellian) energy spectrum. Particles contributing to the second peak have nonthermal kinetic energies. The emission of halogen atoms having nonthermal energies decreases with an increase in the concentration of In impurities. At the same time, the emission of thermal particles does not seem to be sensitive to variation of In⁺ concentration. At the temperatures of interest here, In⁺ impurities are known to be very efficient traps for migrating holes but not to influence the migration of H-centers. The obtained results support the model of nonthermal halogen desorption which requires a long range diffusion of holes from the bulk to the surface as a necessary step of the process.

1. Introduction

The ESD of alkali halides has been a subject of numerous investigations during the last two decades [1]. It has been found that the flux of desorbing particles consists predominantly of neutral atoms of both solid components (alkalis and halogens) as well as neutral molecules and clusters. A small fraction of positive and negative ions has also been observed [2,3]. Most of the ejected neutral particles have low, thermal kinetic energies and are emitted with cosine-like angular distributions [4]. For several alkali halides, however, a considerable fraction of halogen atoms is ejected with nonthermal energies of approximately 0.3 eV. The angular distribution of these particles is peaked along the <001> direction for well defined single crystalline surfaces [4,5].

This contribution focuses on the desorption of halogen atoms with nonthermal energies. We will report here the experimental data obtained recently in our laboratory on ESD of In-doped (001)KBr crystals. These measurements enable us to determine the role of holes diffusion in the desorption of nonthermal halogen atoms. The electron–hole pairs are created in the initial steps of energy deposition by penetrating projectiles. They can be created anywhere in

the valence band of alkali halides, thus acquiring a rather wide distribution of initial kinetic energies [6]. For example, in KBr the width of the valence band is about 2.6 eV [7] so that, on average, the holes could have as much as 1.3 eV excess energy. Such holes are often called “hot holes” [8]. High initial energy makes “hot” holes very mobile providing an efficient transport mechanism of the energy deposited originally in the bulk of the crystal to the surface. In one of our previous papers we have shown that in order to describe properly the experimental dependence of the nonthermal Br yield on the energy of primary electrons impinging on (001)KBr, one should assume the mean diffusion length of carriers leading to desorption to be longer than 100 Å [9]. Unfortunately, no more direct evidence about a nature of such carriers could be drawn from that experiment. It is known, however, that the migration of holes can be altered significantly by monovalent mercury-like ion impurities (Tl⁺, In⁺, etc.) [10–12]. When added in minor amount, these ions occupy the alkali ion sites, thus, preserving the overall crystallographic structure of the crystal. At low temperature, the mercury-like impurities lead to a pronounced stabilization of electrons, holes and other defects near the ion impurity [10–12]. At elevated temperatures, however, only holes are effectively trapped on these ions [13–15]. In result, if diffusion of “hot” holes is indeed supplying the excitation to the surface which results in the emission of nonthermal atoms one can expect that the efficiency of this channel should decrease with the increase of the concentration of “hole

* Corresponding author, tel. +48 12 33 63 77 ext. 560, E-mail: zp@castor.if.uj.edu.pl.

traps". To verify this preposition we have measured the time-of-flight distributions and the total desorption yields of Br atoms emitted from 1 keV electron-bombarded (001)KBr samples having various concentrations of In ions.

2. Experimental

The details of the experimental setup have been described previously [16]. Briefly, the random-correlation time-of-flight (TOF) spectrometer with a flight path of 0.31 m was used to measure TOF distributions of neutral halogen atoms. Neutral atoms leaving the surface along the normal were ionized in an electron-impact ionizer and mass selected in a quadrupole mass spectrometer. The desorption was stimulated by a 1 keV electron beam directed at 45° with respect to the surface normal. The electron current was monitored by a Faraday cup and the spot size of the beam was determined by a CCD camera. Since it is known that the relative contribution of the thermal and nonthermal components depends on the current density of bombarding electrons [17], all measurements were done at the same electron current density. The samples were (001) single crystals of KBr doped with In concentrations ranging from 10^{17} to almost 10^{20} cm^{-3} as determined by an optical absorption technique. All the samples were mounted simultaneously on a sample holder and were cleaned by heating to 470 K in vacuum for several hours. The measurements were taken at 150°C to minimize the effect of In impurities on the diffusion of charge carriers and defects other than holes.

3. Experimental results and discussion

Time-of-flight distributions of Br atoms desorbed by 1 keV electrons from (001)KBr crystals doped with In are

shown in Fig. 1. In general, two components are clearly visible in the spectra. The broad, temperature dependent peak can be fit by a Maxwell–Boltzmann distribution corresponding to a macroscopic surface temperature and is due to thermally emitted particles. The narrow peak with temperature independent maximum corresponding to a kinetic energy of approximately 0.25 eV is due to the ejection of hyperthermal particles. By integrating the areas under each of the peaks shown in Fig. 1 and by measuring the relative halogen desorption yield from all the samples, one can separate the total emission into the thermal and nonthermal components. The result is shown in Fig. 2. Clearly the thermal emission is barely influenced by the presence of indium. At the same time, the emission of nonthermal halogen decreases significantly with an increase in indium concentration.

1 keV electrons incident on alkali halide crystal create predominantly conduction band electrons and valence holes. As we already describe in the introduction, the holes may have quite high kinetic energy and, consequently, they can diffuse over large distances in the crystal. Holes that arrive at the surface can neutralize surface halogen ion and lead to the emission of nonthermal neutral halogen atom. A detailed discussion of possible scenarios for surface halogen emission was given in Refs. [1,18].

The above model can be verified by checking whether the yield of nonthermal emission depends on the number of holes arriving at the surface. It is well known that mercury-like ions, like for example In^+ , are very efficient hole traps. Two different mechanisms of hole trapping have been identified in the literature [10,11]. In the first process, In^+ traps a hole and is converted into doubly ionized In^{2+} . In^{2+} ions are stable, however, they can recombine with an electron or F-center. In result, an excited $(\text{In}^+)^*$ center is formed which can return to its ground-state electronic configuration by emission of a broad band luminescence with a peak energy around 3.0 eV in KBr. In the second channel, In^+ is first neutralized

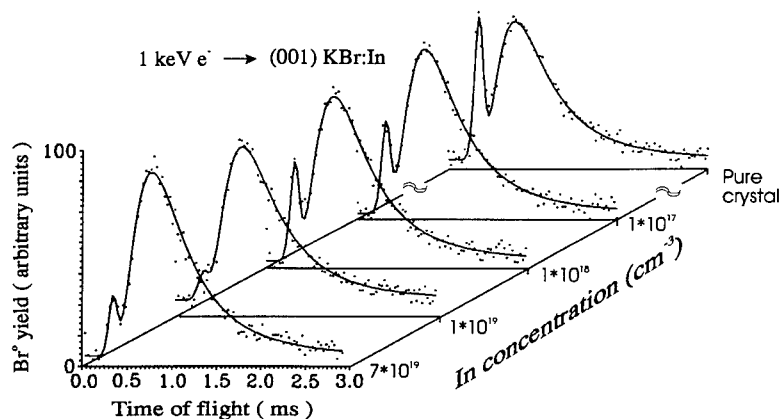
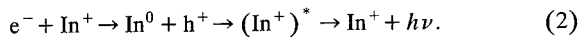
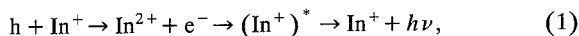


Fig. 1. Time of flight distributions of Br atoms emitted from 1 keV electron-bombarded, In-doped (001)KBr. The measurements were done at 150°C . Solid lines are plotted to guide the eye.

by trapping an electron. Neutral In^0 can be subsequently ionized to the excited state by recombination with a hole, and, finally, the process again results in the emission of radiation. Both processes can be summarized as follows:



The doubly charged mercury-like ions are very stable in alkali halides. For example, the chemical determination of Tl^{2+} concentration indicates that Tl^{2+} ions are present up to 200–800°C depending on the host crystal [13]. On the other hand, it is known that if the temperature exceeds room temperature, the electron trapped in In^0 center is almost instantly thermally promoted to the conduction band [12]. Therefore, at the temperatures of interest in this paper only process (1) should be responsible for hole trapping.

It is visible in Fig. 2. that the emission of nonthermal atoms decreases with the increase of the concentration of In dopant. This observation is strong evidence that hole diffusion is indeed a necessary step for emission of athermal halogen atoms. We have also observed that the emission of nonthermal atoms decreases with the irradiation time for doped crystals, as presented in Fig. 3. For instance, the signal dropped to 50% of its initial value when the target of In-doped KBr (10^{19} cm^{-3}) was bombarded for 60 min with an electron beam with a current density of $20 \mu\text{A}/\text{cm}^2$. The rate of decay decreases with a decrease

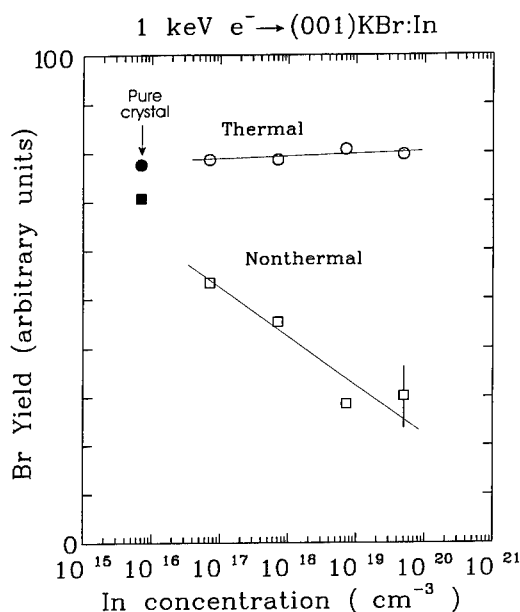


Fig. 2. Dependence of the thermal and nonthermal Br^0 yield on Indium concentration in 1 keV electron-irradiated (001)KBr:In single crystals. Black markers indicate results for pure sample. The measurements were done at 150°C. The solid lines are drawn to guide the eye.

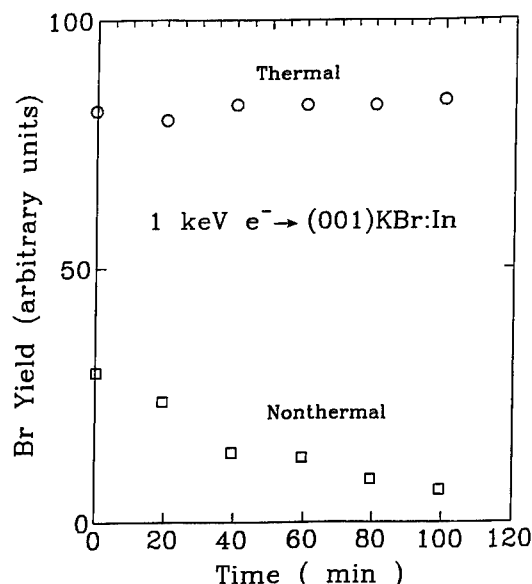


Fig. 3. Time dependence of the thermal and nonthermal Br^0 desorption yield electron-irradiated (001)KBr:In (10^{19} cm^{-3}). The measurements were done at 150°C. The sample was bombarded by 1 keV electrons with a current density of $20 \mu\text{A}/\text{cm}^2$.

of concentration of indium and the nonthermal emission is constant from a pure sample. We believe that this phenomenon is caused by an increase of In concentration in the surface region due to removal of halogen and alkali atoms by bombarding electrons. During electron irradiation In impurities are not desorbed from the surface and, in result, their concentration will increase. The ESD of alkali halides is a very efficient process. A total desorption yield equivalent to 14 NaCl molecules atoms has been measured for NaCl single crystal at 300°C [19]. If we assume the desorption yield for KBr sample at 150°C of the order of 5 we can estimate that approximately 40 monolayers are removed during 1 min of electron bombardment. As a consequence, all In ions located in this volume will be accumulated in the surface zone and the concentration of In impurity in the surface region will be enhanced. This, in turn, will reduce the nonthermal emission due to the process described earlier. The initial yield of nonthermal emission can be recovered by annealing the crystal at 470 K for 30 min. Therefore, we assume that during annealing the excess In evaporate and/or diffuses into the bulk of the crystal and the initial In concentration is restored.

It is also visible in Figs. 2 and 3 that the yield of thermally emitted Br atoms is very weakly, if at all, dependent on both the In-concentration and irradiation time. The emission of thermal halogens is a secondary process with respect to the ejection of nonthermal particles. When the thermalized valence hole in bulk of alkali halide quickly localizes (self-traps) on a pair of lattice halide ions [20] they relax toward each other symmetri-

cally along $\langle 110 \rangle$ in NaCl-type crystals forming so called V_k center. A self-trapped exciton (STE) results when an electron becomes bound to the site of the self-trapped hole. Such self-trapping occurs on a sub-picosecond time-scale [21] and can result in the emission of polarized light. This decay channel dominates at low temperature [22]. At higher temperatures STE can decay nonradiatively leading to the formation of F- and H-centers [20]. At the temperatures of interest in this paper, H-centers can migrate inside the crystal, arrive at the surface and the neutral halogen atom can desorb thermally [23]. The yield of thermally emitted halogen atoms depends on the diffusion range of the interstitial halogen atoms but also on the depth of deposited energy. In the doped crystals diffusing H-centers can be stabilized in the vicinity of a monovalent impurity at low temperatures [14,15]. This process is assumed to be responsible for the enhanced F-center coloration of irradiated In or Tl doped crystals [24]. Ashimova and Usarov have reported, however, that H_A centers (H-center trapped on impurity) are only stable below 110 K in In-doped KCl and below 90 K in In-doped KBr [15]. This observation indicates that mercury-like impurities become “transparent” to the diffusion of H-centers at high temperature. It is also very unlikely that the highest concentration of In used in our experiments, roughly 1 In atom to 10^3 lattice atoms, could influence the deposition of energy by primary electrons. As a consequence, one can expect that the emission of thermal halogens at high temperatures should not be altered by the presence of In impurities, which is indeed observed in our experiment.

4. Conclusions

The time-of-flight distributions of neutral Br atoms have been measured from electron-bombarded indium-doped (001)KBr single crystals at 150°C. It has been observed that the emission of nonthermal atoms decreases with the increase of indium concentration, while, the emission of thermal Br atoms is rather insensitive to the concentration of this impurity. It is known that In^+ ions are very efficient hole traps and are “transparent” to the diffusion of H-centers at elevated temperatures. These results strongly support the model in which diffusion of holes is a necessary step for nonthermal halogen emission.

Acknowledgements

The authors appreciate financial support from the KBN Program no. PB2603 and from the M. Curie-Skłodowska Program no. MEN/NSF-93-144.

References

- [1] M. Szymonski, K. Dan. Vidensk. Selsk., Mat.-Fys. Medd. 43 (1993) 495.
- [2] R.E. Walkup, Ph. Avouris and A.P. Gosh, Phys. Rev. B 36 (1987) 4577.
- [3] Z. Postawa, J. Kolodziej, P. Czuba, P. Piatkowski, M. Szymonski, E. Bielanska, J. Camra, T. Ciach, M. Faryna and A. Rakowska, Nucl. Instr. and Meth. B 78 (1993) 314.
- [4] J. Kolodziej, P. Czuba, P. Piatkowski, Z. Postawa, M. Szymonski and J. Fine, Nucl. Instr. and Meth. B 65 (1992) 507.
- [5] M. Szymonski, J. Kolodziej, P. Czuba, P. Piatkowski, A. Poradzisz, N.H. Tolk and J. Fine, Phys. Rev. Lett. 67 (1991) 1906.
- [6] M.A. Elango, V.N. Kadchenko, A.M. Saar and A.P. Zhukowski, J. Lumin. 14 (1976) 375.
- [7] P. Kowalczyk, F.R. McFeely, L. Ley, R.A. Pollack and D.A. Schirley, Phys. Rev. B 9 (1974) 3573.
- [8] M. Elango, Radiat. Eff. 128 (1994) 1.
- [9] Z. Postawa, J. Kolodziej, P. Czuba, P. Piatkowski, A. Poradzisz, M. Szymonski and J. Fine, in: Desorption Induced by Electronic Transitions DIET V, Springer Series in Surface Sciences, eds. A.R. Burns, E.B. Stechel and D.R. Jennison (Springer, Berlin, 1993) p. 299.
- [10] W.B. Hadley, S. Polick, R.G. Kaufman and H.N. Hersh, J. Chem. Phys. 45 (1966) 2040.
- [11] C.J. Delbecq, A.K. Ghosh and P.H. Yuster, Phys. Rev. 151 (1966) 599.
- [12] Y. Toyotomi and R. Onaka, J. Phys. Soc. Jpn. 46 (1979) 1861.
- [13] J.S. Butterworth and G. Harbottle, Radiochim. Acta 10 (1968) 57.
- [14] S. Zazubovich and V. Osminin, J. Appl. Spectroscopy 23 (1975) 90.
- [15] S. Ashimova and E. Usarov, Opt. Spectroscopy 63 (1987) 1054.
- [16] Z. Postawa, P. Czuba, A. Poradzisz, and M. Szymonski, Radiat. Eff. Def. Solids 109 (1989) 189.
- [17] J. Kolodziej, P. Czuba, P. Piatkowski, Z. Postawa, V. Kempter and M. Szymonski, Vacuum 45 (1993) 353.
- [18] M. Szymonski, J. Kolodziej, Z. Postawa, P. Czuba and P. Piatkowski, Prog. Surf. Sci., in press.
- [19] M. Szymonski, J. Rutkowski, A. Poradzisz, Z. Postawa and B. Jorgensen, Springer Series in Surface Science, vol. 4 (Springer, Berlin, 1985) p. 60.
- [20] R.T. Williams, K.S. Song, W.L. Faust and C.H. Leung, Phys. Rev. B 33 (1986) 7232.
- [21] R.T. Williams, Radiat. Eff. Def. Solids 109 (1989) 175.
- [22] M.N. Kabler, Phys. Rev. A 136 (1964) 1296.
- [23] M. Szymonski, Radiat. Eff. 52 (1980) 9.
- [24] J.S. Butterworth, P.D. Esser and P.W. Levy, Phys. Rev. A 2 (1976) 3340.



ELSEVIER

Inelastic inert gas ion collisions with metal targets. Rearrangement and adsorbate effects

V.A. Esaulov^{*}, L. Guillemot, S. Lacombe, Vu Ngoc Tuan

Laboratoire des Collisions Atomiques et Moléculaires, (Unité Associée au CNRS), bât. 351, Université de Paris Sud, 91405 Orsay, France

Abstract

Results of recent studies of inert gas ion scattering on metal surfaces obtained in this laboratory and elsewhere are briefly reviewed. These have focussed on a study of He, Ne and Ar ion scattering on Na, Mg, Al and Si surfaces for energies in the 500 eV to 15 keV energy range. Measurements of scattered ion and neutral energy and angular distributions, charge fraction determinations and electron and photon spectroscopy results are reported. These demonstrate the role of electronically inelastic “binary” small impact parameter collisions with surface atoms. These are responsible for production of singly and doubly excited states and ionisation. The results of ion solid collisions are analysed and compared to results of gas phase studies of similar collisional systems. Analogies and some major differences are pointed out. The main trends in excitation processes follow the prediction of the molecular orbital promotion model, at least insofar as the prediction of the type of excited particle produced: projectile or target. This suggests that the primary orbital promotion mechanism is the same. Significant differences are encountered and have been discussed in terms of electron capture and loss processes involving the excited species resulting from the binary collision. The existence of core rearrangement processes have been shown to exist on the example of $\text{Ne}^{2+} \text{ } ^1\text{D}$ to ^3P rearrangement. Models of this core rearrangement process have been proposed. The presence of adsorbates has been shown to modify the outcome of scattering. This is partly due to collisions with both metal target atoms and adsorbate atoms, leading to a modification of the primary excitation process. Further modifications occur due to a change in the secondary electron loss and capture processes leading to a modification of the final state distributions.

1. Introduction

Over the past years a large number of studies of inert gas ion scattering on a variety of metal targets have been performed. This work has been concerned both with structure determination and charge transfer processes. It soon became quite obvious that ion scattering was not determined only by elastic binary collisions with surface atoms and that ion neutralisation processes were not exclusively governed by resonant and Auger neutralisation on the ingoing and outgoing trajectories. Thus for instance it was found that in a number of cases of scattering of Ne ions on metal surfaces, one observes an enhancement of scattered ion charge fractions (see e.g. Boers [1] and references therein) and anomalous energy losses (see e.g. Heiland and Taglauer [2]), not understandable in usual binary elastic collision theory. Furthermore, electron spectroscopy studies have shown the production of doubly excited autoionising states of Ne and of various metal target atoms [3]. These experiments clearly pointed to the existence of

electronically inelastic scattering in violent, small impact parameter collisions of the incident ion with a surface atom. Up till now the description of these has mainly relied on a rather arbitrary direct application [4,5] of the Barat–Fano–Lichten molecular orbital promotion model [6,7], which had been developed for the description of gas phase collisions. It therefore seems interesting to perform systematic measurements of excited state production of ion scattering on surfaces and compare them, when possible to the results of studies of similar atom–atom collisional systems in the gas phase. Some attempts at this have been done [4] and some similarities and differences have been observed. The differences have been ascribed [8] to the existence of resonant and Auger electron transfer processes which affect final state distributions.

Here we shall discuss results of investigations of inelastic inert gas ion scattering on some simple targets like Na, Mg, Al and Si performed in our laboratory and elsewhere. The characteristic of the work performed in our laboratory are angle resolved studies of ion scattering and electron spectroscopy. The choice of these systems was dictated by two considerations. Firstly in the gas phase, collisions of Na, Mg and Al ions with Ne atoms have been studied [9–14] and these results can thus serve for comparison

^{*} Corresponding author, tel. +33 1 6941 7680, fax +33 1 6941 7671, E-mail: esaulov@lcam.u-psud.fr.

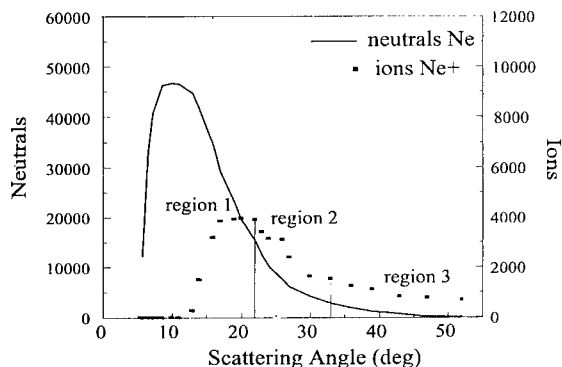


Fig. 1. Angular distribution of scattered neutral and ions in 2 keV Ne^+ incident on Mg at a 6° grazing angle.

with surface data. Secondly these correspond to simple metals, for which a free electron description may be applied and which are thus excellent objects for theoretical investigations. In the following we shall discuss results of some measurements of ion and neutral scattering spectroscopy, charge fraction measurements and electron and photon spectroscopy. We shall try to delineate effects related to the binary violent collisions and compare the data to existing results of gas phase studies in order to analyse the modifications brought about by the neighbouring surface. Finally the effect of adsorbate atoms will be considered. Our aim here is the illustration of the main physical phenomena.

2. Ion scattering spectroscopy and charge fraction measurements

Angular distributions ($N(\theta)$) of scattered ions and neutrals and some energy loss measurements have been performed for He, Ne and Ar ion scattering on Na, Mg, Al and Si surfaces [15–18].

Examples of $N(\theta)$ measured for grazing incidence angles (ϕ) of 6° are shown in Fig. 1 for Ne scattering on Mg. One finds that for small ϕ , the maximum of the neutral distribution lies close to the specular angle, while at larger ϕ it tends to appear at smaller θ and the distributions broaden. Thus for instance for $\phi = 6^\circ$ the maximum of the neutral distribution lies at $\theta = 11^\circ$, while for $\phi = 22^\circ$ it lies at $\theta = 32^\circ$. The maximum of the ion distribution appears at larger angles and with increasing ϕ this angle increases. For smaller impact energies the distributions broaden and the maximum of the ion distribution shifts out to significantly larger angles.

Charge fractions ($Y^+ = \text{ions}/(\text{ions} + \text{neutrals})$) for $\phi = 6^\circ$ are shown in Fig. 2 for some collision energies. A noteworthy feature of these charge fractions, is that they are found to *depend mainly on exit angle* ($\theta - \phi$). In low energy ion-surface scattering one usually supposes [19] that neutralisation can occur in the incoming and outgoing trajectories and, assuming as usual exponential neutralisation rates, it follows that charge fractions should depend on the perpendicular velocity in the ingoing ($v_{\perp \text{ in}}$) and outgoing ($v_{\perp \text{ out}}$) trajectory:

$$Y^+ \propto \exp \left(-A \left(\frac{1}{v_{\perp \text{ in}}} + \frac{1}{v_{\perp \text{ out}}} \right) \right).$$

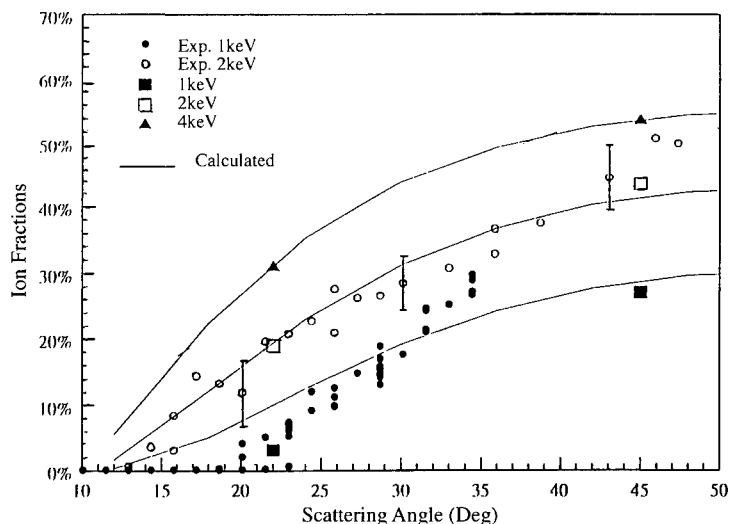


Fig. 2. Charge fractions for a 6° incidence angle of Ne ions for various incident energies. Squares and triangles are data of Ref. [5].

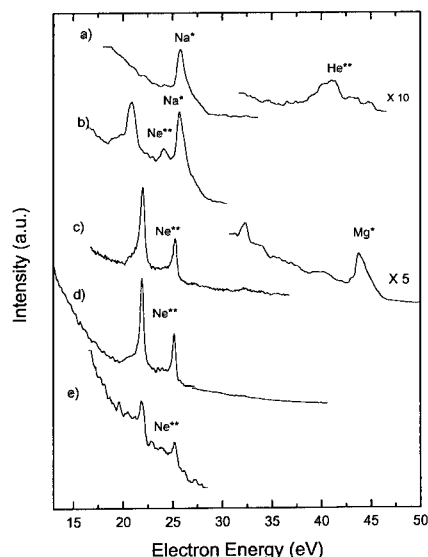


Fig. 3. Energy spectra of electrons produced in (a) 3 keV He collisions with a Na target and detected at 45° and 2 keV Ne collisions with (b) Na detected at 90°, (c) Mg, (d) Al, and (e) Si targets detected at 45°.

This expression is unable to reproduce our data. We found that our charge fractions agree reasonably well (Fig. 3a) with a simple exponential dependence:

$$Y^+ \propto \exp\left(-\frac{A}{v_{\perp \text{ out}}}\right),$$

where $v_{\perp \text{ out}}$ is the outgoing velocity perpendicular to the surface calculated for elastic single scattering conditions and $A = 0.6 \times 10^7$ cm/s. This form also gives results that are very close to the data of Rabalais et al. [5] in the 1 to 10 keV range of energies ($\theta = 22^\circ$ and 45°) (Fig. 2). We would attribute the small discrepancies observed to the fact that ions are presumably due to more than one process for which differences in the value of A may exist. However, as may be seen, the main characteristics are reproduced with even a simple expression, which must represent an average value. Our results are therefore compatible with a model in which all incoming ions are neutralised, a violent collision leading to excitation/ionisation then occurs and ions we observe are those which survive neutralisation in the outgoing stage. This implies that incoming ion neutralisation is extremely efficient.

In the case of Ar scattering on Mg a very small charge fraction was reported by Rabalais et al. [5]. It is also interesting to point out here that the charge fractions for Ar^+ scattering reported by Rabalais et al. [5] can also be closely reproduced by such an exponential dependence, with $A = 1.2 \times 10^7$ cm/s.

The Mg target is not an exception and large fractions are also obtained for Ne scattering on other targets as shown by Lacombe et al. [20]. It is interesting to compare

their values for low keV energies. Thus for 2 keV Ne^+ ions incident at 6° the total ion fractions integrated over scattering angles are of 35%, 14%, 10% and 5% for Na, Mg, Al and Si surfaces, respectively. Thus the general trend is that for a given energy the charge fractions increase as one goes from Si to Mg.

The existence of electronically inelastic processes also follows from energy loss measurements. Thus Grizzi et al. [16] found that the maxima in the Ne^+ ISS peaks lie beyond the value expected from single scattering conditions. They report an inelasticity of about 45 eV. They suggest that the large ion fractions and the large inelastic losses may be related to the production of doubly excited autoionising states of Ne. This idea seemed appealing, since in keV collisions, the excited atoms can be expected to decay at a sufficiently large distance from the surface, where neutralisation would be inefficient. Indeed, e.g. the lifetime of Ne^{**} is of the order of 5×10^{-14} s, and so a 1 keV atom would decay at distances of tens of atomic units from the surface.

In the case of He scattering in the 500–1660 eV range experiments of Bertrand [17] suggested the existence of an energy loss in the 20 to 40 eV range. For this and the other surfaces, inelastic energy losses of about 20 eV have been reported by Souda and Aono [15], whose measurements suggest that ionisation in the binary collision can occur for energies below 200 eV for the Na and Mg targets and below 300 eV for the Al and Si targets. These were observed not only for He^+ but also for *ground state He atom* scattering. Note that low energy losses indicate that increased ion production is not exclusively due to autoionising state production.

Finally it is interesting to mention also the observation of Ne^{2+} ions produced in the scattering of Ne^+ on Si [21].

Thus these ion scattering studies clearly demonstrate the existence of electronic excitation in collisions of incident and surface atoms. The identification of some of the possible excitation channels is rendered possible by photon and electron spectroscopy measurements. These are presented in the next section.

3. Electron spectroscopy measurements

3.1. General characteristics of the electron spectra

A number of investigations of electrons emitted in He, Ne and Ar ion scattering have been performed. Typical electron spectra obtained for 2 keV Ne ions incident at 6° to the target surfaces are shown in Fig. 3 for a 45° detection angle (α). These consist of a continuous distribution on which are superposed a series of structures or peaks. The continuous distribution is due to kinetic and potential electron emission from various neutralisation and de-excitation processes of the incident and, as we shall see below, scattered particles.

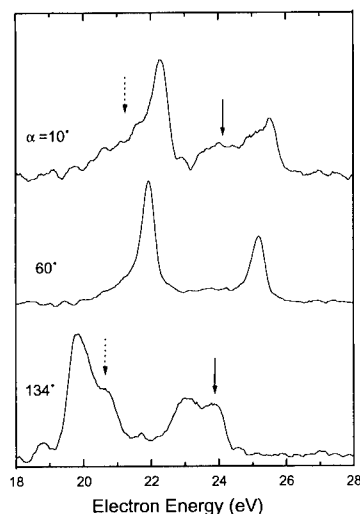


Fig. 4. Energy spectra of electrons produced in 2 keV Ne^+ scattering on Al, for various observation angles.

The energy position and the shape of these peaks in the electron spectrum are dependent on the observation angle (Fig. 4). As was first suggested by Zampieri et al. [4] and later confirmed by Aron and Pepper [22] these shifts are determined by ejection kinematics related to emission occurring from a moving source: an excited atom rapidly receding from the surface. Indeed the peaks are ascribed to scattered excited Ne atoms. In the lower energy part of the spectrum there are two main large peaks due to the decay of $\text{Ne}^{**} 2p^4 ({}^3P \text{ and } {}^1D) 3s^2$ states, whose center of mass energy is close to the 20.35 eV and 23.55 eV positions corresponding to the decay of the excited atom in its free state. At higher energies one generally observes a series of smaller structures (Fig. 3c) the largest of which lies close to 30 eV, also attributable to higher lying autoionising states of Ne and also of Ne^{++} with a $2p^3 nln'1'$ configuration [23,24].

The electron spectrum for scattering on a bulk like Na film [20], also shows peaks due to the autoionisation of Ne^{**} states. The spectrum also displays a peak at 25 eV, which is situated on a large shoulder. The peak is attributed to decay of excited *sputtered* Na atoms in the $2p^5 3s^2$ state. Similar sputtered target emission has been observed in other cases [3]. Thus Fig. 3b shows the spectra for a Mg target, where the structures lying at about 35, 39.5 and 44 eV are due to excited states of Mg^+ and Mg. These are again situated atop of a broad structure, which is attributable to bulk LVV emission, involving transitions from the valence band. Indeed this structure has a characteristic sine dependence on the observation angle with respect to the surface plane.

In the early experiments of Aron and Pepper [22] on Ne^+ scattering on Al, a very large structure was also observed in the vicinity of the Ne^{**} peaks, extending

from about 20 to 35 eV energies. This was attributed to implanted excited atom decay. The existence of such a structure was not confirmed by subsequent measurements of scattering on Al by Gallon and Nixon [23] and by us. We also did not find any signs of this phenomenon for other targets [20].

These observations of course do not rule out contributions from potential electron emission processes: Auger neutralisation of incident Ne^+ and Auger deexcitation of incident resonantly neutralised Ne^* as well as from Auger neutralisation of collisionally formed Ne ions (Ne^+ , Ne^{2+}) and Auger deexcitation of Ne^* and Ne^{++} produced in and after the binary collision. These would appear to merge into a more or less continuous distribution, which it appears difficult to identify in our spectrum. There does appear to exist a broad feature situated *between* the peaks due to the $\text{Ne}^{**} 2p^4 ({}^3P/{}^1D) 3s^2$ states. This may be due to high energy tails in the natural line shapes due to decay near the surface [25].

Finally it is interesting and important to note that similar spectra are obtained in ground-state neutral Ne atom scattering on Mg [4] and on Al [26]. In these collisions one also observes dominant excitation of the $\text{Ne}^{**} 2p^4 ({}^3P/{}^1D) 3s^2$ states, which are observed in similar proportions as for the ionic projectile.

Similar peaks due to the production of autoionising states of He atoms scattered on Na (Fig. 3a), Mg and Al have also been observed in our experiments [18,26]. In the case of Ar scattering on these targets peaks due to autoionising states of the Ar^{**} were *not* observed. Only *target excitation* is observed in this case. On the other hand it is interesting to note that in the case of Ar^+ scattering on K, Ar^{**} is observed [27].

All these observations clearly show the existence of electronically inelastic scattering in which two electrons of e.g. Ne find themselves in a Rydberg orbital. The energy loss for such an excitation process is of the order of 50 eV and can account for the some of the large inelastic losses mentioned above.

3.2. Characteristics of angle resolved spectra and scattered excited atom angular distributions

As mentioned above the peak positions and the shapes of the peaks are found to change when the observation angle changes. An example of this is given in Fig. 4 for the case of Ne scattering on Al. As may be seen the spectra are broad, with a low energy tail for small α , thin down for larger α , and for still larger values are very broad, with a high energy tail. A most interesting aspect of the spectra in Fig. 4 is the difference in the shape of the two Ne peaks. As pointed out by arrows the peak due to the ${}^1D3s^2$ state for a 135° observation angle has a larger low energy shoulder than that due to the ${}^3P3s^2$ state.

We have shown on the example of Ne scattering on Mg [18], that the shape of the spectra can be well accounted

for using an experimentally determined scattered ion energy and angular distribution, which extends to rather large angles and is characterised by large energy losses. Depending upon the position of the spectrometer, ions for a given θ are scattered towards or away from it resulting in higher or lower energy shifts of the electrons. Thus ions in the vicinity of the sharp rise and the maximum in $N(\theta)$ (region 1 in Fig. 1), contribute to the high energy side of the spectrum for small α and to the low energy side at large α . For small α the long low energy tail is due to low energy particles scattered into large angles (region 3), with large energy losses. At large α the high energy tail is also due to these (region 3) atoms scattered into large θ , which now happen to be small angles ($\psi = \theta - \alpha$) for electron emission and therefore result in higher energies. At intermediate α one can encounter a situation, when high energy atoms scattered into $\theta < \alpha$ result in electrons, with the same energies as lower energy ions scattered into $\theta > \alpha$. This results in a “bunched” narrow spectrum. Various other intermediate situations are encountered.

It was shown furthermore [28] that inversely, information about the scattered excited particle angular distributions can be deduced from the analysis of the measured displacements and forms of the Ne^{**} peaks. Such a procedure was used to estimate the shape of the angular distributions for the triplet and the singlet core states of Ne^{**} . It was found that the $^3\text{P}3s^2$ distribution is somewhat narrower and peaks at a smaller scattering angle than that of the $^1\text{D}3s^2$ state. The larger low energy hump in the $^1\text{D}3s^2$ state peak is due to the greater intensity of excited atoms scattered into large angles. Thus these angular measurements indicate a very interesting point, i.e. that the $^3\text{P}3s^2$ is formed preferentially close to the surface.

Preliminary estimates of the location of the maxima of scattered Ne^{**} angular distributions with this method indicated scattering angles of about 25° for Si, 25° for Al, 20° for Mg and a rather broad distribution extending down to about 16° for Na.

3.3. Energy dependence of excited state production

The intensities of the main autoionisation peaks have been measured as a function of incident energy and incidence angles. These intensities correspond to integrals of peak areas after background subtraction and normalising to the incident ion beam current.

Fig. 5 shows the results for a 6° incidence angle for Mg [20,29]. In all cases it is found that:

- the efficiency of autoionising state production generally increases with collision energy up to about 3 keV,
- the intensities of the peaks decrease with increasing incidence angle
- the ratio of the peaks due to $^3\text{P}3s^2$ and the $^1\text{D}3s^2$ states decreases with increasing collision energy, and
- the ratio of the intensity of the peak due to the $^1\text{D}3s^2$

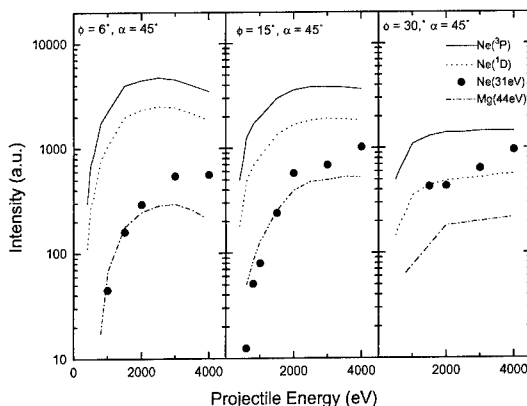


Fig. 5. Energy dependence of autoionising state production in Ne scattering on Mg for various incidence angles (ϕ) and a detection angle of $\alpha = 45^\circ$.

to that due to the $^3\text{P}3s^2$ state decreases as the incident angle increases.

Fig. 6 shows a comparative plot of the intensities summed over the $\text{Ne } ^3\text{P}3s^2$ and the $^1\text{D}3s^2$ states for the different targets. As may be seen, in the studied energy range, the intensity increases as we go from the Si to the Na target. This trend in the excited state production is similar to the trend observed in the ion fractions discussed above.

4. Photon spectroscopy measurements

Additional information about excited state production may be obtained from studies of photon emission. In the case of Ne scattering strong resonance line emission at 743.7 nm and 735.9 nm has been observed indicating that

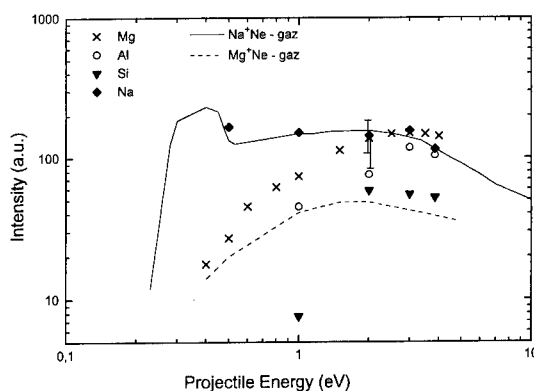


Fig. 6. Energy dependence of the summed $3s^2$ autoionising state intensity for both core states for Mg, Al and Si targets for Ne ions incident at 15° . The detection angle was 45° . The Na data refer to the triplet core state only. The gas phase data is a sum over various states (see text).

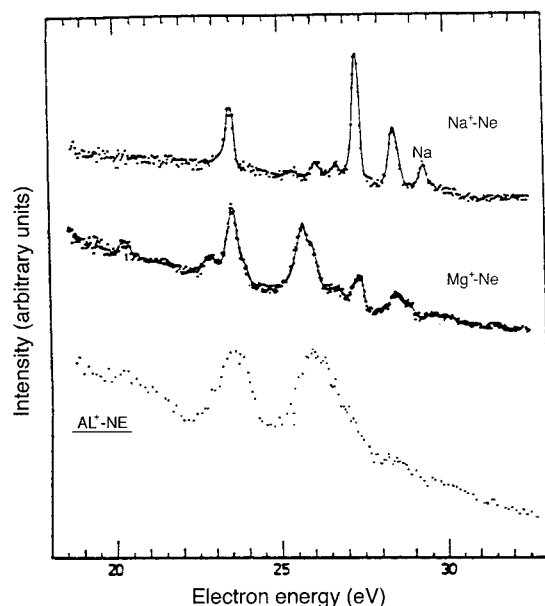


Fig. 7. Autoionising states produced in gas phase 6 keV Na^+ , 5 keV Mg^+ and 2 keV Al^+ collisions with Ne.

a substantial number of resonantly neutralised ions are scattered off the surface [5].

Additionally VUV lines have been observed recently by Bandurin and Daschenko (see Ref. [29]) in 15 keV scattering on Mg and Al surfaces for 10° incidence angles. These are due to the $(2p^4)^3P3s/3p$, the $(2p^4)^1D3s/3p$ and also the $2s2p^6$ excited states of Ne^+ . One also observes a line due to Ne^{2+} in the $2s2p^5$ state.

The production of these states correlates nicely with the observation of the autoionising states of Ne and Ne^{2+} production discussed above.

5. Comparison with collisions in the gas phase

A number of studies of collisions of Na^+ , Mg^+ and Al^+ ions with inert gas targets have been performed in the gas phase [9–14]. In the following we shall now briefly delineate the similarities and differences in the results obtained.

Energy loss measurements for scattering of these ions on He and Ne targets shows the excitation of both the projectile and the target. Production of singly and doubly excited states is observed. Electron energy spectra measured for a Ne target, show peaks due to autoionising states of Ne, Fig. 7. Some of the differences observed between the spectra are related to the conservation of the total spin of the systems, which is expected for light systems, where spin–orbit coupling effects are small. Thus in Na^+ and Al^+ –Ne the total spin is zero and only singlet states are expected, whereas for Mg^+ –Ne with a total doublet state

both singlet and triplet states may be produced. In the case of Na^+ and Mg^+ ions mainly 1D core states of Ne are produced, whereas for the Al^+ system the rather large peak at about 26 eV has been assigned to the 3P core $3s4s(^3S)$, $3s3d(^3D)$ and $3p^2(^3P)$ singlet states [14].

The excitation cross section for the Ne^{**} states decreases when one goes from the more symmetric Na target [9] to Mg [12]. These cross sections are illustrated in Fig. 6.

As opposed to He and Ne, in the case of collisions with Ar mainly target excitation is observed.

We find these general trends in our data on inert gas ion scattering on solid targets. Thus we observe excitation of He and Ne and not that of Ar. The excited state production appears to decrease with increasing Z . As may be seen in Fig. 6 the Ne^{**} production for Na and Mg occurs in proportions which are similar to the gas phase ones at low energies. Also as we saw above the excited particle angular distributions appear to be shifted to somewhat larger angles as Z increases.

There do exist some differences in excited state production. The most dramatic one concerns the electron spectra in Fig. 7, which are quite different from those in Fig. 3 for solid targets. For solid targets the spectra are dominated by the peak due to the $^3P3s^2$ state, which is only very weakly excited in Mg^+ and Al^+ Ne collisions. The higher lying states, e.g. $3s3p$, $3p^2$, etc. are very weakly excited for solid targets.

Differences are also observed in the efficiency of excited state production as a function of energy and as we saw for solids there is a dependence on angles of incidence.

Some of these differences can be related to effects of changes of particle reflection from the solid as a function of incidence angle and collision energy. One can also expect differences induced by resonant and Auger neutralisation and Auger de-excitation of excited states close to the surface. Thus Zampieri and Baragiola [8] explained the weakness of the higher lying autoionising states as due to their resonant ionisation near metal surfaces. Indeed the binding energy of an electron in the $\text{Ne}^{**} 2p^43s^2$ state relative to its parent $\text{Ne}^{**} 2p^43s$ state is of about 7 eV, while that of the higher lying states is less than 5 eV. These can be resonantly ionised near the surface in particular because of image potential shifts and clearly the more strongly bound $3s^2$ states remain stable for smaller atom surface distances. The modifications in the $3s^2$ state intensities discussed above are also related to surface induced transitions, as we shall see below.

6. Quasimolecular interpretations

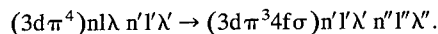
The above comparisons, showing a strong similarity in the basic trends of excited state production suggest that at least the basic primary excitation mechanisms in atom–

atom and atom–surface collisions are similar. In the following we shall briefly examine the mechanisms of excited state production within the framework of the Barat–Lichten molecular orbital promotion model. In terms of the quasimolecular interpretation of inelastic scattering, the excited state production in e.g. Ne collisions, occurs when the 2p orbitals of the colliding partners start to overlap [6,7]. Excitations originate as a result of the promotion of the outermost 2p Ne orbital. The similarity between the gas phase and solid data may arise if the inner 2p core energies of the metal ions, which in the solid are situated at a fairly large distance, are not significantly different from their values in the gas phase, so that the orbital promotions are not swapped. There remains a basic problem concerning outer valence orbitals to which we shall return below.

In the framework of the electron promotion model, in a gas phase He–Na, Mg (or Al) collision, He ($n = 2$) excitations would be due to the promotion of the $3d\sigma$ orbital which correlates to He(1s). Production of autoionising states is due to two electron transitions from the $3d\sigma$ orbital to Rydberg orbitals. In collisions with a metal surface an excitation mechanism leading to $n = 2$ (and higher) level population can result in resonant ionisation, because of level shifts close to the surface. Production of ions as a result of resonant ionisation subsequent to collisional excitation could explain the observation of inelastic losses of about 20 eV in ion production [9]. Autoionising state production would lead to still higher energy losses.

In the case of $\text{Mg}^+ \text{Ar}$ collisions, the MO model predicts the excitation of Mg rather than Ar, in agreement with experimental observation [13]. This is also what we find for collisions of Ar^+ with Mg and Al surfaces, where no significant excitation of Ar states is observed. If we were to consider Ar^+ collisions with K, then in this quasisymmetric system one would expect and one observes production of Ar excited states in gas phase collisions. This was also observed on Ar scattering on chemisorbed K [27].

In collisions with Ne (see the MO diagram in Fig. 8), excitations occur due to the promotion of the $4f\sigma$ orbital, that correlates to Ne(2p) and transitions of one or two $4f\sigma$ electrons to higher lying Rydberg orbitals. In case of ground state Ne collisions with Na, Mg or Al, we deal with an initial molecular state with a $3d\pi^4 4f\sigma^2$ configuration. The singlet $3d\pi^4$ [9–14] will lead to the dominant production of the $(^1\text{D})n1n'1'$ states at low energies. The observation of a strong component due to the triplet core $((^3\text{P})3s3p$ and $(^3\text{P})3p^2$) in the Al^+Ne case, indicates the existence of core $(3d\pi^4)$ -Rydberg electron exchange [14], i.e. a two electron rearrangement process:



This has been studied theoretically for $\text{Na}^+ \text{Ne}$ collisions [9]. In the latter system it was not found to be an important process. The observation of the very large $^3\text{P}3s^2$ state

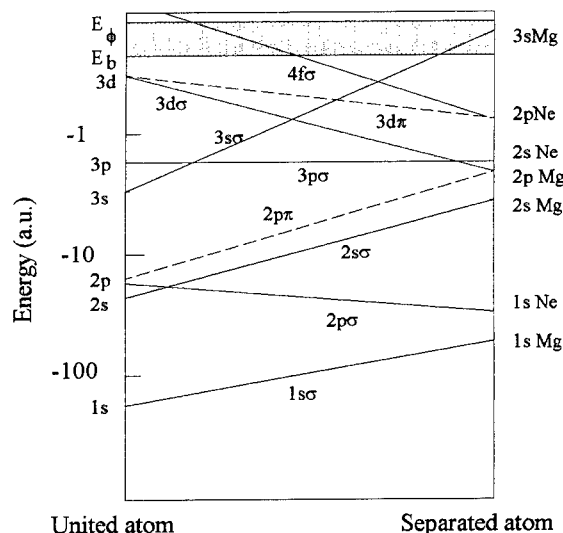


Fig. 8. Molecular orbital correlation diagram showing also the Mg valence band.

peak, led Zampieri et al. [4] to suggest that this rearrangement process may be enhanced by electrons from the solid. The existence of “solid assisted” rearrangement appears to agree with the perpendicular velocity dependent behaviour of the ratio of the singlet and triplet core states and has been discussed by us [18,20,30] and other authors [24]. It should be pointed out that if we were dealing with a Ne^+ or Ne^* projectile the situation would be different. Indeed in this case there are two initial possibilities corresponding to scattering in the $3d\pi^4 4f\sigma$ and the $3d\pi^3 4f\sigma^2$ states. Scattering in the latter state can lead to the formation of excited states of the ^3P core. However we saw above that neutralisation is very efficient and that for Ne ground state projectiles the situation is similar to that due to Ne^+ . It is of course possible that multiple collisions play an important role. The existence of the 31 eV peak, attributed to a $(2p^3)3s^2/3s3p$ configurations in the $\text{Ne}^0 + \text{Mg}$ spectrum [4], points to this. However a careful analysis of various possibilities shows that there are in fact a number of processes that would lead to the above core rearrangement [29,31].

7. Core rearrangement processes

The *quasimolecular rearrangement* process envisaged initially [4,18,20,30,34] is schematised in Fig. 9a. In the gas phase this occurs at a crossing of the $(3d\pi^4)n1\lambda n'1'\lambda' \rightarrow (3d\pi^3 4f\sigma) n'1'\lambda' n''1''\lambda''$ states. The $3d\pi^3 4f\sigma$ core state with an inner vacancy should be more repulsive than the $3d\pi^4$ core state [9]. In the case of a solid target we can envisage an Auger transition between these states, which would be active in the *outgoing* leg of the collision for distances larger than the crossing point of these states. It

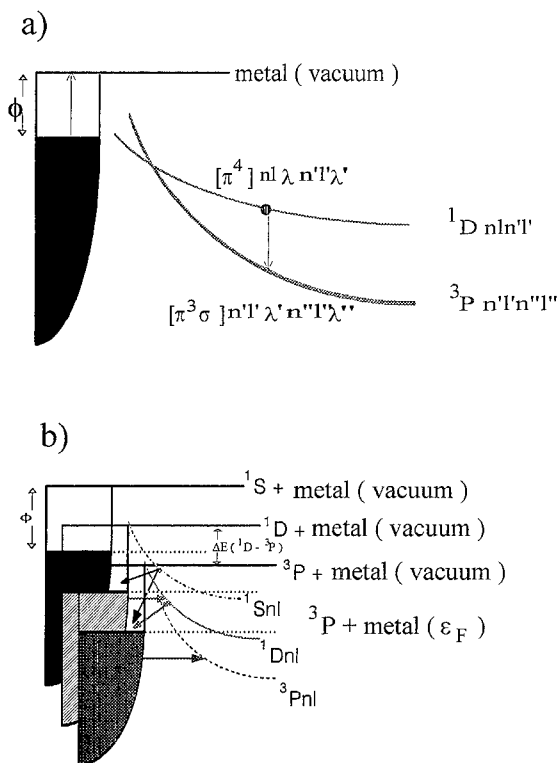


Fig. 9. Core rearrangement processes. (a) the quasimolecular gas phase analogue process, and (b) the resonant autoionisation process.

would involve electrons close to the Fermi level with energies comprised between zero (at the crossing point) to ones corresponding to the energy difference between these states at infinity. There are actually two problems with this interpretation. Firstly the energetics of the process is not very clear, because the positions of the energy levels of these states are shifted and are not known. Secondly this process would only be active for the rather short time of the separation of the quasimolecule for distances larger than the crossing point (circa 10^{-15} s for 1 keV Ne).

An alternative to this are atomic rearrangement processes [29,31], which are active after the collision has occurred as the excited particle flies away from the surface. In this case the effective distances are larger and the process would obviously be the more effective the longer the particle spends near the surface, i.e. for small perpendicular velocities.

A *resonant autoionisation rearrangement* process was suggested recently by us [31]. We attribute rearrangement to ionisation into the continuum represented by: metal + Ne^{2+} (^3P), followed by electron capture processes (Fig. 9b). This ionisation is the *analogue of the autoionisation of open shell atoms in their free states*. In case of these atoms we also deal with systems with several core states. Most singly excited states of the higher Rydberg series,

e.g. $\text{F}((2\text{p}^4)^1\text{Dnl})$ lie “naturally” above the $\text{F}^+((2\text{p}^4)^3\text{P})$ continuum and autoionise [32]. In case of Ne, most ^1D core states lie *below* the $^3\text{P} \text{Ne}^{2+}$ continuum limit. However, when we consider an atom or ion near a metal surface, we must consider level shifts induced by image charge effects, due to which excited state levels will lie above the Fermi level at small distances. Actually a level can be bound with respect to its parent continuum: metal + Ne^{2+} (^1D) (MDC), *but be autoionising with respect to the continuum*: metal + Ne^{2+} (^3P) (MPC). An excited atom or ion formed collisionally in the ^1Dnl configuration can thus autoionise into its parent *and* into the ^3P core related continuum. The resulting $\text{Ne}^{2+} \ ^3\text{P}$ or $\text{Ne}^{+*} \ ^3\text{Pnl}$ can then capture electrons giving the final state distribution. A numerical simulation of this process was performed and the results were in agreement with experimental trends. Note that a modification of the rearrangement process will occur if the workfunction changes since this will affect the range of atom surface distances during which resonant autoionisation can occur.

Additionally, autoionising states such as $\text{Ne}^{+*} (1\text{D} 3\text{s}^2)$ can decay into $\text{Ne}^{+*} (3\text{Pnl})$, a process observed by us in e.g., $\text{F}^{-**} (1\text{D} 3\text{s}^2)$ autodetachment [33].

A *direct Auger rearrangement* process was suggested by Drobnich [29], involving a direct transition between atomic excited states corresponding to the two cores. This process involves electrons from a band of an approximately 3.2 eV width, corresponding to the $(^3\text{P}-^1\text{D})$, located at the Fermi level. This process may be envisaged for Ne^{2+} , Ne^{+*} and Ne^{**} particles.

Finally we should also consider Auger capture processes into states with 2p vacancies such as the $2\text{p}^3 3\text{s}^2$ state seen at 31 eV in the electron spectrum. The filling of this 2p vacancy will lead to the production of 2p^4 core states and if we consider a sudden filling this would occur in a statistical ratio of $9(^3\text{P}):5(^1\text{D}):1(^1\text{S})$.

In a “real” situation all of these processes should exist and we see that the dominant observation of the ^3P core states can thus be explained.

8. Effects of adsorbates

In this section we shall discuss mainly the effects of oxygen adsorption. The effects of Na adsorption [34] are discussed elsewhere in these Proceedings [35].

In early experiments on Ne ion scattering on Mg surfaces, Rabalais et al. [5] noted that ion fractions decreased considerably on an oxydised surface. Grizzi et al. reported disappearance of the peaks due to autoionising states upon exposure of a Mg surface to 10 L of oxygen. Modifications in the proportions of the target excited state production in Ar scattering on Mg [36] and Al [37] surfaces have been observed.

We performed a study of the effects of initial stages of oxydation on the production of autoionising states in scat-

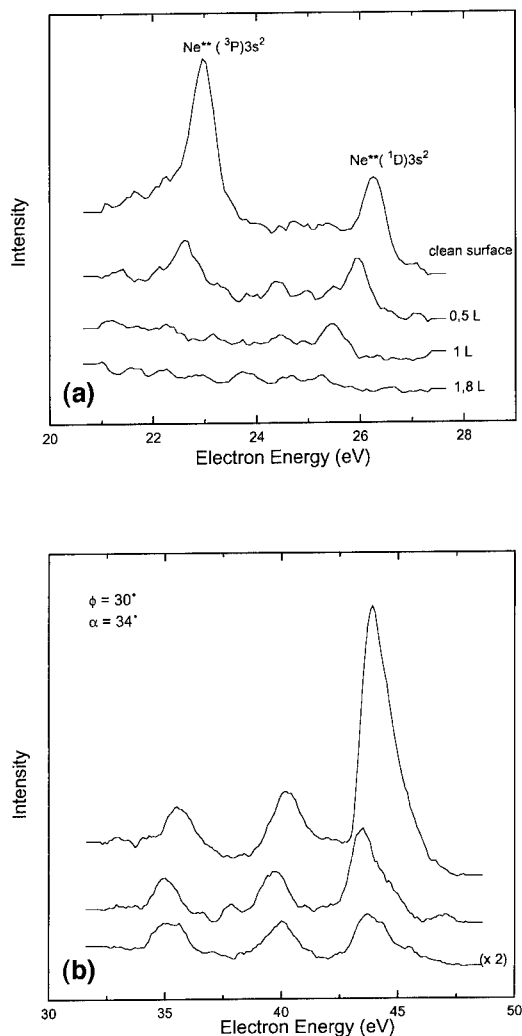


Fig. 10. Effect of initial stages of oxidation on (a) Ne^{**} states produced in 3.5 keV in Ne^+-Mg collisions (3° incidence, 34° detection), and (b) $\text{Mg}^+/\text{Mg}^{++}$ states in 4 keV Ar scattering on Mg (30° incidence, 34° detection).

tering on Mg and Al. It should be noted that we observed saturation of the O KLL AES intensity for exposures of about 2 L for Mg and for about 100 L for Al. In both cases we observed a drop in the surface workfunction. This was of about 1 eV for Mg, reached essentially at 1 L and of about 0.4 eV for a 30 L exposure on Al.

Fig. 10 shows the results of exposing an Mg surface to small doses of O_2 . As may be seen a dramatic drop in intensity of the $3s^2$ states is observed. The most intriguing feature is the initial strong drop and disappearance of the peak due to the ${}^3\text{P}3s^2$ state. A similar effect was observed for the Al target. In case of He scattering one also observes the attenuation of the He^{**} peak. In the case of Ar collisions the 44 eV peak assigned to neutral $\text{Mg}^* 2p^5 3s^2 3p$ is the most affected at small coverages. Actually

it is this attenuation of this peak by O_2 , which first led Baragiola [36] to propose the state assignment on the basis of the assumption that this peak is formed by neutralisation of Mg^{++} and this neutralisation should decrease upon oxygen adsorption.

It is interesting to note that the decrease of the intensities of the He, Ne (${}^1\text{D}$) $3s^2$ and of the Mg^{++} states on the one hand and of that of the Ne (${}^3\text{P}$) $3s^2$ and the Mg^* states follows different trends. This led us to suggest that the initial drop in the Ne (${}^1\text{D}$) $3s^2$ state intensity is due to a decrease of the core rearrangement rate. Note that an initial decrease of this state is also observed for Na adsorption, where the workfunction also decreases [34]. As described by us [31] and pointed out above, this effect is compatible with the prediction of the resonant autoionisation model of core rearrangement discussed above, since in this model the decrease of the workfunction will lead to a stabilisation of ${}^1\text{D}$ core states against resonant autoionisation and hence lead to a decrease in rearrangement.

We ascribed the general decrease of the intensity of all the peaks and also the above mentioned drop in charge fractions to screening of substrate Mg atoms by oxygen atoms. This is compatible with results of direct recoil measurements under grazing incidence conditions, which show a drop of Mg recoil and increase of O recoil ones [38]. As shown by Boumsellek and Esaulov Ne excitation is not observed in Ne–O collisions [39]. On the other hand the situation is different for Na adsorption because the efficiency of excited state production is greater at low energies on a Na target.

9. Concluding remarks

Collisions of inert gas ions with Na, Mg, Al and Si surfaces were investigated in the low keV energy range. Electronically inelastic excitation events in binary collisions of projectile and target atoms are observed. The general trend of excitations, i.e. excitation of He and Ne and not of Ar appears to correspond to what may be expected in atom–atom collisions in the gas phase and the primary excitation mechanism follows the predictions of diabatic MO diagrams [6,7]. A complex and not very clear question regards Rydberg orbitals. It has been suggested by Joyes [40] that as a result of promotion e.g. the $4f\sigma$ (see Fig. 8 for the Ne–Mg system) MO would cross above the Fermi level and this would lead to resonant ionisation and formation of Ne^{2+} . In terms of molecular states, which is what should be considered, this signifies that the energy level of the corresponding state in the quasimolecule would lie above the Fermi level. The production of excited states is then simply due to various electron capture processes. Capture processes will favour the production of the lowest lying excited states, which lie below the Fermi level, or cross under the Fermi level for relatively small atom–surface distances where capture processes are efficient

[31]. The alternative approach of considering transitions between states, that in fact may lie above the Fermi level and have acquired a certain width, is not clear.

An interesting difference between the results for Ne collisions and known gas phase data is that in our case dominant excitation of the autoionising $2p^4$ (3P) $3s^2$ state is observed. This dominance was attributed to core rearrangement processes near the surface. These concern transitions in the transient quasimolecule and scattered atoms.

Strong modifications are observed upon adsorption of oxygen and alkali atoms. Part of these modifications are due to changes in electron transfer rates and rearrangement processes and some are due to modifications due to collisions on both substrate and target atoms.

Additional experiments are being conducted to gain further insight into this complex problem. Theoretical studies of resonant and Auger electron capture and loss rates, and studies of the core rearrangement processes suggested here would be of much interest.

Acknowledgements

The authors would like to thank Yu. Bandurin, M. Barat, R. Baragiola, A. Borisov, D. Doweck, V. Droblich, J. Fayeton, J.P. Gauyacq, O. Grizzi, N. Mandarino, P. Nordlander, S. Pop, W. Rabalais, V. Sidis, I. Urazgildin and F. Xu for many interesting discussions.

References

- [1] L.K. Verhey, B. Poelsema and A.L. Boers, *Radiat Eff.* 34 (1977) 163.
- [2] W. Heiland and E. Taglauer, *Inelastic Ion-Surface Collisions*, eds. N.H. Tolk, J.C. Tully, W. Heiland and C.W. White (Academic Press, 1977) p. 27.
- [3] S. Valeri, *Surf. Sci. Rep.* 17 (1993) 85.
- [4] G. Zampieri, F. Meier and R. Baragiola, *Phys. Rev. A* 29 (1984) 116.
- [5] J.W. Rabalais, J.N. Chen and R. Kumar, *Phys. Rev. Lett.* 55 (1985) 1124.
- [6] M. Barat and W. Lichten, *Phys. Rev. A* 6 (1972) 211.
- [7] U. Fano and W. Lichten, *Phys. Rev. Lett.* 14 (1965) 627.
- [8] G.E. Zampieri and R. Baragiola, *Phys. Rev. B* 29 (1984) 1480.
- [9] J. Ostgaard Olsen et al., *Phys. Rev. A* 19 (1979) 1457.
- [10] J. Ostgaard Olsen and N. Andersen, *J. Phys. B* 10 (1977) 101.
- [11] N. Andersen and J. Ostgaard Olsen, *J. Phys. B* 10 (1977) L719.
- [12] J. Fayeton, Thesis, Université de Paris Sud, 1978, private communication.
- [13] J. Fayeton, N. Anderson and M. Barat, *J. Phys. B* 9 (1976) L149.
- [14] D. Doweck, Thèse de 3ème cycle, Université de Paris Sud, 1978; private communication.
- [15] R. Souda and M. Aono, *Nucl. Instr. and Meth. B* 15 (1986) 114.
- [16] O. Grizzi, M. Shi, H. Bu, J.W. Rabalais and R.A. Baragiola, *Phys. Rev. B* 41 (1990) 4789.
- [17] P. Bertrand, *Nucl. Instr. and Meth.* 170 (1980) 489.
- [18] S. Lacombe, L. Guillemot, M. Huels, Vu Ngoc Tuan and V.A. Esaulov, *Surf. Sci.* 295 (1993) L1011.
- [19] H.D. Hagstrum, *Phys. Rev.* 94 (1954) 336.
- [20] S. Lacombe, V. Esaulov, L. Guillemot, O. Grizzi, M. Maazouz, N. Mandarino and Vu Ngoc Tuan, submitted to *J. Phys. C*.
- [21] B. Hird, R.A. Armstrong and P. Gauthier, Submitted to *Phys. Rev. A* (1993).
- [22] S.V. Pepper and P.R. Aron, *Surf. Sci.* 169 (1986) 14.
- [23] T.E. Gallon and A.P. Nixon, *J. Phys.: Condens. Matter* 4 (1992) 9761.
- [24] F. Xu, N. Mandarino, A. Oliva, A. Bonanno, P. Zoccoli, M. Camarca and R. Baragiola, submitted to *Phys. Rev.*
- [25] V.A. Esaulov, submitted to *J. Phys. C*.
- [26] V.A. Esaulov, L. Guillemot and S. Lacombe, *Nucl. Instr. and Meth. B* 90 (1994) 305.
- [27] F. Xu and N. Mandarino private communication 1994.
- [28] S. Lacombe, L. Guillemot, M. Huels, Vu Ngoc Tuan and V.A. Esaulov, *Izvestia of the Russian Academy of Sciences* 58 (1994) 8.
- [29] L. Guillemot, S. Lacombe, M. Maazouz, Vu Ngoc Tuan, V.A. Esaulov, E. Sanchez, Yu. Bandurin, A. Daschenko and V. Droblich, to be published.
- [30] S. Lacombe, L. Guillemot and V.A. Esaulov, *Surf. Sci.* 304 (1994) L431.
- [31] V. Esaulov, *J. Phys. C* 6 (1994) L699.
- [32] S. Bomsellek and V.A. Esaulov, *J. Phys. B* 23 (1990) 279.
- [33] J.P. Grouard, V.A. Esaulov, R.I. Hall, J.L. Montmagnon and Vu Ngoc Tuan, *J. Phys. B* 19 (1986) 1483.
- [34] F. Xu, A. Baragiola, A. Bonanno, P. Zoccoli, M. Camarca and A. Oliva, *Phys. Rev. Lett.* 72 (1994) 4041.
- [35] A. Bonanno, presented at this Conference (IISC-10).
- [36] R. Baragiola, in: *Inelastic Particle-Surface Collisions*, eds. E. Taglauer and W. Heiland, Springer Series in Chemical Physics, vol. 17 (Springer, 1981) p. 38.
- [37] F. Xu and A. Bonanno, *Surf. Sci. Lett.* 273 (1992) L414.
- [38] S. Bomsellek and V.A. Esaulov, *J. Phys. B* 23 (1990) 1303.
- [39] J.A. Shultz, M.H. Mintz, T.R. Schuler and J.W. Rabalais, *Surf. Sci.* 146 (1984) 438.
- [40] P. Joyes, *J. Phys. (Paris)* 30 (1969) 243.

Auger deexcitation of $\text{Na}(2p^{-1})$ near alkali-halide surfaces

Raúl A. Baragiola *

Laboratory for Atomic and Surface Physics, University of Virginia, Thornton Hall, Charlottesville, VA 22901, USA

Abstract

This paper discusses recent observations of Na-2p Auger electron spectra produced during collisions of low energy ions with sodium halide surfaces. The spectra are explained on the basis of a model which considers that sharp Auger features originate from $\text{Na}^* 2p^5 3l 3l'$ atoms decaying in vacuum and that the outer shell ($3l 3l'$) populations are determined at curve crossings outside the surface.

1. Introduction

Shallow core levels of light elements can be excited during low energy ion surface collisions and studied by measuring the electron spectra resulting from the Auger decay. Such studies provide very detailed insight on different inelastic collision mechanisms, because electron spectroscopy gives information on inner- and outer-shell populations, on the atomic environment at the point of decay, and on the velocity distribution of the excited atoms. Discussions in the field of ion-induced Auger emission from solids have included many controversies regarding the main excitation process (projectile-target vs. target-target collisions), the assignment of atomic or solid-state transitions to Auger spectral features, and the location where deexcitation takes place (inside vs. outside the solid).

These controversies – summarized in recent reviews [1,2] – have been extended recently by reports by Fine et al. [3,4] on measurements of the energy spectra of electrons ejected from the (100) surfaces of sodium halide salts by impact of Ne and Ar ions in the energy range 0.4–5 keV. For NaCl, NaF and NaI, the electron spectra (Fig. 1) show three narrow (~ 1.6 eV) Auger peaks of similar height with energies of 25.7, 28.0 and 30.9 eV, which agree with those of free $\text{Na}^* 2p^5 3s 3l$ atoms decaying in vacuum [5]. The spectra are different from those for ion impact on Na adsorbed on metals, or on metallic Na, where the $\text{Na}^* 2p^5 3s^2$ Auger peak dominates the spectra [6–8]. They also differ from electron spectra induced by electron bombardment of the undamaged salts which show no visible Na-2p Auger structure at these energies. Based on these differences, Fine et al. conclude that the narrow

peaks are from 2p-excited Na, formed by a presumably new class of inelastic collision processes, and undergoing collisional deexcitation inside the solid. Below, it will be shown that this interpretation is not valid, and propose an alternative picture: the sharp electron peaks originate from Auger, rather than *collisional* deexcitation occurring *outside*, rather than *inside* the solid.

2. Model

The interpretation that the Auger lines are from atoms decaying *outside* the solid follows directly from these key observations: i) the Auger energies in these experiments are like those of free Na^* , and not like those of electron bombarded Na halides, ii) the energies of bulk core-excited ($\text{Na}^{+*} 2p^5 3l$) and Auger transitions [9] differ very much among different Na halides, unlike the spectra of Fine et al. and iii) the $\text{Na}^* 2p^5 3s 3l$ energies inside the solid should also differ from those outside, since the $3l$ orbits overlap with halogen valence orbitals or are even larger than the lattice spacing. For instance, the extent (mean diameter) of the 3s, 3p and 3d orbitals of this configuration are ~ 3 , 5, and 10 Å, respectively [10], while the lattice spacing of NaCl is 2.8 Å.

To explain the formation of the core-excited neutral Na, one needs to extend to insulators, the mechanisms used successfully to explain other ion-induced 2p Auger spectra in second-row elemental solids [1,2]. In these materials, electron excited atoms decay inside giving “bulk” Auger lines with energies that reflect twice the width of the valence band. Under ion bombardment, in addition to the bulk feature, sharp “atomic” lines are observed which correspond to excited atom decaying in vacuum. This is possible since the close atomic collisions needed to promote the 2p orbitals [2] can sputter the excited atom.

For instance, in metallic Na, some 2p-excited atoms which decay inside the solid, yield a broad Auger line [6],

* Corresponding author. Tel. +1 804 982 2907, fax +1 804 924 1353.

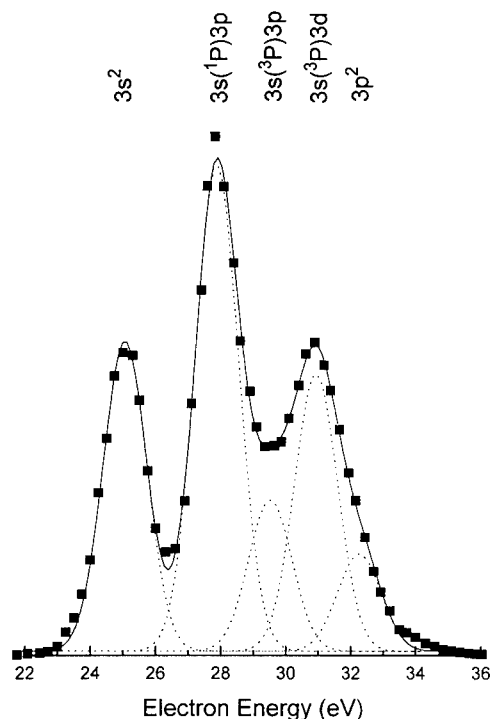


Fig. 1. Decomposition of background-subtracted electron spectra from NaCl from Fine et al. [3,4] into atomic Auger lines.

very similar to that excited by electron bombardment. The proportion of atoms decaying inside vs. outside the solid depends sensitively on the lifetime of the 2p-vacancy [11]. Bulk Auger transitions have been observed in sodium halides by Kamada et al. [9] under electron bombardment of undamaged crystals. Narrow Na-2p Auger lines are observed at energies between 10 and 16 eV with respect to the vacuum level, much lower than those reported by Fine et al. under ion bombardment. These lines are weak, possibly because radiative decay is important due to the short transition rates expected for inter-atomic Auger decay in ionic crystals.

Contrary to the case of bombardment with electrons or X-rays, excitation by collisions with keV heavy ions usually results in substantial momentum transfer to the Na atom, displacing it from the lattice site. If the Na atom suffers an additional violent collision with another lattice atom, it can transfer its core vacancy [12]. This is an unlikely event since the crystalline structure of the solid acts to prevent multiple hard collisions at low energies. After being excited, the Na atom will then slow down in the solid or be ejected from it, a case not considered by Fine et al. The slowing down or the ejection will occur faster than the Auger decay if τ_{2p} , the lifetime of the 2p-hole, is long. There are no reports on τ_{2p} in alkali-halides, but one can expect that due to the decreased overlap of the hole with valence electrons at the cation site, it will be larger than the values $\geq 10^{-13}$ s calculated

for free neutral Na* [5], i.e., larger than the lifetime of collision cascades. Therefore, the Na⁺⁺ will either decay at rest after the collision cascade has quieted or outside the solid after it is ejected. If the Na⁺⁺ decays while at rest in the solid, it will emit an X-ray or an electron from an inter-atomic Auger process, with energies similar to those resulting from electron or X-ray bombardment. Auger electrons from transitions inside the solid (at 10–16 eV, see above) are not evident in the ion bombarded spectra, possibly because their intensities are too weak to be discerned above the background of the cascade of low energy electrons induced by the bombarding ions. Atoms decaying by the Auger process outside the solid will produce electrons with energies typical of those of free atoms, as observed. The intensity of Auger emission from atoms decaying outside the solid will decrease with halogen loss from the sample caused by radiation damage, as observed, due to a decrease in the hole lifetime caused by the increased overlap of the 2p hole with “metallic” electrons.

The outer-shell population of excited, sputtered atoms will be determined by the competition of electron capture and loss processes with the surface. This population will be different for atoms receding from a metal than from an insulator surface, due to the different density and localization of electron states at the surface. This is confirmed by the difference in the spectra of pure and oxidized metals [2] and by the difference between metallic Na and the Na halides being analyzed here.

In metallic Na, a sputtered Na⁺⁺ 2p⁵3s ion will capture an electron in a resonant transition from states near the Fermi level. Only excited atomic states with an ionization potential I larger than the work function of the surface can survive resonant ionization into the metal conduction band [13]. Taking into account a 1–2 eV image shift near the surface, then only 2p⁵3s² and, marginally, 2p⁵3s(¹P)3p and 2p⁵3p² can form even at sites with low local work function, as observed by Brenten et al. [7].

Let us consider now the case of an alkali halide, like NaCl, where, in contrast with metallic Na, there is no continuum of empty states available for resonance ionization. Since sodium exists essentially as Na⁺ inside the ionic crystal, a 2p-excitation in a violent collision will lead to either Na²⁺2p⁵ or to the core excitons Na⁺⁺ 2p⁵3s,p,d. These ionic configurations will have a long range attractive Coulomb interaction with the surface and the bandgap electron state left behind. This attractive ionic state (Na⁺⁺ + crystal⁻) will approach closely or cross neutral states (Na* + crystal) that lead to the final Na* 2p⁵3/3' configurations observed. An electron can be transferred when the states are close or cross, leading to the excited neutral Na* that can decay by the Auger process.

To calculate which crossings can occur, one needs to know the relative positions of the asymptotic energy levels. For a crossing to occur at distances > 2 Å from the surface, the asymptote of the ionic curve has to be above

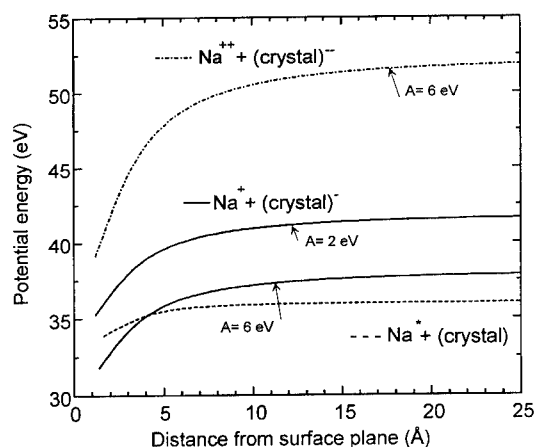


Fig. 2. Schematic potential curves for 2p-excited sodium near a NaCl surface. The ionic curves are estimated using a Born–Haber cycle and atomic state energies, as done by Williams for the case of SIMS of alkali halides [14,15]. The separation is $\Delta = I - A$, where I (< 7.1 eV [5]) is the ionization potential of the excited Na in vacuum and A is the energy gained by the electron when it drops to the affinity level in the solid. The formation of the different $\text{Na}^* 2p^5 3l'$ states from different $\text{Na}^{++} 3l$ requires A less than 5–7 eV. Different affinity states in the bandgap exist, depending on what is the state of the crystal during the ejection process. Since we are dealing with a surface process where a cation vacancy is created during ejection, one should not use the value of A for a bulk halogen site ($A \sim 9.3$ eV for NaCl [16]), as proposed in Ref. [4]. Values of surface states are in the range $A \sim 2$ –4 eV [17], whereas $A \sim 2.4$ if the electron is left in a configuration similar to that of a bulk F-center. Values of A as low as 0.8 eV result from photoemission thresholds of ion damaged alkali halides [18]. It should be pointed out, however, that the required band-gap state does not have to exist or be populated before impact since it is created dynamically near the ejection site in the collision cascade.

that of the neutral curve by $0 < \Delta \leq 7$ eV. The asymptotic separation Δ can be estimated using a Born–Haber cycle and atomic state energies, as done by Williams for the case of SIMS of alkali halides [14,15]. The separation is $\Delta = I - A$, where I (< 7.1 eV [5]) is the ionization potential of the excited Na in vacuum and A is the energy gained by the electron when it drops to the affinity level in the solid. The formation of the different $\text{Na}^* 2p^5 3l'$ states from different $\text{Na}^{++} 3l$ requires A less than 5–7 eV. Different affinity states in the bandgap exist, depending on what is the state of the crystal during the ejection process. Since we are dealing with a surface process where a cation vacancy is created during ejection, one should not use the value of A for a bulk halogen site ($A \sim 9.3$ eV for NaCl [16]), as proposed in Ref. [4]. Values of surface states are in the range $A \sim 2$ –4 eV [17], whereas $A \sim 2.4$ if the electron is left in a configuration similar to that of a bulk F-center. Values of A as low as 0.8 eV result from photoemission thresholds of ion damaged alkali halides [18]. It should be pointed out, however, that the required band-gap state does not have to exist or be populated before impact since it is created dynamically near the ejection site in the collision cascade.

As an example, Fig. 2 illustrates processes leading to the observed $\text{Na}^* 2p^5 3s^2 \rightarrow \text{Na}^+ 2p^6$ Auger line, for core excited $\text{Na}^{++} 2p^5$ and $\text{Na}^+ 2p^5 3s$ and two values of A . Actual potential curves will differ according to the degree of lattice relaxation during ejection, which is not known due to the complexity and the variability of the sputtering process. One can see that $\text{Na}^* 2p^5 3s^2$ ($I = 7.2$ eV) can be formed at a crossing; similar crossings which occur for the other final outer-shell neutral states, and starting from different $\text{Na}^{++} 2p^5 3p, d$ core excitons, have been omitted from the figure for clarity. One can notice in Fig. 2 that it is unlikely to form the neutral state from the doubly

charged Na^{2+} configuration, which explains the lack of Auger emission from ejected cations in high-valency insulators [19].

3. Summary and final remarks

In summary, Auger emission from ion bombarded alkali halides can be explained by a model that is consistent with previous results and which does not require to postulate a new mechanism in the solid. Although I propose, like Fine et al., that Na^* is formed from Na^{++} by electron capture, this does not occur in a close, energetic, collision in the bulk but at a crossing when the excited sodium leaves the solid. While the model described here is similar to the bond-breaking model in SIMS [14,15], it is important to note that the ejection of a core-excited atom is not a typical ion sputtering event [2] and that different surface sites may play the dominant role in different ejection processes. Also, and for completeness, I point out that an additional mechanism, the Auger decay of excited sodium halide molecules in vacuum, can occur but was not considered here since the Auger energies would depend on the type of molecule, contrary to observations.

References

- [1] S. Valeri, Surf. Sci. Rep. 17 (1993) 85.
- [2] R.A. Baragiola, in: Low Energy Ion–Surface Interactions, ed. J.W. Rabalais (Wiley, 1994) Chap. 4.
- [3] J. Fine et al., M. Szymonsky, J. Kolodziej, M. Yoshitake and K. Frazzeb, Nucl. Instr. and Meth. B 78 (1993) 129.
- [4] J. Fine, Phys. Rev. Lett. 71 (1993) 3585.
- [5] O.I. Zatsarinny and L.A. Bandurina, J. Phys. B 26 (1993) 3765.
- [6] J.-F. Hennequin and P. Viaris de Lesegno, Surf. Sci. 42 (1974) 50.
- [7] H. Breiten, H. Müller and V. Kempter, Surf. Sci. 271 (1992) 103.
- [8] F. Xu, R.A. Baragiola, A. Bonanno, P. Zoccali, M. Camarca and A. Oliva, Phys. Rev. Lett. 72 (1994) 4041.
- [9] M. Kamada, O. Aita, K. Ichikawa and K. Tsutsumi, Phys. Rev. B 36 (1987) 4962.
- [10] C. Froese-Fischer, Phys. Rev. A 34 (1986) 1667.
- [11] O. Grizzi and R.A. Baragiola, Phys. Rev. A 30 (1984) 2297.
- [12] R.A. Baragiola, Phys. Rev. A 19 (1979) 2470.
- [13] G.E. Zampieri and R.A. Baragiola, Surf. Sci. 114 (1982) 15.
- [14] P. Williams, Appl. Surf. Sci. 13 (1982) 241.
- [15] P. Williams, Intl. J. Mass Spectr. Ion Phys. 53 (1983) 101.
- [16] N. Itoh, A.M. Stoneham and A.H. Harker, Surf. Sci. 217 (1989) 573.
- [17] E.C. Honea, M.L. Homer, P. Labastie and R.L. Whetten, Phys. Rev. Lett. 63 (1989) 394.
- [18] F. Yan and N. Tolk, Vanderbilt University, private communication.
- [19] K. Franzreb, M. Yoshitake, J. Fine, M. Szymonsky and J. Kolodziej, presented at this Conference (IISC-10).

Spin-dependent studies of the dynamics of $\text{He}(2^3\text{S})$ atom deexcitation at surfaces

F.B. Dunning*, P. Nordlander

Department of Physics and the Rice Quantum Institute, Rice University, P.O. Box 1892, Houston, TX 77251, USA

Abstract

Electron spin labelling techniques provide a powerful technique with which to probe the dynamics of $\text{He}(2^3\text{S})$ atom deexcitation at surfaces. Studies with a clean $\text{Cu}(100)$ surface reveal that deexcitation occurs exclusively through resonance ionization followed by Auger neutralization and that the electrons involved in Auger neutralization are correlated in spin. Model calculations suggest that this can be explained by considering the local perturbation in the surface electronic structure induced by the presence of the (polarized) He^+ ion. The calculated induced densities of states are spin dependent and exhibit sharp Kondo-like resonances near the Fermi level. Measurements at an adsorbed Xe film are also described and suggest that electron ejection results both from direct Auger deexcitation (surface Penning ionization) and from resonance ionization of incident atoms, the resulting ions being neutralized through an interaction that involves neighboring Xe atoms in the film. The Xe film data provide an unusual example of a surface at which resonance ionization and Auger deexcitation occur in parallel with comparable rates.

1. Introduction

Spin labelling techniques, specifically the use of electron-spin-polarized $\text{He}(2^3\text{S})$ atoms coupled with energy-resolved measurements of the ejected electron polarization, provide a powerful means to investigate the dynamics of $\text{He}(2^3\text{S})$ metastable atom deexcitation at surfaces. This approach complements earlier studies of reaction dynamics that were based solely on analysis of the energy distributions of product electrons. Conventional models suggest that at clean high-work-function metal surfaces $\text{He}(2^3\text{S})$ atoms will be deexcited exclusively by the two-step process diagrammed in Fig. 1a [1]. An incident 2^3S atom first undergoes resonance ionization (RI) in which the excited 2s electron tunnels into a vacant level above the Fermi level. The resulting He^+ ion continues toward the surface where it is neutralized by a conduction electron from the metal. The energy released is communicated to a second electron which, if the energy transfer is sufficient, may be ejected from the surface. This Auger neutralization (AN) process results in a relatively structureless ejected electron energy distribution that reflects, approximately, a self-convolution of the local density of electronic states at the surface. At low-work-function surfaces RI cannot occur because, as shown in Fig. 1b, there are no unfilled levels

of appropriate energy available. The 2^3S atoms may then be deexcited by an Auger deexcitation (AD) process in which an electron from the metal tunnels into the 2^3S 1s core hole. The energy released is communicated to the excited 2s electron which may be ejected. Since AD is a

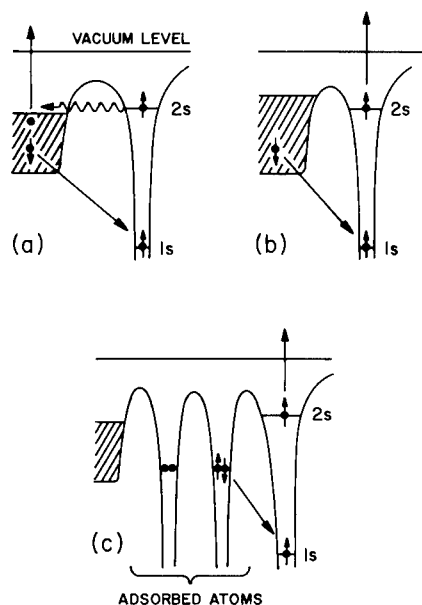


Fig. 1. Schematic diagram of the electron ejection processes that can occur at clean and adsorbate-covered surfaces.

* Corresponding author. Tel. +1 713 527 8101 (3544), fax +1 713 285 5143, e-mail fhd@spacsun.rice.edu.

quasi-one-electron process, the ejected electron energy distribution reflects directly the local density of electronic states and can contain relatively sharp features. As illustrated in Fig. 1c, the presence of adsorbed layers on a high-work-function surface can also impede RI by reducing the overlap between the 2s electron wavefunction and vacant levels in the metal. Deexcitation may again occur by AD and, because the electron that tunnels into the 2^3S 1s core hole originates from the adsorbate layer, the process is analogous to gas-phase Penning ionization (PI) [2] and is frequently termed surface Penning ionization (SPI).

The ejection processes operative can be probed directly by spin labelling. In RI + AN, the electron originates in the surface suggesting that, for non-magnetic surfaces and in the absence of any spin correlations, the ejected electron polarization should be zero. In contrast in AD (SPI) it is the (polarized) 2s electron that is liberated and the ejected electron polarization should equal that of the incident 2^3S atoms. Data obtained at a clean Cu(100) surface show that $\text{He}(2^3\text{S})$ deexcitation occurs exclusively through RI + AN, but that the electrons involved in the AN process are correlated in spin. Model calculations are presented that suggest that the observed correlation is due to perturbations in the local surface electronic structure induced by the (polarized) He^+ ion. The He^+ ion–surface interaction is characterized by strong electron correlation, and many-body effects can be significant. These result in a strongly enhanced local density of electrons near the Fermi energy with the same spin orientation as the incident He^+ ion through the formation of a Kondo-like resonance. Studies with adsorbed Xe films are also described and suggest that electron ejection results both from AD (SPI) and from RI of incident 2^3S atoms followed by neutralization of the resulting He^+ ion through an interaction that involves neighboring atoms in the film. The Xe data provide one of the few examples of a surface at which AD and RI occur in parallel with comparable rates.

2. Experimental technique

The present apparatus is shown schematically in Fig. 2, and has been described in detail elsewhere [3–5]. Briefly, a

fraction of the atoms contained in a ground-state helium beam formed by a multichannel array is excited to the $2^{1,3}\text{S}$ metastable levels by a coaxial electron beam. The 2^1S atoms may be removed from the beam by illuminating it with $2.06\text{ }\mu\text{m}$ radiation from a helium discharge lamp that excites $2^1\text{S} \rightarrow 2^1\text{P} \rightarrow 1^1\text{S}$ transitions. Charged particles produced by electron impact are removed by a transverse electric field. A weak ($\sim 0.5\text{ G}$) magnetic field is applied perpendicular to the beam to establish a well-defined quantization axis. Circularly-polarized $1.08\text{ }\mu\text{m}$ $2^3\text{S} \leftrightarrow 2^3\text{P}$ radiation from a high-power rf-excited lamp, incident along the magnetic field direction, is used to optically pump the 2^3S atoms to increase the relative populations in the $M_J(M_S) = +1$ or -1 magnetic sublevels. The resultant beam polarization P_z , defined as

$$P_z = \frac{n_+ - n_-}{n_+ + n_0 + n_-}, \quad (1)$$

where n_+ , n_0 and n_- are the numbers of atoms in the $M_J(M_S) = +1, 0$ and -1 magnetic sublevels, respectively, is measured by moving the target surface and allowing the beam to enter a Stern–Gerlach analyzer.

Depending as the measurement being undertaken, the target surface is positioned normal to the axis of either a retarding-potential energy analyzer or a Mott polarimeter. The retarding-potential analyzer (energy resolution $\sim 0.6\text{ eV}$ FWHM) is used to measure directly ejected electron energy distributions (EEDs). For comparison purposes, EEDs were determined for $\text{He}(2^1\text{S})$ and $\text{He}(2^3\text{P})$ atoms as well as for $\text{He}(2^3\text{S})$ atoms. EEDs for 2^3S atoms were observed directly using a pure 2^3S incident beam. EEDs for 2^1S atoms were determined by taking the difference between distributions measured with and without the 2^1S quench lamp turned on. The 2^3P atoms were created by transversely illuminating the 2^3S atom beam at the target surface with $1.08\text{ }\mu\text{m}$ $2^2\text{S}_1 \rightarrow 2^3\text{P}_2$ radiation from a single-mode, Coherent CR899-21 Ti:sapphire laser. Tests revealed that the 300 mW output power provided by the laser, which was optimized for operation at $1.08\text{ }\mu\text{m}$, was more than sufficient to saturate the $2^3\text{S} \rightarrow 2^3\text{P}$ transition [6]. EEDs for 2^3P atoms were obtained by measuring the distribution for a mixed $2^3\text{S}/2^3\text{P}$ beam and subtracting the 2^3S contribution.

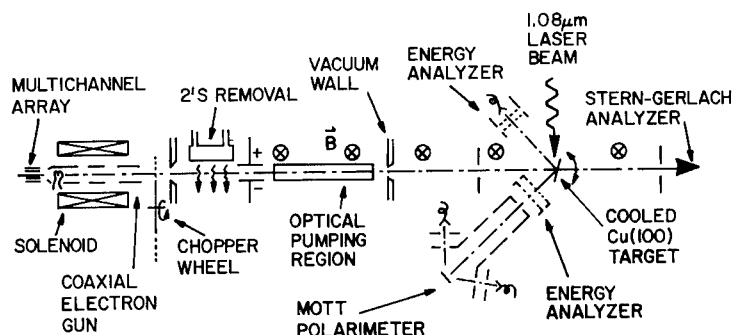


Fig. 2. Schematic diagram of the apparatus.

Ejected electron polarizations were determined using a compact Mott polarimeter equipped with a retarding-potential energy analyzer at its input to permit energy-resolved measurements. The electron polarization P is defined as

$$P = \frac{n_{\uparrow} - n_{\downarrow}}{n_{\uparrow} + n_{\downarrow}}, \quad (2)$$

where n_{\uparrow} and n_{\downarrow} are the numbers of electrons with spin up ($m_s = +\frac{1}{2}$) and spin down ($m_s = -\frac{1}{2}$), respectively. (Using Eqs. (1) and (2) it can be shown that the net spin polarization of the $\text{He}(2^3\text{S})$ atomic electrons is numerically equal to the atomic polarization P_z .) In all measurements, a mechanical chopper is used, in conjunction with time-of-flight techniques, to discriminate against electron ejection caused by fast neutrals or photons that might be produced in the source.

The Cu(100) target surface was mounted on a LHe-cooled dewar. It was initially prepared by repeated cycles of 500 eV Ar^+ ion sputtering followed by annealing. Surface cleanliness and order were monitored by Auger electron spectroscopy (AES) and low energy electron diffraction (LEED). Sputtering/annealing cycles were continued until surface contamination levels were below the AES detection limit and a sharp LEED pattern was obtained. To prepare Xe adsorbate films, the substrate was cooled to ~ 25 K and Xe gas admitted to the system, typically at pressures of 10^{-6} to 10^{-7} Torr, until the required exposure was obtained.

3. Results and discussion

3.1. Clean Cu(100)

The electron energy and polarization distributions observed following $\text{He}(2^3\text{S})$ deexcitation at a clean Cu(100) surface are shown in Fig. 3. The electron polarization is expressed as a percentage of that of the 2^3S atoms. Ejection at a Cu(100) surface is expected to occur through RI + AN because its work function ϕ (4.59 eV) is such that, even at relatively large (~ 10 Å) distances from the surface, the 2^3S level lies well above the Fermi level. The broad relatively featureless EED is consistent with deexcitation via RI + AN. The ejected electron polarization, however, is nonzero and at the highest energies is quite large, which might be explained if some of the incident 2^3S atoms undergo direct AD. To examine this possibility, EEDs were measured using incident 2^1S and 2^3P atoms and these are also included in Fig. 3. It is apparent that the increased internal energy associated with 2^1S and 2^3P atoms does not result in any significant changes in the measured EEDs. (The $2^1\text{S}(2^3\text{P})$ level lies 0.80 (1.14) eV higher than the 2^3S level.) This can only be explained if, in each case, deexcitation occurs exclusively through RI + AN, i.e., if the tunneling rates associated with 2^3S , 2^1S

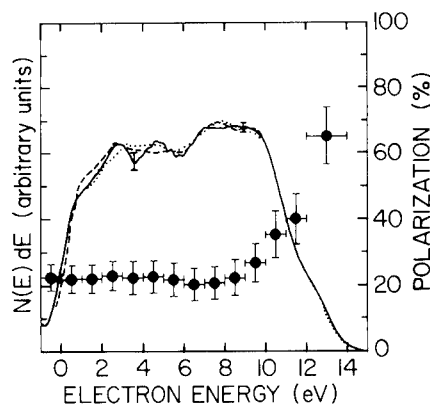


Fig. 3. Electron energy distributions resulting from deexcitation of $\text{He}(2^3\text{S})$ (—), $\text{He}(2^1\text{S})$ (---) and $\text{He}(2^3\text{P})$ (···) atoms at a clean Cu(100) surface. Points: ejected electron polarizations measured with polarized $\text{He}(2^3\text{S})$ incident atoms. The polarization is expressed as a percentage of that of the incident 2^3S atoms.

and 2^3P atoms are such that (for thermal incident energies) each incident atom is converted to a He^+ ion prior to ejection occurring. Thus, even though calculations show that for a given atom–surface separation the tunneling rates are substantially larger for 2^3P atoms than for 2^3S atoms [7], the tunneling rates for 2^3S atoms must still be sufficiently large that none are able to survive passage to regions sufficiently close to the surface that AD can occur. Since 2^3S deexcitation occurs exclusively through RI + AN, the observed electron polarization requires that the electrons involved in the AN process tend to have antiparallel spins resulting in the preferential formation of singlet two-hole final states at the surface. This is evident from Fig. 1a: the He^+ 1s core hole must be filled by a spin down electron (the helium ground state is a spin singlet) but, as shown by experiment, this is accompanied by preferential ejection of a spin up electron. (For definiteness, the incident $\text{He}(2^3\text{S})$ atoms will henceforth be assumed to be polarized as shown in Fig. 1 in the $M_J = +1$ state for which both the 1s and 2s electrons are spin up.) The observed spin correlation is quite large, and might be exploited to analyze the polarization of a low-energy He^+ ion beam.

A model has been developed that accounts for the spin correlation in AN by considering the transition rates associated with ejection of spin-up and spin-down electrons separately [8]. The incident He^+ ion must be neutralized by a spin down electron from the metal, but the ejected electron can have spin up or down. As illustrated in inset (a) in Fig. 4, there is, for specific initial and final states, only a single process by which ejection of a spin-up electron can occur. In contrast, as shown by the solid and dashed arrows in inset (b) in Fig. 4, there are two processes that can give rise to ejection of a spin-down electron. Model calculations, undertaken using approximate metal and atomic wavefunctions, and including surface

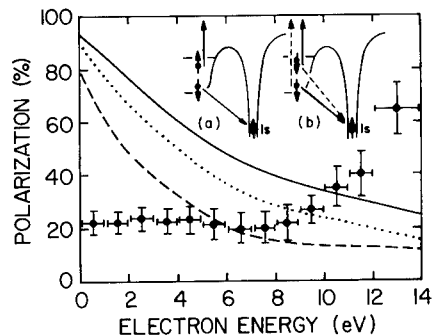


Fig. 4. Ejected electron polarizations calculated taking into account interference effects assuming Auger neutralization occurs 2.5 Å (—), 3.0 Å (· · ·) and 4.0 Å (---) from the surface. Points: experimental results. The insets show schematically the processes that can give rise to ejection of spin-up and spin-down electrons.

screening, suggest that interference between these two processes reduces the probability for ejecting spin-down electrons as compared to that for ejecting spin-up electrons. The predicted ejected electron polarizations resulting from neutralization at several different ion-surface separations are shown in Fig. 4 and depend strongly on ion-surface separation. The predicted energy dependence of the ejected electron polarization, however, is in poor agreement with the experimental data. To account for this discrepancy it is suggested by the authors that unpolarized secondary electrons produced in electron-electron collisions are important and provide a significant contribution to the total ejected electron signal. This would reduce the measured polarizations, especially at lower electron energies where the possible contribution of secondary electrons to the total ejected electron signal is the greatest. The large increase in electron polarization observed at the higher energies was attributed to contributions from AD but, as discussed earlier, EED measurements show that electron ejection results exclusively from RI + AN.

The general characteristics of the experimental data can, however, be explained by considering the perturbation in the surface electronic structure induced by the presence of the polarized He^+ ion. The major perturbation to the density of states is associated with interactions that involve the helium 2s orbital. The 2^1S and 2^3S atomic levels each broaden and shift upwards as the atom-surface separation decreases. Although RI occurs, these levels are sufficiently broad that they extend below the Fermi level ε_F allowing each to be partially filled by electrons from the metal. This will increase the local density of states in the vicinity of ε_F and, because the 2^1S level lies significantly higher in energy than the 2^3S level, this increase will be largest for the triplet state (assuming that the 2^1S and 2^3S widths are comparable) resulting in a marked spin dependence in the induced local density of states. Calculation of secondary electron distributions resulting from Auger neutralization

is a very challenging problem, but a qualitative understanding of the underlying physics can be achieved by adopting some simplifying assumptions.

The helium-induced local density of states can be calculated using the Anderson Hamiltonian [9]

$$H = \sum_{k\sigma} \varepsilon_k n_{k\sigma} + \sum_{\sigma} \varepsilon_{\sigma} n_{\sigma} + \frac{1}{2} \sum_{\sigma \neq \sigma'} U_{\sigma\sigma'} n_{\sigma} n_{\sigma'} + \sum_{k,\sigma} V_{k\sigma} c_{\sigma}^{\dagger} c_{k\sigma} + \sum_{k,\sigma} V_{k\sigma}^* c_{k\sigma}^{\dagger} c_{\sigma}. \quad (3)$$

Here, ε_{σ} denotes the energy of the different electronic states σ of the helium atom. The subscript k refers to the Bloch momentum and band index of the metal conduction electrons. $U_{\sigma\sigma'}$ represents the intra-atomic Coulomb repulsion between the different helium states. $V_{k\sigma}$ is the hopping matrix element between the helium state $|\sigma\rangle$ and the corresponding conduction electron state in the substrate $|k, \sigma\rangle$. It is assumed that spin is conserved during electron tunneling.

The presence of the intra-atomic correlation term U significantly complicates the diagonalization of the Hamiltonian. In the case of helium at a copper surface, the intra-atomic correlation term is large allowing the induced local density of states to be calculated using the slave-boson approach and a Greens function technique [10]. The surface is approximated using a jellium model characterized by a half-filled elliptical conduction band. The unperturbed density of states at the surface thus takes the form

$$\rho_{\sigma}^0(\varepsilon) = \frac{3}{2} \left[1 - \left(\frac{\varepsilon}{D} \right)^2 \right] \quad (4)$$

for $\varepsilon \in (-D, D)$, where D is the half-bandwidth, and is zero elsewhere. For copper, D is taken to be 7.0 eV.

The shift and broadening of the helium 2^3S level near a copper surface has been calculated using the complex scaling method [7]. In the range of atom-surface separations Z of interest here, $2 \text{ a.u.} \leq Z \leq 8 \text{ a.u.}$, the shifts are image-like and can be parameterized as

$$\varepsilon_{\sigma}(Z) = \varepsilon_{\sigma}^0 + \frac{27.2}{4Z} \text{ eV}. \quad (5)$$

In the same range of Z , the widths can be expressed as

$$\Gamma_{\sigma}(Z) = 1.4 \exp(-0.14Z) \text{ eV}. \quad (6)$$

It is assumed that the width of the 2^1S state can be parameterized similarly.

The calculated induced local densities of states $\rho_{\sigma}^{\text{ind}}$ due to the presence of the (polarized) helium ion are shown in Fig. 5a for $Z = 6 \text{ a.u.}$, and are spin dependent. The sharp non-Lorentzian features just below the Fermi energy result from intra-atomic correlation effects and are similar in origin to the Kondo peaks seen in the heavy fermion problem [10]. Although the degeneracy of the $\text{He}(2\text{s})$ level is lifted, the broadening of the singlet and triplet levels is larger than their energy difference resulting

in a non-Lorentzian density of states. A calculation using $U=0$ would have predicted considerably smaller spin polarization. The qualitative features of $\rho_{\sigma}^{\text{ind}}$ are similar for all separations in the range 2 a.u. $< Z < 8$ a.u.

In order to estimate the total effective density of states at the surface relevant for the Auger process, the induced local density of states and assumed unperturbed surface density of states are simply added yielding

$$\rho_{\sigma}^{\text{eff}}(\varepsilon) = \rho_{\sigma}^0(\varepsilon) + \rho_{\sigma}^{\text{ind}}(\varepsilon). \quad (7)$$

The quantity thus constructed provides a measure of the density of states of surface electrons near the helium ion. This effective density of states for $Z=6$ a.u. is shown in Fig. 5. A marked spin dependence in the total density of states is evident.

The energy dependence of the ejected electron polarization can again be obtained by considering separately the probability for ejection of spin-up and spin-down electrons. If energy and spin dependences in the coupling matrix elements are neglected, the ejected currents of spin-up and spin-down electrons will be related by

$$I_{\uparrow}(\omega) \propto \int d\varepsilon' \rho_{\downarrow}^{\text{eff}}(\varepsilon' - \phi) \rho_{\uparrow}^{\text{eff}}(\omega - \varepsilon_{1s} - \varepsilon' + \phi),$$

$$I_{\downarrow}(\omega) \propto \int d\varepsilon' \rho_{\uparrow}^{\text{eff}}(\varepsilon' - \phi) \rho_{\downarrow}^{\text{eff}}(\omega - \varepsilon_{1s} - \varepsilon' + \phi), \quad (8)$$

where ω is the energy of the emitted electron and ε_{1s} is the ionization potential of the helium atom. (The He^+ ion must be neutralized by a spin-down electron.) The predicted polarizations are shown in Fig. 5b for several ion-surface separations. The general agreement between theory and experiment is quite good, especially considering the simple assumptions inherent in the calculations. In particular, the calculations correctly predict the large increase in polarization observed at the highest electron energies. This results because, in this energy regime, both electrons involved in AN must originate near the Fermi level where the spin-dependence in the densities of states is greatest. The predicted polarizations, however, lie somewhat below the measured values. This may be due to matrix element effects or to the assumed shape of the conduction band. The latter possibility will be tested in the future by using more realistic band structures. Kondo-like features, however, will appear in the total density of states independent of the assumed band structure.

3.2. Adsorbed Xe films

Fig. 6 shows EEDs observed for $\text{He}(2^3\text{S})$ deexcitation at a cooled $\text{Cu}(100)$ surface subject to different Xe exposures (1 L corresponds to an exposure of 10^{-6} Torr s, and an exposure of 4 L results in the deposition of approximately one monolayer [11]). No well-defined LEED patterns associated with the adsorbed films were observed. As

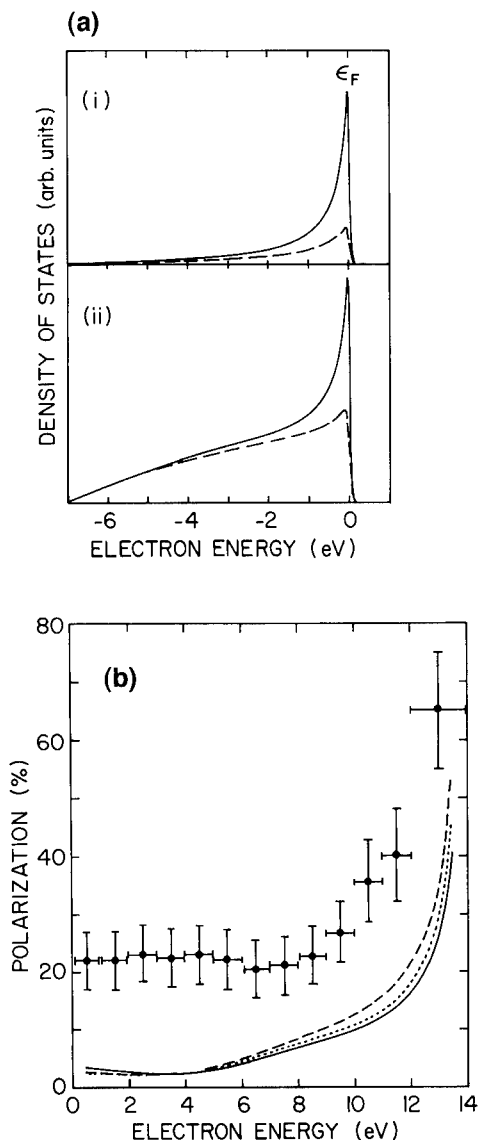


Fig. 5. (a) Calculated induced (i) and total (ii) density of states of spin-up (—) and spin down (---) electrons for an ion-surface separation of 6 a.u. assuming a jellium model characterized by a half-filled elliptical conduction band. (b) Ejected electron polarizations calculated assuming Auger neutralization occurs 5 a.u. (—), 6 a.u. (· · ·) and 8 a.u. (---) from the surface. Points: experimental data.

the surface exposure is increased the broad, relatively-featureless distribution characteristic of clean $\text{Cu}(100)$ evolves into a more structured distribution that, for exposures ≥ 30 L, remains essentially unchanged. The two high-energy peaks are similar to those observed in studies of $\text{He}(2^3\text{S})$ gas-phase PI [12], which correspond to ionization into the $^2\text{P}_{1/2}$ and $^2\text{P}_{3/2}$ states of the product Xe^+ ion, indicating that they result from SPI (AD). Gas-phase PI of Xe is described in terms of a direct transition from

the covalent $\text{He}(2^3\text{S})\text{--Xe}$ entrance potential to the final $\text{He}(1^1\text{S})\text{--Xe}^+$ exit potential. Because neither potential is strongly dependent on internuclear separation, ionization via this “covalent” channel results in narrow peaks in the EED [2]. In gas-phase PI, however, the widths of the $^2\text{P}_{3/2}$ and $^2\text{P}_{1/2}$ features are comparable whereas in SPI the $^2\text{P}_{3/2}$ feature is significantly broader than the $^2\text{P}_{1/2}$ feature. This results because at the surface the $^2\text{P}_{3/2}$ $|M_J| = \frac{3}{2}$, $\frac{1}{2}$ degeneracy is removed by interactions with neighboring atoms [13]. The separation in energy of the $^2\text{P}_{1/2,3/2}$ SPI peaks (~ 1.3 eV) is similar to that observed in gas-phase PI, but their absolute energies are significantly higher. This indicates that the effective ionization potential of Xe atoms at the surface is reduced, which can be attributed to a combination of substrate image charge effects and dielectric screening of the Xe^+ ion by neighboring Xe atoms [14]. The gradual decrease in energy of the SPI features observed with increasing Xe exposure is consistent with the decrease in image charge effects expected as the surface coverage increases. However, even at the highest coverages the energies of the SPI features are ~ 1.3 eV higher than the corresponding gas-phase PI features. The size of this energy shift is similar to that attributed to dielectric screening in earlier studies of photoemission from adsorbed Xe layers [15].

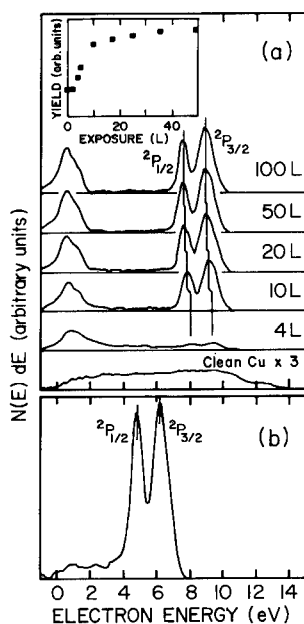


Fig. 6. (a) Ejected electron distributions resulting from $\text{He}(2^3\text{S})$ deexcitation at a cooled $\text{Cu}(100)$ surface following different exposures to Xe. Note the data for clean $\text{Cu}(100)$ are multiplied by a factor three. The inset shows the exposure dependence of the total ejected electron signal. (b) Ejected electron energy distribution resulting from deexcitation of $\text{Ne}(^3\text{P}_{0,2})$ metastable atoms for a surface Xe exposure of 30 L.

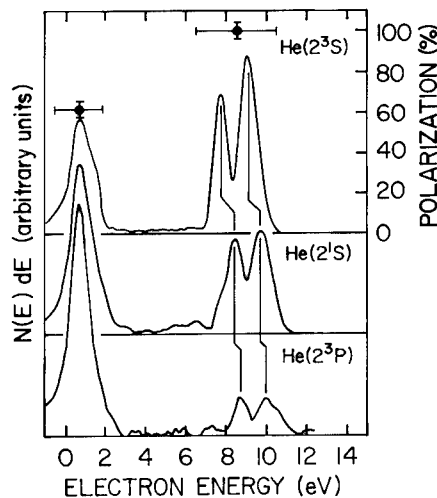
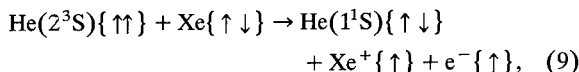


Fig. 7. Electron energy distributions resulting from deexcitation of $\text{He}(2^3\text{S})$, $\text{He}(2^1\text{S})$ and $\text{He}(2^3\text{P})$ atoms at a cooled $\text{Cu}(100)$ surface exposed to 30 L of Xe. Points: ejected electron polarization measured with polarized incident 2^3S atoms. The polarization is expressed as a percentage of that of the incident 2^3S atoms.

The ejected electron polarization associated with the SPI features is indicated in Fig. 7 and, to within experimental error, is equal to that of the incident 2^3S atoms showing that spin is conserved. Ejection must therefore result from an AD (SPI) process of the type



in which a spin-down electron from an atom in the adsorbed film tunnels into the $\text{He}(2^3\text{S})$ 1s core hole with simultaneous ejection of the spin-up 2s electron. Ancillary measurements using a dense Xe crossed-beam target showed that the polarization of electrons produced in gas-phase and surface PI are, to within experimental error, identical indicating that the same dynamical processes are operative. These measurements also show that the polarization of the SPI features is not degraded by secondary electron production. Since the ejected electron polarization is equal to that of the 2^3S atoms, which with laser-induced optical pumping can be very large (≥ 0.98) and can be accurately measured using a SG analyzer, SPI at a Xe film can furnish a valuable source of electrons of known polarization for use in, for example, polarimeter calibration [16].

The measured EEDs, however, contain a low-energy feature that is not observed in gas-phase PI and that therefore cannot be attributed to SPI. Energetically the feature is consistent with AN of Xe^+ ions formed by SPI or with neutralization of He^+ ions formed by RI. To investigate the first possibility EEDs were measured using incident $\text{Ne}(^3\text{P}_{0,2})$ metastable atoms (obtained simply by admitting Ne to the metastable atom source) and represent-

ative data are included in Fig. 6. The EED contains two well-defined peaks that result from production of Xe^+ ($^2\text{P}_{1/2,3/2}$) ions through SPI. However, although Xe^+ ions are created at the surface, no low-energy feature is evident indicating that Xe^+ ions are not the source of the low-energy peak. This is also suggested by Fig. 7 which shows the EEDs resulting from $\text{He}(2^1\text{S})$ and $\text{He}(2^3\text{P})$ deexcitation at a Xe film, together with that for $\text{He}(2^3\text{S})$ atoms. The high energy peaks in each distribution result from SPI and, as expected, their energies increase in proportion to the internal energy of the incident atoms. Each EED contains a low energy feature but it is clear that their sizes do not scale with the size of the SPI peaks, i.e., with Xe^+ ion production. Further, as shown in Fig. 7, the low-energy electrons that result from deexcitation of polarized $\text{He}(2^3\text{S})$ atoms have a sizable polarization. Although SPI (reaction (9)) will result in the production of polarized Xe^+ ions, their polarization will be rapidly degraded by internal spin-orbit coupling and it is unlikely that AN of Xe^+ ions could lead to ejection of electrons having significant spin polarization.

As apparent from Fig. 7, the increased internal energy associated with incident 2^1S and 2^3P atoms does not lead to any significant changes in the profile or position of the low-energy feature. This behavior mirrors that observed with clean Cu(100), and points to the low-energy peaks as being associated with neutralization of He^+ ions formed through RI. This, however, requires the availability of vacant levels at the surface resonant with the excited helium electron. Inverse photoemission studies of adsorbed Xe layers have revealed the presence of unoccupied states ~ 1.5 eV below the vacuum level that may be associated with surface states or Xe negative ion states of configuration $5\text{p}^66\text{s}$ [17]. Solid Xe also has a positive electron affinity, ~ 0.5 eV [18]. As an excited helium atom approaches the surface, image charge interactions and hybridization effects raise the electronic energy levels relative to the vacuum level [7]. This could move the electronic levels into resonance with unoccupied states in the surface and facilitate RI. Such a mechanism is consistent with the observed shift in the branching ratio between the low (RI + AN) and high (SPI) energy features evident in Fig. 7, the relative size of the low-energy feature growing as the internal energy of the incident atoms, and hence the energy overlap with available empty states at the surface, increases.

Following formation of He^+ ions through RI there are a number of neutralization processes that could give rise to the observed low-energy feature. It might result from an interaction that involves two Xe atoms in the film in which the He^+ ion is neutralized by a 5p electron from one Xe atom, the energy liberated being used to eject a 5p electron from a neighboring atom. (Similar three-center Auger processes have been discussed previously [19].) The gas-phase ionization potential of He, 24.58 eV, is more than twice that of Xe, 12.13 eV, suggesting that the process is al-

lowed energetically. However, the product Xe^+ ions must be formed in relatively close proximity and the energy associated with their final mutual electrostatic interaction must be accounted for. Nonetheless, the process might still be allowed energetically because, as noted earlier, surface effects lower the atomic binding energies. Although Auger processes that involve neighboring Xe atoms may be slow, the kinetic energy of the incident atoms is very low (~ 40 meV) and He^+ ions formed by RI may be bound by their image charges allowing time for reaction to occur. Since the He^+ ion formed by RI is spin polarized, spin correlation effects similar to those discussed earlier might account for the observed polarization of the low-energy feature. Alternately, reaction might proceed through near-resonant charge transfer between the He^+ ion and a Xe atom in the surface to form an excited Xe^{++} ion of configuration $5\text{s}5\text{p}^6$ that undergoes rapid AD through tunneling of a 5p electron from a neighboring Xe atom into the Xe^{++} 5s core hole with simultaneous ejection of a 5p electron from the ion. For polarized He^+ ions, the 5s core hole created by charge transfer must also be polarized and spin correlation effects might again account for the observed polarization.

Assigning the low energy feature to neutralization of He^+ ions formed by RI is also consistent with the observation that, as evident from Fig. 6, this feature initially grows more rapidly than the high-energy SPI features with increasing exposure to Xe. For low surface exposures (coverages) the electron may tunnel directly into the Cu(100) substrate through the adsorbed layer. For thick films, however, such direct tunneling is not possible and a balance is established between RI and SPI. Observation of such a balance is remarkable in that at high-work-function metal surfaces $\text{He}(2^3\text{S})$ deexcitation occurs exclusively through RI + AN whereas for thin films of Ar, and a variety of other gases [4], only SPI is observed. The reason that RI can occur at Xe films may be related to the positive electron affinity of solid Xe and two factors might contribute to the balance between RI and SPI. The unoccupied states in the film may be sufficiently close to the vacuum level that the separation between the incident excited atom and the surface must become very small before energy resonance is obtained, thereby allowing SPI to be competitive. Alternately, the density of unoccupied states may be sufficiently low as to limit the rate for RI and permit SPI to compete effectively.

As shown in the inset in Fig. 6, exposure of a cooled Cu(100) surface to Xe results in a large increase in the total ejected electron signal. The probability that AN of a low-energy He^+ ion at a clean high-work-function metal surface will lead to electron ejection is ~ 0.3 [20]. Since, as shown here, $\text{He}(2^3\text{S})$ deexcitation at such surfaces proceeds exclusively via RI + AN, it is reasonable to assume that the probability γ that electron ejection will accompany deexcitation of a $\text{He}(2^3\text{S})$ atom at a clean Cu(100) surface is also ~ 0.3 . The large increase in

electron yield observed following Xe exposure suggests that the value of γ for a Xe film of a few monolayers or greater thickness is ~ 0.9 . A possible explanation for this large yield is provided by studies of gas-phase PI of Xe which show that the angular distribution of the product electrons is asymmetric and is strongly peaked in the direction from which the 2^3S atoms are incident [21]. If this is also true for SPI, the majority of the product electrons will be directed out of the surface, increasing the probability for electron ejection. In addition, electrons initially directed into the film may be backscattered by elastic collisions with other atoms in the film and reemerge, further increasing the electron yield. (This will not degrade the electron polarization because the Xe atoms are closed-shell spin singlets precluding spin-flip exchange scattering.) Given the large value of γ for adsorbed Xe films, they appear attractive for application as an efficient detector of thermal-energy $\text{He}(2^3\text{S})$ metastable atoms.

4. Conclusions

As shown by the preceding examples, spin labelling techniques (coupled with measurement of EEDs) provide a powerful probe of the mechanisms by which $\text{He}(2^3\text{S})$ metastable atoms are deexcited at surfaces and of spin correlation effects. By optical pumping of the $^3\text{P}_2$ metastable level the technique can be extended to the heavier rare gases allowing study of a wide variety of excited atom–surface interactions. Polarized metastable atoms can also provide information on surface magnetic properties through measurements of the asymmetry in the ejected electron current with the incident beam polarized parallel and antiparallel to the majority spin direction in the (magnetized) target. For example, studies using polarized $\text{He}(2^3\text{S})$ atoms and $\text{Ni}(110)$ and $\text{Fe}(110)$ surfaces have shown that minority spin electrons are dominant at distances of $\sim 3 \text{ \AA}$ from the surface where AN occurs [22]. These measurements have established polarized metastable atoms as an extraordinarily sensitive probe of the surface magnetic environment and of the marked changes that can occur in the presence of adsorbed atoms.

Acknowledgements

This research by the authors and their colleagues discussed here is supported by the Office of Basic Energy Sciences, U.S. Department of Energy, the National Science

Foundation under grant #DMR 9117479, the Robert A. Welch Foundation, and the NATO Collaborative Research Grants Programme.

References

- [1] See, for example, H.D. Hagstrum, in: *Electron and Ion Spectroscopy of Solids*, eds. L. Furmans, J. Vennick and W. Dekeyser (Plenum, New York 1978) p. 273.
- [2] For a review of Penning ionization, see A.J. Yencha in: *Electron Spectroscopy: Theory, Techniques and Applications*, Vol. 5, eds. C.R. Brundle and A.D. Baker (Academic Press, New York, 1984) p. 197.
- [3] W.H. Butler, D.M. Oró, F.B. Dunning and G.K. Walters, *Surf. Sci.* 261 (1992) 382.
- [4] D.M. Oró, Q. Lin, X. Zhang, F.B. Dunning and G.K. Walters, *J. Chem. Phys.* 97 (1992) 7743.
- [5] D.M. Oró, P.A. Soletsky, X. Zhang, F.B. Dunning and G.K. Walters, *Phys. Rev. A* 49 (1994) 4703.
- [6] D.M. Oró, Q. Lin, P.A. Soletsky, X. Zhang, F.B. Dunning and G.K. Walters, *Phys. Rev. B* 46 (1992) 9893.
- [7] F.B. Dunning, P. Nordlander and G.K. Walters, *Phys. Rev. B* 44 (1991) 3246.
- [8] L.A. Salmi, *Phys. Rev. B* 46 (1992) 4180; L.A. Salmi, R.M.C. Monreal and S.P. Apell, *Solid State Commun.* 77 (1991) 495.
- [9] D.M. Newns, *Phys. Rev.* 178 (1969) 1123.
- [10] H. Shao, D.C. Langreth and P. Nordlander, *Phys. Rev. B* 49 (1994) 13929.
- [11] H.H. Rotermund and K. Jacobi, *Surf. Sci.* 126 (1983) 32.
- [12] C.E. Brion, C.A. McDowell and W.B. Stewart, *J. Electron Spectrosc. Relat. Phenom.* 1 (1972) 113.
- [13] B. Vogt, B. Kessler, N. Müller, G. Schönhense, B. Schmiedeskamp and U. Heinzmann, *Phys. Rev. Lett.* 67 (1991) 1318, plus references therein.
- [14] See, for example, S. Ishi and B. Viswanathan, *Thin Solid Films* 201 (1991) 373.
- [15] G. Schönhense, *Appl. Phys. A* 41 (1986) 39.
- [16] G.C. Burnett, T.J. Monroe and F.B. Dunning, *Rev. Sci. Instr.* 65 (1994) 1893.
- [17] K. Horn, K.H. Frank, J.A. Wilder and B. Reihl, *Phys. Rev. Lett.* 57 (1986) 1064; K.H. Frank, K. Horn, J. Wilder and E.E. Koch, *Appl. Phys. A* 44 (1987) 97.
- [18] N. Schwentner, F.-J. Himpsel, V. Saile, M. Skibowski, W. Steinmann and E.E. Koch, *Phys. Rev. Lett.* 34 (1975) 528.
- [19] See, for example, S. Dieckhoff, H. Müller, W. Maus-Friedrichs, H. Breiten and V. Kempster, *Surf. Sci.* 279 (1992) 233.
- [20] H.D. Hagstrum, *Phys. Rev.* 96 (1954) 325.
- [21] T. Ebding and A. Niehaus, *Z. Phys.* 270 (1974) 43.
- [22] M.S. Hammond, F.B. Dunning, G.K. Walters and G.A. Prinz, *Phys. Rev. B* 45 (1992) 3674.



ELSEVIER

Electronic structure of collision cascades in semiconductors

Z. Šroubek ^{a,*}, J. Fine ^b

^a Institute of Radio Engineering and Electronics, Academy of Sciences of Czech Republic, Chaberská 57, 182 51 Prague 8, Czech Republic

^b Surface and Microanalysis Science Division, National Institute of Standards and Technology, Gaithersburg, MD 20899, USA

Abstract

Electron density of states and electron elastic mean free path in collision cascades in silicon bombarded by 600 eV atomic particles have been calculated using the pseudopotential technique and the large unit cell method. The results clearly show a metalization of the semiconductor and the formation of deep localized states within the collision cascade. The knowledge of the electronic structure of bombarded Si allows to estimate the electronic diffusion constant ($D = 5 \text{ cm}^2/\text{s}$) and the spatial and temporal evolutions of the excitation in the cascade. A possible contribution of these excitations to the ionization of sputtered atoms from semiconductors is deduced from the transport analysis and the results are compared with new experiments on GaAs bombarded with Xe and He particles.

1. Introduction

The valence and conduction bands in typical semiconductors like Si, Ge, GaAs are several eV wide and electronic excitations induced in these materials by bombarding particles should resemble more the excitations in metals than in narrow band insulators. Also ionization processes of particles sputtered from semiconductors should be of different nature than ionization processes in insulators like LiF where localization of holes in the narrow fluorine valence band can take place [1–3].

In this paper we wish to discuss in more detail specific aspects of excitation and ionization processes in semiconductors. In particular we present the results of the calculation of the Si electronic density of states (EDS) in the region of a collision cascade, which is produced by the impact of a 600 eV particle. The EDS in the collision cascade has been found to be metal-like, resembling the EDS of Al. Because of the forbidden gap in the unperturbed Si the electronic excitations with energies in the gap are virtually confined within the region of the cascade. This, together with the observation that the elastic mean free path inside the cascade is small, can lead to a strong localization of the electronic energy in the cascade region and can influence charge states of emitted particles.

Besides this theoretical study of ionization the ionization processes in GaAs, which electronically resembles Si, were analyzed experimentally using primary ion beams

(He⁺, Xe⁺) and neutral beams (He⁰, Xe⁰) with impact kinetic energies E_k between 500 and 4000 eV. The absolute yields of As⁺ and As[−] were measured as a function of E_k . The measured dependence of the yields on E_k agrees with the conjecture that the substrate is highly electronically excited.

2. Theory

The electronic structure of collision cascades has been calculated in the large-unit-cell approach using the pseudopotential technique. This approach has been successfully used to calculate impurity levels in semiconductors [4] and has been recently used to estimate energies of deep localized levels in bombarded solids [5].

The large unit cell of Si is formed by a cube with the side L equal to 20.41 a.u. and contains 64 Si atoms. The used Si pseudopotential is given by (in a.u.) [5]:

$$V_{\text{Si}}(r) = 4.838 \exp(-0.828r^2) - 3.246 \exp(-0.359r^2). \quad (1)$$

This potential gives correct values of the Friedel sum and of the transport scattering cross section. The electronic wave function is expanded in plane waves with reciprocal lattice vectors of the large unit cell. Altogether 485 plane waves have been used.

When the atoms are situated in their regular positions in the Si lattice the calculated EDS (see Fig. 1, dashed line) resembles very well the known EDS of crystalline Si. To simulate a collision cascade, positions of Si atoms were then randomly changed from their equilibrium positions

* Corresponding author, tel. +422 66422804, fax +422 66410222, E-mail: sroubek@ure.cas.cz or.

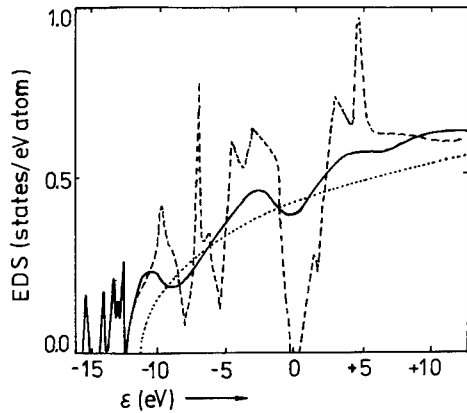


Fig. 1. Calculated electronic density of states (EDS) of the collision cascade formed in Si by 600 eV Ar particles (full line), EDS of unperturbed silicon (dashed line) and of unperturbed aluminum (dotted line). The Fermi energies in all three cases are at $\epsilon = 0$.

and the corresponding change of the interatomic potential energy was calculated. Only those configurations were chosen for which the total change of the interatomic potential energy is about 400 eV as this roughly corresponds to the change of the potential energy in the first 100 fs of the collision cascade created by the impact of a 600 eV Ar particle. A typical EDS of such heavily randomized Si is shown in Fig. 1 by the full line. For comparison EDS of Al metal is shown in Fig. 1 by the dotted line. The density resembles the EDS of pure metals except of a small hump around the energies of the forbidden gap of the crystalline Si and a set of localized levels below the valence band [5]. As mentioned in Section 1, also the states in the amorphised Si which lie in the band gap of the crystalline Si are essentially localized within the cascade because they do not have counterparts in the unperturbed material.

We have also calculated the mean free path of electrons in the cascade region. For this purpose we have calculated the projection $\langle \Psi_a | \Psi_k \rangle$ of some selected eigenfunctions Ψ_a of the perturbed Si into the eigenfunctions Ψ_k with energies ϵ_k of the crystalline Si. The values of $|\langle \Psi_a | \Psi_k \rangle|^2$ $\rho(\epsilon_k)$, where $\rho(\epsilon_k)$ is the EDS of the crystalline Si, have a maximum at $\epsilon_k = \epsilon_a$ and a width Δ . The inverse value of Δ can be interpreted as the life-time of Ψ_a . The value of Δ has been found to be typically around 1.5 eV, thus the life-time τ_a would be $\tau_a = 4 \times 10^{-16}$ s $S = 4 \times 10^{-1}$ fs. The corresponding diffusion constant D at energies close to the Fermi energy is approximately equal to $\frac{1}{3} v_F^2 \tau_a = 5.3$ cm²/s = 53 Å²/fs where v_F is the electron velocity. The source term, it is the amount of the electronic energy E_e deposited in the collision cascade in the space of 1 Å³ in 1 fs, is estimated as in Ref. [6], i.e.

$$\frac{dE_e}{dt} = 2.3 \times 10^{-3} E_0, \quad (2)$$

where E_0 is the density (in eV/Å³) of the kinetic energy of the moving substrate particles. For our case, i.e. for 600 eV Ar impinging on the surface of Si, the total kinetic energy in the cascade in the first 100 fs is about 400 eV. We have further assumed that the collision cascade spreads around the point of impact with a constant velocity, reaching a radius of 10 Å in 100 fs and that the diffusion constant is infinitely large outside and is equal to 50 Å²/fs inside the cascade region. Then from the solution of the diffusion equation we have estimated the density E_e at the surface at 100 fs after the impact to be 1.6×10^{-4} eV/Å³. Using the results shown in Fig. 1 and the assumption of a complete thermalization we have calculated the corresponding electronic temperature T_e from the free-electron specific heat [7],

$$T_e = \left(\frac{2 \epsilon_F E_e}{\pi^2 k^2 N} \right)^{1/2}, \quad (3)$$

where ϵ_F is the Fermi energy and N is the number of electrons per Å³ and k is Boltzmann's constant. Then the ionization probability of the sputtered particle would be proportional to $\exp(-B/(E_e)^{1/2})$, where B is a constant. For $E_e = 1.6 \times 10^{-4}$ eV/Å³, the temperature is $T_e = 580$ K. In the other extreme of a complete confinement of excitations within the cascade, the energy E_e is 2.3×10^{-2} eV/Å³ and the corresponding temperature would be $T_e = 6900$ K. The actual values of E_e and T_e are between these two extremes. It should be noted that the concept of electronic thermalization in collision cascades used in this paper is a conjecture which has not been proved either experimentally or theoretically. It allows, however, to formulate the problem in a simple way and, as a first approximation, it may be not far from reality because thermalization of excited carriers in less than 100 fs has been observed in femtosecond laser experiments on Si [8].

3. Experiments

The highly excited electronic systems at 100 fs after the impact of the primary particle should influence the charge state of sputtered atomic particles because most of them are sputtered at $t \approx 100$ fs. We have recently measured [9] the emission of Ga⁺, As⁺ and As⁻ from GaAs, which is electronically very similar to Si. It turns out that the Ga⁺ ionization is independent of the substrate excitation within the precision of our measurement and it is also independent of bombarding conditions. The observed independence is probably due to the small ionization energy of Ga⁺ which makes the electron transfer from the sputtered Ga atom very efficient and largely insensitive to substrate excitations. On the other hand the ionization energy of As is large and the electron affinity is small. The ionization processes are consequently very sensitive to substrate excitations and thus also to bombarding conditions. The mea-

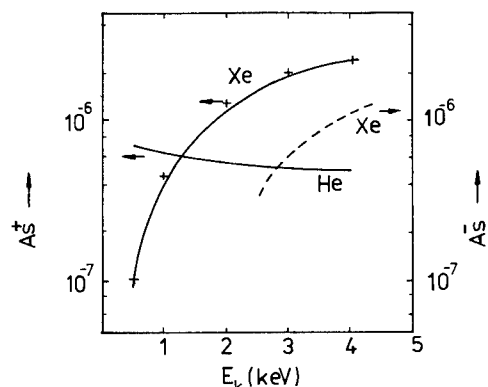


Fig. 2. The ionization probabilities of As^+ (full line) and As^- (dashed line) ions sputtered from GaAs under Xe and He bombardments. The probabilities are plotted as a function of the primary particle energy E_k . The crosses mark the theoretical dependence on E_k for the Xe bombardment, deduced from the analysis discussed in the text.

sured absolute yields of As^+ and As^- as a function of the energy E_k are shown in Fig. 2 for the perpendicular impact of Xe and He. If the primary particles were not penetrating into the substrate and the collision cascades had the same radius independent of E_k , the density of electronic energy E_e would be proportional to E_k and, after thermalization, the effective electronic temperature T_e would be proportional to $(E_k)^{1/2}$. Because the bombarding particles penetrate into the substrate along the direction of the impact the deposited energy would be for the perpendicular impact approximately proportional to E_k/L , where L is the sum of the penetration depth and the radius of the cascade. The value of L would then be proportional to $a + bE_k$, where a and b are constants depending on the bombarding particles. If the penetration depth is large then $L = bE_k$ and the deposited energy is independent of E_k . This is indeed confirmed in the case of He bombardment where the ionization probability of As^+ is practically independent of E_k (see Fig. 2). In the case of Xe the penetration depth is small. Using a tentative assumption that the penetration depth at $E_k = 4$ keV is equal to the radius of the cascade at $E_k = 500$ eV, the relative values of the ionization yield have been calculated with respect to the yield at $E_k = 500$ eV and are marked by crosses in Fig. 2. The agreement with the experiment is good. It should be

noted that the ionization yield dependence of As^+ for Ar bombardment (not shown in Fig. 2) lies between the He and Xe dependences.

The ionization processes leading to As^- were not analyzed in this paper but experimental results from Fig. 2 indicate that As^- behaves similarly as As^+ . Thus we may expect that the ionization processes in GaAs are governed by similar excitation processes for both positive and negative As ions.

4. Conclusion

We have shown that the electronic structure inside low energy collision cascades of semiconductors like Si and GaAs are very similar to electronic structures of free-electron amorphous metals except of the broadening due to localized states. Using this observation we have discussed possible electronic excitations and their confinement within the cascades. The excitations may significantly influence the charge state of sputtered particles. Such ionization processes seem to be relevant in the case of As^+ and As^- formations during GaAs sputtering.

Acknowledgements

This work is supported by the US–CR Science Technology Program under Grant no. 92001 and by the Intracademical Grant no. 16757.

References

- [1] P.M. Thompson and Y.W. Taylor, *Surf. Sci.* 176 (1986) 610.
- [2] P. Varga, U. Diebold and D. Wutte, *Nucl. Instr. and Meth. B* 58 (1991) 417.
- [3] Z. Šroubek and H. Oechsner, *Surf. Sci.* 311 (1994) 263.
- [4] S.G. Louie, M. Schlüter, J.R. Chelikowski and M.L. Cohen, *Phys. Rev. B* 13 (1976) 1654.
- [5] Z. Šroubek, *Phys. Rev. Lett.* 70 (1993) 4019.
- [6] J. Lindhard and M. Scharff, *Phys. Rev.* 124 (1961) 128.
- [7] C. Kittel, *Introduction to Solid State Physics* (Wiley, New York, 1971), p. 249.
- [8] J.R. Goldman and J.A. Prybyla, *Phys. Rev. Lett.* 72 (1994) 1364.
- [9] Z. Šroubek and H. Oechsner, submitted to *Surf. Sci.*



ELSEVIER

Z_1 oscillations in yields of doubly and singly charged ions emitted from a germanium surface when bombarded by light ions

B. Hird*, R. Armstrong, P. Gauthier

Ottawa-Carleton Institute for Physics, Ottawa University Campus, Ottawa, Ontario, K1N 6N5, Canada

Abstract

The interaction radii at which holes are created in the L-shell of light projectiles and in the M-shell of germanium during ion-surface atom collisions have been determined from the thresholds for doubly charged ion production. In contrast to the data with a silicon target, the interaction radius at which electron promotion occurs does not decrease with projectile atomic number (Z_1) as it should if promotion occurs at a definite level crossing. In addition, the yields of doubly charged ions do not follow the Z_1 dependence predicted by the Fano–Lichten–Barat electron promotion model.

1. Introduction

We report measurements of the doubly charged ions scattered and recoiled from a clean amorphous germanium target when bombarded with C^+ , N^+ , O^+ , F^+ , Ne^+ , Na^+ , P^+ , S^+ , Cl^+ , and Ar^+ ions of a few keV energy. The M-shell energy of Ge matches the L-shell energy of light atoms at about $Z = 14$, so that a discontinuity is expected in the Z_1 dependence of the yields. We have reported similar measurements with a silicon target [1].

The last stages in the production of multicharged ions are mainly Auger transitions in which the excitation energy of the ion is in part converted to ionization energy of one or more valence electrons, thus increasing the charge state. The excitation must have been created earlier in the same collision and is likely to have been initiated by the electron promotion process [2,3], which produced one or more inner shell vacancies. At the energy threshold for multicharged ion creation the interaction radius for electron promotion is just reached at the distance-of-closest-approach.

2. Experiment

The instrumental requirements for low energy ion scattering measurements using an electrostatic analyser system has been described in previous publications [4,5]. The beams were produced using pure gases (N_2 , O_2 , Ne , and Ar) in a discharge-type ion source. C^+ , F^+ , and Cl^+ beams were produced with CO , Freon-14 (CF_4) and Freon-12 gas (CCl_2F_2), respectively. Whereas P^+ , S^+ and Na^+ beams

were obtained by placing small amounts of the element in solid form inside the ion source while operating the plasma on argon gas. The ions of the most common isotope of each element were selected with a high resolution 30° deflection magnet. The beam passed through a differentially pumped section between two small apertures, which both defined the beam geometry and isolated the scattering chamber, allowing a pressure of 2×10^{-10} Torr during measurements. The target was a Ge(100) crystal with its surface amorphized and cleaned by 500 eV Ar^+ bombardment. Following each sputtering the target was heated to about $500^\circ C$ for 10 s, during which time the pressure rose due to desorption of the absorbed argon, and then returned almost to the pressure before heating. An amorphous surface was chosen for the measurements so as to avoid any uncertain crystallographic effects from a single crystal surface damaged by the ion beam.

A typical voltage spectrum of the ions emitted at 45° to the incident oxygen beam direction is shown in Fig. 1. The voltages at which the peaks appear all agree well with the energies expected from events in which an incident O^+ ion is either scattered out from the surface after colliding with a single germanium atom, or it is scattered inwards at an angle close to 78° , and the germanium ion recoils outward at 45° . To within the resolution of the analyzer, all the multicharged ions had the same energy as the singly charged ions, since the doubly charged ion peaks occur, to within one channel, at exactly half the voltage of the corresponding singly charged ion peak. The scattering angles were judiciously chosen to resolve the singly and doubly charged peaks for both scattered and recoiled particles. No triply charged ions were observed for the germanium target, although significant Si^{3+} yields had been found previously

* Corresponding author. Tel. +1 613 562 5800/6754, fax +1 613 562 6190, e-mail hird@physics.uottawa.ca.

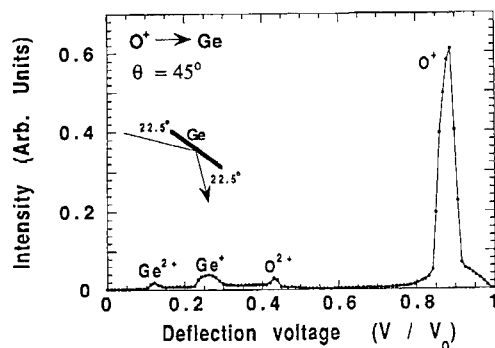


Fig. 1. Electrostatic analyzer spectrum of ions which have been scattered through an angle of 45° by a clean amorphous germanium surface. V is the analyzer deflection voltage, and V_0 is the voltage required to deflect the full energy incident beam.

with a silicon target [1,5].

3. Results

3.1. Variation with beam energy

Fig. 2 shows a typical variation of the scattered ion intensity with beam energy, and Fig. 3 shows the corresponding yields of recoiling germanium target atoms which escape from the surface as singly and doubly ionized ions. Intensities were determined from the areas under the elastically scattered ion peaks.

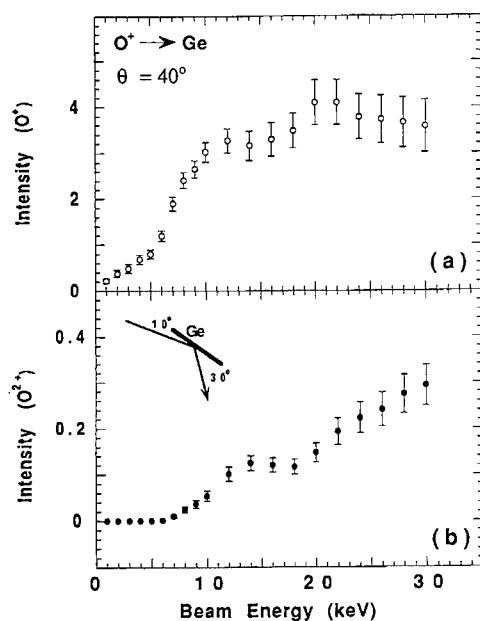


Fig. 2. Yields of (a) O^+ and (b) O^{2+} ions which have been scattered through an angle of 40° by collisions with surface atoms, plotted as a function of the incident O^+ ion energy.

The general shape of the yields as a function of beam energy will probably be affected by shadowing effects since, at the average surface atomic spacing, the shadow cone is 12° for 10 keV oxygen ions, and measurements were made with ions incident on the germanium surface at an angle of 10° . The shadow cone angle decreases with energy and increases with Z_1 . The observed ion yields are thus reduced by surface shadowing effects mostly at our lowest energies and with the heavier projectiles.

Definite energy thresholds are found for creation of doubly charged ions when measured at fixed scattering angles. They occur when the distance-of-closest-approach equals the crossing radius r_0 in the molecular orbital correlation diagram where electron promotion occurs to create the shell vacancies. The ion trajectories are well defined in the measurements and each distance-of-closest-approach was calculated using the "Universal" potential of O'Connor and Bier-sack [6] at the threshold energy and scattering angle.

3.2. Scattered ion yields

Measurements were made at a constant ion beam velocity so as to minimize the effect of kinematic contributions to the cross sections. A velocity of 0.53 keV/amu was chosen as a compromise to be well above the energy thresholds for doubly charged ion production, but low enough to avoid significant subsurface and multiple scattering contributions to the binary collision peaks.

The singly charged scattered ion yield (Fig. 4) increases from a small value for C^+ , to a large value for Na^+ , returning

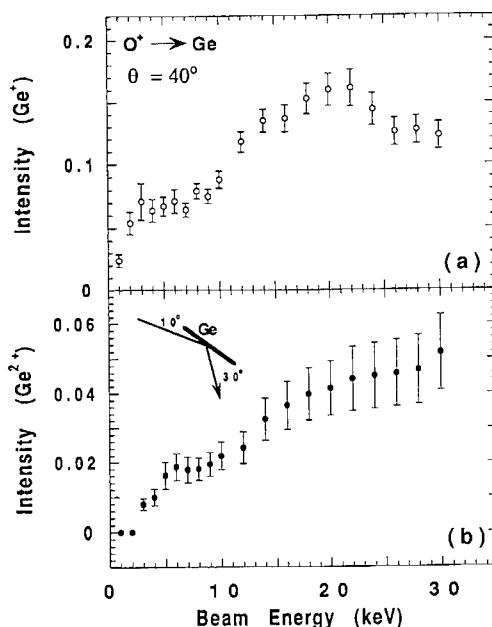


Fig. 3. Yields of (a) Ge^+ and (b) Ge^{2+} ions which have recoiled from surface, or near surface locations and were emitted at 40° to the incident ion direction.

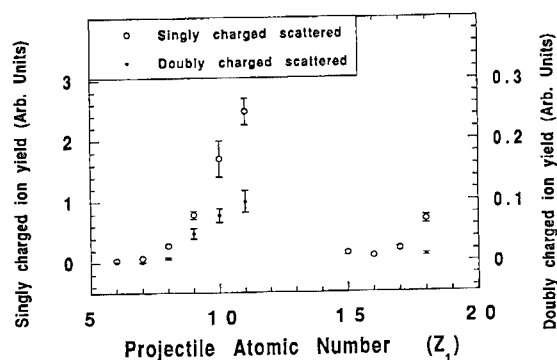


Fig. 4. Yields of singly and doubly charged scattered ions as a function of the atomic number of the incident beam (Z_1).

to small values for P^+ , S^+ and Cl^+ with some indication of an increase for Ar^+ . The doubly charged scattered ion yield (Fig. 4) shows a similar behaviour, with a rise from undetectably low values for C^{2+} to significant values for F^{2+} , Ne^{2+} and Na^{2+} . The yield then returns to an undetectably small value for P^{2+} , with a small increase for higher Z_1 ions. The ratio of yields goes through a maximum in the region $Z_1 = 9-11$, with very small ratios elsewhere.

3.3. Recoil ion yields

Both the Ge^+ and Ge^{2+} recoiled ion yields (Fig. 5) increase from $Z_1 = 6$ to $Z_1 = 11$, as do the scattered ion yields. However, the recoiled ion yields are much smaller than the corresponding scattered ion yields. For $Z_1 > 14$, in contrast, where the scattered ion yields are undetectably small, significant Ge^+ and Ge^{2+} yields were found. Both recoiled ion yields appear to go through a broad maximum.

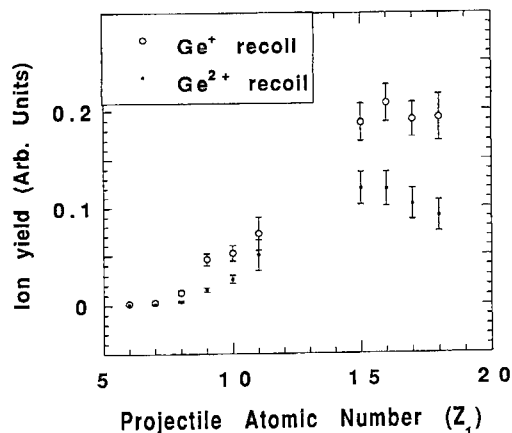


Fig. 5. Yields of Ge^{2+} and Ge^+ ions emitted at 40° to the incident ion direction, as a function of Z_1 .

Table 1

Energy thresholds E_t , and distances-of-closest-approach r_0 , calculated with the "universal" screened Coulomb potential of O'Connor and Biersack [6]. θ is the angle between the incident ion direction and the detected ion direction. θ' is the scattering angle when recoil Ge^{2+} ions are detected at θ .

Beam	θ	θ'	Scattered ions		Recoil Ge^{2+}	
			E_t [keV]	r_0 [a.u.]	E_t [keV]	r_0 [a.u.]
C^+	45°	80.6°	3.6 ± 0.2	0.609	3.4 ± 0.2	0.510
N^+	45°	79.1°	4.4 ± 0.1	0.593	2.3 ± 0.2	0.648
O^+	45°	77.6°	5.7 ± 0.1	0.558	1.1 ± 0.2	0.862
F^+	45°	75.3°	6.8 ± 0.1	0.542		
Ne^+	45°	74.6°	8.0 ± 0.1	0.525	< 1.0	> 1
Na^+	50°	63.5°	8.9 ± 0.1	0.500	2.7 ± 0.7	0.5
P^+	35°	84.8°	14.1 ± 0.1	0.527	2.3 ± 0.1^a	0.818
S^+	35°	84.0°	9.4 ± 0.1	0.646	2.0 ± 0.1^b	0.879
Cl^+	40°	72.2°	4.2 ± 0.1	0.665	1.2 ± 0.2	0.969
Ar^+	40°	69.1°	3.8 ± 0.1	0.714	1.2 ± 0.2	1.09

^a $\theta = 40^\circ$, $\theta' = 75.6^\circ$.

^b $\theta = 40^\circ$, $\theta' = 74.8^\circ$.

4. Crossing radii

The scattered and recoiled crossing radii r_0 , calculated from the energy thresholds (Table 1, and Fig. 6), show distinctly different behaviour from our previous silicon target data. If electron promotion occurs at the same level crossing over a range of projectiles then, because of the general decrease in size of the orbitals with increasing nuclear charge, the crossing radius should decrease with increasing Z_1 [7–

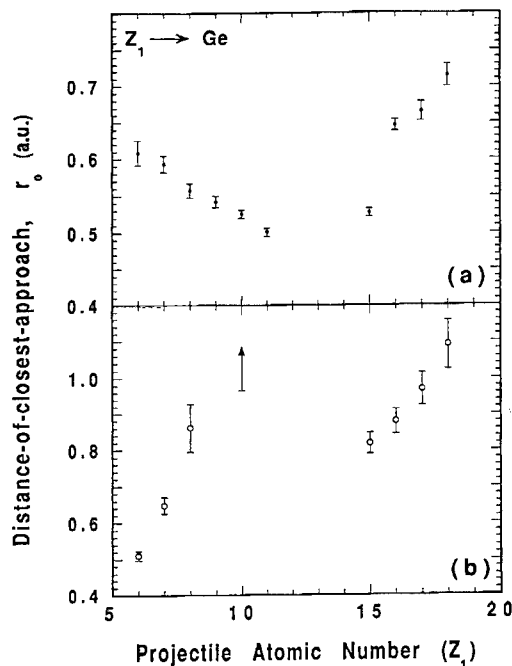


Fig. 6. Crossing radii r_0 , determined from the distances-of-closest-approach at the lowest beam energies at which doubly charged ions were detected, as a function of Z_1 .

9]. We find an increase for recoiled, and scattered ions on the higher Z_1 side of the level match, with a clear discontinuity in the trends of the data between $Z_1 = 11$ and $Z_1 = 15$.

5. Discussion

The increase in r_0 with Z_1 is hard to explain if electron promotion follows the correlation diagram crossings closely. However the Z variation of the X-ray yields [10–12] does not show a discontinuous rise at the Z_1 value where the correlation diagram predicts a change in the electron promotion level. Instead it oscillates, with a gradual rise to a maximum at the level match, suggesting that transitions at both level crossings occur with gradually changing relative probabilities. It is possible that our observed rising values of r_0 are in a region of gradual change from one level crossing to another. It will be necessary to make measurements over a wider range of Z_1 projectiles to establish whether there are level matching oscillations in the r_0 values, as occur in the X-ray yields. There may also be oscillations in the total ion yield if electron promotion at level crossings is the main interaction process which initiates the complicated sequence of interactions by which most energetic ions, including singly charged ions, are produced following quasi-elastic ion–atom surface collisions.

The similarity in the recoiled ion yields on either side of the M–L shell energy match can only be understood if there is significant level mixing before the molecule becomes two separate atoms, so that preferential ionization of the lower Z atom, which is clearly established in ion–gas collisions, has only a weak effect on the ratios of the higher Z to the lower Z ion yields. Holes created in orbitals, which at large

separations promote electrons in the lower Z atom, seem to sometimes result in doubly charged ions, and also singly charged ions of the higher Z atom.

After the ions are initially formed and before they leave the surface, there is a significant probability in a solid that the charge will be reduced as the ion picks up electrons. The interactions which determine the decay rates probably depend on the ionization potential of the projectile and target atom, and on other electronic surface properties such as the valence band width and the density of states at the surface. All these factors complicate the interpretation of the ion yields, but should not affect significantly the determination of the crossing radii.

References

- [1] B. Hird, R.A. Armstrong and P. Gauthier, Nucl. Instr. and Meth. B 90 (1994) 243.
- [2] U. Fano and W. Lichten, Phys. Rev. Lett. 14 (1965) 627.
- [3] M. Barat, and W. Lichten, Phys. Rev. A 6 (1972) 211.
- [4] B. Hird, R.A. Armstrong and P. Gauthier, Phys. Rev. Lett. 67 (1991) 3575.
- [5] B. Hird, R.A. Armstrong and P. Gauthier, Phys. Rev. A 49 (1994) 1107.
- [6] D.J. O'Connor, and J.P. Biersack, Nucl. Instr. and Meth. B 15 (1986) 14.
- [7] B. Fastrup, G. Herman and K.J. Smith, Phys. Rev. A 3 (1971) 1591.
- [8] E.G. Bøving and G. Sørensen, Phys. Rev. Lett. 40 (1978) 315.
- [9] U. Wille and R. Hippler, Phys. Rep. 132 (1986) 129.
- [10] T.M. Kavanagh, M.E. Cunningham, R.C. Der, R.J. Fortner, J.M. Khan and E.J. Zharis, Phys. Rev. Lett. 25 (1970) 1473.
- [11] T.M. Kavanagh, R.C. Der, R.J. Fortner and M.E. Cunningham, Phys. Rev. A 8 (1973) 2322.
- [12] F.W. Saris, Physica 52 (1971) 290.



ELSEVIER

Non-adiabatic effects in charge transfer caused by electron correlation

Hongxiao Shao ^{a,*}, Peter Nordlander ^b, David C. Langreth ^c

^a The Center for Quantized Electronic Structures (QUEST), University of California, Santa Barbara, CA 93106, USA

^b Department of Physics and Rice Quantum Institute, Rice University, Houston, TX 77251-1892, USA

^c Department of Physics and Astronomy, Rutgers University, Piscataway, NJ 08855-0849, USA

Abstract

Using a recently developed many-electron theory, we investigate the velocity dependence of charge transfer probabilities in atom–surface scattering. By analysis of the instantaneous spectral function of the atomic levels, the microscopic origins of non-adiabaticity can be determined. We show that, under certain conditions, intra-atomic correlation effects can introduce novel and non-trivial sources of non-adiabaticity, due to the formation of the Kondo resonance near the Fermi level of the substrate. The narrow width of the Kondo resonance introduces an additional long time scale, which persists even at low velocities.

1. Introduction

Recently there has been considerable experimental and theoretical interest and development in the dynamic processes of charge-transfer between the adsorbate and solids [1–9]. Charge transfer processes are of crucial importance in understanding of a number of fundamental physical processes on surfaces, such as sticking and desorption. Quantum tunneling of electrons, in general, plays a key role for the understanding of the effects of the impurities, quantum dots, etc. on the transport and the optical properties of novel materials [10–15]. Charge-transfer in atom–surface scattering covers a wide range of parameter space, and thus provides an excellent arena for the study of the non-adiabatic, non-equilibrium many-electron phenomena associated with quantum tunneling.

So far, most of the theoretical investigations of charge-transfer reactions in atom–surface scattering have been based on the single-level Anderson model [16,17], where the electron–electron interaction within the atomic species is ignored. Although theoretically appealing this model is too crude for the proper description of realistic systems. For example, there will always be a degeneracy of at least 2 due to the spin of the electron. The electron–electron interaction between the degenerate states (intra-atomic Coulomb interaction) is often large and needs to be included for a realistic description of the interaction of the atom with the surface. In the case of large intra-atomic

Coulomb interaction, the occupation of one atomic state would prevent the occupation of all other atomic states.

There are other more subtle effects caused by intra-atomic correlation. One particularly interesting feature, the Kondo effect has been the subject of numerous studies [18–20]. The Kondo effect can drastically affect the transport and/or optical properties of bulk materials when certain impurities are present. The Kondo effect results from the formation of a narrow resonance, the Kondo peak, near the Fermi level. Although it is well known that the Kondo peak will appear in certain atom–surface scattering situations [8,21], its effect on the dynamics of charge transfer has not yet been investigated in a systematic way.

The multi-level Anderson Hamiltonian is quite complex and an exact analytic solution to the Anderson model is not possible even in equilibrium. Several approaches for the solution of the time-dependent multi-level Anderson model with electron–electron interaction have been developed [7,22–28]. Recently we developed a general method for approximately solving the time-dependent Anderson model using a slave-boson technique [8,29].

In this paper we will use the time-dependent slave-boson method to investigate the velocity dependence of charge transfer processes in atom–surface scattering. Our investigation will focus on correlation effects caused by intra-atomic Coulomb interaction between the atomic levels. The calculations are performed for a system characterized by realistic parameters. By analyzing the instantaneous spectral function of the atomic states, we explicitly demonstrate that the presence of the Kondo peak can influence the charge transfer. In typical situations when the atom is close to the surface, the width of the Kondo peak

* Corresponding author, tel. +1 805 893 3700, fax +1 805 893 8170, E-mail: hshao@toad.metiu.ucsb.edu.

will be very small in comparison to the adiabatic width of the atomic level. The time constant associated with the formation or the decay of this peak is therefore relatively long. We show that the final charge transfer is characterized by two different time scales, the width of the atomic levels and the width of the Kondo resonance.

We will start this paper with a brief description of the time-dependent slave-boson method, with which we will calculate the instantaneous population and spectral function of the atomic states. We will then proceed to show the results of a series of calculations based on a multi-channel tunneling model. The effect due to large intra-atomic Coulomb interaction among degenerate atomic states and between non-degenerate atomic levels will be investigated.

2. Brief description of the formalism

The charge transfer between atoms and a surface can be described by a time-dependent Anderson Hamiltonian [17,30]

$$H(t) = \sum_{k\sigma} \epsilon_k n_{k\sigma} + \sum_{l\sigma} \epsilon_l(t) n_{l\sigma} + \frac{1}{2} \sum_{\{l\sigma\} \neq \{l'\sigma'\}} U_{l\sigma l'\sigma'}(t) n_{l\sigma} n_{l'\sigma'} + \sum_{k,l,\sigma} [V_{kl}(t) C_{l\sigma}^\dagger c_{k\sigma} + \text{H.c.}], \quad (1)$$

where $c_{k\sigma}$ destroys an electron of spin σ in substrate band state k , $C_{l\sigma}$ destroys an electron of spin σ in atomic level l , $n_{k\sigma} = c_{k\sigma}^\dagger c_{k\sigma}$, $n_{l\sigma} = C_{l\sigma}^\dagger C_{l\sigma}$, $\epsilon_l(t)$ is the instantaneous energy of the atomic level l , ϵ_k is the energy of the substrate band state k , U is intra-atomic Coulomb interaction [31], V_{kl} the overlap between electronic wave function of the substrate band and atomic state, and H.c. denotes the Hermitian conjugate.

For the case where $U = 0$, the solution to Hamiltonian Eq. (1) is analytical [16]. In the limit of large U , a slave-boson technique [32] can be used for the approximate solution of Hamiltonian Eq. (1). The slave-boson method expands the Hilbert space for Eq. (1) by adding a zero mass boson, b , which represents an atomic configuration where none of the atomic states is occupied. In the expanded Hilbert space, the creation operator for an atomic state becomes $C_{l\sigma}^\dagger b$ [8], and Hamiltonian Eq. (1), without the U term, takes the form:

$$H(t) = \sum_{k\sigma} \epsilon_k n_{k\sigma} + \sum_{l\sigma} \epsilon_l(t) n_{l\sigma} + \sum_{k,l,\sigma} [V_{kl}(t) C_{l\sigma}^\dagger b c_{k\sigma} + \text{H.c.}]. \quad (2)$$

A generalized charge Q , defined as

$$Q = b^\dagger b + \sum_{l,\sigma} n_{l\sigma}, \quad (3)$$

is a conserved quantity. In the large U limit, the solution to Hamiltonian Eq. (2) within the $Q = 1$ subspace of the Hilbert space is equivalent to that to Hamiltonian Eq. (1) [32].

The instantaneous occupations and correlation functions of the atomic states can be calculated numerically using a non-equilibrium Green's function technique described elsewhere [8,29,33]. The less than correlation function of an atomic state is given by

$$A_{l\sigma}^<(t, t') = G_{l\sigma}^<(t, t') [B^>(t', t) - B^<(t', t)], \quad (4)$$

where $G^<$ and $B^>$ are the appropriate correlation functions respectively for the $C_{l\sigma}$ and b in Hamiltonian Eq. (2). The population of an atomic state is given by

$$\langle n_{l\sigma}(t) \rangle = G_{l\sigma}^<(t, t), \quad (5)$$

and the instantaneous occupied spectral functions (OSF) of an atomic state can be evaluated using

$$\rho_{l\sigma}^{\text{occ}}(\omega, t) = \frac{1}{2\pi} \int_{-\infty}^{\infty} d\tau A_{l\sigma}^<(t + \tau/2, t - \tau/2) e^{i\omega\tau}. \quad (6)$$

The population of the atomic levels can be obtained directly from their spectral function,

$$\langle n_{l\sigma}(t) \rangle = \int_{-\infty}^{\infty} d\omega \rho_{l\sigma}^{\text{occ}}(\omega, t). \quad (7)$$

The usefulness of a spectral decomposition of the population of atomic levels in analyzing charge transfer will be illustrated in the results section.

As an atom approaches a metal surface, the energy levels shift and broaden. The qualitative features of these shifts can be understood from the image potential [34]. For a discussion how the parameters of the time-dependent Anderson model can be related to the energy shifts and broadenings of atomic levels using a classical trajectory approximation see Ref. [8].

3. Results and discussions

The calculations will be performed for a model system in which a two-level atom is scattered against a surface characterized by a band with a parabolic density of states. Both levels are assumed to have a spin degeneracy of 2. The atomic levels are assumed to shift downwards with decreasing atom-surface separation (e.g., the affinity level of neutral species). The width of an atomic level (FWHM) is parameterized as:

$$\Gamma_\sigma(Z(t)) = 2 \Delta_\sigma \exp(-\alpha Z(t)). \quad (8)$$

The shifts and widths of the atomic levels are illustrated respectively in the upper panels of Fig. 1.

The trajectory of the atom will be assumed linear. The atom is taken to move with constant velocity towards the surface and to instantaneously reverse its direction at the

turning point $Z = 0$. We will investigate the dependence of the charge transfer on whether various components of the intra-atomic Coulomb interaction $U_{l\sigma l'\sigma'}$ are large or small. We will show that a microscopic understanding of the dynamics of charge transfer between adsorbates and a solid surface can be obtained with an analysis of the spectral function of the atomic levels.

In Section 3.1 we consider the case where all components of U vanish, in order to establish a reference for discussing the more realistic cases where U is large. The $U = 0$ results are based on Hamiltonian Eq. (1) with $U = 0$. In Section 3.2 we take the U between the up and down spins in a given level l to be large, but the U between electrons in the upper level and those in the lower level to still be zero. This allows many-body (Kondo) resonances to appear in the spectral functions in certain instances, and we discuss the effect of these on the predicted charge transfer. We note that in these two cases the upper and lower levels have no effect on each other, so

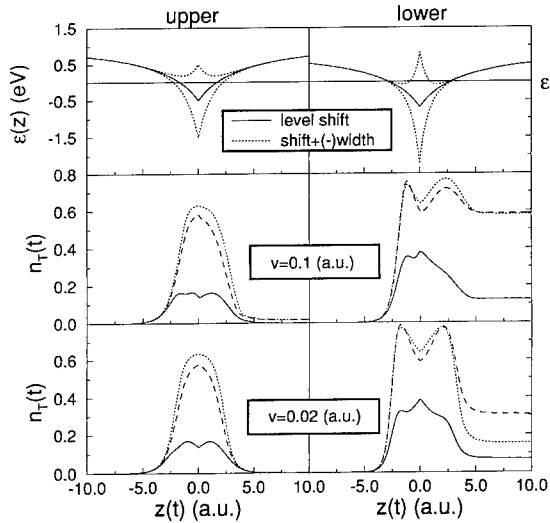


Fig. 1. Shown in the top panel, the energy shift and broadening of the atomic levels along the trajectory. The dotted lines are defined as $\epsilon_i(Z) \pm \Delta(Z)$. The shifts are parameterized as $\epsilon_i(Z) = \epsilon_i^0 - 27.2/4(Z+4)$ eV, with Z in a.u., and with $\epsilon_i^0 = 1.2$ eV for the upper level and 1.0 eV for the lower level. The widths are parameterized as in Eq. (8) with $\Delta_0^u = 1.0$ eV and $\alpha_u = 1.0$ a.u. for the upper level and $\Delta_0^l = 1.5$ eV and $\alpha_l = 1.5$ a.u. for the lower level. The positive, zero, and negative values along the horizontal axis corresponding to the incoming, turning point, and outgoing portion of the trajectory respectively. The two panels below show the calculated instantaneous populations of the atomic levels along the trajectory. The middle panel is for $v = 0.1$ a.u. and the panel at the bottom is for $v = 0.02$ a.u. The solid curves are for the case where the e-e interaction (U) among all states are large; the dashed curves for the case where U is large between the degenerate spin states, but zero between the upper and lower levels; and the dotted curves for the case where U is zero everywhere with $N = 1$. The width of the conduction band is $D = 5.0$ eV and the temperature of the substrate is $T = 300$ K.

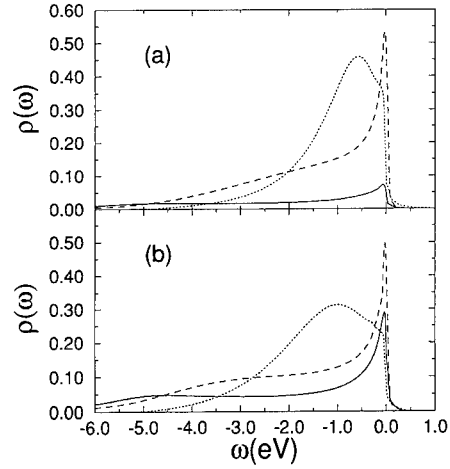


Fig. 2. Instantaneous occupied spectral functions (OSF) of the levels at the turning point for the system described in Fig. 1 at incident velocity $v = 0.1$ a.u. Panel (a) refers to the upper level and (b) refers to the lower level. The dotted curves are for the case where the intra-atomic Coulomb repulsion U is zero between all states. The dashed curve is for the case where the Coulomb repulsion between the different spin states of the same atomic level is taken into account, i.e., $U_{l\uparrow l\downarrow}$ large. The solid line is for the case where the Coulomb repulsion between all the levels is taken into account, i.e., $U_{l\sigma l'\sigma'}$ large for all $l\sigma l'\sigma'$.

that the charge transfer to each of them is the same as it would have been if the other were not present; thus our results would also apply to each of two single level problems with spin. Finally in Section 3.3 we take all components of U to be large. Then, in addition to the Kondo resonances of case 3.2, the inter-level blocking effect which we have discussed earlier [8,29] comes in to play.

3.1. Case of $U_{l\sigma l'\sigma'} = 0$

The instantaneous populations of the atomic levels along the atomic trajectory are shown in Fig. 1. For the $U = 0$ case, the population of the upper level increases until the atom reaches the turning point during the incoming trajectory, and decreases monotonically during the outgoing trajectory. The population of the lower level, however, experiences one maximum each during incoming and outgoing trajectory. In Fig. 2, we show the occupied spectral function (OSF) at the turning point for both levels. The spectral functions are characterized by an impurity peak centered around the energies of the atomic levels. The half-width at the half maximum (HWHM) of the impurity peak is approximately equal to the adiabatic half width of the atomic levels. For the upper level, the level shifts and its width increases during the incoming trajectory in such a way, as illustrated in Fig. 1, that the total weight of the OSF grows continuously until the turning point. So does the population. During the outgoing trajec-

tory, the weight of the OSF decreases continuously, and so does the population.

For the lower level, however, during the incoming and outgoing trajectory, there is a region of atom–surface separation (A), where in equilibrium the spectral function would be totally submerged under the Fermi level (both of the dotted curves get below the Fermi level). This is why in this region, the increase in population during the incoming trajectory and outgoing trajectory is most dramatic. When an atom passes through region A and gets closer to the surface, the width increases faster than the level shifts down. As a result, the portion of the spectral function below the Fermi level is smaller. This reduction in the total weight below the Fermi level leads to the decrease in the population of the lower level. During the outgoing trajectory, the population of the lower level increases when the atom passes through region A and then decreases as the atom recedes further away from the surface.

3.2. Case of $U_{l\uparrow l\downarrow}$ large

Now let us turn to the investigation of the effects caused by Coulomb repulsion between the degenerate states of the atomic levels. The instantaneous populations of the atomic level along the trajectory are plotted in Fig. 1. The general shape of the curves is similar to the zero U case. The differences are more significant for the upper level than for the lower level during the incoming trajectory, and in particular, for the lower level at smaller velocity. These observations can be readily explained by an analysis of the OSF.

As can be seen in Fig. 2, the OSF for this case looks very different from the $U = 0$ case. An additional feature, a resonant peak near the Fermi level is formed as a result of the Coulomb repulsion between the two spin states. We will refer to this peak as the Kondo peak. The spectral weight under the Kondo peak is taken from the impurity peak. The width of the Kondo peak is given qualitatively by the Kondo temperature [18–20], T_K , which can be written as

$$T_K \approx D \exp\left(-\frac{|\epsilon_l - \epsilon_F|}{N\Delta}\right), \quad (9)$$

where D is the distance between the Fermi level ϵ_F and the bottom of the conduction band, $N\Delta$ is the adiabatic total half width for the atomic level of degeneracy N (here $N = 2$), and ϵ_l is the energy level of the degenerate atomic state. Since the adiabatic width for the upper level is larger than that of the lower level for $Z > 1$ a.u., the width of the Kondo peak for the upper level is expected to be larger than that for the lower level. The electron transfer process is determined by two time scales, the inverse of the adiabatic width and the inverse of the width of the Kondo peak. The difference between the large U and zero U for both levels is mainly caused by the difference in the width

of the Kondo peak. A wider peak is formed more rapidly than a narrow one. For this reason, the effects of including $U_{l\uparrow l\downarrow}$ will be largest for the upper level during the incoming trajectory.

The differences between large $U_{l\uparrow l\downarrow}$ and zero U depend on the substrate temperature. In the present calculation, we have assumed that the substrate is kept at $T = 300$ K. When the upper level is above the Fermi level, the Kondo temperature is very small compared to the substrate temperature. Thermal fluctuations strongly decrease the effects of the Kondo peak on the charge transfer. For lower substrate temperatures, a larger effect of intra-atomic correlation would be expected. In the region where the adiabatic atomic level is near the Fermi level, the charge transfer dynamics becomes temperature dependent. The effect of substrate temperature on charge transfer is an interesting subject which will be discussed elsewhere [35].

Now let us try to understand the significant effect of large $U_{l\uparrow l\downarrow}$ on the population of the lower level at low velocities during the outgoing trajectory. Again this can be accomplished by an analysis of the spectral function of the atomic levels. From Fig. 2, we know that at the turning point, the Kondo peak in the spectral function of the lower level is relatively well formed even at as high a velocity as $v = 0.1$ a.u. [36]. Once the Kondo peak is formed, due to the fact that it is narrow, the removal of spectral weight from the Kondo peak will be much harder than the decrease in spectral weight from the impurity peak. During the outgoing trajectory, the atomic level shifts above the Fermi level. Since the population of an atomic level is equal to its integrated OSF, and the integrated weight is nearly the same around the turning point for zero U and large $U_{l\uparrow l\downarrow}$, if the system changes sufficiently fast, neither part can go through adequate depopulation and the atomic population at large distances remain similar to the population at the turning point. The difference between zero and large U is expected to be small, as shown for the large velocity in Fig. 1. However, when the atom moves more slowly, it is predominantly the spectral weight associated with the Kondo peak that will contribute to the final population of the atomic level. This argument explains why the effect of including $U_{l\uparrow l\downarrow}$ has a relatively large effect on the final population of the lower level at a smaller velocity as seen in Fig. 1.

For larger velocities than $v = 0.1$ a.u., at which the Kondo peak barely forms at the turning point, the final population for zero U case will be larger than for large $U_{l\uparrow l\downarrow}$. The buildup of spectral weight in the Kondo peak is at the expense of spectral weight in the impurity peak. In other words, the spectral weight in the impurity peak is lower when $U_{l\uparrow l\downarrow}$ is large. For large velocities, only the broad features of the Kondo peak have time to build up at the turning point. During the outgoing trajectory, the depopulating process for weight under the Kondo peak is almost as efficient as that for the impurity peak. Since the spectral weight under the Kondo peak is smaller, what is

left in the final population derives from the tails of the impurity peak. Therefore, the final population is larger for zero U system than that for large $U_{l\uparrow l\downarrow}$. This fact will become more evident when we discuss the behavior of the final population of the upper level as a function of the incident atomic velocity.

3.3. Case of $U_{l\sigma l'\sigma'}$ large

Now let us turn to the case where large Coulomb repulsion exists among all states. This is a case, where a dramatic blocking effect can occur [29]. The charge transfer from the substrate to one atomic state depends on the total atomic population, among other things. The larger the total atomic population is, the less likely the electron transfer from the substrate into the atom.

In Fig. 1, the instantaneous population of the two atomic levels along the trajectory is plotted. During the initial part of the trajectory, the population is low in both of the levels. For this reason, the influence of intra-atomic correlation is very limited. At a distance $Z \approx 4$ a.u., the curves become markedly different. This happens because once there is substantial population in any level, the unoccupied portion of the atomic states is reduced. As a result of the reduction in the unoccupied states, the atomic levels cannot populate as much. Although the final population in upper level is very small, the temporary population of the upper level in the dynamic process nonetheless dramatically reduces the total charge transfer into the lower level.

In Fig. 2, the instantaneous occupied spectral functions of the two atomic levels at the turning point are shown for large $U_{l\sigma l'\sigma'}$. They look similar to those for the case where only the intra-level $U_{l\uparrow l\downarrow}$'s are large, except that their amplitudes are smaller due to the inter-level blocking effect, as expected.

3.4. Velocity dependence of charge transfer

In order to further investigate the effects of electron correlation effect on charge transfer, we calculated the total final population of the upper level as a function of the incident velocity for the large $U_{l\uparrow l\downarrow}$ case. For comparison, we also include a calculation for $U = 0$. The results of the calculation are shown in Fig. 3. For the $U = 0$ case, the logarithm of the final population as a function of inverse incident velocity shows a linear behavior at low velocities. This linearity can be analytically derived in the master equation limit [29]. This linearity can be understood intuitively by an analysis of the OSF.

In Fig. 4, the instantaneous spectral function at the turning point is shown for different velocities for $U = 0$ and large $U_{l\uparrow l\downarrow}$. At low temperature and small velocities, the OSF of the atomic level is a simple distorted Lorentzian, sharply cut-off at the Fermi level due to Fermi factor. The population is determined by the adiabatic width and position of the atomic level with respect to the Fermi level.

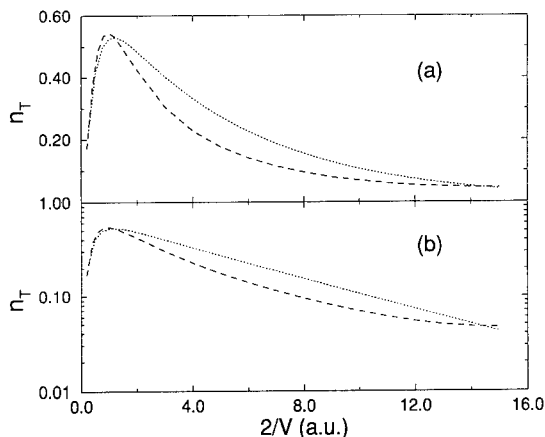


Fig. 3. Final population of the upper level, described in Fig. 1, as a function of inverse incident atomic velocity. Panel (a) is a linear-linear plot and panel (b) is linear-log plot. The dashed curves are for large e-e interaction (U) and the dotted ones for zero U .

The charge transfer at low temperature is then controlled by the level width and whether the level position is above or below the Fermi level, and is insensitive to the specific energy of the atomic level. Therefore, only one time scale, the inverse of adiabatic half level width, is present.

For large U , however, as shown in Fig. 4, a Kondo peak is formed in the OSF at the turning point. As discussed earlier, the inverse of the width of the resonant peak provides an extra time scale for the charge transfer dynamics. Due to this very existence of the additional time scale, the linearity present in zero U case does not exist in large U case any more. Therefore it is possible to experimentally investigate large correlation effect by measuring

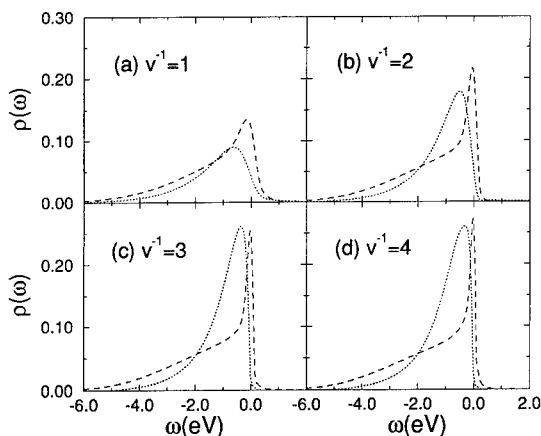


Fig. 4. Occupied spectral function (OSF) at the turning point of one atomic state in the upper level, described in Fig. 1, at different incident velocities. The dashed curves are for large e-e interaction (U) and the dotted ones for zero U .

the final population of the scattered species as a function of inverse incident velocity.

From Fig. 4, we see that for the largest velocities, the Kondo peak is incompletely formed. The spectral functions for zero U and large U are similar. Consequently, the final charge transfer will be similar. For the lowest velocities, the Kondo peak appears in its full glory. As discussed in Section 3.2, the final population will therefore be larger due to the inertness of this feature. For intermediate velocities, the formation of the Kondo peak is incomplete, yielding a broad structureless feature near the Fermi level. The incompletely formed Kondo structure decays relatively fast. The intra-atomic correlation term reduces the spectral weight of the impurity peak. For this reason, in the intermediate velocity regime, the final population is smaller for large $U_{\sigma'\sigma'}$ than for $U = 0$.

4. Summary

We have presented a series of model calculations illustrating the effects of intra-atomic correlation on charge transfer. We have demonstrated the usefulness of the spectral function for understanding the microscopic origins on non-adiabaticity. We have been able to confirm the drastic blocking effects among correlated non-degenerate atomic levels [29]. We have also been able to show that the formation of a Kondo peak in the spectral function of degenerate atomic levels can introduce novel sources of non-adiabaticity in the problem by introducing an extra long time scale (the inverse of the narrow width of the resonant peak) and by altering the spectral weight near the Fermi level. This novel many-electron effect is expected to be most prominent when the degeneracy of the atomic level is large and/or the substrate temperature is smaller than the Kondo temperature. More detailed studies of the effects of substrate temperature, atomic velocities and substrate work function will be published in a forthcoming paper [35].

The results from the calculations described in this paper show that the study of charge transfer processes in atom-surface scattering can provide interesting information of the physics of strongly correlated fermion systems in non-equilibrium situations. Atom-surface scattering experiments can be performed for a very wide range of parameters and may in fact be the ideal arena for studies of the dynamics of many-electron systems.

Acknowledgements

One of the authors (HS) is especially grateful for the generous support from Prof. Horia Metiu. This work is supported in part by the National Science Foundation under grants DMR 91-20007 (HS), DMR 91-17479 (PN,HS) and DMR 91-03466 (DCL) and DMR 94-07055

(DCL). Part of this work was done when one of us (DCL) was a member of the Institute for Theoretical Physics, University of California, Santa Barbara, and partially supported by NSF grant PHY 89-04035. Acknowledgement is made to the donors of the Petroleum Research Fund, administered by the American Chemical Society for the partial support of this research, under grants 27240-AC5 (PN,HS).

References

- [1] G.A. Kimmel, D.M. Goodstein, Z.H. Levine and B.H. Cooper, Phys. Rev. B 43 (1991) 9403.
- [2] M.S. Hammond, F.B. Dunning, G.K. Walters and G.A. Prinz, Phys. Rev. B 45 (1992) 3674.
- [3] P.D. Johnson, A.J. Viescas, P. Nordlander and J.C. Tully, Phys. Rev. Lett. 64 (1990) 942.
- [4] A.L. Johnson, S.A. Joyce and T.E. Madey, Phys. Rev. Lett. 61 (1988) 2578.
- [5] C.C. Hsu, H. Bu, A. Bousetta, J.W. Rabalais and P. Nordlander, Phys. Rev. Lett. 69 (1992) 188.
- [6] J. Los and J.J.C. Geerlings, Phys. Rep. 190 (1990) 133.
- [7] J.B. Marston, D.R. Andersson, E.R. Behringer and B.H. Cooper, Phys. Rev. B 48 (1993) 7809.
- [8] H. Shao, D.C. Langreth and P. Nordlander, Phys. Rev. B 49 (1994) 13929.
- [9] H. Shao, D.C. Langreth and P. Nordlander, Phys. Rev. B 49 (1994) 13948.
- [10] C. Liu and Q. Niu, Phys. Rev. B 47 (1993) 13031.
- [11] G.W. Bryant, Phys. Rev. B 48 (1993) 8024.
- [12] C.A. Stafford and S. Dassarima, Phys. Rev. Lett. 72 (1994) 3590.
- [13] A.D. Stone and H. Bruus, Surf. Sci. 305 (1994) 490.
- [14] C. Bruder and H. Schoeller, Phys. Rev. Lett. 72 (1994) 1076.
- [15] P.A. Maksym and T. Chakraborty, Phys. Rev. Lett. 65 (1992) 108.
- [16] A. Blandin, A. Nourtier and D. Hone, J. Phys. (Paris) 37 (1976) 369.
- [17] R. Brako and D.M. Newns, Rep. Prog. Phys. 52 (1989) 655.
- [18] H.R. Krishna-Murthy, J.W. Wilkins and K.G. Wilson, Phys. Rev. B 21 (1980) 1003.
- [19] N. Andrei and C. Destri, Phys. Rev. Lett. 52 (1984) 364.
- [20] N.E. Bickers, Rev. Mod. Phys. 59 (1987) 845.
- [21] A. Yoshimori and K. Makoshi, Solid State Comm. 74 (1990) 693.
- [22] W. Bloss and D. Hone, Surf. Sci. 72 (1978) 277.
- [23] T.B. Grimley, V.C.J. Bhasu and K.L. Sebastian, Surf. Sci. 124 (1983) 305.
- [24] A. Yoshimori, H. Kawai and K. Makoshi, Prog. Theor. Phys. Suppl. 80 (1984) 203.
- [25] K.L. Sebastian, Phys. Rev. B 31 (1985) 6976.
- [26] R. Brako and D.M. Newns, Solid State Comm. 55 (1985) 633.
- [27] H. Kasai and A. Okiji, Surf. Sci. 183 (1987) 147.
- [28] K.W. Sulston, A.T. Amos and S.G. Davison, Phys. Rev. B 37 (1988) 9121.
- [29] D.C. Langreth and P. Nordlander, Phys. Rev. B 43 (1991) 2541.
- [30] P.W. Anderson, Phys. Rev. 124 (1961) 41.

- [31] Intra-atomic Coulomb interaction between atomic states, U , depends on the atomic distance from the surface. Detailed discussions in this regard can be found in Refs. [33,37]. Throughout this report, U is assumed large at all time during the scattering.
- [32] P. Coleman, Phys. Rev. B 29 (1984) 3035.
- [33] H. Shao, D.C. Langreth and P. Nordlander, in: Low Energy Ion–Surface Interactions, ed. J.W. Rabalais (Wiley, 1993) pp. 117–187.
- [34] P. Nordlander and J.C. Tully, Phys. Rev. B 42 (1990) 5564.
- [35] H. Shao, P. Nordlander and D.C. Langreth, to be published (1994).
- [36] For lower velocities, the Kondo peak will be even more pronounced. See Fig. 9 in Ref. [8] and Fig. 4 in the present paper for a detailed discussion of how the instantaneous spectral function of an atomic level depends on the velocity of the atom.
- [37] P. Nordlander, H. Shao and D.C. Langreth, Nucl. Instr. and Meth. B 78 (1993) 11.



ELSEVIER

Evidence for electron correlations in secondary ion formation

A.B. Popov^{*}, B.N. Makarenko, A.P. Shergin*Ioffe Physical Technical Institute, 194 021 St. Petersburg, Russian Federation*

Abstract

The velocity dependences of ionization probabilities for positive and negative ions sputtered under ion bombardment of metals are investigated. It is shown that the Auger-like transitions caused by the intra-atomic Coulomb interaction are the main mechanism in the formation of negative Cu, Ag, Au and Pt ions.

1. Introduction

The mechanisms of charge state formation of particles sputtered under ion bombardment of solids are the important subject of modern theoretical and experimental investigations. The conventional theoretical description of the charge exchange between a moving particle and a metal surface is based on the time-dependent Newns-Anderson Hamiltonian and treats the electron exchange as a resonant tunneling transition between an atomic level and the conduction band of a metal [1]. The electron tunneling model neglects spin effects and the effect of the intra-atomic Coulomb repulsion between electrons captured into different states of secondary particle. The model [1] is valid if only one atomic level is involved in the exchange process (for instance, it may be the neutralization of a positive ion or the formation of a negative ion separately, but not both at the same time). This condition is very seldom realized in practice.

At present the role of electron correlations is intensively studied theoretically [2–9]. Recently it has been confirmed in few experiments [10,11] that the correlation effects can considerably alter the probability of charge transfer in atom scattering on metal surfaces. The task of this work is the experimental observation of the electron correlations in secondary ion formation during sputtering.

The charge exchange in the particle-surface interaction has the same nature in both scattering and sputtering. However, there are significant differences. The most prominent of them is the much stronger excitation of the surface in ion sputtering. How it can affect the manifestation of the electron correlations is the question which

should be clarified. It should be only emphasized that the de-excitation process is as a rule faster than the charge state formation process. At the same time, the low-velocity nature of secondary particles (the energies of the majority of sputtered atoms are a few eV) will probably result in an increase of the role of correlation effects because of a long time scale of particle-surface interaction in comparison with atom scattering (the usual particle energy interval in scattering experiments is decades of eV – a few keV). In any case, because the charge exchange processes in scattering and sputtering have more common features than their differences, we could expect an essential effect of the electron correlations on secondary ion formation.

In the present study the yields and the energy spectra of neutral atoms, positive and negative ions sputtered from polycrystalline Ag and Pt targets were measured. The metals Ag and Pt with positive affinity energy were selected as objects under investigation because the correlation effects can be more definitely manifest when ions of both signs can be ejected. The results of our previous investigations of Cu and Au targets [12,13] were involved in the present consideration.

2. Experimental technique and results of energy spectra measurements

The experimental setup for studying the sputtered neutrals, positive and negative ions, is described in details previously [14]. The angle of incidence of 5.5 keV Ar⁺ primary ion beam was 50° and the emission angle with respect to the surface was 90°. The neutrals were post-ionized by electron impact before analysis. The intensity of neutral particles was obtained by the ratio of the intensity of post-ionized neutral atoms to the post-ionization efficiency α . The value of α is expressed by

$$\alpha = \sigma j l / v, \quad (1)$$

^{*} Corresponding author, tel. +7 812 247 9142, fax +7 812 247 1017, E-mail: shergin@eos.pti.spb.su.

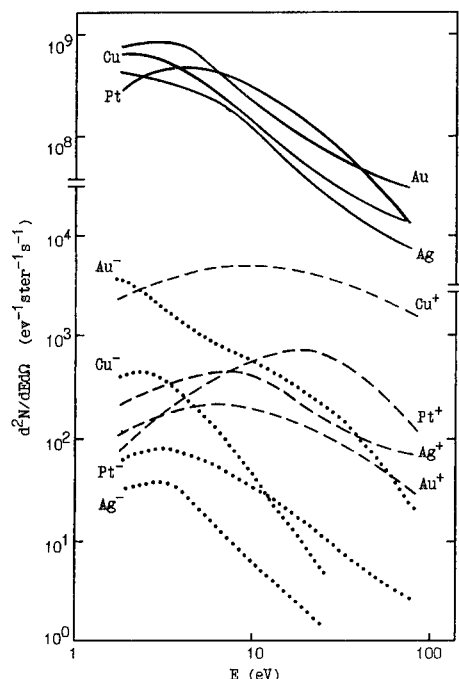


Fig. 1. The energy spectra of neutral atoms (solid lines), positive (dashed lines) and negative (dotted lines) ions sputtered from Cu, Ag, Pt and Au polycrystalline targets by 5.5 keV Ar⁺ ions.

where v is the velocity of sputtered particles, σ is the cross section for electron impact ionization, j is the electron current density and l is the dimension of the ionization area.

The experimental energy spectra of neutral atoms, positive and negative ions for Ag and Pt are shown in Fig. 1 together with the spectra for Cu and Au measured earlier [12,13]. As seen from the figure, the spectra of positive ions exhibit distributions with maxima occurring at 10–20 eV and relatively long “tails” in the high energy region. The spectra of negative ions differ considerably from those of positive ions. The maxima occur at energies $E < 4$ eV and the distributions fall down faster with increasing energy.

It should be noted that for neutral Pt atoms the energy distribution was found to be described well by the Thompson formula [15] $dN/dE \approx E/(E + U_b)^{3-2m}$ with the surface binding energy $U_b = 8$ eV and the parameter $m = 0$. For Cu, Ag and Au atoms this equation fits experimental curves only in the energy region $E < 25$ –30 eV with $U_b = 3$, 4 and 4 eV, respectively. At energies higher than 30 eV the dependence $dN/dE \approx E^{-2}$ fails to describe the experimental distributions. The increase of the sputtered particle yield for high energies can be explained by the direct recoil mechanism. This effect, as was shown in Ref. [16], is most pronounced under the angles of incidence different from 0°.

3. Velocity dependences of ionization probabilities

Fig. 2 shows the ionization probabilities P^+ and P^- as a function of the normal component v_\perp of the velocity of sputtered particles, which were obtained by comparing the energy spectra of positive and negative ions, correspondingly, with the spectra of neutral atoms. The investigation of the velocity dependence of ionization probabilities is one of the main test, which allows to make a choice from different theoretical approaches because the particle velocity defines the interaction time and is considered in all theoretical models of the charge exchange. As follows from Fig. 2, the ionization probabilities P^+ for positive ions agree well with the exponential dependence on v_\perp^{-1} : $P^+ \approx \exp(-v_0^+/v_\perp)$, where v_0^+ is the characteristic velocity in the system “sputtered ion-surface”. Such a behavior of $P^+(v_\perp^{-1})$ shows an evidence for the electron tunneling mechanism [1] in the formation of positive ions. The same conclusion was derived also in Refs. [12–14,17]. It should be noted that in these works the ionization probabilities $P^+(v_\perp^{-1})$ were obtained by direct measurements of the energy spectra of ions and neutral atoms.

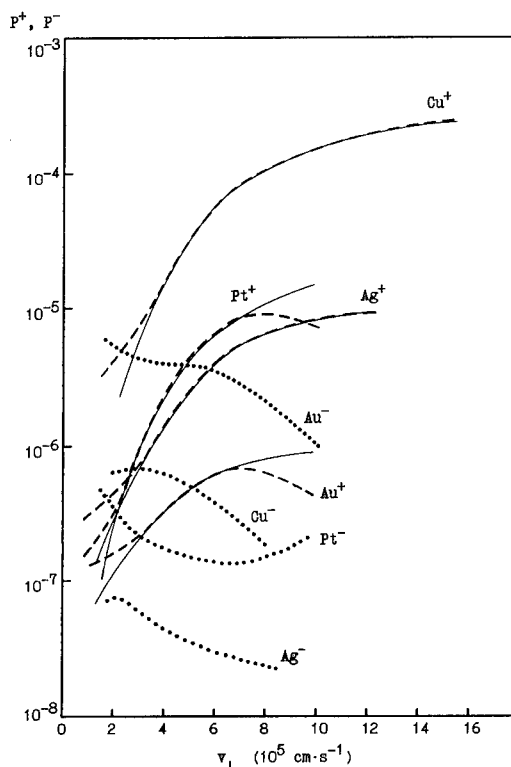


Fig. 2. The ionization probabilities P^+ (dashed lines) and P^- (dotted lines) as a function of velocity of sputtered particles. Thin solid lines are the dependences $P^+ \approx \exp(-v_0^+/v_\perp)$.

As seen in Fig. 2, unlike $P^+(v_\perp)$, the velocity dependences of $P^-(v_\perp)$ for Cu, Ag and Au prove to be decreasing functions of the velocity. $P^-(v_\perp)$ for Pt has a minimum. Such a behavior of $P^-(v_\perp)$ disagrees strongly with the predictions of the electron tunneling model [1] as this model predicts simply an exponential dependence of the ionization probability on the velocity for both positive and negative ions ($P^\pm \approx \exp(-v_0^\pm/v_\perp)$).

4. Auger-like transitions in formation of negative ions

The observed behavior of $P^-(v_\perp)$ can be caused by the effect of the intra-atomic Coulomb interaction on the process of population of the ionization and affinity levels of the emitted particle. As shown theoretically [2–4,7], one of the results of influence of the intra-atomic correlations on the charge transfer is a strong (compared to the one-level model) redistribution of the charge states during simultaneous population of the ionization and affinity levels through resonant transitions. This effect would be more significant when the electron affinity level is energetically close to the Fermi level [3,4,7]. As a consequence, $P^-(v_\perp)$ may be a decreasing function of the velocity. However, in the case of pure metals the difference $\phi - A$ (here ϕ is the work function and A is the affinity energy) is usually large and the decreasing behavior of $P^-(v_\perp)$ cannot be explained by the resonant transitions in our case.

Electron correlations can also manifest themselves during formation of the negative ion from a positive ion through the Auger-like transition caused by the intra-atomic Coulomb interaction. This mechanism leading to the decreasing function of P^- on the velocity has been proposed recently by Nakanishi et al. [5] in analysis of the scattering of H^+ ions on W surface: an electron from the conduction band fills the unoccupied ionization ε^+ level and the energy released thereby is carried away by a second electron of the conduction band which is captured by the affinity ε^- level (Fig. 3). The Auger-like transition is possible as long as the sum of the energies of two hopping

metal electrons $\varepsilon_k + \varepsilon_l$ is equal to the sum of $\varepsilon^+(z) + \varepsilon^-(z)$, where z is the distance of the atomic particle from the surface. Evidently, the charge transfer through the Auger-like transitions is enhanced as the particle velocity decreases. Thus, the decrease of P^- observed with increasing v during sputtering of Cu, Ag, Au and Pt is an essential argument in favor of the Auger mechanism of the secondary negative ion formation.

Additional evidence for this mechanism follows from an analysis of the absolute values of transition rates for the Auger-like and one-electron resonant processes which are probably two main channels leading to the secondary ion formation for the metals under study. The width Γ_A corresponding to the Auger-like process will be higher the wider the energy interval $\Delta\varepsilon$ within the conduction band from which the electrons participating in the Auger process can be captured by the particle. If we accepted $\varepsilon^+(z) = I$ (here I is the ionization potential) and $\varepsilon^-(z) = A$, the equation $\varepsilon_k + \varepsilon_l = \varepsilon^+(z) + \varepsilon^-(z)$ leads to the following expression for the energy interval $\Delta\varepsilon$:

$$\Delta\varepsilon = I + A - 2\phi. \quad (2)$$

The widths Γ_A and Γ^\pm (Γ^\pm correspond to the one-electron transitions) can be estimated in the quasiclassical approximation for a particle moving at velocity $v_\perp = z/t$ using a system of master equations for the occupations n^+ and n^- of the atomic ε^+ and ε^- levels, respectively. As was shown in Ref. [6] the quasiclassical approximation is valid if the secondary particle has a low velocity and the atomic energy levels lie far from the Fermi level. These conditions are satisfied in our case and the system takes the form:

$$dn^+/dt = (1 - n^+)(1 - n^-)\Gamma_A + (1 - n^+)\Gamma^+, \quad (3)$$

$$dn^-/dt = (1 - n^+)(1 - n^-)\Gamma_A - n^-\Gamma^-. \quad (4)$$

This system is most easily solved if we assume $\Gamma_A = \Delta_A \exp(-\gamma_A z)$, $\Gamma^\pm = \Delta^\pm \exp(-\gamma^\pm z)$, $\gamma_A = \gamma^+ = \gamma^-$ and the initial conditions at $t = 0$ are $n^+(0) = n^-(0) = 0$, which seem to be realistic. Here γ^{-1} is the characteristic decay length of the electron wavefunction. In addition, since the yield of negative ions in sputtering of metals is very low, the factor $(1 - n^-)$ can be set to be equal to unity. Moreover, since $1 - n^+(\infty) \ll 1$ and $n^-(\infty) \ll 1$, we find $P^+ \approx 1 - n^+(\infty)$ and $P^- \approx n^-(\infty)$. As a result, the solution of Eq. (3) and (4) can be written as

$$P^+ = \exp\left(-\frac{\Delta^+ + \Delta_A}{h\gamma v_\perp}\right), \quad (5)$$

$$P^- = P^+ \frac{\Delta_A}{\Delta^+ + \Delta_A - \Delta^-} \left[\exp\left(\frac{\Delta^+ + \Delta_A - \Delta^-}{h\gamma v_\perp}\right) - 1 \right]. \quad (6)$$

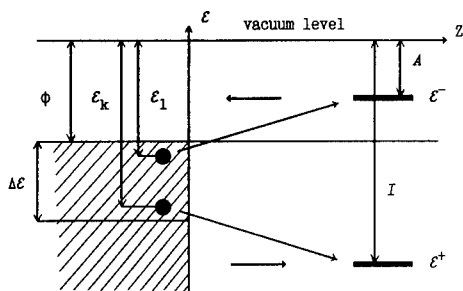


Fig. 3. The scheme of the Auger-like and resonant transitions between the sputtered particle and the surface.

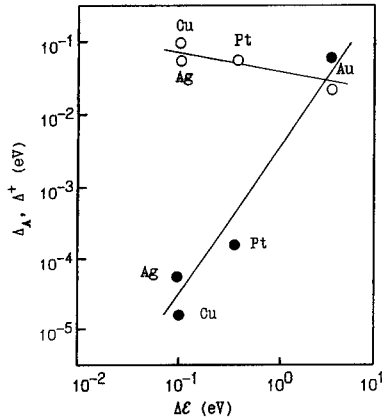


Fig. 4. The dependence of the absolute values of Δ_A (●) and Δ^+ (○) on the energy interval $\Delta\varepsilon$.

As seen, for P^+ we obtain the exponential dependence on v_\perp^{-1} , while $P^-(v_\perp)$ is a more complicated function. Eq. (5) and (6) lead to

$$P^-(v_\perp)/P^+(v_\perp) = \frac{\Delta_A}{\Delta^+ + \Delta_A - \Delta^-} \left[\exp\left(\frac{\Delta^+ + \Delta_A - \Delta^-}{h\gamma v_\perp}\right) - 1 \right], \quad (7)$$

where Δ_A and $\Delta^+ + \Delta_A - \Delta^-$ are parameters which can be found from a best fit of the values of $P^-(v_\perp)/P^+(v_\perp)$ (Eq. (7)) and the experimental ones. The widths Δ_A obtained in this way are plotted in Fig. 4 as a function of the energy interval $\Delta\varepsilon$ calculated using Eq. (2). As one should expect, there is a distinct correlation between Δ_A and $\Delta\varepsilon$ for all elements under study. In addition, as follows from Fig. 4, the values of Δ_A increase about proportionally to $(\Delta\varepsilon)^2$. Such a dependence of Δ_A on $\Delta\varepsilon$ follows from the golden-rule expression for the Auger-like transition rate $W(z)$:

$$W(z) = 2\pi \int \int d\varepsilon_k d\varepsilon_1 \rho(\varepsilon_k) \rho(\varepsilon_1) V_{abkl}^2 \times \delta(\varepsilon^+ + \varepsilon^- - \varepsilon_k - \varepsilon_1), \quad (8)$$

where V_{abkl} is the matrix element, a and b denote the secondary particle states corresponding to the ionization ε^+ and affinity ε^- levels, respectively, and $\rho(\varepsilon_i)$ are the densities of states in the conduction band. For simplicity, we assume that $\rho(\varepsilon_k) = \rho(\varepsilon_1) = \rho$, $V_{abkl}(z) = V_0 \exp(-\gamma z)$, $\varepsilon^+(z) = I$ and $\varepsilon^-(z) = A$. Then, $W(z)$ can be written as $W(z) = 2\pi\rho^2(\Delta\varepsilon)^2 V_0^2 \exp(-2\gamma z)$. As seen, the value of $W(z)$ at $z=0$ is proportional to $(\Delta\varepsilon)^2$, which agrees well with the experiment.

Fig. 4 shows also the widths $\Delta^+ = v_0^+ h\gamma$ of the ionization level responsible for the positive ion formation. The parameters v_0^+ are determined from the slope of the $\ln P^+(v_\perp^{-1})$ experimental curves [14,17]. In calculating Δ^+ we have used the average value $\gamma = 1 \text{ \AA}^{-1}$ as it was

proposed in Ref. [18]. As might be expected, $\Delta^+ \gg \Delta_A$ for all metals except Au (for which Δ^+ and Δ_A are comparable) and Δ^+ are almost independent on $\Delta\varepsilon$, which indicates that resonant processes dominate in the formation of positive ions and there is only a small contribution from the Auger-like transitions. Such a behavior of the absolute values of Δ_A and Δ^+ results from the two-electron nature of the Auger process: its probability should be lower than the probability of the one-electron resonant transition to the ε^+ level. At the same time, the slight drop in Δ^+ with increasing $\Delta\varepsilon$ can probably be attributed to a redistribution of the probabilities in favor of a higher yield of negative ions.

The existence of a minimum on the $P^-(v_\perp)$ curve for Pt is likely a consequence of the competition between the Auger-like transitions and the nonadiabatic transitions described by the electron tunneling model. For low v the Auger-like transitions are dominant and we observe the decreasing function of the velocity dependence $P^-(v_\perp)$. For high v the contribution of the quiresonant transitions becomes greater and the ionization probability P^- begins to increase with increasing velocity.

5. Conclusion

In this work the yields and the energy spectra of secondary neutral atoms, positive and negative ions sputtered from metal targets have been measured and the velocity dependences of ionization probabilities P^+ and P^- have been obtained. The dependences $P^-(v)$ were found to be decreasing functions of v , which is in disagreement with the electron tunneling model. The results obtained provided evidences for the Auger-like transitions in the formation of negative ions.

References

- [1] M.L. Yu and N.D. Lang, Nucl. Instr. and Meth. B 14 (1986) 403.
- [2] H. Kasai and A. Okiji, Surf. Sci. 183 (1987) 147.
- [3] K.W. Sulston, A.T. Amos and S.G. Davison, Phys. Rev. B 37 (1988) 9121.
- [4] H. Nakanishi, H. Kasai and A. Okiji, Surf. Sci. 197 (1988) 515.
- [5] H. Nakanishi, H. Kasai and A. Okiji, Surf. Sci. 242 (1991) 410.
- [6] D.C. Langreth and P. Nordlander, Phys. Rev. B 43 (1991) 2541.
- [7] B. Helling and V.P. Zdanov, Surf. Sci. 274 (1992) 411.
- [8] H. Shao, D.C. Langreth and P. Nordlander, Phys. Rev. B 49 (1994) 13929.
- [9] H. Shao, D.C. Langreth and P. Nordlander, Phys. Rev. B 49 (1994) 13948.
- [10] E.R. Behringer, D.R. Andersson, D.M. Goodstein, B.

- Kasemo, B.H. Cooper and J.B. Marston, *Nucl. Instr. and Meth. B* 78 (1993) 3.
- [11] U. van Slooten, T.C. Horn and A.W. Kleyn, *Surf. Sci.* 243 (1991) 12.
- [12] B.N. Makarenko, A.B. Popov and A.P. Shergin, *Izv. AN SSSR, Fiz.* 54(7) (1990) 1331; Engl. transl.: *Bull. Acad. Sci. USSR Phys. Ser. (USA)* 54 (7) (1990) 96.
- [13] A.B. Popov, S.B. Kablukov, B.N. Makarenko and A.P. Shergin, *Vacuum* 44 (1993) 903.
- [14] B.N. Makarenko, A.B. Popov, A.A. Shaporenko and A.P. Shergin, *Radiat. Eff. Def. Solids* 113 (1990) 263.
- [15] H.W. Thompson, *Phyl. Mag.* 18 (1968) 337.
- [16] Y. Dembowski, H. Oechsner, Y. Yamamura and M. Urbassek, *Nucl. Instr. and Meth. B* 18 (1987) 467.
- [17] A. Wucher and H. Oechsner, *Surf. Sci.* 199 (1988) 567.
- [18] R. Brako and D.M. Newns, *Rep. Progr. Phys.* 52 (1989) 655.



ELSEVIER

Resonant coherent excitation of N^{6+} and Mg^{11+} in planar channeling: anisotropies in ionization probabilities and X-ray emission

S. Datz ^{a,*}, P.F. Dittner ^a, H.F. Krause ^a, C.R. Vane ^a, O.H. Crawford ^a, J.S. Forster ^b,
G.S. Ball ^b, W.G. Davies ^b, J.S. Geiger ^b

^a Physics Division, P. O. Box 2008, Oak Ridge National Laboratory, Oak Ridge, TN 37831-6377, USA

^b AECL Research, Chalk River Laboratories, Chalk River, Canada

Abstract

Hydrogenic ions penetrating a crystal are perturbed by the frequency with which they pass atoms lying in rows or ordered planes. This frequency, when resonant, can cause excitation of the ion with subsequent collisional ionization or radiative relaxation following escape from the crystal. The various possible m states being non-degenerate in the channel are separable. The associated alignment is observed in both the separate ionization probabilities and X-ray anisotropy.

1. Introduction

The thrust of the conference in which this paper is presented is toward inelastic interactions of ions with surfaces. The work described in this paper deals with inelastic interactions of ions in planar channeling inside the crystal. We are, however, not too far off the mark because the planar channeling potential is made up from the sum of two (sheet) surface potentials. The difference, if you will, is similar to that between an ordinary sandwich and an open faced one (smørebrød), and in the future these techniques may well be applied to the single surface.

In earlier work on resonant coherent excitation (RCE) of channeled ions, it was shown that for H-like ions ($Z = 4 - 9$) moving in axial crystal channels in the velocity range $6v_0 \leq v_i \leq 12v_0$, collisional lifetimes are sufficiently long to give well-defined $n = 1$ and $n = 2$ states. It was also shown that the effect of the spatially (time) coherent field caused by correlated collisions with atoms arranged in crystal rows can give rise to resonant excitation of the penetrating ion [1,2]. Thus, an ion moving at velocity v_i past a row of atoms with interatomic spacing d experiences periodic perturbation at frequencies $\nu = K(v_i/d)$, $K = 1, 2, 3 \dots$. The ion can be resonantly excited when a frequency $\Delta E_{ij}/h$ is attained, where ΔE_{ij} is the energy difference between states i and j of the moving ion. We showed that the energy levels of the penetrating ion differed measurably from the vacuum states. These differences reflected the influence of the static crystal field which removed the degeneracy of the $2p_x$, $2p_y$, and $2p_z$

orbitals, and of the influence of wake field which acted to Stark mix the $2s$ and $2p_z$ states.

It was then shown that, while in axial channeling, the excitation frequencies are determined by the fixed spacing along rows in a given lattice direction, in planar channeling, the frequencies are vector sums of components in the hkl directions [3]. Hence, at a given velocity (see Fig. 1), a continuously tunable range of resonant frequencies is available depending on the angle in the plane low index axial directions. In both cases, (axial and planar), the resonances were previously observed by varying the ion beam energy for a fixed crystal orientation.

An example of the resonances that can be attained is shown in Fig. 2 for N^{6+} in the (100) planar channel of Au, where a plot of the velocities and angles required to achieve RCE for $n = 1 \rightarrow n = 2$ is shown. The condition for resonance in the (100) plane of an FCC lattice is given by

$$E_r (\text{MeV}/\text{amu}) = 3.03 \frac{2}{(\gamma + 1)} \left[\frac{\Delta E_{ij} (\text{keV}) \times a (\text{\AA})}{l \cos \theta + k \sin \theta} \right]^2, \quad (1)$$

where E_r is the resonant ion energy, γ is the relativistic factor $(\sqrt{1 - \beta^2})^{-1}$, a is the lattice constant and l and k are field components. The resonances are denoted by (l, k) in the diagram.

For the low- Z (4–9) hydrogenic ions used, the resonances were demonstrated by observing the increase in the fraction of totally stripped ions which occurred as the ion passed through the crystal channel as a function of v_i . The reason for this increase is the increase in the ionization cross section (factor ~ 10) which occurs when the ion is pumped up from $n = 1 \rightarrow n = 2$. For the ions in question,

* Corresponding author. Tel. +1 615 574 4779 or +1 615 576 4473, fax +1 615 574 1118.

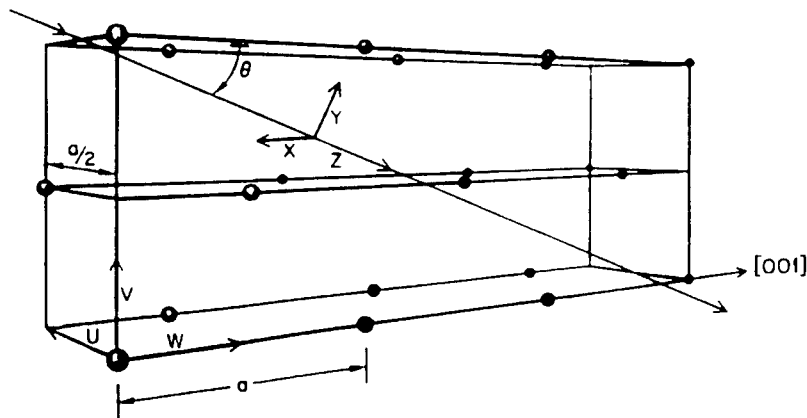


Fig. 1. Coordinate system for planar channeling in the (100) plane of an FCC crystal.

there is a reasonable chance ($\sim 50\%$) of the ion in its 1s state, passing through the electrons in the channel without electron loss, however, in the $n = 2$ state, the probability of emergence from even these very thin (1000–5000 Å) crystals is vanishingly small.

This is not true for higher- Z ions at higher velocities. Here the ionization cross section of even the $n = 2$ state

may be small enough to allow the ion to escape from the crystal intact where it is then free to relax via radiative decay. This was demonstrated in a later paper [4] using Mg^{11+} ions and observing RCE in the 7th harmonic in the $\langle 111 \rangle$ axial channel in Au at resonant velocities of $\sim 16v_0$ (~ 160 MeV). Here the resonance could be observed by either an increase in Mg^{12+} population or by an increase in Mg^{11+} Ly_α X-radiation from those ions which escaped the crystal in the $n = 2$ state. Differences in the relative population of the $2p_z$ and $2p_x$ states were noted between the radiative and ionization channels implying differences in the electron bombardment ionization cross sections for these two orbitals.

This result led to a curious conclusion: namely, that the specific m state population created by RCE retained its identity long enough to participate in an ionizing collision, i.e., the alignment was not destroyed by electron collisions prior to the ionizing collision. This result could be due to the creation of these states in different parts of the channel, e.g., the $2p_x$ state might be created closer to the atomic strings than the $2p_z$ and result in a higher probability for ionization of $2p_x$ states. Since trajectories in axial channeling are extremely complex, we sought to carry out the experiments in planar channels where the trajectories are considerably simpler to follow. In addition, we would like to work with low harmonics where the transition strength is large and to use ions which can give X-rays which are measurable with a SiLi detector (≥ 1 keV), i.e., we must use high energy beams to achieve low harmonics.

These requirements lead to a dilemma if we are to carry out these experiments as we have in the past, i.e., to use H-like ions and vary the ion beam energy in small steps. To achieve the high energies in question requires the use of a cyclotron or linac where small variations in ion beam energy by varying machine conditions are not achieved on a short time scale. The usual method is to accelerate to a higher energy and then “degrade” the energy by passing it through an absorber and selecting the final energy via magnetic deflection. Unfortunately, at the desired high

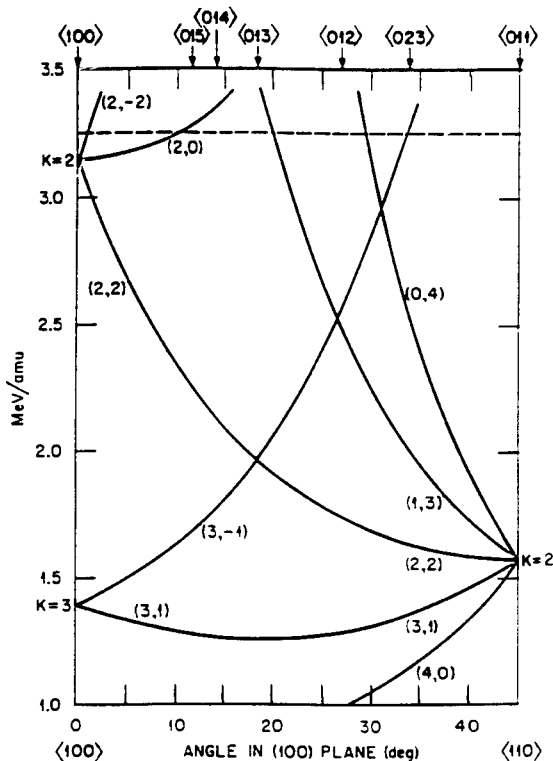


Fig. 2. Positions in energy and angle in the (100) plane for RCE resonances in the $\text{N}^{6+} + \text{Au}$ (100) system. The horizontal dashed line indicates the region of angle scan of 3.25 MeV/amu N^{6+} discussed in this paper.

energies, almost all the ions emerging from the degrader would be totally stripped with very little H-like component remaining. This led us to examine the possibility of studying these resonances using a beam of fixed velocity and varying instead the distance d between perturbing centers, i.e., using planar channeling with a fixed ion beam energy and varying angle (see Eq. (1)).

The lowest achievable planar harmonic is the (2,0) which lies in energy above the 2nd harmonic in the $\langle 100 \rangle$ axis (see Fig. 2). We investigated the feasibility of the angle variation technique N^{6+} ions from the ORNL EN Tandem Van de Graaff at an energy of 3.25 MeV/amu where excitation to $n = 2$ is tantamount to ionization. To investigate the region where escape with subsequent radiation contributes, we employed Mg^{11+} ions at an energy of 25 MeV/amu using the Chalk River CSCC Tandem Cyclotron Facility.

2. Experimental arrangement

The general experimental arrangement has been described previously [4]. For the nitrogen experiment, a beam of N^{6+} ions at an energy of 3.25 MeV/amu was supplied by the ORNL EN Tandem accelerator. After suitable collimation, it was passed through an Au crystal (1800 Å thick). The Au crystal was epitaxially grown on rock salt with the surface parallel to a (100) plane, mounted in a 3-axis goniometer and oriented so that it could be rotated about a $\langle 100 \rangle$ axis toward a $\langle 110 \rangle$ axis, i.e., in the (100) plane. The emergent charge-state distribution was analyzed by electrostatic deflection followed by a solid-state position-sensitive detector. Charge states 5, 6, and 7 were simultaneously detected.

In the case of Mg^{11+} (see Fig. 3), the beam was supplied at an energy of 25 MeV/amu by the CSCC Tandem Cyclotron Facility at Chalk River, Canada, and passed through a Ni crystal 4000 Å thick which was epitaxially grown with the surface parallel to a (100) plane. As above, the crystal could be rotated about a $\langle 100 \rangle$ axis in the (100) plane. The beam was charge state analyzed by

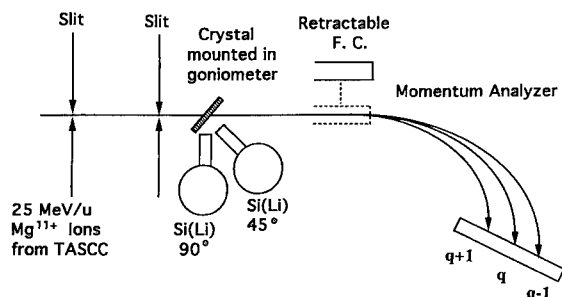


Fig. 3. Schematic for the RCE experiment using the 25 MeV/amu Mg^{11+} beam at the Chalk River TASCC. The experiment on N^{6+} at ORNL did not use Si(Li) detectors.

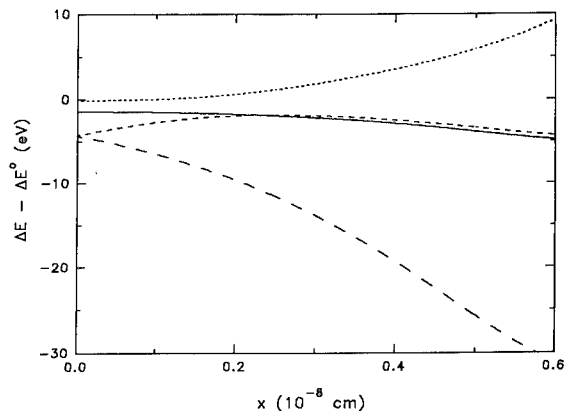


Fig. 4. Energy shifts of the various $n = 2$ substates from vacuum level ΔE^0 , as a function of distance from the planar channel midplane. The calculation here is for 3.25 MeV/amu N^{6+} in a (100) channel of Au 10° from $\langle 100 \rangle$ axis. (short-dashed line) $2p_x 2s(c)$, (solid line) $2p_y$, (dashed line) $2p_z$, (long-dashed line) $2p_x 2s(w)$.

a Q3D magnetic analyzer in which charges 11 + and 12 + were registered. At the energy in question, almost no 10 + fraction is visible. Two Si(Li) X-ray detectors aimed at 90° and 45° recorded the emission of $Mg^{11+} Ly_\alpha$ ($n = 2 \rightarrow 1$) X-rays.

3. Results and discussion

We expect that different substates in the $n = 2$ manifold will be non-degenerate and will occur at different exciting frequencies. Further, these energy levels may be a function of distance from the center of the channel. Calculations of these energy levels have been carried out and the results for, e.g., N^{6+} at 3.25 MeV/amu in (100) Au are shown in Fig. 4. The vertical scale denotes the energy difference between these states and the level they would have in vacuum. The horizontal axis corresponds to the distance from the center of the channel. The energy shifts of the excited states and the transition strengths were calculated from a time-dependent effective-Hamiltonian theory described previously [5]. Inputs to the calculation included electron scattering factors [6], and the plasmon energies of Ni and Au (assumed to be 20.7 eV and 25.8 eV, respectively). The wave functions for these states also depend on the distance between the ion and the atomic planes. These are represented by the cartoons in Fig. 5. At the center of the channel, the $2p_z$ state is Stark mixed with the 2s to form two states: one with a forward pointing lobe and the other with a rear pointing lobe. Moving away from the channel center, the transverse field dominates the Stark mixing and the 2s mixes with $2p_x$, the $2p_z$ becomes a single symmetric state. The $2p_x$ state, which at channel center is a symmetric state, mixes with 2s to form two

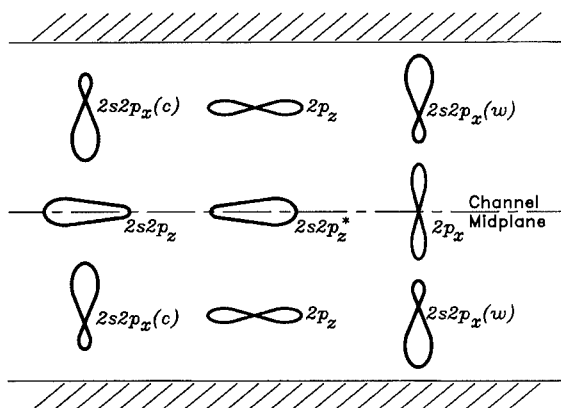


Fig. 5. Wave function shapes for the substates as a function of distance from the channel midplane.

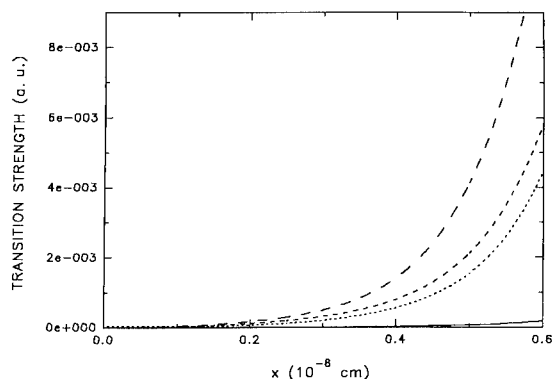


Fig. 6. Transition strengths for the substates calculated here for 3.25 MeV/amu N^{6+} in (100) Au 10° from $\langle 100 \rangle$ axis. (short-dashed line) $2p_x2s(c)$, (solid line) $2p_y$, (dashed line) $2p_z$, (long-dashed line) $2p_x2s(w)$.

states; one $2p_x2s(c)$ with the largest lobe pointing toward the center and the other $2p_x2s(w)$ with its largest lobe pointing toward the channel wall. Since there is no gradient in its direction, the $2p_y$ state is symmetric at all distances.

Fig. 6 shows the calculated transition strength for each of these states as a function of distance from the channel center. Extending furthest into the potential gradient, the $2p_x2s(w)$ state has the highest value. The $2p_y$ has by far the lowest. The main point here, however, is that the transition strength is least at the channel center and increases sharply as the “wall” is approached. Returning to Fig. 4, we see that the energy of the $2p_z$ state is relatively constant with distance and should therefore appear as a sharp line at an energy just ~ 2 –5 eV below the vacuum level. The $2p_x2s(w)$ state, on the other hand, should appear as a broad feature extending to ~ 30 eV below the vacuum level. The $2p_x2s(c)$ should appear as a narrower feature on the high energy side extending up to ~ 8 eV above vacuum level. The $2p_y$, although relatively flat, has a very small transition strength at all distances and can be neglected.

The question arises as to where in the channel the excitation takes place? Motion of ions in planar channels have been extensively studied [7] and the answer is relatively simple. The ions oscillate in an almost harmonic potential of the form $V(x) \sim A \cosh(bx)$ as shown in Fig. 7. Because of the relative flatness of the $2p_z$ state energy

with position, it will, at the proper angle, receive continuous excitation almost everywhere along its path; the greatest will occur at its maximum amplitude. The situation for, e.g., the $2p_x2s(w)$ is quite different. Its energy level is changing continuously with position in the channel. In order to build up phase coherence at a given velocity, it must move in a region where the eigenstate is relatively constant. This it does only when it is at its maximum amplitude. It is here also that the transition strength is a maximum. Therefore, when we observe a resonance at a given angle, we can associate with it a given transition energy and a given position in the channel.

The observed charge state fractions of N^{6+} exiting the Au crystal are shown in Fig. 8. Along the top, we plot the angle in the (100) plane from the $\langle 100 \rangle$ axis. Along the bottom, we plot the energy required for a (2,0) planar resonance as calculated from Eq. (1). The main (2,0) structure is contained in the region of 5 to 25° . The $\Delta E_{1s \rightarrow 2p}$ in vacuum for the N^{6+} ion is at 500 eV. Three main features are contained in the spectrum, two peaks centered on either side of the vacuum level energy, and a broad feature extending out to almost 30 eV below the vacuum level. The feature on the high energy side extends to ~ 6 eV. Using Fig. 3, these features can be identified below.

The sharp feature centered at -3 eV is due to the $2p_z$ resonance. Its sharpness arises from the relative insensitiv-

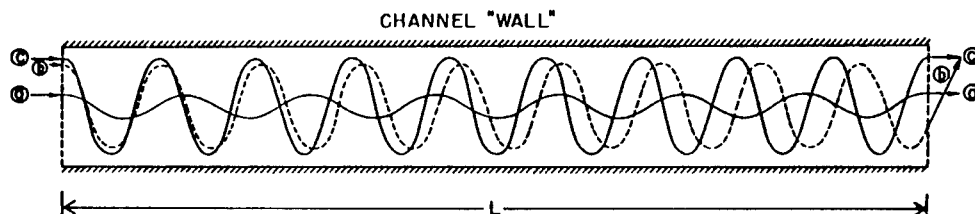


Fig. 7. Trajectories of ions entering a planar channel as a function of entrance point.

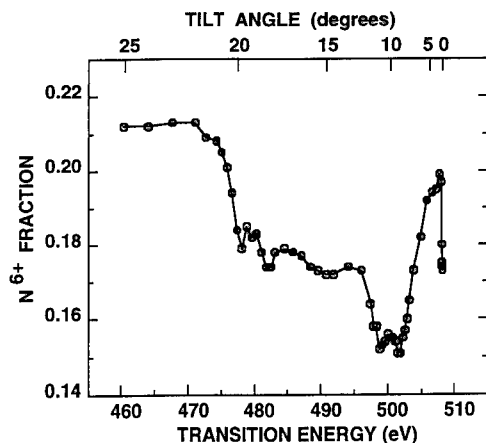


Fig. 8. Surviving change fraction of N^{6+} (3.25 MeV/amu) in (100) Au as a function of tilt angle from $\langle 100 \rangle$ (top scale). This angle can be related to transition energy through Eq. (1). Aside from the overall structure due to the (2,0) resonance, a fraction of the (2,2) resonance can be seen near 0° and features due to higher order (3,1) resonances can be seen near 20° , see Fig. 2. The structure ranging from ~ 475 to 500 eV is attributable to the $2p_x 2s(w)$ state, the peak at 502 eV is due to the $2p_z$ state, and the shoulder going up to ~ 506 eV is due to the $2p_x 2s(c)$ state.

ity of ΔE_{ij} to position in the channel. If one includes the fact that the transition strength increases with increasing distance (Fig. 4), we expect a downshift of the $2p_z$ peak of -3 to 5 eV. The shoulder on the high energy side is identified with the $2p_x 2s(c)$ resonance which we expect to extend up to ~ 5 – 8 eV. The very broad feature extending down to ~ 470 eV is the $2p_x 2s(w)$ resonance. (Note: The small features at 482 eV and 479 eV are due a higher order resonance (3,1) which overlays the (2,0) extended resonance (see Fig. 2). The feature at ~ 509 eV is a portion of the (2,2) resonance which lies very close to the axis.)

The corresponding information for Mg^{11+} at 25 MeV/amu in (100) Ni is shown in Figs. 9, 10 and 11. Nickel was chosen for this experiment rather than gold because the smaller lattice constant $d = 3.524$ Å as against $d = 4.078$ Å in Au allowed us to reach the desired (2,0) resonance with the 25 MeV/amu beam available.

Because of the higher velocity and the higher Z of Mg^{11+} as compared with N^{6+} , the displacements from $\Delta E_{1s \rightarrow 2p}$ are smaller. (Fig. 9 vis a vis Fig. 4). The transition strengths are of the same order of magnitude. However, in contrast to N^{6+} in Au (Fig. 6), the transition strength for $2p_z$ lies slightly below that for $2p_x 2s(c)$, see Fig. 10. Similar identifications of the features can be made. The vacuum level $\Delta E_{1s \rightarrow 2p}$ for Mg^{11+} is at 1472 eV. The $2p_z$ peak is virtually coincident with this value. The $2p_x 2s(c)$ forms a shoulder on the high energy side extending up to ~ 10 eV above $2p_z$ and the $2p_x 2s(w)$ forms a bulge on the low energy side extending down to ~ 20 eV below the vacuum resonance level.

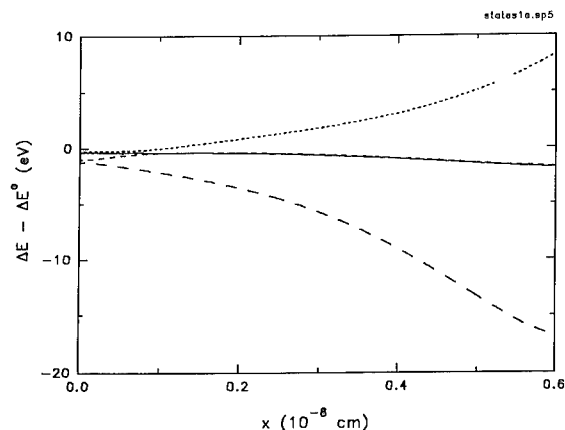


Fig. 9. Energy shifts of the various $n=2$ substates from vacuum level ΔE° , as a function of distance from the planar channel midplane. The calculation here is for 25 MeV/amu Mg^{11+} in a (100) channel of Ni 10° from $\langle 100 \rangle$ axis. (short-dashed line) $2p_x 2s(c)$ state, (solid line) $2p_y$, (dashed line) $2p_z$, (long-dashed line) $2p_x 2s(w)$.

Thus far, we have looked for effects due to $n=1 \rightarrow n=2$ excitation followed by ionization. We now look for effects for ions which have been excited and survive to exit the crystal and then relax radiatively by X-ray emission. The results of the X-ray measurements on Mg^{11+} are shown in Fig. 12 and compared with the ionization measurements. The first obvious observation is that the X-rays attributable to states excited to the $2s 2p_x(w)$ are strongly suppressed when compared to emission from ions excited to the $2p_z$ state. The relative probability of excitation to $2s 2p_x(w)$ and $2p_z$ is almost independent of position (amplitude), see Fig. 10. Hence, the difference in ionization probability is attributable to the shape of the wave function. This is not an unexpected result since the bulk of the square of the wave function for the $2p_x 2s(w)$ state lies

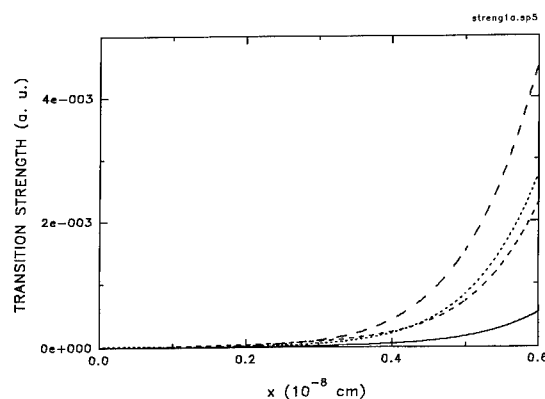


Fig. 10. Transition strengths for the substates calculated here for 25 MeV/amu Mg^{11+} in (100) Ni 10° from $\langle 100 \rangle$ axis. (short-dashed line) $2p_x 2s(c)$, (solid line) $2p_y$, (dashed line) $2p_z$, (long-dashed line) $2p_x 2s(w)$.

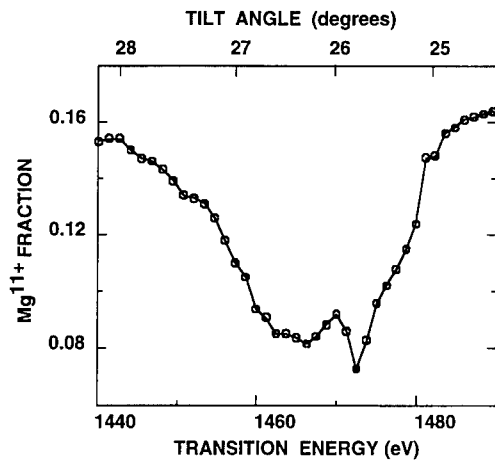


Fig. 11. Surviving charge fraction of Mg^{11+} (25 MeV/amu) in (100) Ni as a function of tilt angle from $\langle 100 \rangle$ (top scale). The angle can be related to transition energy through Eq. (1). The region from 1440 eV to 1470 eV can be attributed to the $2p_x 2s(w)$ state, the peak at 1472 eV is due to the $2p_z$, and the shoulder extending up to ~ 1485 eV is due to the $2p_x 2s(c)$ state.

perpendicular to the direction of the bombarding electron flux and extends into regions of higher electron density near the planes of atomic cores. Although the shapes of the wave functions for these two states (i.e., $2p_z$ and $2p_x 2s(w)$) vary with position (Fig. 5), their identities are reasonably clear. A $2p_z$ mixed with 2s on axis becomes almost pure $2p_z$ far off axis. The $2p_x 2s(w)$ state is a pure $2p_x$ on axis but mixes with 2s as it moves away from the axis. The case for the $2p_x 2s(c)$ state is not as clear. The wave function for this state changes character drastically as it moves through its oscillation in the channel. In its on-axis manifestation, it is a 2s mixed with $2p_z$. In its extreme form far off-axis, it is a 2s mixed with a $2p_x$. In between, it has s, p_z and p_x character.

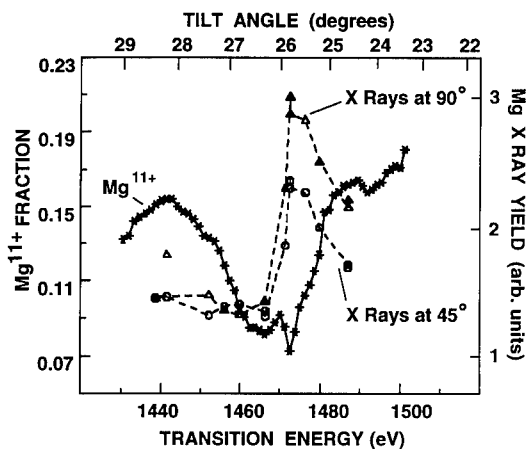


Fig. 12. X-ray yields in detectors placed at angles of 45° and 90° to the beam as a function of transition energy (tilt angle) as compared with charge state fraction (i.e., Fig. 11).

Moving at 25 MeV/amu ($\beta = 0.23$), the velocity of the Mg ions is 6.8×10^9 cm s $^{-1}$ in which case they spend 0.6×10^{-14} s in the 4000 Å crystal. The lifetime of $2p \rightarrow 1s$ transition in Mg^{11+} is 7.6×10^{-14} s so that almost all the observed radiation takes place outside the crystal. When the excited ions emerge from the crystal into vacuum, they must assume discrete states, $2p_x$, $2p_z$ or 2s. The fraction appearing in a given state will depend on the vertical displacement in the planar channel at the exit point. The radiative lifetime for the $2s \rightarrow 1s$ transition in Mg^{11+} is 3×10^{-7} s so that very little 2s radiation will occur within the field of view of the Si(Li) detectors. The radiation pattern of the $2p_x$ state is orthogonal to the x direction. It should be isotropic in the y - z plane and no differences in intensity should be observed between the 90° and 45° detectors (after correction for lab-frame to projectile-frame solid angles). The radiation pattern for the $2p_z$ state is orthogonal to the z direction, isotropic in the x - y plane and should display an increased intensity of 90° detector compared with the 45° . Such an effect is visible in Fig. 12. Here again the $2p_x 2s(c)$ state is more complex. Although the state lies perpendicular to the electron flux, it always extends into regions of lower electron density. Its state depends on vertical displacement at the exit point. From the X-ray yield, it is evident that there is a chance for escape from the crystal without ionization and that it shows evidence for alignment.

In conclusion, there is strong evidence that once a given ionic state is excited, a large fraction of the ions remain in that state and are either ionized or radiate from that state. The result is counter to the expectation that electron-ion collisions in the channel would have a large enough cross section to destroy the alignment before either of these two events could take place. At this point, the reasons for the observed retention of anisotropy are open to conjecture.

Acknowledgements

The authors wish to express their appreciation to J. Chevallier of the Institute of Physics and Astronomy at Aarhus University, Denmark for his preparation of the crystals used in these experiments. The research by the Oak Ridge National Laboratory group is sponsored by the U.S. Department of Energy, Office of Basic Energy Sciences, Division of Chemical Sciences, under Contract No. DE-AC05-84OR21400 with Martin Marietta Energy Systems, Inc.

References

- [1] S. Datz, C.D. Moak, O.H. Crawford, H.F. Krause, P.F. Dittner, J. Gomez del Campo, J.A. Biggerstaff, P.D. Miller, P. Hvæplund and H. Knudsen, Phys. Rev. Lett. 40 (1978) 843.

- [2] C.D. Moak, S. Datz, O.H. Crawford, H.F. Krause, P.F. Dittner, J. Gomez del Campo, J.A. Biggerstaff, P.D. Miller, P. Hvelplund and H. Knudsen, *Phys. Rev. A* 19 (1979) 977.
- [3] S. Datz, C.D. Moak, O.H. Crawford, H.F. Krause, P.D. Miller, P.F. Dittner, J. Gomez del Campo, J.A. Biggerstaff, H. Knudsen and P. Hvelplund, *Nucl. Instr. and Meth.* 170 (1980) 18.
- [4] S. Datz, P.F. Dittner, J. Gomez del Campo, K. Kimura, H.F. Krause, C.R. Vane, Y. Iwata, K. Komaki, Y. Yamazaki, F. Fujimoto and Y. Honda, *Radiat. Eff. Def. Solids* 117 (1991) 73.
- [5] O.H. Crawford and R.H. Ritchie, *Phys. Rev. A* 20 (1979) 1848.
- [6] P.A. Doyle and P.S. Turner, *Acta Crystallogr. A* 24 (1968) 390, I used their Eq. (4), with parameters from Table 4(a).
- [7] See, e.g.; S. Datz and C.D. Moak, Heavy Ion Channeling, in: *Heavy Ion Science*, Vol. 6, ed. D.A. Bromley (Plenum, 1983) p. 169.

Nonlinear screening effects in the interaction of slow multicharged ions with metal surfaces

A. Arnau ^{a,*}, P.A. Zeijlmans van Emmichoven ^b, J.I. Juaristi ^a, E. Zaremba ^c

^a Departamento de Física de Materiales, Universidad del País Vasco, San Sebastián, Spain

^b Debye Institute, Universiteit Utrecht, Utrecht, Netherlands

^c Department of Physics, Queen's University, Kingston, Ontario, Canada

Abstract

Density functional theory is used to treat the problem of screening of highly charged ions in an electron gas when inner shell vacancies are present. Results are presented for N and Ne ions in various electronic configurations. These include information about screening charge densities, induced densities of states in the conduction band, bound energy levels and KLL Auger lines.

1. Introduction

Since the pioneering work of Hagstrum [1] in the early fifties there has been an increasing interest in the interaction of multicharged ions (MCI) with metal surfaces. The large variety of electronic processes that take place as the ion approaches the surface [2] (resonant capture, Auger neutralization, autoionization) makes the complete understanding of the physics taking place a challenging problem for both the theoretical and experimental physicist. It is also of practical interest in studies of plasma-wall interactions, the material modification by ion beams and surface analysis involving elastic and inelastic ion beam scattering.

It is generally accepted that as the ion approaches the metal surface it captures electrons into highly excited Rydberg states that subsequently deexcite by a sequence of autoionization events. However, the time scale for inner-shell neutralization is typically much larger than the time it takes the ion to reach the surface. Experiments indicate that a major part of the relaxation process takes place at and below the surface [3–5] (assuming of course that the ion is sufficiently energetic to penetrate the solid) and the subsequent filling of the inner shells takes place in the presence of the screening electrons of the solid. As the time scale on which this screening occurs is relatively short (typically 10^{-16} s) compared to the inner shell relaxation times, the metallic screening can be considered to be essentially complete except for the presence of the instantaneous distribution of inner shell vacancies (or holes).

In this work we study the interaction of a MCI with an electron gas which is used to represent the metallic conduction band of a nearly free electron material. Assuming that the metal electrons screen sufficiently rapidly, we can consider the ion as a static point charge Z_1 with some configuration of inner shell holes immersed in an electron gas. The quantities we are interested in are: the induced electron densities, the induced densities of states in the band, the energy levels and the total energy differences between two different configurations that represent the initial and final states of an Auger process. On the other hand, we will not attempt to determine the relative probabilities with which the different configurations occur. This more detailed information requires knowledge of transition rates and is beyond the scope of the present investigation.

2. Theory

We have used density functional theory (DFT) to treat the problem of screening of excited state ions embedded in an electron gas [6] of mean density n_0 . The static approximation is adequate as long as the ion velocity (v) is lower than the Fermi velocity (v_F) of the metal electrons [7], while linear response theory is not expected to be valid for such a strong perturbation ($Z_1/v_F \gg 1$; atomic units are used in this paper unless otherwise stated).

In this model one has to solve self-consistently the equations

$$\left\{ -\frac{1}{2}\nabla^2 + v_{\text{eff}}[n] \right\} \phi_i = \epsilon_i \phi_i, \quad (1)$$

where

$$v_{\text{eff}} = v_{\text{ext}} + v_{\text{ind}} + v_{\text{xc}},$$

* Corresponding author. Tel. +34 43 216600, fax +34 43 212236, e-mail waparpia@sq.ehu.es.

with

$$v_{\text{ext}} = -\frac{Z_1}{r}, \quad v_{\text{ind}} = \int d\mathbf{r}' \frac{n(\mathbf{r}')}{|\mathbf{r} - \mathbf{r}'|} \quad (2)$$

and $v_{\text{xc}}[n]$ is the exchange correlation potential in the local density approximation (LDA) [8]. The density $n(\mathbf{r})$ appearing in Eq. (2) is

$$n = \sum_{i \in \text{occ.}} |\phi_i|^2, \quad (3)$$

where the sum includes both the sum over occupied discrete bound states and an integration over the continuum up to the Fermi level. This set of equations is solved self-consistently by iteration.

Due to the short range of the self-consistent screened potential $v_{\text{eff}}[n]$ in Eq. (1) a finite number of bound states (n_b) appear. When inner shell holes are present, we define the number of holes n_h by the relation

$$n_h = n_b - n_s, \quad (4)$$

where n_s is the number of bound states occupied.

In the usual DFT calculations one is interested in the ground state electronic configuration. This means that $n_h = 0$ and all available bound states below the continuum of metallic states are fully occupied. In most cases the number of bound states satisfy $n_b \leq Z_1$, although there are particular cases in which a negatively charged core exists. In either case the scattering phase shifts at the Fermi level satisfy the Friedel sum rule [9]

$$Z_1 = \frac{2}{\pi} \sum_l (2l+1) \delta_l(k_F), \quad (5)$$

which expresses the total screening condition for a static impurity in a metal. However, when (n_h) inner shell holes are present the number of occupied bound states (n_s) is lower than the number of bound states (n_b) supported by the self-consistent potential. In this case it may happen that $n_b > Z_1$. Eq. (5) is then no longer valid and must be generalized to

$$Z_1 + n_h = \frac{2}{\pi} \sum_l (2l+1) \delta_l(k_F). \quad (6)$$

In other words, the self-consistent potential accommodates a total of $Z_1 + n_h$ extra states below the Fermi level but the deficit of n_h occupied states ensures charge neutrality of the system.

It is often useful to split the induced electron density ($\delta n = n - n_0$) into its bound (δn^{bound}) and scattering (δn^{scatt}) contributions according to:

$$\begin{aligned} \delta n &= \sum_{n \in n_s} |\phi_n|^2 + \sum_{|k| < k_F} |\phi_k|^2 \\ &= \delta n^{\text{bound}} + \delta n^{\text{scatt}}. \end{aligned} \quad (7)$$

Angular momentum and spin degeneracy is taken into account when specifying the occupancy of the levels. For

partially filled shells we note that in general δn^{bound} is not spherically symmetric. In this case we take a spherical average of the charge density to be used in Eq. (1) and (2). It is also useful to define the displaced charge within a distance r from the ion by

$$Q(r) = 4\pi \int_0^r dr' r'^2 \delta n(r'). \quad (8)$$

The integrals of δn^{bound} and δn^{scatt} over all space separately give n_s and $Z_1 - n_s$, respectively.

Although there is no rigorous theoretical justification for treating excited state configurations within density functional theory, the method provides reasonable estimates of the energies associated with these states [10], as demonstrated by earlier core-hole level shift calculations [11–13]. The total energy for each configuration is obtained from the sum of three terms: kinetic energy (T), electrostatic energy (E_{es}) and exchange and correlation energy (E_{xc}). These three terms can be expressed as:

$$T = \sum_i \varepsilon_i - \int d\mathbf{r} n(\mathbf{r}) v_{\text{eff}}(\mathbf{r}), \quad (9a)$$

$$E_{\text{es}} = \int d\mathbf{r} n(\mathbf{r}) \left\{ v_{\text{ext}}(\mathbf{r}) + \frac{1}{2} \int d\mathbf{r}' \frac{n(\mathbf{r}')}{|\mathbf{r} - \mathbf{r}'|} \right\}, \quad (9b)$$

$$E_{\text{xc}} = \int d\mathbf{r} n(\mathbf{r}) \varepsilon_{\text{xc}}[n(\mathbf{r})], \quad (9c)$$

where $\varepsilon_{\text{xc}}[n]$ is the exchange and correlation energy density. We subtract the background values from the total energies $E[n]$ taking into account that when $v_{\text{ext}} = 0$ the density $n = n_0$, and that there is a positive background of charge keeping charge neutrality in the system. The results we obtain in this way for the total energy differences between two different configurations corresponding to $N + 1$ and N electrons of the initial and final states of an Auger process are in good agreement with other estimations [14]; the differences being of the order of 2%.

3. Results

In Fig. 1a, 1b and 1c we plot the radial dependence of the induced electron densities for three different electronic configurations of nitrogen ions ($Z_1 = 7$) in an electron gas with $r_s = 3$ (a.u.) [$r_s = (3/4\pi n_0)^{1/3}$]. The ground state configuration ($1s^2 2s^2$) in Fig. 1a shows an efficient screening within a distance of about 2 a.u. from the position of the ion by 4 bound electrons in the K and L shells plus an additional 3 electrons in the valence band. In Figs. 1b and 1c we show that when inner shell holes are present the extent of the screening cloud is larger, and in this particular case it is about two times that of the ground state configuration depicted in Fig. 1a. This is due to the elimination of the more compact screening charge density of the inner core states. At the same time, the self-con-

sistent potential becomes stronger with the appearance of new bound states (2p and 3s) and the increasing importance of the screening from higher angular momentum scattering states (for example, d-wave scattering in Fig. 2c). Typically, when holes are present in shells with quantum numbers up to including n , the total screening cloud (bound plus scattering contribution) extends into the

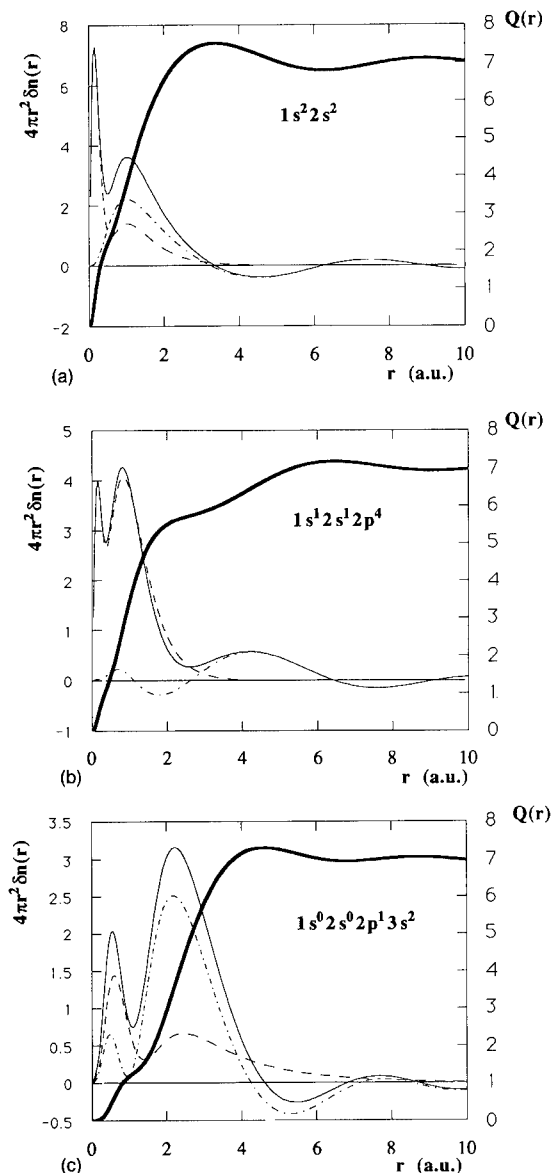


Fig. 1. (a) Radial dependence of the induced electron density δn (thin solid) and its bound contribution δn^{bound} (dashed) and scattering contribution δn^{scatt} (dashed-dotted) for $N(1s^2 2s^2)$ configuration for $r_s = 3$. The displaced charge $Q(r)$ is also shown (thick solid) in the figure. See Eq. (8) in the text. (b) Same as (a) for $N(1s^1 2s^1 2p^4)$ configuration. (c) Same as (a) for $N(1s^0 2s^0 2p^1 3s^2)$ configuration.

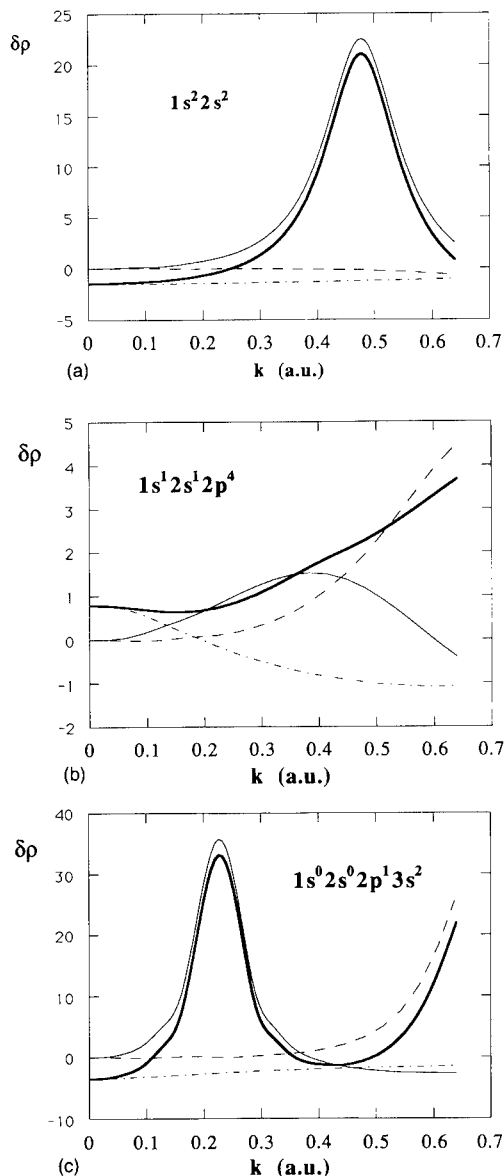


Fig. 2. (a) Induced density of states $\delta\rho$ (thick solid) for $N(1s^2 2s^2)$ configuration for $r_s = 3$ and its angular momentum components: s-wave $\delta\rho_0$ (dashed dotted), p-wave $\delta\rho_1$ (thin solid) and d-wave $\delta\rho_2$ (dashed). See Eq. (10) in the text. (b) Same as (a) for $N(1s^1 2s^1 2p^4)$ configuration. (c) Same as (a) for $N(1s^0 2s^0 2p^1 3s^2)$ configuration.

region with $(n+1)$ -shell character, apart from the long range Friedel oscillations. We have checked that the total screening cloud is not too different when a weakly bound state appears or when screening takes place by continuum electrons having the same l -wave character (s, p or d in our case), e.g. screening by a weakly bound s-state or screening by low energy s-wave continuum electrons.

In Figs. 2a, 2b and 2c we plot the total change in the density of states $\delta\rho(k)$ induced by the impurity ion in the valence band of the metal and its angular momentum components $\delta\rho_l$ given by:

$$\delta\rho(k) = \frac{2}{\pi} \sum_l (2l+1) \frac{d}{dk} \delta_l(k) \equiv \sum_l \delta\rho_l. \quad (10)$$

This quantity helps in understanding the type of screening by continuum electrons when inner shell holes are present. For example, for the ground state configuration in Fig. 2a, the dominant feature is the p-wave resonance which accommodates the 3 p-state electrons of the free atom. At low energies toward the bottom of the band, the screening is of course always dominated by s-wave continuum states. On going to the $1s^1 2s^1 2p^4$ configuration the p-wave resonance is virtually eliminated since p-wave screening is provided by the 4 bound p electrons. At the same time, s- and d-wave screening is becoming increasingly important. The latter is an indication of the increasing radial extent of the self-consistent potential when inner shell holes are present. Finally, Fig. 2c shows an extreme configuration in which relatively few of the inner core states are occupied. In this case much of the screening is provided by the p-wave resonance associated with the atomic 3p state, and an appreciable d-wave component at the Fermi energy.

It is clear that the induced density in the valence band shown in Fig. 1 is significant and in turn will affect the atomic energy levels. As an example we show the results for $r_s = 3$ for a N ion with 2 K-shell vacancies as a function of the total number of vacancies in the 1s, 2s, and 2p shells in Fig. 3. The 1s level was found to be constant within roughly 20% and is not shown in the figure. The eigenvalues strongly depend on the total number of vacancies, whereas the specific combination of 2s and 2p vacan-

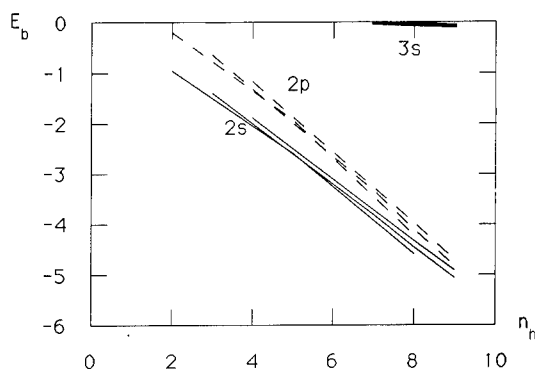


Fig. 3. Bound state energy levels (in Rydbergs) of N ions for $r_s = 3$ with 2 K-shell vacancies as a function of the total number of vacancies. Thin solid lines denote the 2s levels, thin dashed lines the 2p levels and the thick solid line the 3s level. Different line for each level indicate different combination of 2s and 2p holes.

Table 1

KLL Auger energies for Ne and N ions

Ion/electron density	K-shell holes in the initial state	Auger energy [eV]
$N/r_s = 3$	1	$366 < E_{\text{KLL}} < 418$
$N/r_s = 3$	2	$408 < E_{\text{KLL}} < 440$
$Ne/r_s = 2$	1	$768 < E_{\text{KLL}} < 825$
$Ne/r_s = 2$	2	$829 < E_{\text{KLL}} < 880$

cies seems to be only of minor importance. For ions with at least 7 vacancies (at most 3 L-shell electrons) the occurrence of a weakly bound 3s level was found. For all charge states of the embedded ion the atomic 3p state lies in the continuum (see, e.g., Fig. 2c). At higher densities ($r_s = 2$) our calculations indicate that the 3s level is also pushed into the continuum for all charge states of N. Due to the proximity of the $n = 3$ levels to the continuum, we speculate that previously measured peaks associated with LMM transitions may, in fact, be due to LVV transitions in which the p-state resonance shown in Fig. 2c is playing a role. For larger- Z_1 ions this of course would not be true due to stronger binding of the $n = 3$ electrons.

We have calculated the KLL Auger energies from total energy differences for various configurations in which the initial state has one or two K-shell vacancies. We have chosen N and Ne ions in an electron gas with $r_s = 3$ and 2, respectively. We have not attempted to generate the Auger electron spectra, by adding the different lines with a statistical weight, due to the lack of knowledge about the population of each of the configurations and the energy loss suffered by the Auger electrons as they pass through the solid and subsequently cross of the surface into vacuum; thus these Auger line positions may be taken as upper bounds. We prefer to give an energy range for the KLL Auger energy and wait for some reliable results for Auger rates and population of each configuration. Thirty-four different transitions of the type $|n_K n_L\rangle \rightarrow |n_K + 1 n_L - 2\rangle$ have been considered for each Auger energy range. Our results are summarized in Table 1. The energy range in which these KLL Auger electrons are emitted is around 40 to 50 eV. The KLL Auger spectra measured in the experiments [14,15] for Ne and N projectiles are centered around 800 and 380 eV, respectively, which correspond more closely to our calculations with a single K-shell vacancy in the initial state. It therefore appears that LDA scheme of density functional theory can be used to obtain reasonable estimates of total energy differences but not an accurate quantitative estimate of the peak positions. The main effect due to the metallic electrons in the solid state (screening) as compared to the ions in vacuum, as far as the KLL Auger peak positions is concerned, comes from the larger energy shift in the L-shell levels as compared to the K-shell (which is almost negligible) and consequently

the KLL Auger lines are expected to appear at slightly higher energies. This latter effect depends, of course, on the electronic density of the target. It is also worth mentioning that the bottom of the conduction band (the zero of our electron energy scale) is $E_F + \phi$ below the vacuum level (typically 15 eV) where E_F is the Fermi energy and ϕ the work function of the metal.

4. Conclusion

DFT may be used to study the nonlinear screening of MCI in an electron gas when inner shell holes are present. One could also use the self-consistent potential (see Eq. (1)) to calculate the transport cross section at the Fermi level and consequently the stopping power as has previously been done by Echenique et al. [16,17] for ground state electronic configurations of different ions. The information one obtains helps in the understanding of the physical processes that take place once the ion has crossed the metal surface and penetrates into the bulk. However, if one wishes to obtain the Auger electron spectra one also needs to estimate the Auger transition rates for each of the different channels and the transport of the continuum energetic electrons through the solid. Work along these lines is currently in progress.

Acknowledgements

We are indebted to P.M. Echenique and N. Stolterfoht for many stimulating and helpful discussions. Financial support by Eusko Jaurlaritza, Gipuzkoako Foru Aldundia, Euskal Herriko Unibertsitatea and the Commission of European Communities (Human Capital and Mobility program) is also acknowledged.

References

- [1] H.D. Hagstrum, Phys. Rev. 96 (1954) 325.
- [2] F. Aumayr and H. Winter, Comments At. Mol. Phys. 29(5) (1994) 27.
- [3] H. Kurz, K. Töglhofer, H.P. Winter, F. Aumayr and R. Mann, Phys. Rev. Lett. 69 (1992) 1140.
- [4] F.W. Meyer, S.H. Overbury, C.C. Havener, P.A. Zeijlmans van Emmichoven and D.M. Zehner, Phys. Rev. Lett. 67(3) (1991) 72.
- [5] S. Schippers, S. Hustedt, W. Heiland, R. Köhrbrück, J. Bleck-Neuhaus, J. Kemmler, D. Lecler and N. Stolterfoht, Nucl. Instr. and Meth. B 78 (1993) 106.
- [6] E. Zaremba, L.M. Sander, H.B. Shore and J.H. Rose, J. Phys. F 7 (1977) 1763.
- [7] P.M. Echenique, F. Flores and R.H. Ritchie, in: Solid State Physics: Advances in Research and Applications, Vol. 43, eds. H. Ehrenreich and D. Turnbull (Academic Press, New York, 1990) p. 230.
- [8] O. Gunnarsson and B.I. Lundqvist, Phys. Rev. B 13 (1976) 4274.
- [9] J. Friedel, Philos. Mag. 43 (1952) 153.
- [10] A.R. Williams and U. von Barth, in: Theory of the inhomogeneous electron gas, eds. S. Lundqvist and N.H. March (Plenum, New York, 1983) Chap. 4.
- [11] C.O. Almbladh and U. von Barth, Phys. Rev. B 13 (1976) 3307.
- [12] A.R. Williams and N.D. Lang, Phys. Rev. Lett. 40 (1978) 954; Phys. Rev. B 20 (1979) 1369.
- [13] R.M. Nieminen and M.J. Puska, Phys. Rev. B 25 (1982) 67.
- [14] R. Köhrbrück, S. Hustedt, S. Schippers, W. Heiland, J. Bleck-Neuhaus, J. Kemmler, D. Lecler and N. Stolterfoht, Nucl. Instr. and Meth. B 78 (1993) 93.
- [15] J. Limburg, J. Das, S. Schippers, R. Hoekstra and R. Morgenstern, Surf. Sci. 313 (1994) 355.
- [16] P.M. Echenique, R.M. Nieminen and R.H. Ritchie, Solid State Commun. 37 (1981) 779.
- [17] P.M. Echenique, R.M. Nieminen, J.C. Ashley and R.H. Ritchie, Phys. Rev. A 33 (1986) 897.



ELSEVIER

Electron emission from polycrystalline lithium fluoride bombarded by slow multicharged ions

M. Vana, F. Aumayr, P. Varga, HP. Winter *

Institut für Allgemeine Physik, Technische Universität Wien, Wiedner Hauptstraße 8–10, A-1040 Wien, Austria

Abstract

Total electron yields have been determined from electron emission statistics measured for impact of H^+ , N^{q+} ($q = 1, 5, 6$) and Ar^{q+} ($q = 1, 3, 6, 9$) on clean, polycrystalline lithium fluoride. Ion impact energies have been varied from almost zero up to $10 \times q$ keV. The obtained total electron yields deviate considerably from available data derived via ion- and electron current measurements for LiF single crystal targets. Our results are explained by comparison with a recent model for MCI induced potential electron emission from clean metal surfaces, which has been properly adapted, available theory for kinetic electron emission from alkali-halide surfaces, and by considering also measured secondary electron yields for LiF. Dependences of the electron emission statistics and -yields on projectile impact energy and -charge differ strongly from corresponding properties for clean metal surfaces, which can be explained from the different roles of potential- and kinetic emission and, in particular, a relatively stronger contribution from secondary electron emission induced by fast electrons from finally neutralising projectiles inside the LiF bulk.

1. Introduction

For bombardment of insulator surfaces with slow multicharged ions (MCI) Z^{q+} , at given impact energy E_p , strong increase with the ion charge state q has been observed for the total emission yields of both electrons [1–3] and secondary ions (SI) [3]. Furthermore, microscopic surface damages induced on alkali-halide crystals (AHC) by slow MCI impact also increase with q [4]. Considering these observations, Parilis et al. have proposed the so-called “Coulomb explosion” (CE) mechanism [5] as an efficient means for MCI induced ejection of particles from insulator surfaces, following an assumed strong electron depletion in the uppermost surface layer due to multi-electron capture by the approaching MCI. This CE mechanism should manifest itself in total sputtering yields increasing with the MCI charge. However, no such behaviour could be found for atomically clean Si(100) bombarded by Ar^{q+} ($q \leq 9$, $E_p = 20$ keV) ions [6]. On the other hand, impact of slow highly charged ions (up to Th^{74+} , $E_p \approx 2$ keV/amu) on $KAl_3Si_3O_{10}(OH)_2$ (mica) produced larger microscopic damages for higher q [7], and slow, doubly charged noble gas ions ($q = 1, 2$) caused larger SI yields for atomically clean LiF than singly charged

ones [8]. In summary, MCI impact on AHC surfaces gives rise to strongly q -dependent yields for emission of neutral and/or ionized target particles as well as electrons.

At very low ion impact energies, where kinetic electron emission (KE) can still be neglected, for any solid surface the potential electron emission (PE) yield strongly increases with q , because of its direct relation with the total potential energy carried by the MCI toward the surface [9]. Referring to the well established process of electron stimulated desorption from AHC surfaces [10], we speculate that slow MCI induced electron emission from AHC might be correlated, either directly or indirectly, with the not yet well understood processes responsible for the above-mentioned q -dependent MCI induced sputtering and SI emission. We have therefore investigated electron emission induced by slow MCI on clean LiF, for which target already numerous studies on photon-, electron- and ion stimulated sputtering and desorption have been carried out [10]. However, absolute yields for electron emission induced by singly charged ions from AHC surfaces are rather scarce [11,12], and practically no such data are available for impact of slow MCI, apart from the already mentioned ones [1,3], which have not been obtained under ultrahigh vacuum (UHV) conditions (background pressure above 10^{-6} Pa). However, since PE processes critically depend on the target surface conditions, they need to be studied under UHV conditions. For reproducible yield measurements, it must also be taken into account that insulator surfaces can charge up under ion impact [12]. For

* Corresponding author, tel. +43 1 58801 5710, fax +43 1 5864203, E-mail: winter@eapv38.tuwien.ac.at.

our present studies, we have applied a special technique for determination of particle induced total electron yields, which both assured appropriate experimental conditions and delivered various useful informations on the electron emission processes of interest.

2. Experiment

The LiF target has been prepared as a polycrystalline $50 \mu\text{g}/\text{cm}^2$ film (thickness about 200 nm), by deposition of LiF under high vacuum conditions on a stainless steel backing, and transferring the latter into a setup for measuring particle-induced electron emission statistics (ES) as described in Ref. [9].

For these measurements, the LiF target was kept at room temperature and regularly cleaned by Ar^+ sputtering (ion energy and flux typically 1 keV and $10^{14}/\text{cm}^2\text{s}$, respectively) between subsequent runs with the projectile ions of actual interest. The latter ion fluxes were kept below $10^3/\text{s}$, which both was necessary for the proper working of our ES technique and avoided any target charging-up effects, which otherwise could only be achieved by target heating up to 400°C .

As projectile species, H^+ , N^{q+} ($q = 1, 5, 6$) or Ar^{q+} ($q = 1, 3, 6, 9$) ions have been delivered from our 5 GHz ECR source [13]. Impact energy E_p on the target surface could be varied from almost zero up to $10 \times q$ keV. Absolute total electron yields γ were derived from the measured ES as described in our earlier work for a clean Au surface [9]. The target could also be bombarded by electrons extracted from the sputter gun for target cleaning, after reversing its bias voltage.

Total electron yields obtained from ES measurements with atomically clean metal surfaces have been shown to be accurate within $\pm 4\%$ [9]. However, in the present study we observed some unusually large data scattering from different experimental runs under apparently equal conditions. This resulted mainly from the limited q/M resolution in primary MCI beam analysis, where selected MCI beams were somewhat contaminated by small amounts of other ion species with nearly equal q/M . Especially at higher impact energies the ES measurements for LiF could be disturbed from overlapping ES for the admixed ion species with similar q/M . This effect is more severe than in measurements with clean Au [14], since the ES for LiF are generally broader (see below). Furthermore, preparation of the LiF surface by Ar^+ sputtering without subsequent thermal annealing created radiation damages with a slightly variable surface- and bulk exciton population [10]. This could have caused slightly different ES for measurements under otherwise equal experimental conditions, since more PE could be produced from the interaction of MCI with exciton states than with the much deeper LiF valence band states. Because of these reasons, the here presented total electron yields for LiF are accurate within typically

$\pm 10\%$ only, which still is sufficiently precise for our conclusions to be presented.

We like to point out that, in comparison with the common way of measuring total electron yields from currents of projectile ions and emitted electrons, our here applied technique not only delivers total electron yields with comparable accuracy (see above), but also delivers the respective electron emission statistics, which themselves are quite useful for investigating the basic mechanisms for the observed electron emission. Furthermore, the ES technique is much more sensitive and thus avoids excessive radiation damage and charging-up of the target surface. It also rules out erroneous total electron yield measurements due to negative ion desorption [8], because pulses from our surface barrier detector following the impact of fast negative ions are much broader than the ones from impact of electrons with the same kinetic energy.

3. Results

Fig. 1 shows total electron yields γ versus ion energy E_p for impact of Ar^{q+} ($q = 1, 3, 6, 9$) on LiF over the full impact energy range covered by our present measurements. Fig. 2 presents ES measured for Ar^{9+} impact with $E_p = 0.9, 13.5$ and 63 keV, respectively.

In contrast to the symmetric, Gaussian-shaped ES resulting from MCI impact on clean Au [9,15], at higher projectile energies the here presented ES become asymmetric with a tail toward higher emission multiplicities. This could have been caused by a superposition of several ES distributions, resulting from electron emission from target regions with different work functions W_ϕ . Variation of the projectile flux within a factor of 30 showed, that the asymmetric ES were not caused by pile-up effects from the ES detector and its subsequent electronics, as has been

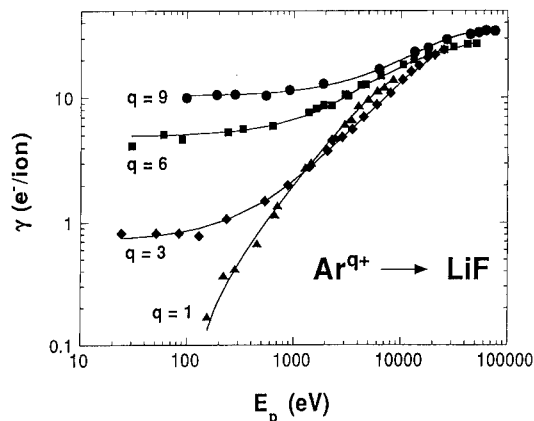


Fig. 1. Total electron yield γ for impact of Ar^{q+} ($q = 1, 3, 6, 9$) on LiF, versus impact energy E_p .

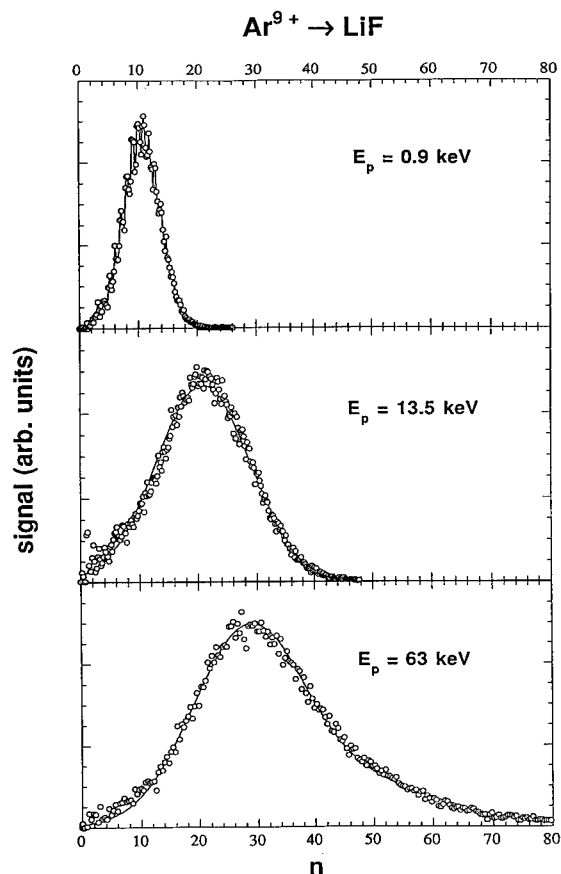


Fig. 2. Measured electron emission statistics for impact of Ar^{9+} on LiF, at three different impact energies E_p .

concluded in a study on singly charged ion impact on CsI [16]. By means of low-energy ion scattering on a LiF surface cleaned via Ar^+ sputtering under similar condi-

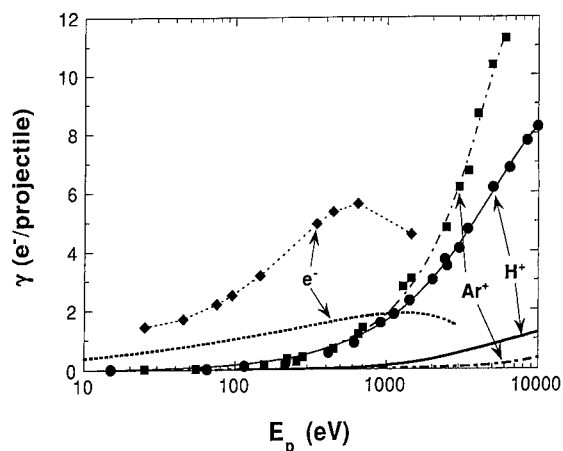


Fig. 3. Total electron yields γ for impact of electrons, protons and Ar^+ on clean gold (thick curves) and LiF (data points connected by thin curves), respectively, versus impact energy E_p .

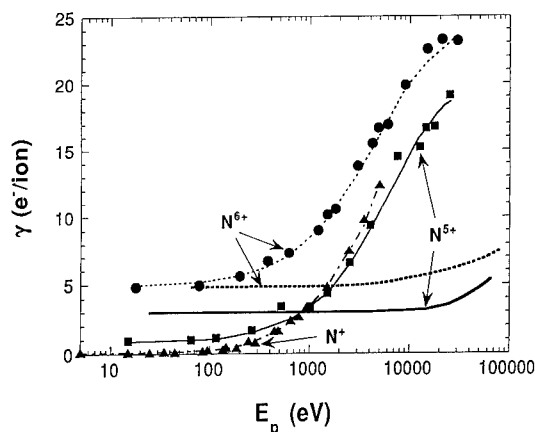


Fig. 4. As Fig. 3, for impact of N^{q+} ($q = 1, 5, 6$).

tions as in the present experiments, the formation of metallic lithium on the LiF surface could be ruled out. Therefore, the observed ES asymmetry could not have resulted from Li island formation, which is observed for electron impact on AHC at room temperature [17,18]. We thus concluded, that the observed asymmetric ES structure is typical for the particular target material and can be explained in a similar way as for impact of singly charged ions on metal oxide surfaces [19], see also discussion in Section 4.

Fig. 3 shows total electron yields for impact of H^+ , Ar^+ and electrons on LiF, respectively, versus projectile energy E_p . Note that our present measurements for electron impact have been carried out with such low electron fluxes (typically less than $10^3/\text{s}$), that no formation of a lithium metal film on the LiF surface (see above) could take place during data accumulation. Also plotted in Fig. 3 were total electron yields for impact of the same projectile species on clean polycrystalline gold (for H^+ and Ar^+ from Ref. [20], and for electrons from Ref. [21]).

In Fig. 4, measured total electron yields γ have been plotted versus projectile energy E_p for impact of N^{q+} ($q = 1, 5, 6$) on LiF and Au [22].

4. Discussion

Projected ion ranges have been estimated (G. Betz, private communication) for impact of H^+ , N^+ and Ar^+ , respectively, on polycrystalline LiF, by applying the computer codes MARLOWE [23] and TRIM [24]. The polycrystalline LiF target was simulated, respectively, by an appropriately scaled NaCl structure, screened Coulomb potentials for the Li- and F atoms, and random projectile impact directions (MARLOWE), and by “amorphous” LiF (TRIM). Projected ranges for 500 eV impact energy are 12, 2 and 1.5 nm, respectively, and increase approximately linearly with E_p toward higher impact energy.

Consequently, at least up to $E_p = 20$ keV for both N^{q+} and Ar^{q+} the projected ranges are much smaller than the thickness of our LiF film target (about 200 nm, cf. Section 2).

Our present total electron yields may be compared with data from earlier investigations for impact of 5–25 keV Ar^+ [11], 0.1–1 keV Kr^{q+} ($q \leq 5$) [1] and ≥ 50 eV MCI from metal species ($q \leq 8$) [3], respectively, on heated (above 300°C) monocrystalline LiF targets. All these data have been derived from measured projectile ion- and emitted electron currents, while no corresponding ES data are known. In general, the published total electron yields are smaller than ours by more than a factor of 2, which might be caused by different experimental situations in the earlier studies, which involved other target composition and vacuum conditions and, in particular, much higher projectile currents. Consequently, a more detailed comparison with the earlier published data is not very meaningful.

In Ref. [9], our present understanding of electron emission from a clean metal surface under impact of slow MCI has been described within a scenario basically consisting of three steps. During step #1 the MCI approaches the surface and rapidly captures electrons from the latter via resonance neutralisation (RN), in which way it is turned into a so-called “hollow atom”, i.e. a neutral, multiply excited particle. This hollow atom loses electrons both into vacuum due to auto-ionisation (AI) and into the solid via resonance ionisation (RI), but these electron losses are quickly replaced by the ongoing RN, until surface impact takes place. During the following step #2, all highly excited electrons carried by the hollow atom into the surface are “peeled off” (PO) due to screening. In the subsequent step #3 the particle moves further into the solid and becomes reneutralized, after which it will relax into its neutral ground state via different transitions, among which ejection of fast projectile Auger electrons in the course of inner shell neutralisation is especially noteworthy. These fast electrons may either escape into vacuum or induce slow secondary electrons inside the solid, which can contribute to the total electron yield. Depending on the MCI species and its charge state and impact energy, and on the type and surface conditions of the solid, the various above mentioned contributions to the total electron yield may greatly differ [9].

Referring now to our Fig. 4, we observe that in comparison with MCI induced electron emission from clean gold ($W_\phi \approx 5.1$ eV), for LiF the PE contribution to the total electron yield dominates only at considerably lower ion impact energy over the respective KE contributions, and is also comparably less important. This clearly different role can be explained by a lower threshold and a higher importance for the concomitant KE processes (see below), and by the much higher effective work function ($W_\phi \approx 12$ eV, [8,17,25]) of LiF.

For impact of singly charged ions, the electron emission apparently starts at $E_p \approx 100$ eV, without a clearly

defined threshold. It increases first gently and then rather steeply up to about 10 keV, above which it gradually levels off. As shown in detail in Ref. [2], this behaviour results from conditions relevant for KE from AHC, in particular the projectile energy dependence of electron production via quasi-molecular autoionisation in close collisions of the projectiles with the negative halogen ions, and the rather large mean free paths for electrons diffusing through the AHC (typically 5–10 nm [2,26]). Saturation of KE at high impact energy results from an increasingly deeper projectile penetration into the target bulk, which causes a correspondingly stronger attenuation of electrons to be ejected into vacuum. In contrast to KE from AHC, for a clean metal surface principally different collision processes contribute to KE. In particular, the threshold impact energy for dominant KE processes in a metal is much higher (e.g. $E_p \approx 1$ keV for Ar^+ on Au [20]), and KE yields are considerably smaller (for Ar^+ on Au cf. Fig. 3, and for N^+ on Au $\gamma \approx 3$ at 30 keV [27]).

The particular KE mechanisms within the AHC bulk are also responsible for the fact that, at a given E_p , this KE becomes less efficient with higher primary ion charge [2]. As already shown for MCI impact on NaCl [3], “crossings” of γ versus E_p curves related to the different ion charge states can be observed in our measurements, see curves for N^+ and N^{5+} in Fig. 4, and curves for Ar^+ and Ar^{3+} , and for Ar^{3+} and Ar^{6+} in Fig. 1, respectively. Whereas for $q = 1$ projectiles practically no PE arises from LiF, at high E_p for $q = 1$ the more efficient KE compensates for the PE contributions induced by multiply charged ions.

The change of PE yields when going from N^{5+} to N^{6+} (cf. Fig. 4) is considerably larger for LiF than Au. As explained in Ref. [29], for impact of N^{6+} inside the target bulk one projectile K-shell vacancy gives rise, via respective Auger transitions, to production of comparably fast electrons ($E_e \approx 350$ eV). Fig. 3 shows that for the electron impact energy range of 100–500 eV, secondary (i.e. electron-induced) electron emission yields are typically by a factor of 3 larger for LiF than for Au. Consequently, secondary emission induced by fast electrons inside the AHC is more efficient than inside a metal target, from which fact the above noted, relatively larger change in the PE yields for LiF can be explained. A similar, however less pronounced behaviour is apparent for Ar^{q+} when changing q from 8 to 9, since then one L-shell vacancy can give rise to emission of fast ($E_e \approx 200$ eV) Auger electrons [28]. This change in PE yields is probably less pronounced due to the influence of the above-surface electron emission processes, which follow the principally different surface-densities-of-states (S-DOS) for Au and LiF, respectively.

In summary, the largely different work functions and S-DOS make MCI induced “above-surface” PE contributions for LiF less important than for Au, whereas the subsequent “below-surface” PE- and KE contributions

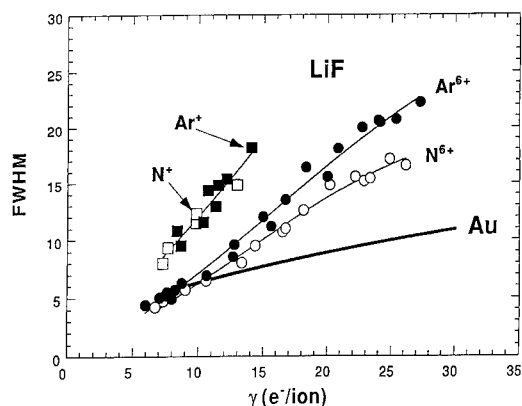


Fig. 5. Full widths at half maximum (FWHM) of measured electron emission statistics versus resulting total electron yields γ , for impact of N^{q+} and Ar^{q+} ($q=1, 6$) on LiF (data points connected by thin lines), and for impact of various slow multi-charged ions on clean gold (thick solid curve), respectively (for further details cf. text).

behave just in the opposite way, because of the considerably larger electron mean free paths in the LiF bulk, and also the much larger secondary electron yields. However, in a more detailed treatment we should consider all processes relevant for electron production before, at and after the MCI impact on the LiF surface, just in the same way as for a clean Au surface [9]. Such a refined treatment might show, e.g., that the MCI induced above-surface electron production from LiF is changed due to blocking of resonance ionisation (RI) of the intermediately formed “hollow atoms” in front of the surface, since the LiF band gap constitutes forbidden final states for RI.

At last, with reference to Fig. 2 we shortly comment on the observed electron emission statistics (ES). For impact of Ar^{9+} , at lower impact energies the PE contribution is dominant or still important, and we observe relatively narrow, Gaussian shaped (i.e. symmetric) ES. However, for higher E_p (i.e. dominant KE) considerably broader and clearly asymmetric ES are produced. At a given total electron yield, in comparison with ES for MCI impact on clean Au [15], for LiF the FWHM of ES is generally larger. Fig. 5 compares the FWHM of ES measured for Au and LiF, respectively, for given total yields γ , which shows that the FWHM for Au is smaller than for LiF, and that for LiF the ES is also broader for singly than for multiply charged ions. From this observation we conclude that at given values of γ the ES will be the broader, the less PE contributes to the respective total electron emission. Recent investigations [19,29,30] have explained the formation of asymmetric ES from a larger projected range of ions and larger mean free paths of electrons in the LiF bulk, which both favour contributions from backscattered projectiles and recoil particles to primary electron production inside the solid, and the generation of secondary

electron cascades. Consequently, at higher E_p the observed ES deviate from the symmetric Gaussians as found for clean metal surfaces. Such asymmetric ES can be described by two parameter-dependent Polya distributions [19].

5. Conclusions

We have presented total electron yields derived from electron emission statistics measured for impact of singly and multiply charged ions on clean polycrystalline LiF. Ion impact energies have been varied from the exclusive potential emission (PE) regime up to the regime for dominant kinetic emission (KE). The applied experimental technique is almost ideally suited for PE and KE studies with insulator target surfaces. Our results on KE can be explained with an existing theory for KE from alkali halide crystal surfaces. At high impact energy asymmetric electron emission statistics were found, in agreement with published results for singly charged ion impact on metal oxide surfaces. In order to explain the observed PE, we have adapted our earlier developed model for slow MCI induced electron emission from clean metal surfaces, by taking into account characteristic differences in total electron emission above, at and below the target surface, respectively. As a particularly important deviation from metallic targets, for LiF and probably other alkali halides the role of subsurface secondary electron emission is much more pronounced, which might be of interest for the not yet well understood MCI-induced sputtering and secondary ion emission processes from alkali halide crystals.

Acknowledgements

This work has been supported by Austrian Fonds zur Förderung der wissenschaftlichen Forschung and by Kommission zur Koordination der Kernfusionsforschung at the Austrian Academy of Sciences. The authors acknowledge very useful contributions to different parts of this work from G. Betz and C. Lemell.

References

- [1] Sh.S. Razhabov, R.R. Rakhimov and D. Abdusalamov, *Izv. Akad. Nauk SSSR Ser. Fiz.* 40 (1976) 2543.
- [2] L.M. Kishinevskii and E.S. Parilis, *Sov. Phys. Tech. Phys.* 27 (1982) 784.
- [3] S.N. Morozov, D.D. Gruich and T.U. Arifov, *Izv. Akad. Nauk SSSR Ser. Fiz.* 43 (1979) 612.
- [4] Sh.S. Razhabov and R.R. Rakhimov, *Izv. Akad. Nauk SSSR Ser. Fiz.* 49 (1985) 1812.
- [5] L.S. Bitensky, M.N. Mirakhmedov and E.S. Parilis, *Sov. Phys. Tech. Phys.* 24 (1979) 618;

- I.S. Bitensky and E.S. Parilis, *J. Phys. (Paris)* 50 (1989) C2-227, and refs. therein.
- [6] S.T. de Zwart, T. Fried, D.O. Boerma, R. Hoekstra, A.G. Drentje and A.L. Boers, *Surf. Sci.* 177 (1986) L939.
- [7] D. Schneider, M.A. Briere, J. McDonald and J. Biersack, *Radiat. Eff.* 127 (1993) 113.
- [8] P. Varga and U. Diebold in: *Low Energy Ion–Surface Interactions*, ed. J.W. Rabalais (Wiley, 1994) ch. 7.4.
- [9] H. Kurz, F. Aumayr, C. Lemell, K. Töglhofer and HP. Winter, *Phys. Rev. A* 48 (1993) 2182; F. Aumayr and HP. Winter, *Comm. At. Mol. Phys.* 29 (1994) 275, and refs. therein.
- [10] P.D. Townsend, in: *Sputtering by Particle Bombardment II*, ed. R. Behrisch, (Springer, Berlin, 1983) p. 147; M. Szymon-ski, in: *Desorption induced by Electronic Transitions/DIET IV*, eds. G. Betz, P. Varga, Springer Series in Surface Sciences 19, (Springer, Berlin, 1990) p. 270. K.S. Song and R.T. Williams, *Self-Trapped Excitons*, Springer Series in Solid-State Sciences 105 (Springer, Berlin, 1993) ch. 6.5.
- [11] K.H. Krebs and S. Rogaschewski, *Wiss. Z. der Humboldt-Universität zu Berlin, Math.-Nat.R.* XXV (1976) 3.
- [12] D. Hasselkamp, in: *Particle Induced Electron Emission II*, Springer Tracts in Modern Physics 123 (Springer, Berlin, 1992) pp. 66–68.
- [13] M. Leitner, D. Wutte, J. Brandstötter, F. Aumayr and HP. Winter, *Rev. Sci. Instr.* 65 (1994) 1091.
- [14] F. Aumayr, H. Kurz, HP. Winter, D. Schneider, M.A. Briere and J.W. McDonald, *Rev. Sci. Instr.* 64 (1993) 3499.
- [15] H. Kurz, F. Aumayr, C. Lemell, K. Töglhofer and HP. Winter, *Phys. Rev. A* 48 (1993) 2192.
- [16] B. Moshhammer and R. Matthäus, *J. Phys. (Paris)* 50 (1989) C2-111.
- [17] P. Wurz, J. Sarnthein, W. Husinsky, G. Betz, P. Nordlander and Y. Wang, *Phys. Rev. B* 43 (1991) 6729.
- [18] P. Wurz and C.H. Becker, *Surf. Sci.* 224 (1989) 559.
- [19] L.A. Dietz and J.C. Sheffield, *Rev. Sci. Instr.* 44 (1973) 183; L.A. Dietz and J.C. Sheffield, *J. Appl. Phys.* 46 (1975) 4361.
- [20] G. Lakits, F. Aumayr, M. Heim and HP. Winter, *Phys. Rev. A* 42 (1990) 5780.
- [21] E.W. Thomas, ed., in: *Atomic Data for Controlled Fusion Research*, ORNL-6088/V3, Oak Ridge National Laboratory (1985).
- [22] M. Vana, H. Kurz, HP. Winter and F. Aumayr, these Proceedings (IISC-10), *Nucl. Instr. and Meth. B* 100 (1995) 402.
- [23] M.T. Robinson, *Phys. Rev. B* 40 (1989) 10717.
- [24] W. Eckstein and J.P. Biersack, *Nucl. Instr. and Meth. B* 2 (1984) 550; J.P. Biersack, *Nucl. Instr. and Meth. B* 27 (1987) 21.
- [25] S. Pülm, A. Hitzke, J. Günster, H. Müller and V. Kempter, *Radiat. Eff.* 128 (1994) 151.
- [26] B.L. Henke, J. Liesegang and S.D. Smith, *Phys. Rev. B* 19 (1979) 3004.
- [27] R.A. Baragiola, E.V. Alonso, J. Ferron and A. Oliva-Florio, *Surf. Sci.* 90 (1979) 240.
- [28] P. Varga and HP. Winter, in: *Particle Induced Electron Emission II*, Springer Tracts in Modern Physics 123 (Springer, Berlin, 1992) pp. 183 and 184.
- [29] K. Ohya, F. Aumayr and HP. Winter, *Phys. Rev. B* 46 (1992) 3101; K. Ohya and I. Mori, *Jpn. J. Appl. Phys.* 31 (1992) 3686.
- [30] M. Vicanek and H.M. Urbassek, *Phys. Rev. B* 47 (1993) 7446.



ELSEVIER

Electron emission in the neutralization of multiply-charged ions at low velocities on metal surfaces: the effect of secondary-electron cascades

N. Lorente ^{*}, R. Monreal, M. Maravall*Departamento de Física de la Materia Condensada, C-XII, Universidad Autónoma de Madrid, E-28049 Madrid, Spain*

Abstract

We present the results of secondary-electron cascade calculations of several systems and determine the relative yield due to these metal electron cascades depending on the nature of the electron emitting process and its energy. We conclude that for slightly charged systems such as He^{2+} and Ne^{2+} the cascade emission can account for 60% of the total electron yield, while it is irrelevant for highly charged species such as Ar^{12+} when subsurface neutralization is not included.

1. Introduction

Many techniques that study multiply-charged ion (MCI) neutralization on metal surfaces measure the number of electrons emitted in the process [1–12]. Among the common features of MCI neutralization at low velocity which can be found are that the electron emission spectra have a similar overall shape with prominent peaks at low electron energy, and that the total electron yield scales linearly with the potential energy of the incident ion: for examples see the above references. The potential energy of an ionic species, W_q , is defined as the sum of one-electron ionization thresholds up to the charge of the studied ion. Thus, in one-electron emission processes the ion can yield a total energy of W_q plus the ion's kinetic energy. In the present work we are going to be concerned with potential electron emission (PEE) and the effect of these electrons on the metal electrons, leading to new total electron yields and spectra once metal electron cascades are included.

In 1963, Propst [13] estimated using electron cascade data that 50% of the total electron yield in the neutralization of He^+ on W was due to metal electron cascades. The low energy electron amounts for his calculated spectra were considerably enhanced by these electrons. Salmi [14] reached a similar conclusion with the model used in our present work. Arifov et al. [2] considered that about 50% of the electrons leaving a metal in ion neutralization, arise from metal electron cascades. More recently Lorente and Monreal [15] estimated that 60% of the electrons produced

in the neutralization of He^{2+} on Cu was due to these cascades, and showed the effect of electron piling-up at low energy in the electron spectra. One could conclude that for singly and doubly charged ions, such secondary electron cascades are fundamental both in the electron yield and spectra.

Regarding more highly MCIs, Hughes et al. [16] explained the difference in electron yield between the neutralization of N^{4+} and N^{6+} because of the cascade of metal electrons caused by subsurface KLL electrons, available in the N^{6+} case. However, the two- to three-order-of-magnitude difference between the low-energy peak and the KLL peak in the electron spectra suggests that the effect of these secondary cascades may be irrelevant to the electron spectra. We could still expect that secondary emission be important due to the high energy of the KLL electrons.

The above facts have induced us to analyze the importance of metal electron cascades. In Section 3 several systems are studied. First we summarize the results presented elsewhere for He^{2+} [15]. Afterwards we apply an “ad-hoc” model for Ne^{2+} following a reasoning akin to that of the He^{2+} model, despite the differences between these two systems. We conclude the study by calculating the ratio of the electron cascade yield to the total yield for different sources, as a function of neutralization process and energy of the primary electron originating the cascade.

Section 2 is devoted to the theory we have used [13,15]. It is based on an isotropical model by Wolff [17,18] in which the nature of the electron–electron interaction is unimportant insofar as it is of short range. We present how the theory must be modified in order to account for the effect of the different emitting processes in the secondary

^{*} Corresponding author. Tel. +34 1 397 4906, fax +34 1 397 4950, e-mail nico@uamc13.fmc.uam.es.

electron cascade. We calculate several transmission functions by integrating over solid angle. In this way we can study the cascade processes produced by electrons injected from either above the surface, the surface itself or the bulk. Finally, in Section 4 there are a summary and the conclusions of the present work.

2. Theory

2.1. Model

The model we have assumed in carrying out the secondary-electron calculations is the one described by Penn et al. [18] and Salmi [13], among others (see also Refs. [15,17,19]). The following is a summary of the approach.

The estimation of secondary electron production is given by iterations of a Volterra equation based on the semiclassical Boltzmann equation [13].

$$\frac{dN_T}{dE}(E) = S(E) + \int_E^\infty F(E, E') \frac{dN_T}{dE}(E') dE'. \quad (1)$$

Here dN_T/dE is the total electron spectrum and the source $S(E)$ is the amount of electrons giving rise to the cascades. The factor $F(E, E')$ is the integration kernel. It gives the probability per unit energy that an electron in a state with energy E' is scattered, and an electron is found in a state with energy E . An approximation to $F(E, E')$ can be obtained in the following way: Since each electron which undergoes a scattering process produces an output of two, $F(E, E')$ must satisfy the following sum rule [17]:

$$\int_{E_F}^{E'} dE F(E, E') = 2. \quad (2)$$

Then the simplest choice becomes, when the zeroth-order harmonic is the only one considered in the spherical harmonic expansion of Boltzmann's equation [17],

$$F(E, E') = \frac{2}{E' - E_F}, \quad (3)$$

where an obvious condition for applicability is that the scattering electron energies be high enough to avoid divergence (a useful guideline is $E' - E_F > E_F$). This form of the integral equation's kernel is very different from its exact form. In the present problem we are not interested in the calculation of fine details of the secondary electron distribution, but in the estimation of the amount of secondary electron produced. The fulfilment of Eq. (2) makes sure that we are going to obtain the electron multiplication in each cascade of the secondary process. The present theory only considers the cascade process in an isotropic electron gas originated by an impinging low-energy electron.

As stated above we are using a zeroth-order spherical-harmonic approximation when calculating Boltzmann's

equation; see Ref. [17]. In doing so, we assume that electrons are isotropically produced during both Auger emission and the subsequent cascade processes. For a discussion on the importance of the degree of accuracy in the different orders of spherical-harmonic approximation see Refs. [17,20]. Then the escape of electrons from the surface can be described by a symmetric transmission function, $T_{out}(E)$. A discussion of the specific choices is given in Section 2.2. Regarding the first step of the cascade, it is produced by the scattering of electrons ejected through the relevant process:

In the case of Auger emission (AC) in which a metal electron is produced as a result of electron capture by the impinging ion, the emitting electron is produced within the first few surface monolayers [20]; then many of these electrons will be emitted before they collide with metal electrons. This means that the first cascade is $[1 - T_{out}(E)]$ times dN_{AC}/dE , where dN_{AC}/dE , the Auger spectrum, is the source $S(E)$ in Boltzmann's equation, Eq. (1), and $[1 - T_{out}(E)]$ is the fraction of electrons which cannot surmount the surface barrier. This is just the fraction which, for every generation of cascade electrons, will originate the next. Then we can multiply $F(E, E')$ times $[1 - T_{out}(E)]$ in the kernel of Eq. (1). Finally, the total spectrum of emitted electrons is obtained by summing up all the contributions to give dN_T/dE and by multiplying times the transmission function $T_{out}(E)$.

On the other hand, in the particular case of autoionization processes (AU) where a multiply excited ion de-excites via electron emission and relaxation of the remaining ion, the source of electrons is above surface. Then the transmission function is different, $T_{in}(E)$, since it says what fraction of the electron current enters the solid; and so $T_{in}(E)$ itself is the factor multiplying dN_{AU}/dE for the first cascade. As we are dealing with low energy electrons, we expect them to have a small mean free path and suffer collisions on the surface. Thus, the same treatment as for Auger electrons is applied in the rest of the cascade calculation.

For bulk electrons we could expect to have a complete cascade process before reaching the surface. Then we use the original scheme by Wolff [17], with $F(E, E')$ given by Eq. (3), in every step of the cascade, including the first step. The integral equation is solved to obtain dN_T/dE , and finally we use the transmission function on the total distribution.

2.2. Transmission function

For a highly isotropical model like the one used, we take the average of the barrier transmission coefficient $T(E, \Omega)$ over solid angle, Ω . $T(E, \Omega)$ is obviously independent of the inward or outward direction of incidence, but the average quantity is not, due to the refraction condition on the surface [21].

As regards the transmission function, we have performed calculations for three different choices, as can be seen in Fig. 1. The dotted lines are the result for a step-like surface in which the quantum transmission coefficient is used [21]. The curve with higher values corresponds to an electron current entering the solid. In dashed lines we have shown the results for a classical step barrier: the escape-cone transmission function [10]. There is a clear difference due to the presence of quantum interference on the surface. The triangle markers are the quantum calculation for a jellium surface with image potential [22]. The good agreement with the escape-cone calculation is remarkable. This may justify the unexplained success of the escape-cone function in electron emission calculations. We will be using it in the rest of the paper.

3. Results and discussion

3.1. He^{2+}

The neutralization of He^{2+} , $W_q = 78.7$ eV, on metal surfaces of high work function $\phi \approx 4$ eV has been widely studied [15,23–27]. The emerging picture of the charge exchange process can be summarized in a few steps. At a distance of 6 Å from the jellium edge, the $n = 2$ manifold of He^+ crosses the bottom of the band allowing resonance capture (RC). At about 2 Å the same manifold crosses the Fermi level, allowing resonance ionization (RI) to take place. Thus, we expect to find an important population of He^{2+} at 2 Å. This resonance capture mechanism is an effective means of preventing neutralization of He^{2+} to its ground state as it passes through the region where this process would be most probable. Then one concludes that AC in two steps to the ground state is the dominant contribution to the electron yield and spectra [15,23,25]. In Ref. [15] we calculated both AC spectra and the metal electron cascade brought up by the AC electrons. We found a good qualitative agreement with experimental data [23], taking into account the fact that our calculations are solid-angle integrated, while in the experiments electrons are collected at a fixed angle.

3.2. Ne^{2+}

Since Ne^{2+} , $W_q = 62.6$ eV, is energetically similar to He^{2+} and their electron spectra have some common features we expect that secondary electron cascades be important for neon. We have not calculated neutralization rates or electron spectra for Ne^{2+} neutralization on metal surfaces. We have simply fitted two peaks representing possible AC or AD (Auger de-excitation) to the experimental spectra [3]. These are drawn with a dashed line in Fig. 2. They are two triangles of area 0.05 and 0.15 electrons respectively, while the corresponding calculated values for He^{2+} were 0.03 and 0.14 electrons. After postulating the

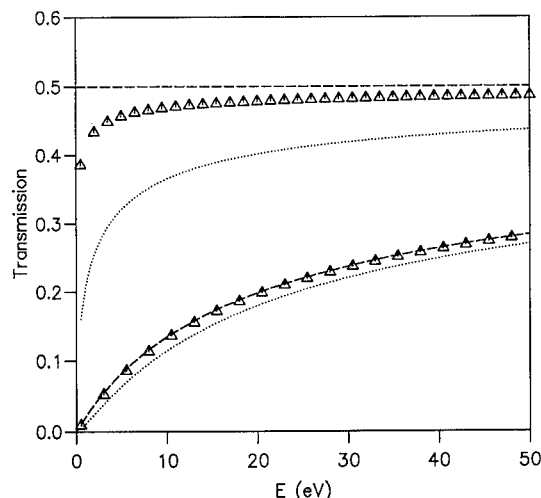


Fig. 1. Transmission functions for three different calculations. The classical escape-cone transmission function is plotted in dashed lines. The line at 0.5 transmission is the transmission function for an electron current entering a solid surface, while the curve at smaller transmission numbers is the outgoing transmission current. In dotted lines we find the transmission functions for quantum calculations of the transmission for a step barrier surface. Again the above curve is the transmission function for an entering current while the one below is the transmission function for an electron current which is leaving the metal. In triangles we have plotted the quantum calculation for a realistic jellium surface in which the image potential is taken into account. For ingoing electrons the image potential favors the transmission, and thus we obtain higher values than the step-barrier calculation in which quantum interference diminishes the transmitted current. Similar results are obtained for outgoing electrons. The softer image-potential barrier allows a higher emission of electrons into the vacuum. The agreement of a more realistic surface with the classical escape-cone function is remarkable, probably explaining the success of the escape-cone transmission. The metal density used in this calculation is the one for $r_s = 2.67a_0$.

electron source, we have calculated the electron cascades caused by it. The total electron spectrum is plotted in full, Fig. 2. The agreement with the experimental data [3] suggests that metal electron cascades are fundamental towards explaining the electron yields and spectra of Ne^{2+} neutralization on metals of high work function.

Approximately, 60% of the total yield is due to metal electron cascades in the two systems studied above, with the characteristic low-energy spectra being basically explained by the piling-up effect of metal electron cascades.

3.3. Yield due to metal electron cascades

We would like to study the electron cascade production in other systems. However, this task is difficult due to the detailed analysis of the charge-exchange processes that one has to do in order to obtain the sources for the metal

electron cascades. In the work being described, we idealize the problem so that we can compute different yields for several inducing processes. As we shall see the model is quite robust against changes in the chosen parameters, giving some confidence about its reliability.

The total electron yield γ_{total} is calculated by integrating over energy the total spectrum $T_{\text{out}}(E) dN_T/dE$, dN_T/dE given by Eq. (1). The secondary cascade yield γ_{sec} is the total yield minus the yield of the primary electrons, the latter being the integration of the source S of Eq. (1) times the corresponding transmission function.

A single Lorentzian is chosen as the source for the cascades. Since what we are calculating is the ratio of cascade yield to total yield, the number of primary electrons is unimportant and so we take the area of the curve as one. By changing the width and the energy peak of the Lorentzian, and assuming different neutralization processes following the guidelines given in Section 2, we find that the ratio of the metal electron cascade yield over the total yield is practically independent from finer details of the source. We can vary the Lorentzian width from 2 eV to 35 eV without appreciable change except at low peak energies. So, for the Lorentzian peaked at 10 eV one has the biggest difference (less than 20%) between yield ratios depending on the width used. When the peak is at 20 eV the difference is less than 3%. The reason for the low energy result is that 7.5 eV of the 35-eV wide curve are below the vacuum energy, while this does not happen for

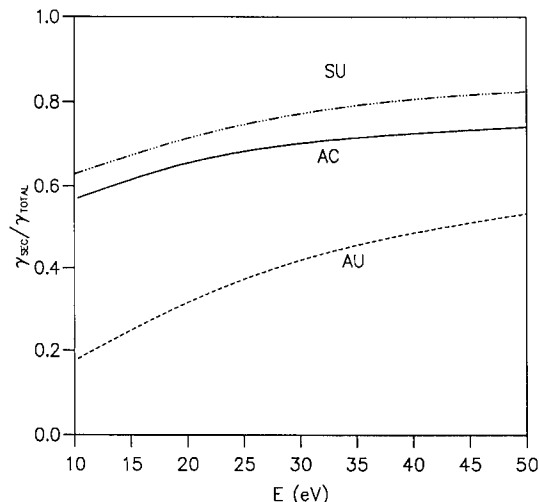


Fig. 3. These are the calculated ratios of secondary cascade to total yield for three different processes, plotted versus the peak energy of the source measured from the vacuum level. AU stands for electrons emitted in an autoionization process, which takes place over the metal surface. AC depicts the electrons emitted in an Auger capture process where the electron originates on the metal surface. SU is a complete bulk calculation of the cascade processes, where the final yields take into account the transmission by the metal surface. Once the emitting process and the emitted electron energy have been determined we can estimate the percentage of cascade electrons in the electron yield by reading in this figure.

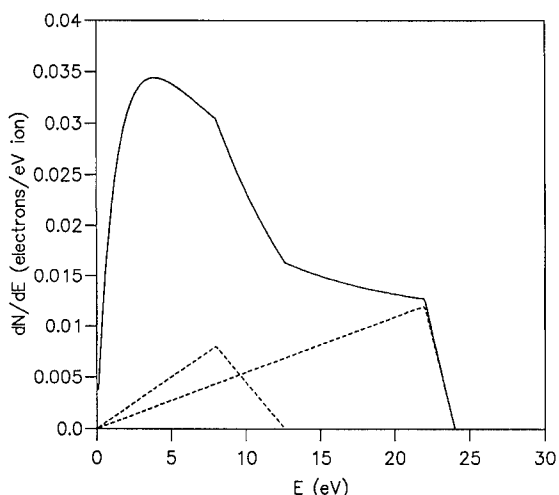


Fig. 2. The total spectrum of Ne^{2+} neutralized on Cu is plotted in full line. The fitted electron source is shown in dashed lines, assuming two contributing processes to the electron emission. These primary spectra have been fitted according to the results of a calculation for He^{2+} neutralization on Cu [15], and to the experimental result of Varga et al. [3]. This figure shows that 60% of the emission in this system may also come from metal electron cascades.

the 2-eV wide Lorentzian. We have also checked that the actual shape of the electron source matters little as long as we have a defined peak. As examples, we tested triangles and Gaussians besides the Lorentzians. Here the discrepancy among the results due to the different shapes is less than 5%, being bigger for higher energy due to the different tails of the distributions.

Fig. 3 shows the yield ratio of secondary cascade electrons to total emitted electrons ($\gamma_{\text{sec}}/\gamma_{\text{total}}$) for three emission processes. In all cases, the ratio is plotted versus the peak energy of the source, measured from the vacuum level.

In dashed line we have drawn autoionization processes, labeled AU. For a 10-eV peak less than 20% of total electron yields are metal cascades, while at 30 eV the proportion climbs to 40%. This indicates that for very highly charged ions where AU emission is dominant under 10 eV, such as Ar^{12+} , one is going to find that much less than 20% of the total yield is made up by metal electron cascades. Using the estimations of Kurtz et al. [28] we found proportions of less than 10% of the yield due to electron cascades since the AU emission peaks at 4–6 eV. However secondary electron emission is not unimportant

at higher energies: At 30 eV 40% of the yield is metal electron cascades.

The second line in full represents the ratios induced by Auger capture processes. AC gives rise to more electron cascade emission: it is almost constant at 60%–70%, in good agreement with the helium and neon results. We calculated the yield ratio for a 20-eV peak of 2-eV width for jellium densities ranging from $r_s = 2.0a_0$ to $r_s = 5.0a_0$, finding changes of less than 0.03 in the corresponding value of the curve (around 0.7). This indicates that the above results may be applied to almost all free-electron metals.

What are the differences between these curves due to? We can already see them in the origin of the cascade. The fraction of the source used in the first step of the cascade is $1 - T_{\text{out}}$ for AC processes, while it is T_{in} for the AU emission as explained in Section 2. While $1 - T_{\text{out}}$ ranges from almost one to 0.7, T_{in} is constant and equals 0.5. Definitely, there are more electrons in the AC induced cascades than in the AU ones. This explains the big difference between AU and AC, and also explains why the AC yield ratio is almost constant when the one for AU is clearly increasing with the electron source's energy, since this behavior is lessened by the $1 - T_{\text{out}}$ decrease.

We also calculate the contribution of subsurface or bulk processes, labeled SU in Fig. 3. We assume that in these processes the whole source is used in creating the cascade, in opposition to the other cases in which a fraction of it was lost. Obviously then, we obtain a higher ratio of electron cascades here, skirting 80%.

Fig. 3 is an easy way of estimating the amount of metal electron cascades in the total yield once the emitting processes are known. One can see what the yield percentage due to electron–electron collisions in the metal is, by reading it off the graph at the corresponding source energy.

4. Summary and conclusions

By means of an isotropical model, in which nuances of electron–electron interactions are not important as far as yield calculations and qualitative electron distributions are concerned, we have performed an extensive study of the effects of metal electron cascades on the electron yields and spectra of MCI neutralization on metal surfaces.

For ion species of potential energy, W_q , smaller than 100 eV we find that 60% of the electron yield is due to metal electron cascades, piling up at low energy in the electron spectra. This agrees well with a schematic approach using a Lorentzian as an electron source since for $W_q \approx 50$ eV Auger capture (AC) is one of the dominant mechanisms. For AC in Fig. 3 we find that the metal electron cascades are 60%–70% of the total yield. For autoionization (AU) the yield ratio is no longer constant against the source energy, and varies from less than 20% for 10 eV to 40% for 30 eV.

Highly charged ions like Ar^{12+} present a dominant AU peak at 4–6 eV and this yields less than 10% of cascade electrons in the total electron yield. High energy subsurface electrons have not been included in our calculations.

Acknowledgements

Helpful discussions with P. Apell are gratefully acknowledged. This work has been funded by Dirección General de Investigación Científica y Técnica (DGICYT) of Spain under Contract No. PB93-0260.

References

- [1] H.D. Hagstrum, Phys. Rev. 96 (1954) 325.
- [2] U.A. Arifov, L.M. Kishinevskii, E.S. Mukhamadiev and E.S. Parilis, Sov. Phys.-Tech. Phys. 18 (1973) 118.
- [3] P. Varga, W. Hofer and H. Winter, Surf. Sci. 117 (1982) 142.
- [4] D.M. Zehner, S.H. Overbury, C.C. Havener, F.W. Meyer and W. Heiland, Surf. Sci. 178 (1986) 359.
- [5] M. Delauney, M. Fehringer, R. Geller, D. Hitz, P. Varga and H.P. Winter, Phys. Rev. B 35 (1987) 4232.
- [6] S.T. de Zwart, A.G. Drentje, A.L. Boers and R. Morgenstern, Surf. Sci. 217 (1989) 298.
- [7] P.A. Zeijlmans van Emmichoven, C.C. Havener and F.W. Meyer, Phys. Rev. B 43 (1991) 1405.
- [8] J. Das, L. Folkerts and R. Morgenstern, Phys. Rev. A 45 (1992) 4669.
- [9] H. Kurz, K. Töglhofer, H.P. Winter and F. Aumayr, Phys. Rev. Lett. 69 (1992) 1140.
- [10] R.A. Baragiola, in: Low Energy Ion-Surface Interactions, ed. J.W. Rabalais (Wiley, 1993).
- [11] R. Köhrbrück, N. Stolterfoht, S. Schippers, S. Hustedt, W. Heiland, D. Lecler, J. Kemmler and J. Bleck-Nehaus, Phys. Rev. A 48 (1993) 3731.
- [12] P. Eeken, J.M. Fluit, A. Niehaus and I. Urazgil'din, Surf. Sci. 273 (1992) 160.
- [13] F.M. Propst, Phys. Rev. 129 (1963) 7.
- [14] L.A. Salmi, Phys. Rev. B 46 (1992) 4180.
- [15] N. Lorente and R. Monreal, Surf. Sci. 303 (1994) 253.
- [16] I.G. Hughes, J. Burgdörfer, L. Folkerts, C.C. Havener, S.H. Overbury, M.T. Robinson, D.M. Zehner, P.A. Zeijlmans van Emmichoven and F.W. Meyer, Phys. Rev. Lett. 71 (1993) 291.
- [17] P.A. Wolff, Phys. Rev. 95 (1954) 56.
- [18] D.R. Penn, P. Apell and S. M. Girvin, Phys. Rev. B 32 (1985) 7753.
- [19] M. Rösler and W. Brauer, Phys. Status Solidi B 126 (1984) 629.
- [20] M. Rösler, Nucl. Instr. and Meth. B 78 (1993) 263.
- [21] V. Heine, Phys. Rev. 151 (1966) 561.
- [22] N. Lorente, R. Monreal and M. Alducin, Phys. Rev. A 49 (1994) 4716.
- [23] P.J. Jennings, R.O. Jones and M. Weinert, Phys. Rev. B 37 (1988) 6113.
- [24] P.A. Zeijlmans van Emmichoven, P.A.A.F. Wouters and A. Niehaus, Surf. Sci. 195 (1988) 115.

- [25] S. Schippers, S. Oelschig, W. Heiland, L. Folkerts, R. Morgenstern, P. Eeken, I.F. Urazgil'din and A. Niehaus, *Surf. Sci.* 257 (1991) 289.
- [26] H. Breiten, H. Müller and V. Kemper, *Surf. Sci.* 274 (1992) 309.
- [27] K. Töglhofer, F. Aumayr and H.P. Winter, *Surf. Sci.* 281 (1993) 143.
- [28] H. Kurz, F. Aumayr, C. Lemell, K. Töglhofer and H.P. Winter, *Phys. Rev. A* 48 (1993) 2192.



ELSEVIER

Multi-electron and multi-state effects in the charge transfer processes between oxygen and metal surfaces

D. Teillet-Billy ^{a,*}, B. Bahrim ^{a,b}, J.P. Gauyacq ^a^a *Laboratoire des Collisions Atomiques et Moléculaires (unité de recherches associée au CNRS 281), Université de Paris-Sud, Bât. 351, 91405 Orsay Cedex, France*^b *Atomic Physics Institute, Laser department, P.O. Box MG-6, Bucarest Magurele, Romania*

Abstract

Oxygen atoms and molecules and their negative ions have an electronic structure containing a few equivalent outer electrons. In the course of an atom (molecule)–metal surface collision, each of them can participate in charge transfer processes. It is shown that this multi-electron aspect has to be taken into account, it generates multi-state and polarization effects. The consequences for the resonant charge transfer process are discussed and two examples are discussed: polarization effects in sputtering of O^- ions and quenching of oxygen singlet states. A generalisation to other systems and electronic structures is presented.

1. Introduction

The charge transfer process is an important process in atom (molecule)–surface collisions. It manifests itself as a change in the charge state of particles scattered from a surface (neutralisation of positively charged particles, ionization of excited neutral atoms or formation of negative ions). It corresponds to an electron jump from the metal surface to the atomic or molecular center or inversely from the particle to the metal surface. These capture or loss processes may both occur in the course of a given particle–surface interaction, depending on the relative energy position of the atomic level and of the Fermi level. Various processes can be induced in atoms or molecules by a charge transfer i.e. the presence of one extra electron: electronic transitions as well as excitation of the internal heavy particle movement in the case of molecules. Charged or excited species formed by charge transfer are thus invoked as reaction intermediates in different processes on surfaces: reactive scattering [1], desorption [2], electronic (or vibrational) excitation [3,4], quenching of excited states [5,13].

Among the different charge transfer mechanisms, the resonant charge transfer process will be studied in the present article. Auger processes can also take place in the vicinity of a surface (Auger de-excitation, Auger neutralisation). Usually the range of atom–surface distances where

they are efficient is smaller than that for the resonant process. Such two electron processes will not be considered in the present paper.

Resonant charge transfer is generally viewed as a one active electron process: there exists a potential barrier between the metal and the atom in the potential felt by the electron and the resonant charge transfer process corresponds to a tunneling through this barrier or to transitions over this barrier. The efficiency of the resonant process is strongly dependent on the tunnelling process characteristics: the higher and broader the potential barrier is, the smaller the tunnelling rate is. The tunnelling probability also depends on the angular properties of the active electron wave function. For example, the presence of a node in the angular part of the electron wave function in the direction of the surface where the potential barrier is narrow will decrease the tunnelling rate, this angular property induces polarisation effects in the capture/loss process; it is one of the aspects of the resonant charge transfer process that deserves attention and it will be discussed here. However, only a few systems can be considered as one electron systems. Indeed in open shell systems with a few equivalent electrons, any of these can participate in the charge transfer process. In a system with a few equivalent electrons, the capture (or loss) of an electron can result in the formation of different electronic states depending on the quantum number of the captured (lost) electron and on its angular momentum coupling with the rest of the electronic cloud. A multi-state effect can then be associated with the multi-electron effect. In addition, the various possible quantum numbers of the captured (lost) electrons

* Corresponding author, tel. +33 1 6941 7863, fax +33 1 6941 7671, E-mail: billy@lcam.u-psud.fr.

can correspond to spin variables but also to orbital angular momentum variables and then, this introduces polarization effects in the problem. In open shell systems, one can then have multi-electron effects associated with multi-state and polarization effects which influence the charge transfer process. It is the aim of this paper to stress the importance of the electronic structure description of the atomic (molecular) particle in the treatment of particle metal-surface charge transfer process, as well as to present the peculiarities introduced by an open shell structure. In Section 2, these effects will be presented on the examples of atomic and molecular oxygen. Results of quantitative studies of resonant charge transfer rates will be presented, and the various effects discussed. Then, examples of applications of these calculations to practical systems will be presented: study of polarization effects in the charge state of sputtered oxygen negative ions (Section 3) and a study of a quenching process for oxygen excited states due to the multi-state aspect of the resonant charge transfer process (Section 4). Finally, as a conclusion, the general characteristics of these multi-electron multi-state effects will be presented with a discussion of their occurrence in various systems (Section 5).

2. Electronic structure of the atomic (molecular) particle and resonant charge transfer

2.1. Polarization effect in one electron problems

In a few systems, the resonant charge transfer problem can be considered as a one electron problem. A prototype is a closed shell system capturing an electron, the neutralization of alkali ions is an example of such a structure. The captured electron can have the spin up or down, and due to the different spin degeneracies of the initial and final states of the capture/loss process, spin statistics factors must be incorporated in the treatment and this makes the capture and loss rates different one from the other [6,7]. For a capture (lost) electron with a non-zero angular momentum, the resonant charge transfer rate depends on the angular momentum of the electron, in fact on its projection m on an atomic axis perpendicular to the metal surface. This was first shown in perturbative studies by Gadzuk [8] and was later confirmed by non-perturbative studies [7,9,10]. The polarization effect can be easily understood; let us consider the case of a p-electron. $m = 0$ orbitals are pointing along the surface normal and thus, due to a better overlap, they are more coupled with the metal states than the $m = \pm 1$ orbitals that present a node in this direction. It can also be viewed in another way: the coupling with the surface results in a mixing of the different symmetries in the atom, in particular a p-electron mixes with all the possible angular momenta; the mixture of $m = 0$ and $m = \pm 1$ levels is indeed different: only the $m = 0$ level can mix with the s state which does not present any centrifugal

barrier and this leads to large atom-surface charge transfer couplings (see discussion in Ref. [7]). This polarization effect is quite general and was found in a variety of systems. It can be significantly modified when hybridization is present. Indeed, in that case, atomic states with different l values are mixed by their interaction with the surface, leading to hybrids which have very different charge transfer properties (see e.g. in Refs. [9,10]).

2.2. Structure of O and O⁻

The case of atomic oxygen and its negative ion is chosen here to illustrate the role of the electronic structure of the atomic (molecular) particle in the charge transfer problem. The O atom and its O⁻ ion have an incomplete p shell structure. The free O atom has 4 equivalent 2p electrons, the O⁻ ion has 5 equivalent 2p electrons and these 5 electrons can a priori participate in the charge transfer. Any of the 5 equivalent electrons of O⁻ can tunnel through the potential barrier leaving the O atom in the O(2p⁴) configuration, that is to say in one of the 3 electronic states, the ground ³P or the two excited ¹D, ¹S electronic states. Thus the multi-electron aspect of the loss process is also associated to a multi-state aspect.

Let us consider the O⁻(2p⁵) ²P($M_L = 1$, $M_S = \frac{1}{2}$) sublevel. It can be represented by a unique Slater determinant O⁻(2p⁵) ²P ($M_L = 1$, $M_S = \frac{1}{2}$) = $|2p_+ 2\bar{p}_+ 2p_0 2\bar{p}_0 2p_-|$. The bar labels the $m_s = -\frac{1}{2}$ spin state and the subscripts $+, 0, -$ label the $m_l = +1, 0, -1$ projections of the electron orbital momentum on the quantization axis. When expanding the Slater determinant with respect to its column, we obtain 5 terms, each one corresponding to any of the five 2p electrons of O⁻ coupled to a neutral O atom state.

$$\begin{aligned} & |2p_+ 2\bar{p}_+ 2p_0 2\bar{p}_0 2p_-| \\ &= 2p_+ |2\bar{p}_+ 2p_0 2\bar{p}_0 2p_-| - 2\bar{p}_+ |2p_+ 2p_0 2\bar{p}_0 2p_-| \\ &\quad + 2p_0 |2p_+ 2\bar{p}_+ 2\bar{p}_0 2p_-| - 2\bar{p}_0 |2p_+ 2\bar{p}_+ 2p_0 2p_-| \\ &\quad + 2p_- |2p_+ 2\bar{p}_+ 2p_0 2\bar{p}_0|. \end{aligned} \quad (1)$$

The O⁻ wavefunction can then be splitted in a sum of terms, each of them being related to one electronic sublevel of the neutral oxygen and being associated to a one electron wavefunction defined by its orbital and spin quantum numbers. This correspondence can be made more explicit by relating the 4 electrons Slater determinants to the oxygen states. (see e.g. in Ref. [11] for details).

The coefficients in the expansion are called parentage coefficients [12] and correspond to the weight of each neutral oxygen electronic state in the O⁻ wavefunction. The formation of the O⁻ ion then implicitly includes the excitation of the oxygen atomic core. The formation/decay of an O⁻ ion cannot be considered as a one electron process (this would correspond to simply attaching an

electron to a ground state O atom), a priori it implies the 5 outer p-electrons and the three O electronic states (3P , 1D and 1S) associated with the $2p^4$ electronic configuration. It is also noteworthy that the polarization effect (dependence of the charge transfer rate on the orbital angular momentum) is associated with this multi-state effect: indeed, as mentioned above, the symmetry of the captured/lost electron that connects a given state O^- to a given state of O is well defined (Eq. (1)) and so, certain pairs of states (O, O^-) will be more or less coupled according to the polarization effect.

2.3. Coupled angular mode (CAM) method

The non perturbative coupled angular mode (CAM) method was developed [7] to handle the problem of electron capture and loss by ionic or neutral, atomic or molecular systems in front of a metal surface. It has been applied to a variety of different systems: atomic negative ions [7], neutral and positive ions [10], transient negative molecular ions in molecule vibrational excitation processes [4], transient atomic negative ions in quenching processes [13]. Only the general principle of the method will be presented here. It consists in studying electron scattering by the compound system formed by the atom (or molecule) and the metal surface. The atomic (molecular) states appear as resonances in this scattering study and the analysis of the resonance properties yields the level energy and the level widths (total and partial). The CAM method considers a jellium metal and describes the electron–metal interaction by a local potential only function of z , the electron–surface distance, and taken from the work of Jennings et al. [14]. In the present work, the surface was chosen as an aluminum (111) surface. The electron–atom (molecule) interaction is described in the multi-channel effective range approximation (ERT), previously developed to treat electronic excitation in electron-free molecule collisions [15–17]. In the ERT, the long range e^- -atom interactions are explicitly included, whereas the short range forces are implicitly incorporated via a boundary condition on the atom boundary. In the single channel version of ERT and CAM [7,15], one considers a one electron wavefunction for the collisional electron. In the multi-channel version of ERT [16,17] and CAM [11,18], one considers multi-electron wavefunctions. In both cases, the boundary condition on the atom boundary consists in matching the electron–atom scattering wavefunction outside, to an equivalent electron wavefunction inside the atom. A detailed description of the multi-electron multi-state version of the CAM method can be found in Ref. [11].

2.4. O^- negative ions interacting with an Al surface

The energy positions and widths of the two sublevels $^2P_{M_L=0}$ and $^2P_{M_L=\pm 1}$ of O^- are calculated by the CAM method as functions of the atom–surface distance Z . The

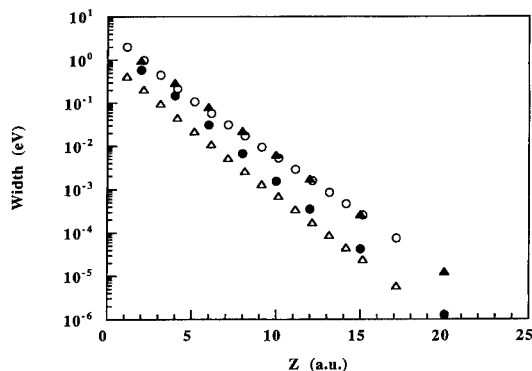


Fig. 1. Total decay widths of the O^- levels in front of an Al surface as functions of the atom–surface distance (measured from the image reference plane). Present CAM results: full triangles ($M_L = \pm 1$); full circles ($M_L = 0$). Results from Ref. [19]: open triangles ($M_L = \pm 1$); open circles ($M_L = 0$).

energies [18], not presented here, shift down as the ion approaches the surface and roughly follow the image charge potential at the ion center. Fig. 1 presents the total detachment widths as a function of Z , measured from the image reference plane. The total widths display the usual almost exponential decrease with Z , corresponding to the overlap between the metal and atom wavefunctions. The width of the O^- ($^2P_{M_L=\pm 1}$) is found larger than that of the O^- ($^2P_{M_L=0}$). Polarisation effects come from the larger coupling with a surface of a $m = 0$ electron as compared with a $m = 1$ electron (see the discussion above in Section 2.1). For the multi-electron case, one has to look at the electronic structure to deduce the difference between the widths of the two $^2P_{M_L=\pm 1}$ and $^2P_{M_L=0}$ states from the difference between the $m = 0$ and $m = \pm 1$ one electron coupling terms (indeed m and M_L are different!). A first easy argument is to look at the number of $m = 0$ and $m = \pm 1$ electrons in each of the 2P states: one for the $M_L = 0$ and two for the $M_L = \pm 1$, thus leading to a larger charge transfer coupling, i.e. width, for the $M_L = \pm 1$. A better more detailed argument consists in analyzing the parentage coefficients of the O^- states and in comparing the weights of the various m terms for the various O states (see in Ref. [11]): it shows that the $m = 0$ terms are mainly efficient in the $^2P_{M_L=\pm 1}$ O^- state, thus accounting for the larger width of this state. It is noteworthy that the multi-electron effect apparently reverses the polarization effect (it is only apparent since m and M are different quantum numbers, one refers to the transferred electron and the other to the entire atom).

Fig. 1 also presents the results of Nordlander [19] obtained in a one electron study neglecting the multi-electron effects. As expected from the above discussion, they display a larger width for the 0 state than for the ± 1 state.

Fig. 2 presents the partial decay widths of the O^- ($^2P_{M_L=\pm 1}$) negative ion towards the various neutral

channels (3P , 1D , 1S) according to the angular momentum of the ejected electrons ($m = 0$ and $m = \pm 1$). The largest partial decay width corresponds to the 3P electronic O state associated to a $m = 0$ electron and the smallest partial decay width is associated to the 1S O state. The different binding energies of the O^- ion with respect to the different neutral states explain the 3 different Z behaviours of the partial widths at large atom–surface distances: the exponential decrease with Z of the width is linked to the exponential decrease of the outer electron wavefunction of O^- i.e. to its binding energy with respect to each neutral state.

2.5. Molecular oxygen and its $^2\Pi_g$ negative ion

The oxygen molecule presents an open shell structure similar to that of atomic oxygen. The ground state O_2^- negative ion of $^2\Pi_g$ symmetry corresponds to the $1\pi_u^4 1\pi_g^3$ electronic configuration. The electronic configuration of molecular oxygen is $1\pi_u^4 1\pi_g^2$ (for the outer shell), and is associated with three states: $X^3\Sigma_g^-$, $a^1\Delta_g$ and $b^1\Sigma_g^+$. The O_2/O_2^- charge transfer process, associated with the capture/loss of a $1\pi_g$ electron then has a multi-state character associated with the π_g multi-electron character, similarly to the case of atomic oxygen: the electronic structure of the O_2^- ground state ion contains terms associated with the excited a and b states. In addition, studies of the electronic excitation of O_2 by electron impact [16] showed that the $1\pi_u$ electronic shell is also playing a role in the resonance formation and decay and thus the multi-electron effects also incorporates the O_2 electronic states associated with the $1\pi_u^3 1\pi_g^3$ configuration. Molecular systems such as O_2^- present some specific characteristics that are not present in atomic systems. The internuclear distance can play a role in the charge transfer process: first, the electron affinity

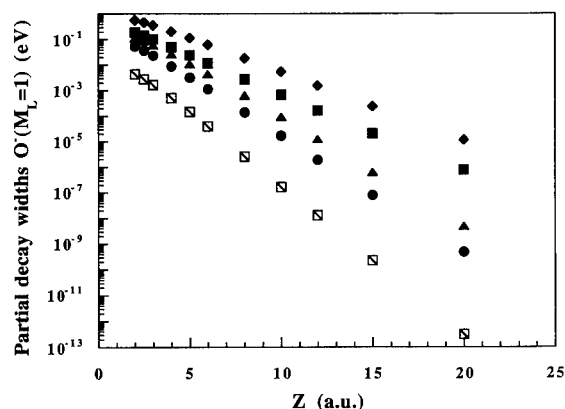


Fig. 2. Partial decay widths of the O^- ($M_L = \pm 1$) level in front of an Al surface: full diamonds (O^3P , $m = 0$ channel), full squares (O^3P , $m = \pm 1$ channel), full triangles (O^1D , $m = 0$ channel), full circles (O^1D , $m = \pm 1$ channel), squares with a bar (O^1S , $m = \pm 1$ channel).

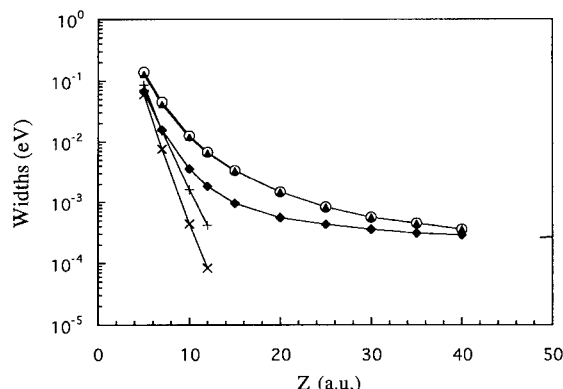


Fig. 3. Total decay width of the O_2^- ($^2\Pi_g$) level in front of an Al surface, for various internuclear distances and orientations. Equilibrium distance of the free O_2 : open circles (perpendicular geometry), full diamonds (parallel geometry, S state), full triangles (parallel geometry, A state). Equilibrium distance of the free O_2^- , parallel geometry: + (A state), \times (S state).

depends on the internuclear distance and this influences the charge transfer coupling and secondly, for low energy collisions, the molecule can vibrate during a collision. Another molecular character concerns the orientation of the molecular axis: the symmetry of the molecule + surface system depends on this axis orientation. For a molecular axis normal to the surface, the system is invariant by rotation around this axis and the molecular symmetry is preserved. For other orientations, the plane containing the molecular axis and perpendicular to the surface is the only symmetry element: in the case of the doubly degenerate $^2\Pi_g$ O_2^- state, the two components mix together to form two states: one symmetric (S) and one antisymmetric (A) with respect to this plane. These two components couple differently with the metal surface. As a result, the $^2\Pi_g$ O_2^- resonance is splitted in two components with different charge transfer properties. This feature is quite general in molecule–surface interactions and has been already discussed in the context of electron-adsorbed N_2 molecule collisions [20].

The energy and width of the O_2^- ($^2\Pi_g$) ion interacting with an Al surface have been determined with the multi-channel CAM method. The energy is found to follow the usual image charge shift. Fig. 3 presents the width of the O_2^- state as a function of the molecule–surface distance for two geometries (molecular axis perpendicular and parallel to the surface) and for two internuclear distances (the free O_2 and O_2^- equilibrium distances, $Re(O_2)$ and $Re(O_2^-)$). Only the total width is presented here. The partial widths corresponding to the various O_2 states present a behavior similar to that seen on the atomic oxygen case. The free O_2^- energy is quite different at the two internuclear distances: at $Re(O_2)$, O_2^- is a resonance located around +0.1 eV and at $Re(O_2^-)$, O_2^- is bound by around −0.93 eV with respect to the O_2 ground state.

This energy difference explains the quite different widths of O_2^- in front of an Al surface at the two internuclear distances: at $Re(O_2)$, the width goes to a constant at infinity and at $Re(O_2^-)$ it goes to zero. The effect of the molecular axis orientation on the width is also quite effective. In the case of the parallel geometry, the two components S and A have quite different widths: the symmetric component is significantly less coupled to the surface than the antisymmetric one, which is quite comparable to the two components in the perpendicular geometry. This result is quite similar to that of N_2^- ($^2\Pi_g$) [20] and it can be interpreted by considering the symmetry of the active orbital [20]: in the perpendicular geometry and in the A component of the parallel geometry the active orbital is a $d\pi$, whereas it is a $d\delta$ for the S component of the parallel geometry (quantization axis normal to the surface) and this accounts for the coupling differences.

The large variations of the O_2^- width, i.e. of the charge transfer rate, with both the internuclear distance and the molecular axis orientation show that both these variables have to be taken into account in a charge transfer study; it means that the charge transfer will occur preferentially for certain symmetries and certain internuclear distances.

3. Example of polarization effects: sputtering of O^- ions

The resonant charge transfer process determines the final charge state of particles sputtered from a surface. We studied the case of oxygen atoms sputtered from a vanadium surface covered by variable amounts of alkali to vary its workfunction, in connection with the experimental study of Yu [21]. The basic idea is that the large variation of the O^- yield with the surface work function is due to the variation of the O^- survival probability during its escape from the surface and not to variations in the sputtering process. We used the position and charge transfer rates obtained with the CAM method, together with a semiclassical rate equation approach for the dynamical treatment [22]. The latter consists in assuming that the atoms follow a classical trajectory, along which the various populations are evolving, following rate constants (note that the capture and loss rates are not equal). In the case of O^- sputtering, the equation reduces to (in atomic units):

$$\frac{dP^-}{dt} = -\Gamma P^-,$$

where P^- is the O^- ion population and Γ its decay rate.

At small atom-surface distance, the O^- level is below the Fermi level, and for $Z > Z_c$, the O^- level becomes unstable and can lose its electron. When the workfunction varies, Z_c varies and this changes the survival probability. Fig. 4 presents our results for an O^- velocity of 16 km/s. Three sets of theoretical results are presented according to the initial state of the O^- ion: it is assumed to be initially

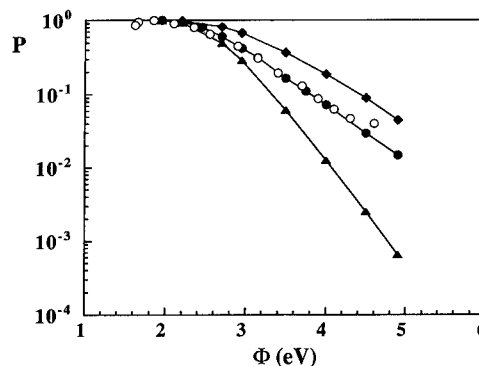


Fig. 4. Survival probability of O^- ions sputtered from an alkali coated V surface with a variable surface workfunction ($v = 16$ km/s): black diamonds (O^- , $M_L = 0$ state), black triangles (O^- , $M_L = \pm 1$ state), black circles (O^- , statistical population of M_L states). Open circles: experimental results of Yu [21].

in the $M_L = 0$ or $M_L = \pm 1$ state or in a statistical mixture of the three states. The results for $M_L = 0$ and $M_L = \pm 1$ are quite different. For comparison with experiment, we chose a statistical mixture, because of the polycrystalline structure of the target and of the sputtering conditions. These statistical results are found to reproduce quite well the experimental results of Yu [21] (see also in Ref. [18]). One can then conclude on the large importance of polarization effects which lead to a well defined population of magnetic sublevels in the sputtered O^- ions.

4. Example of multi-state effects: quenching of oxygen singlet states

The multi-electron, multi-state structure of the O/O^- charge transfer process leads to the existence of a quenching process for the O singlet states. The general idea can be obtained from Fig. 5: it presents in two different ways the energetics of the O/O^- system. The existence of two possible (and equivalent) diagrams comes from the fact that the energetics of resonant charge transfer is usually presented on one electron diagrams which are not suited for multi-state, multi-electron effects. Fig. 5a presents a unique continuum of metallic states in front of the three different electron affinities of O^- , with respect to the 3P , and 1D and 1S states. The electron affinities increase when Z decreases due to the image charge shift and cross the Fermi level at different critical distances $Z_c(^3P)$ and $Z_c(^1D)$. For the Al surface, the crossing $Z_c(^1S)$ does not exist. Fig. 5b presents an alternate picture with a unique O^- state in front of three continua: they correspond to the continuum of metallic electrons associated to the various O states (3P , 1D and 1S) and are then shifted in energy, one with respect to the other. The three bands of occupied levels (hatched areas on Fig. 5b) are then simply shifted

one with respect to the other. There are also three vacuum levels for the metal + O system corresponding to the three O states. The two figures contain the same Z_c distances which define different zones with different charge transfer characteristics:

- for $Z < Z_c(^3P)$: electron capture is possible in all channels,
- for $Z_c(^3P) < Z < Z_c(^1D)$: electron capture by 1D and 1S atoms is possible, while O^- can decay to form a 3P atom,
- for $Z > Z_c(^1D)$: electron capture by 1S atoms is possible, while O^- can decay to form 3P or 1D atoms.

These three regions lead to the existence of a singlet state quenching process induced by the charge transfer: when a singlet oxygen atom approaches the surface, it can capture an electron to form an O^- ion which decays by emitting an electron, forming an $O(^3P)$ atom. With such a process, what happens of an oxygen atom at small atom–surface distances is then independent of the initial state of

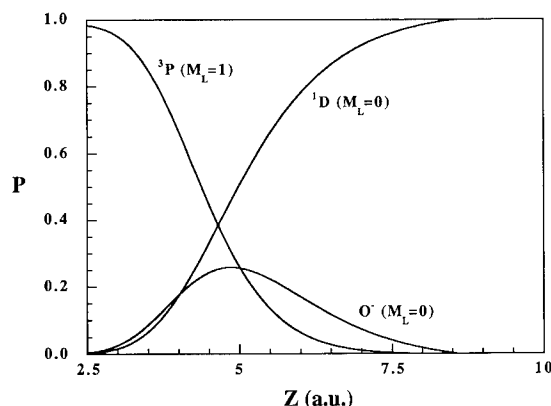


Fig. 6. Populations of the various oxygen states populated during the approach of an Al surface by an O (1D) state. The system is initially in the 1D ($M_L = 0$) state and its collision energy is 1 eV. The populations are shown as functions of the atom–surface distance, the collision proceeding from the right to the left.

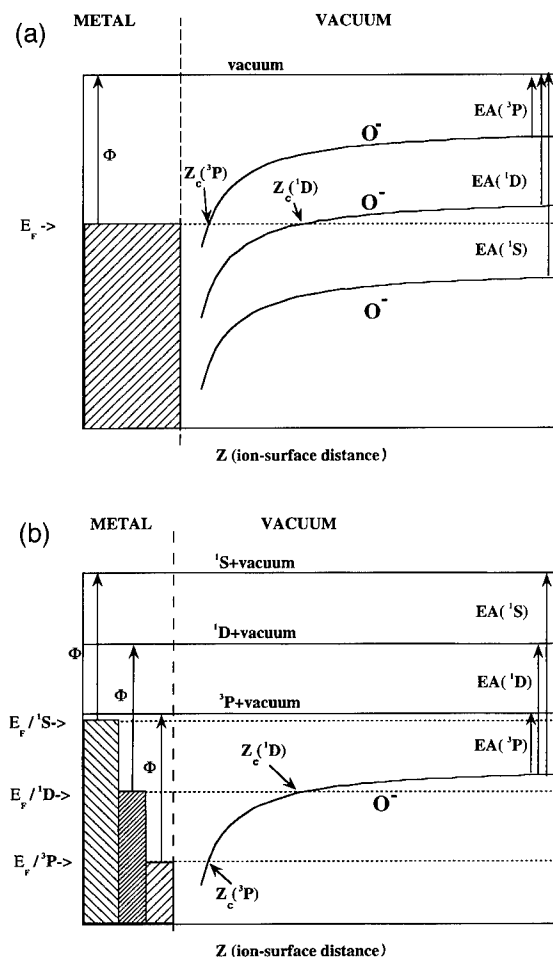


Fig. 5. (a) and (b): Schematic energy diagrams of the O^-/O -Al surface system.

the O atom. Fig. 6 presents the results of a study of this quenching process. It is performed by solving the rate equations describing the evolution of the populations of the various states as the atom approaches the surface. Fig. 6 presents the case of an oxygen atom, initially in the 1D ($M_L = 0$) state approaching an Al surface with a collision energy of 1 eV (perpendicular motion). As the atom approaches, the 1D level captures an electron to form an O^- ion (preferentially in the $M_L = 0$ state) which in turn decays by electron emission, forming an $O(^3P)$ atom, preferentially in the 3P ($M_L = 1$) state. The precise sub-levels of O^- and $O(^3P)$ that actually participate in the quenching process are determined by the relative value of the various capture/loss rates (Fig. 2). For the example of Fig. 6, the quenching occurs around $5a_0$ from the surface. Its characteristics indeed depend on the initial state and on the collision velocity (see in Ref. [11]). This quenching process for excited states is rather important, excited states approaching a surface are deexcited before touching the surface, the excitation energy going into an electron–hole pair creation.

5. Conclusion and extensions

The effect of the open shell structure of oxygen (atomic and molecular) on the atom (molecule)–surface resonant charge transfer has been presented. As a main result, the resonant charge transfer process cannot be reduced to a simple one electron problem involving only one atomic (molecular) state: it implies a few electronic states and transitions can occur via different electrons with different quantum numbers; this leads to large differences between the charge transfer rates for the various states and sub-states. In addition, the multi-state character of the charge

transfer directly leads to the existence of a quenching process for the excited states that proceeds via charge transfers.

These features are not specific to oxygen and appear in a variety of systems. Indeed, the polarization effect (“angular selection rules”) has been invoked by Van Pinxteren et al. [23] to explain the peculiarities of the two electron capture by C^+ and O^+ ions; it has also been invoked in the context of recoil spectroscopy by Hsu et al. [24]. The effects discussed on oxygen are indeed not limited to the case of incomplete p (π) shells, in particular the quenching process discussed in Section 4 can occur via any open shell structure. As a further example, the well known He^- resonance ($1s\ 2s^2\ ^2S$) corresponds to binding an electron to both the He metastable states ($1s\ 2s\ 2^1S$ and 2^3S); it has been invoked as an efficient intermediate in a singlet to triplet conversion mechanism similar to the one discussed in Section 4 [5] and quantitative studies confirmed the efficiency of this charge transfer induced conversion on low workfunction surfaces [13]. The He^- resonance is often considered as the prototype of Feshbach resonances, formed by adding an electron on an open shell structure and many systems present similar resonances that can act as intermediates in conversion mechanisms. Species with excited electrons have been invoked recently as intermediates in a few quenching processes: conversion of Ne cores [25], quenching of excited N and N_2 electronic states [26]. In all these systems, a resonant electron capture from a surface by an atomic (molecular) particle triggers an internal electronic evolution.

Acknowledgement

One of us (B.B.) gratefully acknowledges support from the “Réseau de formation-recherche, France–Roumanie” du Ministère de la Recherche et de l’Enseignement Supérieur.

References

- [1] J.W. Gadzuk, *Com. Atom. Mol. Phys.* 5 (1985) 219; A.W. Kleyn, 16th ICPEAC, Book of invited papers (1989) p. 451.
- [2] J.W. Gadzuk and C.N. Clarke, *J. Chem. Phys.* 91 (1989) 3174;
- R. Azria, L. Parenteau and L. Sanche, *Phys. Rev. Lett.* 59 (1987) 638.
- [3] L. Sanche, *J. Phys. B* 23 (1990) 1597; R. Palmer and P.J. Rous, *Rev. Mod. Phys.* 64 (1992) 383.
- [4] V. Djamo, D. Teillet-Billy and J.P. Gauyacq, *Phys. Rev. Lett.* 71 (1993) 3267.
- [5] R. Hemmen and H. Conrad, *Phys. Rev. Lett.* 67 (1991) 1314; H. Brenten, H. Müller and V. Kempter, *Z. Phys. D.* 22 (1992) 563.
- [6] R. Zimny, H. Nienhaus and H. Winter, *Radiat. Eff. Def. Solids* 109 (1989) 9.
- [7] D. Teillet-Billy and J.P. Gauyacq, *Surf. Sci.* 239 (1990) 343.
- [8] J.W. Gadzuk, *Surf. Sci.* 180 (1987) 225.
- [9] P. Nordlander and J.C. Tully, *Phys. Rev. Lett.* 61 (1988) 990.
- [10] A. Borisov, D. Teillet-Billy and J.P. Gauyacq, *Nucl. Instr. and Meth. B* 78 (1993) 49.
- [11] B. Bahrim, D. Teillet-Billy and J.P. Gauyacq, *Phys. Rev. B* 50 (1994) 7860.
- [12] J.L. Slater, *Quantum theory of atomic structure* (McGraw-Hill, New York, 1960).
- [13] A. Borisov, D. Teillet-Billy and J.P. Gauyacq, *Surf. Sci.* 284 (1993) 337.
- [14] P.J. Jennings, P.O. Jones and M. Weinert, *Phys. Rev. B* 37 (1988) 3113.
- [15] J.P. Gauyacq, *Dynamics of Negative Ions* (World Scientific, Singapore, 1987).
- [16] D. Teillet-Billy, L. Malegat and J.P. Gauyacq, *J. Phys. B* 20 (1987) 3201.
- [17] D. Teillet-Billy and J.P. Gauyacq, *J. Phys. B* 22 (1989) L335.
- [18] B. Bahrim, D. Teillet-Billy and J.P. Gauyacq, *Surf. Sci.* 316 (1994) 189.
- [19] P. Nordlander, *Phys. Rev. B* 46 (1992) 2584.
- [20] V. Djamo, D. Teillet-Billy and J.P. Gauyacq, in: *Electron Collisions with Molecules, Clusters and Surfaces*, eds. L. Morgan and H. Ehrhardt (Plenum, New York, 1994) p. 227.
- [21] M.L. Yu, *Phys. Rev. Lett.* 47 (1981) 1325.
- [22] J.J.C. Geerlings and J. Los, *Phys. Rep.* 190 (1990) 133; A. Nourtier, *J. Phys. (Paris)* 50 (1989) 311; J.P. Gauyacq, A. Borisov and D. Teillet-Billy, to appear in: *Negative Ions*, ed. V. Esaulov (Cambridge University Press).
- [23] H.M. van Pinxteren, C.F.A. van Os, R.M.A. Heeren, R. Roding, J.J.C. Geerlings and J. Los, *Europhys. Lett.* 10 (1989) 715.
- [24] C.C. Hsu, H. Bu, A. Bousetta, J.W. Rabalais and P. Nordlander, *Phys. Rev. Lett.* 69 (1992) 188.
- [25] V. Esaulov, S. Lacombe, L. Guillemot and Vu Ngoc Tuan, these Proceedings (IISC-10), *Nucl. Instr. and Meth. B* 100 (1995) 232.
- [26] H. Müller, R. Hausmann, H. Brenten and V. Kempter, *Surf. Sci.* 303 (1994) 56.

Resonant electron transfer in ion–metal-surface interactions: The case of large quantum numbers

U. Wille *

Bereich Theoretische Physik, Hahn–Meitner-Institut Berlin, Glienicker Str. 100, D-14109 Berlin, Germany

Abstract

Some theoretical aspects of resonant electron transfer processes occurring in the interaction of slow atoms and ions with metal surfaces are surveyed. The emphasis is on cases involving atomic states with large quantum numbers, i.e., on surface interactions of Rydberg atoms and of highly charged ions. Resonant transition rates calculated in first-order adiabatic approximation are examined with regard to their scaling properties, and universal behavior of the rates is disclosed by analyzing the limit of large quantum numbers. Quasiclassical aspects of these results are discussed, and comparison is made with purely classical estimates for the transition rates. Angular momentum effects in resonance ionization of Rydberg atoms are considered explicitly.

1. Introduction

In the interaction of slowly moving atoms and ions with metal surfaces, electron transfer processes are induced by the one-electron potential acting in the ion–metal system (“resonant electron transfer”) as well as by the direct two-body interaction between conduction band electrons (“Auger transfer”) [1–5]. Resonant electron transfer is effective both in the neutralization of ions and in the ionization of excited atoms near surfaces, whereas Auger transfer is a mechanism that contributes to ion neutralization.

Recent studies of surface interactions of atoms and (positive) ions include cases in which electron transfer takes place out of, or into, atomic or ionic states with large quantum numbers. One example is the ionization of laser-excited Rydberg atoms at metal surfaces [6–8], which is effected by resonant transitions of atomic electrons into empty conduction band states. In the case of surface interactions of slow, highly charged ions [9–12], multiple electron transfer out of the conduction band into initially empty ionic states with large quantum numbers leads to rapid neutralization of the ions. Resonant transfer is supposed to be the principal mechanism of this neutralization process, but Auger transfer is likely to have some influence at small ion–surface distances [12].

The present paper deals with resonant electron transfer at metal surfaces, under conditions where large atomic or

ionic quantum numbers are involved. The study of this kind of process offers, at least in principle, the opportunity to obtain information on the electronic potential at large distances from the surface [7,8,10]. Progress in this direction is still hampered by difficulties in finding unequivocal experimental signatures for resonant electron transfer, as well as by the complexity of the theoretical analysis. Here, we elaborate on some general aspects that may be relevant to this analysis, and consider the case of resonance ionization of Rydberg atoms explicitly. Our discussion relies on resonant transition rates calculated within the first-order adiabatic approximation [13]. We employ a simple model [14,15] that is based on a step-like jellium potential for the conduction band states and on the hydrogenic approximation for the ionic states, and in which image-charge effects are neglected. This model allows the transition matrix elements to be evaluated in closed form for arbitrary values of the parameters characterizing the ion–metal system. From the transition rates, atomic occupation probabilities as a function of time or ion-surface distance are obtained by solving a simple rate equation [13,16].

Unless stated otherwise, we use atomic units ($e = m_e = \hbar = 1$).

2. Scaling properties and universal behavior

When entering the realm of large quantum numbers, we encounter huge manifolds of atomic states with highly intricate wave functions. This suggests to look for simplifications in the theoretical treatment of resonant electron transfer, which emphasize common features of the transi-

* Tel. +49 30 80622685, fax +49 30 80622098, E-mail: wille@vax.hmi.d400.de.

tion rates. One possibility to achieve this goal is to introduce scaling concepts. As is well known from many branches of physics, such concepts may be useful in establishing a description of a dynamical system in terms of universal functions which no longer depend on the full set of system parameters.

Our analysis of the scaling properties of resonant electron transfer is based [17] on first-order transition rates $\Gamma_{nlm}^{(Z;V_0)}(D)$ written as

$$\Gamma_{nlm}^{(Z;V_0)}(D) = 2\pi \int d^3k \rho(k) \delta(\epsilon_k - \epsilon_n) |\mathcal{M}_{nlm}^{(Z;V_0)}(k;D)|^2, \quad (1)$$

where D is the ion–surface distance, Z is the effective ion core charge, and V_0 is the depth of the conduction band potential. The matrix element $\mathcal{M}_{nlm}^{(Z;V_0)}(k;D)$ (for its explicit definition and closed-form evaluation, see Ref. [14]) describes transitions of electrons or holes out of the ionic initial state with spherical quantum numbers n, l, m and energy $\epsilon_n = -Z^2/2n^2$ into the final conduction band state with electronic momentum k and energy $\epsilon_k = k^2/2 - V_0$. For the density of conduction band states, $\rho(k)$, we take the free-electron density of states (the metal is assumed to be at zero temperature).

A clue to the scaling properties of the transition rates is found in their behavior as a function of the ion–surface distance D . In the upper panel of Fig. 1, the D -dependence of $\Gamma_{nlm}^{(Z;V_0)}(D)$ is shown for $Z = 1$ (this case corresponds to resonance ionization of neutral atoms), $V_0 = 0.5$ a.u., $l = m = 0$, and a sequence of values of the principal quantum number n . The curves are qualitatively similar in that they exhibit a fairly weak, near-exponential decrease (with superimposed oscillations caused by the nodal structure of the atomic wave function) extending from small D -values, followed by a turn-over to rapid decrease, which occurs in a narrow D -range. The turn-over point is found to coincide approximately with the classical threshold distance D_n which is given, in our model, by

$$D_n = 2n^2/Z. \quad (2)$$

This distance separates the range $D < D_n$ in which resonant transitions are classically allowed, from the range $D > D_n$ in which these transitions can occur only via quantal tunneling through the potential barrier separating metal and ion. Introducing the scaled ion–surface distance \tilde{D} as

$$\tilde{D} = D/D_n, \quad (3)$$

we define the scaled representation $\tilde{\Gamma}_{nlm}^{(Z;V_0)}(\tilde{D})$ of the transition rate $\Gamma_{nlm}^{(Z;V_0)}(D)$ by setting

$$\tilde{\Gamma}_{nlm}^{(Z;V_0)}(\tilde{D}) = \Gamma_{nlm}^{(Z;V_0)}(D_n \tilde{D}). \quad (4)$$

In scaled representation (cf. lower panel of Fig. 1), the similarities among the transition rates for different quantum numbers become particularly apparent.

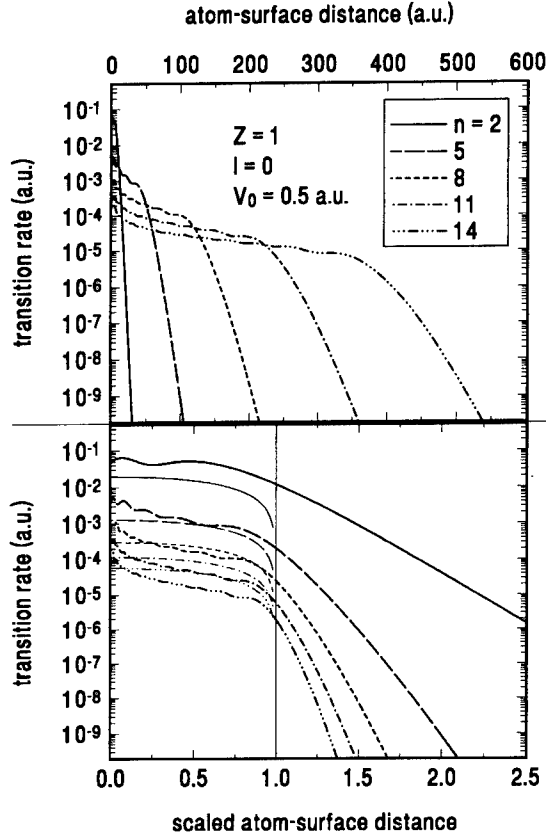


Fig. 1. Upper panel: transition rates $\Gamma_{nlm}^{(Z;V_0)}(D)$ for $Z = 1$, $V_0 = 0.5$ a.u., $l = m = 0$ and a sequence of n -values, plotted as a function of the atom–surface distance D . Lower panel: transition rates for the case shown in the upper panel, plotted as a function of the scaled atom–surface distance \tilde{D} (cf. Eq. (4)). The thin curves correspond to the classical approximation (14). The vertical thin line marks the classical threshold distance $\tilde{D} = 1$.

The systematic analysis of the scaling properties of the transition rates $\tilde{\Gamma}_{nlm}^{(Z;V_0)}(\tilde{D})$ [17] proceeds from a study of the transition matrix elements as a function of \tilde{D} and of the scaled momentum component of the conduction band electron parallel to the surface, \tilde{k}_{\parallel} . The latter component is defined in terms of the original component k_{\parallel} and the mean electronic momentum in the ionic n -shell, $\kappa_n = Z/n \equiv (2|\epsilon_n|)^{1/2}$, as

$$\tilde{k}_{\parallel} = k_{\parallel}/\kappa_n. \quad (5)$$

Exploiting scaling properties of the wave functions used to describe the initial and final electronic states and of the perturbing potential, we find that the scaled representation $\tilde{\mathcal{M}}_{nlm}^{(Z;V_0)}(\tilde{k}_{\parallel};\tilde{D})$ of the transition matrix element factorizes in the form

$$\tilde{\mathcal{M}}_{nlm}^{(Z;V_0)}(\tilde{k}_{\parallel};\tilde{D}) = \kappa_n^{3/2} \left[\frac{2}{V_0} \left(\frac{2V_0}{\kappa_n^2} - \tilde{k}_{\parallel}^2 - 1 \right) \right]^{1/2} \bar{\mathcal{M}}_{nlm}(\tilde{k}_{\parallel};\tilde{D}) \quad (6)$$

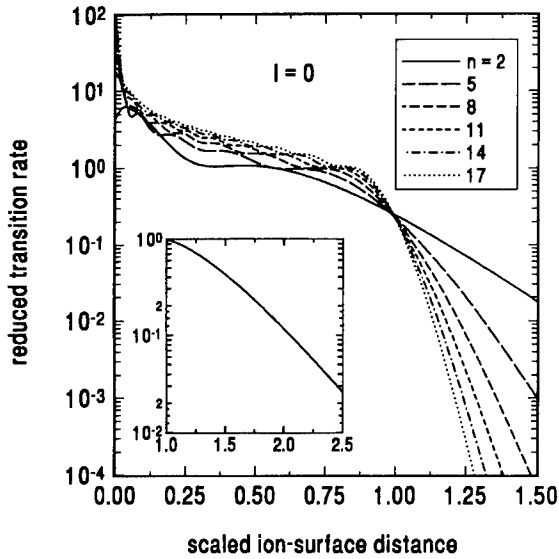


Fig. 2. Reduced transition rates $\bar{\gamma}_{nlm}(\tilde{D})$ for $l=m=0$ and a sequence of n -values, plotted as a function of the scaled ion-surface distance \tilde{D} . The inset shows the \tilde{D} -dependence of the universal function $\Xi(\tilde{D})$ introduced in Eq. (11).

(note that, except for an irrelevant phase factor, the resonant transition matrix element depends on \mathbf{k} via k_{\parallel} only). The (dimensionless) “reduced” matrix element $\bar{M}_{nlm}(\tilde{D})$ is independent of the potential parameters Z and V_0 . Using Eqs. (1), (4) and (6), we further find that the transition rate $\tilde{F}_{nlm}^{(Z;V_0)}(\tilde{D})$ can be written in the large- n limit (at fixed l and m) as

$$\tilde{F}_{nlm}^{(Z;V_0)}(\tilde{D}) = \frac{8}{\pi} V_0 \left(\frac{|\epsilon_n|}{nV_0} \right)^{3/2} \bar{\gamma}_{nlm}(\tilde{D}), \quad (7)$$

where the (dimensionless) “reduced” transition rate

$$\bar{\gamma}_{nlm}(\tilde{D}) = n^{3/2} \int_0^\infty d\tilde{k}_{\parallel} \tilde{k}_{\parallel} |\bar{M}_{nlm}(\tilde{k}_{\parallel}; \tilde{D})|^2 \quad (8)$$

is independent of Z and V_0 .

As a function of n , the reduced rates $\bar{\gamma}_{nlm}(\tilde{D})$ exhibit qualitatively different behavior in the classically allowed range $\tilde{D} < 1$ and the classically forbidden range $\tilde{D} > 1$, respectively. Confining ourselves in the following to the case $l=0$, we display in Fig. 2 reduced rates $\bar{\gamma}_n(\tilde{D})$ for a sequence of (equidistant) n -values. In the range $\tilde{D} < 1$, the oscillatory structure tends to become less pronounced when n increases, and it appears that, except for the vicinity of $\tilde{D}=0$, the rates converge towards a smooth limiting function. We therefore write

$$\lim_{n \rightarrow \infty} \bar{\gamma}_n(\tilde{D}) = \Omega(\tilde{D}), \quad 0 < \tilde{D} < 1, \quad (9)$$

with a *universal* function $\Omega(\tilde{D})$ that depends on the scaled ion-surface distance only. The curve in Fig. 2 corresponding to $n=17$ is expected to provide a fairly good numerical approximation to $\Omega(\tilde{D})$. In the range

$0.2 < \tilde{D} < 0.9$, the decrease of $\Omega(\tilde{D})$ appears to follow closely an exponential dependence. For finite n , we obtain from Eq. (7)

$$\tilde{F}_n^{(Z;V_0)}(\tilde{D}) = \frac{2^{3/2}}{\pi} \frac{Z^3}{V_0^{1/2} n^{9/2}} \Omega(\tilde{D}), \quad 0 < \tilde{D} < 1 \quad (10)$$

as an explicit, approximate expression for the transition rates $\tilde{F}_n^{(Z;V_0)}(\tilde{D})$.

Universal behavior of the transition rates in the range $\tilde{D} > 1$ is revealed by considering *ratios* of rates for pairs of equidistant n -values. These ratios turn out to be independent of n in the large- n limit (cf. Fig. 2), so that we may write

$$\lim_{n \rightarrow \infty} [\bar{\gamma}_n(\tilde{D}) / \bar{\gamma}_{n-1}(\tilde{D})] = \Xi(\tilde{D}), \quad \tilde{D} \geq 1, \quad (11)$$

with a *universal* function $\Xi(\tilde{D})$ (cf. inset in Fig. 2) which, to very good approximation, can be analytically represented as

$$\Xi(\tilde{D}) = 118.2(\tilde{D}^2 - 0.5381\tilde{D})\exp(-4\tilde{D}). \quad (12)$$

For finite n , we find from Eqs. (7) and (11) the *scaling law*

$$\tilde{F}_{n_1}^{(Z;V_0)}(\tilde{D}) = \left(\frac{n_2}{n_1} \right)^{9/2} [\Xi(\tilde{D})]^{n_1 - n_2} \tilde{F}_{n_2}^{(Z;V_0)}(\tilde{D}), \quad \tilde{D} \geq 1 \quad (13)$$

as an approximate relation connecting transition rates for arbitrary principal quantum numbers n_1 and n_2 .

Using Eqs. (10) and (13), we can approximately generate the full \tilde{D} -dependence of the transition rate $\tilde{F}_n^{(Z;V_0)}(\tilde{D})$ for arbitrary n from the universal functions $\Omega(\tilde{D})$ and $\Xi(\tilde{D})$ and the transition rate for a fixed n -value in the classically forbidden range. On a more qualitative level, our scaling procedure is likely to be useful as a guideline for introducing scaling concepts into more sophisticated treatments of resonant electron transfer. In extensions of the present analysis within the first-order adiabatic approximation, nonzero angular momenta should be considered at all stages of the analysis. Further, the inclusion of image potentials and of more realistic forms of the density of conduction band states is indicated. By adopting the parabolic (Stark) representation for the (hydrogenic) ionic states [18], effects of orbital hybridization [19] can possibly be incorporated into our scaling scheme.

3. Quasiclassical and classical aspects

The limit of large quantum numbers is the quasiclassical limit for the electronic motion in the unperturbed ionic system. The universal behavior of the transition rates which we have disclosed in the large- n limit is therefore supposed to reflect, to a certain degree, quasiclassical properties of resonant electron transfer.

An analysis of the quasiclassical limit of resonant electron transfer can be attempted, within the adiabatic approximation, by applying WKB-type methods to solve the stationary one-electron Schrödinger equation. However, the implementation of these methods is feasible only for asymptotically large ion–surface distances ($D \gg D_n$) [20,21], whereas the range of physically important distances extends from the asymptotic regime far down into the classically allowed range [10,22]. In first-order adiabatic approximation, one may think of analyzing the quasiclassical limit by replacing the unperturbed ionic wave function in the transition matrix element with its WKB approximant. Unfortunately, when doing so, one destroys the possibility to evaluate the transition matrix elements in closed form [14]. In principle, this difficulty can be avoided by introducing large- n approximations only *after* the matrix element has been reduced to a one-dimensional momentum space integral. Then one may use asymptotic approximations for the radial momentum space wave function, but it turns out that this approach does not even qualitatively reproduce the characteristic features of the transition matrix elements and rates. Therefore, it appears that the large- n results we have obtained in Section 2 are the only results available at present that characterize the quasiclassical limit of resonant electron transfer over the full range of ion–surface distances.

In connection with surface interactions of highly charged ions, resonant electron transfer has been treated within purely classical concepts [23,24]. In the model of Burgdörfer et al. [23], classical rates have been introduced separately to describe resonance neutralization (“electron capture”) and resonance ionization (“electron loss”), respectively, of a manifold of states with principal quantum number n . For a rough estimate, it is appropriate to define a single classical transition rate $\Gamma_n^{(cl)}(D)$ describing “loss of a hole” or “loss of an electron”, depending on whether the initial ionic or atomic state is unoccupied or occupied:

$$\Gamma_n^{(cl)}(D) = \begin{cases} \nu_n P_n(D), & D < D_n, \\ 0, & D \geq D_n, \end{cases} \quad (14)$$

where

$$\nu_n = \frac{Z^2}{2\pi n^3} \quad (15)$$

is the classical orbital frequency for a hydrogenic state with principal quantum number n , and

$$P_n(D) = \frac{D_n^2 - D^2}{D_n^2} \equiv 1 - \tilde{D}^2 \quad (16)$$

is the “geometrical” probability that the orbiting electron hits the “loophole” at the potential saddle between ionic core and surface (note that our estimate for $P_n(D)$ differs slightly from that used in Ref. [23]).

In the lower panel of Fig. 1, quantal transition rates $\tilde{F}_n^{(Z;V_0)}(\tilde{D})$ in the classically allowed range $\tilde{D} < 1$ are

contrasted with rates calculated from the classical estimate (14). While agreement is found within less than an order of magnitude, there are characteristic qualitative differences between the two cases. The slope of the classical rates, which is determined by the area of the potential loophole, is small except for the vicinity of $\tilde{D} = 1$. The slope of the quantal rates, on the other hand, shows a near-exponential behavior for not too small n . In the first-order approach pursued here, this behavior must be understood as arising from changes in the overlap of the unperturbed metal and ionic wave functions that persist down to small ion–surface distances. If the same behavior would show up in a complete, nonperturbative treatment, it would be appropriate to discuss it in terms of the “over-barrier” reflection which an electron wave in the ion–metal system experiences in the classically allowed range of ion–surface distances. A noteworthy quantitative difference between quantal and classical rates is the occurrence of an overall factor $n^{-3/2}$ in the quantal rate relative to the classical rate (cf. Eqs. (10) and (14)). The agreement of quantal and classical results in the parameter range chosen in Fig. 1 is therefore somewhat fortuitous.

4. Resonance ionization of Rydberg atoms

As a specific example involving large quantum numbers, we consider resonance ionization of Rydberg atoms. In particular, we will look at the dependence of the ionization distance associated with a Rydberg state (i.e., that ion–surface distance at which ionization of this state is most likely to take place) on the angular momentum quantum numbers l and m .

We assume an atom to approach a metal surface along a straight-line trajectory, with velocity component v_z perpendicular to the surface. In adiabatic approximation, the survival probability for a state with quantum numbers n, l, m is then given [13,16,22], in scaled representation, by

$$\tilde{S}_{nlm}^{(Z;V_0)}(v_z; \tilde{D}) = \exp \left\{ - \frac{2n^2}{Zv_z} \int_{\tilde{D}}^{\infty} d\tilde{D}' \tilde{F}_{nlm}^{(Z;V_0)}(\tilde{D}') \right\}. \quad (17)$$

This probability is a monotonically decreasing function of \tilde{D} that drops from unity to zero in a narrow \tilde{D} -range. Accordingly, we can define the scaled ionization distance of the state with quantum numbers n, l, m as that distance $\tilde{A}_{nlm}(v_z)$ for which $\tilde{S}_{nlm}^{(Z;V_0)}(v_z; \tilde{D} = \tilde{A}_{nlm}) = 0.5$.

In Fig. 3, we display the dependence of \tilde{A}_{nlm} on the magnetic quantum number m for $n = 15$, $l = 14$ and on the orbital angular momentum quantum number l for $n = 15$, $m = 0$. The velocity $v_z = 1 \times 10^{-5}$ a.u. is chosen to correspond to the thermal-velocity, grazing-incidence experiments of Ref. [8]. Also shown (cf. inset) is the n -dependence for $l = 0$. The decrease of \tilde{A}_n with n is proportional to $\ln n$ in the large- n limit, so that the

unscaled ionization distance increases as $n^2/\ln n$. Since \tilde{A}_{nlm} exhibits a weak (logarithmic) dependence on v_z , it follows from Fig. 3 that under typical conditions the ionization distances for $l=0$ Rydberg states are close to, or smaller than, the classical threshold distance D_n . This implies that even for very slow Rydberg atoms the time spent at large distances from the surface is too short for the ionizing transitions to occur with substantial probability in the “subbarrier” (tunneling) regime $\tilde{D} > 1$. We note here that in previous theoretical studies of resonance ionization of Rydberg atoms [20,21], transition rates were calculated at asymptotically large ion–surface distances ($D \gg D_n$) only and no attempts were made to evaluate ionization distances. Rather, it was presupposed that resonance ionization is effected by a tunneling mechanism.

As a function of l and m , the ionization distances \tilde{A}_{nlm} decrease essentially in a monotonic way, and for large l and m acquire values much smaller than the classical threshold distance. The l - and m -dependence of \tilde{A}_{nlm} can be surprisingly well reproduced by a simple model [22] that emphasizes the connection between the ionization distance and the spatial extent of the atomic wave function along the surface normal (in a qualitative picture, one may assume the ionizing transitions to set in when the atomic orbital begins to “touch” the surface). Taking the expectation value of z^2 in the state with wave function $\psi_{nlm}^{(Z)}(r)$,

$$\langle z^2 \rangle_{nlm} = \frac{n^2}{2Z^2} [5n^2 + 1 - 3l(l+1)] \times \left[\frac{1}{3} + \frac{2}{3} \frac{l(l+1) - 3m^2}{(2l+3)(2l-1)} \right], \quad (18)$$

as a measure for this extent, we define scaled ionization distances $\tilde{\delta}_{nlm}$ as

$$\tilde{\delta}_{nlm} = [\langle z^2 \rangle_{nlm}]^{1/2} / D_n. \quad (19)$$

In Fig. 3, the dashed curves have been obtained by multiplying the distances $\tilde{\delta}_{nlm}$ calculated from Eq. (19) by a common “normalization factor” of 2.09 (which makes the solid and dashed curves coincide at $l=7, m=0$). The good agreement between solid and dashed curves for the m -dependence of the ionization distance shows that this dependence reflects nothing but the strong change in shape (from “cigar-like” to “pancake-like”) that the atomic orbital undergoes when m varies from small to large values.

The ionization distances we have calculated correspond to a situation in which the Rydberg atoms are asymptotically prepared in states with definite spherical quantum numbers n, l, m and in which the mixing of these states induced by the metal and image potentials (“hybridization”) remains small until the ionizing transition occurs. If the mixing is strong throughout, Stark-like hybridized orbitals form whose ionization distances are expected to be considerably different from those of the spherical states.

Calculations within our model employing the parabolic (Stark) representation of the hydrogenic states [18] are therefore indicated.

5. Summary and conclusions

We have surveyed a number of theoretical aspects of resonant electron transfer in ion–metal–surface interactions for cases where large ionic quantum numbers are involved. Scaling properties of first-order transition rates were discussed within a simple model. A key role in this discussion is played by the scaled ion–surface distance which is defined in terms of the classical threshold distance for resonant electron transfer. For ionic states with zero orbital angular momentum, the transition rates for large principal quantum numbers were found to be determined essentially by two universal functions of the scaled ion–surface distance. The quasiclassical character of this result has been emphasized, and a comparison of quantal transition rates with purely classical estimates has been made. Resonance ionization of Rydberg atoms has been considered explicitly. The ionization distances were found to lie in the vicinity of, or below, the classical threshold distance. Their dependence on the atomic angular momentum quantum numbers was shown to follow closely the predictions of a simple model.

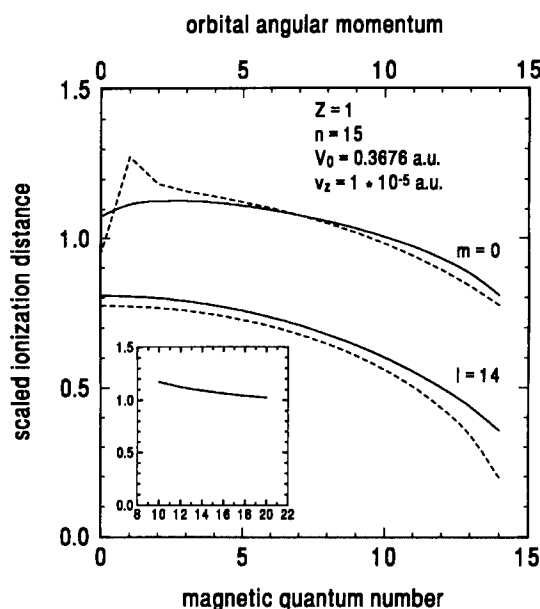


Fig. 3. Scaled ionization distances \tilde{A}_{nlm} (solid curves) and $\tilde{\delta}_{nlm}$ (dashed curves) for Rydberg atoms with perpendicular velocity $v_z = 1 \times 10^{-5}$ a.u. Upper curves: l -dependence for $n=15, m=0$; lower curves: m -dependence for $n=15, l=14$. The inset shows the n -dependence for $l=m=0$.

In conclusion, we mention that experimental information relating directly to the theoretical results discussed here is not available at present and apparently will be difficult to obtain. Methods for accurately determining ionization distances of Rydberg atoms are desirable since they would allow details of resonant electron transfer to be examined under particularly simple conditions. Applications of the results of our scaling procedure, especially of Eqs. (10) and (13) for the transition rates, are conceivable in conjunction with the theoretical analysis of surface interactions of highly charged ions in terms of coupled rate equations [23].

References

- [1] H.D. Hagstrum, in: *Inelastic Ion–Surface Collisions*, eds. N.H. Tolk, J.C. Tully, W. Heiland and C.W. White (Academic Press, New York, 1977) p. 1.
- [2] A.T. Amos, K.W. Sulston and S.G. Davison, *Adv. Chem. Phys.* 76 (1989) 335.
- [3] J. Los and J.J.C. Geerlings, *Phys. Rep.* 190 (1990) 133.
- [4] R.A. Baragiola, in: *Low-Energy Ion–Surface Interactions*, ed. J.W. Rabalais (Wiley, New York, 1994) p. 187.
- [5] B.H. Cooper and E.R. Behringer, in: *Low-Energy Ion–Surface Interactions*, ed. J.W. Rabalais (Wiley, New York, 1994) p. 263.
- [6] C. Fabre, M. Gross, J.M. Raimond and S. Haroche, *J. Phys. B* 16 (1983) L671.
- [7] C.A. Kocher and C.R. Taylor, *Phys. Lett. A* 124 (1987) 68.
- [8] D.F. Gray, Z. Zheng, K.A. Smith and F.B. Dunning, *Phys. Rev. A* 38 (1988) 1601.
- [9] H.J. Andrä, A. Simionovici, T. Lamy, A. Brenac, G. Lamboley, A. Pesnelle, S. Andriamonje, A. Fleury, M. Bonnefoy, M. Chassevent and J.J. Bonnet, in: *Electronic and Atomic Collisions*, eds. W.R. MacGillivray, I.E. McCarthy and M.C. Standage (Adam Hilger, Bristol, 1992) p. 89.
- [10] J. Burgdörfer, in: *Review of Fundamental Processes and Applications of Atoms and Ions*, ed. C.D. Lin (World Scientific, Singapore, 1993) p. 517.
- [11] J. Das and R. Morgenstern, *Comm. At. Mol. Phys.* 29 (1993) 205.
- [12] F. Aumayr and H.P. Winter, *Comm. At. Mol. Phys.* 29 (1994) 275.
- [13] J.C. Tully, *Phys. Rev. B* 10 (1977) 4324.
- [14] U. Wille, *Phys. Rev. A* 45 (1992) 3004.
- [15] U. Wille, *Nucl. Instr. and Meth. B* 67 (1992) 132.
- [16] H. Shao, D.C. Langreth and P. Nordlander, in: *Low-Energy Ion–Surface Interactions*, ed. J.W. Rabalais (Wiley, New York, 1994) p. 117.
- [17] U. Wille, *Phys. Rev. B* 50 (1994) 1888.
- [18] U. Wille, *Nucl. Instr. and Meth. B* 79 (1993) 132.
- [19] P. Nordlander and J.C. Tully, *Phys. Rev. B* 42 (1990) 5564.
- [20] A.V. Chaplik, *Zh. Eksp. Teor. Fiz.* 54 (1968) 332 [*Sov. Phys. – JETP* 27 (1968) 178].
- [21] R.K. Janev, *J. Phys. B* 7 (1974) 1506, L359.
- [22] U. Wille, *Surf. Sci.* 307–309 (1994) 874.
- [23] J. Burgdörfer, P. Lerner and F.W. Meyer, *Phys. Rev. A* 44 (1991) 5674.
- [24] J.N. Bardsley and B.M. Penetrante, *Comm. At. Mol. Phys.* 27 (1991) 43.

Depth of origin of ions in desorption induced by electronic transitions (DIET): ion transmission through ultrathin films

Theodore E. Madey^{*}, Norbert J. Sack, Mustafa Akbulut

Department of Physics and Astronomy and Laboratory for Surface Modification, Rutgers University, Piscataway, NJ 08855-0849, USA

Abstract

Measurements to address a fundamental issue in transport of low energy (< 10 eV) ions through the surface layers of a solid are described. Our goal is to identify the dominant energy-transfer and charge-transfer processes that limit the survival probability of ions excited below the surface. Our approach is to study the interaction of low energy positive and negative ions (O^+ , F^+ , F^-) with ultrathin films of condensed gases (Ar, Kr, Xe, H_2O , NH_3) ranging from fractional monolayer to six monolayers in thickness. The ions are produced by electron stimulated desorption from an appropriate substrate (e.g., oxidized W(100) for O^+ , PF_3 on Ru(0001) for F^+ , F^-). The ions desorb from the surface with well defined energy (< 10 eV) and angular distributions, and their yield, mass/energy and desorption angle are measured using a digital, time-of-flight ESDIAD detector (electron stimulated desorption ion angular distribution). The gases are condensed at < 25 K onto the crystal substrate, and their film thickness is determined by means of thermal desorption spectroscopy. We find that 10% of the O^+ ESD signal can be transmitted through 1.6 atomic monolayers (ML) of Ar, 2.9 ML of Kr and 4.0 ML of Xe. In contrast, the O^+ signal is attenuated to $< 1\%$ by 0.5 ML of H_2O . We attribute the attenuation of O^+ in rare gas films mainly to elastic backscattering, whereas the attenuation of O^+ by H_2O and NH_3 films is dominated by charge transfer neutralization. F^+ ions are almost completely attenuated by 1 monolayer of Xe, while F^- ions experience a four-fold increase in yield when the substrate is covered by 1 monolayer of Xe. We discuss these results in terms of charge and energy transfer models, and draw conclusions about the depth of origin of ions produced in DIET (desorption induced by electronic transitions) processes.

1. Introduction

Stimulated desorption of ions from surfaces is the basis of several well known surface analysis probes, including SIMS (secondary ion mass spectrometry) ESD (electron stimulated desorption) and PSD (photon stimulated desorption) [1–4]. The usual tacit assumption is that ions desorb mainly from the topmost surface layer, and that subsurface contributions to the ion signal in these methods are negligible [5–9]. In recent experiments, we have found evidence that the situation is more complicated: ions ($E < 10$ eV) may be completely attenuated by a fractional monolayer film or may penetrate a film 4 or 5 atomic layers thick depending on the overlayer and ion [10–13].

In the work described here, we address a fundamental issue in transport of low energy (< 10 eV) ions through the surface layers of a solid: what are the dominant

energy-transfer and charge-transfer processes that limit the survival probability of ions excited below the surface of a solid? It is commonly assumed that both elastic scattering and neutralization are the dominant types of interaction in this range of collision energies [14]. Although there exists a wealth of information on the interaction of keV and MeV ions with rare gas solids [15], molecular solids [16,17], and other insulators [18], only little is known about the ion–solid interaction in the collision energy regime less than 10 eV [14,19]. In order to gain insight into this subject we are currently performing a series of experimental investigations on the transmission of low energy ions through ultrathin films of various atomic and molecular solids.

We use a novel experimental approach to characterize ion transport through surfaces. The essence of the experiments is illustrated in Fig. 1. We generate a beam of atomic O^+ , F^+ , or F^- ions with known kinetic energy and angular distribution by bombarding an appropriate surface with a focused electron beam, and causing electron stimulated desorption (ESD). (For example, to produce a beam of O^+ ions with intensity I_0 that desorb with an angular width $\Delta\theta_0 \approx 15^\circ$ centered about the normal to the surface,

^{*} Corresponding author. Tel. +1 908 445 5185. fax +1 908 445 4991, e-mail madey@physics.rutgers.edu.

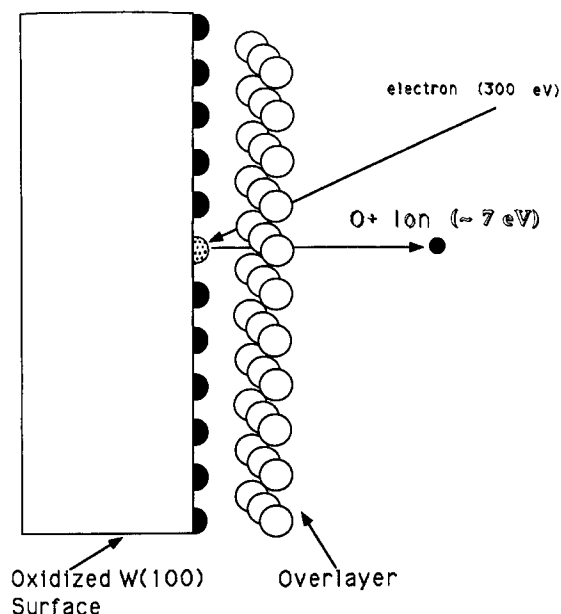


Fig. 1. Schematic of experimental approach.

and with a kinetic energy E_{ko} of 7 eV, we use a lightly-oxidized W(100) substrate [20,21]). This is our reference ion beam. We then cover the surface, cooled to 20 K, with an ultrathin film of a condensed atomic or molecular solid (Ar, Kr, Xe, NH_3 , H_2O). Film thicknesses range from fractional monolayers to multilayers, and are determined using thermal desorption spectroscopy (TDS) of the overlayer. During electron bombardment of the layered surface, we measure the changes in the intensity, kinetic energy distributions, and angular distributions (mass resolved) of the ion beam as a function of film thickness.

In this paper, we summarize results of the study of transmission of 7 eV oxygen ions desorbed from an oxidized W(100) crystal, through ultrathin films of rare gases (argon, krypton and xenon) and condensed molecules (H_2O and NH_3). Surprisingly, we find that a small fraction of the oxygen ions can penetrate more than 5 monolayers of Kr or Xe, whereas less than 0.5 monolayer of H_2O suppresses the O^+ signal nearly completely. We also present recent results for the transmission of F^- through Xe films in which the measured F^- ESD signal is *enhanced* by the presence of one Xe monolayer.

2. Experimental

The experiments have been carried out in an ion-pumped and turbo-pumped stainless steel ultrahigh vacuum (UHV) chamber equipped with instrumentation for surface analytical techniques [10–12]. There are two unique aspects of this apparatus that are essential for the proposed experiments: a manipulator on which a sample can be cooled to

~ 20 K, and a high sensitivity digital ESDIAD (electron stimulated desorption ion angular distributions) detector that allows mass, energy, and angle-resolved ion detection. Other components include a 50 mm radius concentric hemispherical analyzer (CHA) used for Auger electron spectroscopy (AES) and low energy ion scattering (LEIS); 0–5 keV electron gun for AES; differentially pumped ion gun for sputtering, and for LEIS; 0–1 keV electron gun for ESDIAD and LEED; quadrupole mass analyzer.

The sample (a metal single crystal) is cooled to 20 K by means of a closed-cycle He refrigerator. The sample is heated by radiative heating and electron beam heating from a tungsten filament mounted behind it. Different samples are used as sources for different ion beams. The surface used to generate O^+ beams is a W(100) crystal that has been heated to 860 K in an oxygen atmosphere (5×10^{-6} Pa) to form a thin oxide film [20,21]. The oxidized surface is clean as determined by means of AES, and exhibits a (1×3) LEED pattern [11]. ESD of this surface produces a single O^+ desorption beam centered on the surface normal with a full width at half maximum (FWHM) $\sim 15^\circ$, and kinetic energy ~ 7 eV. The surface used to generate F^+ and F^- beams is a Ru(0001) crystal that has been dosed with 0.33 ML of PF_3 ; both normal and off-normal beams are observed [22]. In all cases, the primary electron beam energy for ESD is ~ 300 eV, and the sample temperature is ~ 20 K for the ESD measurements.

The overlayer gases are deposited onto the cold, clean substrate using a directional gas doser. Coverages are determined using thermal desorption spectroscopy (TDS) by which we separate the first monolayer from subsequent layers.

The ESDIAD analyzer comprises a series of planar grids, a stack of five microchannel plates, and a position sensitive resistive anode encoder that is connected to a position analyzing computer. By pulsing the electron beam that is focused onto the sample and by gating the detector, we can perform time-of-flight (TOF) analysis of the desorbing ions. For appropriate bias and pulse conditions, we can detect both positive and negative ions in a mass-resolved mode and directly acquire digital 2d data; thus, we obtain information about the total yield, the angular distribution and the mass/energy distribution of the desorbing ions. Under conditions of zero electric field between sample and detector (0 V sample bias), the maximum polar angle for ion detection is $\sim 22^\circ$. Application of a sample bias of +100 V allows detection of O^+ ions with polar desorption angles of up to $\sim 70^\circ$. Energy analysis of desorbing ions is accomplished by use of retarding field methods in the ESDIAD analyzer, and by careful analysis of ion signals in TOF measurements. The quadrupole mass spectrometer is mainly used for confirmation of results obtained with the ESDIAD detector and for high resolution mass analysis of the desorbing species. Details of the ESDIAD detector are given elsewhere [23].

3. Results and discussion

3.1. Transmission of O^+ through rare gas films

Adsorption of a rare gas on top of the oxidized W(100) surface at 20 K leads to attenuation of the ESD oxygen ion signal. Fig. 2 shows a semilogarithmic plot of total angle integrated O^+ signal as a function of overlayer thickness for Xe, Kr, and Ar films [11]. All data have been obtained with a sample bias of +100 V (large collection angle) and an electron energy of 300 eV for a total electron fluence of $< 5 \times 10^{13} \text{ cm}^{-2}$. Both as deposited and annealed films are included, and no systematic differences are seen. Despite the similar attenuation of O^+ by all 3 rare gases for coverages up to ~ 1.5 ML, the attenuation by thicker films varies greatly for different gases. The rare gas thickness at which the O^+ signal is decreased to 10% of the value from the clean oxidized surface is 1.6 ML for Ar, 2.9 ML for Kr, and 4.0 ML for Xe. The decrease is roughly exponential for the thicker films, and the slope is steepest for Ar (strongest attenuation) and least steep for Xe.

From Fig. 2 we can derive the attenuation cross section σ_{exp} , for the exponential (thick film) regime, using an equation which is based on a continuum model of attenuation in a solid:

$$\sigma_{\text{exp}} = -\frac{1}{N_{\text{RG}}} \frac{\partial(\ln \Phi)}{\partial d}, \quad (1)$$

where d is the rare gas film thickness, N_{RG} the rare gas number density, and Φ the total O^+ flux reaching the detector. Using bulk values for N_{RG} of $2.66 \times 10^{22} \text{ cm}^{-3}$ for Ar, $2.17 \times 10^{22} \text{ cm}^{-3}$ for Kr, and $1.64 \times 10^{22} \text{ cm}^{-3}$ for Xe,

for Xe, we find the cross section to be largest for Ar and smallest for Xe: $6.2 \pm 2 \times 10^{-15} \text{ cm}^2$ for Ar, $2.2 \pm 0.3 \times 10^{-15} \text{ cm}^2$ for Kr, and $1.4 \pm 0.2 \times 10^{-15} \text{ cm}^2$ for Xe.

Both angular distributions and energy distributions of the oxygen ions have been measured as a function of rare gas thicknesses up to 3 monolayers for Kr and Xe. For coverages less than 2 ML, neither the energy nor angular distributions change significantly. For films thicker than two monolayers, we find changes in both quantities. For example, a fraction of the O^+ ions passing through Xe and Kr films greater than 2 ML thick lose about 2 eV and 3 eV of kinetic energy, respectively. Moreover, the ions that have lost kinetic energy leave the surface with large polar angles: the evidence for this comes from a comparison of O^+ yield at 0 V sample bias (collect polar angles $\leq 22^\circ$) and at +100 V bias (polar desorption angles up to $\sim 70^\circ$).

Before interpreting these results, we must consider both film uniformity and the interaction of the primary electron beam with the overlayer film. As discussed in Refs. [10–12], the evidence is persuasive that disturbance of the film by either primary or secondary electrons (via ionization, desorption, exciton formation) is not a significant problem for these measurements. Moreover, thermal desorption studies and annealing experiments on the rare gas films [24] provide evidence that the films grow in a layer-by-layer fashion (at least for the first few monolayers). Hence, the films appear to be sufficiently uniform and continuous that the observed attenuation of the oxygen ions can be correlated with scattering processes between O^+ ions and rare gas atoms.

We propose a microscopic model in which the passage of O^+ ions through the rare gas film is determined by elastic and inelastic scattering events between ions and rare gas atoms [10–12]. Elastic scattering (es) by large angles, or backscattering, can prevent an ion from desorbing. We assume that charge transfer (ct) is the most probable inelastic interaction to affect ion survival and transmission. We express the total experimental attenuation cross section σ_{exp} as

$$\sigma_{\text{exp}} = \sigma_{\text{es}} + \sigma_{\text{ct}}. \quad (2)$$

For Kr and Xe, the observation of large angle scattering and the loss of kinetic energy during passage of O^+ through films > 2 ML thick is strong evidence that elastic scattering effects are important. Further evidence for the role of elastic scattering is provided by recent molecular dynamics simulations of O^+ transmission through ideal fcc rare gas films a few monolayers in thickness, by Klein, Urbassek and Vicanek [25]. When using only elastic scattering cross sections between O^+ and rare gas atoms in the simulation (and completely neglecting charge transfer), they find rather good quantitative agreement with our measured transmission yield, energy and angular distributions, for Kr and Xe films. They attribute the surprisingly large fraction of transmitted oxygen ions to the small radius of O^+ relative to Kr and Xe. The ions are able to

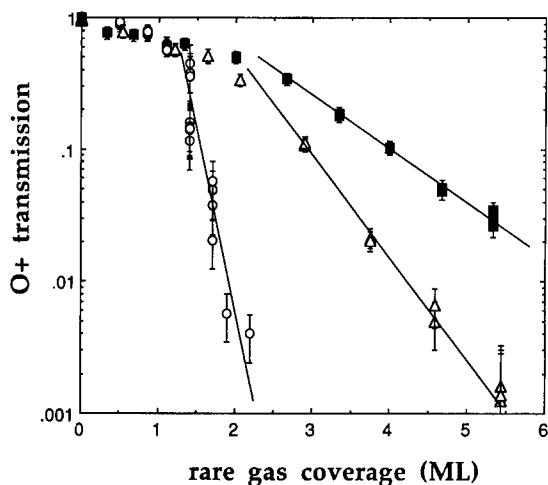


Fig. 2. Attenuation of angle-integrated O^+ ion signal by ultrathin films of Ar (open circles), Kr (open triangles) and Xe (closed squares) adsorbed on oxidized W(100) at 20 K.

pass through “channels” in the fcc rare gas structure [11,12,25].

The interpretation of the Ar data (Fig. 2) is not clear. Based on O^+ -rare gas atom potentials of Guest et al. [26], we expect the total elastic scattering cross section [25] to be much larger for Xe than for Ar, which is opposite to the trend in Fig. 2. Furthermore, the simulations of Klein et al. show that elastic scattering alone is not sufficient to account for the strong attenuation of O^+ by Ar films. The attenuation must be partly caused by another mechanism, such as enhanced charge transfer, structural effects in the films, or ion lifetime influenced by ESD final state effects [27].

We conclude this section by noting that elastic scattering effects appear to be dominant in attenuation of O^+ by Kr and Xe, while other effects (charge transfer, etc.) affect the attenuation of O^+ by Ar.

3.2. Transmission of O^+ through condensed molecular films, H_2O and NH_3

For studies of O^+ transmission through condensed molecular films, isotopically labeled $H_2^{18}O$ and NH_3 are dosed onto the clean, oxidized W(100) crystal at 25 K. The use of $H_2^{18}O$ allows us to distinguish $^{16}O^+$ from the substrate and possible $^{18}O^+$ from the overlayer water.

Thermal desorption spectroscopy measurements for NH_3 and $H_2^{18}O$ demonstrate that the majority of NH_3 and $H_2^{18}O$ adsorbed in the first monolayer on oxidized W(100) remain molecular (only about 0.2 ML of NH_3 and 0.08 ML of H_2O dissociate). H_2O desorbs from the monolayer with a peak temperature of ~ 155 K, while desorption from multilayer H_2O has its onset at a lower temperature. The peak temperature for a monolayer of NH_3 is ~ 148 K. The monolayer coverages are believed to be $\sim 4.25 \times 10^{14}$ molecules/cm 2 for NH_3 , and $\sim 8.5 \times 10^{14}$ molecules/cm 2 for H_2O [28].

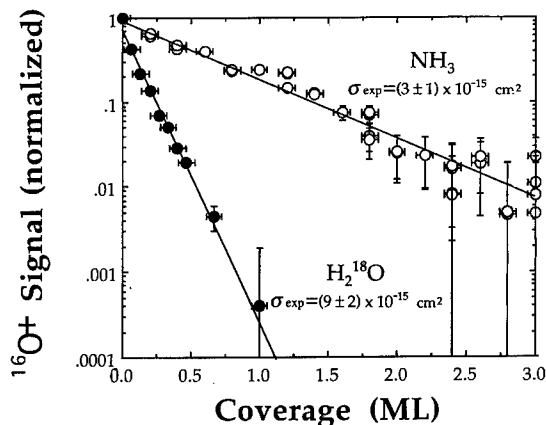


Fig. 3. Attenuation of angle-integrated O^+ ion signal by ultrathin films of H_2O and NH_3 adsorbed on oxidized W(100) at 20 K.

Fig. 3 is a semilogarithmic plot of the total angle-integrated $^{16}O^+$ yield (100 V sample bias, includes possible large angle scattering) as a function of the overlayer coverages of NH_3 and $H_2^{18}O$, respectively [28]. About 20% of the initial $^{16}O^+$ ions penetrate more than one monolayer of NH_3 , whereas only $\sim 10^{-2}$ of the initial $^{16}O^+$ ions survive after adsorption of 0.5 monolayers of H_2O . The ion yields decrease exponentially as a function of the NH_3 and H_2O coverages over several orders of magnitude of intensity.

Comparing ion yields for 0 V and +100 V sample bias demonstrates that there is essentially no large angle scattering ($> 22^\circ$) in passage of O^+ through H_2O or NH_3 . There is a small increase ($\sim 2^\circ$) in the FWHM of the $^{16}O^+$ beam after passing through the low coverage H_2O or NH_3 films, which we attribute to small angle elastic scattering.

Using a procedure similar to Eq. (1), one can calculate the attenuation cross sections σ_{exp} for O^+ from the data of Fig. 3,

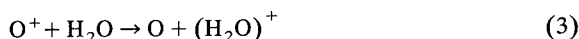
$$\sigma_{exp} = (3 \pm 1) \times 10^{-15} \text{ cm}^2 \text{ for } NH_3,$$

$$\sigma_{exp} = (9 \pm 2) \times 10^{-15} \text{ cm}^2 \text{ for } H_2O.$$

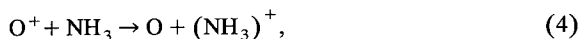
Note also that our measured attenuation cross section ($3 \pm 1 \times 10^{-15} \text{ cm}^2$) for an NH_3 overlayer is in good agreement with the cross section ($2.8 \pm 0.5 \times 10^{-15} \text{ cm}^2$) measured for attenuation of 5 eV O^+ with an adsorbed NH_3 layer on TiO_2 [13]. Based on our measured cross sections, we can estimate the collision radius, R , by assuming $\sigma_{exp} = \pi R^2$. We find $R \approx 5.3 \text{ \AA}$ for H_2O and $R \approx 3.1 \text{ \AA}$ for NH_3 . These collision radii are considerably larger than the molecular Van der Waals radii (1.45 \AA for H_2O and 1.8 \AA for NH_3); they are also too large to attribute the attenuation of O^+ to elastic backscattering and large angle scattering, for which smaller impact parameters are necessary. Moreover, if elastic scattering were a dominant process, one would expect similar O^+ attenuation cross sections (rather than a factor of 3 difference) for NH_3 and H_2O , which have similar mass and dipole moment. There is direct experimental evidence only for small angle scattering and not for large angle scattering, so we conclude that the measured O^+ attenuation cross sections cannot be explained by elastic backscattering.

Since we rule out elastic backscattering as a dominant O^+ attenuation process, we must consider inelastic processes, e.g., ion-molecule reactions and charge transfer processes. No evidence for ionic ion-molecule products in the desorbing species have been found, and we focus on charge transfer processes.

For one-electron charge transfer reactions in the gas phase,



and



the energy defects are 1 eV and 2.2 eV, respectively; both reactions are exothermic. Theory and experiment show that the smaller the energy defect, the larger the charge transfer cross section; our O^+ attenuation cross sections for H_2O and NH_3 are consistent with this trend.

We can compare our experimental attenuation cross sections with gas-phase one-electron charge-transfer cross sections between O^+/H_2O and O^+/NH_3 in the thermal energy range. Based on rate coefficients measured at room temperature [29,30], the cross section is $\sim 5.8 \times 10^{-14} \text{ cm}^2$ for O^+/H_2O and $\sim 2.2 \times 10^{-14} \text{ cm}^2$ for O^+/NH_3 . Both the gas phase measurements and our cross sections show the same trend: the O^+/H_2O cross section is about 3 times larger than that for O^+/NH_3 .

In concluding this section, we observe that charge transfer processes appear to dominate the attenuation of O^+ by overlayers of H_2O and NH_3 .

3.3. Transmission of F^- through Xe films

The next of our series of investigations involves the transmission of positive and negative fluorine ions (F^+, F^-) through a rare gas overlayer, Xe. The F^+ ion signal is attenuated monotonically with increasing Xe film thickness, and decreases to $\sim 2\%$ at 1 ML of Xe. The attenuation of F^+ is considered in a later publication; we focus now on the unusual behavior of F^- .

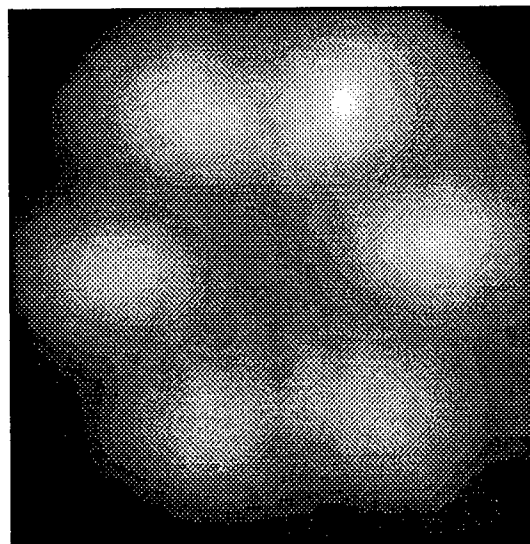
The saturation coverage of $PF_3/Ru(0001)$ (0.33 molecules PF_3 per Ru atom) gives rise to a hexagonal F^- ESDIAD pattern [22], Fig. 4a. In contrast to the behavior described above for attenuation of O^+ and F^+ by condensed films, we find that the adsorption of Xe films on this substrate leads to an increase of the F^- yield of up to four times that observed in the absence of Xe [31]. The F^- yield exhibits a maximum at a Xe coverage of 1 ML, and a decrease for higher coverages (Fig. 5). This increase is accompanied by a dramatic change in the ion angular distribution: the hexagonal ESDIAD pattern seen in the absence of Xe displays broad, normal F^- emission in the presence of a Xe overlayer (Fig. 4b).

We develop a model in which the presence of Xe leads to an enhancement of the electron stimulated desorption yield of F^- from PF_3 , which causes an increase in the intensities of the hexagonal ESDIAD spots. With increasing Xe coverage, more and more F^- ions scatter elastically from Xe atoms and thereby change their trajectories.

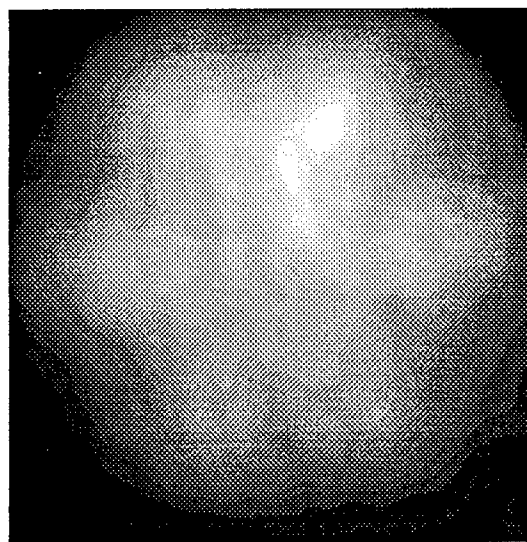
We assume that F^- can be formed either by dipolar dissociation or by dissociative electron attachment. Dipolar dissociation requires an electron with an energy higher than ~ 20 eV:



The electrons capable of initiating this process are mainly the primary electrons, and their flux does not change significantly with Xe coverage; hence this process should be independent of Xe coverage. (Note that the primary 300



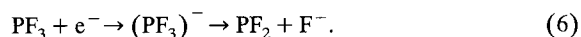
(a)



(b)

Fig. 4. F^- ESDIAD patterns. (a) saturation coverage of PF_3 on $Ru(0001)$; (b) 0.25 ML of Xe on $PF_3/Ru(0001)$.

eV electrons lose only a small fraction of their energy in the Xe film). Dissociative electron attachment is initiated by low energy (< 10 eV) secondary electrons from the Ru substrate:



Irrespective of the mode of formation of F^- ions, an F^- ion may undergo charge exchange with the substrate upon desorption and be neutralized. Joyce et al. have studied the influence of coadsorption of potassium on the F^- ESD yield from $PF_3/Ru(0001)$ and have concluded

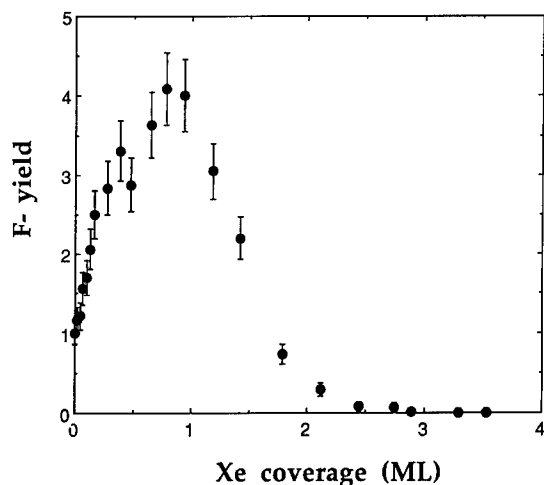


Fig. 5. Angle-integrated F^- ESD signal as a function of Xe film thickness for Xe on $PF_3/Ru(0001)$ at 20 K.

that a decrease in the work function (caused by the adsorption of potassium) decreases the neutralization probability and causes an enhancement of the F^- yield [32].

We suggest that the Xe adsorbate may increase the rate at which F^- is produced through dissociative electron attachment, e.g., by a reflection of the secondary electrons (which stem from the Ru substrate) at the Xe film back towards the PF_3 . A Xe layer may also decrease the neutralization probability of F^- by dielectric screening and hence increase their lifetime and escape probability. A lowering of the surface work function by Xe on $PF_3/Ru(0001)$ has been measured recently [31].

The F^- yield maximizes at around 1 ML of Xe (Fig. 5); in the thickness regime from 0–1 ML there is a competition between enhancement of F^- through increase in the production and survival rate, and attenuation of F^- through elastic backscattering of F^- from Xe. We suggest that the decrease in F^- for Xe films thicker than 1 ML is caused predominantly by elastic scattering of the F^- in the Xe film. Charge transfer from F^- to Xe is not favored energetically.

The change in angular distribution of the F^- appears to be caused by elastic scattering of the ions by the Xe atoms. The ions which desorb initially with a polar angle of $\sim 60^\circ$ from the clean $PF_3/Ru(0001)$ surface are steered towards the surface normal, which results in a broad normal emission. Upon completion of 1 ML of Xe, all ions are scattered and can be found in the broad normal distribution. This picture is consistent with the channel model [11,12] that we have proposed for the transmission of O^+ through rare gas films: Bulk rare gas solids have the fcc structure, which means a layer structure of A–B–C–A... Close-packed (111) oriented rare gas films exhibit channels perpendicular to the surface for a coverage of up to 3 ML. We suggest, by analogy, that the reason for the

steering of the F^- ions is the existence of the channels perpendicular to the surface.

4. Summary and conclusions

We have made a series of measurements to identify the dominant energy transfer and charge transfer processes that limit the survival probability of ions created below a surface. We find that a substantial fractional of 7 eV O^+ ions can survive transmission through Kr and Xe films several monolayers in thickness. Based on changes in angular and energy distributions, we attribute the attenuation of O^+ in Kr and Xe films mainly to elastic backscattering. This conclusion is reinforced by the results of recent molecular dynamics simulations by Klein et al. [25]. In contrast, the attenuation of O^+ by H_2O and NH_3 is dominated by charge transfer neutralization, and 0.5 monolayers of H_2O attenuate the O^+ signal to $<1\%$. A surprising enhancement of F^- intensity (by a factor of four) is observed for F^- through Xe, together with a striking change in the angular distribution of F^- . The Xe film enhances the production and survival rate of F^- while causing elastic scattering of F^- by Xe atoms.

These data indicate that under the appropriate conditions, low energy anions and cations produced below the topmost surface layer of a solid by electron, photon or ion excitation may have a substantial probability of survival and escape from the surface. Depending on the electronic properties of the ion and target film, both elastic scattering and charge transfer processes are observed to limit the ion survival probability. Future studies will focus on the survival of anions and cations in condensed H_2O films (relevant to electrochemistry) and in other condensed molecular films.

Acknowledgements

The authors acknowledge, with pleasure, helpful discussions and valuable collaboration with H. Urbassek, M. Vicanek and P. Klein (who made Ref. [25] available to us before publication), as well as helpful discussions with R. Baragiola and R. Johnson. This work has been supported in part by the National Science Foundation, Grant CHE-9408367.

References

- [1] T.E. Madey, *Science* 234 (1986) 316.
- [2] N.H. Tolk, M.M. Traum, J.C. Tully and T.E. Madey (eds.), *Desorption Induced by Electronic Transitions, DIET-I*, Springer Series in Chemical Physics 24 (Springer, Berlin, 1983).
- [3] W. Brenig and D. Menzel (eds.), *DIET-II*, Springer Series in Surface Sciences 4 (Springer, Berlin, 1985).

- [4] R.G. Ramsier and J.T. Yates, Jr., *Surf. Sci. Rep.* 12 (1991) 243.
- [5] P. Sigmund, A. Oliva and G. Falcone, *Nucl. Instr. and Meth.* 194 (1982) 541.
- [6] M. Vicanek, J.J. Jimenez Rodriguez and P. Sigmund, *Nucl. Instr. and Meth. B* 36 (1989) 124.
- [7] P. Sigmund et al., *Nucl. Instr. and Meth. B* 36 (1989) 110.
- [8] J.W. Burnett, J.P. Biersack, D.M. Gruen, B. Jorgensen, A.R. Kraus, M.J. Pellin, E.L. Schweitzer, J.T. Yates, Jr. and C.E. Young, *J. Vac. Sci. Technol. A* 6 (1988) 2064.
- [9] M.F. Dumke, T.A. Tombrello, R.A. Weller, R.M. Housley and E.H. Cirlin, *Surf. Sci.* 124 (1983) 407.
- [10] N.J. Sack, M. Akbulut and T.E. Madey, *Nucl. Instr. and Methods B* 90 (1994) 451.
- [11] N.J. Sack, M. Akbulut and T.E. Madey, *Phys. Rev. Lett.* 73 (1994) 794.
- [12] N.J. Sack, M. Akbulut and T.E. Madey, *Phys. Rev.*, in press.
- [13] U. Diebold and T.E. Madey, *Phys. Rev. Lett.* 72 (1994) 1116.
- [14] H. Massey and H. Gilbody, *Electronic and Ionic Impact Phenomena* (Clarendon, Oxford, 1974).
- [15] C.T. Reimann, W.L. Brown and R.E. Johnson, *Phys. Rev. B* 37 (1988) 1455.
- [16] W.L. Brown, W.M. Augustyniak, L.J. Lanzerotti, R.E. Johnson and R. Evatt, *Phys. Rev. Lett.* 45 (1980) 1632.
- [17] D.B. Chrissey, J.W. Boring, J.A. Phipps, R.E. Johnson and W.L. Brown, *Nucl. Instr. and Meth. B* 13 (1986) 360.
- [18] W.L. Brown, *Nucl. Instr. and Meth. B* 32 (1988) 1.
- [19] R.E. Johnson, *Energetic Charged-Particle Interactions with Atmospheres and Surfaces* (Springer, 1990).
- [20] T.E. Madey, J.J. Czyzewski and J.T. Yates, Jr., *Surf. Sci.* 49 (1975) 465.
- [21] D.A. King, T.E. Madey and J.T. Yates, Jr., *J. Chem. Phys.* 55 (1971) 3247.
- [22] A.L. Johnson, S.A. Joyce and T.E. Madey, *Phys. Rev. Lett.* 61 (1988) 2578.
- [23] N.J. Sack, L. Nair and T.E. Madey, *Surf. Sci.* 310 (1994) 63.
- [24] N.J. Sack, M. Akbulut and T.E. Madey, in press.
- [25] P. Klein, H.M. Urbassek and M. Vicanek, *Phys. Rev. B*, in press.
- [26] M.F. Guest et al., *Mol. Phys.* 38 (1979) 1427.
- [27] V.N. Ageev, to be published.
- [28] M. Akbulut, N.J. Sack and T.E. Madey, in preparation.
- [29] D.L. Albritton, *Atom. Data Nucl. Data Tables* 22 (1978) 1.
- [30] D. Smith, N.G. Adams and T.M. Miller, *J. Chem. Phys.* 69 (1978) 308.
- [31] N.J. Sack, M. Akbulut and T.E. Madey, in press.
- [32] S.A. Joyce, C. Clark, V. Chakarian, D.K. Shuh, J.A. Yarmoff, T.E. Madey, P. Nordlander, B. Maschhoff and H.-S. Tao, *Phys. Rev. B* 45 (1992) 14264.



ELSEVIER

Velocity dependence of ionization probability of secondary ions emitted from metal surfaces

D.V. Klushin, M.Yu. Gusev, I.F. Urazgil'din *

Department of Physics, Moscow State University, Moscow 119899, Russia

Abstract

Two mechanisms of the charge state formation during secondary ion emission from metals are shown to predominate: the tunneling one (resonant neutralization while the atomic level crosses the Fermi level of the metal) and the thermalization one (the establishment of the occupation of the atomic level corresponding to the local electronic temperature). Generally, both mechanisms are present, but under certain conditions (type of metal, etc.) one of them can predominate. The calculated results agree quantitatively with the experimental data and are in favour of the existence of a locally high electronic temperature in the collision cascade area.

1. Introduction

Charge exchange between an atomic particle and a solid surface is one of the fundamental aspects of the atom–surface interaction. The charge state formation of an escaping atomic particle in secondary ion emission is the field of interest of many experimental and theoretical groups during the last years. In spite of this attention and importance the mechanism of secondary ion formation is still poorly understood (see, for example, the review of Yu [1]). In particular, the effect of the secondary particle velocity on the ionization probability is a subject of intensive discussions. From experimental results, it is tempting to write down two empirical laws: exponential dependence of the ionization probability P^+ on the inverse of the normal component of the velocity $P^+ \propto \exp[-v_0/v_\perp]$ [2,3] and a power-law dependence on the normal component of the velocity $P^+ \propto (v_\perp)^\alpha$ [4,5] (v_0 and α are constants). Theoretically, the Anderson–Newns Hamiltonian [6] is employed to describe the nonadiabatic charge transfer processes between a moving atom and a metal surface [7–10]. In this model, charge state formation is a result of the interaction between the valence level $E_a(z)$ (here and below, all the energies are reckoned from the Fermi level) of the escaping (sputtered) atom and substrate continuum states. This interaction leads to the broadening of $E_a(z)$, and the half-width of $E_a(z)$ is normally assumed to depend exponentially on distance z from the surface: $\Delta(z) = \Delta_0 \exp[-\gamma z]$, where γ is the inverse of the

characteristic length ($\gamma \sim 1 \text{ \AA}^{-1}$, Δ_0 is on the order of eV).

For the case where $E_a(z)$ crosses the Fermi level at a distance z_0 from the metal surface and the temperature is supposed to be zero, Brako and Newns [10] analytically derived the exponential dependence of P^+ on inverse velocity: $P^+ = \exp[-2\Delta(z_0)/\gamma v_\perp]$. This result can also be derived from the rate-equation and is just what the electron-tunneling model leads to (see Ref. [9]).

The electron-tunneling model gives a qualitative account of many regularities in the secondary ion emission from metals and semiconductors [1,11,12], including the effect of the presence of adsorbates on the surface [13]. However, the model fails to give a quantitative description. Furthermore, some experimental results cannot be described by this model even qualitatively. Partly to explain the discrepancies between the electron-tunneling model and the experimental results, Sroubek formulated the semiphenomenological substrate-excitation model of secondary-ion production [14]. Assuming the electrons in the sputtering site are excited to a high effective temperature T_e , Sroubek showed that the ionization probability can be approximated by $P^+ = \exp[-|E_a(z^*)|/T_e]$, where $z^* = \gamma^{-1} \ln(2\Delta_0/\gamma v_\perp)$. If a linear approximation is used for $E_a(z)$, power-law $P^+(v_\perp)$ dependence results (see Ref. [14]).

Now, the electron-tunneling model and Sroubek's model are most widely used. The qualitative difference between these two models is evident; however, none of them has so far received priority. It is not still a quantitative comparison between experiment and theory [1,12].

In this work, the quantum description of the charge exchange process was applied, and two charge state forma-

* Corresponding author. Tel. +7 095 4270079, fax +7 095 2926511 box 10395, e-mail uraz@elec60.phys.msu.su.

tion mechanisms were shown to operate simultaneously, namely the tunneling and the thermalization mechanisms which can be related to the two above mentioned models. The theory gives a quantitative description of the experimental data. The theoretical results achieved are not inconsistent with either the electron-tunneling model or that by Sroubek. Moreover, under certain conditions either of these models becomes a particular case of the suggested theory.

2. Theory

Considering electron exchange in secondary ion emission from metals it should be noted first that the atomic level $E_a(z)$ varies significantly with the distance z from the surface, so the “memory” effects can be neglected [8,10]. In this case, the final charge state in the “wide band” approximation (which is valid for ordinary wide-band metals) is given by (see Ref. [10])

$$n_a(\infty) = \frac{1}{\pi} \int_{-\infty}^{\infty} d\omega F_F(\omega, T_e) \left| \frac{1}{v_{\perp}} \int_{-\infty}^{\infty} dz (\Delta(z))^{1/2} \times \exp \left[\frac{1}{v_{\perp}} \left(i\omega z + \int_z^{\infty} (iE_a(z') - \Delta(z')) dz' \right) \right] \right|^2, \quad (1)$$

where $F_F(\omega, T_e)$ is the Fermi distribution with temperature T_e .

We apply this general expression for the different temperature ranges. When $T_e \rightarrow 0$ (more precisely, in the low-temperature case $T_e \ll \gamma v_{\perp}$ when the electronic temperature is much less than the energy of the excitation resulting from the finite-time hopping interaction switching-off), and after it is taken into account that $|\Delta'(z_0)| \ll |E'_a(z_0)|$ where $\Delta'(z) = \partial\Delta(z)/\partial z$, $E'_a(z) = \partial E_a(z)/\partial z$, and $E_a(+\infty) < 0$, Eq. (1) leads to a well-known result for the ionization probability of the secondary ion [10]:

$$P^+ = \exp \left[-\frac{2}{v_{\perp}} \int_{z_0}^{\infty} \Delta(z) dz \right] = \exp \left[-\frac{2\Delta(z_0)}{\gamma v_{\perp}} \right] \quad (2)$$

(as above, we are assuming that $\Delta(z) = \Delta_0 \exp[-\gamma z]$).

However, the high-temperature case ($T_e \gg \gamma v_{\perp}$) is the most interesting. Note that the distinction between the high- and the low-temperature cases uses the parameter $T_e/\gamma v_{\perp}$, and therefore depends on both the temperature and the inverse velocity: for the same temperature, the situation may require either the high- or the low-temperature treatment depending on the component of the atom velocity normal to the surface. The energy distribution of the secondary ions sputtered from a metal usually has a maximum between 5 and 15 eV. If the situation is estimated for this range of kinetic energies, one finds that,

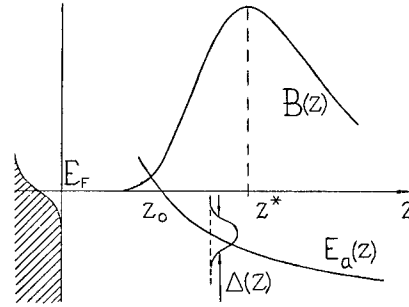


Fig. 1. The atomic level energy $E_a(z)$ and the $B(z)$ dependence (see Eq. (3)) as a function of the distance from the jellium edge of the metal; z_0 is the effective neutralization distance, and z^* is the effective thermalization distance.

e.g., for Cu the high-temperature case is realized for $T_e > 500$ K, and this temperature is even lower for heavier metals. The electron temperature T_e in the bombarded region is still a problem; anyway, there are reasons to expect that it differs (and, probably, to a large extent) from the ionic one (some estimations suggest that T_e can be as high as few thousands of K [15]).

Integrating Eq. (1) over ω , we obtain

$$n_a(\infty) = -i \frac{T_e}{2v_{\perp}} \int_{-\infty}^{\infty} dz B(z) \times \int_{-\infty}^{\infty} d\tau \frac{\exp \left[-\frac{1}{v_{\perp}} \int_{z-\tau}^z iE_a(x) dx \right]}{\sinh(\pi T_e \tau / v_{\perp} - i0)} \quad (3)$$

where

$$B(z) = \frac{\partial}{\partial z} \left\{ \exp \left[-\frac{2}{v_{\perp}} \int_z^{\infty} \Delta(z') dz' \right] \right\}$$

$B(z)$ is bell-shaped (but with a certain asymmetry); it has a maximum at $z^* = \gamma^{-1} \ln(2\Delta_0/\gamma v_{\perp})$ and its width is of the order of γ^{-1} , see Fig. 1. In Eq. (3), it was taken into account that $\Delta(z)$ varies only slightly with an order of $v_{\perp}/\pi T_e$ variation of its argument (i.e. $\Delta(z) \gg |\Delta'(z)| v_{\perp}/\pi T_e = \Delta(z) \gamma v_{\perp}/\pi T_e$), and that $\Delta(z^*) = \gamma v_{\perp}/2 \ll T_e$ (we consider here the high-temperature case $T_e \gg \gamma v_{\perp}$).

We recall that z_0 is the point where $E_a(z)$ crosses the Fermi level (normally, for metals $z_0 \sim \gamma^{-1}$). What is more, in the high-temperature case we have $z^* > z_0$ (see Fig. 1). We split the integration over z in Eq. (3) into two intervals: from $-\infty$ to \tilde{z} and from \tilde{z} to $+\infty$. The \tilde{z} point can be anywhere between z_0 and z^* , with only one more restriction that $\tilde{z} - z_0 \gg v_{\perp}/\pi T_e$. For definiteness, let $\tilde{z} - z_0 \sim \gamma^{-1}$ (see Fig. 1). The \tilde{z} point plays an auxiliary part and, as we will see later, its choice does not affect the results. The important fact is that $|E_a(z)| \gg |E'_a(z)| v_{\perp}/\pi T_e$ when $z > \tilde{z}$. For $z < \tilde{z}$, we can approxi-

mate $E_a(z)$ by $E_a(z) = E'_a(z_0)(z - z_0)$ because the vicinity of z_0 gives the major contribution. Then Eq. (3) becomes

$$n_a(\infty) = -i \frac{T_e}{2v_{\perp}} \int_{-\infty}^{\infty} dz B(z) \int_{-\infty}^{\infty} d\tau \frac{\exp \left[-i \frac{E'_a(z_0)\tau}{v_{\perp}} (z - z_0) + i \frac{E'_a(z_0)\tau^2}{2v_{\perp}} \right]}{\sinh(\pi T_e \tau / v_{\perp} - i0)} \\ + i \frac{T_e}{2v_{\perp}} \int_{\bar{z}}^{\infty} dz B(z) \int_{-\infty}^{\infty} d\tau \frac{\exp \left[-i \frac{E'_a(z_0)\tau}{v_{\perp}} (z - z_0) + i \frac{E'_a(z_0)\tau^2}{2v_{\perp}} \right]}{\sinh(\pi T_e \tau / v_{\perp} - i0)} \\ + \int_{\bar{z}}^{+\infty} dz B(z) F_F(E_a(z), T_e).$$

Consider the second term of the above sum. In integration over τ , the segment defined by $|\tau| < v_{\perp} / \pi T_e$ is most important. Then, the exponent $i E'_a(z_0) \tau^2 / 2v_{\perp}$ can be neglected in comparison with $i E'_a(z_0) \tau (z - z_0) / v_{\perp}$ (since $z > \bar{z}$; $\bar{z} - z_0 \gg v_{\perp} / \pi T_e$; $\bar{z} - z_0 \sim \gamma^{-1}$; $v_{\perp} / \pi T_e \ll \gamma^{-1}$). Thus, we have

$$n_a(\infty) = -i \frac{T_e}{2v_{\perp}} \int_{-\infty}^{\infty} dz B(z) \int_{-\infty}^{\infty} d\tau \frac{\exp \left[-i \frac{E'_a(z_0)\tau}{v_{\perp}} (z - z_0) + i \frac{E'_a(z_0)\tau^2}{2v_{\perp}} \right]}{\sinh(\pi T_e \tau / v_{\perp} - i0)} \\ + \int_{\bar{z}}^{\infty} dz B(z) [F_F(E_a(z), T_e) - F_F(E'_a(z_0)(z - z_0), T_e)] \\ = I_1 + I_2.$$

We consider I_1 first. After integrating over z by parts, and withdrawing the imaginary term from the denominator using the Sokhotsky formula $1/(x - i0) = 1/x + i\pi\delta(x)$ ($\sinh(\pi T_e \tau / v_{\perp} - i0) \approx \cosh(\pi T_e \tau / v_{\perp}) [\tanh(\pi T_e \tau / v_{\perp}) - i0]$), we obtain:

$$I_1 = 1 + \frac{T_e}{2v_{\perp}} \int_{-\infty}^{\infty} d\tau \frac{E'_a(z_0)\tau}{v_{\perp} \sinh(\pi T_e \tau / v_{\perp})} \\ \times \exp \left[i \frac{E'_a(z_0)\tau^2}{2v_{\perp}} \right] Q(\tau),$$

where

$$Q(\tau) = \int_{-\infty}^{\infty} dy \exp \left[-i \frac{E'_a(z_0)\tau}{v_{\perp}} y - \frac{2}{v_{\perp}} \int_{z_0+y}^{\infty} \Delta(x) dx \right] \\ (y = z - z_0).$$

The function $|Q(\tau)|$ is a sharp peak (of width $\gamma v_{\perp} / \pi |E'_a(z_0)|$) located at $\tau = 0$. To see that it is so, one can substitute $\Delta(z) = \Delta_0 \exp[-\gamma z]$, which results in $Q(\tau) \sim \Gamma(-i E'_a(z_0) \tau / \gamma v_{\perp})$ and recall that $|\Gamma(i\eta)|^2 = \pi / \eta \sinh(\pi \eta)$, where Γ is a gamma-function. Normally, $|E'_a(z_0)| \gamma^{-1} \gg T_e$; therefore, the vicinity of $\tau = 0$ that plays a role is much smaller than $v_{\perp} / \pi T_e$, so we can write

$$I_1 = 1 + \frac{E'_a(z_0)}{2\pi v_{\perp}} \int_{-\infty}^{\infty} d\tau \exp \left[i \frac{E'_a(z_0)\tau^2}{2v_{\perp}} \right] Q(\tau).$$

Integration over τ yields

$$I_1 = 1 - \int_{-\infty}^{\infty} dy \exp \left[-\frac{2}{v_{\perp}} \int_{z_0+y}^{\infty} \Delta(x) dx \right] \\ \times \frac{1}{2} \left(i \frac{2 |E'_a(z_0)|}{\pi v_{\perp}} \right)^{1/2} \exp \left[-i \frac{|E'_a(z_0)| y^2}{2v_{\perp}} \right].$$

This integral can easily be taken by the saddle-point method ($y = 0$ is the saddle point):

$$I_1 = 1 - \exp \left[-\frac{2}{v_{\perp}} \int_{z_0}^{\infty} \Delta(z) dz \right] = 1 - \exp \left[-\frac{2\Delta(z_0)}{\gamma v_{\perp}} \right].$$

Let us consider the integral I_2 . By taking into account that $|E_a(z)| \gg T_e$ and $|E'_a(z_0)(z - z_0)| \gg T_e$ when $z > \bar{z}$, I_2 becomes

$$I_2 = - \int_{\bar{z}}^{\infty} dz B(z) \left(\exp \left[\frac{E_a(z)}{T_e} \right] - \exp \left[\frac{E'_a(z_0)(z - z_0)}{T_e} \right] \right) \\ \approx - \int_{\bar{z}}^{\infty} dz P(z) \exp \left[\frac{E_a(z)}{T_e} \right].$$

We neglect the term $\exp[E'_a(z_0)(z - z_0)/T_e]$ as compared to $\exp[E_a(z)/T_e]$ because $|E_a(z)| < |E'_a(z_0)(z - z_0)|$ at $z > \bar{z}$ (see Fig. 1).

It remains to show that I_2 depends only slightly on \bar{z} . Using the linear approximation $E_a(z) = E_a(z^*) + E'_a(z^*)(z - z^*)$ near z^* (we recall that $z^* = \gamma^{-1} \ln(2\Delta_0/\gamma v_{\perp})$ is the point where $B(z)$ has the maximum), we obtain

$$I_2 = -\tilde{\gamma}(\xi; 2\Delta(\bar{z})/\gamma v_{\perp}) \exp \left[-\frac{|E_a(z^*)|}{T_e} \right] \\ \approx -\Gamma(\xi) \exp \left[-\frac{|E_a(z^*)|}{T_e} \right]$$

where

$$\xi = \frac{|E'_a(z^*)|}{\gamma T_e} + 1;$$

$$\tilde{\gamma}(\xi; 2\Delta(\bar{z})/\gamma v_{\perp}) = \Gamma(\xi) - \Gamma(\xi; 2\Delta(\bar{z})/\gamma v_{\perp});$$

$\tilde{\gamma}(\xi; 2\Delta(\bar{z})/\gamma v_{\perp})$ is an incomplete gamma-function; $\Gamma(\xi)$ is a gamma-function; $\Gamma(\xi; 2\Delta(\bar{z})/\gamma v_{\perp})$ is an incomplete complementary gamma-function. It was taken into account that $\Gamma(\xi) \lesssim 1$, $\Gamma(\xi; 2\Delta(\bar{z})/\gamma v_{\perp}) \sim \exp[-2\Delta(\bar{z})/\gamma v_{\perp}]$, and $2\Delta(\bar{z})/\gamma v_{\perp} > 1$.

Summarizing the above, we finally have

$$n_a(\infty) = 1 - \exp\left[-\frac{2\Delta(z_0)}{\gamma v_{\perp}}\right] - \Gamma\left(\frac{|E'_a(z^*)|}{\gamma T_e} + 1\right) \times \exp\left[-\frac{|E_a(z^*)|}{T_e}\right].$$

Now, the expression for the ionization probability can be written as

$$P^+ = \exp\left[-\frac{2\Delta(z_0)}{\gamma v_{\perp}}\right] + \Gamma\left(\frac{|E'_a(z^*)|}{\gamma T_e} + 1\right) \times \exp\left[-\frac{|E_a(z^*)|}{T_e}\right]. \quad (4)$$

3. Discussion and comparison with experimental data

First of all it is worth noting that when $|E_a(z^*)|/T_e > 2\Delta(z_0)/\gamma v_{\perp}$, Eq. (4) for the ionization probability P^+ coincides with the result of the electron-tunneling model. In contrast, when $|E_a(z^*)|/T_e < 2\Delta(z_0)/\gamma v_{\perp}$ and $|E'_a(z^*)|/\gamma T_e \ll 1$, Eq. (4) passes to the limit given by the expression for P^+ in the model suggested by Sroubek.

The first term in Eq. (4) for the ionization probability P^+ coincides with the low-temperature expression for P^+ , and results for the most part from kinetic effects induced by the reasonably rapid change of $E_a(z)$ with z when it crosses the Fermi level at z_0 . We will refer to z_0 as the effective distance of neutralization, since for distances above z_0 the electron tunneling onto the atomic level occurs with high intensity. The second term represents “thermalization” of the atomic level, i.e., the tendency towards equilibrium occupation with the local electronic temperature T_e (z^* is the effective thermalization distance).

Thus, two mechanisms of the charge state formation can be differentiated: the “tunneling” one (the term “tunneling mechanism” is a matter of convention: it is related to the accepted term “electron-tunneling model” used to refer to such mechanism) and the “thermalization” one. The predomination of one of them is governed by numerous factors (velocity of the secondary ion, behavior of the level E_a with z , the distance z_0 , the half-width Δ of the E_a level, local electronic temperature, etc.), so a special treatment is needed in each particular case. However, one can predict in general the behavior of P^+ as a function of the inverse velocity ($1/v_{\perp}$) (Fig. 2). At large velocities v_{\perp} (i.e. small $1/v_{\perp}$), the low-temperature regime is real-

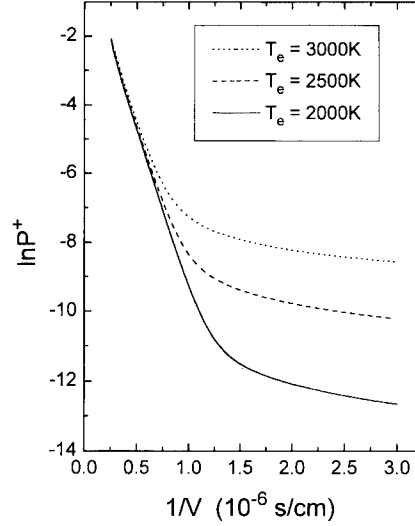


Fig. 2. Characteristic dependence of the ionization probability in the secondary ion emission on the inverse velocity of the escaping particle at different local electronic temperatures. The parameters are as follows: $\Delta_0 = 2$ eV, $\gamma = 0.5 \text{ \AA}^{-1}$, $E_a(z)$ (in a.u.) = $E_a^0 + 1/4(z - z_{im})$, $E_a^0 = -3$ eV, $z_{im} = 0.5 \text{ \AA}$.

ized and the only mechanism for the formation of the ion is the tunneling one, which results in linear dependence of $\ln P^+$ on $(1/v_{\perp})$ at small $1/v_{\perp}$ independent of T_e (Fig. 2). As the velocity decreases, we pass to the high-temperature case. However, even in the high-temperature regime the tunneling mechanism can predominate up to a certain v_{\perp} . Further decrease in v_{\perp} favors the establishment of the equilibrium (with temperature T_e) occupation of the level, and the thermalization mechanism dominates the charge state of the ion (as is seen from saturation of the $\ln P^+$ curves in Fig. 2).

Consider the experimental results [16] for the ionization probability in secondary-ion emission from several metals (Cu, Nb, and Ta) represented by dark squares in Fig. 3. In fact, dependencies similar to those given in Fig. 3 have been reported in numerous publications and present the typical behavior of $\ln P^+$ as a function of $1/v_{\perp}$ at small v_{\perp} [2,16,17].

Solid lines in Fig. 3 represent the calculated data. There are five parameters in Eq. (4) for the ionization probability of secondary particle: Δ_0 , γ , z_0 , T_e , and $E_a(z)$. We define all of them except T_e : the amplitude of the atomic level width is $\Delta_0 = 2$ eV in all three cases; the inverse characteristic length γ is valued as $\gamma = \sqrt{2\phi}$ for γ in (a.u.) $^{-1}$, where ϕ is the work function of the metal. The calculations of the energy shifts of atom levels near the metal surface can be performed using the complex scaling [18] and the coupled angular mode [19] techniques. We use a simpler but sufficiently good approximation for the dependence of E_a (reckoned from the Fermi level) on z in the case of metals $E_a(z) = E_a^0 + 1/4(z - z_{im})$, where $E_a^0(z)$ is

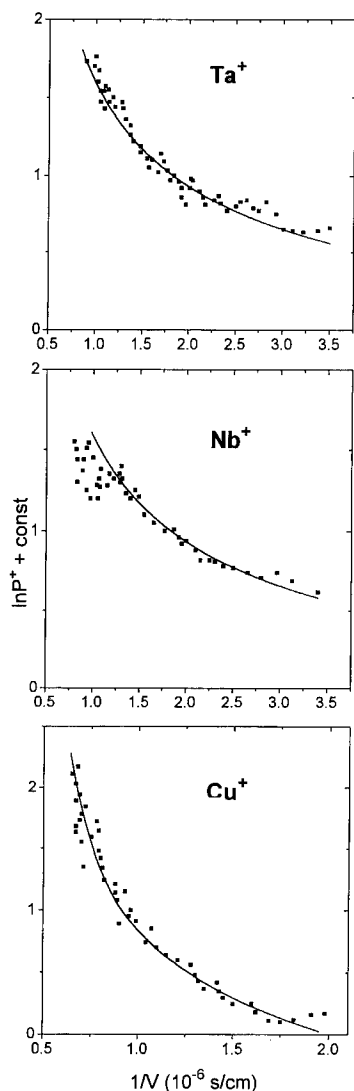


Fig. 3. Velocity dependence of ionization probability of metal atoms ejected under 45° from sputter cleaned polycrystalline Ta, Nb, and Cu. The dark squares are experimental points; the solid lines show the calculated data. The vertical scale is chosen according to the figure from Ref. [16].

in a.u.; z_{im} is the location of the image plane; $E_a^0 = \phi - I$; I is the ionization potential of the metal atom, i.e., E_a^0 is the energy of the atomic level at infinite distance from the surface ($E_a^0 = -3.4$ eV, -2.9 eV, and -3.6 eV for Cu, Nb, and Ta, respectively). In the $E_a(z)$ dependence it is also taken into account that the image plane is displaced by z_{im} from the jellium edge of the metal being the coordinate origin in the outward direction. This distance was set at $z_{\text{im}} = 1$ a.u. for all three cases. Now, the location of the point z_0 where $E_a(z)$ crosses the Fermi level (which is the energy origin) can be easily calculated from the equation $E_a(z) = 0$.

Thus, after the amplitude of the half-width of the atomic level Δ_0 is chosen and the parameters γ , z_0 together with the $E_a(z)$ dependence are found from table values of I and ϕ , the fitting parameter that remains is the local electronic temperature T_e . The calculation was best fitted to the experimental data (see Fig. 3) by choosing T_e to be 2800, 3100, and 3200 K for Cu, Nb, and Ta, respectively.

We emphasize that the calculated ranges of P^+ corresponding to the range of velocities $1/v_\perp$ in Fig. 3, $P^+ = (0.4-3) \times 10^{-4}$ for Cu, $P^+ = (3-8) \times 10^{-4}$ for Nb, and $P^+ = (0.4-1) \times 10^{-4}$ for Ta are in good agreement with the experimental data on the absolute values of P^+ for these metals [16] (the experimental ranges of P^+ are $P^+ = (0.7-3) \times 10^{-4}$ for Cu, $P^+ = (4-8) \times 10^{-4}$ for Nb, and $P^+ = (0.6-1) \times 10^{-4}$ for Ta). Thus, the theory correctly predicts not only the shapes of the $P^+(1/v_\perp)$ dependence, but the absolute values of P^+ as well.

4. Conclusion

In conclusion, a general description of the charge exchange processes in secondary ion emission from metals is given. Two mechanisms of the charge state formation can be differentiated: the tunneling one (resonant neutralization while the atomic level crosses the Fermi level of the metal) and the thermalization one (the establishment of the occupation of the atomic level corresponding to the local electronic temperature). Generally, both mechanisms are present, but under certain conditions one of them can predominate. The theory quantitatively describes the experimental data.

Acknowledgement

The research described in this publication was made possible in part by Grant N MQ1000 from the International Science Foundation.

References

- [1] M.L. Yu, in *Sputtering by Particle Bombardment III*, eds. R. Behrish and K. Wittmaack, Springer Series in Topics in Appl. Phys. Vol. 64 (Springer, Berlin, 1991) p. 91.
- [2] M.J. Vasile, *Phys. Rev. B* 29 (1984) 3785.
- [3] R.F. Garrett, R.J. MacDonald, and D.J. O'Connor, *Nucl. Instr. and Meth.* 218 (1983) 333.
- [4] A.R. Krauss and D.M. Gruen, *Surf. Sci.* 92 (1980) 14.
- [5] R.G. Hart and C.B. Cooper, *Surf. Sci.* 94 (1980) 105.
- [6] P.W. Anderson, *Phys. Rev.* 124 (1961) 41;
D.M. Newns, *Phys. Rev.* 178 (1969) 1123.
- [7] A. Blandin, A. Nourtier, and D.W. Hone, *J. Phys. (Paris)* 37 (1976) 369.

- [8] J.K. Norskov and B.I. Lundqvist, *Phys. Rev. B* 19 (1979) 5661.
- [9] N.D. Lang, *Phys. Rev. B* 27 (1983) 2019.
- [10] R. Brako and D.M. Newns, *Surf. Sci.* 108 (1981) 253.
- [11] Y.L. Wang, *Phys. Rev. B* 38 (1988) 8633.
- [12] I.F. Urazgil'din, *Nucl. Instr. and Meth. B* 78 (1993) 271.
- [13] I.F. Urazgil'din, *Phys. Rev. B* 47 (1993) 4139.
- [14] Z. Sroubek, *Phys. Rev. B* 25 (1982) 6046, *Nucl. Instr. and Meth.* 194 (1982) 533.
- [15] Z. Sroubek, G. Falcone, *Surf. Sci.* 166 (1986) L136; Z. Sroubek, *Appl. Phys. Lett.* 45 (1984) 850.
- [16] A. Wucher and H. Oechsner, *Surf. Sci.* 199 (1988) 567.
- [17] V. Makarenko, A. Popov, A. Shaporenko, A. Shergin, *Rad. Eff. Def. Solids* 113 (1990) 263.
- [18] P. Nordlander, J.C. Tully, *Phys. Rev. Lett.* 61 (1988) 990; P. Nordlander, N.D. Lang, *Phys. Rev. B* 44 (1991) 13681.
- [19] D. Teillet-Billy, J.P. Gauyacq, *Surf. Sci.* 239 (1990) 343.

Line shifts in mass spectra of secondary ions ejected from solids by MeV-ion impact

K. Wien^{*}, Ch. Koch, Nguyen van Tan

Institut für Kernphysik der Technischen Hochschule, Schlossgartenstrasse 9, 64289 Darmstadt, Germany

Abstract

Emission of hydrogen ions has been used to investigate the charging of the nuclear track being produced by fission fragments in organic solids. The question of interest is, if in insulating material the lifetime of ionisation along the nuclear track is sufficiently long to allow atomic motion driven by Coulomb repulsion of neighbouring ionized atoms. It is shown in this article that the hydrogen ions experience the potential produced by the ionized track core, but weaker than Auger electrons (see Schiwietz et al., Phys. Rev. Lett. 69 (1992) 628). In order to determine the mean initial energy of emission, we measured the time-of-flight distributions of secondary ions by means of a linear TOF instrument being equipped with 2 acceleration grids and converted them into axial energy distributions. Monte Carlo simulations were used to simulate the time distributions and to estimate the mean charge along the nuclear track causing the observed line shifts.

1. Introduction

A few years after Macfarlane and coworkers had adopted PDMS (plasma-desorption-mass-spectrometry) to the field of mass spectrometry [1], the same laboratory discovered that in time-of-flight mass spectra of organic solids the line of the H^+ ion is generally shifted towards shorter flight times than expected from time-mass calibration. The present article is addressed to line shifts of the hydrogen ions H^+ , H_2^+ , H_3^+ , H^- and for comparison also the alkali ions K^+ and Cs^+ and the halide ion I^- . The impetus for these experiments came from a work of Schiwietz et al. [2], who observed shifts also of K-Auger electron lines. The Auger energies were considerably smaller than expected from the level scheme of the emitting ions. The Auger electrons were emitted from carbon atoms being ionized by high energetic (40 MeV) Ne ions penetrating a thin polypropylene foil. The authors emphasised that these line shifts towards lower energies are mainly caused by a positive charge along the nuclear track. They estimated that the corresponding track potential during the time of the Auger transitions ($4-8 \times 10^{-15}$ s) can have values up to about 45 V. If this relatively high track potential lives sufficiently long ($> 10^{-14}$ s), it should also influence the movement of ions leaving the track zone at the sample surface after heavy-ion impact.

Energy distributions of secondary ions desorbed from

solids by fast heavy ions have been measured with numerous samples (see, for instance, the review articles [3–5]), line or energy shifts, respectively, were deduced for hydrogen ions and a few light ions. It has already been suggested that the shifts are related to a positive charge along the nuclear track [6–8]. A mean track potential – as in the case of Auger electron emission [2] – is difficult to deduce, because neither the time of ion emission nor the position of ion formation are sufficiently well known. In the last section, the measured line shifts are therefore analysed in terms of a model, which is based on a continuous line charge along the nuclear track.

2. Experimental method

The time- and corresponding axial energy-distributions of secondary were studied by the double-grid method, a TOF technique first applied to PDMS mass lines by Becker [9]. The instrument used for the present experiments is sketched in Fig. 1. Sample films deposited on metal foils are traversed by ^{252}Cf -fission fragments ejecting the secondary ions from the sample front side. The ions are accelerated in two successive electric fields towards the stop detector. The flight time is a function of the initial kinetic energy of the ion and the local potential of the point at the sample, from where the ion is ejected. The distribution of these initial energies causes a broadening of the ion mass lines.

The samples were either blank metal foils or thin films of organic material or alkali halides being evaporated or

^{*} Corresponding author, tel. +49 615 1 1622 121, fax +49 6151 164321.

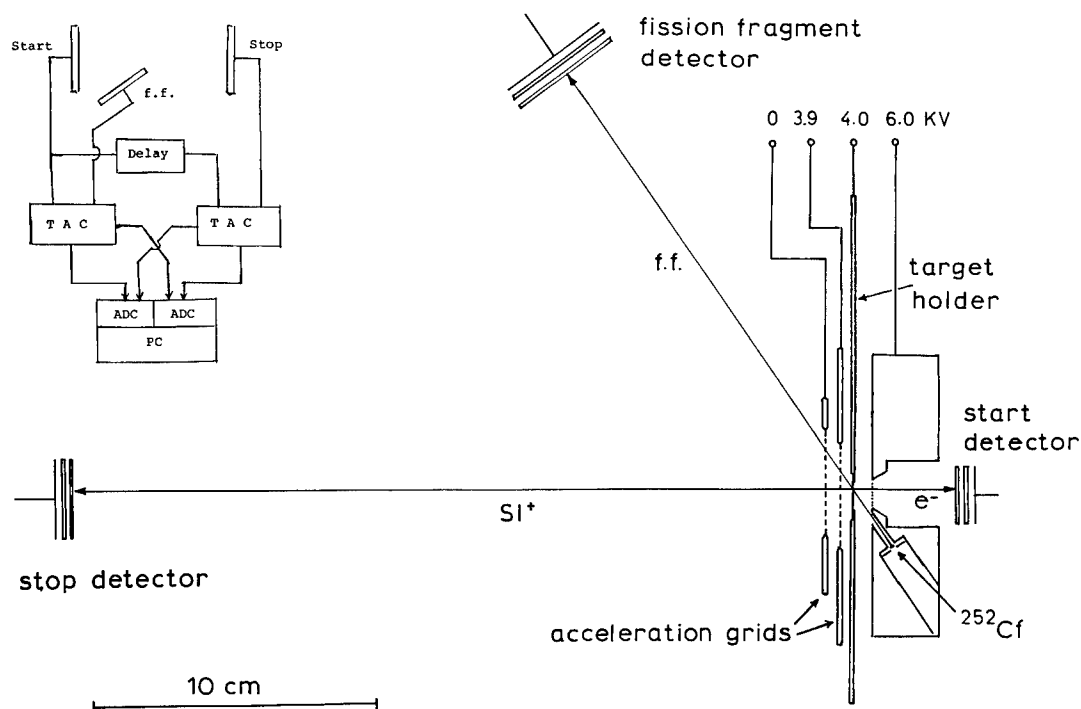


Fig. 1. Time-of-flight setup for measuring time distributions of secondary ions. In the inset, the principle electronic setup is sketched. TAC: time-to-amplitude converter, ADC: analog-to-digital converter.

electrosprayed onto these metal foils. The metal foils as well as the sample surfaces were generally contaminated by impurities during fabrication or storage in natural air. Even, when they were ion etched inside the vacuum chamber of the TOF instrument (5×10^{-7} mbar), contamination via rest gas adsorption was unavoidable.

The fission fragments of a 20 μCi Cf-source pass the target under an angle of 55° against the surface normal and impact a micro-channel plate detector. This second TOF branch (see inset in Fig. 1) is used to determine the velocity or energy of the fission fragments, when they have left the uppermost layers of the sample. Setting

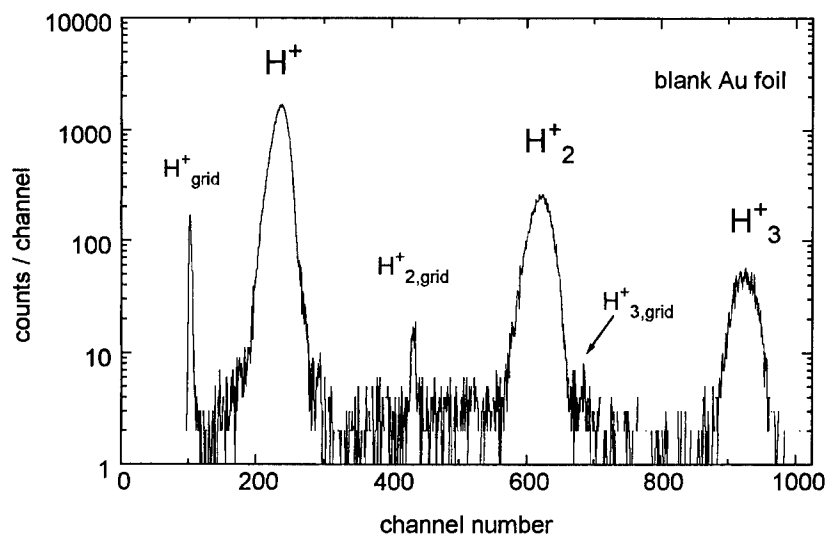


Fig. 2. Spectrum of the 3 positive hydrogen ions ejected from a blank Au foil by fission fragments. The narrow hydrogen lines are caused by ion emission from the 1st grid.

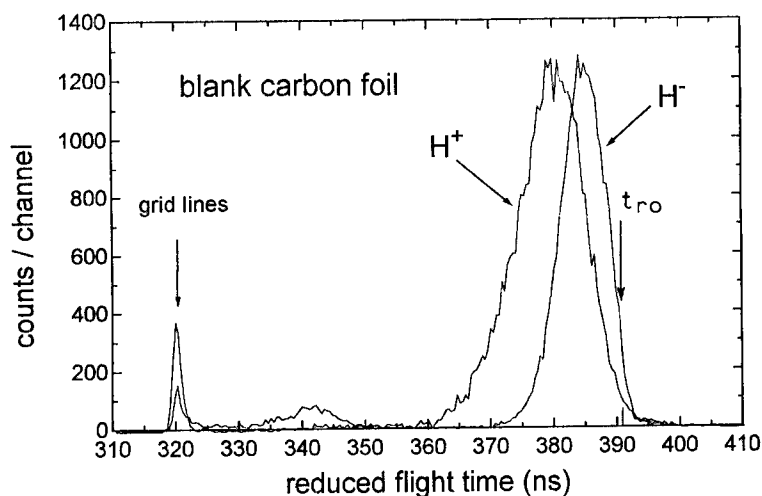


Fig. 3. Reduced time distributions of the H^- and H^+ ions emitted from a blank carbon foil. t_{ro} is marked by an arrow.

windows on sections of the fission fragment TOF spectrum, the time distributions of the secondary ions were measurable as function of primary ion velocity. The energy loss of the fission fragments in the sample material at the exit surface was evaluated by means of the measured velocities and the stopping-power tables of Northcliffe and Schilling [10].

3. Measurement of time distributions and time to energy conversion

The principle of the method used by us was, to broaden the mass lines of secondary ions by a weak first acceleration field in front of the target and to measure the distribution of their absolute flight times relative to the position of corresponding grid lines, in order to reduce the influence of electronic instabilities and uncertainties of flight distances.

A typical TOF spectrum extended over the time range of the 3 positive hydrogen ions is presented in Fig. 2. Beside the broadened H^+ , H_2^+ , and H_3^+ lines, also 3 narrow lines of hydrogen ions are seen, which are ejected

by fission fragments from the bars of the 1st grid. They were used as fix points in the time scale of the spectra, this means, the position of a time distribution was determined relative to the corresponding grid line, if such a line was visible.

For a quick and direct comparison of time distributions measured with different ions, we converted the channel numbers of the spectra into absolute flight times and eliminated the mass dependence by dividing these times by the square root of the ion mass m :

$$t_r = t/\sqrt{m} = (K + K_0)(\Delta t/\Delta K)/\sqrt{m}. \quad (1)$$

Here, $\Delta t/\Delta K$ is the time/channel calibration and K_0 the offset of the channel scale associated to $t = 0$. K_0 was determined with help of the secondary-electron line in the negative ion spectrum. Under the assumption that the track potential $U_i(x, y, z) = 0$, the reduced flight time t_r depends – apart from the spectrometer parameters – only on E_a , the axial initial energy of the ions. In Fig. 3 we show as an example the reduced time distributions of H^+ and H^- emitted from a blank carbon foil. The comparison indicates that the mean axial energy of H^- is smaller than that of H^+ (see Table 1).

Table 1

Experimental data of axial energy distributions measured for H^+ and H^- with metal foils. a and b : parameter of the function $E^a \exp(-bE)$ fitted to the measured energy distributions. E_m : mean axial energies. The energy window on the fission-fragment TOF spectrum was set on the light fragment group

Foil:	C	Au	Ni	Ti	Al
	H^+, H^-	H^+, H^-	H^+, H^-	H^+, H^-	H^+, H^-
dE/dx [keV/Å]	1.25	1.8	0.7	0.95	1.0
a	0.42, 0.65	0.82, 0.44	0.77, 0.33	0.91, 0.39	1.42, 0.28
b [eV $^{-1}$]	0.71, 0.27	0.29, 0.76	0.52, 0.86	0.27, 0.76	0.34, 0.79
E_m [eV]	4.4, 1.28	5.2, 1.30	3.2, 1.12	5.6, 1.43	6.0, 1.02

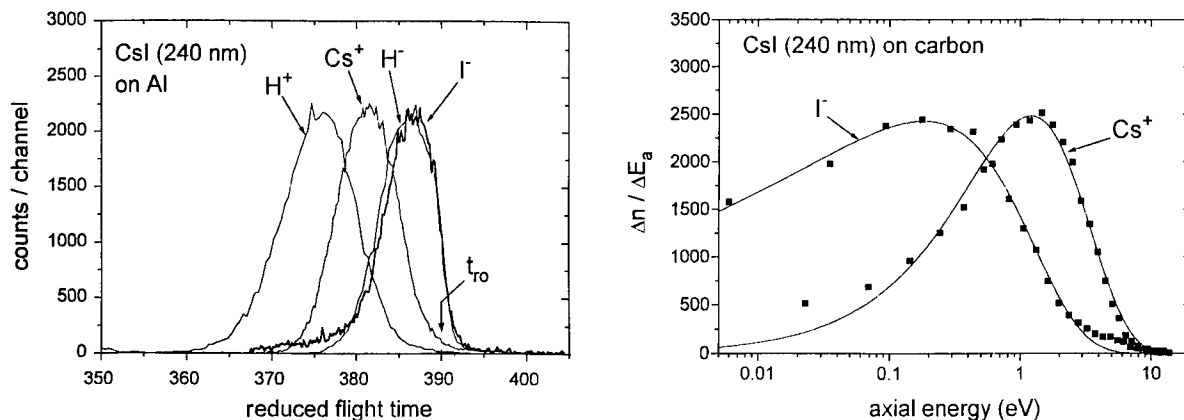


Fig. 4. Reduced time distributions and corresponding axial energy distributions of various ions ejected from a 240 nm thick CsI film. The curves have been normalized to the same height. Solid lines in the right figure are fits of Eq. (3).

The reduced time distributions $\Delta n / \Delta t_r$ can be converted into an axial energy distribution $\Delta n / \Delta E_a$ by the expression

$$\frac{\Delta n}{\Delta E_a} = \frac{\Delta n}{\Delta t_r} \frac{dt_r}{dE_a}. \quad (2)$$

The derivative dt_r/dE_a of the spectrometer function $t_r = t/\sqrt{m}$ is an analytical expression [11]; its values for a certain energy E_a were calculated using the precisely measured acceleration voltages U_i and distances d_i and d . The distances between target and grids were determined with help of an optical microscope. The main problem of the conversion is the evaluation of the time value t_{ro} under a broadened mass line, which corresponds to zero initial energy ($E_a = 0$). Using the grid lines as reference in the time scale, the remaining uncertainty of t_{ro} is caused by

the distance between the target and the 1st grid. The accuracy of measuring this distance was $\pm 30 \mu\text{m}$.

4. Results and discussion

4.1. Metal foils

Due to the rapid contamination with organic adsorbants [12], even sputter-cleaned metal foils emit hydrogen ions under fission fragment bombardment. Comparing their relative yields per impact (1:0.15:0.04 for H^+ , H_2^+ and H_3^+) and their energy distributions with corresponding data obtained with organic gases under electron bombardment [13], it is obvious that the hydrogen ions are formed by

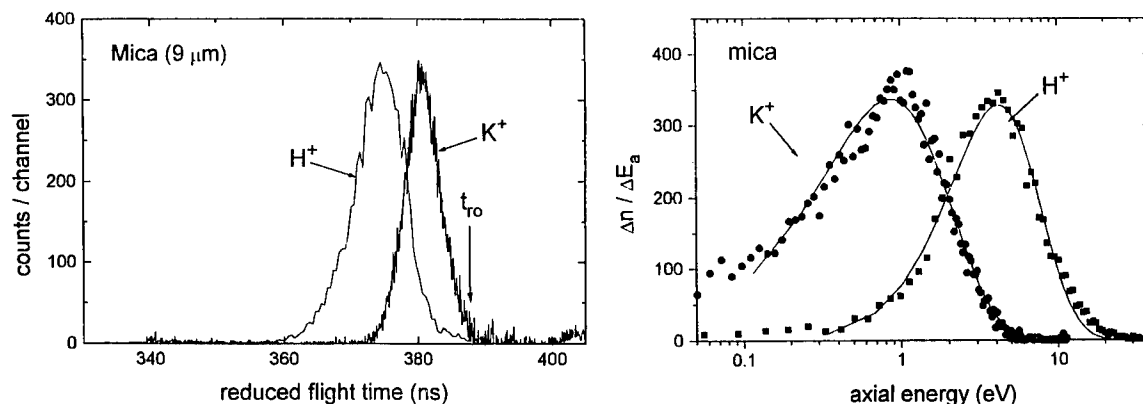


Fig. 5. Reduced time distributions and corresponding axial energy distributions of H^+ and K^+ ejected from mica by about 10 MeV fission fragments (light group).

dissociation of molecular ions located at the surface of the samples and being excited in the shower of δ -electrons emerging from the track area after fission fragment impact. This seems to be true also for organic samples as proven with completely deuterated glycine samples. The hydrogen ions are therefore spectators of the track potential at and above the sample surface.

The time distributions of hydrogen ions measured with Au, C, Ni and Ti foils do not exhibit an indication of a line shift. As seen in Fig. 3, the right slope of the H^+ -distribution arises sharply from the same point of the time scale as the H^- -distribution. The energy distributions obtained with metal foils are generally describable by

$$\frac{\Delta n}{\Delta E} \propto E^a \exp(-bE). \quad (3)$$

This expression does not fit as well to the distributions of Al – probably due to a thick layer of insulating Al_2O_3 , in which a positive track charge can remain. The parameters a and b and the mean axial energy E_m evaluated for H^+ and H^- are listed in Table 1. The groups of light and heavy fission fragments did not give different E_m values.

4.2. CsI and mica

A CsI film was prepared by vacuum evaporation on a carbon foil, the cleaved mica foil was covered by a thin Al film at the backside. Examples of reduced time distributions are displayed in Figs. 4 and 5. Line shifts are obviously present for the H^+ ion, but not for Cs^+ and K^+ . A possible energy shift of the Cs^+ ion relative to that of the I^- ion is certainly not larger than 1 eV. Additional experimental results are given in Table 2. The mean axial energy $E_m = 1.8$ eV of Cs^+ is in fair agreement with values measured by Becker et al. (2.0 eV [14]) and Moshhammer (1.5 eV [11]), but a factor of at least 3 larger than a value evaluated from a work of Macfarlane and

Table 2

Experimental data of axial energy distributions measured with a CsI film and mica. I_{rel} : intensities of ions normalized to the intensity of the H^+ ion. a and b : parameter of the function $E^a \exp(-bE)$ fitted to the measured energy distributions. E_m : mean axial energies

Sample	dE/dx [keV/Å]	H^+	H_2^+	H_3^+	H^-	K^+	Cs^+	I^-
CsI (240 nm)	0.72	I_{rel}	1	0.14	0.04	0.76	2.68	0.82
		a					0.81	0.18
		b [eV $^{-1}$]					0.66	1.0
		E_m [eV]	5.5	5.0	3.2	0.67	1.8	0.86
Mica (9 μ m)	0.39	I_{rel}	1	0.17	0.03	0.68	2.85	
		a					1.1	
		b [eV $^{-1}$]					1.3	
		E_m [eV]	5.3	5.1	3.7	0.83	1.2	

Jacobs (0.50 eV [6]), who used a different method for calibrating the time scale.

Energy distributions of alkali and halide ions (see Figs. 4 and 5) having the form of Eq. (3) can be compared with theoretical predictions being published, for instance, by Ziv et al. [15] and Kelly [16]. Ziv et al. assumed that after energetic particle impact, aggregates of atoms or molecules are generated, which are weakly bound to the surface, and in which the excitation energy is dispersed via vibrational relaxation before dissociation. Kelly expounded a thermal evaporation process. In both cases, the critical parameter is the exponent a in Eq. (3). Predicted is $a = 0.5$ and 0.5 or 1, respectively. For Cs^+ and K^+ the agreement is fair, for I^- the experimental value of a is too small. Angular distributions measured by Moshhammer [11] exhibit, that Cs^+ emission from CsI is strongly forward peaked ($\sim \cos^3\theta$) and I^- emission almost isotropic ($\cos^{0.5}\theta$). This is not expected by both models. We suggest two possible processes for the formation of I^- : either electron capture

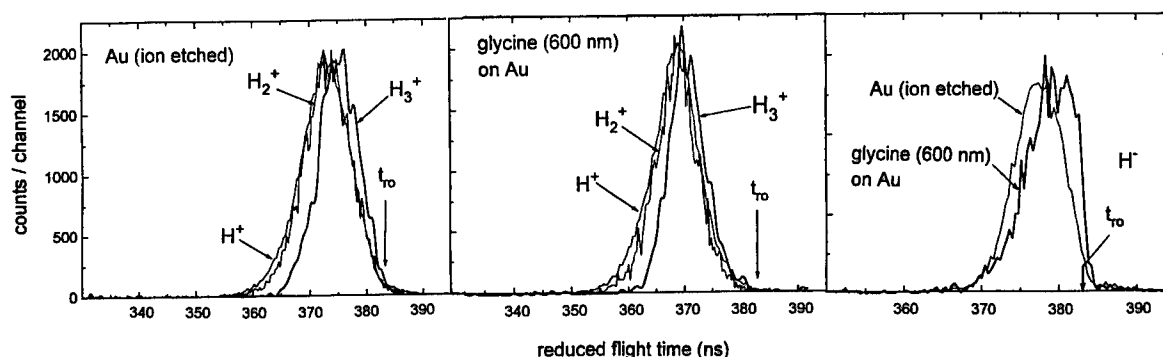


Fig. 6. Time distributions of hydrogen ions ejected by fission fragments from an Au foil being cleaned by 3.5 keV-Ar $^+$ ion etching and from a 600 nm thick glycine film being evaporated onto a Au foil. The curves of the H_3^+ ion were smoothed in order to display better their general shape.

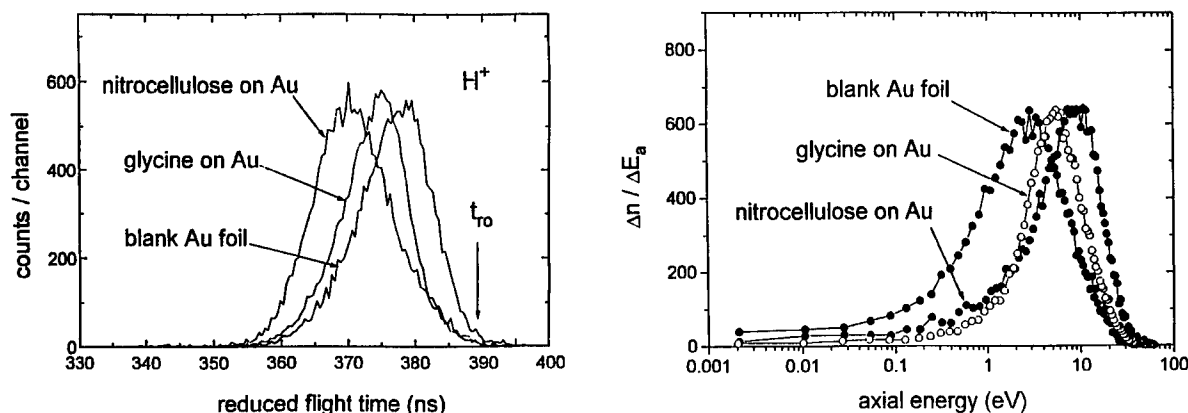


Fig. 7. Time- and axial energy-distributions of H^+ ions ejected by fission fragments from a blank Au foil and two organic samples deposited on Au foils. The distributions are normalized to the same height.

of neutral I-atoms in front of the surface or decay of CsI-molecules after electron capture again close to the surface. The latter process might also work with H_2 -molecules leading to H^- , which shows a similar angular distribution as I^- [11].

4.3. Organic layers on metal foils

Typical for organic layers are the shifts of the positive hydrogen lines towards shorter flight times. As shown in Fig. 6, these shifts are manifested by more or less pronounced gaps between t_{ro} and the right falling off of the time distributions. Obviously, the three ions H^+ , H_2^+ and H_3^+ ejected from the 600 nm-thick glycine film on Au experience nearly the same shift. The largest shifts were observed with electrosprayed nitrocellulose films. In Fig. 7, time distributions obtained with blank Au, glycine and nitrocellulose and the corresponding axial energy distributions are compared. The mean initial energies E_m are listed in Table 3.

For the positive ions, the line shifts are associated with enlarged mean energies E_m . When the thickness of the glycine layer on the Au substrate increases, the line shifts of H^+ , H_2^+ and H_3^+ grow and also the mean initial E_m as illustrated in Fig. 8. Saturation is reached at a layer thickness of about 1000 Å. Contrary to the positive hydrogen ions, the E_m values of H^- decrease for thicker glycine layers. Comparing the opposite trends of E_m for positive and negative ions, it seems to be evident, that a positive charge close to the area of ion emission and growing with layer thickness influences ion ejection: the initial energies of positive ions are shifted towards higher kinetic energies and those of negative ions to smaller kinetic energies. The corresponding electric potential in the area of ion emission generates a barrier, which hinders low energetic negative ions of leaving the surface. The intensity of H^- relative to that of H^+ is in fact decreasing with increasing layer thickness as illustrated in the right diagram of Fig. 9. This cut-off of low energetic negative ions leads to a sharp increase of the ion intensity at the time t_{ro} . As seen in Fig.

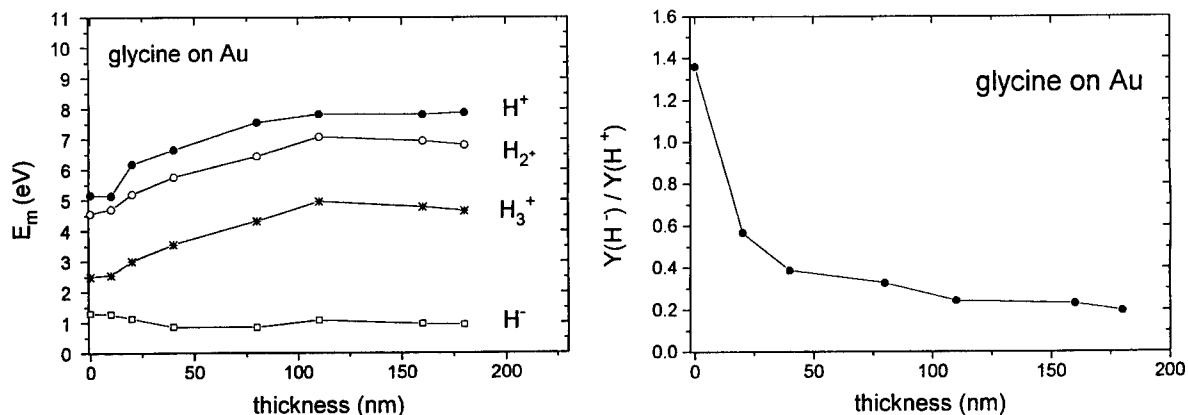


Fig. 8. Left: mean initial energies of hydrogen ions as function of the thickness of glycine layers deposited on Au foils, right: the ratio of H^- and H^+ yields as function of the glycine layer thickness.

Table 3

Experimental data of axial energy distributions measured with comparatively thick organic films deposited on metal foils. Glycine and valine were evaporated on Au and Cu foils, respectively, and nitrocellulose electrosprayed. E_m : mean axial energy. (L) and (H): light and heavy group of fission fragments

Sample	dE/dx [keV/Å]		H^+	H_2^+	H_3^+	H^-
Glycine (160 nm)	0.58 (L)	E_m [eV]	7.8	7.0	4.8	0.95
		ΔE_m [eV]	2.62	2.35	2.28	
Valine (400 nm)	0.41 (H)	E_m [eV]	7.8	7.3	4.8	1.07
		ΔE_m [eV]	8.3	7.6	5.2	1.02
Nitrocellulose	0.44 (L)	E_m [eV]	10.4	9.0	6.4	1.29
		ΔE_m [eV]	5.2	4.4	3.9	
		ΔE_m [eV]				

6, H^- emission from the uncharged blank Au foil is not accompanied by such a sharp increase of intensity.

5. The mean track potential

In the following, the measured line shifts will be used to evaluate the mean track potential at the time and in the area of ion creation. At the surface and in the surrounding of the point of projectile impact this potential is supposedly not constant. Due to the local variation of the ion emission probability and the variation of the potential, the mean values derived here can be only rough estimates. In the case of positive ions, a measure for the mean track potential U_m is simply the difference between E_m (metal), the mean energy obtained with a blank metal, and E_m , the mean energy for the insulating film deposited on the same metal (see ΔE_m values Table 3).

For CsI and mica, ΔE_m of the positive hydrogen ions would be comparatively small, probably smaller than 1 eV. Lines of alkali ions, which are virtually not shifted, were not available, ΔE_m was not evaluated, but is certainly smaller than 0.8 eV. The results of the glycine samples measured as function of film thickness are plotted in Fig. 9.

We have set $U_m \approx \Delta E_m$ under the assumption that the initial energy distributions of the ions ejected from the blank metal and the insulating film are identical. This seems to be nearly fulfilled for ion emission from glycine regarding two observations: (1) As shown in Fig. 9, the difference of the energies E_{max} , where the energy distributions reach their maximum, delivers the same values of U_m as the mean energies E_m . (2) The width of the energy distributions at half maximum (FWHM) does not change considerably, when the film thickness is enlarged, it increases from 8.1 to 9.5 eV. This means in addition, that also the track potential does not vary much within the surface area, from where the ions are ejected. For the H^+ ion, the smallest halfwidth was found for mica (FWHM = 6.7 eV), the largest one for nitrocellulose (FWHM = 16.0 eV). We suppose that this difference is related to the surface structure being nearly epitaxial for mica and very irregular for electrosprayed nitrocellulose.

Regarding the ΔE_m values of glycine, the mean track potential U_m increases steadily from zero for a 10 nm thick layer till about 2.5 eV for a 110 nm thick layer. Beyond 110 nm saturation seems to be established. By means of Monte Carlo simulations we proved that image charging of the metallic substrate surface can not reduce the potential at the organic surface as far as observed. Even for the 10 nm thick film the reduction should be smaller than 20%.

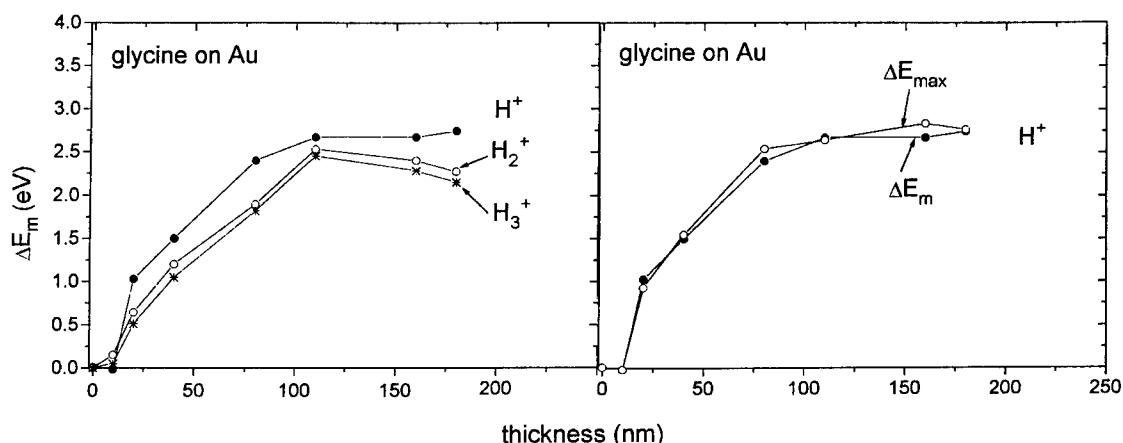


Fig. 9. Left: the difference $\Delta E_m = E_m - E_m(\text{metal})$ is plotted versus the thickness of a glycine film on Au for the three positive hydrogen ions, right: ΔE_m is compared with $\Delta E_{max} = E_{max} - E_{max}(\text{metal})$, the difference of the energies, where the maximum of the H^+ -energy distributions is reached for the glycine film and the blank Au foil.

As seen from Table 3 and Fig. 9, the values of ΔE_m decrease slightly with increasing number of atoms per hydrogen ion. This implies that H_2^+ and H_3^+ experience a lower track potential than H^+ . In principle, this can be caused by a rapid decay of the track potential acting longer on the slower H_2^+ and H_3^+ ions than on H^+ , or H_2^+ and H_3^+ are created further away from the point of impact than H^+ , where the track potential is weaker.

6. Monte Carlo simulations of time- and energy distributions

To investigate these possibilities as well as the thickness dependence of ΔE_m we performed Monte Carlo simulations of the ion emission, of the subsequent ion acceleration in a track potential and of the ion trajectories in the spectrometer under the actual experimental conditions. These simulations delivered time distributions, which were converted into energy distributions by means of the same procedure as described in Section 3. We assumed that the ions are released from the top layer of the sample under the following initial conditions:

- The distribution of the initial kinetic energy E_0 has the form of Eq. (3). The parameters a and b were chosen to reproduce the measured energy distributions of the hydrogen ions being ejected from the blank Au foil.
- The angular distributions are proportional to $\cos^n\theta$ with $n = 3$ for H^+ and 2 for H_2^+ and H_3^+ .
- The local emission probability as function of the distance from the point of impact is a Gauss function having a width of 20 Å. This means the ions are ejected mainly out of a cross section equivalent to the in-track.
- The distribution of the azimuth angle is isotropic.
- The track potential at the surface was derived from a line-charge along the nuclear track in normal direction to the surface. Dielectric reduction of the potential was included ($\epsilon = 4$). The first charged element of the line charge was located 7 Å underneath the surface.

Using these input parameters, the mean energy E_m of H^+ measured with the 160 nm glycine film on Au as well as the energy shift ΔE_m were reproducible by a charge line-density of $\rho_c = +0.85$ e/nm. ρ_c turned out to be rather sensitive to the width of the emission area. A width of 10 Å resulted in a charge density of only +0.27 e/nm. The calculated energy shifts of H_2^+ and H_3^+ were identical with the calculated value of H^+ ($\Delta E_m = 2.62$ eV), but slightly larger than the measured shifts (see Table 3 and Fig. 9). The simulations showed that the smaller experimental value of the H_3^+ ion is explainable by a life time of the track potential of $\tau = 2 \times 10^{-11}$ s.

Also the dependence of ΔE_m on the thickness of the glycine film was analysed in terms of a line-charge decreasing exponentially with time. Macfarlane and Jacobs

[6] and Fenyő et al. [8] suggested that a current from the metallic substrate into the nuclear track core neutralizes its charging. The life time τ of the charging was assumed to depend on the layer thickness d . The charge density is then given by

$$\rho_c = \rho_{c0} \exp(-t/\tau(d)).$$

Introducing this expression in the simulations, τ was fitted to the ΔE_m values of H^+ measured as a function of d . The result was

$$\tau = 0.5 \times 10^{-15} d^2 \text{ [s]} \quad \text{for } d = 20\text{--}100 \text{ nm.}$$

Fenyő et al. [8], who studied H^+ emission from nitrocellulose films on Si, have reported a linear dependence of τ on d and 2–10 times smaller values of τ . They deduced the life time of the track charge from radial energy distributions and assumed hydrogen emission out of the inner track core.

7. Conclusions

Experimental observation as well as Monte Carlo simulations have revealed that the shifts of mass lines in time-of-flight mass spectra measured with fission fragments as primary ions can be explained by positive charges located in the vicinity of the nuclear track. Compared with energy shifts of Auger electrons [2], these shifts of secondary ions are distinctly smaller – values between 1 and 5.2 eV have been deduced from mass lines of hydrogen ions. The shifts depend on the irradiated material – they are about zero for contaminated metals and largest for electrosprayed nitrocellulose films. The experiments on Auger electrons were performed with the electrons emitted from ionized atoms inside the highly energized track core. The hydrogen ions investigated in the present work stem most probably from excited molecules decaying at the sample surface. Differences of line shifts measured for the three hydrogen ions and also the thickness dependence of the shifts can be considered as an indication for a decay in time of the track potential. By means of Monte Carlo simulations we evaluated for a 100 nm thick glycine film on Au a lifetime of 5×10^{-12} s. This is certainly much longer than the neutralisation time of the charge, which is generated directly by the traversing fission fragment. The charging required to explain the observed line shifts is relatively small – more than two orders of magnitude smaller than the original charge density (about 160 e/nm [8]). The small number of charges could be associated with a few trapped holes in the surrounding of the nuclear track produced by δ -electron collisions. We think, that the hydrogen ions observed in the present experiments did not participate in a Coulomb explosion process being considered as the driving process of fast heavy ion induced sputtering.

Acknowledgement

The authors would like to thank Dr. H. Folger and his coworkers of the GSI/Darmstadt/FRG for preparing the carrier foils.

References

- [1] R.D. Macfarlane and D.F. Torgerson, *Science* 191 (1976) 920.
- [2] G. Schiwietz, P. Grande, B. Skogvall, J.P. Biersack, R. Köhrbrück, K. Sommer, A. Schmoldt, P. Goppelt, I. Kadar, S. Ricz and U. Stettner, *Phys. Rev. Lett.* 69 (1992) 628.
- [3] K. Wien, *Nucl. Instr. and Meth. B* 65 (1992) 149.
- [4] P. Hakansson, in: *Fundamental Processes in Sputtering of Atoms and Molecules (SPUT92)*, ed. P. Sigmund, K. Dan. Vidensk. Selsk., *Mat. Fys. Medd.* 43 (1993) 593.
- [5] G. Betz and K. Wien, *Int. J. Mass Spec. Ion Proc.* 140 (1994) 1.
- [6] R.D. Macfarlane and D.L. Jacobs, *Proc. of the 4th Int. Conf. on Ion Formation from Organic Solids (IFOS IV)*, ed. Benninghoven, Münster, 1987 (Wiley, Chichester, 1989) p. 71.
- [7] K. Wien, *Radiat. Eff. Def. Solids* 109 (1989) 137.
- [8] D. Fenyö, P. Hakansson and B.U.R. Sundqvist, *Nucl. Instr. and Meth. B* 84 (1994) 31;
S. Widdiyasekera, P. Hakansson and B.U.R. Sundqvist, *Nucl. Instr. and Meth. B* 33 (1988) 836.
- [9] O. Becker, *Nucl. Instr. and Meth.* 198 (1982) 53.
- [10] L.C. Northcliffe and R.F. Schilling, *Nucl. Data Tables A* 7 (1970) 233.
- [11] R. Moshhammer, thesis, Technische Hochschule Darmstadt/FRG, 1991.
- [12] M. Wagner, K. Wien, B. Curdes and E. Hilf, *Nucl. Instr. and Meth. B* 82 (1993) 362.
- [13] M.D. Burrow, S.R. Ryan, W.E. Lamb Jr. and L.C. McIntyre Jr., *J. Chem. Phys.* 71 (1979) 4931.
- [14] O. Becker and K. Wien, *Nucl. Instr. and Meth. B* 16 (1986) 456.
- [15] A.R. Ziv, B.V. King, S.H. Lin and I.S.T. Tsong, *Nucl. Instr. and Meth.* 218 (1983) 742;
S.H. Lin, I.S.T. Tsong, A.R. Ziv, M. Szymonski and C.M. Loxton, *Phys. Scripta T6* (1983) 106.
- [16] R. Kelly, *Surf. Sci.* 90 (1979) 280.



ELSEVIER

Time-of-flight elastic recoil analysis of ion beam modified nitrocellulose thin films

James H. Arps, Robert A. Weller *

Vanderbilt University, Nashville, Tennessee 37235-1807, USA

Abstract

The erosion properties of nitrocellulose ($C_6H_7N_3O_{11}$) thin films on Si have been studied under exposure to 270 keV H, He, C, and Ar ions. Time-of-flight elastic recoil spectrometry has been applied to determine the atomic composition of the films as a function of deposited charge. All exposed films exhibit an initial removal of N and O consistent with RO–NO₂ bond breaking, proceeding at a rate that appears to depend on the density of electronic excitation. A non-volatile, carbon-rich residue remains after prolonged exposure to H, He, and C ions, while the film is effectively removed under Ar irradiation. Experimental evidence supports the proposition that binary collisions are an important mechanism affecting desorption of the H and C components. The results are consistent with a suggestion that complete volatilization of the film is determined by the nuclear stopping power of the incident ion.

1. Introduction

The response of nitrocellulose to energetic ions is quite unusual. The material volatilizes completely under certain irradiation conditions, otherwise forming a radiation-hard residue. This property, frequently referred to as “self-development”, can be practically applied in lithography as a positive resist, or as a negative resist using the residue, to produce structures with lateral dimensions less than 100 nm [1]. Previous workers have attempted to identify the parameters affecting the nitrocellulose etch rate and the conditions under which a residue is formed. Kaneko et al., have reported that both the ion mass and energy play a role in the observed erosion behavior, suggesting a mechanism dependent on the electronic and nuclear energy losses of the ion in the material [2,3]. Mühle and Götz observed an initial etch rate independent of ion mass and found no correlation between the removed thickness and the total deposited ion energy [4]. Moliton et al., report etch rates dependent on the total energy loss with no effects tied to the individual nuclear and electronic losses [5].

A common method for measuring nitrocellulose film evolution has been surface profilometry. Unfortunately, the technique is insensitive to any changes in chemical composition during exposure. The use of a profilometer may also restrict the minimum thickness of films that may be stud-

ied. Perhaps because of this, many previous experiments have used films with an initial thickness greater than the projected range of the irradiating ions. Attempts to identify the individual contributions due to electronic or nuclear energy loss are complicated by significant variation in these values along the ion trajectory. Infrared spectroscopy has also been applied to study the evolution of the nitrocellulose chemical structure, and a number of reaction pathways have been suggested [6]. However, it may not be possible to identify the dominant reactions without quantitative information on the film stoichiometry.

In an attempt to further understand the erosion behavior of nitrocellulose, we have applied medium energy time-of-flight elastic recoil detection to the analysis of 270 keV H, He, C, and Ar ion irradiated thin films on silicon. This technique can simultaneously measure in situ the evolution of the individual atomic components in the film as a function of the accumulated dose. Thicknesses less than 20 nm were studied to minimize the variation in the nuclear and electronic energy loss as ions penetrate the film. The initial loss of nitrogen and oxygen for all exposures is generally compatible with desorption of NO₂. Further, the change in N and O content appears to scale with the total deposited electronic energy density. These results provide at least circumstantial evidence that RO–NO₂ bond breaking is one of the dominant processes. For the cases of H, He and C exposure, a carbonaceous layer persists after prolonged exposure. The complete removal of the film by Ar irradiation suggests that binary collisions associated with nuclear energy loss are an important factor in determining the onset of volatilization.

* Corresponding author. Tel. +1 615 343 7225, fax +1 615 343 7263, e-mail weller@vuse.vanderbilt.edu.

2. Experiment

A stock solution of nitrocellulose $(C_6H_7N_3O_{11})_n$ in amyl acetate was diluted to a concentration of 1.5%. Using a syringe and a #18 needle, a single drop of liquid was cast on the surface of a deionized water bath. After allowing the solvent to partially evaporate, the film was drawn onto a clean 1-inch silicon wafer (Virginia Semiconductor). Each sample was dried in air for 30 minutes, then heated in a N_2 ambient at $80^\circ C$ for another 30 minutes to remove any remaining solvent. A thickness of 17 nm was estimated based on the weight of a drop of solution, the area of the cast film, and a density of 1.2 g/cm^3 for nitrocellulose.

The samples were placed in a vacuum chamber with a nominal base pressure of 10^{-8} Torr. H^+ , He^+ , C^+ and Ar^+ ions were accelerated to 270 keV and directed at normal incidence to the samples. During each irradiation, the ions were rastered over a $0.6 \pm 0.1 \text{ cm}^2$ area with a current density of approximately $0.02 \mu A/\text{cm}^2$. At predetermined intervals, the exposures were interrupted and time-of-flight elastic recoil detection was used to measure the atomic composition of the film.

Complete descriptions of the time-of-flight detection scheme and its application to the detection of light elements are given elsewhere [7,8]. Briefly, a beam of 810 keV Ar^{3+} ions is directed at an angle of 21° to the sample surface. Light element recoils from the film, Si atoms from the substrate, and the scattered beam are detected at a 42° forward scattering angle relative to the initial beam direction. The particles pass through a thin carbon foil and generate one or more secondary electrons that, when detected by a microchannel plate, trigger a start pulse. The particles themselves generate a stop signal at a second microchannel plate after traversing a 37 cm flight path. Although the recoil energies determined by collision kinematics are usually larger for high-mass recoils, light atom recoils have the greater velocity and are well separated from Si and Ar events in the time-of-flight spectrum. The total number of ions needed to obtain each measurement was 1×10^{11} . By working at beam energies lower than for conventional elastic recoil detection, the total energy deposited in the sample is reduced and sensitivity to light elements is enhanced, due to the larger recoil cross sections. Hence, the damage to radiation sensitive material is minimized during analysis.

3. Results and discussion

A representative time-of-flight spectrum for a pristine nitrocellulose film is shown in Fig. 1a. Recoil H is easily identified, while overlap of the recoil C, N, and O features is observed due to straggling and energy loss in the film from both the incident Ar and recoil species. In short, the film is of sufficient thickness to cause a light element

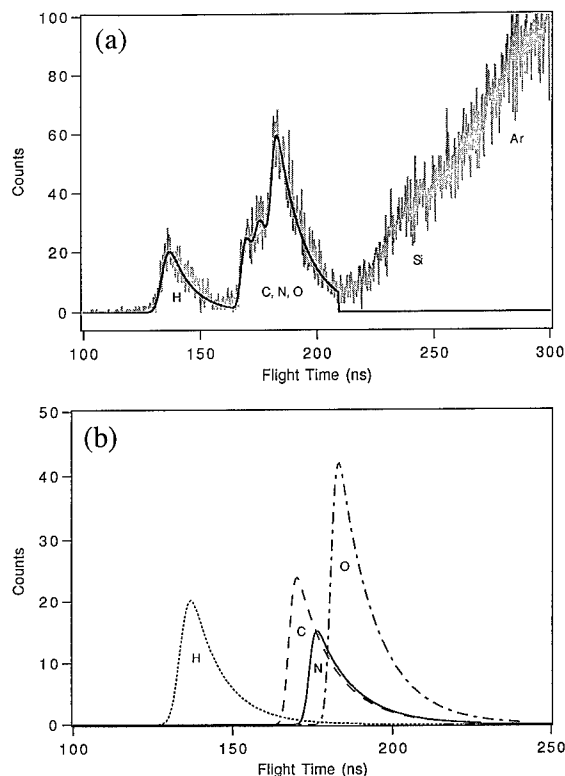


Fig. 1. (a) 810 keV Ar^{3+} time-of-flight spectrum and least-squares fit for a nitrocellulose thin film on Si. 1×10^{11} ions were deposited in the analysis. (b) Individual contributions of recoil H, C, N and O from the fit in (a).

recoil emerging from some depth within the film to have the same velocity as a heavier recoil near the surface. Though the profiling of much thinner layers could have reduced or eliminated this overlap, the erosion of the film then progresses too rapidly for a detailed series of measurements to be made. In order to extract the atomic concentrations of H, C, N, and O for each analysis, a peak fitting algorithm was employed. The time-of-flight distribution $f(z)$ of a particular recoil species from a thin uniform layer, modified by energy loss and straggling, can be described empirically by a function that is the convolution of a Gaussian with a decaying exponential.

$$f(z) = \frac{Ak}{2} \exp \left[\frac{k(k\sigma^2 - 2(z - z_0))}{2} \right] \times \left(1 - \operatorname{erf} \left[\frac{\sigma}{\sqrt{2}} \left(k - \frac{z - z_0}{\sigma^2} \right) \right] \right), \quad (1)$$

where $f(z)$ has been normalized so that A gives the total yield, k is the decay constant, σ the Gaussian standard deviation, and z_0 is the calculated flight time corresponding to recoils from the surface. The complete fitting function is the sum of the contributions in the form given in

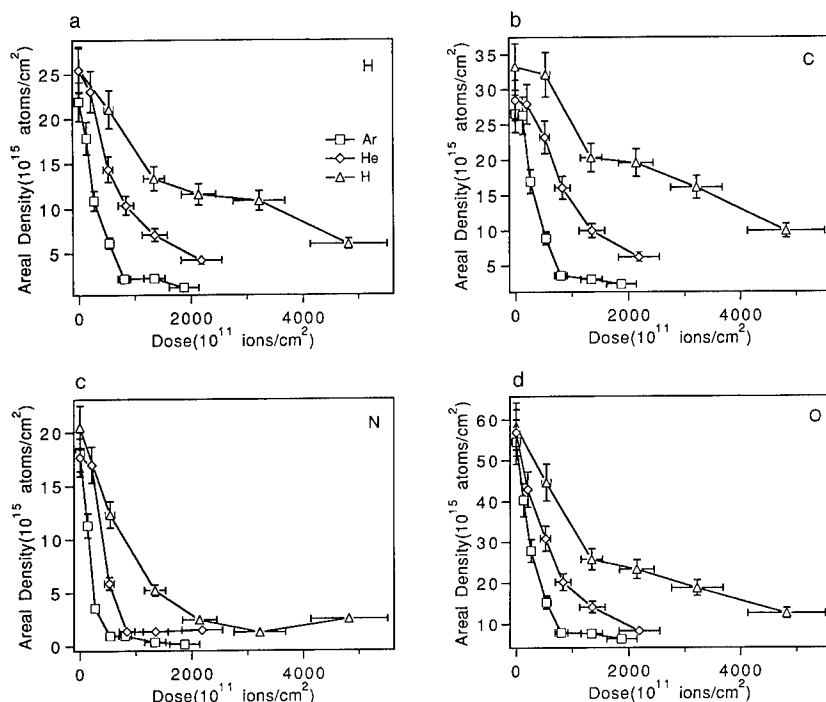


Fig. 2. (a)–(d) Change in the components H, C, N and O as a function of dose for Ar (\square), He (\diamond), and H (\triangle) irradiation. The points are connected to aid the eye.

Eq. (1) for each component of the film. A total of eight parameters were used, including a yield for each of the four elements and a decay constant and width for H. A

single decay constant and width were assumed in describing C, N, and O, since the recoil velocities and energy loss characteristics are similar. The result of this general, non-

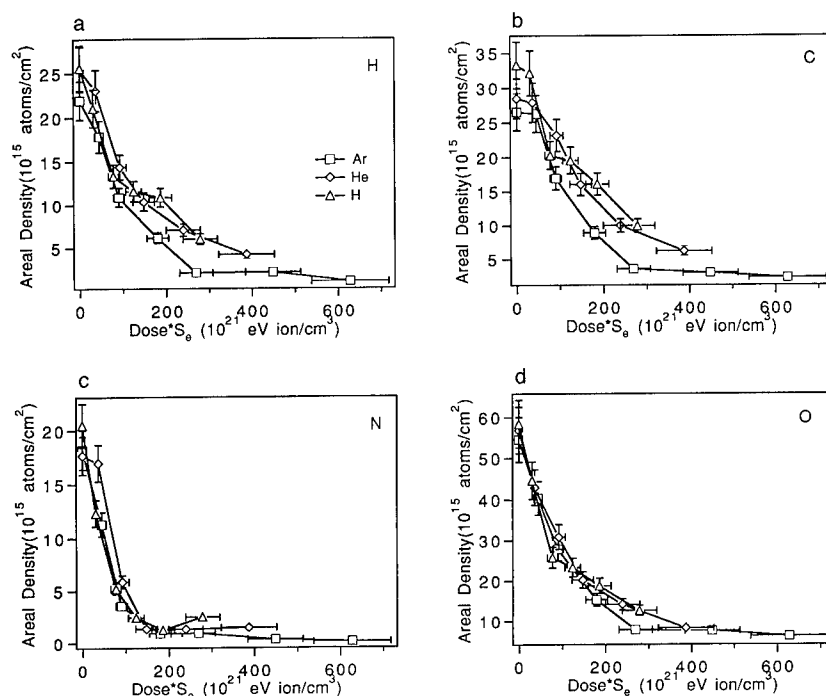


Fig. 3. (a)–(d) Change in the components H, C, N and O with the electronic energy density for Ar (\square), He (\diamond), and H (\triangle) irradiation.

linear least squares fit to the data, with uncertainties determined by counting statistics, is also shown in Fig. 1a. The observed value of χ^2 for this fit, 376.2 for 368 degrees of freedom, was typical of the results obtained for all analyses. Fig. 1b shows the individual contributions of each species to the time-of-flight spectrum in Fig. 1a. For each computed yield, the areal density was calculated based on measured values for the detector efficiency, the Lenz–Jensen recoil cross section, and the number of incident ions. The initial stoichiometry and thickness generally agree with predicted values to within the $\pm 10\%$ estimated uncertainty.

The evolution of the atomic components of the nitrocellulose film, subject to H, He, and Ar irradiation, is shown in Fig. 2 as a function of the dose. The data for C exhibits a rate of removal between those for He and Ar but are omitted from the graphs in order to simplify presentation and because of a smaller initial sample thickness. Not unexpectedly, the removal rate increases with the mass of the incident ion. It is important to note that the ions used in erosion differ greatly in both their relative and absolute values of the electronic and nuclear energy loss, S_e and S_n . Using an implementation of the TRIM algorithm [9], the electronic stopping power in nitrocellulose has been calculated to be 57.9, 177, 305, and 335 eV/nm for 270 keV H, He, C, and Ar ions while the nuclear stopping is 0.055, 0.735, 13.7 and 198 eV/nm, respectively. Studies of the ion beam modification of polymers other than nitrocellulose have suggested that electronic excitations alter the chemical structure creating ionized molecules, collective excitations, and highly excited species [10]. Fig 3 shows the variation of H, C, N, and O with the product of dose and electronic energy loss. While a scaling with the total deposited energy may not be ruled out completely, the overlap of the N and O curves suggests that the density of electronic energy deposition is a key parameter influencing the desorption of these components. From the basic structure of the nitrocellulose repeat unit, shown in Fig. 4, a

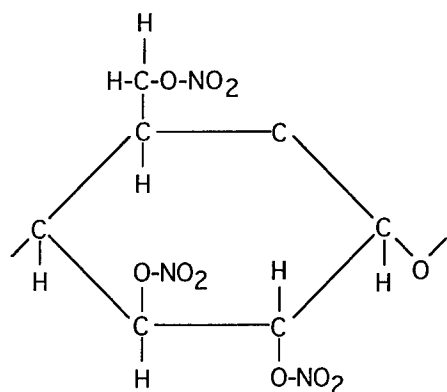


Fig. 4. Chemical structural formula of the nitrocellulose.

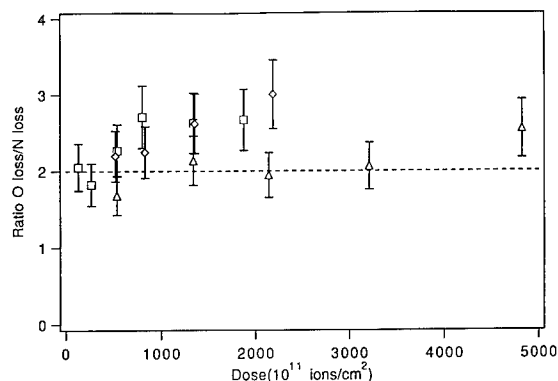


Fig. 5. Ratio of oxygen to nitrogen loss as a function of dose for Ar (\square), He (\diamond), and H (\triangle) irradiation. The dashed line indicates the ratio consistent with the stoichiometry of NO_2 .

likely path for the removal of N and O is the breaking of radical O– NO_2 bonds. It has been previously suggested that under thermal annealing, RO– NO_2 bond breaking acts as a trigger for the total decomposition of the molecule [11]. Additional evidence for this mechanism can be seen in the stoichiometry of the removal of N and O. The ratio of removed oxygen to removed nitrogen is plotted as a function of the accumulated dose in Fig. 5. For each of the incident ions, the initial ratio is consistent with the selective excision of NO_2 fragments. For H irradiation, this ratio is effectively maintained throughout the exposure and may indicate the formation of a residue.

Examination of the erosion curves in Figs. 2a and 2b shows essentially complete removal of H and C under Ar irradiation. The remaining coverage of light elements is approximately the same as that found on a clean Si wafer. This result is not inconsistent with an earlier suggestion of a threshold based on a total energy loss of 350 eV/nm for volatilization of the residue [4]. For H, He and C irradiation, a carbon-rich, oxygen-depleted layer remains, suggesting that highly cross-linked, carbon networks could be formed by the reaction between adjacent radicals. The remaining residue is nearly twice as thick after H exposure compared with similar data for He while no statistically significant difference in stoichiometry is noted. For H and He irradiation, the overlap of the plots of removed H and C in Figs. 3a and 3b may point to a common bond breaking mechanism also based on electronic excitation. The H and C curves for Ar irradiation appear to overlap initially but decrease quickly as the film is removed. An additional mechanism is needed to explain the removal of the residue by Ar. As evidenced by the large difference in nuclear stopping between Ar and H or He, binary collisions could likely play a key role. Using the empirical formula of Matsunami et al. [12], comparative estimates of sputtering yields for carbon by 270 keV Ar, He, and H are 0.72, 0.002, and 9.7×10^{-5} atoms/ion, respectively.

Given that roughly 5×10^{15} atoms/cm² of carbon remain after He erosion, an exposure equal to the accumulated Ar dose, $\sim 2 \times 10^{14}$ ions/cm², could not remove this residue. Hence, simple differences in physical sputtering appear inadequate to explain complete removal of the film by Ar given the residue left by He. It appears more likely that a desorption mechanism incorporating collisional sputtering would proceed in conjunction with the bond breaking generated by electronic excitations rather than after the formation of a residue.

4. Conclusion

Medium energy time-of-flight elastic recoil detection has been applied in the study of the real-time evolution of the atomic composition of nitrocellulose under H, He, C, and Ar ion irradiation. The technique has been shown to be a useful tool for the study of these radiation sensitive materials. The initial stoichiometry of desorbed N and O is consistent with a reaction involving the breakage of RO–NO₂ bonds. Good correlation is obtained between the removal of N and O and the electronic energy loss under all irradiation conditions. Removal of H and C show a similar scaling for H and He ions but differs for Ar because of the complete removal of the residue. The larger number of binary collisions experienced by Ar ions, as indicated by the higher nuclear stopping power and sputtering yield, is probably responsible for this observed behavior.

Acknowledgments

This work was supported in part by the U.S. Army Research Office under contract DAAL 03-92-G-0037.

References

- [1] M.W. Geis, J.N. Randall, T.F. Deutsch, N.N. Efremow, J.P. Donnelly and J.D. Woodhouse, *J. Vac. Sci. Technol.* 3 (1985) 343.
- [2] H. Kaneko, Y. Yasuoka, K. Gamo and S. Namba, *Jpn. J. Appl. Phys.* 28 (1989) 716.
- [3] H. Kaneko, Y. Yasuoka, K. Gamo and S. Namba, *Jpn. J. Appl. Phys.* 28 (1989) 1113.
- [4] R. Mühle and G. Götz, *Nucl. Instr. and Meth. B* 46 (1990) 347.
- [5] J.P. Moliton, T. Triguad and A. Moliton, *Nucl. Instr. and Meth. B* 65 (1992) 428.
- [6] L. Merhari, J.P. Moliton, and C. Belorgeot, *J. Appl. Phys.* 68 (1990) 4837.
- [7] M.H. Mendenhall and R.A. Weller, *Nucl. Instr. and Meth. B* 40/41 (1989) 1239.
- [8] J.H. Arps and R.A. Weller, *Nucl. Instr. and Meth. B* 79 (1993) 539.
- [9] J.P. Biersack and L.G. Haggmark, *Nucl. Instr. and Meth.* 147 (1980) 257.
- [10] G. Marletta, *Nucl. Instr. and Meth. B* 46 (1990) 295.
- [11] H. Kaneko, Y. Yasuoka, K. Gamo and S. Namba, *J. Vac. Sci. Technol B* 1 (1989) 1778.
- [12] N. Matsunami et al., *Atom. Data Nucl. Data Tables* 31 (1984) 1.



ELSEVIER

Accurate calculation of atomic resonances near surfaces

Stefan A. Deutscher^{a,b,*}, Xiazhou Yang^{a,b}, Joachim Burgdörfer^{a,b}

^a University of Tennessee, Department of Physics, A.H. Nielsen Bldg. 401, Knoxville, TN 37996, USA

^b Oak Ridge National Laboratory, Oak Ridge, TN 37831, USA

Abstract

We present first results of new accurate calculations for atomic resonances near an Al surface. We employ large-scale matrix diagonalization involving ≥ 1000 basis states and realistic effective single-particle potentials. We implement two complementary techniques – the complex rotation method and the stabilization method. We also investigate strongly perturbed atomic wave functions near the surface and relate their evolution as a function of the distance, d , to the Wigner–von-Neumann non-crossing rule. The distance dependence of the resonance parameters can be analyzed in terms of semiclassical mechanics.

1. Introduction

Resonant charge exchange between metal surfaces and ions plays an important role in many surface-diagnostic methods such as Auger electron spectroscopy (AES), ion neutralization spectroscopy (INS), and secondary ion mass spectrometry (SIMS), as well as for emerging technological applications (e.g. surface catalysis, thin film growth, and molecular beam epitaxy (MBE)).

On a fundamental level, the interaction of multiply charged ions (MCI) with surfaces has become the focus of interest in the field of atomic physics in strong Coulomb fields. Neutralization and relaxation of MCI represent an intriguing many-body problem which involves transitions of a large number of “active” electrons and leads to the dissipation of large amounts of potential energy (typically ~ 1 keV). The understanding of the MCI–surface interaction requires detailed information on the behaviour of atomic resonances near and at surfaces. Both positions and widths of atomic resonances provide the input for coupled-states calculations for inelastic processes near metal surfaces [1].

We have implemented two complementary methods for the calculation of resonances. First, we use the method of complex scaling [2–6] which provides an efficient tool for calculating complex eigenenergies (positions and widths) of atomic resonances. Second, the recently developed stabilization method [7,8] allows the direct determination of the resonant wave function, i.e. the local density of states, and permits larger basis sizes since the calculation is performed on the real axis.

In the following progress report we present first benchmark calculations for the simple system of hydrogen near an aluminium surface. Applications to other systems are in progress. Atomic units are used throughout unless stated otherwise.

2. Model

We consider a hydrogenic ion in front of a metal surface. The Hamiltonian \hat{H} of the problem reads

$$\hat{H} = -\frac{\hbar^2}{2m}\hat{\Delta} + \hat{V}(\mathbf{r}, d), \quad (1)$$

where the potential

$$V(\mathbf{r}, d) = V^A(\mathbf{r}) + V^{\text{surf}}(\mathbf{r}, d) \quad (2)$$

consists of the atomic core potential $V^A(\mathbf{r})$, and of additional contributions $V^{\text{surf}}(\mathbf{r}, d)$ due to the presence of the surface. The core potential for hydrogenic atoms with atomic number Z is a Coulomb potential $-Z/r$. The surface potential of a metal reads

$$V^{\text{surf}}(\mathbf{r}, d) = V_p^{\text{SI}}(d) + V_e^{\text{SI}}(\mathbf{r}) + V_{\text{pe}}^{\text{I}}(\mathbf{r}, d). \quad (3)$$

For the self-image interaction of the electron, V_e^{SI} , we use an accurate numerical fit to test-functions of the model potential proposed by Jennings, Jones, and Weinert [9]. It reproduces the self-consistent LDA calculation of Kohn and Lang [10] near and inside the surface (apart from the Friedel oscillations) while giving the correct asymptotic behaviour

$$\lim_{d \rightarrow \infty} V_e^{\text{SI}}(\mathbf{r}) = -\frac{1}{4z}, \quad (4)$$

* Corresponding author, tel. +1 615 974 7838, fax +1 615 974 7843, E-mail: sad@utkux.utk.edu.

where d is the distance from the surface. The potential contains only three parameters which reflect the properties of the metal; the saturation or bulk value of the potential, U_0 , the width of the interface region, λ , and the image plane position, z_0 , which for aluminium ($r_s = 2.07$) was found to be located at 0.70 a.u. in front of the surface. For the interaction potential between the electron and the ionic image V_{pe}^I , we apply the dynamical response formulation of de Abajo and Echenique [11], and derive the zero velocity limit using the plasmon–pole approximation with dispersion. This approach avoids the well-known difficulties with the singular behaviour of V_{pe}^I near the surface [6], and reproduces the correct asymptotic limit as $d \rightarrow \infty$,

$$V_{pe}^I(r, d) = \frac{Z}{\sqrt{(z+d)^2 + \rho^2}}. \quad (5)$$

The first term in Eq. (3) describes the interaction of the ion with its own image and equals at large distances $V_I^{SI}(d) = -Z^2/(4d)$. It will not be taken into account in the following since in the quasistatic limit the energy positions and widths do not depend on this interaction. It plays, however, a crucial role for the image acceleration of the projectile and, hence, for the scattering dynamics [14].

3. Method

In order to obtain positions and widths of these resonances we solve the eigenvalue problem

$$\hat{H}|\psi\rangle = E|\psi\rangle, \quad (6)$$

where \hat{H} is the Hamiltonian of the problem, E the (possibly complex) eigenenergy and $|\psi\rangle$ the corresponding eigenstate. We carry out a large-scale basis expansion to convert Eq. (6) into an N dimensional matrix equation yielding a set of energy eigenvalues $\{E_k\}_1^N$. Hydrogenic basis functions are not well-suited as their continuum part is not square-integrable. To circumvent this problem we choose an expansion in terms of Sturmian functions which give a good description of both bound and continuum states while remaining complete and square-integrable

$$\Phi_{n,l,m}^{(\sigma)}(r, \theta, \phi) = \frac{1}{r} S_{n,l}^{(\sigma)}(r) Y_l^m(\theta, \phi), \quad (7)$$

where $S_{n,l}^{(\sigma)}(r)$ are the Coulomb–Sturmian functions given in coordinate representation by

$$S_{n,l}^{(\sigma)}(r) = h_{n,l} e^{-\sigma r} (2\sigma r)^{l+1} L_n^{(2l+1)}(2\sigma r), \quad (8)$$

where

$$h_{n,l} = \sqrt{\frac{n!}{(n+2l+1)!}}, \quad \text{and } n, l = 0, 1, \dots \quad (9)$$

They contain the Sturmian parameter σ which allows for variational optimization. n , l , and m represent the radial,

angular momentum, and magnetic quantum numbers, respectively, Y_l^m the surface spherical harmonics, and $L_n^{(\alpha)}$ denotes the generalized Laguerre polynomials. The basis states (Eq. (7)) form a non-orthogonal basis set which results in a generalized eigenvalue problem. The matrix elements can be expressed analytically with exception of $\langle i | \hat{V}^{\text{surf}} | j \rangle$ which must be computed numerically. Within the method of complex coordinate rotation we use up to 1000 basis states. The stabilization method allows considerably larger basis sizes (we use up to 4000). The standard complex rotation method [1–6] consists of the canonical transformation in the complex plane

$$\begin{aligned} r &\rightarrow r e^{i\Theta}, \\ p &\rightarrow p e^{-i\Theta}. \end{aligned} \quad (10)$$

It converts resonant wave functions into square-integrable functions by effectively projecting out the P space (continuum space) portion of the wave function. Consequently, the Hamiltonian becomes dependent on Θ :

$$\hat{H}(r, p) \rightarrow \hat{H}(r, p, \Theta) = -\frac{\hbar^2}{2m} e^{-2i\Theta} \hat{\Delta} + \hat{V}(r e^{i\Theta}). \quad (11)$$

Converged resonances are characterized by the stability of the complex eigenvalue E with respect to the rotation angle Θ , the Sturmian parameter σ , and the basis size N . The analytic continuation of the potential $\hat{V}(r e^{i\Theta})$ into the complex plane is explicitly known only in simple cases. For realistic potentials we adopt the “passive” rather than the “active” complex rotation, rotating the wave function $\Phi_{n,l,m}^{(\sigma)}(r e^{-i\Theta})$ rather than the Hamiltonian. The price to pay for complex rotation is that the physical interpretation of the resonant wave function is less obvious.

An attractive, alternative method [7,8] recently developed uses the fact that stabilization diagrams, well-known as a tool for the determination of the positions of resonances, can also reveal information on their widths. One advantage is that the calculation proceeds on the real axis. The spectral density of resonances (the Feshbach Q space complement) is given by

$$\rho^Q(E) = -\frac{1}{\pi} \Im \left(\sum_k \frac{1}{(E - E_k) + i\Gamma_k} \right), \quad (12)$$

with $E_k - i\Gamma_k$ as the complex poles of the Green’s function. $\rho^Q(E)$ can be calculated by repeated diagonalization of Eq. (6) on the real axis (i.e. $\Theta = 0$) for a range of σ between σ_{\min} and σ_{\max} . The spectral density follows from

$$\rho^Q(E) = -\frac{1}{\sigma_{\max} - \sigma_{\min}} \int_{\sigma_{\min}}^{\sigma_{\max}} d\sigma \rho_\sigma(E), \quad (13)$$

where

$$\rho_\sigma(E) = \sum_j \delta(E_j(\sigma) - E). \quad (14)$$

Eq. (13) is now readily evaluated as

$$\rho^Q(E) = -\frac{1}{\sigma_{\max} - \sigma_{\min}} \sum_j \left| \frac{dE_j(\sigma)}{d\sigma} \right|_{E_j(\sigma)=E}^{-1} \quad (15)$$

Thus $\rho^Q(E)$ can be obtained by binning all energies $E_j(\sigma)$ for $\sigma_{\min} \leq \sigma \leq \sigma_{\max}$ into a histogram and then fitting a smooth function. Fig. 1 displays a typical stabilization diagram for hydrogen in front of an aluminium surface. The resulting histogram from which the spectral density $\rho^Q(E)$ can be determined is shown in Fig. 2. Eq. (15) can be visualized as a projection of the line density of the stabilization diagram onto the energy axis. From the fit of the “raw” spectrum of Eq. (15) to a sum over Lorentzian lines, both positions and widths can be extracted with high accuracy. Moreover, the structure of the resonant wave functions can be directly determined. The local spectral density of the corresponding resonance wave function $|\Psi_k^Q(\mathbf{r}; E_k)|^2$ at the energy E_k is analogous to Eq. (15) given by

$$|\Psi_k^Q(\mathbf{r}; E_k)|^2 = \frac{1}{\sigma_{\max} - \sigma_{\min}} \sum_j |\psi_j(\mathbf{r}, \sigma)|^2 \left| \frac{dE_j(\sigma)}{d\sigma} \right|_{E_j(\sigma)=E_k}^{-1} \quad (16)$$

The local spectral density assists in the physical interpretation of the properties of the shape and Feshbach resonances.

4. Result

The level positions and widths calculated as outlined above show the same qualitative behaviour that has previ-

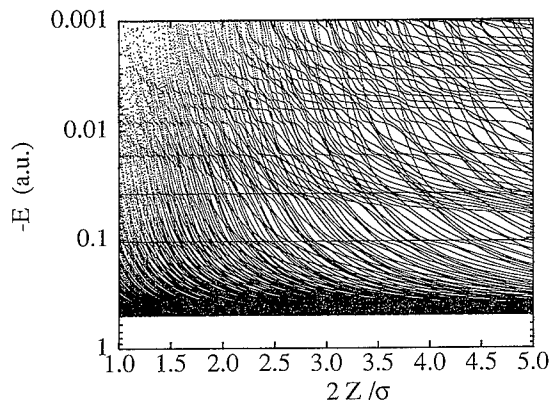


Fig. 1. The figure shows a typical stabilization diagram for a hydrogen atom at $d = 11$ a.u. in front of an aluminium ($r_s = 2.07$) surface. Here, E is the energy and σ the Sturmian parameter. Note the stabilized horizontal “lines” which correspond to resonances (e.g. near $E = -0.1$ a.u. for $n = 2$). Resonances up to $n = 8$ can be clearly distinguished.

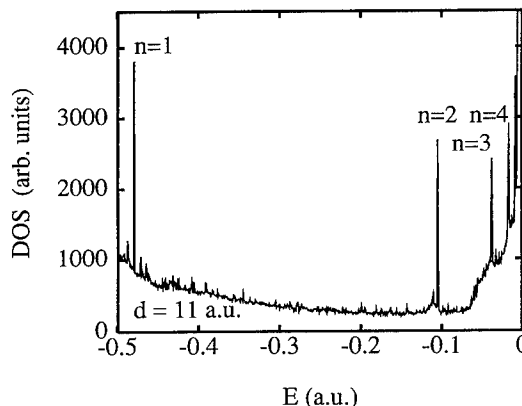


Fig. 2. Density of states (DOS) extracted from the data shown in Fig. 1. Here, n denotes the principal quantum number. For $n = 2$ the two parabolic substates can be distinguished. Note the obvious difference of their respective widths which is explained in the text.

ously been obtained by means of complex rotation [6] and by means of the nonperturbative coupled angular mode (CAM) method [12] if the same surface potentials are used. Differences due to the use of other, more realistic potentials are more pronounced for the ground state ($n = 1$) than for excited states ($n \geq 2$) and will be discussed in detail elsewhere [13]. We focus in the following on the behaviour of the wave functions.

As pointed out previously [14], the classical dynamics near the top of the barrier is crucial for the structure of resonances and for the charge transfer process. Properties of the classical phase space structure are reflected in the wave functions. Figs. 3 and 4 show the resonant $n = 2$ wave functions from the $m = 0$ subspace near the surface. At large distances when both states form narrow thick-barrier resonances, they closely resemble parabolic states of hydrogen (Fig. 3). As soon as the energy level lies in the vicinity of the saddle point of the potential barrier, resonances undergo structural changes which are reflected in the shape of the wave function, as well as in the position and width of the resonance. The “up-hill” resonance, pointing away from the surface, maintains its approximate parabolic character well above the saddle point energy and the continuum part of the wave function (the leakage current) is small (Fig. 4). This is because the inner classical turning point of the corresponding orbit lies far away from the saddle. Consequently, a fast over-barrier transition, while energetically possible, remains dynamically blocked. Therefore, narrow, high-lying resonances exist close to the surface. In contrast, as soon as the “downhill” resonance, facing the surface, touches the saddle, the resonant wave function experiences a morphological change and the delocalized continuum part represents a significant fraction of the wave function. In other words, the electron undergoes “over-barrier transitions”. Nevertheless, the resonance can be clearly identified even in the

over-barrier region. Its destruction (i.e. promotion to the smooth continuum) can be related to the semiclassical dynamics of over-barrier reflections [13]. It is closely related to the “avoided crossings” of resonances in the complex plane. Unlike proper bound states, resonances of the same exact symmetry do not satisfy the Wigner–von-Neumann non-crossing rule. Curves of the positions of resonances $E_k(d)$ as a function of the distance, d , from the surface can therefore cross. A generalization of the Wigner–von-Neumann non-crossing rule can be derived

for the complex energy plane [15]. Typically, the trajectories of resonance energies avoid “collisions” in the complex plane. Fig. 5 illustrates the trajectories for the $n = 2$ resonances with d as the continuous parameter. While the position curves (projection of $E_{1,2}(d)$ onto the real axis) cross, the trajectories in the complex plane do not since the widths repel each other. Extension to higher n shells shows [13] that the suppression of “collisions” in the complex plane is generic. The point to be noted is that collisions imply the coalescence of complex eigenenergies

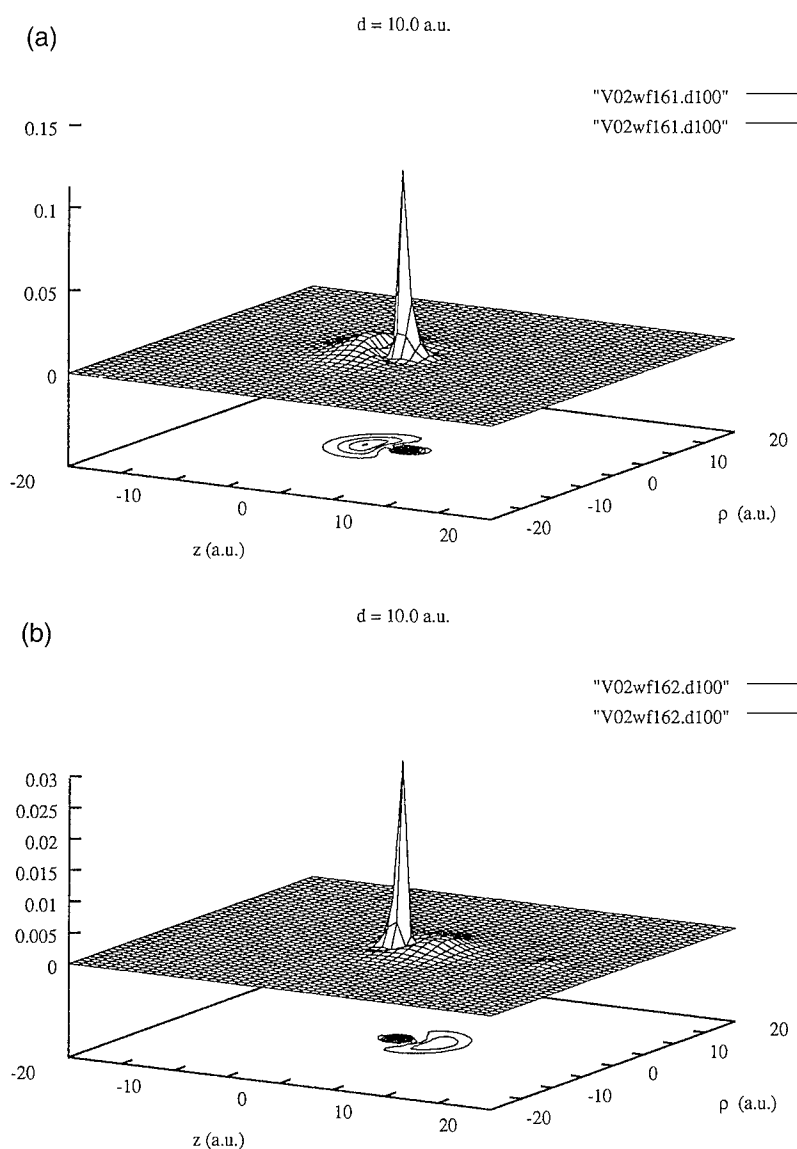


Fig. 3. The behaviour of the two $n = 2, m = 0$ wave functions at a distance of $d = 10$ a.u. Both wave functions closely resemble parabolic states. The resonance pointing away from the surface (a) is nearly unperturbed whereas the one pointing towards the surface (b) shows already a very small leakage current. The surface is located at $z = d$ parallel to the ρ and perpendicular to the z axis, respectively. The origin was chosen to be the position of the hydrogenic ion.

for a given d . Crossings of trajectories belonging to different parameter values, d , are however possible.

5. Conclusions

We have presented first results on atomic resonances near the surface employing a new stabilization technique.

It allows the detailed analysis of the structure of these resonances. A close correspondence to the classical over-the-barrier dynamics can be established. This correspondence is of crucial importance for highly charged ion surface interactions and for the behaviour of resonances very close to the surface at distances d smaller than the orbital radius, $d \leq \langle r \rangle$.

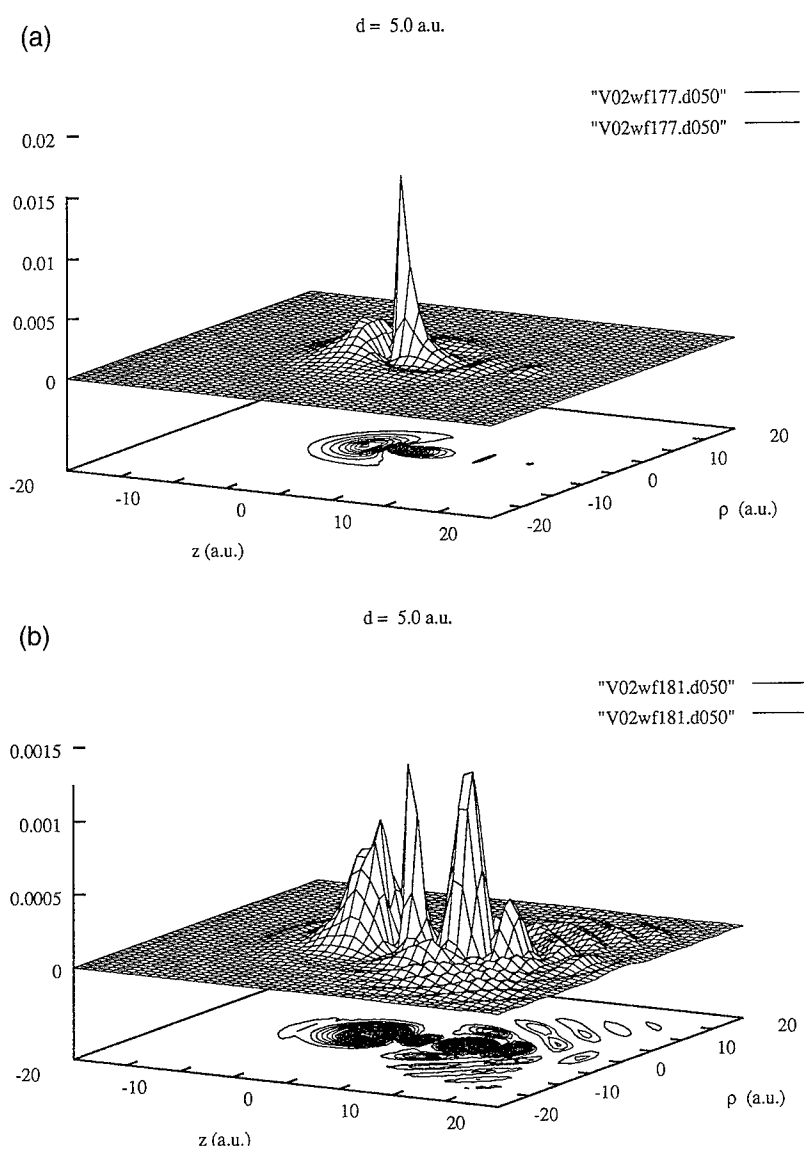


Fig. 4. The behaviour of the $n=2, m=0$ wave functions at a distance of $d=5$ a.u. The resonance pointing away from the surface (a) shows already a noticeable leakage current while still somewhat resembling a parabolic state. The other resonance (b) pointing towards the surface, however shows a significant leakage and shows already characteristics of a spherical wave function.

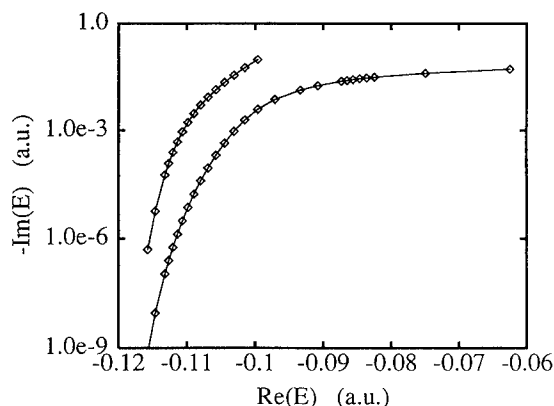


Fig. 5. Trajectory of the $n=2$ resonances in the complex energy plane. $\text{Re}(E)$ and $\text{Im}(E)$ denote the real and imaginary parts of the complex eigenenergy obtained with complex rotation. The figure shows that in accordance with the Wigner–von-Neumann non-crossing rule, generalized as outlined in the text, the $n=2$, $m=0$ states do *not* cross. The diamonds correspond to different distances d of the hydrogen atom from the aluminium surface ranging from 24 to 5 or 0.5 a.u., respectively.

Acknowledgements

We would like to thank Lars Anderson, Carlos Reinhold, and Jörg Müller for many helpful discussions. Work supported by US Department of Energy, Office of Basic Energy Sciences, Division of Chemical Sciences, under contract no. DE-AC05-84OR21400 with Martin Marietta Energy Systems, Inc.

References

- [1] J. Burgdörfer, in: Review of Fundamental Processes and Applications of Atoms and Ions, ed. C.D. Lin (World Scientific, Singapore, p. 517.
- [2] E. Baslev and J.M. Combes, *Commun. Math. Phys.* 22 (1971) 280.
- [3] W. Reinhardt, *Ann. Phys. Rev. Chem.* 33 (1982) 232.
- [4] B.R. Junker, in: Advances in atomic and molecular physics, eds. D. Bates and B. Bederson (Academic Press, New York, 1982) p. 208.
- [5] Y.K. Ho, *Phys. Rep.* 99 (1983) 1.
- [6] P. Nordlander and J.C. Tully, *Phys. Rev. Lett.* 61 (1988) 990; *Surf. Sci.* 211/212 (1989) 207; *Phys. Rev. B* 42 (1990) 5564.
- [7] V.A. Mandelshtam, T.R. Ravuri and H.S. Taylor, *Phys. Rev. Lett.* 70 (1993) 1932.
- [8] J. Müller, X. Yang and J. Burgdörfer, *Phys. Rev. A* 49 (1994) 2470.
- [9] P.J. Jennings, R.O. Jones and M. Weinert, *Phys. Rev. B* 37 (1988) 6113.
- [10] N.D. Lang and W. Kohn, *Phys. Rev. B* 1 (1970) 4555.
- [11] F.J. García de Abajo and P.M. Echenique, *Phys. Rev. B* 46 (1992) 2663; F.J. García de Abajo, Dissertation, The University of the Basque Country, San Sebastián, Spain (1993).
- [12] A.G. Borisov, D. Teillet-Billy and J.P. Gauyacq, *Nucl. Instr. and Meth. B* 37 (1993) 49.
- [13] S.A. Deutscher, X. Yang and J. Burgdörfer, to be published (1994).
- [14] J. Burgdörfer, P. Lerner and F.W. Meyer, *Phys. Rev. A* 44 (1991) 5674; J. Burgdörfer and F.W. Meyer, *Phys. Rev. A* 47 (1993) 1220.
- [15] J. Burgdörfer, X. Yang and J. Müller, in: Chaos, Solitons and Fractals (in press, 1994).



ELSEVIER

Singlet levels of an He atom interacting with an Al surface: Interaction between quasi stationary states in the $n = 2-6$ manifolds

G.E. Makhmetov^b, A.G. Borisov^{a,b}, D. Teillet-Billy^a, J.P. Gauyacq^{a,*}

^a *Laboratoire des Collisions Atomiques et Moléculaires (unité de recherches associée au CNRS 281), Université de Paris-Sud, Bât. 351, 91405 Orsay Cedex, France*

^b *Physics Department, Chair of Physical Electronics, Moscow State University, Moscow 119 899, Russian Federation*

Abstract

The excited singlet states ($n = 2-6$) of He atoms interacting with an aluminum surface are studied with the Coupled Angular Mode (CAM) method, which provides their energy positions and widths as functions of the atom–surface distance. The results show very strong couplings between the various states inside each manifold, induced both by direct couplings and indirect couplings via the metal states. These couplings can lead to an attraction as well as to a repulsion of the interacting states. The state mixing results in the formation of hybrids with a rather small width.

1. Introduction

The modification of atomic levels due to their interaction with a metal surface has been the subject of numerous studies, in particular in the context of atom–surface charge transfer studies. Indeed, due to the interaction with a neighbouring metal surface, the atomic level energies are shifted from their value for the free atom and they acquire a finite lifetime (see e.g. the reviews on the charge transfer process [1]). Since a few years, non perturbative methods (complex scaling [2] and Coupled Angular Mode methods, CAM [3]) are available, they enable quantitative studies of these problems and were applied to a few different physical problems.

In the present work, we report on a study of singlet excited states of helium interacting with an Al surface, performed with the Coupled Angular Mode method. This work was initiated for the study of He^{*} (2^1S) conversion to the He^{*} (2^3S) state via resonant ionization of the He^{*} atom [4]. The study of the 2^1S level revealed unexpected features [5] which motivated a further study of the higher excited He states. It revealed the existence of important interactions between the states inside the $n = 2$ manifold, which, surprisingly, lead to an attraction between the levels [5]. Here, we report on a further study of this problem in the $n = 3-6$ singlet manifolds of helium.

2. Coupled angular mode (CAM) method

The method will be only briefly outlined here, it has been presented with more details elsewhere [3]. It consists in studying the electron scattering by a compound system formed by the superposition of the metal surface and the atom. The e[−]–surface interaction is represented by a local potential, a function only of z , the e[−]–surface distance and taken from the work of Jennings et al. [6] The e[−]–atom interaction is represented by a model potential taken from the work of Aymar and Crance [7]. The electron scattering by the compound potential is studied in the spherical harmonics basis centered around the atom. The axis going through the atomic center and perpendicular to the surface is a symmetry axis and as a result, m , the projection of the electron angular momentum on this axis is a good quantum number. Looking at the scattering properties of the electron for negative energies (i.e. below the vacuum level) reveals the existence of resonances, which are associated with the atomic levels, perturbed by the surface. The analysis of this resonant scattering in terms of the time delay matrix yields the energy position and the width of the atomic levels. In the present study, where a few resonances are found to overlap, the analysis was performed by fitting the sum of the eigenvalues of the time delay matrix [8], a function of the collision energy, to a sum of Lorentzian profiles [9]. The CAM method is well suited to determine the level characteristics for atoms (or molecules) interacting with metal surfaces. It has been applied successfully to a few different physical situations: charge transfer in atom–surface interactions [3], dynamical resonant charge transfer in fast grazing collisions [10],

* Corresponding author, tel. +33 1 6941 7863, fax +33 1 6941 7671, E-mail: gauyacq@lcam.u-psud.fr.

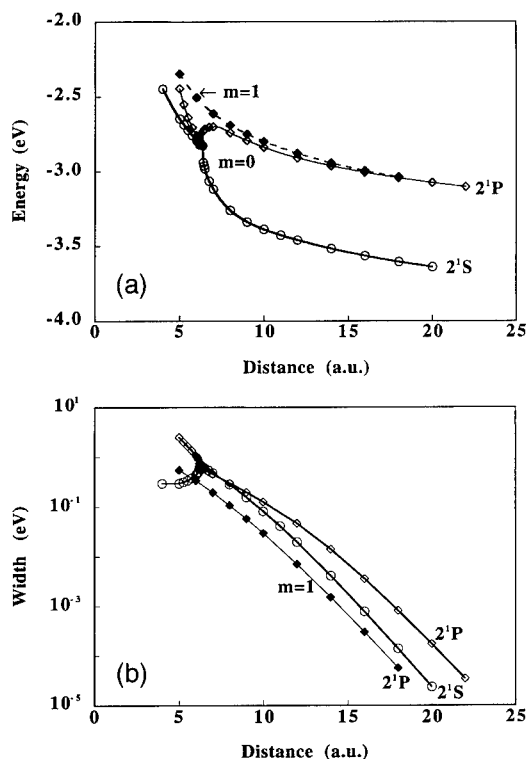


Fig. 1. (a) Energy of the helium atom singlet levels ($n=2$ manifold) in front of an Al surface, as function of the atom-surface distance, measured from the image reference plane. Open circles: level correlated at infinity with the 2^1S level. Open and closed diamonds: levels correlated at infinity with the 2^1P level ($m=0$ and $m=\pm 1$ resp.). (b) Width of the helium atom singlet levels ($n=2$ manifold) in front of an Al surface, as function of the atom-surface distance. Same symbols as in (a).

open shell systems [11], deexcitation of excited states via a charge transfer [12], resonant vibrational excitation of adsorbed molecules by electron impact [13]. Its results have also been shown to agree with those of another, independent, non perturbative method, the complex scaling method [2,14].

3. Results and discussion

3.1. ($n=2$) singlet He manifold

We will first look at the He ($n=2$) manifold which presents the most striking features. Figs. 1a and 1b present the positions and widths of the 2^1S and 2^1P He levels in front of an Al surface as a function of the atom-surface distance Z (The distance is measured from the image reference plane). The 2^1S and 2^1P ($m=0$) level energies are found to come very close one to the other in a rather drastic variation, to coalesce and then split. The level

splitting is associated with the creation of two mixed states (hybrids) with very different widths. The most stable level appears to have a width which decreases when the atom-surface distance decreases. In the coalescence region, it is difficult to follow one precise state. For drawing the Fig. 1, we assumed that the correlation was done following the ordering of the real part of the energy. For comparison, Figs. 1a and 1b also present the results for the 2^1P ($m=1$) level which cannot mix inside the $n=2$ manifold. It presents the usual smooth behaviour: its energy increases when Z decreases due to the image charge interaction and its width steadily increases when Z decreases.

This structure has been interpreted [5] as due to an interaction between the two ($m=0$) states of the ($n=2$) manifold. However, although a “usual” coupling corresponding to a hermitian operator leads to a splitting between the states, in the present case, it leads to an attraction of the levels. The interaction responsible for this effect is complex and corresponds to transitions between the 2^1S and 2^1P levels via the continuum. As shown by Devdariani et al. [15], the usual derivation of the Local Complex Potential Approximation leads, in the case of two interacting quasistationary states, to the following 2×2 reduced Hamiltonian in the basis of the two quasistationary states:

$$H = \begin{pmatrix} E_1 - i\frac{\Gamma_1}{2} & V - \frac{i}{2}\sqrt{\Gamma_1\Gamma_2} \\ V - \frac{i}{2}\sqrt{\Gamma_1\Gamma_2} & E_2 - i\frac{\Gamma_2}{2} \end{pmatrix}, \quad (1)$$

where the diagonal terms are the complex energies of the quasistationary states and V is a direct coupling between the two states. The non-Hermitian complex coupling terms corresponds to an interaction between the two states via the continuum. This coupling has this form if the two quasistationary states interact with the same continuum. This reduced Hamiltonian was derived in the context of model semiclassical studies of interacting quasistationary states. The diagonalization of the above Hamiltonian, depending on the energy distance between the two states and on the relative importance of the direct and indirect couplings, leads to an attraction or a repulsion of the two states. For the ($n=2$, $m=0$) manifold, it was shown [5] that this reduced Hamiltonian can effectively model the CAM results. Model studies with the Hamiltonian (1) shows that the situation displayed on Fig. 1 with a coalescence of the two states is rather peculiar and require a special set of terms in Eq. (1). It is also noteworthy that the mixing between the s and p levels shown on Fig. 1 is quite different from the mixing found in studies of the H ($n=2$) manifold [2,14]. Indeed, the H levels are degenerate at infinity and very close one from the other at finite Z distances and this changes the character of the hybrid formation (see the discussion in Ref. [5]), compared to the present situation where the 2^1S and 2^1P levels are well separated in energy.

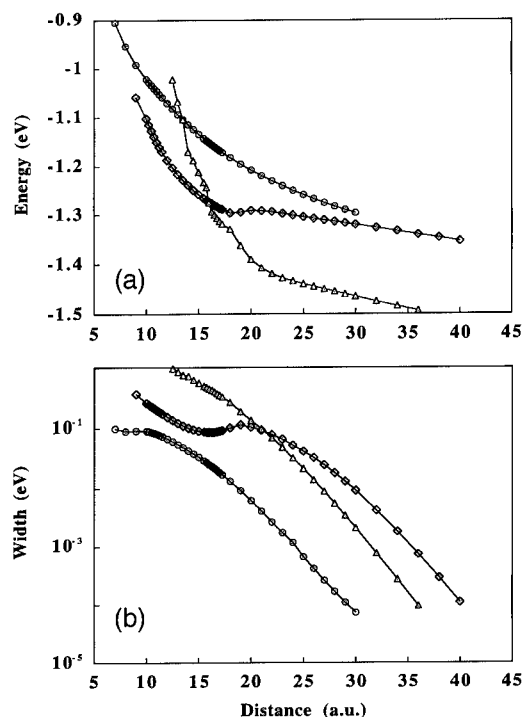


Fig. 2. (a) Energy of the helium atom singlet levels ($m=0$, $n=3$ manifold) in front of an Al surface, as function of the atom-surface distance, measured from the image reference plane. Open triangles: level correlated at infinity with the 3^1S level; open diamonds: level correlated at infinity with the 3^1D level; open circles: level correlated at infinity with the 3^1P level. (b) Width of the helium atom singlet levels ($m=0$, $n=3$ manifold) in front of an Al surface, as function of the atom-surface distance. Same symbols as in (a).

The feature discussed above should be rather general and could appear in any atomic system with nondegenerate levels. Indeed, indications of attractions, however without coalescence of the levels can be found in other systems: alkali atoms interacting with an aluminum surface [16], the triplet levels of He in front of a Cu(100) surface [17].

3.2. ($n=3$) singlet He manifold

Figs. 2a and 2b present the results for the positions and widths of the $m=0$ states of the ($n=3$) He manifold (singlet levels). At small and large Z the calculations were stopped when the width was becoming too large or too small to be easily obtained with the CAM method. The Z variation of the levels is less drastic than the one seen in Fig. 1 however, one can recognize variations similar to the ones present in Fig. 1. First at large Z , the 3^1P and 3^1D levels are almost degenerate (the coupling between them is much larger than their energy separation), so that the hybrid formation is similar to that for the H atom. The p and d levels mix to form two levels with very different

widths (two orders of magnitude of difference). The hybrids can be interpreted in the same way as for H: the hybrid pointing toward the surface has the largest width and the smaller energy. At smaller Z distances ($16\text{--}19 a_0$), one can recognize an interaction between the two lowest levels; they present an attraction and, at small Z , this leads to two hybrids with very different widths. At even smaller Z , all the levels are mixed, leading to the existence of a hybrid with a rather moderate width, much smaller than the one that can be extrapolated from the large Z almost exponential behaviour. The width of this hybrid is also not varying much with the atom-surface distance. As for the other two hybrids in the ($n=3$) manifold, at small Z , they have large widths (in the few eV range), the determination of their characteristics by the CAM method is not accurate and they cannot really be considered as quasistationary states anymore). The global result is then that as Z decreases, the hybridization results in the formation of a state with a moderate width which is the only one to survive as a quasistationary state.

3.3. Higher manifolds

The above result was further checked by studying the higher lying ($m=0$) singlet states of He for a rather small atom-surface distance: $Z=7a_0$. For this distance, one can think that the mixing between the states inside the ($n>3$) manifolds is rather important and that hybrids are formed. Indeed, the higher the principal quantum number n of the manifold is, the larger is the Z distance where the hybrids form. As a result, we only find a limited number of levels, rather narrow; all the other hybrids formed in each manifold being too broad to be accurately located by the CAM method. The positions and widths of these hybrids are shown in Figs. 3a and 3b as functions of n . The $n=2$ results in Fig. 3 might look a little bit out of the trend shown by the others. This should be due to the fact that $Z=7a_0$ is not such a small distance for the ($n=2$) manifold and hybrids are not yet completely formed; in particular the width of the ($n=2$) most stable hybrid is decreasing when Z decreases (see Fig. 1).

A few remarks can be made on the results of Figs. 3a and 3b.

(i) As n increases, the width of the level decreases. The decrease roughly follows a n^{-2} variation. This is rather surprising, and at least, it is contrary to what is found at large atom-surface distances. Indeed for large Z , the higher n is, the larger the spatial extension of the atomic orbital is, the more efficiently it couples with the metal states and hence, the larger the level width is. Here the hybridization is able to reverse this effect. A possible explanation is that, in the higher n manifolds there are more states to be mixed and hence an increased flexibility for forming stable hybrids. This trend was already observed in the case of degenerate levels in the study of the $n=2, 3$ manifold in the H/Al system [16].

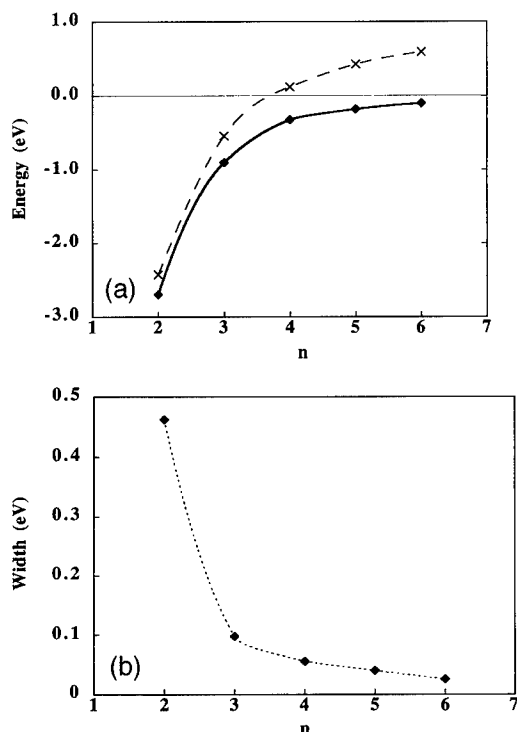


Fig. 3. (a) Energy of the most narrow ($m=0$) hybrid of each n manifold of helium singlet levels (black diamonds). The crosses indicate the position of a hydrogenic level n simply shifted by an image charge shift. The lines are only guides for the eye. (b) Width of the most narrow ($m=0$) hybrid of each n manifold of helium singlet levels (black diamonds). The line is only a guide for the eye.

(ii) The energy of these stable hybrids are well below the usual estimates that can be made from the image charge shifts. Fig. 3a presents such an estimate for the energy, obtained as:

$$\epsilon(n) = \frac{1}{4Z} - \frac{1}{2n^2}, \quad (2)$$

i.e. a pure image shift of a hydrogenic level (this choice is motivated by the complete mixing of the levels inside a manifold). The higher level in Fig. 3a is well below this estimate (0.7 eV) and thus still at negative energies, whereas the image charge shift predicts it to be at positive energies (the $n=4$ level is already in this situation). The binding energy of these quasi-stable hybrids was found to decrease with n like n^{-3} in the $n=3$ –6 range. Levels higher than $n=6$ were not calculated; indeed, they are very close to the vacuum threshold and this makes the CAM calculation difficult. The electron scattering by the compound atom–surface system was also studied at positive energies (above the vacuum level) for this atom–surface distance. It did not reveal the existence of any state with a moderate width.

In Fig. 3, the levels are labelled according to the manifold principal quantum number. For small atom–surface distances, intermanifold interactions could play a role, in addition to the intramanifold interactions, and this would result in mixings between the stable hybrids discussed here.

4. Conclusions

We have reported on a study of the ($m=0$) singlet states of He in front of an aluminum surface. The main result is that the states are strongly mixed in front of the surface, both by a direct coupling and by an indirect coupling via the continuum of metal states. This effect is particularly important in the higher n manifolds. The result of this mixing is that at small atom–surface distances, hybrids are formed with a rather small width, much smaller than what one can expect from the large Z behaviour. One can then expect to find states with a rather long lifetime, close to the surface. The different hybrids have very different properties and then one can expect that the excited state formation will favour certain states with a given polarization. In addition, in the case of multiple electron capture by multicharged ions, this effect will favour the formation of multiply excited states with a given symmetry and hence with a given autoionization deexcitation scheme.

The state mixings should deeply influence the charge transfer process in atom–surface collisions. In most of the charge transfer studies, only one active state and one active electron are considered. Various attempts have been made to incorporate multistate and multi-electron aspects in the charge transfer approaches. In particular, they can be incorporated in the semiclassical rate equation approach by adding spin statistics factors and extra equations for the additional states. However, the present study shows the existence of strong mixing between the states and hence of non-adiabatic couplings between the atomic states in front of the metal surface. Those can indeed influence the charge transfer process and should be taken into account in dynamical studies of atomic excited states near metal surfaces.

Acknowledgement

We gratefully acknowledge the PICS program of the CNRS which made this collaborative work possible.

References

- [1] A. Nourtier, J. Phys. (Paris) 50 (1989) 311; J.J.C. Geerlings, and J. Los, Phys. Rep. 190 (1990) 133; J.P. Gauyacq, A. Borisov and D. Teillet-Billy, in: Negative Ions, ed. V. Esaulov (Cambridge University Press, 1995).

- [2] P. Nordlander, and J.C. Tully, Phys. Rev. Lett. 61 (1988) 990.
- [3] D. Teillet-Billy and J.P. Gauyacq Surf. Sci. 239 (1990) 343.
- [4] J. Lee, C. Hanrahan, J. Arias, F. Bozso, R.M. Martin and H. Metiu, Phys. Rev. Lett. 54 (1985) 1440;
B. Woratschek, W. Sesselmans, J. Küppers, G. Ertl and H. Haberland, Phys. Rev. Lett. 55 (1985) 611; 1231;
R. Hemmen and H. Conrad, Phys. Rev. Lett. 67 (1991) 1314;
H. Breiten, H. Müller and V. Kemper, Z. Phys. D 22 (1992) 563.
- [5] G.E. Makhmetov, A.G. Borisov, D. Teillet-Billy and J.P. Gauyacq, Europhys. Lett. 27 (1994) 247.
- [6] P.J. Jennings, R.O. Jones and H. Weinert, Phys. Rev. B 37 (1988) 6133.
- [7] M. Aymar and M. Crance, 1980 J. Phys. B 13 (1980) 2527.
- [8] F.T. Smith, Phys. Rev. 118 (1960) 349.
- [9] U. Fano, Phys. Rev. 124 (1961) 1866.
- [10] A.G. Borisov, D. Teillet-Billy and J.P. Gauyacq, Phys. Rev. Lett. 68 (1992) 2842.
- [11] B. Bahrim, D. Teillet-Billy and J.P. Gauyacq, Surf. Sci. 316 (1994) 189.
- [12] A.G. Borisov, D. Teillet-Billy and J.P. Gauyacq, Surf. Sci. 284 (1993) 337.
- [13] V. Djamo, D. Teillet-Billy and J.P. Gauyacq, Phys. Rev. Lett. 71 (1993) 3267.
- [14] A. Borisov, D. Teillet-Billy and J.P. Gauyacq, Nucl. Instr. and Meth. B 78 (1993) 49.
- [15] A.Z. Devdariani, V.N. Ostrovsky and Yu.N. Sebyakin, Sov. Phys. JETP 44 (1976) 477.
- [16] P. Nordlander and J.C. Tully, Phys. Rev. B 42 (1990) 5564.
- [17] F.B. Dunning, P. Nordlander and G.K. Walters, Phys. Rev. B 44 (1991) 3246.



ELSEVIER

Isotope effects in the formation of MCs^+ molecular secondary ions

Hubert Gnaser *

Fachbereich Physik and Institut für Oberflächen- und Schichtanalytik, Universität Kaiserslautern, D-67663 Kaiserslautern, Germany

Abstract

Bombardment of solid surfaces by Cs^+ ions results in the emission of molecular secondary ions of the type MCs^+ , where M stands for an element contained in the sample. Generally, these molecular species exhibit emission characteristics distinctly different from those of the atomic ions. Previous experiments ascribed this observation to the possible formation mechanism of MCs^+ ions: the association of a *neutral* M atom with a Cs^+ ion in the sputtering event. To further elucidate these formation processes, the possible influence of isotopic mass differences was investigated: the yields of MCs^+ ions sputtered from various elements ($\text{M} = \text{B}, \text{Si}, \text{Ge}, \text{and Mo}$) under 5.5 keV Cs^+ bombardment were measured as a function of the emission energy for two (or more) isotopes of any of those elements. While the atomic ions M^+ exhibit a pronounced (up to $\sim 10\%$) light-isotope enrichment in the flux which decreases with increasing energy, for MCs^+ species the isotope effects are much smaller and show a different emission-energy dependence. Above ~ 10 eV the light/heavy ratio of the MCs^+ flux tends to increase with increasing emission energy; with MCs^+ ions probing the emission of *neutral* M atoms, this finding agrees with the predictions of computer simulations which indicate a pronounced enrichment of the lighter isotope in the flux of sputtered neutral atoms at higher energies. At very low energies (< 5 eV), MCs^+ ions from Si, Ge, and Mo show an isotope fractionation similar to that of atomic ions, while the flux of BCs^+ is enriched in the heavier B isotope.

1. Introduction

It is known for some time that Cs^+ ion bombardment of surfaces produces a fair number of molecular species MCs^+ , where M stands for a sample constituent [1]. Since the yields of these ions were found [2–4] to exhibit little (or even no) dependence on sample composition (for atomic ions these variations, called matrix effect [5], have severely limited the quantification of secondary-ion mass spectrometry data), these ions are frequently utilized for analytical purposes [2–4,6,7]. The reduction (or absence) of matrix effects for those species is rationalized [2–4] by their possible formation/ionization mechanism, namely the combination of a neutral M atom with a Cs^+ ion in the sputtering event. The implanted and resputtered Cs atoms often have very high ion yields (close to unity) and, in many cases, will be present as ions at the surface [8]. Thus, under steady-state conditions the flux of MCs^+ ions will reflect (via that of M atoms) the atomic concentration of the element M. Obviously, some dependence on the actual Cs^+ yield is expected and, in fact, found experimentally [6]. Several experimental findings corroborate this proposal; among them the close similarity of the energy

spectra of Cs^+ and MCs^+ ions [9], the invariability of MCs^+ intensities under oxygen exposure [7,9], and the observation [10] that the yield of MCs^+ ions scales (quadratically) with the polarizability of the atom M, a dependence which can be reproduced theoretically by applying a suitable potential to model the interaction between the Cs^+ ion and the neutral atom M. Here, the argument was the following [10]: for the alkali ion-neutral atom interaction a potential of the form [11]

$$V(r) = Ar^{-12} - 0.5\alpha e^2 r^{-4}$$

has been applied, where r is the distance between the neutral atom and the ion, α is the polarizability of the former and A is a constant which characterizes the repulsive term. The attraction is of the Langevin-type [12] and is that arising between the ion and the ion-induced dipole moment of the neutral species. Then, the potential minimum (i.e. the value of $V(r)$ at the equilibrium distance r_m , which is the dissociation energy for the MCs^+ molecule) is given by

$$D \equiv V(r_m) \propto \alpha^{3/2} A^{-1/2}.$$

On the other hand, the distribution function for sputtering a dimer scales with its dissociation energy, D , according to [13,14]: $\Phi^{(2)} \propto D^{3/2}$. Therefore, the dimer distribution function $\Phi^{(2)}$ will exhibit a dependence on the polarizability α given by

$$\Phi^{(2)} \propto \alpha^{9/4} A^{-3/4},$$

* Tel. +49 631 205 4038, fax +49 631 205 4301, E-mail: gnaser@hrk.unikl.de.

with an exponent for α ($n = 2.25$) which is very close to what has been observed experimentally, namely $Y_{\text{MCs}^+} \propto \alpha^n$, with $n = 2.07 \pm 0.20$ and $n = 1.92 \pm 0.14$ for two different sets of samples [10].

As an extension of these investigations [7,9,10], the present work aimed at studying the influence of the isotopic mass on the emission of MCs^+ ions. The intention was twofold: first, the formation of MCs^+ species might depend on the density of M atoms in the association volume, i.e., for a given emission energy, should be different for the isotopes of an element. Second, in the aforementioned scenario of MCs^+ emission, the flux of MCs^+ ions will reflect the flux of *neutral* M atoms; isotope effects observed for MCs^+ (e.g. in dependence of emission energy) should thus relate directly to those of neutral atoms. Based on these objectives, the experiments investigated isotope fractionation effects for MCs^+ sputtered from various elemental specimens (B, Si, Ge, and Mo) as a function of emission energy ε . Contrary to *atomic* secondary ions [15–19], isotopic fractionation effects for *molecular* secondary ions have been studied rarely [18,19]; from the limited data no consistent picture for the observed fractionation emerged. To some extent this might be due to the rather complex formation and ionization processes involved for the oxide molecules investigated.

2. Experimental

The experiments were carried out in a secondary-ion mass spectrometer (Cameca IMS-4f) [20] employing a 5.5 keV Cs^+ primary ion beam (impact angle 42° off the surface normal). The beam was raster-scanned across a surface area of $(125 \mu\text{m})^2$ to ensure homogeneous sample erosion. The primary current was in the range from 5 to 70 nA and was adjusted depending on the emission energy selected, in order to obtain sufficient secondary-ion count rates. Positive molecular (MCs^+) and atomic (M^+) secondary ions were accepted from a circular area (defined by ion optical means and centered within the sputtered area) of $60 \mu\text{m}$ diameter. By closing the respective slits, the energy bandpass of the instrument was set to $\Delta E \approx 2 \text{ eV}$. The emission energy ε of secondary ions was selected by offsetting the sample potential from its normal value of 4500 V, while keeping the remainder of the secondary-beam optics unchanged. The origin of the energy scale was derived from the steepest slope, on the low-energy side, of the measured energy distributions; the uncertainties of this procedure appear to be less than about 1 eV (see below).

All measurements were done at low mass resolution ($M/\Delta M = 300$). Because of the elemental nature of the specimens, no molecular interferences apart from hydrides were observed; the magnitude of the latter was monitored and was in no case found to exceed 2×10^{-3} of the respective parent isotope. Thus, no corrections were performed for these contributions.

The specimens investigated were polycrystalline boron and molybdenum and single crystals of silicon and germanium. As the latter rapidly amorphize under ion irradiation [21], both semiconductors were in an amorphous state for these experiments. The intensities of the isotopes of an element were recorded by cyclic, automated magnetic peak switching between the respective mass values; usually, at least 100 such cycles were carried out. The measured ion intensities were corrected for dead-time counting losses of the electron multiplier according to established procedures [22]. Because of the moderately low count rates ($\leq 10^5 \text{ c/s}$), these corrections are rather small (1% or less). The signals were ratioed to that of a reference isotope (here the elements' heaviest ones) and the mean and the standard deviation were derived from all cycles. This measured isotope ratios R are normalized by the natural abundance ratios R_0 of the respective isotope pairs. In Section 3 these values R/R_0 will be presented as a function of emission energy both for molecular MCs^+ and atomic M^+ ions. As an additional check, these ratios R/R_0 were inspected also as a function of the mass difference relative to the reference isotope. For the isotopes of an element the corresponding values should fall on a straight line for a given emission energy if the isotope effects are linear in the mass difference. Within the experimental errors such a behavior was usually found to exist. Deviations from such a correlation are, on the other hand, well suited to identify outliers in the measured isotope ratios.

3. Results and discussion

Typical energy spectra for molecular MCs^+ and atomic M^+ ions are shown in Fig. 1 for the Si target. Also depicted is the spectrum of resputtered Cs^+ projectiles. The latter is found to be very similar to that of SiCs^+ , both

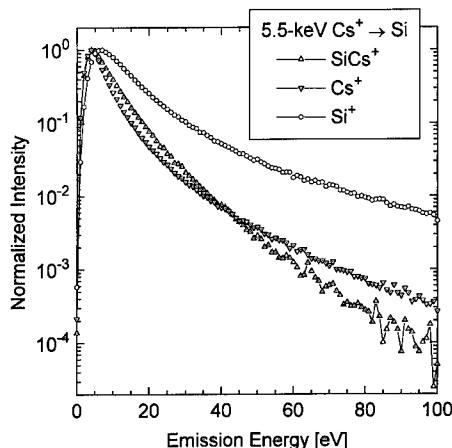


Fig. 1. Energy spectra of SiCs^+ , Si^+ , and Cs^+ ions sputtered from silicon under 5.5 keV Cs^+ ion bombardment.

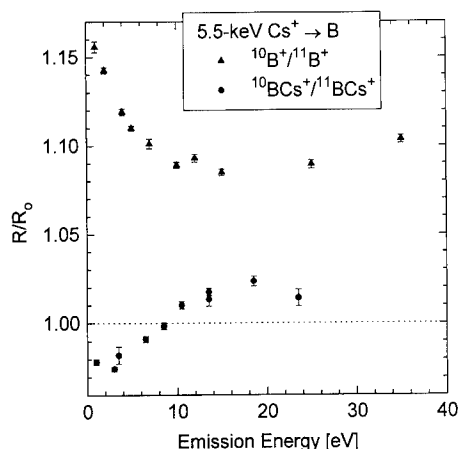


Fig. 2. The measured isotope ratio R normalized to the abundance ratio R_0 versus the emission energy for BCs^+ and B^+ secondary ions sputtered from boron by 5.5 keV Cs^+ ions. The values of R represent the mean of a set of (100 or more) individual ratios; the errors are $\pm 1\sigma_{\text{mean}}$.

in peak position and width as well as in the high-energy fall-off. These observations are in agreement with other data on semiconductors [9], but are valid also for the metallic specimens (B and Mo) investigated here. By contrast, the Si^+ and the other atomic-ion distributions are distinctly broader and decrease more gradually towards higher energies. As discussed [9], this finding supports the formation of MCs^+ ions from a neutral M atom and a Cs^+ species.

The isotope fractionation for MCs^+ ions was investigated for MCs^+ ions sputtered from elemental B, Si, Ge, and Mo specimens. Fig. 2 shows the yield ratio $^{10}\text{BCs}^+ / ^{11}\text{BCs}^+$ normalized to the $^{10}\text{B} / ^{11}\text{B}$ abundance ratio as a function of the emission energy. Since the energy distributions of MCs^+ species are rather narrow, the accessible energy range is limited to about 25 eV. Nevertheless, over this range the fractionation clearly varies: at low energies the heavier isotope is enhanced, while at higher energies the lighter isotope is formed preferentially (the shift amounts to $\sim 4\%$). The variation of the isotopic fractionation is opposite to what is generally observed for atomic secondary ions, that is, a pronounced preferentiality of the lighter isotope at low emission energies. Such a behavior is also found for B^+ ions sputtered under the same conditions (see Fig. 2). This light-isotope enrichment and its gradual decrease with emission energy (velocity) was previously observed [15–18] for a large number of atomic ions sputtered from a variety of ionic specimens (like alkali halides and oxides); it was shown to agree quantitatively with the predictions of the bond-breaking model [23–25] of secondary-ion emission which results in an exponential scaling of the ionization probability with the inverse emission velocity. Although the bond-breaking model is probably not applicable for the present speci-

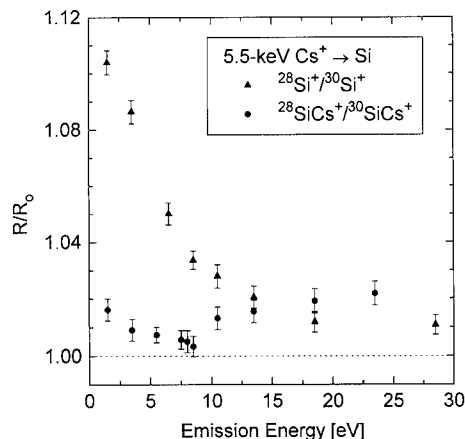


Fig. 3. The measured isotope ratio R normalized to the abundance ratio R_0 versus the emission energy for SiCs^+ and Si^+ secondary ions sputtered from silicon by 5.5 keV Cs^+ ions. The values of R represent the mean of a set of (100 or more) individual ratios; the errors are $\pm 1\sigma_{\text{mean}}$.

mens, the atomic isotope fractionation is qualitatively similar to what has been observed for the afore-mentioned ionic solids. Figs. 3, 4 and 5 depict the atomic and the MCs^+ isotope ratios versus the emission energy for Si, Ge, and Mo, respectively. Similar to B^+ , also Si^+ , Ge^+ , and Mo^+ exhibit a pronounced enrichment (up to 10%) of the light isotope(s) for $\varepsilon \leq 5$ eV. With increasing ε the enrichment (i.e., R/R_0) decreases and levels off to a roughly constant value ($R/R_0 \approx 1.09$ for B^+ and ~ 1 for the other atomic ions) at about $\varepsilon \approx 25$ eV. Due to a lack of sufficient signal, much higher energies are not accessible.

MCs^+ secondary ions, by contrast, show a rather different picture, with some general observations emerging:

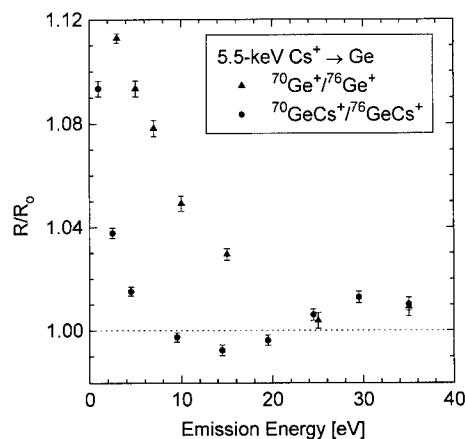


Fig. 4. The measured isotope ratio R normalized to the abundance ratio R_0 versus the emission energy for GeCs^+ and Ge^+ secondary ions sputtered from germanium by 5.5 keV Cs^+ ions. The values of R represent the mean of a set of (100 or more) individual ratios; the uncertainties are $\pm 1\sigma_{\text{mean}}$.

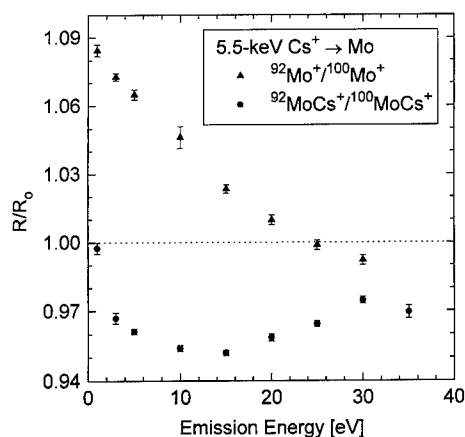


Fig. 5. The measured isotope ratio R normalized to the abundance ratio R_0 versus the emission energy for MoCs^+ and Mo^+ secondary ions sputtered from molybdenum by 5.5 keV Cs^+ ions. The values of R represent the mean of a set of (100 or more) individual ratios; the uncertainties are $\pm 1\sigma_{\text{mean}}$.

(i) the overall variations of the isotopic fractionation with emission energy are smaller than for atomic ions with the exception of GeCs^+ and MoCs^+ at energies below ~ 2 eV; (ii) at emission energies above about 10 eV, the fractionation of MCs^+ ions tends to increase slightly with ε and, with the exception of MoCs^+ , is positive (i.e., lighter M species are enriched); (iii) at low energies, on the other hand, the ratio R/R_0 is distinctly different for the elements; with increasing ε , it increases for BCs^+ , but decreases for SiCs^+ , GeCs^+ , and MoCs^+ . For the latter two molecular ions the tendency in this energy regime is similar to that of the respective atomic ions (cf. Figs. 4 and 5).

According to the MCs^+ formation mechanism discussed in Section 1, the isotopic fractionation for MCs^+ ions should reflect the fractionation of *neutral* M atoms. While the emission-energy dependence of the preferential sputtering of neutral isotopes has not been investigated experimentally, computer simulations [26,27] indicate an increasing preferential ejection of the *lighter* isotope with *increasing* emission energy. For example, in the simulation data of Eckstein [27] for Mo-isotopes the preferential sputtering of the lighter isotope rises by about 2.5% by increasing the emission energy from 1 eV to 30 eV. In the present experiments, the isotope ratios of all MCs^+ ions exhibit (above $\varepsilon \approx 10$ eV) an increase which is somewhat similar to Eckstein's results [27]: the corresponding shifts of R/R_0 amount to 3.7% for BCs^+ (Fig. 2), 1.5% for SiCs^+ (Fig. 3), 1.7% for GeCs^+ (Fig. 4), and 1.8% for MoCs^+ (Fig. 5). It is noted that the relative mass differences for these four isotope pairs are 0.1, 0.071, 0.086, and 0.087, while the computations were done for the $^{92}\text{Mo}/^{100}\text{Mo}$ isotopes (0.087 mass difference). If this reasoning is valid, the data presented in Figs. 2–5 would

constitute a verification of an emission-energy dependent preferential light-isotope sputtering as predicted by computer simulations and, albeit of a considerably smaller magnitude, also by the analytical sputtering theory [28] via an increasing value of m , the exponent in the screened Coulomb interaction potential.

On the other hand, in the *absence* of an emission-energy dependent fractionation of neutral atoms, a preferential formation of the *heavier* MCs^+ species could be expected for the proposed formation mechanism of MCs^+ ions, since the density of M atoms will be important for the combination with Cs^+ ions. Such an enhancement of the heavier species is in fact seen in the data for BCs^+ at low energies and for MoCs^+ over the whole range of ε investigated.

The data for GeCs^+ and MoCs^+ show an emission-energy dependence at the lowest values of ε which is similar to that of the atomic ions. It could be argued, therefore, that in this energy regime *atomic* ions also contribute to the formation of MCs^+ molecules (e.g. $\text{M}^+ + \text{Cs}^0 \rightarrow \text{MCs}^+$). Such a contribution should, then, reflect the isotopic fractionation of the atomic ions which is very large (cf. Figs. 4 and 5). Apparently, such an effect is absent for BCs^+ and SiCs^+ (the latter is, with respect to R/R_0 at low ε , somewhat intermediate between the very light B and the heavy Ge and Mo). The isotopic fractionation R/R_0 of MCs^+ secondary ions depicted in Figs. 2–5 may thus be a superposition of these effects; the differences in the observed emission-energy dependence indicate, however, that the individual contributions are not necessary of equal importance for different elements.

In summary, isotope effects for MCs^+ molecular ions sputtered from boron, silicon, germanium, and molybdenum under Cs^+ bombardment are distinctly different from those of the atomic ions. While the latter show the rather well-documented light-isotope enrichment for emission energies ≤ 30 eV, the isotopic fractionation for MCs^+ species is generally smaller and more variable in this energy range. The observed effects may, to some extent, reflect the increase of the light/heavy isotope ratio of *neutral* atoms with increasing emission energy which is predicted in computer simulations.

Acknowledgement

The author is grateful to H. Oechsner for his support of this work.

References

- [1] H.A. Storms, K.F. Brown and J.D. Stein, *Anal. Chem.* 49 (1977) 2023.
- [2] Y. Gao, *J. Appl. Phys.* 64 (1988) 3760.

- [3] C.W. Magee, W.L. Harrington and E.M. Botnick, *Int. J. Mass Spectrom. Ion Proc.* 103 (1990) 45.
- [4] H. Gnaser and H. Oechsner, *Fres. J. Anal. Chem.* 341 (1991) 54; *Surf. Interf. Anal.* 17 (1991) 646.
- [5] A. Benninghoven, F.G. Rüdenauer and H.W. Werner, *Secondary Ion Mass Spectrometry* (Wiley, New York, 1987).
- [6] W. Bock, H. Gnaser and H. Oechsner, *Anal. Chim. Acta* 297 (1994) 277.
- [7] H. Gnaser, *J. Vac. Sci. Technol. A* 12 (1994) 452.
- [8] J.E. Ortega, E.M. Oellig, J. Ferron and R. Miranda, *Phys. Rev. B* 36 (1987) 6213.
- [9] H. Gnaser and H. Oechsner, *Surf. Interf. Anal.* 21 (1994) 257.
- [10] H. Gnaser and H. Oechsner, *Surf. Sci. Lett.* 302 (1994) L289.
- [11] S. Bloom and H. Margenau, *Phys. Rev.* 85 (1952) 670.
- [12] H.S.W. Massey, E.H.S. Burhop and H.B. Gilbody, *Electronic and Ionic Impact Phenomena*, vol. 3 (Pergamon, Oxford, London, 1971).
- [13] H.M. Urbassek, *Nucl. Instr. and Meth. B* 18 (1987) 587.
- [14] G.P. Können, A. Tip and A.E. de Vries, *Radiat. Eff.* 21 (1974) 269; 26 (1975) 23.
- [15] H. Gnaser and I.D. Hutcheon, *Phys. Rev. B* 35 (1987) 877; 38 (1988) 11112.
- [16] H. Gnaser and I.D. Hutcheon, in: *Secondary Ion Mass Spectrometry, SIMS VI*, eds. A. Benninghoven et al. (Wiley, Chichester, 1988) p. 29.
- [17] H. Gnaser, *Radiat. Eff. Def. Solids* 109 (1989) 265.
- [18] S.A. Schwarz, *J. Vac. Sci. Technol. A* 5 (1987) 308.
- [19] E.U. Engström, A. Lodding, H. Odelius and U. Södervall, *Mikrochim. Acta* (1987) 387.
- [20] H.N. Migeon, C. Le Pipec and J.J. Le Goux, in: *Secondary Ion Mass Spectrometry, SIMS V*, eds. A. Benninghoven et al. (Springer, Berlin 1986) p. 155.
- [21] W. Bock, H. Gnaser and H. Oechsner, *Surf. Sci.* 282 (1993) 333.
- [22] J.C. Huneke, J.T. Armstrong and G.J. Wasserburg, *Geochim. Cosmochim. Acta* 47 (1983) 1635.
- [23] G. Slodzian, *Surf. Sci.* 48 (1975) 161; *Phys. Scripta* T6 (1983) 54.
- [24] P. Williams, *Surf. Sci.* 90 (1979) 588; *Appl. Surf. Sci.* 13 (1982) 241.
- [25] M.L. Yu and K. Mann, *Phys. Rev. Lett.* 57 (1986) 1476.
- [26] U. Conrad and H.M. Urbassek, *Nucl. Instr. and Meth. B* 61 (1991) 295.
- [27] W. Eckstein, *Nucl. Instr. and Meth. B* 83 (1993) 329.
- [28] P. Sigmund, in: *Sputtering by Particle Bombardment I*, ed. R. Behrisch (Springer, Berlin, 1981) p. 9.



ELSEVIER

Charge exchange of swift molecules H_2^+ , H_2 , CO_2^+ and CO_2 , at Pd(111) surfaces

T. Schlathölter, W. Heiland *

Universität Osnabrück, Fachbereich Physik, Postfach 4496, Barbarastrasse 7, Osnabrück, D-49 069, Germany

Abstract

Molecular ions and neutral molecules are scattered at 500 eV and at grazing incidence from metal surfaces. H_2^+ and CO_2^+ are subject to charge exchange processes which lead in part to dissociation. In the case of CO_2 evidence for negative molecular ion formation is found. Potassium “poisons” the dissociation of H_2 on Pd. These findings are supported by comparison of different metals, Pd(111) and Pd(111) covered with a monolayer of K. The dissociation probability of H_2^+ and H_2 decreases at the K-covered surface, in the case of CO_2^+ and CO_2 an increase is found. CO_2^+ on Pd(111) + K dissociates completely.

1. Introduction

The scattering of swift molecular particles from surfaces is of interest in nuclear fusion experiments and in effects at the surface of satellites. Another aspect is the use of molecular ions in film growth experiments. In any case the molecules transfer momentum and energy to the solid and the molecules initiate charge exchange processes [1]. The charge exchange processes turn out to be of interest for surface chemistry too, i.e. in scattering negative molecular states are observed whenever in surface chemistry experiments negative “precursors” are found (Table 1). The precursors are intermediate states in dissociative chemisorption or associative desorption. It is an open question how directly the ionic states found in scattering experiments correlate with the intermediate states in chemisorption experiments. However, there is supporting evidence when observing the effects of alkali adsorption on the dissociation of either scattered or adsorbed molecular species. Whenever the alkali “promotes” the dissociative chemisorption [19] an increase of the dissociation is found in the scattering experiments and vice versa. In this context hydrogen plays a special role since in that case the dissociative adsorption is “poisoned” by the presence of alkali metals [20–23]. In qualitative agreement we find in scattering experiments the dissociation probability of H_2^+ and H_2 to decrease when adsorbing K on Ni (111) [5] and on Pd(110) [24]. Here we report results for H_2^+ on Pd(111) in comparison with results using CO_2^+ and CO_2 .

2. Experiment and results

The experimental details are given elsewhere [1,8,11]. We use a time-of-flight system (TOF) to measure the energy distributions of scattered particles. Since the primary beam is pulsed the measurement of neutral particles is possible, too. Neutrals are in fact in most cases the majority of the scattered particles. Neutral primary particles are produced in a gas cell which is placed between the analyzing magnet and the target chamber. Since the beam pulsing system is located before the ions enter the magnet we obtain pulsed, neutral, and mass analyzed beams behind the gas cell. Fig. 1 shows the TOF distributions for 564 eV H_2^+ and 551 eV H_2^+ scattered from clean Pd(111) and Pd(111) with 1 monolayer of K resp. The intensity scale is logarithmic. The time scale is reversed, i.e. the spectra are almost equivalent to energy spectra (“almost” because there is a distortion due to the difference of Δt and ΔE when converting time to energy). The spectra contain the large neutral peak around t_0 . The time t_0 marks the position where surviving molecules without energy loss, i.e. preserving the primary energy, would be found. The ions are separated from the neutral peak by postacceleration after the target. Off the clean surface the positive ion yield is below 10%, off the K covered surface the positive ion yield is below 1%. For the negative ions the situation is qualitatively inverted, i.e. more negative H is found for the K covered surface.

The other observation of interest is the change of the molecular yield. The surviving H_2 molecules are distinguished as a “hat” on the top of the broad distribution of dissociated molecules. There is an obvious increase of molecular survival due to the K adsorption. The dissociated particles spectrum extends above the primary energy,

* Corresponding author, tel. +49 541 9690, fax +49 541 969 2670, E-mail: wheiland@dosuni1.bitnet.

Table 1

Molecule	Surface	Scattering	Chemisorption
O ₂	Ag(111)	Pan Haochang et al. [2] Reijnen et al. [4] Schubert et al. [6] van Slooten et al. [7]	Backx et al. [3] Campbell (1986) [5]
CO ₂	Ni(110)	Schubert et al. [8,9]	Bartos et al. [10]
CO ₂	Pd(110)	Schmidt et al. [11]	Wambach et al. [12] Wohlrab et al. [13]
O ₂	Pt(111)	Reijnen et al. [14]	Luntz et al. [15] Wurth et al. [16]
NO	Pt(111)	Reijnen et al. [17]	Kiskinova et al. [18]
O ₂	Ni(111)	Schubert et al. [6]	Shayegan et al. [19]

marked by t_0 , due to the transformation of the center of mass energy gain owing to the dissociation into the laboratory frame of reference. This effect is seen from the

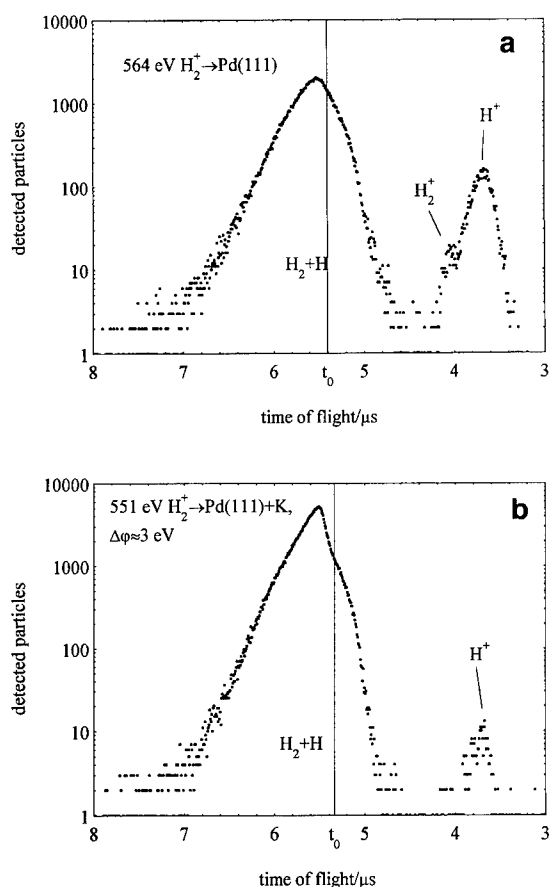


Fig. 1. (a) Time of flight spectra of H, H₂ and positive ions from the interaction of 564 eV H₂⁺ interacting with a clean Pd(111) surface. The grazing angle of incidence is 5°, the laboratory scattering angle is 10°. The ions are separated from the neutrals by postacceleration. (b) As in Fig. 1a but from a K covered Pd(111) surface with 551 eV H₂⁺ as primary ions.

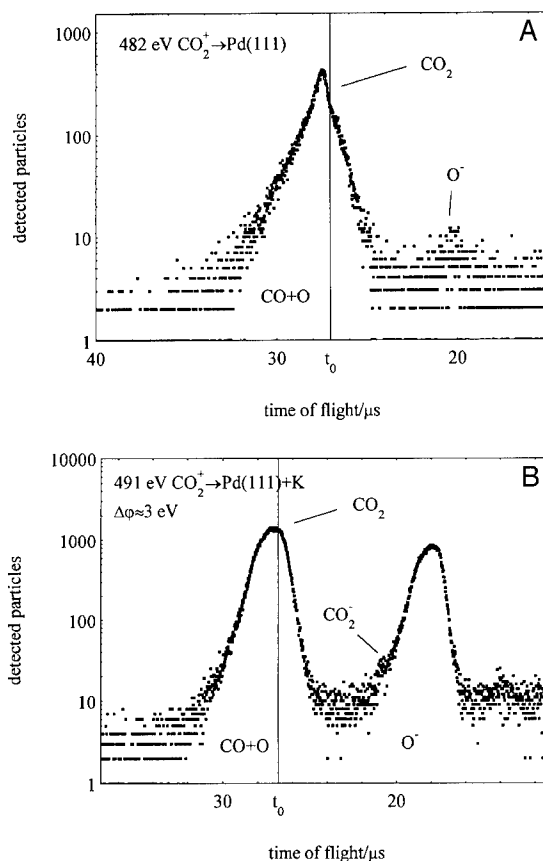


Fig. 2. (a) Time of flight spectra of CO₂, CO + O and negative ions from the interaction of CO₂⁺ with a clean Pd(111) surface. Geometrical conditions as in Fig. 1. (b) Same as Fig. 2a but for a K covered Pd(111) surface.

formula of energy conservation for diatomic molecules which gives for the energy E of the dissociated particles in the lab. system

$$E = \frac{1}{2}E_0 + \frac{1}{2}E_D \pm \sqrt{E_0 E_D} \cos \alpha,$$

where E_0 is the primary energy, E_D the dissociation energy and α the angle between the molecular axis and the incident beam direction. The orientation of the molecules is isotropic. The spectra are “scrambled” by energy loss straggling and by the differences in trajectories which occur even under surface channeling conditions.

For CO₂⁺ as primary particles we obtain an “inverse” result (Fig. 2), i.e. the molecular survival is high for the clean Pd(111) surface whereas the K causes the complete destruction of the incident CO₂⁺. For the results of Fig. 2 a positive voltage was used for the post-acceleration in order to show the negative ions. As expected, the negative ion yield is high from the K covered surface. In case of the K-surface a small CO₂⁻ peak is visible. The total negative ion yield, mainly O⁻, is in the 10% range. The yields have to be corrected for the higher detection probabilities for

ions compared to neutrals. In the case of clean Pd(111) we find also a “hat” of neutral CO_2 coming from the interaction of CO_2^+ with the surface. When using neutral CO_2 as primary particle the molecular survival is enhanced for both clean Pd(111) and Pd(111) + K [25]. Especially the CO_2^- peak is very distinct for the interaction of CO_2 with Pd(111) + K.

3. Discussion and summary

The hydrogen results are in line with previous results for Ni(110), Ni(111) and Pd(110). The dissociation – at these low energies – is clearly charge exchange dominated. From considering the possible atomic structure of K on these metal targets it is not likely that the surfaces are “smoothed” by K-adsorption. Increasing roughness in contrast would cause an enhanced dissociation if the dissociation would be collisional.

The formation of H_2 is quite clearly due to an Auger type electron capture from the metal into the ground state of H_2 , as discussed previously [1,24]. The dissociation can proceed at least via two channels, (i) by resonant capture into the anti bonding H + H molecular state, or (ii) by the screening action of the electrons in the selvedge of the solid. The final state of any hydrogenic species in the metals discussed here will be a “screened proton” independent of the initial state, H^+ , H, H_2^+ , H_2 , etc. Since we observe an appreciable dissociation also for neutral incident H_2 and we can exclude collisional dissociation, the dissociation by screening is the natural solution of the problem [24,26]. Since the screening is part of the energy loss scheme due to electron–hole pair excitation [26,27] we have to remember that Lucas [28] proposed that the dissociation of swift molecules is due to elementary excitations in the solid albeit to excitation of plasmons. However, the energies used here are probably too small to excite plasmons [29]. Hence, only electron–hole pairs are excited. The lower dissociation probability found with K-layers can be attributed to the lower electron density of the K-layer compared to the clean Pd surface.

The CO_2 –surface system is comparably more complicated. We give a more detailed account elsewhere [25]. In short, the CO_2 is moving slowly, $v_{\perp} = 4 \times 10^{13} \text{ Å s}^{-1}$ only, i.e. $v_{\perp} = 2 \times 10^{-3} \text{ a.u.}$ Therefore all possible electronic processes will be finished at rather large distances of the CO_2 from the surface. In case of CO_2^+ single and double electron capture will lead to neutral ground state CO_2 , electronically excited CO_2 and excited states of the CO_2^- system. In case of neutral incident CO_2 a different set of CO_2^- states may be populated. The capture mechanisms are in part supported by results from electron spectroscopy [30]. The discussion is complicated by the fact that in contrast to CO_2 the CO_2^- energetically prefers a bent geometry. In case of neutral CO_2 as incident particle we still find the “promotion” effect of K, which indicates

that very probably the bent species are more important. The difference to the H_2 case is that CO_2 is moving more slowly and is also larger than the H_2 molecule. Therefore most charge exchange processes will occur at larger distance from the surface, and the processes will be resonant. Since the K electron density extends further than the Pd electron density, resonant processes are favored.

Acknowledgements

This work is supported by the Deutsche Forschungsgemeinschaft and the Deutsche Akademische Austauschdienst. We thank H.J. Freund for providing the Pd(111) crystal.

References

- [1] W. Heiland, in: *Low Energy Ion–Surface Interaction*, ed. J.W. Rabalais (Wiley, New York, 1994) p. 313.
- [2] P. Hoachang, T.C.M. Horn and A.W. Kleyn, *Phys. Rev. Lett.* 27 (1986) 3035; *J. Electron Spectr. Rel. Phen.* 45 (1987) 361.
- [3] C. Backx, C.P.M. de Groot and P. Biljoen, *Surf. Sci.* 104 (1981) 300.
- [4] P.H.F. Reijnen, P.J. van den Hoek, A.W. Kleyn, U. Imke and K.J. Snowdon, *Surf. Sci.* 221 (1989) 427.
- [5] C.T. Campbell, *Surf. Sci.* 173 (1986) L 641.
- [6] S. Schubert, U. Imke and W. Heiland, *Vacuum* 41 (1990) 252.
- [7] U. van Slooten, D.R. Andersson, A.W. Kleyn and E.A. Gislason, *Chem. Phys. Lett.* 185 (1991) 440.
- [8] S. Schubert, U. Imke, W. Heiland, K. J. Snowdon, P.H.F. Reijnen and A.W. Kleyn, *Surf. Sci.* 205 (1988) L793.
- [9] S. Schubert, U. Imke and W. Heiland, *Surf. Sci.* 219 (1989) L576.
- [10] B. Bartos, H.J. Freund, H. Kuhlenbeck, M. Neumann, H. Lindner and K. Müller, *Surf. Sci.* 179 (1987) 59.
- [11] K. Schmidt, H. Franke, T. Schlathölter, C. Höfner, A. Nörmann and W. Heiland, *Surf. Sci.* 301 (1994) 326.
- [12] J. Wambach, G. Odörfer, H. J. Freund, H. Kuhlenbeck and M. Neumann, *Surf. Sci.* 209 (1989) 159.
- [13] S. Wohlrab, D. Ehrlich, J. Wambach, H. Kuhlenbeck and H.J. Freund, *Surf. Sci.* 220 (1989) 243.
- [14] P.H.F. Reijnen, A. Rankema, U. van Slooten and A.W. Kleyn, *Surf. Sci.* 253 (1991) 24.
- [15] A.C. Luntz, M.D. Williams and D.S. Bethune, *J. Chem. Phys.* 89 (1988) 4381.
- [16] W. Wurth, J. Stöhr, P. Feulner, X. Pan, K.R. Bauchspiess, Y. Baba, E. Hudel, G. Rocker and D. Menzel, *Phys. Rev. Lett.* 65 (1990) 2426.
- [17] P.H.F. Reijnen and A.W. Kleyn, *Chem. Phys.* 139 (1989) 489.
- [18] M. Kiskinova, G. Pirug and H.P. Bonzel, *Surf. Sci.* 136 (1984) 285.
- [19] M. Shayegan, J.M. Cavallo, R.E. Glover and R.L. Park, *Phys. Rev. Lett.* 53 (1984) 1578.
- [20] H.P. Bonzel, *Surf. Sci. Rep.* 8 (1988) 43.
- [21] A. Berko and F. Solymosi, *Surf. Sci.* 171 (1986) L498.
- [22] F. Solymosi and I. Kovacs, *J. Chem. Phys.* 93 (1989) 7537.

- [23] F. Solymosi, J. Mol. Catalysis 94 (1991) 337.
- [24] K. Schmidt, T. Schlathöler, A. Närmann and W. Heiland, Chem. Phys. Lett. 200 (1992) 465.
- [25] T. Schlathöler and W. Heiland, Surf. Sci. 323 (1995) 207.
- [26] W. Heiland and A. Närmann, Nucl. Instr. and Meth. B 78 (1993) 20.
- [27] P.M. Echenique, F. Flores and R.H. Ritchie, Solid State Physics 43 (1990) 229.
- [28] A.A. Lucas, Phys. Rev. Lett. 43 (1979) 1350.
- [29] W. Heiland, U. Imke, S. Schubert and K.J. Snowdon, Nucl. Instr. and Meth. B 27 (1987) 167.
- [30] V. Kempter, private communication.



ELSEVIER

Energy loss straggling of 0.5-MeV protons specularly reflected from a SnTe(001) surface

Kenji Kimura *, Hideaki Kuroda, Martin Fritz, Michi-hiko Mannami

Department of Engineering Science, Kyoto University, Kyoto 606-01, Japan

Abstract

Energy spectra of 0.5-MeV protons specularly reflected from a SnTe(001) surface are measured with a high-resolution magnetic spectrometer ($\Delta E/E \sim 0.1\%$). Position-dependent energy loss straggling is derived from the observed energy distributions of the reflected protons. The obtained position-dependent straggling is compared with the theoretical ones caused by plasmon excitations and single electron collisions. The agreement between the experimental and theoretical results is reasonably good. Contrary to the energy loss itself, contribution of the single electron collisions is dominant for the energy loss straggling.

1. Introduction

When fast ions are incident on a flat crystal surface at a small glancing angle, most of the ions are reflected at the angle of specular reflection [1]. This phenomenon, called *specular reflection of fast ions*, is a very suitable technique to study ion-surface interactions because the ions are reflected from the topmost atomic plane after a long interaction time with the surface [2]. We have demonstrated that the position-dependent stopping power of the surface can be derived from the observed energy losses of the specularly reflected ions [3,4]. The derived stopping power was explained by a sum of the stopping powers caused by the plasmon excitation and the single electron collision.

The work presented here extends this research to energy loss straggling. The energy loss process is subject to statistical fluctuations resulting in a finite width for the energy distribution of the ions. In the previous studies, the energy loss straggling has not been discussed because of the poor energy resolution of the solid state detector used before. The present work provides energy spectra of the reflected 0.5-MeV protons from a SnTe(001) surface measured with a high-resolution spectrometer. From the observed energy loss straggling, the position-dependent energy loss straggling per unit path length at the surface is derived. Comparing the derived straggling with the theoretical ones, the origin of the energy loss straggling is discussed.

2. Experimental

A single crystal of SnTe(001) was prepared by epitaxial growth in situ by vacuum evaporation on a cleaved KCl(001) surface, which was mounted on a high precision goniometer in an UHV chamber. A beam of 0.5-MeV protons from a Tandatron accelerator was collimated by a series of apertures to less than $0.1 \times 0.1 \text{ mm}^2$ and to a divergence angle less than 0.3 mrad. The ions scattered from the SnTe(001) surface were energy analyzed by a 90° sector magnetic spectrometer, which could be rotated around the target. The radius of the spectrometer was 300 mm and the dispersion was 1200 mm. The spectrometer had an aperture ($\phi = 60 \text{ }\mu\text{m}$) at the entrance focal point 40 cm down stream from the target. Microchannel plates located in the focal plane served as a position-sensitive detector (length 55 mm, resolution 0.13 mm) for the energy analyzed ions. Including the energy spread of the incident beam the energy resolution of the spectrometer was better than 0.1%.

3. Results

Fig. 1 shows an example of the observed energy spectrum of the 0.5-MeV protons specularly reflected from the SnTe(001) surface, exhibiting several well-defined peaks at $\sim 496.5 \text{ keV}$, $\sim 490 \text{ keV}$ and $\sim 484 \text{ keV}$. Whereas the peak of the highest energy consists of the ions reflected from the topmost atomic plane, the other smaller peaks are related to sub-surface channeling. Some incident ions can penetrate into the crystal through surface steps. These ions travel within the planar channels parallel to the surface

* Corresponding author. Tel. +81 75 753 5253, fax +81 75 771 7286, e-mail kimura@kues.kyoto-u.ac.jp.

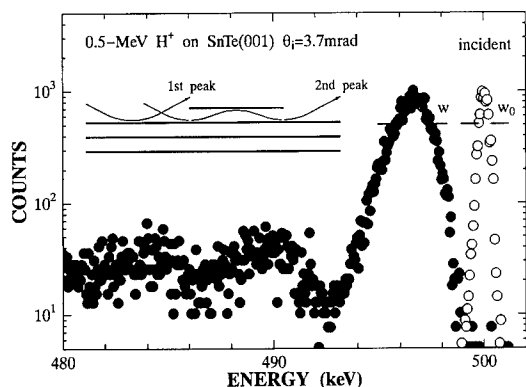


Fig. 1. Energy spectrum of 0.5-MeV protons specularly reflected from a SnTe(001) surface. The glancing incident angle was 3.7 mrad.

plane and may escape from the crystal through the surface steps as shown by the inset in Fig. 1. Here, we concentrate on the highest energy peak, which corresponds to the real specular reflection.

The energy spectrum of the incident beam is also shown in Fig. 1. The peak energy of the specularly reflected ions is about 3.5 keV lower than the incident energy showing the energy loss of the ions. Fig. 2 shows the observed mean energy loss of the specularly reflected 0.5-MeV protons as a function of the incident angle. This energy loss increases gradually with increasing incident angle.

The FWHM of the specular reflection peak, w , is broader than that of the incident peak, w_0 , as can be seen in Fig. 1. Since the observed energy distributions are well

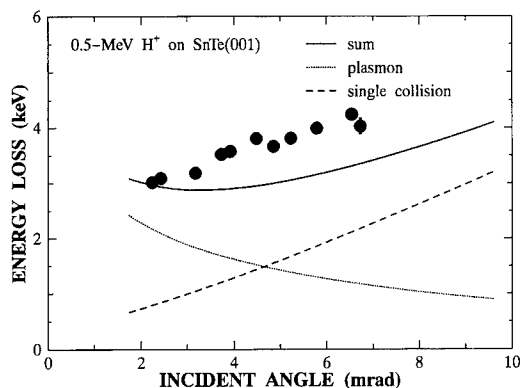


Fig. 2. Mean energy loss of 0.5-MeV protons specularly reflected from a SnTe(001) surface. The energy losses due to plasmon excitation calculated from the theory of Kitagawa (dotted line), due to single electron collision calculated from binary encounter model (dashed line) and their sum (solid line) are also shown. The agreement between the experimental and theoretical ones is reasonably good.

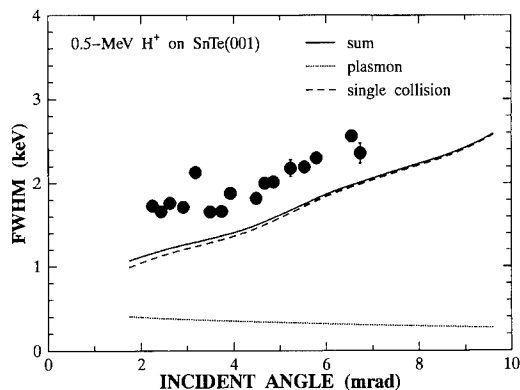


Fig. 3. FWHM of the specular reflection peak at the glancing angle incidence of 0.5-MeV protons on a SnTe(001) surface. Theoretical widths due to plasmon excitation (dotted line), due to single electron collision (dashed line) and their sum (solid line) are presented. The contribution of the plasmon excitation is negligibly small. The agreement between the experimental and theoretical ones is good.

approximated by Gaussians, the intrinsic width can be estimated by $W = (w^2 - w_0^2)^{1/2}$, and the result is shown as a function of the incident angle in Fig. 3. The width increases with the incident angle.

4. Discussion

4.1. Derivation of the position-dependent energy loss straggling

The trajectory of the reflected ion is described by the continuum surface planar potential $V(x)$, just as in the case of planar channeling, where x is distance from the surface. The equation for a trajectory $x(z)$ of an ion of energy E and incident angle θ_i is written as

$$\frac{dx}{dz} = \left(\frac{V(x_m) - V(x)}{E} \right)^{1/2}, \quad (1)$$

where $x_m(\theta_i)$, determined by $V(x_m) = E\theta_i^2$, is the distance of the closest approach of the ion to the surface. The coordinate system is chosen so that the trajectory lies in the x - z plane.

The stochastic equation for the energy distribution $f(\theta_i; z, E)$ of the ions at z , is expressed as

$$\frac{\partial f(\theta_i; z, E)}{\partial z} = \int \{ f(\theta_i; z, E + \epsilon) - f(\theta_i; z, E) \} P(x(z), \epsilon) d\epsilon, \quad (2)$$

where $P(x, \epsilon)dz$ is the probability that the ion loses energy ϵ after travelling an infinitesimal path dz at the distance x from the surface. Expanding $f(\theta_i; z, E + \epsilon)$

with respect to ϵ and neglecting the terms higher than ϵ^2 , a Fokker–Planck equation can be derived,

$$\frac{\partial f(\theta_i; z, E)}{\partial z} = S(x(z)) \frac{\partial f(\theta_i; z, E)}{\partial E} + \frac{\gamma(x(z))}{2} \frac{\partial^2 f(\theta_i; z, E)}{\partial E^2}, \quad (3)$$

where

$$S(x) = \int \epsilon P(x, \epsilon) d\epsilon \quad (4)$$

is the position-dependent stopping power and

$$\gamma(x) = \int \epsilon^2 P(x, \epsilon) d\epsilon \quad (5)$$

is the position-dependent energy loss straggling per unit path length. Eq. (3) is solved with an initial condition $f(\theta_i; -\infty, E) = \delta(E - E_0)$ as

$$f(\theta_i; z, E) = \frac{1}{\sqrt{2\pi} \tilde{\Omega}(\theta_i; z)} \exp \left\{ -\frac{(E - E_0 + \Delta E(\theta_i; z))^2}{2 \tilde{\Omega}^2(\theta_i; z)} \right\}, \quad (6)$$

where

$$\Delta E(\theta_i; z) = \int_{-\infty}^z S(x(z')) dz' \quad (7)$$

is the mean energy loss of the ion at z ,

$$\tilde{\Omega}^2(\theta_i; z) = \int_{-\infty}^z \gamma(x(z')) dz' \quad (8)$$

is its energy loss straggling (the average square fluctuation of the energy loss) at z and the integrations are performed along the ion trajectory. The energy loss straggling of the reflected ions, which depends on the incident angle, can be written as

$$\Omega^2(\theta_i) = \int_{-\infty}^{+\infty} \gamma(x(z)) dz, \quad (9)$$

where the integration is performed along the ion trajectory. The energy loss straggling is related to the observed FWHM as $\Omega^2(\theta_i) = (8 \ln 2)^{-1} W^2$. Substituting Eq. (1) into Eq. (9), the total energy loss straggling is obtained as

$$\Omega^2(\theta_i) = 2E^{1/2} \int_{x_m}^{\infty} \gamma(x) [V(x_m) - V(x)]^{-1/2} dx. \quad (10)$$

This is an integral equation of the Abel type. Eq. (10) can be solved if $V(x)$ is a monotonic function.

$$\gamma(x) = -\frac{1}{2\pi E} \frac{dV(x)}{dx} \left[\Omega^2(0) \left(\frac{E}{V(x)} \right)^{1/2} + \int_0^{\pi/2} \frac{d\Omega^2(\theta_i)}{d\theta_i} \bigg|_{\theta_i = (V(x)/E)^{1/2} \sin(u)} du \right]. \quad (11)$$

Thus the position-dependent energy loss straggling $\gamma(x)$ can be derived from the observed energy loss straggling $\Omega^2(\theta_i)$.

If the image potential of the projectile is taken into account, the sum of the surface planar potential and the image potential has a potential minimum, and Eq. (10) has to be solved numerically. We use the Ziegler–Biersack–Littmark potential [5] for the calculation of the continuum surface planar potential

$$V_U(x) = 2\pi Z_1 Z_2 e^2 n_p a_U \sum_{i=1}^4 \frac{c_i}{d_i} \exp \left(-\frac{d_i x}{a_U} \right), \quad (12)$$

where Z_1 (Z_2) is the atomic number of the projectile ion (target atom), n_p is the atomic density of the surface plane, $\{c_i\} = \{0.028171, 0.28022, 0.50986, 0.18175\}$, $\{d_i\} = \{0.20162, 0.40290, 0.94229, 3.1998\}$ and $a_U = 0.88534 a_B (Z_1^{0.23} + Z_2^{0.23})$. The image potential is given by [6]

$$V_i(x) = -\frac{Z_1^2 e^2 \omega_s}{2v} \int_0^{v/v_F} \frac{J_0(2|x - x_e| \omega_s \xi/v)}{1 + \xi^2} d\xi + \frac{\theta(x_e - x) Z_1^2 e^2 \omega_b}{2v} \times \int_0^{v/v_F} \frac{J_0(2(x_e - x) \omega_b \xi/v) - 1}{1 + \xi^2} d\xi, \quad (13)$$

where ω_s (ω_b) is the surface (bulk) plasmon frequency, v is the ion velocity, x_e is the position of the electronic

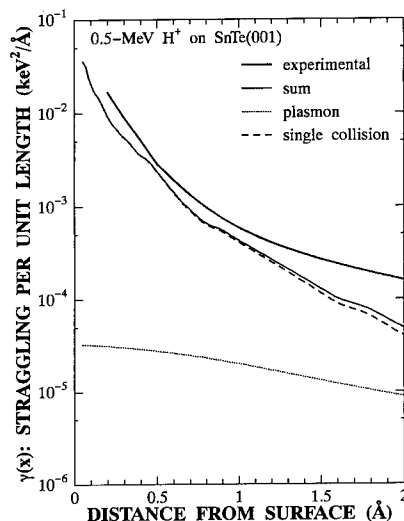


Fig. 4. Position-dependent energy loss straggling, $\gamma(x)$, for 0.5-MeV protons at the surface of SnTe(001) derived from the observed energy loss distributions. Theoretical results due to plasmon excitation (dotted line), single electron collision (dashed line) and their sum (solid line) are presented. Although the theoretical one is slightly smaller than the experimental one, the characteristic features are reproduced quite well by the calculation.

surface, which is usually assumed to be one half of the interplanar distance and v_F is the Fermi velocity of the target crystal. After substituting the sum of Eqs. (12) and (13) into $V(x)$, Eq. (10) was solved numerically. The obtained $\gamma(x)$ is shown in Fig. 4. The energy loss straggling per unit path-length decreases rapidly with increasing x .

4.2. Comparison with the theoretical calculation

The theoretical stopping power at an inhomogeneous electron gas was derived by Kitagawa [7]. The stopping power for an ion at a surface is

$$S_{\text{pl}}(x) = S_b(x) + S_s(x) + S_r(x), \quad (14)$$

$$S_b(x) = \left(\frac{Z_1 e \omega_p(x)}{v} \right)^2 \ln \left(\frac{2v}{v_F(x)} \right),$$

$$S_{s(r)}(x) = \int T_{s(r)}(X, x) \frac{d\omega_p^2(X)}{dX} \frac{x-X}{2|x-X|} \times P \left(\frac{1}{\omega_p^2(x) - \omega_p^2(X)} \right) dX, \quad (15)$$

$$T_s(X, x) = \left(\frac{Z_1 e \omega_p(X)}{v} \right)^2 K_0 \left(\frac{2|x-X|\omega_p(X)}{v} \right),$$

$$T_r(X, x) = \left(\frac{Z_1 e \omega_p(x)}{v} \right)^2 K_0 \left(\frac{2|x-X|\omega_p(x)}{v} \right), \quad (16)$$

where $\omega_p(x) = (4\pi e^2 n_V(x)/m)^{1/2}$, $v_F(x) = (3\pi^2 n_V(x))^{1/3} \hbar/m$, m is the electron mass, $n_V(x)$ is the density of valence electrons averaged along the plane parallel to the surface and $K_0(z)$ is the modified Bessel function. The components $S_b(x)$, $S_s(x)$ and $S_r(x)$ represent the stopping powers due to excitation of bulk mode, surface mode and reflective mode respectively.

The stopping power given by Eq. (14) does not include the single electron collisions. This contribution may be calculated by the binary encounter model as [4,8]

$$S_{\text{s.c.}}(x) = \frac{2\pi Z_1^2 e^4 n(x)}{mv^2} \ln \left(\frac{2mv^2}{\hbar \omega(x)} \right), \quad (17)$$

where $n(x)$ is the density of the electrons averaged along the plane parallel to the surface and $\omega(x) = [4\pi e^2 n(x)/m]^{1/2}$. We used the Hartree–Fock wavefunctions [9] of isolated Sn and Te atoms to calculate $n(x)$.

The energy loss of the reflected proton was derived by integrating the stopping powers given by Eqs. (14) and (17) along the trajectory, and the results are shown in Fig. 2. Although the incident-angle dependences differ from each other, both processes are important for the energy loss of the reflected ions at the surface. The sum of the calculated results is slightly smaller than the observed one.

This is a general tendency for the surface stopping powers for the various combinations of ions and crystal surfaces [4].

The energy loss straggling due to plasmon excitation is calculated from Eqs. (14)–(16). As mentioned above, $S_b(x)$ corresponds to the bulk plasmon excitation and $S_s(x) + S_r(x)$ corresponds to the surface plasmon excitation. The excitation probability of bulk (surface) plasmon after travelling an infinitesimal path dz at distance x is given by $S_b(x)dz/\hbar\omega_b((S_s(x) + S_r(x))dz/\hbar\omega_s)$. Assuming that the excitation processes of the bulk plasmon and the surface plasmon are independent, the probability distribution of energy loss due to plasmon excitation is given by

$$P_{\text{pl}}(x, \epsilon) = \frac{S_b(x)}{\hbar\omega_b} \delta(\epsilon - \hbar\omega_b) + \frac{S_s(x) + S_r(x)}{\hbar\omega_s} \delta(\epsilon - \hbar\omega_s). \quad (18)$$

Substituting Eq. (18) into Eq. (5), the position-dependent energy loss straggling due to plasmon excitation is given by

$$\gamma_{\text{pl}}(x) = \hbar\omega_b S_b(x) + \hbar\omega_s (S_s(x) + S_r(x)). \quad (19)$$

The energy loss straggling due to single electron collisions is calculated with the binary encounter model. The probability distribution of energy loss due to single electron collision is given by

$$P_{\text{s.c.}}(x, \epsilon) = \sum_i n_i(x) \frac{d\sigma_i}{d\epsilon}, \quad (20)$$

where $n_i(x)$ is the density of the i th shell electrons averaged along the plane parallel to the surface and $d\sigma_i/d\epsilon$ is the cross section for the projectile and i th shell electron scattering. Employing the Thomson cross section, $d\sigma_i/d\epsilon = 2\pi Z_1^2 e^4/mv^2 \epsilon^2$, and substituting Eq. (20) into Eq. (5), the position-dependent energy loss straggling due to the single collision is given by

$$\gamma_{\text{s.c.}}(x) = \frac{2\pi Z_1^2 e^4}{mv^2} \sum_i n_i(x) \int_{\epsilon_{\min}}^{\epsilon_{\max}} d\epsilon \approx 4\pi Z_1^2 e^4 n(x). \quad (21)$$

This result is reduced to the Bohr formula [10] if the averaged electron density is used.

The calculated energy loss straggling is compared with the experimental result in Figs. 3 and 4. Contrary to the energy loss, the contribution of the plasmon excitation to the energy loss straggling is negligibly small. This is due to the fact that the process of the large energy transfer contributes dominantly to the energy loss straggling. The maximum energy transfer in the single electron collision, $\epsilon_{\max} = 2mv^2$ (about 1 keV in the present case), is much larger than the plasmon energy ($\hbar\omega_b = 15$ eV for SnTe). Although the calculation reproduces the characteristic fea-

tures of the observed result, the calculated straggling is slightly smaller than the observed one. This fact may be related to the observation that the calculated energy loss is slightly smaller than the experimental result.

It should be noted that the observed energy spectrum deviates slightly from the Gaussian (see Fig. 1) especially at small incident angles, while the theoretical energy spectrum, Eq. (6), is the Gaussian. This difference may be ascribed to the approximation used in the derivation of the Fokker–Planck equation. In the small energy loss region, the Fokker–Planck equation is not a good approximation and the exact stochastic equation has to be solved like the Vavilov theory [11].

5. Conclusion

Energy spectra of 0.5-MeV protons reflected specularly from the SnTe(001) surface are measured with a 90° magnetic spectrometer. From the observed energy loss distributions, the position-dependent energy loss straggling per unit path-length is derived. The theoretical energy loss straggling due to plasmon excitations and single electron collisions is calculated. Contrary to the energy loss, the contribution of the plasmon excitation to the energy loss straggling is negligibly small. Although the theoretical straggling reproduces the characteristic features of the experimental one, the theoretical one is slightly smaller than the experimental one.

Acknowledgement

We are grateful to the members of the Department of Nuclear Engineering of Kyoto University for the use of the Tandetron accelerator. This study was supported in part by a Grant-in-Aid for Scientific Research from the Japanese Ministry of Education, Science and Culture.

References

- [1] M. Hou and C. Varelas, *Appl. Phys. A* 33 (1984) 121.
- [2] K. Kimura, M. Hasegawa, Y. Fujii, M. Suzuki, Y. Susuki and M. Mannami, *Nucl. Instr. and Meth. B* 33 (1988) 358.
- [3] K. Kimura, M. Hasegawa and M. Mannami, *Phys. Rev. B* 36 (1987) 7.
- [4] Y. Fujii, S. Fujiwara, K. Narumi, K. Kimura and M. Mannami, *Surf. Sci.* 277 (1992) 164.
- [5] J.F. Ziegler, J.P. Biersack and U. Littmark, *The stopping and Range of Ions in Solids, The Stopping and Range of Ions in Matter*, Vol. 1, ed. J.F. Ziegler (Pergamon, New York, 1985).
- [6] Y.H. Ohtsuki, *Charge Beam Interaction with Solids* (Taylor & Francis, London, 1983) p. 228.
- [7] M. Kitagawa, *Nucl. Instr. and Meth. B* 33 (1988) 409.
- [8] J.J. Thompson, *Phil. Mag.* 23 (1912) 419.
- [9] H. Herman and S. Skillman, *Atomic Structure Calculations* (Prentice-Hall, Englewood Cliffs, NJ, 1963).
- [10] N. Bohr, K. Dan. Vidensk. Selsk. Mat. Fys. Medd. 18 (8) (1948).
- [11] P.V. Vavilov, *Zh. Eksp. Teor. Fiz.* 32 (1957) 920 [*Sov. Phys. JETP* 5 (1957) 749].

Sputtering of tin and gallium–tin clusters

Th. Lill *, W.F. Calaway, M.J. Pellin

Materials Science, Chemical Technology, and Chemistry Divisions, Argonne National Laboratory, Argonne, IL 60439, USA

Abstract

Tin and gallium–tin clusters have been produced by 4 keV Ar^+ ion bombardment of polycrystalline tin and the gallium–tin eutectic alloy and analyzed by time-of-flight mass spectrometry. The sputtered neutral species were photoionized with 193 nm (6.4 eV) excimer laser light. Neutral tin clusters containing up to 10 atoms and mixed gallium–tin clusters $\text{Ga}_{(n-m)}\text{Sn}_m$ with $n \leq 4$ for the neutrals and $n \leq 3$ for the sputtered ionic species have been detected. The measured distributions of mixed clusters with equal nuclearity have been found to be nonstatistical most likely due to significant differences in the ionization efficiencies of clusters with equal nuclearity but different tin content.

1. Introduction

Cluster emission during ion bombardment of metal surfaces has become the object of intense investigation over the last few years. There are several reasons for this increased interest in metal cluster sputtering. First, the ejection mechanism for clusters appears to be different from that of atomic species. The linear collision cascade model [1–3], that has been proven to describe atom sputtering very satisfactorily, has only limited applicability to cluster sputtering [4]. Therefore, the study of cluster sputtering is anticipated to provide new insights into sputtering, a key process in many leading edge technologies. Second, sputtered metal clusters have been found to play a significant role in laser secondary neutral mass spectrometry of metal thin film interfaces [5,6] and semiconductor materials [7]. Third, cluster sputtering could find important applications in material science, for instance for the growth of nanomaterials.

Until recently, most of the information about sputtered clusters was based on secondary ion cluster experiments, even though most clusters are ejected in the neutral state [8,9]. Sputtered neutral species require postionization prior to detection. Recently, photoionization by means of UV lasers combined with very sensitive detection techniques led to a breakthrough in the experimental accessibility of large sputtered neutral metal clusters. Clusters as large as Cu_{20} [10], Ag_{18} [8], Al_{12} [11], In_{32} [12], Ga_{14} [13] and mixed clusters $\text{Ga}_{(n-m)}\text{In}_m$ with $n \leq 10$ [14] have been

detected. Relative cluster yields and kinetic energy distributions have been measured for these systems.

The mixed cluster experiments have revealed new and unique information about the sputtering process including the depth of origin of sputtered clusters [13,14]. An increasing depth of origin was found for increasing cluster size in sputtering experiments on the liquid gallium–indium eutectic alloy [14]. While 94% of the sputtered atoms originate from the first atomic layer when the gallium–indium eutectic alloy is bombarded with 4 keV Ar^+ ions, only 68% of the atoms comprising clusters containing 8 atoms come solely from this outermost layer. The observation of statistical abundance distributions of the mixed gallium–indium clusters was crucial for deriving information about the depth of origin of metal clusters from the experimental data. It has been proposed that statistical abundance distributions are observed, if chemical effects play a minor role and photoionization probabilities for all species are nearly equal [14]. Since gallium and indium are located in the same column of the periodic table of the elements and atoms as well as clusters of these elements are one photon ionizable using an ArF-excimer laser, these conditions were presumably fulfilled for the mixed clusters detected in the previous experiments.

This is not the case for the gallium–tin system reported herein. The ionization potential (IP) of tin atoms is 7.34 eV and hence exceeds the photon energy of the available laser light (6.4 eV). Furthermore, ionization potentials that are higher than 6.4 eV have been reported for internally cold Sn_n clusters up to a nuclearity $n = 6$ [15]. The experimental work presented in this paper provides first information about signal intensities of the secondary ions and the photoions for sputtered mixed gallium–tin clusters with varying tin content.

* Corresponding author. Tel. +1 708 252 3514.

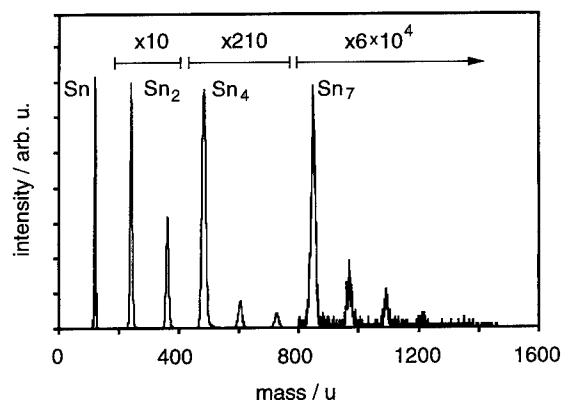


Fig. 1. Typical mass spectrum of neutral clusters ejected from polycrystalline tin during 4 keV argon ion bombardment and postionized with 6.4 eV photons at a power density of 0.3 MW/cm². Portions of the spectrum are magnified by the indicated scaling factors.

2. Experimental

The experiments have been performed in the SARISA IV instrument developed in this laboratory and described in detail elsewhere [16]. This ultra high vacuum apparatus is equipped with an angle- and energy-refocusing time-of-flight mass spectrometer especially designed for high detection efficiencies of photoionized particles. For preparation of unalloyed targets, pure gallium ingots and tin foil (ÆSAR) were used. The gallium–tin eutectic alloy (8.5 at.% Sn) was prepared by dissolving the proper amount of granular tin (Mallinckrodt) in molten gallium at about 100°C overnight. The experiments have been performed near room temperature, where the gallium–tin eutectic alloy is liquid (melting point 20.5°C). As in the experiments with the gallium–indium eutectic alloy, a piece of cobalt was used to support the liquid sample vertically in the instrument [14].

The samples were bombarded with 4 keV Ar⁺ ions at normal incidence, the beam diameter at the sample being about 300 μm. The SARISA IV instrument allows measurements of either sputtered secondary ions or neutral particles. The primary ion pulse length is chosen to be different for both modes, being 160 ns and 2000 ns when detecting sputtered ions and neutrals, respectively. The ion pulse width is kept small in the secondary ion mode to achieve sufficient mass resolution, while in the secondary neutral mode the mass resolution is defined by the laser pulse width (typically 25 ns). The larger ion pulse width in the secondary neutral mode gains signal intensity since the ionization volume can be completely filled with a population that represent the entire velocity distribution and permits velocity integrated measurements of the sputtered neutrals.

In order to clean target surfaces, a continuous argon ion beam with a current of about 3 μA was rastered over a surface area of approximately 2 mm × 2 mm. The samples were cleaned for 1 to 2 hours before every experimental session. No sputter cleaning was necessary between single experimental runs as revealed by comparing spectra taken from the freshly rastered surface and from surfaces that have been kept in the vacuum chamber for several minutes without rastering.

The sputtered neutral atoms and clusters were ionized with 193 nm light from an ArF (6.4 eV) excimer laser that intersected the sputtered particle flux about 1 mm above the target surface with a cross section of 1 mm wide and 2 mm high. Laser power dependent measurements have been performed by attenuating the laser beam with up to 7 partially absorbing quartz plates. Thus, the laser power density could be varied in a range between 0.05 to 3 MW/cm².

3. Results and discussion

A typical composite mass spectrum of neutrals sputtered from a polycrystalline tin surface and photoionized at a laser power density of about 0.3 MW/cm² is shown in Fig. 1. Tin clusters up to Sn₁₀ are clearly visible. The scaling factors reflect the rapid decrease of the cluster signal intensity with increasing cluster size. The rate of change of the cluster signal intensity varies throughout the measured distribution. In particular, there is only a weak intensity change when comparing dimers and trimers for this particular laser power density.

Fig. 2 shows a log–log plot of the integrated signals for clusters sputtered from polycrystalline tin divided by the integrated tin atom signal at four different laser power

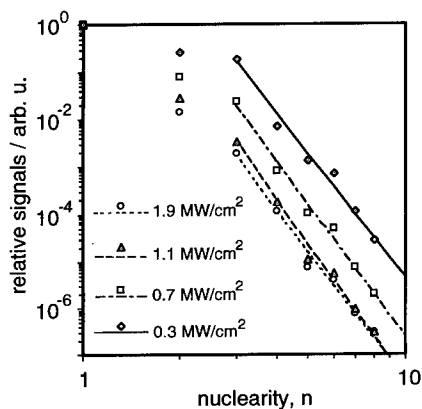


Fig. 2. Relative signals of neutral clusters sputtered from polycrystalline tin and postionized with 6.4 eV photons at 1.9 MW/cm² (circles), 1.1 MW/cm² (triangles), 0.7 MW/cm² (squares), and 0.3 MW/cm² (diamonds) as a function of cluster nuclearity. The lines represent least squares fits to a power law.

densities as a function of cluster nuclearity, n . The data for the relative signals in Fig. 2 have been divided by \sqrt{n} in order to convert the data to flux [4,10,11]. As first demonstrated in Ref. [4] for aluminum and copper clusters, the yields of sputtered neutral and ionic clusters show a power law dependence on cluster nuclearity. As visible in Fig. 2, the relative signals of tin clusters containing more than three atoms can also be fit by a power law. The slopes are -9.0 , -9.5 , -9.3 , and -8.6 for laser power densities of 1.9 , 1.1 , 0.7 , and 0.3 MW/cm², respectively. Thus, the slope of the power law appears to be independent of the laser power density in the investigated range for 6.4 eV photoionization. An average value of -9.1 ± 0.4 has been determined. The data at the different laser power densities do not fall on the same line because the tin atom signal is changing substantially due to its quadratic dependence on the laser power density as measured in a laser power study.

Because tin atoms and clusters are not single photon ionizable with 6.4 eV light, it is difficult to obtain quantitative information about partial sputtering yields. However, we have reason to believe that the measured power law slope is close to the value that would be obtained if the unperturbed cluster yields were measured (i.e., if the cluster photoion signals were saturated without fragmentation). First, the relative intensities of the Sn_7 and Sn_8 clusters, which have been reported to have IPs below 6.4 eV when generated in a pulsed nozzle source [15], lie nicely on the power law fits. Second, the observed slope is in good agreement with results on other materials. In previous studies, a correlation between the power law exponent and the total sputtering yield was identified [4]. The datapoint for tin falls on such a plot and is very close to the value for aluminum. The total sputtering yield for aluminum is 3.0 for 4 keV Ar^+ ion bombardment and the slope of the power law dependence was found to be -9.3 . For tin, the sputtering yield is 2.5 [17]. Therefore the obtained slope of -9.1 seems to be reasonable.

Ion bombardment of the gallium–tin eutectic alloy leads to the ejection of all-gallium and all-tin clusters as well as mixed clusters making the spectrum more complex. Therefore in Figs. 3 and 4, the mass spectra are divided into pieces, each piece showing clusters with equal nuclearity separately. Fig. 3 depicts a mass spectrum of the neutral atoms and clusters, which have been photoionized at a laser power density of 1 MW/cm². Clusters containing up to 4 atoms are shown, although very low pentamer signals have also been detected. The atom and dimer spectra are dominated by the all-gallium species. Among the trimers and tetramers, the most intense peaks belong to Ga_2Sn and Ga_3Sn , respectively. Fig. 4 shows a mass spectrum for the secondary ions. Because ion yields are lower than neutral yields for this system, only clusters as large as trimers were able to be detected.

Despite having IPs that exceed the ArF laser photon energy of 6.4 eV, the all-tin clusters in Fig. 3 have photoion intensities that are only about one order of mag-

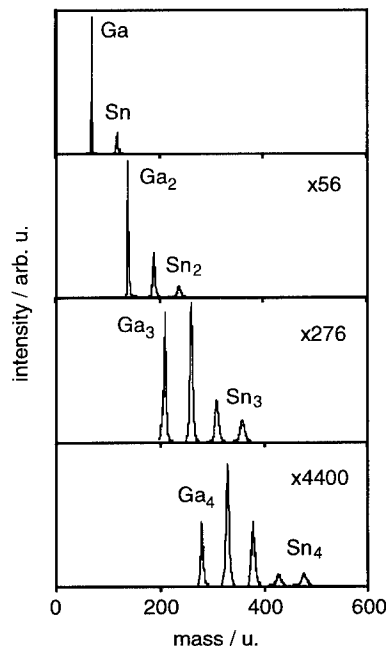


Fig. 3. Typical mass spectrum of neutral clusters ejected from the liquid gallium–tin eutectic alloy during 4 keV argon ion bombardment and postionized with 6.4 eV photons at a power density of 1 MW/cm². The four panels show mass peaks corresponding to clusters with equal nuclearity. The scaling factors are indicated.

nitude smaller than those of the all-gallium clusters. This indicates that mainly internally hot clusters with sufficient energy to be one photon ionized are detected [18]. This

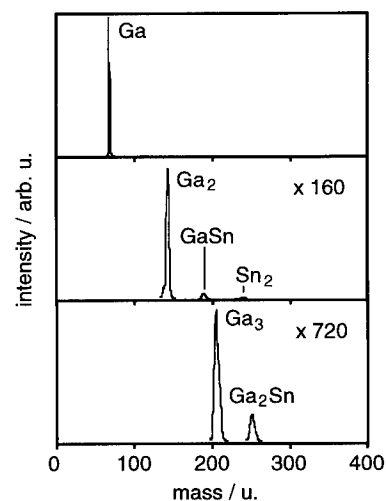


Fig. 4. Typical mass spectrum of positive secondary ion clusters ejected from the liquid gallium–tin eutectic alloy during 4 keV argon ion bombardment. The three panels show mass peaks corresponding to clusters with equal nuclearity. The scaling factors are indicated.

might also be a reasonable explanation for the measured signal distributions in Fig. 2 which do not show “bumps” between the smaller two photon ionizable ($n \leq 6$) and larger one photon ionizable clusters.

Unfortunately, no data on the surface composition of the gallium–tin eutectic alloy is available in the literature. Therefore, our knowledge is restricted to thermodynamic calculations based on a formalism developed by Miedema et al. [19]. Here, the gallium–tin alloy is treated as a regular solution. The parameters that enter the calculation are taken from Ref. [20]. The calculations predict a strong tin surface segregation with a tin concentration of 87 at.% in the first atomic layer. Such a surface segregation of the minor constituent is known and well documented for the gallium–indium eutectic alloy [21–23], where the indium surface concentration was measured to be 94 at.%. A closer look at the spectra in Figs. 3 and 4 indeed suggests that tin is surface segregated in the gallium–tin system. Considering the dimers, for instance, an uniform tin concentration of 8.5 at.% (i.e., a nonsegregating system) would result in an 116-fold stronger Ga_2 abundance compared to Sn_2 (assuming a statistical formation process). This is an order of magnitude more than observed in the experiment. Since Ga_2 is one photon ionized and Sn_2 not, the signal ratio should be larger than the abundance ratio. However, our measurements yield the opposite result. The only explanation for observing such a large Sn_2 signal is that its abundance is large due to segregation. Similarly, the high signal intensities of the gallium containing GaSn_2 and GaSn_3 clusters would not be observed if the surface composition was equal to the bulk composition. Thus, our results confirm that tin is segregated on the surface of the gallium–tin eutectic alloy as predicted.

The measured distributions of the clusters with equal nuclearity in Figs. 3 and 4 are clearly not statistical. This is in contrast to the statistical behavior observed for the gallium–indium eutectic alloy. In particular, the measured photoion intensities drop significantly for clusters containing equal numbers of tin and gallium atoms and for clusters in which tin atoms are the majority. Thus, for the trimers, there is a distinct intensity drop when going from Ga_2Sn to GaSn_2 . For the tetramers, the measured intensity decreases gradually from Ga_3Sn to Ga_2Sn_2 and to GaSn_3 . The question arises as to what extend the departure from a statistical behavior is from a nonstatistical distribution in yields caused by chemical bonding differences in the alloy or from ionization efficiency variations that cause the measured signals to be distorted. Clearly, this question can be answered definitively only by measuring the neutral cluster yields, for instance, with sufficiently high photon energies. We note that statistical as well as nonstatistical combinations of component elements have been found for mixed clusters in laser vaporization experiments [24–28].

This question can be addressed and some information can be obtained from the experimental data by comparing the measured distributions for ionic and photoionized neu-

tral mixed clusters as given in Figs. 3 and 4. The measured distributions for neutral and ionic dimers and trimers differ dramatically from each other. Thus, for the Ga_2Sn cluster, the measured photoion signal is larger than that of Ga_3 , but in the secondary ion mode the Ga_2Sn signal is only about 25% of the all-gallium trimer. The GaSn_2 and Sn_3 ion cluster signals are very low, and therefore, are not visible in the mass spectrum in Fig. 4. The ionic and photoionized neutral clusters are sputtered species in the particle flux that are ionized by two different processes. The trend of decreasing ion and photoion signal intensities for increasing tin content in clusters with equal nuclearity correlates with the higher IP of tin clusters compared to gallium clusters. Clearly, the differences in the measured distributions suggest that the ionization process is crucial for the appearance of nonstatistical distributions of sputtered mixed gallium–tin clusters. We note that for sputtered neutral and ionic gallium–indium clusters, nearly identical abundance distributions have been found [14].

The tendency to produce nonstatistical distributions of mixed clusters due to chemical bonding effects can not be ruled out but is anticipated to be only weak. For mixed clusters composed of group IVA with group VA and group IIIA with group VA metals, the valence-electron-counting model, the so called “Wade’s rules” [29], were used to explain the pattern of the observed nonstatistical distributions. In this model, cluster bonding involves only p orbitals, and a cluster with nuclearity n has stable bonding for configurations of $2n + 2$, $2n + 4$, or $2n + 6$ p -electrons. As can easily be shown, for the group IIIA–group IVA system studied in our sputtering experiments, these configurations do not exist. Another effect that requires consideration is preferential evaporation of one of the elements from the sputtered, internally hot clusters. However, since the vaporization energy of tin is only slightly larger than gallium ($\Delta H_f(298) = 3.16$ and 2.87 eV, respectively [30]), preferential evaporation of gallium, if any, would lead to an enhanced tin concentration of the detectable clusters and therefore can not be responsible for the measured distributions in Figs. 3 and 4.

4. Conclusions

Sputtering of neutral and ionic clusters under 4 keV Ar^+ ion bombardment from the gallium–tin eutectic alloy and of neutral tin clusters from polycrystalline tin has been studied. Neutral clusters as large as $\text{Ga}_{(n-m)}\text{Sn}_m$ with $n \leq 4$ and Sn_{10} as well as ionic clusters $\text{Ga}_{(n-m)}\text{Sn}_m$ with $n \leq 3$ have been detected. The relative cluster signal vs. cluster nuclearity dependences of the neutral clusters sputtered from polycrystalline tin and photoionized with 6.4 eV photons can be fit with a power law dependence, the slope, δ , being -9.1 ± 0.4 , a value that lies on the general linear dependence of δ on the total sputtering yield which was discovered previously for a variety of metals. For the

eutectic gallium–tin alloy, the measured signal distributions of the ionic and neutral (ionized with 6.4 eV photons) sputtered clusters with equal nuclearity are found to be nonstatistical. The observation of different signal distributions for sputtered secondary ions and photoionized neutral clusters suggests that different ionization efficiencies of the various clusters play an important role. The measured signal distributions of the photoionized neutral clusters can therefore be explained by the fact that substitution of gallium atoms for tin atoms leads to an increasing photoionization efficiency for clusters of given nuclearity. The experimental results as well as segregation calculations indicate that tin is segregated at the surface of the gallium–tin eutectic alloy.

Acknowledgements

The authors would like to thank A.R. Krauss for calculations of the tin surface concentration in the gallium–tin alloy and A. Wucher for interesting and helpful discussions. This work was supported by the U.S. Department of Energy, BES-Material Sciences, under Contract W-31-109-ENG-38.

References

- [1] P. Sigmund, in: *Sputtering by Particle Bombardment I*, ed. R. Behrisch (Springer, Berlin, Heidelberg, New York, 1981).
- [2] M.W. Thompson, *Philos. Mag.* 18 (1968) 377.
- [3] H. Oechsner, *Z. Phys.* 238 (1970) 433.
- [4] S.R. Coon, W.F. Calaway, M.J. Pellin and J.M. White, *Surf. Sci.* 298 (1993) 161.
- [5] G. Nicolussi, W. Husinsky and G. Betz, *Phys. Rev. Lett.* 71 (1993) 1518.
- [6] G. Kampwerth, M. Terhorst, E. Niehuis, A. Benninghoven, in: *Secondary Ion Mass Spectrometry SIMS VIII*, eds. A. Benninghoven, K.T.F. Janssen, J. Tümpner and H.W. Werner (Wiley, Chichester, 1992).
- [7] S.W. Downey, A.B. Emerson and R.F. Kopf, *Nucl. Instr. and Meth. B* 62 (1992) 456.
- [8] A. Wucher, M. Wahl and H. Oechsner, *Nucl. Instr. and Meth. B* 83 (1993) 73.
- [9] M. Wahl and A. Wucher, *Nucl. Instr. and Meth. B* 94 (1994) 36.
- [10] S.R. Coon, W.F. Calaway, M.J. Pellin, G.A. Curlee and J.M. White, *Nucl. Instr. and Meth. B* 82 (1993) 329.
- [11] S.R. Coon, W.F. Calaway, J.W. Burnett, M.J. Pellin, D.M. Gruen, D.R. Spiegel and J.M. White, *Surf. Sci.* 259 (1991) 275.
- [12] Z. Ma, S.R. Coon, W.F. Calaway, M.J. Pellin, D.M. Gruen and E.I. v. Nagy-Felsobuki, *J. Vac. Sci. Technol. A* 12 (1994) 2425.
- [13] Th. Lill, W.F. Calaway, Z. Ma and M.J. Pellin, *Surf. Sci.* 322 (1995) 361.
- [14] Th. Lill, W.F. Calaway, M.J. Pellin and D.M. Gruen, *Phys. Rev. Lett.* 73 (1994) 1719.
- [15] K. LaiHing, R.G. Wheeler, W.L. Wilson and M.A. Duncan, *J. Chem. Phys.* 87 (1987) 3401.
- [16] M.J. Pellin, C.E. Young, W.F. Calaway, J.W. Burnett, B. Jørgensen, E.L. Schweitzer and D.M. Gruen, *Nucl. Instr. and Meth. B* 18 (1987) 446.
- [17] N. Matsunami, Y. Yamamura, Y. Itikawa, N. Itoh, Y. Kazumata, S. Miyagawa, K. Morita, R. Shimizu and H. Tawara, *Atom. Data Nucl. Data Tables* 31 (1984) 1.
- [18] A. Wucher, private communication.
- [19] A.R. Miedema and J.W.F. Dorleijn, *Surf. Sci.* 95 (1980) 447.
- [20] A.R. Miedema, *Z. Metallk.* 69 (1978) 455.
- [21] M.F. Dumke, T.A. Tombrello, R.A. Weller, R.M. Housley and E.H. Cirlin, *Surf. Sci.* 124 (1983) 407.
- [22] K.M. Hubbard, R.A. Weller, D.L. Weathers and T.A. Tombrello, *Nucl. Instr. and Meth. B* 40 (1989) 278.
- [23] K.M. Hubbard, R.A. Weller, D.L. Weathers and T.A. Tombrello, *Nucl. Instr. and Meth. B* 36 (1989) 395.
- [24] E.A. Rohlfing, D.M. Cox, R. Petkovic-Luton and A. Kaldor, *J. Phys. Chem.* 88 (1984) 6227.
- [25] M.B. Bishop, K. LaiHing, P.Y. Cheng, M. Peschke and M.A. Duncan, *J. Phys. Chem.* 93 (1989) 1566.
- [26] R.G. Wheeler, K. LaiHing, W.L. Wilson, J.D. Allen, R.B. King and M.A. Duncan, *J. Am. Chem. Soc.* 108 (1986) 8101.
- [27] R.G. Wheeler, K. LaiHing, W.L. Wilson and M.A. Duncan, *J. Chem. Phys.* 88 (1988) 2831.
- [28] D. Schild, R. Pflaum, K. Sattler and E. Recknagel, *J. Phys. Chem.* 91 (1987) 2649.
- [29] K. Wade, *Adv. Inorg. Chem. Radiochem.* 18 (1976) 1.
- [30] R.C. Weast (ed.), *Handbook of Chemistry and Physics* (CRC Press, Boca Raton, 1988).



ELSEVIER

Angular and charge state distributions of highly charged ions scattered during low energy surface-channeling interactions with Au(110)

F.W. Meyer^{a,*}, L. Folkerts^a, S. Schippers^{a,b,1}

^a Oak Ridge National Laboratory, Oak Ridge, TN 37831-6372, USA

^b University of Osnabrück, D-49069 Osnabrück, Germany

Abstract

We have measured scattered projectile angular and charge state distributions for 3.75 keV/amu O^{q+} ($3 \leq q \leq 8$) and 1.2 keV/amu Ar^{q+} ($3 \leq q \leq 14$) ions grazing incident along the [110] and [100] directions of a Au(110) single crystal target. Scattered projectile angular distributions characteristic of surface channeling are observed. For both incident species, the dominant scattered charge fraction is neutral, which varies only by a few percent as a function of incident charge state. Significant O^- formation is observed, which manifests a distinct velocity threshold. For incident Ar projectiles with open L-shell, the positive scattered charge fractions, while always less than about 10%, increase linearly with increasing number of initial L-shell vacancies.

1. Introduction

Most experimental work to date in the area of multi-charged ion–surface interactions has focused on measurement of X-ray [1,2] and electron emission. The latter experiments include measurements of total electron yields, determined either by conventional means [3] or via analysis of the electron emission statistics [4], as well as of ejected electron energy distributions [5–7]. Recently, Winter et al. [8] directed attention to the scattered projectiles, measuring angular distributions of highly charged ions scattered during grazing surface collisions. They found characteristic shifts of the angular distributions away from the specular reflection angle, which they attributed to image charge acceleration of the highly charged ion during its approach to the surface. The only previous measurement of scattered ion charge state distributions was made by de Zwart et al. [9], who measured relative yields of +1, +2, and +3 scattered ions as a function of incident charge state ($q = 1$ to 11) for 20 keV Ne, Ar, and Kr ions incident at 15° on a polycrystalline W target. Since their experiment could not detect neutral scattered projectiles, de Zwart et al. were not able to determine absolute charge state fractions. More recently, Briere et al. [10] have

reported preliminary results of charge state distribution measurements for Kr^{35+} and O^{8+} ions grazing incident on an epitaxially grown Au film on mica.

In this contribution we describe an experiment in which both the angular as well as charge state distributions of the scattered ions are measured using a two-dimensional position sensitive detector (PSD). The method permits detection of all possible scattered charge states (i.e. including positive ions, neutrals and negative ions), making possible the extraction of absolute scattered projectile charge fractions. Furthermore, the present measurements were performed under surface channeling [11] conditions as verified by observation of characteristic angular distributions for the reflected projectiles. Under surface channeling conditions there is minimal penetration of the target surface plane and the projectile trajectories are well defined. As a result the interaction times of the projectile with the target can in principle be accurately determined.

2. Experimental approach

In the present experiment multicharged O and Ar ions, produced by a CAPRICE ECR ion source at the ORNL Multicharged Ion Research Facility, are grazing incident ($\Psi = 1.8^\circ$) on a clean Au(110) surface along the [110] or [001] directions. The incident multicharged ion beam is collimated by two 0.5-mm-diameter apertures to an angular divergence of about 0.1° FWHM. The scattering geometry is indicated schematically in Fig. 1. The single crystal

* Corresponding author. Tel. +1 615 574 4705, fax +1 615 574 4745, e-mail meyer@orph01.

¹ Present address: Kernfysisch Versneller Instituut, Zernikelaan 25, 9747 AA Groningen, The Netherlands.

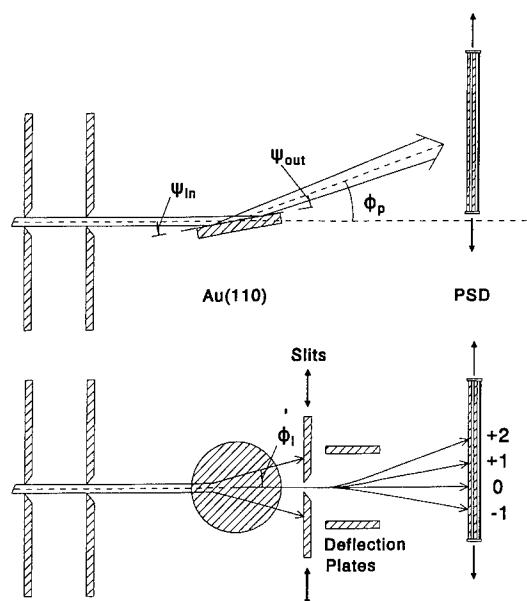


Fig. 1. Schematic side and top views of the collision geometry and experimental layout.

Au(110) target is mounted on an x - y - z manipulator located in a UHV chamber having a base pressure of 3×10^{-10} mbar and is prepared by cycles of surface sputter cleaning with 1-keV Ar^+ ions and crystal annealing at about 700°C. Surface cleanliness is verified using electron-induced Auger electron spectroscopy. Both the angular distribution (polar as well as lateral) and charge state distribution of the scattered (reflected) projectiles were measured using a two-dimensional position sensitive detector (PSD) (quantar technology model 3394A) having a 40-mm-diameter active area. Movable slits located between the target and the PSD were completely opened for measurements of angular scattering distributions. For the charge state distribution measurements they were closed to select a thin vertical slice of the scattered beam, which was then dispersed by charge state across the face of the PSD using a pair of electrostatic deflection plates located immediately downstream of the slit assembly, as shown in Fig. 1. The target-PSD distance is about 560 mm. The PSD is mounted on a second x - y - z manipulator which permits measurement of the polar scattering angle, ϕ_p , in the range -0.8° to $+5.6^\circ$. The position of the primary beam, used to determine $\phi_p = 0^\circ$, as well as its angular spread, can thus be directly measured. In order to avoid saturation of the PSD, beam intensities on target were kept sufficiently low that the total scattered ion flux on the PSD did not exceed 100 kHz.

3. Experimental results

Figs. 2a and 2b show the angular distributions observed on the PSD for two different incident ions and target

azimuthal orientations. The characteristic “banana” shape of the angular distributions displayed in the figure is indicative of surface channeling, which occurs whenever the direction of the grazing incident beam is nearly parallel to one of the low index crystal directions, such that the ions are reflected by a series of relatively soft encounters with successive atoms along a particular lattice row rather than a single hard encounter with an isolated lattice atom. The resulting guided motion down the atomic rows leads to an observed angular distribution of the ultimately reflected particles that mirrors the “corrugation” present in the surface. For the [110] direction, this “corrugation” is 8.15 Å wide due to the known (1×2) reconstruction of the Au(110) surface at room temperature, while for the [001] direction, i.e. transverse to the “missing row” direction, it is 4.07 Å. It is noted that the above “banana” shaped angular distribution is no longer observed when the azimuthal crystal orientation is changed a few degrees away from the low-index directions, or when the crystal is heated above the temperature at which the phase change to the random (1×1) surface reconstruction occurs. It is further noted that already at the above collision energy, the central spot of maximum scattered ion intensity is observed at angles larger than the specular reflection angle, due to image acceleration effects [8] on the incoming projectile trajectory.

As already mentioned in an earlier section, in order to determine the charge distribution of the scattered ions, movable slits were used to select a vertical slice of the scattered beam, which then passes through a set of deflection plates. The electrostatic analysis produces a series of horizontally displaced vertical bands, each corresponding to a particular charge state, while the intensity distribution of each band along the vertical axis reflects its polar angular distribution. The result of such an electrostatic analysis is shown in Fig. 3 for 3.75 keV/amu O^{8+} ions incident on Au(110) under the same conditions already described in connection with Fig. 2a. The movable slits were set to select lateral angles ϕ_l from -0.15° to $+0.15^\circ$, i.e. a central slice from the scattered ion angular distribution, while the PSD was shifted horizontally to permit dispersal of the charge state distribution over the full width of the PSD. The vertical bands corresponding to the different charge states are easily discerned in the figure. The band second from the right is the most intense, and corresponds to the neutral component, with negative ions ($r = -1$) on the extreme right and the positive charge states ($r = +1$ to $+5$) to the left. Individual vertical slices (i.e. charge states) can be projected onto the vertical axis, providing information on the polar angular distribution for a particular scattered charge state. This is illustrated in Fig. 4a for four scattered charge states resulting from grazing interactions of O^{8+} with Au(110) along the [110] direction.

Alternatively, charge state distributions can be obtained by essentially collapsing the 2D spectrum onto the hori-

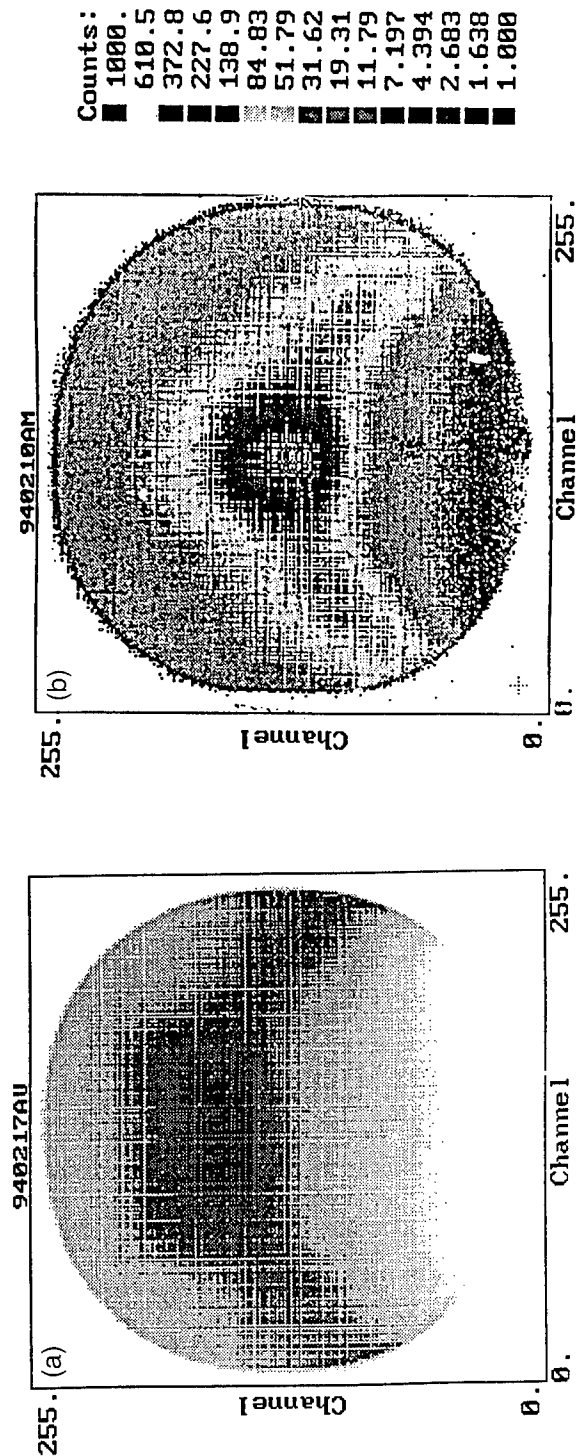


Fig. 2. Intensity distribution of scattered ions recorded on the PSD for (a) 3.75 keV/amu O^{8+} ions incident at 1.8° and (b) for 2.0 keV/amu Ar^{11+} ions incident at 1.5° , both along the [110] direction of Au(110), illustrating the banana-shaped angular scattering distribution characteristic of surface-channeling.

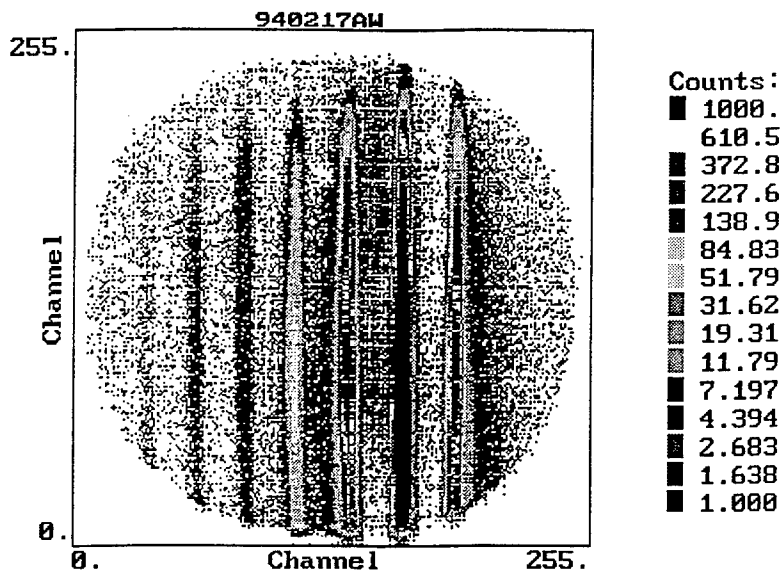


Fig. 3. Intensity distribution recorded on the PSD with narrow slit opening and deflection voltage switched on, for 3.75 keV O^{8+} incident ions, showing charge state -1 (furthest on right) through $+5$ (furthest on left).

zontal axis, as is illustrated in Fig. 4b. Integration under each charge state “peak” then permits determination of the scattered charge state fractions. This was done for oxygen ions in initial charge states down to $q = 3$, and for Ar ions in the incident charge state range 3–14. The measurement results are given in Figs. 5 and 6, where the fractions of final charge states “ r ” are plotted as a function of the incident charge state “ q ”. It is noted that the measured charge state distributions were largely insensitive to changes in front channel plate bias voltage, suggesting that the PSD quantum efficiency of even the lowest scattered charge states (i.e. $+1$, 0 , and -1) was close to 100% at the investigated energies.

Scattered ion charge state distributions were also measured for ion incidence along arbitrary “random” directions, i.e. away from the low-index channels. Only slight variations with incident direction were found in the relative scattered charge fractions. Measurements [12] with incident Ar^{q+} ions, to be discussed in detail elsewhere, showed significant variation of the positive charge fractions as a function of elapsed time since the last annealing cycle, suggesting possible sensitivity of the measured fractions to surface order and/or contamination. It is emphasized, however, that in the present article, the focus is not on the dependences of the charge fractions on target conditions, but rather on their dependence on the incident projectile.

To that end, measurements were also made of the energy dependence of the scattered charge fractions for incident O^{1+} , O^{5+} and O^{7+} ions in the velocity 0.064 to 0.55 (in a.u.). The positively charged scattered ion fractions show significant increases in the investigated energy range, as might be expected in analogy to gas phase

collisions where stripping cross sections steeply increase with energy and the electron capture cross sections are either still flat or have already started to fall. More interestingly, as can be seen in Fig. 7, the fraction of O^- ions, which constitute the most loosely bound system ($E_A = 0.054$ a.u.) in the ensemble of possible charge states, shows a definite velocity or energy “threshold” at $v = 0.1$ a.u., below which the O^- fraction is very small, and above which it steadily increases up to the maximum investigated velocity. This velocity dependence is in contrast to what is expected for thick target gas phase collisions [13] for this energy interval, where the detachment cross section increases and the σ_{0-1} capture cross is approximately flat or already falling.

4. Discussion

In order to gain some insight into the trajectories along which the projectiles travel under the conditions of surface-channeling, a Monte Carlo simulation was carried out in which the equations of motion of the projectile in the periodic potential of the crystal surface were solved for an ensemble of appropriate random initial conditions. Following Niehof and Heiland [14], the scattering potential used was a superposition of individual contributions (assuming a ZBL interaction potential) from a $6 \times 6 \times 2$ lattice cell that was progressively translated along the ion trajectory. The 2×1 reconstruction was created by moving every second (110) row of the [110] surface plane to the third layer. The surface was characterized by an anisotropic Debye temperature, as prescribed by Jackson [15]. Fig. 8 shows the simulation results for 3.75 keV/amu O projec-

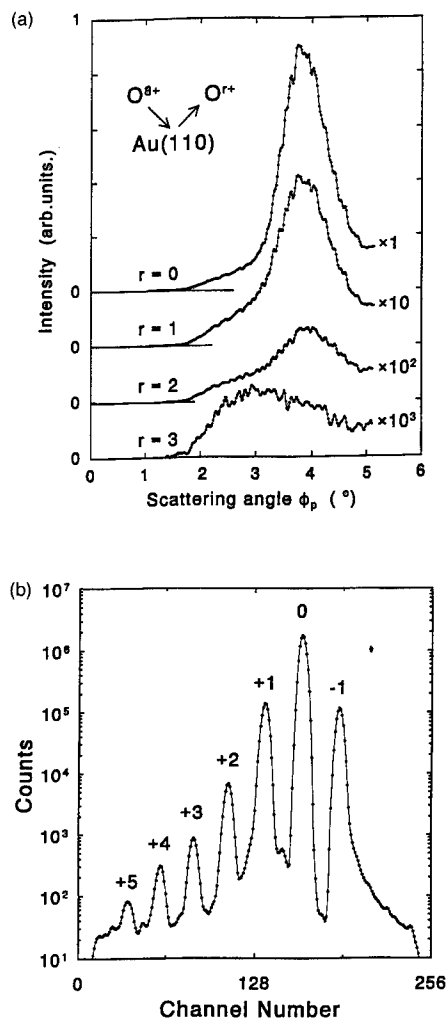


Fig. 4. Collapse of selected portions the 2D spectrum of Fig. 3 onto the (a) vertical axis, showing the angular scattering distribution for four scattered charge states, and onto (b) the horizontal axis showing the charge distribution of the scattered projectiles.

tiles incident along the [110] direction of Au(110) at 1.8°. As can be seen, quite good agreement with the experimentally measured angular distribution shown in Fig. 2a is obtained. The simulation indicates a total trajectory length within 2 Å of the topmost Au surface layer of about 214 Å, corresponding to an interaction time of only about 25 fs, and a maximum penetration depth of 2.2 Å. This result can be used together with the measured charge distributions to determine time scales [16] of projectile charge equilibration during multicharged ion–surface interactions.

As regards the charge state distributions for O^{q+} and Ar^{q+} ions shown in Figs. 5 and 6, a number of remarkable features can be noted. For all incident charge states investigated, the neutral fraction strongly dominates the scattered ion charge state distribution, as has been already noted by Winter et al. [8]. For incident ions not carrying inner shell

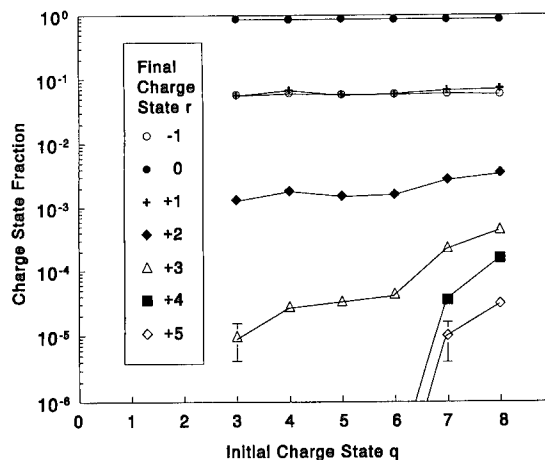


Fig. 5. Scattered projectile charge fractions for 3.75 keV/amu O^{q+} ($3 \leq q \leq 8$) ions incident along the [110] direction of Au(110) at 1.8°.

vacancies, i.e. $q \leq 6$ for the O ions and $q \leq 8$ for the Ar ions, the scattered charge fractions are essentially independent of incident charge, indicating complete charge equilibration. For the incident oxygen ions, a significant fraction of the scattered ions recede from the surface in charge state -1 . As can be seen from Fig. 5, the scattered ion fractions of charge state $+2$ and higher show noticeable increases when the incident ion carries initial K-shell vacancies, i.e. for O^{7+} and O^{8+} . Such a trend has been previously noted by de Zwart et al. [9]. In the case of the Ar^{q+} incident ions, this increase occurs when the incident ion carries one or more L-shell vacancies, and is evident already in the $+1$ charge fraction. As is shown in Fig. 6, there is a monotonic increase in *all* positive charge fractions with increasing initial L-vacancy number, which is seen to become increasingly steeper with increasing

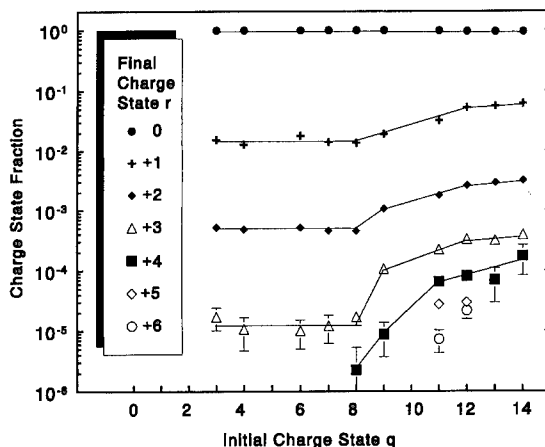


Fig. 6. Scattered projectile charge fractions for 1.2 keV/amu Ar^{q+} ($3 \leq q \leq 14$) ions incident along the [001] direction of Au(110).

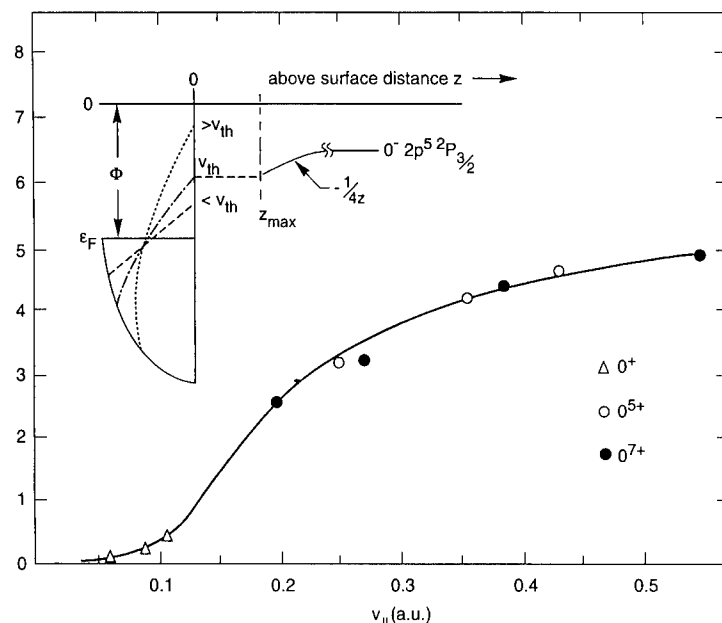


Fig. 7. O^- scattered charge fractions for O^{1+} , O^{5+} , O^{7+} incident ions as a function of parallel velocity; incidence angle 1.8° along the $[001]$ direction of Au(110) – the solid line is drawn to guide the eye; inset schematically indicates O^- formation mechanism (above-surface distance is referenced to surface image plane).

scattered charge state. It should be noted, however, that, independent of incident charge state, the overall contribution of scattered charge states +1 and higher to the total scattered ion intensity is less than 10% for the two systems and energies investigated.

The scattered projectile polar angular distributions shown in Fig. 4a show evidence of two components. The

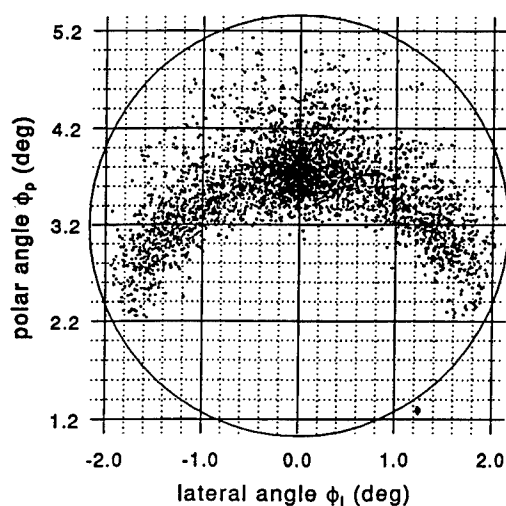


Fig. 8. Simulated scattered projectile intensity distribution on the PSD for 3.75 keV/amu oxygen ions incident along the $[110]$ direction of Au(110) at 1.8° , showing the characteristic banana-shaped angular scattering distribution observed for surface-channeling.

first one, which dominates the low scattered charge state angular distributions, is narrow with FWHM about 1° and peaks close to the angle expected for specular reflection. The second is significantly broader and shifted to smaller scattering angles. The latter component appears to increase in relative importance with increasing charge state, and appears to be the dominant one for scattered charge state +3. It is possible that this broader component results from the small fraction of projectiles in which inner-shell Auger decay takes place on the outgoing trajectory, but the data analysis required to resolve this issue is presently still incomplete.

For the case of the incident oxygen ions, the velocity threshold observed for the scattered O^- fraction (see Fig. 7) can be used [16] to estimate the spatial extent of charge equilibration on the receding part of the projectile trajectory. Negative ion formation velocity thresholds such as displayed in Fig. 7 have been explained as arising due to “kinematic resonance” effects [17] in the case of projectiles having non-zero parallel velocity components with respect to the target surface. In the rest frame of such projectiles, a modification of the Fermi–Dirac distribution of target electrons results in a virtual population of electronic states above the Fermi edge. At sufficiently high parallel velocities, occupied states of the solid can come into resonance with a projectile negative ion level whose electron affinity is significantly less than the surface work function of the target. This scenario is schematically indicated in the inset of Fig. 7. An additional feature of negative ion formation above metal surfaces is the fact

that, unlike ionization energies of positive ions, the negative ion electron affinity increases with decreasing distance to the surface, due to the image charge interaction which shifts the negative ion binding energy by $-\frac{1}{4}z$, where z is the distance above the surface image plane (both energy shift and distance in atomic units). This has the consequence that, from the measured threshold of negative ion formation, the maximum distance of negative ion formation above the surface can be inferred. For the threshold observed in the present case, the top of the kinematically shifted valence electron distribution is energetically within 0.128 a.u. of the vacuum level. Resonant capture of these kinematically shifted valence electrons to form O^- implies a negative ion level shift (due to the image charge interaction) of -0.074 a.u. This shift corresponds to a distance of formation above the image plane of $\sim 3a_0$, which translates to a distance of 2–3 Å above the actual surface plane after the offset between these two reference planes has been taken into account. Under the assumption that the O^- ion is formed by a one electron transfer process, neutral oxygen is a necessary precursor. The fact that both the neutral and O^- fractions are essentially independent of incident charge state indicates that the above noted charge equilibration is already essentially complete while the scattered ions are still within 2–3 Å of the surface.

To estimate the contribution to charge equilibration of the above-surface resonance neutralization and autoionization cascade occurring on the approach trajectory, simulations for various oxygen charge states incident on Au(110) were carried out using the code developed by Burgdörfer et al. [18] to determine the resulting electron populations in the various projectile n -levels at the time of surface impact. Particularly for the highest oxygen charge states, i.e. +7 and +8, which have the longest autoionization cascades to be traversed in order to populate the inner shells, at the perpendicular velocity corresponding to the experimental condition of Fig. 5, only little feeding of the projectile K-, L-, and M-shells via the autoionization cascade was found. The other captured electrons remain in higher lying Rydberg levels, where they will be peeled from the projectile by the increased screening it will experience upon reaching the surface. It is concluded [14] that inner shell electron population along the approach trajectory via the above-surface cascade does not play a significant direct role in the charge equilibration of these highly charged ions during their interaction with the surface.

It thus appears that, at least for the incident O^{q+} ions, even for the grazing collisions studied here, the dominant contribution to the charge equilibration comes from the close interaction with the surface, i.e. within roughly 2–3 Å of the surface.

Acknowledgements

This research was sponsored by the Division of Applied Plasma Physics, Office of Fusion Energy, and by the Division of Chemical Sciences, Office of Basic Energy Sciences of the U.S. Department of Energy under contract No. DE-AC05-84OR21400 with Martin Marietta Energy Systems, Inc. L. Folkerts was supported through a program administered by the Oak Ridge Institute for Science and Education. S. Schippers gratefully acknowledges financial support by the Deutsche Forschungsgemeinschaft (DFG).

References

- [1] B. D'Etat et al., Proc. 6th Int. Conf. on the Physics of Highly Charged Ions, Manhattan, Kansas, USA 1992, AIP Conf. Proc. 274, p. 592.
- [2] H.J. Andrä et al., ICPEAC XVII Invited Papers, Brisbane, Australia, 1991, p. 89.
- [3] M. Fehringer et al., Nucl. Instr. and Meth. B 23 (1987) 245.
- [4] F. Aumayr and H.P. Winter, Comments At. Mol. Phys. 29 (1994) 275.
- [5] F.W. Meyer, S.H. Overbury, C.C. Havener, P.A. Zeijlmans van Emmichoven, J. Burgdörfer, and D.M. Zehner, Phys. Rev. A 44 (1991) 7214.
- [6] R. Köhrbrück et al., Phys. Rev. A 50 (1994) 1429.
- [7] J. Das, H. Limburg and R. Morgenstern, XVIII ICPEAC Invited Papers, Aarhus, Denmark, 1993, AIP Conf. Proc. 295, p. 766.
- [8] H. Winter, Europhys. Lett 18 (1992) 207; H. Winter, C. Auth, R. Schuch and E. Beebe, Phys. Rev. Lett 71 (1993) 1939.
- [9] S.T. de Zwart et al., J. Phys. B 18 (1985) L623.
- [10] M.A. Briere et al., Contributed Papers of the XVIII ICPEAC, Aarhus, Denmark, 1993, p. 774.
- [11] R. Sitzmann and C. Varelis, Nucl. Instr. and Meth. 132 (1976) 633; B.W. Farmery, A.D. Marwick and M.W. Thompson, in: *Atomic Collision Phenomena in Solids* (North Holland, Amsterdam, 1970) p. 589.
- [12] L. Folkerts and F.W. Meyer, Phys. Rev. A, to be submitted (1994).
- [13] B. Hird and F. Rahman, Phys. Rev. A 26 (1982) 3108; B. Hird, F. Rahman and M.W. Orakzai, Can. J. Phys. 66 (1988) 972.
- [14] A. Niehof and W. Heiland, Nucl. Instr. and Meth. B 48 (1990) 306.
- [15] D.P. Jackson, Surf. Sci. 43 (1974) 432.
- [16] L. Folkerts et al., submitted to Phys. Rev. Lett.
- [17] See, e.g.: F. Wyputta, R. Zimny and H. Winter, Nucl. Instr. and Meth. B 58 (1991) 379; A.G. Borisov, D. Teillet-Billy and J.P. Gauyacq, Phys. Rev. Lett. 68 (1992) 2842.
- [18] J. Burgdörfer, P. Lerner and F.W. Meyer, Phys. Rev. A 44 (1991) 5674.

MeV He ion impact desorption of hydrogen isotopes from an InP(001)-p(1 × 1) surface

K. Morita^{*}, H. Ikegami, M. Ueshima

Department of Crystalline Materials Science, School of Engineering, Nagoya University, Furo-cho, Chikusa-ku, Nagoya 464-01, Japan

Abstract

MeV He⁺ ion impact desorption of hydrogen isotopes adsorbed on the InP(001)-p(1 × 1) surface has been studied by continuous measurements of decrease of their surface coverage by means of the elastic recoil detection (ERD) technique using a He⁺ ion beam at different energies. It is found that the surface coverage of hydrogen decreases exponentially as the He⁺ ion fluence increases, while no change of the p(1 × 1) spots by LEED and the In surface composition by AES has been observed even when the surface coverage decreases from 2 ML down to 0.3 ML. The desorption cross sections of MeV He⁺ ions for hydrogen isotopes, determined from the exponential decay curves, are $(8\text{--}10) \times 10^{-17} \text{ cm}^2$ in the range from 0.7 to 1.9 MeV. Their energy dependence corresponds well to that of the electronic stopping cross section for MeV He⁺ ions of In atoms, to which the hydrogen atoms are directly bound. The desorption process of hydrogen by MeV ion impact is discussed on the basis of the experimental data.

1. Introduction

The adsorption of hydrogen on semiconductor surfaces has received intensive attention over the past ten years from fundamental and applied points of view because of its ability to block the activity of dangling bonds and to passivate the surface. The electronic and chemical properties of hydrogen atoms have been studied by means of surface analysis techniques on the cleaned and reconstructed surface of elemental and various compound semiconductors such as Si, GaAs, InP, etc. [1–6]. The hydrogen atoms adsorbed on the crystalline surface also may alter the growth mode of metal films [7]. For detailed understanding of the hydrogen effect, quantitative analysis of the surface hydrogen concentration is of essential importance. MeV ion beam analysis techniques with nuclear reactions and elastic (recoil) collisions are the most powerful for absolute measurements. For their applications, MeV ion impact desorption of hydrogen should be well understood.

In our previous work [8], we have applied a NRA technique using the $^3\text{He(d, } \alpha\text{)H}$ reaction to measure the concentration of deuterium adsorbed on the InP(001)-p(2 × 4) surface. It has been found that the cross section of the probing 700 keV $^3\text{He}^+$ ions for desorption of D is quite high and is roughly 10^{-16} cm^2 . In order to understand the

process of the ion impact hydrogen desorption, it is important to know the dependence of the cross section on ion energy. For this purpose, the elastic recoil detection (ERD) technique with the $^4\text{He}^+$ ion beam should be developed under ultrahigh vacuum conditions.

In this paper, we report the experimental result of the energy dependence of the He⁺ ion impact desorption of hydrogen isotopes from a InP(001)-p(1 × 1) surface in the MeV regime which was measured using the ERD technique. It is shown that the energy dependence of the cross section for hydrogen desorption is almost independent of energy in the range studied, essentially the same as that of the electronic stopping cross section for He⁺ ions [9] of In atoms to which the hydrogen atoms are bound. The process for hydrogen desorption is discussed on the basis of the experimental data.

2. Experimental

The InP specimen used was a (001)-oriented n-type and an undoped single-crystalline wafer. Its carrier concentration and resistivity were $(6.0\text{--}9.5) \times 10^{15} \text{ cm}^{-3}$ and $(2.6\text{--}3.2) \times 10^{-1} \Omega \text{ cm}$, respectively (Showa Electric Industries Ltd.). The specimen surface was mechanically polished, cleaned in standard solvents, etched in a $\text{H}_2\text{O}:\text{H}_2\text{SO}_4$ solution for 1 min at 60°C and in a $\text{H}_2\text{O}:\text{NH}_4\text{F}$ solution for 1 min at room temperature and finally rinsed in de-ionized water. As shown in Fig. 1, the specimen was mounted on a three-axes rotatable goniome-

^{*} Corresponding author, tel. +81 52 789 4686, fax +81 52 789 3791.

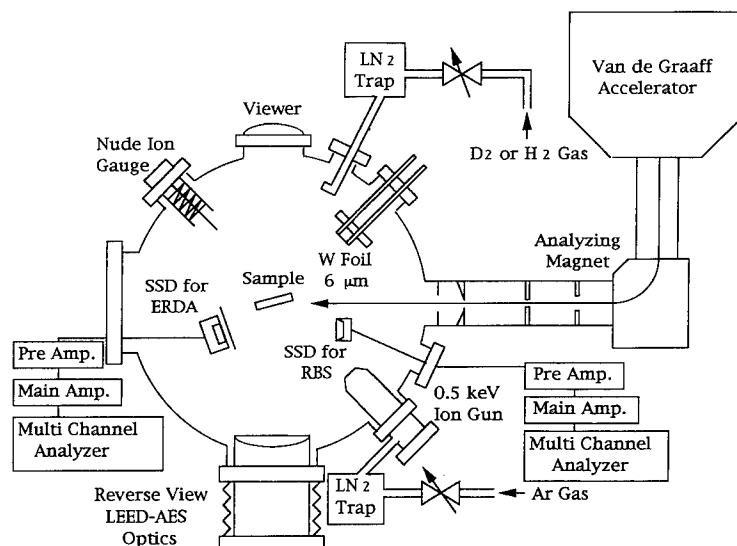


Fig. 1. A schematic arrangement of the experimental apparatus used; SSD: silicon surface-barrier detector, ERDA: elastic recoil detection analysis, RBS: Rutherford backscattering spectrometry and W foil heated for dissociation of H_2 or D_2 .

ter with two-axes linear motion in an ultrahigh vacuum chamber which was connected to a differentially pumped beam line of a 2 MeV Van de Graaff accelerator and equipped with a reverse view LEED-AES optics. A base pressure less than 5×10^{-10} Torr was regularly achieved.

The specimen surface was atomically cleaned by repeating both 0.5 keV Ar^+ sputtering for 20 min at a current density of $0.15 \mu A/cm^2$ and subsequent annealing at $320^\circ C$ for 10 min. A clear LEED pattern of $p(2 \times 4)$ spots could be observed. The Auger electron spectrum showed no traces of C, O, or other impurities. The $p(1 \times 1)$ H(or D) surface was prepared by exposure of the $p(2 \times 4)$ surface at room temperature to atomic hydrogen (H or D) at a high dose above 1700 Langmuir (L). The hydrogen atoms were produced due to dissociation of molecular hydrogen with a hot tungsten foil of $6 \mu m$ in thickness, heated at $1500^\circ C$, which was placed in front of and about 4

cm away from the specimen surface. Exposure doses of hydrogen were estimated from partial hydrogen pressure and the time for the tungsten foil to be heated.

The areal density of H and D adsorbed on the specimen surface was measured by means of the ERD technique, in which the probing He^+ ion beam was incident on the specimen at 80° to the surface normal and the recoil hydrogen was also detected at a recoil angle of 20° and at 80° to the surface normal through a filter. The irradiation fluence of the probing He^+ ion beam during the measurement was monitored by means of the RBS technique. The probing He^+ ion beam was also used at the same time for ion impact desorption of the adsorbed hydrogen atoms.

3. Experimental results

A typical energy spectrum of deuterium ions recoiling from the $InP(001)-p(1 \times 1)$ surface is shown in Fig. 2, where the energy of the probing $^4He^+$ ion beam was 1.5 MeV. The $p(1 \times 1)$ surface was prepared by exposure of the $p(2 \times 4)$ surface to atomic deuterium at a dose of 1700 L. It is clearly seen from Fig. 2 that recoiling deuterium ions form a peak spectrum. Thus, the deuterium coverage at the surface was estimated from the integrated area of the peak. The absolute value of the deuterium coverage was calibrated with the $^3He(d, \alpha)H$ reaction yield at 700 keV which was measured for the $p(1 \times 1)$ surface prepared by the same procedure.

For a preliminary experiment, the thermal stability of the $D/InP(001)-p(1 \times 1)$ surface was investigated by measuring the decay of deuterium coverage after the isochronal annealing. The result is summarized in Fig. 3. It is seen

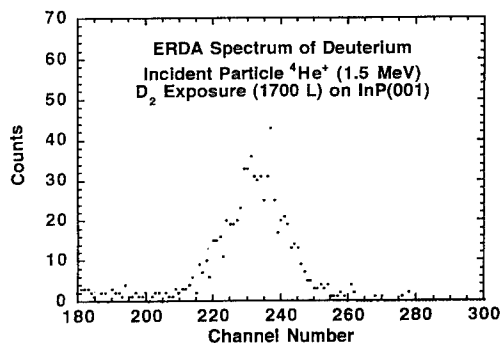


Fig. 2. A typical energy spectrum of deuterons recoiled from the $D/InP(001)-p(1 \times 1)$ surface by 1.5 MeV He^+ ion beam.

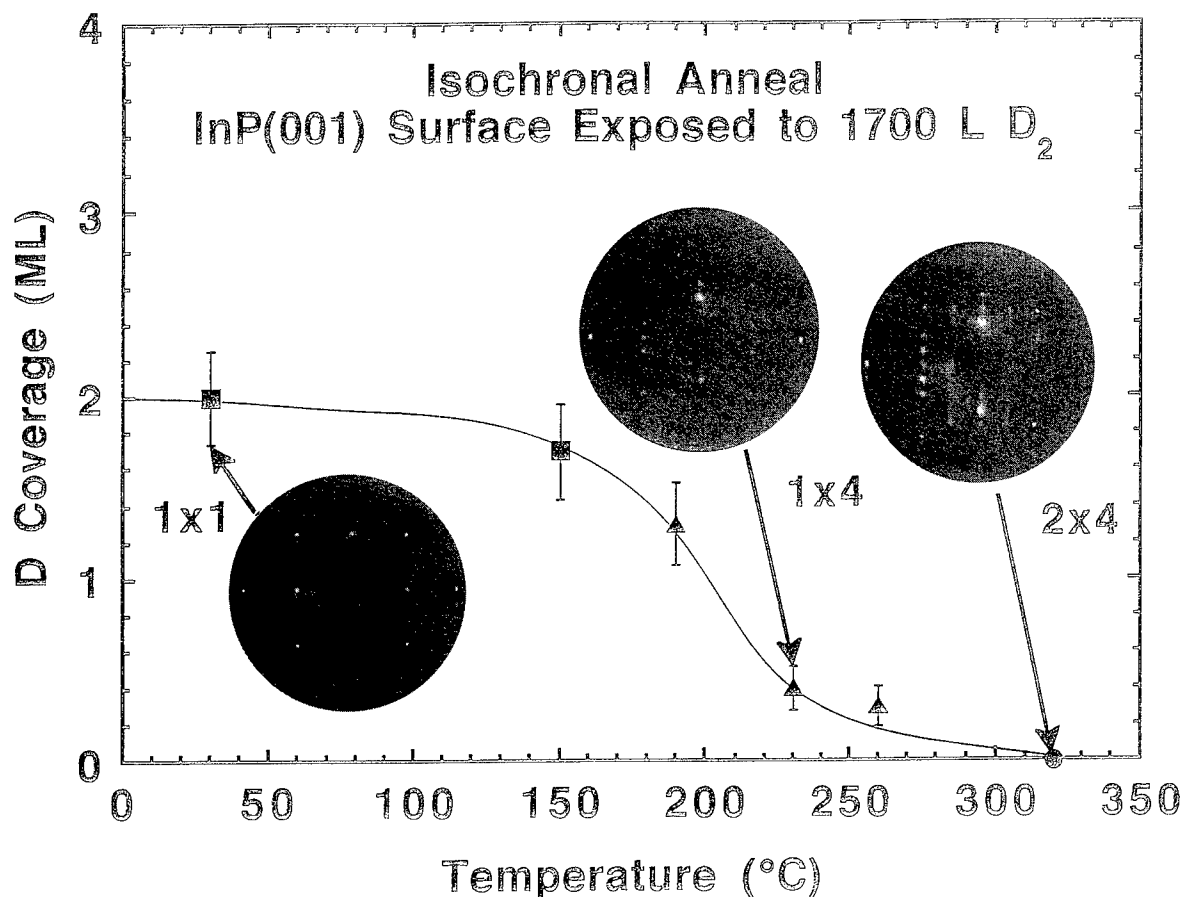


Fig. 3. The temperature dependence of the deuterium coverage at the D/InP(001) surface which was isochronally annealed for 15 min at each temperature. In the figure are inserted the LEED patterns for the D/InP(001) surface which change from $p(1 \times 1)$, through $p(1 \times 4)$, to $p(2 \times 4)$ indicated by ■, ▲, and ● with decreasing deuterium coverage.

from Fig. 3 that as the temperature increases the deuterium coverage decreases and the LEED pattern changes from $p(1 \times 1)$ to $p(2 \times 4)$, through $p(1 \times 4)$, and the AES intensity from In decreases slightly. The latter two results are reversed to changes of the LEED spots and the AES intensity observed during the adsorption process of atomic deuterium onto the InP(001)- $p(2 \times 4)$ surface. From the decay curve of the deuterium coverage during isochronal annealing, the activation energy for thermal desorption of deuterium atoms from the InP(001) surface may be estimated when the order of the desorption reaction is given. However, the desorption process is not well understood yet. When the reaction is assumed to be the first order, the activation energy is estimated to be 0.52 ± 0.2 eV. On the other hand, when the reaction is assumed to be the second order, the activation energy becomes 0.7 ± 0.3 eV.

The decay of the deuterium coverage at the InP(001)- $p(1 \times 1)$ surface induced by the probing MeV He^+ ions at room temperature was measured at different energies. Typical decay curves at energies of 1.5 MeV and 1.9 MeV are

shown in Figs. 4a and 4b, in which no change of the $p(1 \times 1)$ spots and the AES In surface composition was observed even when the surface coverage decreases down to 0.3 ML. These facts indicate that the specimen surface is not locally heated and damaged by the irradiation of MeV He^+ ions up to a fluence of $2 \times 10^{16}/\text{cm}^2$. It is clearly seen from Figs. 4a and 4b that the deuterium coverage decreases approximately exponentially. Bombarding with the probing $^4\text{He}^+$ ions at different energies, similar decay curves were observed. The desorption cross sections, which were determined from the slope of the exponentially decaying curves at different energies, are plotted as a function of He^+ ion energy in Fig. 5, where the data obtained with $^3\text{He}^+$ bombardment at 700 keV of a H/InP(001)- $p(1 \times 1)$ surface are also plotted. Moreover, the electronic stopping cross sections for MeV He^+ ion of In atoms, to which the hydrogen atoms are directly bound, are shown by the solid line. It is clearly seen from Fig. 5 that the He^+ ion impact desorption cross sections are almost constant in the present energy range and have the

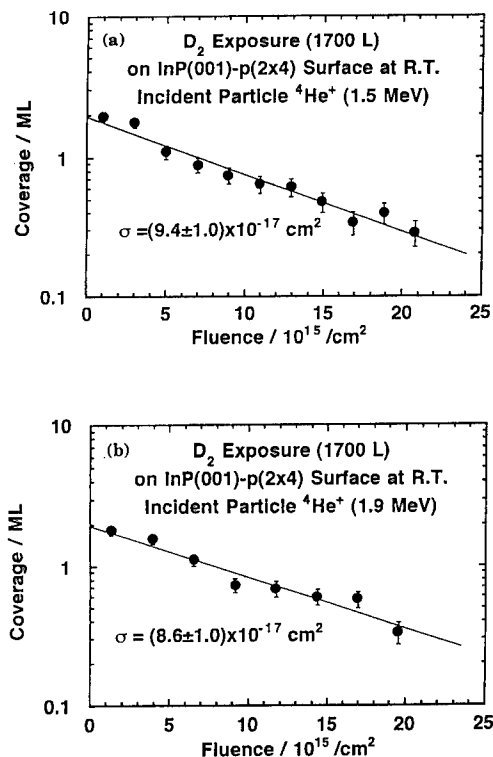


Fig. 4. Change in the deuterium coverages on the InP(001)-p(1×1) surface which were measured continuously by means of the ERD technique with 1.5 MeV $^4\text{He}^+$ ion beam (a) and 1.9 MeV $^4\text{He}^+$ ion beam (b).

same energy dependence as the stopping cross section of In for the He^+ ions. It is also seen that the desorption cross section for D is almost the same as that for H and

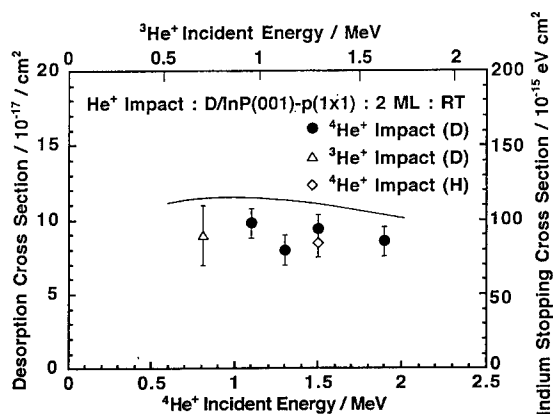


Fig. 5. The desorption cross section of $^4\text{He}^+$ ions for deuterium on the InP(001)-p(1×1) surface as a function of the incident energy. The values of $^4\text{He}^+$ for protium and $^3\text{He}^+$ for deuterium are plotted for comparison. The solid line represents the stopping cross section of In.

that the desorption cross section of $^3\text{He}^+$ ion is also the same as that of $^4\text{He}^+$ ion. These experimental data are discussed in the next section.

4. Discussion

The ion impact desorption of hydrogen adsorbed on the solid surface may be caused by elastic collisions and/or inelastic collisions. The former collision process is separated into the direct collision of projectile ions with adsorbed hydrogen and the secondary collisions of recoiling substrate atoms with hydrogen. The latter collision process is associated with excitation and ionization of substrate atoms at the topmost surface layer to which the hydrogen atoms are bound.

In the direct collision of projectile ions with adsorbed hydrogen, the desorption cross section is simply expressed as the integral of the differential cross sections for displacement from the binding energy to the maximum transfer energy. The theoretical cross section of the direct collision process is proportional to the inverse of the projectile energy in the MeV energy regime. The cross section for H is twice as large as that for D, which is the so-called isotope effect. These theoretical predictions are not consistent with the experimental data in Fig. 5. Moreover, the displacement cross section calculated for a collision of 1 MeV $\text{He}^+\text{-H}$ using the binding energy of 1 eV was roughly $\sim 10^{-18} \text{ cm}^2$, which is two orders of magnitude smaller than the experimental data.

In the secondary collision process, the hydrogen desorption takes place due to displacement by energetic recoiling In atoms at the topmost surface produced in the elastic collision cascade initiated by the projectile ion. In the case of the MeV He^+ projectile, the flux density of energetic recoiling In atoms is proportional to the inverse of the He^+ ion energy and their energy distribution is almost independent of the He^+ ion energy. When the $m = \frac{1}{3}$ power law approximation to the Thomas-Fermi potential [10] was used for the collision of In recoils with D atoms, the cross section for displacement of D at the topmost surface by 1 MeV He^+ bombardment is roughly estimated to be $7 \times 10^{-18} \text{ cm}^2$. The desorption cross sections estimated on the basis of the secondary collision process are also inconsistent with the experimental data.

As seen from Fig. 5, the energy independence of the experimental desorption cross sections shows a good agreement with that of the electronic stopping cross sections of In atoms for MeV He^+ ions. The energy independence of the cross sections rules out a direct inelastic collision process. It has been also shown by the group of Tombrello on sputtering of oxides by MeV Cl ions that there is a linear dependence of the sputtering yields on the electronic stopping cross section [11], as the result of Fig. 5. Since the saturation coverage of hydrogen atoms adsorbed on the p(1×1) surface was 2 ML, the average

energy required for desorption of one hydrogen atom due to an inelastic collision is roughly estimated from Fig. 5 to be 600 eV, which is by an order of magnitude smaller than that for sputtering of Al from Al_2O_3 by MeV Cl ions. The estimated value eventually corresponds to the mean ionization energy in the Bethe-Bloch formula for the electronic stopping cross section. The electrons mainly contributing to the stopping of MeV He^+ ions are valence electrons ($5s^2 5p^1$) and outer-shell electrons ($4s^2$, $4p^6$, $4d^{10}$ and $3s^2$, $3p^6$, $3d^{10}$) rather than inner-shell electrons. Therefore, these facts seem to indicate that the hydrogen desorption due to inelastic collision is not ascribed to direct ionization of bonding electrons, but to an indirect process, such as the Auger process following ionization of the outer-shell electrons and the coupling of the low energy ionized electrons to phonons as a possible energy transfer to hydrogen atoms.

The hydrogen adsorbed on the solid surface may be desorbed in an atomic or molecular state. In the present experiment the hydrogen adsorption at room temperature removes the reconstruction of the cleaned $p(2 \times 4)$ surface to the bulk-like $p(1 \times 1)$ surface through $p(1 \times 4)$ and enriches the surface concentration of In presumably due to the energy released by the chemical reaction with the In atoms at the topmost surface, thus hydrogen being in an atomic state. Upon the MeV He^+ ion impact desorption, however, the surface reconstruction and the depletion of In surface concentration are not induced, thus the desorption process being concluded to be athermal. These facts and the above consideration indicate that hydrogen desorbed via the electronic collisions is atomic. The fact is very consistent with the experimental result that the desorption cross sections for D are the same as those for H. If hydrogen adsorbed in an atomic state would be desorbed as molecule, the cross section for H would be twice as large as that for D due to the isotope effect, via the frequency factor, of the molecular formation probability at the surface [12]. However, we have no direct evidence for the atomic desorption. For a better understanding of the process of ion impact hydrogen desorption, further measurements are required such as the mass spectrometry of desorbed species [13,14].

5. Summary

In order to understand the process of MeV He^+ ion impact desorption of hydrogen isotopes from the $\text{InP}(001)$ -

$p(1 \times 1)$ surface, repeated measurements of the surface coverage have been done using the elastic recoil detection technique with He^+ ion beams at different energies. It is found that the surface coverage decreases exponentially as the He^+ ion fluence increases, while no change of the $p(1 \times 1)$ spots by LEED and of the In surface composition by AES has been observed when the surface coverage decreases from 2 ML to 0.3 ML. The desorption cross sections, determined from the exponential decay curves, have been found to be $(8\text{--}10) \times 10^{-17} \text{ cm}^2$ in the range from 0.7 to 1.9 MeV. Their energy dependence shows a good agreement with that of the electronic stopping cross section for MeV He^+ ions of In atoms, to which the hydrogen atoms are bound. From the experimental data, the MeV He^+ ion impact desorption of hydrogen isotopes from a $\text{InP}(001)$ - $p(1 \times 1)$ surface is concluded to be ascribed to the electronic collision of the He^+ ion with In atoms at the topmost surface layer, to which hydrogen is bound. For a more detailed understanding, systematic measurements of desorbed species are required.

References

- [1] L.H. Doboys and G.P. Schwartz, Phys. Rev. B 26 (1982) 794.
- [2] R.J. Culbertson, L.C. Feldman, P.J. Silverman and R. Height, J. Vac. Sci. Tech. 20 (1982) 868.
- [3] J.A. Schaefer, Surf. Sci. 178 (1986) 90.
- [4] K. Mortensen, F. Besenbacher, I. Stensgaard and W.R. Wampler, Surf. Sci. 205 (1988) 433.
- [5] K. Oura, M. Naitoh, F. Shoji, J. Yamane, K. Umezawa and T. Hanawa, Nucl. Instr. and Meth. B 45 (1990) 521.
- [6] E.J. Petit, F. Houzay and J.M. Moison, Surf. Sci. 269/270 (1992) 902.
- [7] K. Sumitomo, T. Kobayashi, F. Shoji, K. Oura and I. Katayama, Phys. Rev. Lett. 66 (1991) 1193.
- [8] H. Ikegami and K. Morita, Surf. Sci. 295 (1993) 213.
- [9] J.F. Ziegler, The stopping and Ranges of Ions in Matter, vol. 4 (Pergamon, New York, 1977).
- [10] K.B. Winterbon, P. Sigmund and J.B. Sanders, K. Dan. Vidensk. Selsk. Mat. Fys. Medd. 37 (1970) no. 14.
- [11] Y. Qiu, J.E. Griffith and T.A. Tombrello, Radiat. Eff. 64 (1982) 111.
- [12] K. Ashida, K. Ichimura, M. Matsuyama and K. Watanabe, J. Nucl. Mater. 128/129 (1984) 792.
- [13] O. Becker, W. Knippelberg and K. Wien, Physica Scripta T 6 (1983) 117.
- [14] T.A. Tombrello, Int. J. Mass Spectr. Ion Phys. 53 (1983) 307.



ELSEVIER

Simulation of fast electron emission from surfaces

Carlos O. Reinhold^{a,b,*}, Joachim Burgdörfer^{a,b}, Kenji Kimura^c, Michi-hiko Mannami^c

^a Department of Physics and Astronomy, University of Tennessee, Knoxville TN 37996-1200, USA

^b Oak Ridge National Laboratory, Oak Ridge, TN 37831-6377, USA

^c Department of Engineering Science, Kyoto University, Kyoto 606, Japan

Abstract

We present a microscopic simulation of fast electron emission in glancing-angle ion–surface collisions. Our model accounts for both dynamic image interactions and multiple scattering near the surface and predicts a pronounced convoy electron peak for small emission angles. We find that convoy electrons principally originate from target core states which are excited via close collisions with the impinging ions. Polarization of core electrons during emission is found to play an important role. Very good agreement is found with experiments for fast Li^+ ions interacting with $\text{SnTe}(0,0,1)$ surfaces.

1. Introduction

Electron emission in glancing-angle collisions has become a focus of ion–surface interactions. Electron spectra can provide detailed information about the neutralization dynamics of multiply charged ions, the electronic structure of the surface (surface density of states) and the long-ranged image interactions near the surface. From a fundamental point of view, the study of fast electrons emitted in ion–surface interactions provides an important link between atomic physics and condensed matter physics.

Two decades ago a cusp-shaped peak was discovered in the spectrum of electrons arising from ion–atom [1] and ion–solid (transmission) collisions [2]. This cusp is observed for electrons ejected with velocities v_e close to the projectile velocity v_p . In ion–solid collisions this structure is usually referred to as the convoy-electron peak (CEP). Cusp electrons consist of electrons in low-lying continuum states (i.e. near-threshold states) of the projectile. Because cusp electrons recede from the target in close spatial correlation with the projectile, the behavior of the cross sections in the limit $|v_e - v_p| \rightarrow 0$ is governed by threshold laws characteristic of the two-body final state interaction between the electron and the projectile.

Recent experiments concerning glancing-angle ion–surface interactions have revealed a prominent convoy peak. Compared to the peak for transmission conditions, however, the convoy peak for ion–surface interactions is dramatically broadened and shifted in energy. The first evidence for broadening of the CEP was found by de

Ferrais and Baragiola [3] for scattering of protons at an Al surface. A similar broadening was observed for semiconductor surfaces [4,5]. Concurrently, a shift of the CEP to electron velocities larger than v_p was proposed [6] and independently measured [4] for projectile charges greater than 1. Subsequently, large shifts of up to 100 eV have been observed in several laboratories and a number of explanations have been proposed [7–11]. It was readily understood that these effects were closely related to dynamic image interactions. At grazing angles of incidence the impinging ion remains near the target surface for a very long time and, therefore, the effective final-state interaction in which the excited electrons evolve is quite different from ion–atom collisions and foil transmission experiments. The energy shift was identified as “convoy-electron acceleration” and the underlying picture is that of emitted electrons repelled to larger energies by the negative image of the projectile ion travelling in close proximity.

The theoretical description of fast electron emission in glancing-angle surface scattering is still in its infancy. Iitaka et al. [12] and Kimura et al. [9] have shown that a classical trajectory Monte Carlo (CTMC) simulation employing an initial ensemble of electrons distributed in a shell around the projectile yields a shifted CEP when the electrons propagate in the fields of the projectile and its image. As of yet, however, no simulation has been performed that employs realistic initial ensembles (“sources”) of electrons and describes the transport of fast electrons from their birth in a violent collision through a sequence of multiple scattering to their final exit from the surface. In this letter, we present the results of a comprehensive classical simulation of convoy electron emission. Based on our simulation, we have recently identified the peak as a

* Corresponding author, tel. +1 615 974 7826, fax +1 615 974 7843, E-mail: reinhold@uthvx.uth.edu.

result of a classical rainbow singularity for scattering of fast electrons at the induced dynamical screening potential [13].

2. Model

The present simulation is an extension of a model originally developed for fast electron emission from transmission of ions through solids [14]. Ensembles of initial coordinates were calculated for both target and projectile electrons employing the CTMC method as applied to atomic collisions [15]. We decompose target electrons into outermost valence electrons and core electrons. Electrons in the outermost valence band of SnTe (i.e. 5p electrons) are treated as a free electron gas which is constrained to the $z < 0$ region by the surface barrier. Core electrons are assumed to be well localized in bound states of isolated Sn and Te atoms. The electronic evolution is described by a time-dependent effective one-electron Hamiltonian

$$H = \frac{p^2}{2} + V(\mathbf{r}, t) - \mathbf{r} \sum_k \sum_{\alpha=e,i} \Delta p_k^\alpha \delta(t - t_k^\alpha), \quad (1)$$

where \mathbf{r} and \mathbf{p} (in a.u.) are the coordinate and momentum of the electron. This Hamiltonian describes the motion of an electron in the potential field V , perturbed by a stochastic force representing the collisional momentum transfers Δp_k^α due to the inelastic ($\alpha = i$) and elastic ($\alpha = e$) collisions with other electrons and ionic cores in the neighborhood of the surface. Elastic momentum transfers Δp_k^e are calculated from the differential elastic cross section for the scattering of electrons at the Sn and Te cores. Inelastic momentum transfers are obtained from the imaginary part of a single-frequency plasmon-pole dielectric function [16] including dispersion and single-particle single-hole excitations.

The potential field $V = V_p + V_{ip} + V_b + V_t$ consists of: (i) the field of the projectile, V_p , (ii) the dynamic image potential induced by the projectile, V_{ip} , (iii) the surface barrier potential, V_b , containing the interaction of the electron with its own image, and (iv) the field of the initial target core, V_t . The time dependence of the potential results from the motion of the impinging ion which is assumed to follow a curvilinear trajectory for quasi-elastic scattering deduced from a planar averaged Moliere potential representing the interaction with the first layer of atoms and from the ionic self image interaction. In Fig. 1 we display the potential experienced by an electron near a proton moving parallel to a SnTe(001) surface. The well-known wake pattern trailing the ion as well as the surface barrier potential are clearly visible. Dynamic image potentials have been obtained using a single-frequency classical dielectric function [16] ($\omega_{pv} = 15.1$ eV, $\gamma = 8.54$ eV). At the ion velocities $v_p \gg v_F$ (v_F being the Fermi velocity), our induced potential is found to be in good agreement

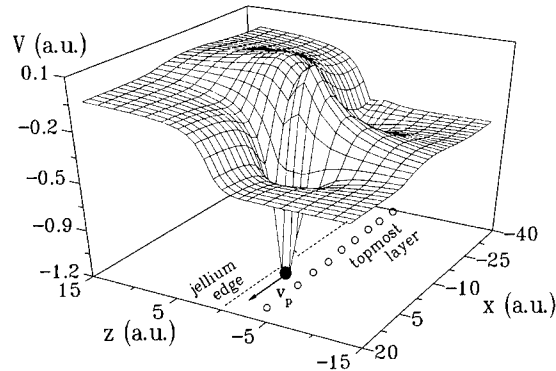


Fig. 1. Electronic potential $V' = V_p + V_{ip} + V_b$ near a 0.3 MeV/u proton moving parallel to a SnTe(001) surface as a function of the position vector of the electron ($x, 1$ a.u., z). The surface plane corresponds to the (x, y) plane and the surface normal is oriented along the z -axis. The position vector the projectile is $(0, 0, -1.5)$, i.e. 1.5 a.u. above the top row of atoms. $z = 0$ corresponds to the jellium edge situated 3 a.u. above the first layer of atoms.

with the one calculated by Garcia de Abajo et al. [17] using the plasmon pole approximation for the dielectric function. We employ the parameterized potential of Jennings et al. [18] for the surface barrier.

3. Results

After the incoming ion crosses the jellium edge (3 a.u. above the topmost layer), electron capture and loss probabilities become so large that the ionic charge state fluctuates very rapidly as a function of time [19]. For 0.3 MeV/u Li^+ ions interacting with a SnTe(001) surface the charge state fractions $q = 2$ and $q = 3$ become approximately equal ($\sim 50\%$). Our simulation (Fig. 2a) consists therefore of an average of the spectra for Li^{2+} and Li^{3+} ions. Typically, 5×10^7 trajectories were included to assure small statistical uncertainties. We compare our simulation with recent experimental data [19] for electron emission in coincidence with outgoing Li^{2+} ions. Remarkably, these data have indicated (see Ref. [19]) the independence of the convoy peak from the outgoing charge state in contradiction to the naive picture of convoy electron acceleration by the asymptotic image field of the projectile.

The present simulation is consistent with this conclusion and provides insight into the mechanism that breaks the correlation between the asymptotic charge state and the convoy electron spectrum: convoy electrons are produced very close to the first layer of target atoms and leave the surface before the projectile completes its charge-changing cycle. This is seen in Fig. 3b where the yield of convoy electrons is plotted as a function of the distance between the ion and the first layer of target atoms at the moment of emission. Clearly, more than 50% of convoy electrons are

emitted when the projectile is at a distance smaller than ~ 1 a.u. from the topmost layer.

The lack of correlation between exit charge state and the shift of the convoy peak points to the local potential in close proximity to the surface as being responsible for convoy electron acceleration. We therefore include the polarization of core electrons in the dynamical screening potential. Pitarke et al. [20] have shown that core polarization gives a significant contribution to the anomalously large shift of the radiative electron capture (REC) peak observed by Vane et al. [21] for titanium ions channeled in a gold single crystal. Core polarization is accounted for in terms of an inhomogeneous electron gas with a local plasma frequency [20]

$$\omega_p(d)^2 = \omega_{pv}^2 + \sum_{n,l} 4\pi\rho_{n,l}(d), \quad (2)$$

where $\rho_{n,l}(d)$ denotes the planar-averaged number density of electrons in the state with quantum numbers n, l and d is the distance between the ion and the first layer of atoms. At large distances (see Fig. 3a) the local plasma frequency in Eq. (2) tends to the volume plasma frequency pertaining to the displacement of 5s and 5p valence electrons: i.e.

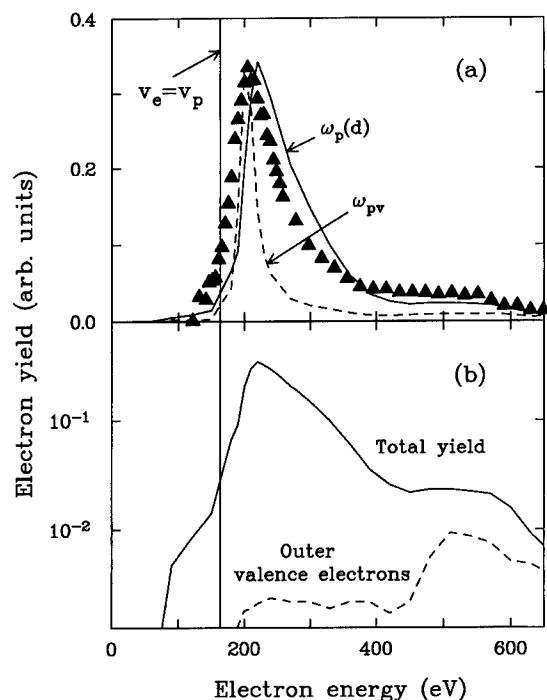


Fig. 2. Spectrum of electrons emitted at 100 ± 50 mrad with respect to the surface resulting from the interaction of 0.3 MeV/u Li^+ with SnTe(001). The angle of incidence of the impinging ions is 6 mrad. (a) Comparison of the full simulations using the valence-band plasma frequency (ω_{pv}) and a distance dependent plasma frequency ($\omega_p(d)$) with the coincidence data [19] (solid triangle). Theoretical and experimental results are normalized to each other at the peak. (b) Comparison of the total yield of electrons with the yield of outermost valence electrons.

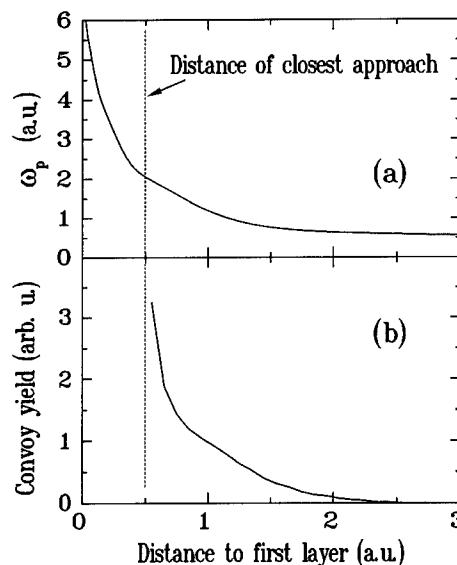


Fig. 3. (a) Local plasma frequency as a function of the distance from the topmost layer. (b) Yield of convoy electrons as a function of the distance between the ion and the first layer of target atoms at the moment of emission.

$\omega_p(d > 2 \text{ a.u.}) \approx \omega_{pv} = 0.55 \text{ a.u.}$ However, at the distance of closest approach $\omega_p(d)$ is about a factor of 4 larger than ω_{pv} . Both simulations using the distance dependent plasma frequency and the volume plasma frequency yield significant convoy electron acceleration (see Fig. 2a). Inclusion of the core polarization increases the peak shift but contributes predominantly to the broadening of the peak which closely resembles the measured spectrum. This is due to the fact that the spectrum is an average over electrons emitted at different distances d , each of which suffers a different amount of image acceleration. It should be stressed that this comparison refers to a small subset of an exceedingly complex multi-electron process involving the emission of several hundred electrons per ion.

After considering all sources of electrons, we find that the dominant contribution to the convoy electron spectrum originates from target core states (see Fig. 2b). This dominance is due to the large number of electrons in the N-shell of Sn and Te whose orbital velocities closely match the projectile velocity v_p . Thus, local processes such as electron capture to bound or low-lying continuum states of the projectile are strongly favored. Emission of outermost valence electrons at forward angles, on the other hand, plays a significant role only for electron energies above 400 eV where the yield of outermost valence electrons exhibits a peak (see Fig. 2b). This peak is the counterpart to the binary encounter peak known from ion-atom collisions and foil transmission experiments and it arises from head-on projectile-electron collisions. However, this is a marginal contribution to the total yield of electrons which exhibits only a weak shoulder in this region. Despite the

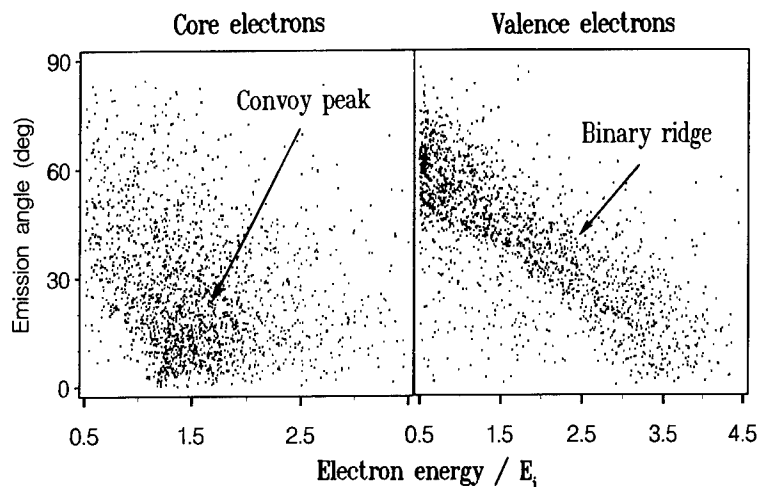


Fig. 4. Theoretical densities of core and outermost valence electrons emitted from SnTe(001) surfaces after the interaction with 0.3 MeV/u Li^+ ions. The points in the figure correspond to electrons emitted in the plane of the trajectory of the ions. The emission angle is measured with respect to the surface.

fact that the ionization probability of electrons initially in the projectile is equal to unity, their contribution to the total yield is also found to be marginal (i.e. many more target electrons are emitted).

At larger emission angles with respect to the surface, head-on projectile–electron collisions are expected to give rise to a “binary ridge” (also known from ion–atom collisions) at electron energies $E_e = 4E_i \cos \theta$, θ being the emission angle with respect to the local ion trajectory and $E_i = (v_p^2/2)$ a.u. This ridge can be clearly seen in the density of outermost valence electrons emitted in the plane of the ion trajectory (see Fig. 4). For emission of core electrons under the current collision conditions, however, the binary ridge is completely swamped by the convoy electron peak clearly visible in the energy range $E_i < E_e < 2E_i$ which extends to relatively large angles (up to 20–30°).

Summarizing, the present classical simulations for 0.3 MeV/u Li^+ –SnTe(001) collisions account for the shift and broadening of the convoy electron peak compared to its counterparts in ion–atom and ion–foil collisions. Both effects are a consequence of the fact that liberated electrons evolve in the dynamically screened field of the projectile. Convoy electrons are found to originate from target core states and emission occurs when the projectile is in very close proximity to the topmost atomic layer of the surface. Agreement with the experimental convoy electron spectrum can be found when core polarization is taken into account.

Acknowledgements

C.O.R. and J.B. acknowledge support by NSF and US DOE, Office of Basic Energy Sciences Division of Chemi-

cal Sciences contract no. DE-AC05-84OR21400 with Martin Marietta. We also acknowledge the support of the Japan–US Cooperative Scientific Program sponsored by JSPS and NSF. K.K. and M.M. acknowledge support of the Grant-in-Aid for Scientific Research from the Japanese Ministry of Education, Science and Culture.

References

- [1] C.B. Crook and M.E. Rudd, Phys. Rev. Lett. 25 (1970) 1599.
- [2] K.G. Harrison and M.W. Lucas, Phys. Lett. 33A (1986) 142.
- [3] L.F. de Ferraris and R. Baragiola, Phys. Rev. A 33 (1986) 4449.
- [4] M. Hasegawa, K. Kimura, M. Mannami, J. Phys. Soc. Jpn. 57 (1988) 1834.
- [5] H. Winter, P. Strohmaier and J. Burgdörfer, Phys. Rev. A 39 (1989) 3895.
- [6] J. Burgdörfer, Nucl. Instr. and Meth. 24/25 (1987) 139.
- [7] A. Koyama et al., Phys. Rev. Lett. 65 (1990) 3156; A. Koyama, Nucl. Instr. and Meth. 67 (1992) 103; H. Ishikawa et al., Nucl. Instr. and Meth. 67 (1992) 160.
- [8] M. Hasegawa, T. Fukuchi, Y. Mizuno, K. Kimura and M. Mannami, Nucl. Instr. and Meth. B 53 (1991) 285.
- [9] K. Kimura, M. Tsuji and M. Mannami, Phys. Rev. A 46 (1992) 2618.
- [10] E.A. Sánchez, O. Grizzi, M.L. Martiarena and V.H. Ponce, Phys. Rev. Lett. 71 (1993) 801.
- [11] R.A. Baragiola, Nucl. Instr. and Meth. B 78 (1993) 223.
- [12] T. Iitaka, Y.H. Ohtsuki, A. Koyama and H. Ishikawa, Phys. Rev. Lett. 65 (1990) 3160.
- [13] C.O. Reinhold, J. Burgdörfer, K. Kimura and M. Mannami, Phys. Rev. Lett. 73 (1994) 2508.
- [14] J. Burgdörfer and J. Gibbons, Phys. Rev. A 42 (1990) 1206; J. Burgdörfer, Lecture Notes in Physics 294 (1988) 344; 376 (1990) 199;

- C.O. Reinhold, J. Burgadoörfer, J. Kemmler and P. Koschar, Phys. Rev. A 45 (1992) R2655.
- [15] R.E. Olson, in: Physics of Electronic and Atomic Collisions, eds. H.B. Gilbody et al. (North-Holland, 1987) p. 271; C.O. Reinhold and R.E. Olson, Phys. Rev. A 39 (1989) 3861.
- [16] P.M. Echenique, F. Flores and R.H. Ritchie, Solid State Phys. 43 (1990) 229.
- [17] F.J. Garcia de Abajo and P.M. Echenique, Phys. Rev. B 46 (1992) 2663.
- [18] P.J. Jennings, R.O. Jones and M. Weinert, Phys. Rev. B 37 (1988) 6113.
- [19] K. Kimura, T. Kishi and M. Mannami, Nucl. Instr. and Meth. 90 (1994) 282.
- [20] J.M. Pitarke, R.H. Ritchie and P.M. Echenique, Phys. Rev. B 43 (1991) 62.
- [21] C.R. Vane et al. Nucl. Instr. and Meth. B 67 (1992) 256.



ELSEVIER

Luminescence of self-trapped excitons induced by single keV ion bombardment

R.G. Kaercher, E.F. da Silveira¹, J.F. Blankenship, E.A. Schweikert^{*}

Center for Chemical Characterization and Analysis, Texas A&M University, College Station, TX 77843-3144, USA

Abstract

We have studied the light emission from CsI and NH₄Cl films that were bombarded simultaneously with H⁺, low mass organic, and (CsI)_nI⁺ ($n = 0-2$) ions in the keV energy range (25–45 keV) at room temperature. Photons were detected from the impact of individual primary ions with a single photon counting photomultiplier, and were analyzed using time resolved and wavelength analysis. For CsI, fast ($\tau \leq 12$ ns) and slow ($\tau \geq 650$ ns) component decays were observed for all projectiles used. The fast component's emission was ~ 300 nm while the slow component's emission was in the visible. Only a fast component ($\tau < 3$ ns) was observed in the UV region for NH₄Cl. Our data suggest that the light emission from both samples is due to the radiative relaxation of self-trapped excitons which are produced by electronic interactions between the primary ions and the target atoms.

1. Introduction

We have recently reported on the simultaneous detection of secondary ions and photons produced by the impact of individual keV energy ions [1]. The approach of event-by-event bombardment and detection allows the identification of coincidental emissions which in turn may reveal physical or chemical correlations relevant to projectile energy dissipation in the target and/or to the formation and emission of secondary ions [2–4]. To further pursue these issues, the characteristics of secondary ion and photon emission must be known.

Previous experiments with keV projectiles have shown that secondary ion yields are strongly dependent upon the complexity of the projectile, i.e., monoatomic or polyatomic [3], while photon yields depend primarily upon the projectile velocity [1]. Photon signals from individual keV projectile–solid interactions are weak, thus the yields were reported as total photon counts, i.e., they were not resolved in terms of wavelength and lifetime. Moreover, the energy loss and transfer mechanisms responsible for photon emission from solids due to keV ion impacts remained to be established. These items are addressed in the present paper.

Specifically, we have examined the light emission from individual collision cascades using the event-by-event analysis mode. Light emission was studied using time resolved and wavelength analysis. H⁺, low mass organic, and (CsI)_nI⁺ ($n = 0-2$) ions in the 25–45 keV energy regime were used as primary ions. We report below on the luminescence produced by these projectiles impacting CsI and NH₄Cl targets, and present the evidence linking this emission to the luminescence of self-trapped excitons (STEs). STEs and their role in the production of defects in insulators has been thoroughly investigated [5–13].

2. Experimental

Fig. 1 is a schematic of the instrument used. It is only briefly described since it has been reported in detail elsewhere [1,14]. A spontaneous desorption based ion source is used to produce negative ions and electrons. The charged particles are accelerated up to 45 keV. Immediately after the acceleration region, the electrons are steered with a weak magnetic field (~ 200 G max) into a microchannel plate (MCP) start detector. The primary ions continue down the drift region and impact the sample at times proportional to the square root of their mass to charge ratios. Secondary electrons produced by the primary ion impacts are accelerated coaxially off the sample surface into the spectrometer where a second magnetic field bends them into a MCP stop detector. Secondary electron signals are used to verify the impact of primary ions and to calculate photon yields (see Ref. [1]). Photons emitted

^{*} Corresponding author, tel +1 4098452341, fax +1 4098451655, E-mail: easgroup@chemvx.tamu.edu.

¹ On sabbatical from Departamento de Física, Pontificia Universidade Católica, C.P., 38701, Rio de Janeiro 22452-970, Brazil.

from the impact site are detected by a single photon counting photomultiplier (PMT). The PMT had an active window from 185 to 715 nm, a maximum quantum efficiency of 22% at 410 nm, a solid angle of 0.85 sr, and a total detection efficiency of $\sim 1\%$.

CsI and NH_4Cl samples were vapor deposited onto

quartz slides. Primary ions impacted the sample surface and light was observed from the back of the sample, looking through the quartz slide. Because of the low light intensities, wavelength analysis could only be accomplished with broad band filters (50 nm resolution). Time resolved analysis was accomplished by means of a time-

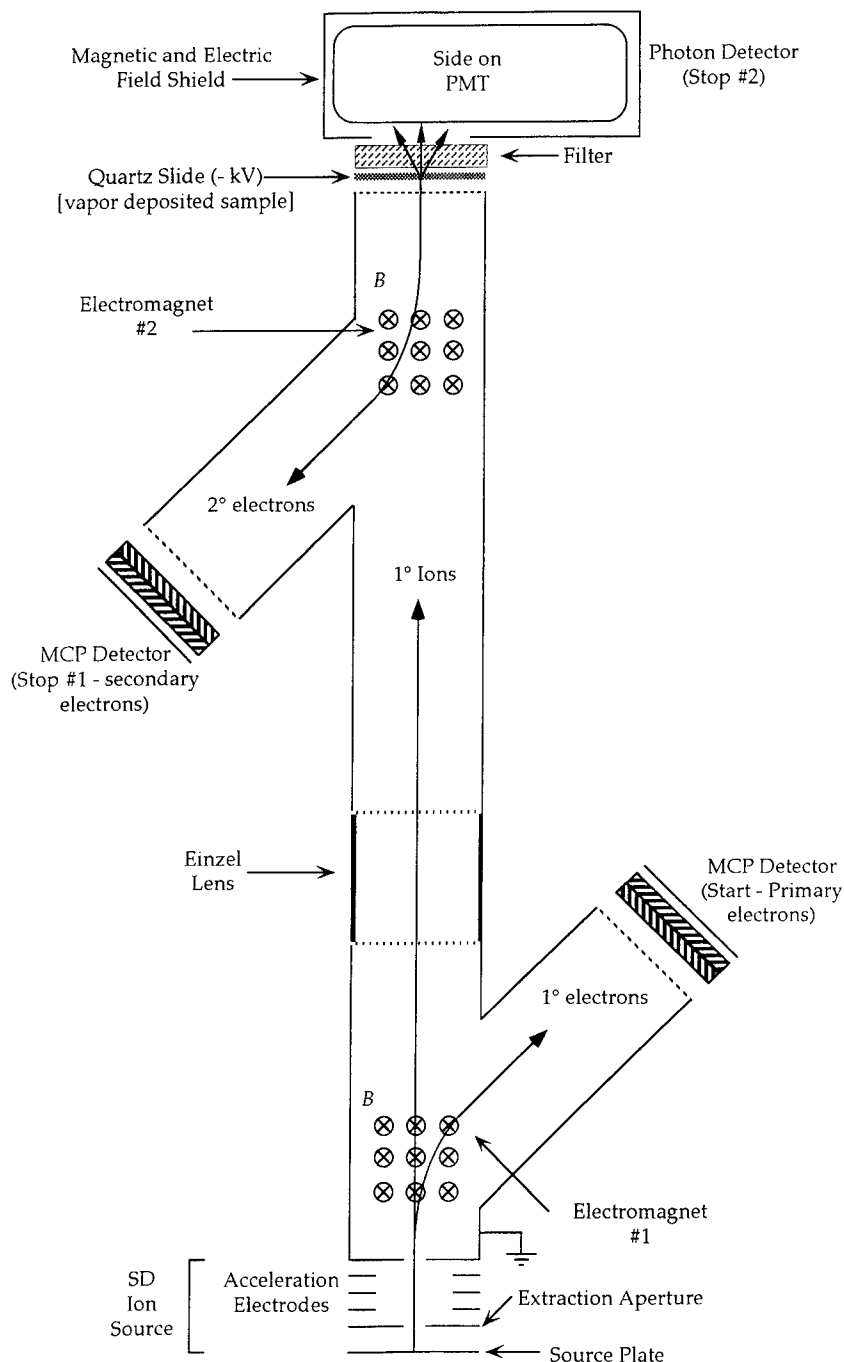


Fig. 1. Schematic of the TOF mass spectrometer.

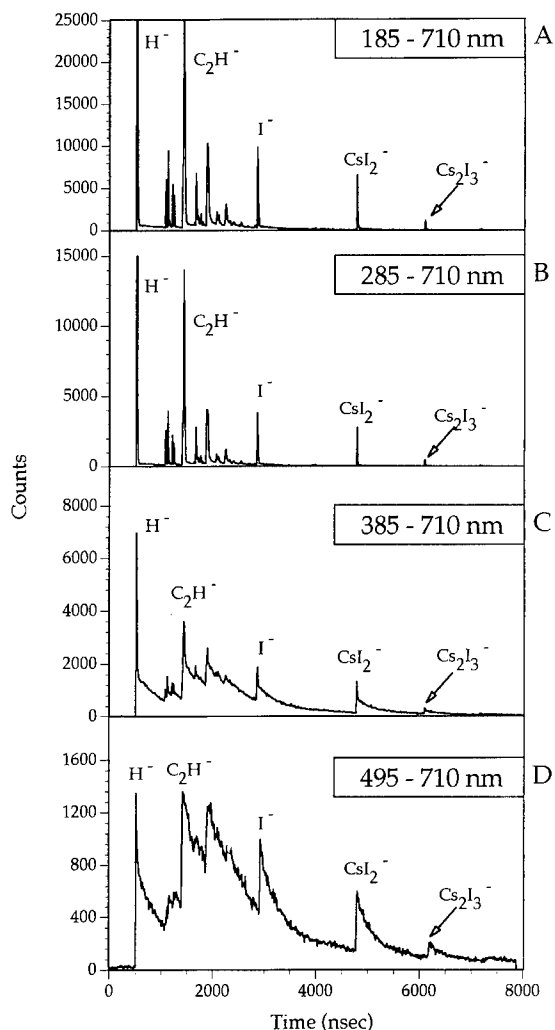


Fig. 2. TOF spectra of 45 keV projectiles detected by light emission from their impacts on a CsI target. Each spectrum is of a different wavelength window.

to-digital converter with 0.5 ns timing resolution. CsI and NH_4Cl were chosen as a model targets because of their reported luminescence [7,15].

All experiments were run at room temperature, and every analysis was performed in the static regime (total dose of all primary ions 10^5 – $10^6/\text{cm}^2$).

3. Results and discussion

TOF spectra of 45 keV projectiles detected by light emission from their impacts on a CsI target are shown in Fig. 2. As stated, wavelength analysis was performed with broad band filters. Fig. 2 shows four spectra at different wavelength windows. Each subsequent filter decreases the high energy side of the window by ~ 100 nm. As noted,

primary ions are mass identified by time. They impact the target sequentially, thus the ordinate has units of time. The abscissa is in units of photon counts. The peaks labeled I^- , CsI_2^- , and Cs_2I_3^- are light signals produced by these primary ions. From Fig. 2, two key observations can be made: (i) in the velocity range examined, all primary ions induce luminescence with two component decays; (ii) the two decay components do not have the same peak emission.

3.1. Wavelength analysis

The emission profile of the fast component was determined by calculating the photon yield for a given wavelength window then subtracting the next most discriminating window [1]. For example, when the light yield from H^- in the 285–710 nm window (Fig. 2b) is subtracted from the H^- light yield in the 185–710 nm window (Fig. 2a), the resulting yield is the relative emission intensity for H^- in the region of 185–295 nm. Using this method, a wavelength resolution of 50 nm was obtained, and the peak emission for the fast component from CsI is estimated to be ~ 300 nm. Two intrinsic emission bands attributed to STE luminescence have been reported for CsI after a crystal was exposed to UV radiation: 290 nm and 338 nm [11,12]. Both of these reported bands fall within the 50 nm resolution of our observed ~ 300 nm emission.

Low photon yields in the slow decay prevented the calculation of a detailed emission profile. However, a comparison of Figs. 2a–2d shows that when the fast UV component is filtered, the slow component remains. We conclude that the slow component's emission is in the visible region. Luminescence in the visible region has been reported for CsI crystals activated with Na or Tl which were bombarded by high energy photons and particles [16,17]. Therefore, the observed visible luminescence may not be intrinsic to CsI but may be due to impurities within the CsI lattice.

3.2. Time resolved analysis

Time resolved analysis of the two component decay for CsI luminescence is plotted in Fig. 3 for three wavelength windows. The luminescence induced by H^- and I^- primary ions is presented. These projectiles were selected to demonstrate well resolved cases of two energy loss regimes. At 45 keV, H^- ions lose $\sim 99\%$ of their energy through electronic stopping, while I^- ions lose $\sim 72\%$ of their energy through nuclear stopping. The intensity of each light signal is proportional to the amount of energy deposited into the electronic system of the target [1]; therefore, at 45 keV, the observed signal is more intense for H^- than I^- .

It is obvious from Fig. 3 that both projectiles produce two component decays with similar emission profiles within the resolution of the filters. However, for both the fast and

slow components, I^- has a shorter lifetime. A possible explanation is the crystal lattice distortion caused by the impact of keV I^- ions. 45 keV H^- ions deposit all their energy over a range of ~ 5000 Å in a CsI crystal through electronic interactions. However, 45 keV I^- ions dissipate their energy through nuclear collisions within ~ 200 Å of the surface. Because of the collision cascade induced by the I^- ions, the crystal lattice near the impact site is disturbed. The generated excitons which are self-trapped within this region will not be in a “perfect” crystal. The perturbation of the electronic structure within the region may alter the stability of the STEs and thereby shorten their lifetimes. (Stopping powers and ranges of ions were simulated by TRIM [18].)

Lamatsch et al. studied STEs in CsI, and reported a temperature dependence on the luminescence lifetime [11,12]. As stated, two intrinsic emission bands attributed to STE luminescence have been reported for CsI: 290 nm and 338 nm. At 64 K, the 338 nm emission band had a reported lifetime of 970 ns. As the temperature of the CsI crystal was increased, the lifetime steadily decreased until 152 K where the lifetime was 80 ns. At temperatures above 152 K, no luminescence was observed. Our instrument allowed us to observe light emission at room temperature. The intensity is low, but at 298 K a lifetime of ~ 10 ns is observed for the fast component. This observation is consistent with the reported trend.

To our knowledge, no work has reported a two component luminescence decay for CsI; however, two component

decays have been observed from the luminescence of STEs for other alkali halide crystals and rare gas solids [19,20]. Matsumoto et al. reported that RbI at 13.8 K, excited with 317 nm radiation, exhibited a fast component (4.4 ns) and a slow component (500 ns) decay.

In contrast to the two component decay of CsI, only a fast component was observed for NH_4Cl . Fig. 4a shows the luminescence from 185–710 nm induced by 45 keV H^- ions impacting a sample of NH_4Cl vapor deposited onto a quartz slide. The width of the observed peak is less than 2 ns. With only 0.5 ns timing resolution, a statistically valid decay could not be determined; however, the lifetime is obviously less than 3 ns. The luminescence of STEs in ammonium halide salts has been reported. Two component decays were observed for NH_4I ($\tau_{fast} = 2.0$ ns, $\tau_{slow} = 200$ ns) and NH_4Br ($\tau_{fast} = 2.0$ ns, $\tau_{slow} = 700$ ns); however, for NH_4Cl only a fast decay was reported ($\tau_{fast} = 2.7$ ns) [15]. Similarly also to the CsI results, the intensity of the NH_4Cl STE luminescence was reported to decrease with increasing temperature. The luminescence intensity was reported to decrease two orders of magnitude between 11 and 250 K, and reportedly vanished around 250 K [21]. As with CsI, our experiments were performed at room temperature. The intensity of the NH_4Cl luminescence was extremely low, but detectable.

Due to the extremely low signal intensity, only crude wavelength measurements could be made. Fig. 4b shows the observed luminescence from a thin NH_4Cl vapor deposit. Sufficiently thin that the 45 keV H^- primary ions

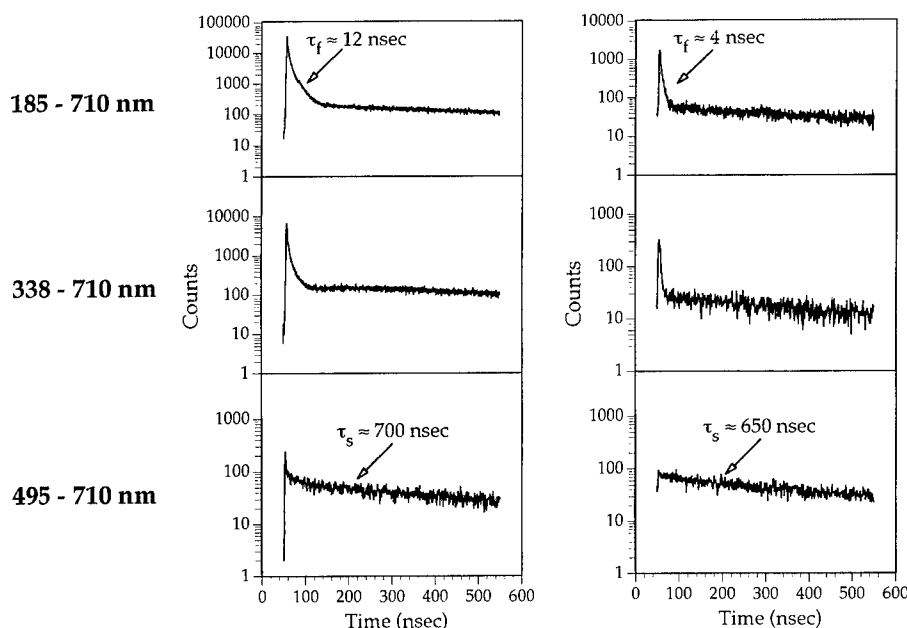


Fig. 3. Semi-log plots of the light emission from a CsI film induced by 45 keV H^- and I^- ions at different wavelength windows. Two component decays are evident.

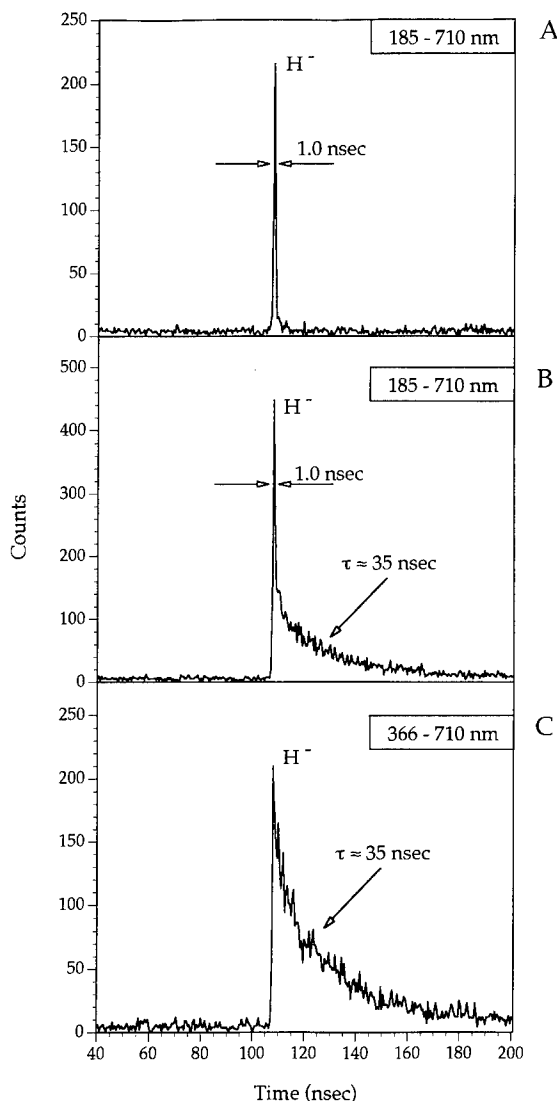


Fig. 4. Light emission from NH_4Cl films bombarded by 45 keV H^- ions. (a) Thick NH_4Cl film (> 5000 Å) with no wavelength discrimination; (b) thin NH_4Cl film (< 5000 Å) with no wavelength discrimination, light from the quartz support is observed; (c) same as in (b) but wavelength window is 366–710 nm, emission from NH_4Cl is removed.

can penetrate the film and impact the quartz slide (< 5000 Å). Two decay components are now observed. The slow component is attributed to the luminescence of the quartz (SiO_2). Luminescence of STE in SiO_2 has been reported [22]. When the observed wavelength window is decreased from 185–710 nm to 366–710 nm, the fast decay attributed to the STE luminescence of NH_4Cl is removed (Fig. 4c). The reported STE luminescence from NH_4Cl has an emission peak at 252 nm [15]. Our results agree with this emission.

4. Conclusion

We have used single keV ions to bombard the surface of CsI and NH_4Cl films, and have detected the light emission from these impacts on an event-by-event basis. Wavelength and time resolved analysis of our results agree with previously reported data obtained with other means of electronic excitation. We conclude that the light emission from both CsI and NH_4Cl is due to the radiative relaxation of self-trapped excitons which are produced by electronic interactions between the primary ions and the target atoms.

Work is in progress on improving the collection efficiency of the light, and on relating the observed light signals to the desorption mechanisms for keV and MeV ions.

Acknowledgements

This work was supported by the National Science Foundation Grant CHE-9208185. EFS gratefully acknowledges the support for a sabbatical leave from CNPq (Brazil).

References

- [1] R.G. Kaercher, E.F. Da Silveira, C.V. Barros Leite and E.A. Schweikert, Nucl. Instr. and Meth. B 94 (1994) 207.
- [2] B.D. Cox, M.A. Park, R.G. Kaercher and E.A. Schweikert, Anal. Chem. 64 (1992) 843.
- [3] M.G. Blain, S. Della-Negra, H. Joret, Y. Le Beyec and E.A. Schweikert, Phys. Rev. Lett. 63 (1989) 1625.
- [4] M. Van Stipdonk, M.A. Park, E.A. Schweikert, P. Sylvester and A. Clearfield, Int. J. Mass Spec. Ion Processes 128 (1993) 133.
- [5] N. Itoh, ed., Defect Processes Induced by Electronic Excitation in Insulators, Directions in Condensed Matter Physics, vol. 5 (World Scientific, London, 1989).
- [6] K. Tanimura and N. Itoh, Nucl. Instr. and Meth. B 46 (1990) 207.
- [7] R.T. Williams and K.S. Song, J. Phys. Chem. Solids 51 (1990) 679.
- [8] K.S. Song and R.T. Williams, eds., Self Trapped Excitons, Springer Series in Solid-State Sciences, vol. 105 (Springer, New York, 1993).
- [9] M. Itoh, K. Tanimura and N. Itoh, J. Phys. Soc. Jpn. 62 (1993) 2904.
- [10] K.-i. Kan'no, K. Tanaka, H. Kosaka and Y. Nakai, J. Lumin 48&49 (1991) 147.
- [11] H. Lamatsch, J. Rossel and E. Saurer, Phys. Status Solidi 41 (1970) 605.
- [12] H. Lamatsch, J. Rossel and E. Saurer, Phys. Status Solidi B 48 (1971) 311.
- [13] K. Tanimura and N. Itoh, Phys. Rev. Lett. 60 (1988) 2753.
- [14] A.Y. Yau, M.A. Park, R.G. Kaercher and E.A. Schweikert, Rev. Sci. Instr. 64 (1993) 1748.

- [15] N. Ohno, M. Itoh and S. Hashimoto, *J. Lumin.* 53 (1992) 121.
- [16] S. Keszthelyi-Léandori and G. Hrehuss, *Nucl. Instr. and Meth.* 68 (1969) 9.
- [17] C.J. Crannell, R.J. Kurz and W. Viehmann, *Nucl. Instr. and Meth.* 115 (1974) 253.
- [18] J.F. Ziegler, TRIM, ver. 90, IBM-Research, 28-0, Yorktown, NY 10598, (1990).
- [19] T. Matsumoto, T. Kawata, A. Mityamoto and K.-i. Kan'no, *J. Phys. Soc. Jpn.* 61 (1992) 4229.
- [20] G. Zimmerer, in: *Proc. Int. School of Physics "Enrico Fermi", Excited-State Spectroscopy in Solids*, Varenna, Italy, 1985, ed. U.M. Grassano and N. Terzi (North-Holland, Amsterdam, 1987).
- [21] M. Itoh, *J. Phys. Soc. Jpn.* 57 (1988) 372.
- [22] C. Itoh, T. Suzuki and N. Itoh, *Phys. Rev. B* 41 (1990) 3794.



ELSEVIER

Charge exchange in low-energy D^+ scattering from O-, CO-, and CsCl-adsorbed Pt(111) surfaces

R. Souda^{*}, K. Yamamoto, W. Hayami, T. Aizawa, Y. Ishizawa

National Institute for Research in Inorganic Materials, 1-1 Namiki, Tsukuba, Ibaraki 305, Japan

Abstract

The capture and loss of valence electrons during low-energy (~ 100 eV) D^+ scattering from solid surfaces have been studied from a combination of experiments and molecular-orbital-energy calculations based on the discrete variational $X\alpha$ method. The surface peak of D^+ surviving neutralization is almost absent for O at the oxygenated Pt(111) surface whereas it is remarkable at the CO-adsorbed Pt(111) surface. The enhancement of the neutralization probability of D^+ at the O/Pt(111) surface is caused by the band effect of resonance neutralization mediated by the O–Pt bond, but the band effect is not remarkable in scattering from molecularly-adsorbed CO. The other example of the band effect is presented concerning CsCl adsorption: Almost complete neutralization occurs when D^+ is scattered from CsCl dissociatively adsorbed on the Pt(111) surface, whereas neutralization probability is suppressed to some extent if D^+ is scattered from CsCl adsorbed ionically on the H-terminated Si(001) surface.

1. Introduction

It is well established that an ion captures a surface electron via resonant neutralization (RN) and/or Auger neutralization (AN). The relative role of these processes is thought to be dependent upon the energy position of the ion vacant level relative to that of the target valence band. So far, a considerable research effort has been devoted to alkali-metal ions and noble-gas ions, but a few investigations had been made of the other ions which might be classified as “reactive” ions. Among them, hydrogen is of particular interest since it is the simplest projectile and its neutralization behavior is known to be unique [1]. In general, ions scattered from the outermost surface layer are more likely to survive neutralization than those scattered from the deeper layers, and form surface peaks in their energy distributions. This is the case for the noble-gas ions such as He^+ . However, the surface peak in H^+ or D^+ scattering is almost completely absent for metal and semiconductor surfaces and appears only at highly ionic-compound surfaces such as alkali halides [2]. In order to gain better insight into the charge exchange phenomena, D^+ scattering experiments have been made at a variety of chemisorption systems on metal and semiconductor surfaces [3]. In this paper, attention is mainly focused on O-, CO- and CsCl-adsorbed Pt(111) surfaces. The mechanism

of neutralization and electronic excitation will be discussed from a combination of experiments and molecular-orbital (MO) energy calculations.

2. Experiment

The experiments were performed in an ultrahigh vacuum (UHV) chamber equipped with facilities for standard surface characterization. The D^+ ion was generated in a discharge-type ion source and was mass analyzed by using a Wien filter. A D^+ beam was incident upon a surface with an angle of 80° measured from the surface, and the D^+ ions scattered specularly through a laboratory scattering angle of 160° were detected by means of a hemispherical electrostatic energy analyzer operating with a constant energy resolution of 1 eV. The Pt(111) surface was prepared with a standard oxygen treatment and exhibited an excellent 1×1 pattern in low-energy electron diffraction. CsCl was evaporated in UHV from the tantalum basket and was deposited on the clean Pt(111) surface and the hydrogen-terminated Si(001) surface, which were kept at room temperature.

3. Results and discussion

Fig. 1 shows energy spectra of $E_0 = 100$ eV D^+ ions scattered from CsCl (~ 0.4 monolayer) deposited on (a) the H-terminated Si(001) surface and (b) the Pt(111) sur-

^{*} Corresponding author, tel. +81 298 51 3351, fax +81 298 52 7449, E-mail: souda@nirim.go.jp.

face. The arrows on the abscissa indicate the positions of the elastic binary-collision energy for individual target atoms. The D^+ ions scattered from the substrates themselves are almost completely neutralized and the ion yield is increased with the amount of deposited CsCl. In Fig. 1a, the surface peaks (peak A) for Cs and Cl appear accompanied by the energy-loss peak labeled B. One may think that peak B comes from multiple scattering rather than the electronic excitation. But, this assumption should be discarded by considering the fact that the energy loss value is almost identical even when the incident energy is changed. The energy spectrum shown in Fig. 1a is characteristic of the intrinsic CsCl surface. Peak B can be ascribed to the

electron-hole-pair excitation because of the good correlation between the energy-loss value of peak B and the band-gap energy of CsCl [2,3]. By contrast, the D^+ spectrum in Fig. 1b exhibits no marked surface peaks for Cs as well as Cl, and the spectrum is composed mainly of a broad background indicated by the broken line. The background stems from D^+ ejected from the surface after penetration into the Pt substrate.

The Pt(111) surface is also exposed to oxygen (200 L; 1 L = 1 langmuir = 1.3×10^{-4} Pa s) and carbon monoxide (10 L) at room temperature, and the results of D^+ scattering ($E_0 = 100$ eV) are displayed in Figs. 2a and 2b, respectively. The intensities are normalized relative to each

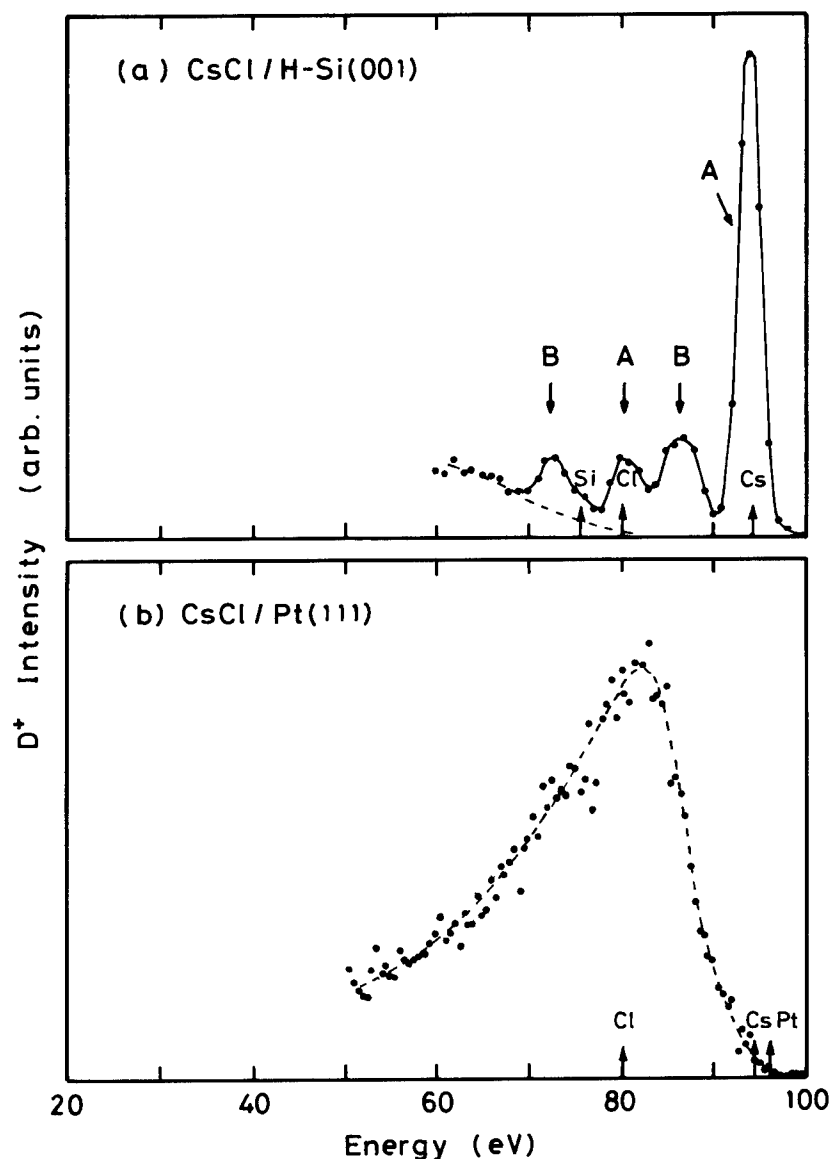


Fig. 1. Energy spectra of $E_0 = 100$ eV D^+ scattered from CsCl (0.4 ML) deposited on (a) the H-terminated Si(001) surface and (b) the clean Pt(111) surface. The energies for the elastic binary collision are shown by arrows with chemical symbols on the abscissa.

other through beam current. The oxygenated Pt(111) surface shows a very small O surface peak relative to the background, whereas the O peak is remarkable at the CO/Pt(111) surface. It should be noted that the backgrounds in Figs. 1b and 2 are quite similar in shape irrespective of the species of the adatoms and have a cutoff energy at around 90 eV.

In the literature [2,3], it has been revealed from a large number of D^+ scattering experiments that the presence or

the absence of the surface peak in the D^+ spectra is correlated closely to the ionicity of the surface atomic bond. Indeed, Fig. 1a is typical of the D^+ spectra for the highly ionic-compound surfaces. On the other hand, the absence of the marked surface peaks in Fig. 1b is thought to be caused by the breakdown of the ionic Cs–Cl bond, that is, the occurrence of the dissociative adsorption and the covalent orbital hybridization with the Pt atom [2,3].

As regards neutralization of the D^+ ions, it is believed

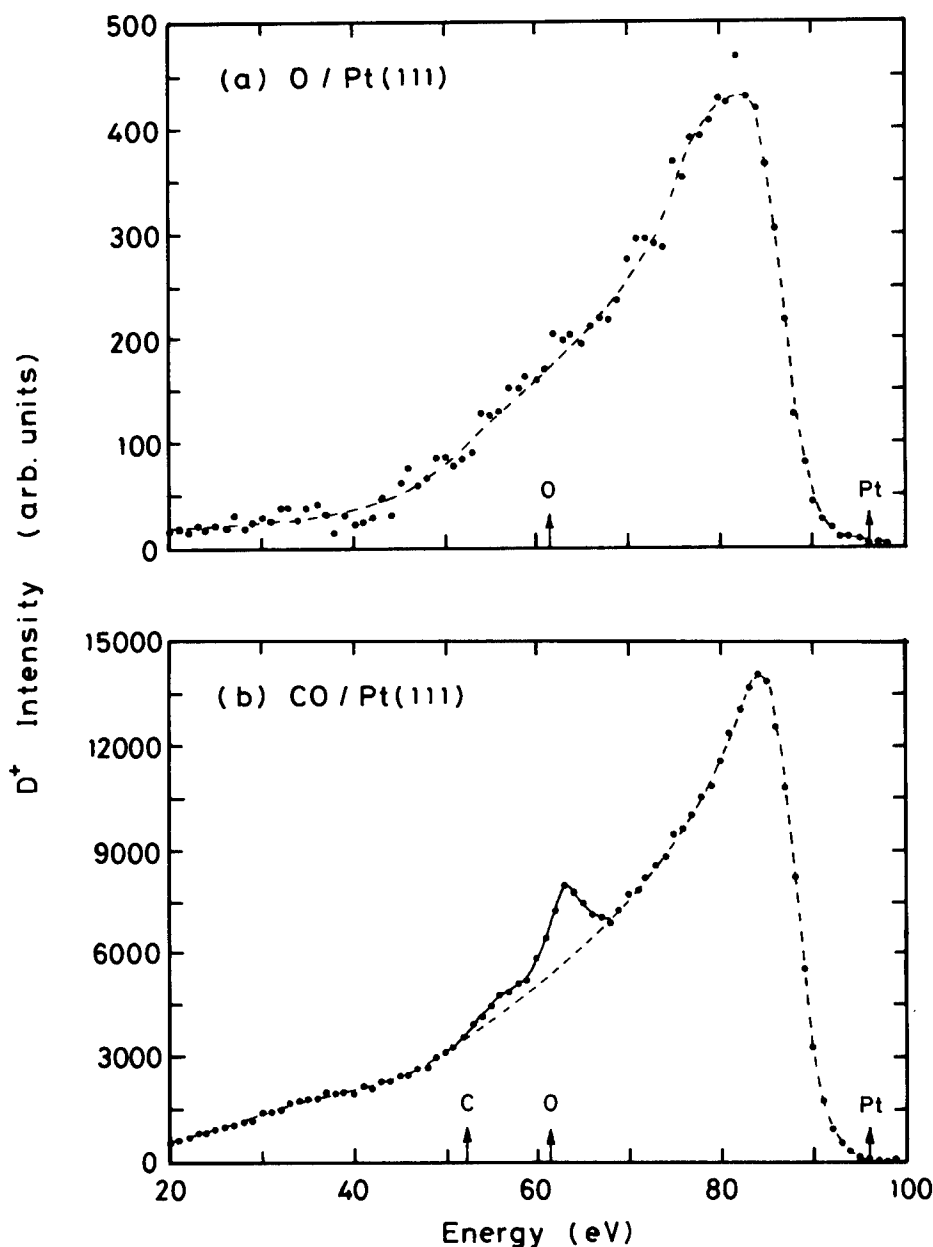


Fig. 2. Energy spectra of $E_0 = 100$ eV D^+ scattered from the Pt(111) surface exposed to (a) 200 L O_2 , and (b) 10 L CO. The intensities are normalized relative to each other.

that the AN process makes important contribution, but AN cannot explain the observed remarkable chemical effect on the neutralization probability. On the basis of the experiments, we have suggested that RN plays an important role in neutralization of D^+ [2,3]. This assumption has recently been confirmed from the MO energy calculations for hydrogen interacting with various surface clusters [4]. In what follows, the demonstration is made for the O- and CO-adsorbed Pt(111) surfaces since their structures are well established.

The MO energy level is numerically calculated using the self-consistent-charge discrete variational X α (SCC-

DV-X α) method; the strategy of the calculation has been shown elsewhere [5]. CO is molecularly adsorbed at the on-top site of Pt(111) with the C end towards the Pt atom. Although a small 5σ donation/ 2π back-donation type interaction exists between the MOs of CO via the valence band of the Pt surface [6], the calculation is made for $(C-O-D)^+$ linear chain by changing the O–D separations. It might be possible that the ion-beam bombardment causes the dissociation of CO or the change of the adsorption site. However, the beam intensity is too small to induce such a structural change. On the other hand, oxygen is dissociatively adsorbed at the fcc three-fold hollow site of the

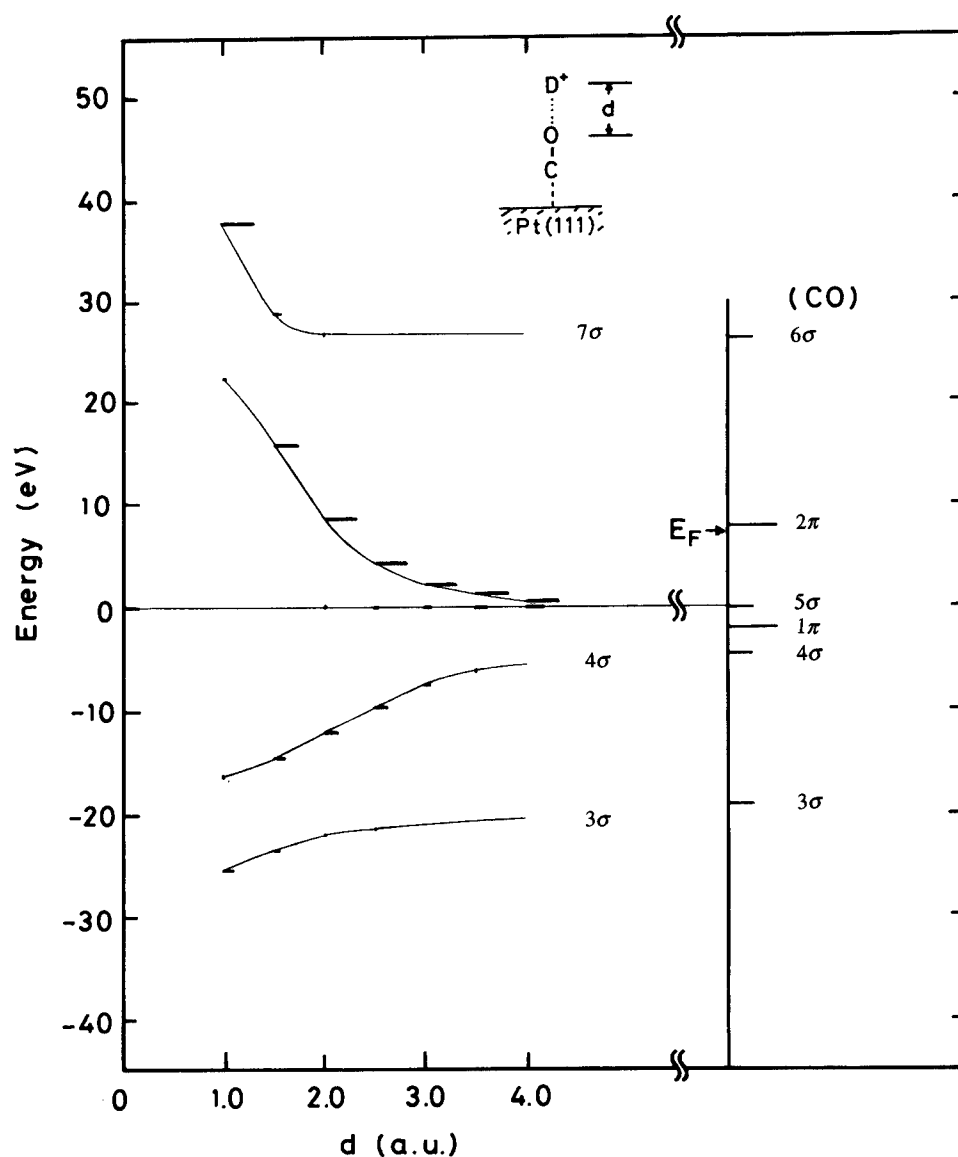


Fig. 3. Energy-level diagram for the $(COD)^+$ cluster simulating D^+ scattering from O of CO adsorbed molecularly on the Pt(111) surface. The D is component is shown as a function of the internuclear distance. The calculated molecular-orbital energies for CO are displayed on the right-hand side.

Pt(111) surface with a height of 0.85 \AA [7]. The simulation is made by taking the simplest $(\text{Pt}_3\text{--O--D})^+$ cluster.

Figs. 3 and 4 show the σ -orbital energies for the $(\text{COD})^+$ cluster and the a_1 -orbital energies for the $(\text{Pt}_3\text{OD})^+$ cluster, respectively. The results are plotted relative to the valence-band-top (or the highest occupied molecular orbital; HOMO) positions so that the variations of orbitals with the D 1s character can be surveyed as a function of the separation, d , of the deuteron from the O atom. The distance of closest approach for $E_0 = 100 \text{ eV}$ D^+ on O is 0.65 a.u. ($1 \text{ a.u.} = 0.53 \text{ \AA}$). The population of the D 1s atomic orbital in each MO is indicated by the length of the horizontal bar. Also displayed on the right-

hand side of the diagram are the electronic structures calculated by using the (CO) and (Pt_3O) clusters.

In Fig. 3, the D 1s character appears mainly in the 5σ and 6σ orbitals at a large separation. With decrease of the separation, the 6σ orbital is promoted and, finally, the D 1s character is concentrated on the 7σ orbital. The position of the Fermi level at the Pt(111) surface is also indicated in the figure by considering the experimental fact that 4σ orbital is located at about 12 eV below the Fermi level position [8].

The a_1 orbital energies shown in Fig. 4 have basically the same behavior as in the $(\text{COD})^+$ system. Note that, at a large separation, the D 1s character appears in the MOs

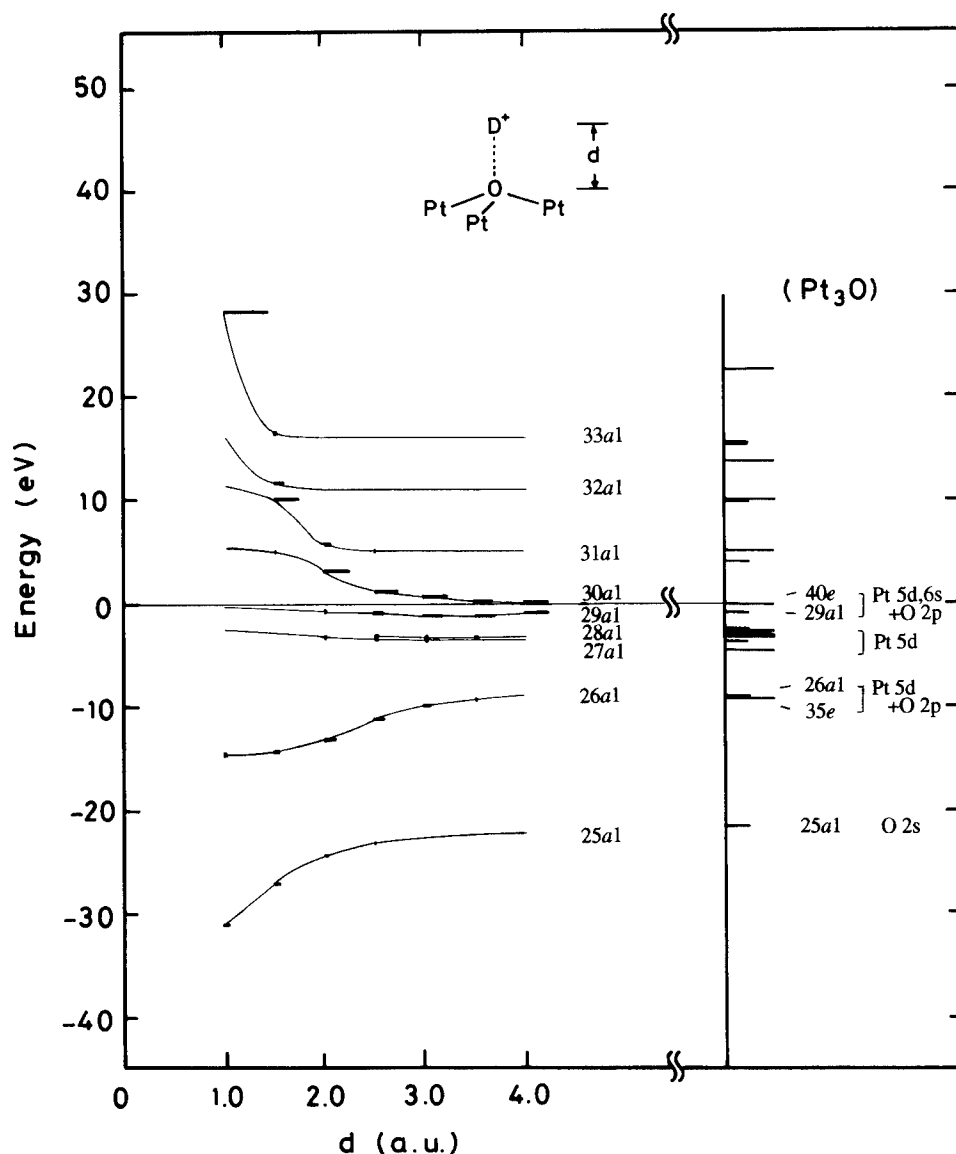


Fig. 4. Energy-level diagram for the $(\text{Pt}_3\text{OD})^+$ cluster simulating D^+ scattering from O dissociatively adsorbed at the fcc 3-fold hollow site of the Pt(111) surface.

around the HOMO position, which in this case coincides with the Fermi-level position. The distribution of the D 1s character in $27a_1$, $28a_1$ and $29a_1$ orbitals at moderate separations indicates that D 1s does satisfy the resonance condition in energy with the valence band states. Before interaction with D^+ , the $29a_1$ orbital has the Pt 5d, 6s and O 2p characters, whereas the $28a_1$ and $27a_1$ orbitals are composed mostly of the Pt 5d atomic orbital. The $30a_1$ orbital originates from D 1s and is hybridized with the Pt 5d, 6s and O 2p orbitals. With the decrease of the separation, the orbital character changes and the D 1s component is, in turn, transferred to the MOs with higher energies. Such an orbital promotion is caused by the antibonding interaction with the O 2s, 2p orbitals as evidenced by the downward shift of the correlated bonding orbitals. It is notable that the D 1s character disappears almost completely in the valence-band orbitals for $d < 2.0$ a.u. This state is the so-called “surface molecule” [9].

The above calculation clearly shows that D^+ captures a valence electron via RN. However, the calculated MO energy diagrams are not sufficient to elucidate the experimental results shown in Fig. 2. In reality, ion neutralization is a highly dynamical process and the neutralization probability is thought to be determined at least by two competitive factors. One is the duration of the ion–surface interactions, $T \approx 10^{-15}$ s, and the other is the lifetime of the D 1s hole. The occurrence of complete neutralization at metal [Pt(111)] and semiconductor [Si(001), H-terminated Si(001)] surfaces can be ascribed to the band effect of RN, that is, the D 1s hole cannot be localized in the MOs formed by D^+ and the target atom, and diffuses irreversibly into the valence-band states of the surrounding atoms within the collision time T . On the other hand, the presence of the O peak for the CO/Pt(111) surface shows that the hole is rather localized in the molecular orbitals of the $(COD)^+$ complex and cannot diffuse into the band of the Pt(111) substrate. The situation is similar to the well-known quasi-resonant neutralization of the He^+ ions [10–13], where the electron (or the hole) is localized in the MOs formed by He 1s and the resonating semi-core orbital of the target. In these cases, the average neutralization probability is shown to be at most 0.5 [9,13].

The considerably small O peak at the O/Pt(111) surface suggests that the D 1s hole is diffusive. The MO calculation shown in Fig. 4 reveals that RN, though suppressed in the close encounters due to the formation of the surface molecule, occurs at moderate separations ($d > 2.0$ a.u.) as a consequence of the hybridization of D 1s with the 27 – $29a_1$ orbitals of the (Pt_3O) cluster. Among them, the $29a_1$ orbital formed with O 2p and Pt 5d, 6s states is of most importance due to the strong hybridization with the D 1s orbital. In this case, RN occurs such that the hole of D^+ is initially transferred to the $29a_1$ orbital and subsequently diffuses into the valence-band states of the Pt surface. It is thus concluded that the absence of the O peak at the O/Pt(111) surface is caused by the band effect of the

Pt(111) surface mediated by the O–Pt bond. The same mechanism holds for neutralization of D^+ scattered from dissociatively-adsorbed Cs and Cl on the Pt(111) surface. On the other hand, the ionicity of the Cs–Cl bond causes the bottleneck of hole diffusion [2–4], which results in the appearance of the surface peaks as is typically seen in Fig. 1a.

The spectral backgrounds shown in Figs. 1b and 2 are assignable not to survival of D^+ but to re-ionization of neutralized D^+ ($D^+ \rightarrow D^0 \rightarrow D^+$). Re-ionization occurs in the collision with the adatoms just before leaving the surface due to the electron promotion mechanism [4]. As is seen in Figs. 3 and 4, indeed, the D 1s electron can be promoted along antibonding MO in the close encounter ($d < 2.0$ a.u.). This is followed by ionization (resonance ionization; RI) due to electron diffusion into the open conduction-band states of the Pt(111) substrate. If the resulting ions survive RN on the receding path from the surface, they form the background in the D^+ energy spectra. Re-ionization results in excitation of the D 1s electron to the conduction-band state, so that the leading edge of the background is located by several eV below the elastic collision energy for Pt. It is remarkable that the intensity of the background at the CO/Pt(111) surface is considerably large compared to that at the O/Pt(111) surface, although the coverage of the adatoms is not known. It is likely that the background intensity depends on the microscopic surface atomic structures; oxygen of the molecularly-adsorbed CO is located farther from the Pt(111) surface than the dissociatively-adsorbed O atom. Since the orbitals of the empty conduction-band states are spatially extended toward the vacuum side compared to the occupied valence-band state, the antibonding 6σ and 7σ orbitals in the $(COD)^+$ complex may interact preferentially with the former rather than the latter, leading to the enhancement of RI relative to RN in probability.

4. Conclusion

The mechanism of charge exchange in low-energy D^+ scattering from the O-, CO-, and CsCl-adsorbed Pt(111) surfaces has been discussed within the framework of the electron promotion mechanism and the band effect of resonant tunneling. It is revealed that neutralization of D^+ scattered from molecularly-adsorbed CO on the Pt(111) surface is suppressed in probability because of the localized nature of the D 1s hole in the $(D-O-C)$ complex. The same is essentially true for D^+ scattering from ionically adsorbed CsCl on the H-terminated Si(001) surface. On the other hand, the atomically adsorbed O, Cs, and Cl on Pt(111) have significant orbital hybridization with the Pt 5d, 6s states through which the D 1s hole can diffuse irreversibly into the valence-band states of Pt(111), resulting in almost complete neutralization of D^+ . (Re)ionization of D^0 occurs if the 1s electron is promoted along the

antibonding molecular orbitals and diffuses into the conduction-band state. The spectral background in D^+ scattering becomes remarkable if the surface is covered with the adatoms on which D^0 can be ionized during collision. It is suggested that the background intensity is enhanced if the adatom is situated farther from the surface since the D 1s orbital interacts with the empty conduction-band state rather than the occupied valence-band state.

Acknowledgement

We are indebted to Professor H. Adachi of Kyoto University for use of the DV-X α calculation program.

References

- [1] W. Eckstein, in: *Inelastic Particle–Surface Collisions*, Springer Series of Chemical Physics vol. 17, eds E. Taglauer and W. Heiland (Springer, New York, 1981) p. 157.
- [2] R. Souda, W. Hayami, T. Aizawa, S. Otani and Y. Ishizawa, *Phys. Rev. B* 42 (1990) 7761; *B* 43 (1991) 10062; *B* 45 (1992) 14 358; *B* 50 (1994) 1934; 4733.
- [3] R. Souda, W. Hayami, T. Aizawa, S. Otani and Y. Ishizawa, *Phys. Rev. Lett.* 69 (1992) 192; *Phys. Rev. B* 48 (1993) 17255; *Surf. Sci.* 290 (1993) 245.
- [4] R. Souda, K. Yamamoto, W. Hayami, B. Tilley, T. Aizawa and Y. Ishizawa, *Phys. Rev. B*, in press.
- [5] H. Adachi, M. Tsukada and C. Satoko, *J. Phys. Soc. Jpn.* 45 (1978) 875.
- [6] H.P. Bonzel, *Surf. Sci. Rep.* 8 (1987) 43.
- [7] K. Mortensen, C. Klink, F. Jensen, F. Besenbacher and I. Stensgaard, *Surf. Sci.* 220 (1989) L701.
- [8] M. Kiskinova, G. Pirug and H.P. Bonzel, *Surf. Sci.* 133 (1983) 321.
- [9] S. Tsuneyuki, N. Shima and M. Tsukada, *Surf. Sci.* 186 (1987) 26.
- [10] R.L. Erickson and D.P. Smith, *Phys. Rev. Lett.* 34 (1975) 297.
- [11] N.H. Tolk, J.C. Tully, J. Kraus, C.W. White and S.H. Neff, *Phys. Rev. Lett.* 36 (1976) 747.
- [12] A. Zartner, E. Taglauer and W. Heiland, *Phys. Rev. Lett.* 40 (1978) 1259.
- [13] J.C. Tully, *Phys. Rev. B* 16 (1977) 4324.

Energy loss of fast protons scattered from an Al(111)-surface under grazing incidence

M. Wilke, R. Zimny, H. Winter *

Humboldt-Universität zu Berlin, Institut für Physik, Invalidenstr. 110, 10 115 Berlin, Germany

Abstract

Protons with energies ranging from about 6 to 30 keV are scattered under grazing angles of incidence from a flat and clean Al(111)-surface. We observe angular and energy distributions of the scattered projectiles with high resolution and find for the mean energy loss a pronounced increase with projectile energy and a slight decrease for an increasing angle of incidence. We present model calculations based on the assumption that the energy loss is predominantly due to binary collisions with conduction electrons. These calculations reproduce main features of our data fairly well.

1. Introduction

Ion-surface scattering under a grazing angle of incidence allows one to perform defined studies of the interaction mechanisms of fast ions with surfaces. Ions of energy E , scattered under a grazing angle of incidence from a flat crystal surface, cannot overcome the planar surface potential, since the energy of the motion perpendicular to the surface $E_{\perp} = E \sin^2 \Phi_{\text{IN}}$ (Φ_{IN} : angle of incidence) amounts to typically some eV. The projectiles are scattered in front of the topmost layer of target atoms (“semiplanar channeling”).

Energy loss phenomena in this geometry of scattering have attracted some attention in recent years. At high projectile velocities ($v \gg v_F$, v_F = Fermi velocity of the target electrons) experimental data for proton stopping have been reported by Kimura et al. [1] and Winter et al. [2]. At low velocities ($v \lesssim 0.6 v_F$) Närmann et al. [3,4] studied the energy loss of protons scattered from Ni-surfaces. For intermediate velocities ($v \approx v_F$) experiments with protons specularly reflected from a C(0001)-surface and estimates on the position- and velocity-dependent stopping power $S(v, y)$ have been presented by Stölzle and Pfandzelter [5,6].

In this work we study in more detail the interaction mechanisms in the intermediate velocity regime, where the projectile velocities are comparable to those of the conduction electrons in the metal. We have measured the energy loss of protons specularly reflected from an Al(111)-surface in dependence on the projectile velocity ($0.5 \lesssim v/v_F \lesssim 1.1$)

and on the angle of incidence ($0.1^\circ \lesssim \Phi_{\text{IN}} \lesssim 1.5^\circ$). This projectile-target combination provides a good basis for a theoretical treatment, since protons have no electronic structure and Al is generally accepted as the prototype of a free-electron-like metal.

A general first principles and unified theoretical treatment of the interrelated aspects of dynamical ion screening, charge exchange between metal and moving projectiles along the trajectory, dynamic excitation of surface electrons and of the potentials governing the trajectory of the projectiles has not been performed so far. This will be an extremely difficult task. Instead we present here a simplified scheme for the calculation of proton stopping at surfaces and deduce position dependent stopping powers for low and intermediate velocities [7]. From a comparison with our experimental results we conclude that the energy loss of protons at an aluminum surface is dominated by inelastic binary collisions with conduction electrons in the selvage of the surface.

Atomic units are used unless noted otherwise.

2. Experiment and results

A fast proton beam is collimated to a divergence of less than 0.04° and is directed onto the (111) face of an aluminum single crystal under a grazing angle of incidence Φ_{IN} , deduced from the reflection of a laser beam with an accuracy of about 0.05° . Energy spectra of scattered protons are recorded with a 90° cylindrical analyzer positioned at an angle of emergence Φ_{OUT} in the scattering plane, i.e. the plane which contains incident beam and surface normal.

The analyzer is positioned about 700 mm behind the

* Corresponding author, tel. +49 30 2803 491, fax +49 30 2803 496, E-mail: winter@physik.hu-berlin.de.

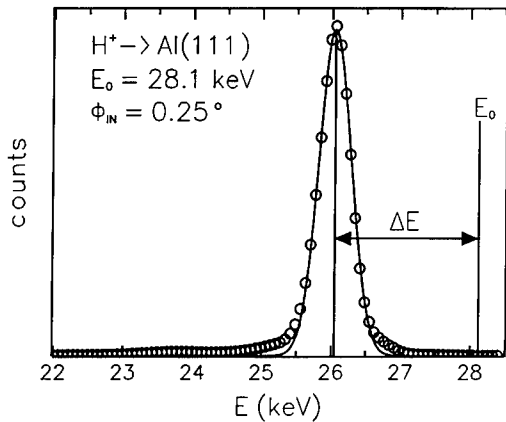


Fig. 1. Energy spectrum of H^+ ($E_0 = 28.1$ keV) reflected from an Al(111)-surface, with $\Phi_{IN} \approx \Phi_{OUT} \approx 0.25^\circ$. The solid line represents a Gaussian fit to the data.

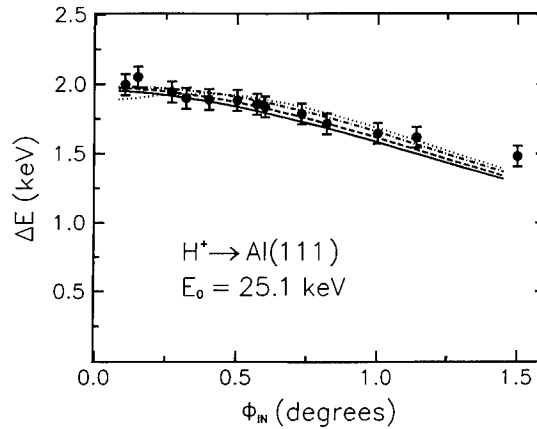


Fig. 2. Energy loss of specularly reflected protons with incident energy of 25.1 keV as a function of the incident angle. The lines represent results of calculations for different “switching distances” y_F (see text), solid line: $y_F = 3.5a_0$, dashed line: $y_F = 4a_0$, dash-dotted line: $y_F = 5a_0$, dotted line: $y_F = 7a_0$.

target and has an energy resolution $\Delta E/E \approx 3 \times 10^{-3}$ at an angular acceptance of $\pm 0.02^\circ$. The clean and flat Al(111) surface is prepared by cycles of grazing sputtering and of annealing up to about 500°C . After final preparation no traces of impurities can be detected in the electron-induced Auger spectra. From SPA-LEED studies we deduce a well-ordered surface with an average terrace width of 500–700 Å. The projectile beam is directed along a high-indexed (“random”) crystallographic direction in the surface plane in order to avoid effects of axial channeling. This allows us to apply a continuum surface potential in the description of trajectories of the projectiles.

We have measured energy spectra of specularly reflected H^+ with an energy E_0 for the incident beam ranging from about 6 to 30 keV and varying the angle of incidence up to 1.5° . As a representative example we show in Fig. 1 a spectrum for 28.1 keV protons scattered from Al(111) under $\Phi_{IN} = 0.25^\circ$. The spectrum is dominated by an intense peak with a Gaussian lineshape so that the most probable and the mean energy loss ΔE of the specularly reflected protons are practically identical and are evaluated by a Gaussian fit to the data (solid line in Fig. 1). The spectra exhibit additional weak peak structures at lower energies, which are attributed to “skipping motion” and subsurface channeling. (see e.g. Refs. [1,8–10]). These latter effects are beyond the scope of the present paper and will be reported elsewhere.

In Fig. 2 the energy loss for specularly reflected protons with $E_0 = 25.1$ keV is displayed in dependence on the angle of incidence Φ_{IN} . We observe a slight decrease of ΔE with increasing angle, which is less pronounced as observed for a graphite surface [5,6]. The various lines represent results from our model calculations outlined in the following sections.

The dependence of the mean energy loss on projectile

energy is shown in Fig. 3. In our experiments the angular setting of the target is adjusted in such a way that the initial energy E_\perp^0 of the motion normal to the surface plane is kept constant. Note that close to the surface E_\perp is raised by about 1 eV due to image interaction between charged particle and metal surface [11]. We show data for $E_\perp^0 = 0.5$ eV and 2.5 eV, respectively. The slight reduction of the energy loss for the larger normal energy is equivalent with the decrease of ΔE with increasing angle, as shown in Fig. 2.

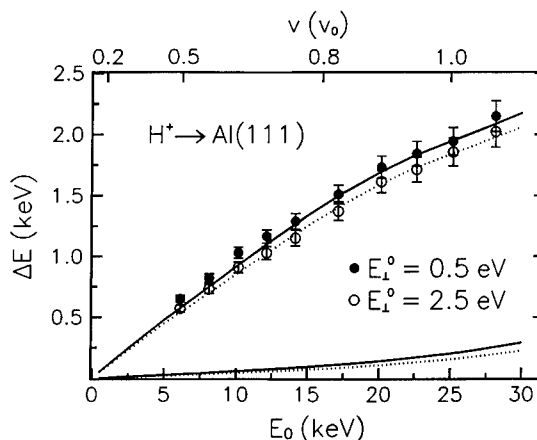


Fig. 3. Energy loss of specularly reflected protons as a function of the incident energy E_0 for two initial transverse energies E_\perp^0 of 0.5 eV (solid circles) and 2.5 eV (open circles). The solid lines are calculated for $E_\perp^0 = 0.5$ eV, the dotted lines for $E_\perp^0 = 2.5$ eV. The lower lines represent the contributions of the “vacuum region” to the total energy loss. The “switching distance” y_F (see text) was chosen as $y_F = 4a_0$.

3. Model for energy loss

Protons with energies in the range of these studies and scattered under grazing angles $\Phi_{\text{IN}} \leq 1.5^\circ$ along a random crystallographic direction from a surface do not penetrate into the bulk of the solid. Then the energy loss of fast projectiles is primarily due to interactions with the conduction electrons. Since these interactions depend on the distance y of the projectile from the surface plane, the concept of a surface stopping power $S(v_{\parallel}, y)$ has been introduced [1,5,6], where v_{\parallel} is the actual velocity component parallel to the surface plane. Integration along the mean trajectory of the projectiles yields the mean energy loss

$$\Delta E = \int_{\text{trajectory}} S(v_{\parallel}, y) dx. \quad (1)$$

The electron density at the metal surface decays smoothly into the vacuum from its bulk value n_0 to zero. Since the protons penetrate into this sea of surface electrons two regions of interaction may be distinguished: the “vacuum region” and the region of finite electron density above the topmost surface layer (“electron selvage”). Electronic stopping in each of these zones will be treated here by a different formalism. A demarcation between both regions is discussed at the end of Section 3.3.

3.1. Stopping in the vacuum region

In our experiments incident and detected particles are positive ions. A proton moving outside the sea of surface electrons is seen from the metal as a time-varying long-ranged Coulomb field of an external point charge. The metal electrons respond to this perturbation by setting up a dynamical screening cloud. The resulting time-dependent total potential causes real electronic excitations in the surface on cost of the kinetic energy of the projectile. The stopping power for this *nonlocal* process can be derived within the dielectric linear response theory [12,13] for $v_{\perp} \rightarrow 0$ and an external charge Z (here: $Z = 1$) as

$$S_{\text{VAC}}(v_{\parallel}, y') = \frac{2Z^2}{v_{\parallel}} \int_0^{\infty} d\omega \omega \int_0^{\infty} dQ_y \frac{1}{Q} S(Q, \omega) \exp(-2Qy'), \quad (2)$$

where $Q = \sqrt{(\omega/v_{\parallel})^2 + Q_y^2}$. The distance y' is measured from the jellium edge at $y_{\text{JE}} = 2.21a_0$ above the topmost lattice plane of Al(111) [14]. Eq. (2) is derived for a semi-infinite jellium metal. The surface loss function $S(Q, \omega)$ depends on energy $\omega \geq 0$ and parallel momentum $Q = |Q|$ absorbed by electrons in the surface. $S(Q, \omega)$ reflects the elementary excitation spectrum of a jellium surface: electron–hole pair continuum and surface–plasmon resonance [15]. It depends on the microscopic details of the surface electron density distribution. Unfortunately, no quantitatively reliable unified function $S(Q, \omega)$ is

presently available even for the idealized jellium metal. Following Penzar and Sunjić we assume that $S(Q, \omega)$ can be splitted into a low-energy electron–hole pair contribution $S_{\text{EH}}(Q, \omega)$ and a surface–plasmon contribution $S_{\text{PL}}(Q, \omega)$, i.e. $S(Q, \omega) = S_{\text{EH}}(Q, \omega) + S_{\text{PL}}(Q, \omega)$. For the latter we have chosen a semiempirical surface–plasmon pole model [16], whereas S_{EH} is taken from [15]: $S_{\text{EH}}(Q, \omega) = 0.65(\omega/E_F)(Q/k_F) \exp(-3.445(Q/k_F)) \times \Theta(Qv_F - \omega)$, where E_F and k_F denote Fermi-energy and -momentum of the metal electrons. In this model electron–hole pairs (Q, ω) are more effectively excited, if their phase velocity (ω/Q) is less than v_F . Following Gumhalter [17] we cut $S_{\text{EH}}(Q, \omega)$ at $\omega = Qv_F$. This contribution to stopping in grazing ion–surface scattering clearly calls for a better determination of the surface-loss spectrum up to intermediate values of both Q and ω . The uncertainty of $S(Q, \omega)$ is moderated however by the finding that in the present case of an Al(111)-surface electronic stopping in the vacuum region contributes only between 5 and 10% to the total energy loss of the protons.

3.2. Stopping in the electron selvage

The dielectric approach for an *external* charge breaks down, when the proton penetrates into the sea of surface electrons, where a negative screening cloud is built up around the projectile. However, it holds again on the outgoing trajectory, where the screening charge can't follow the proton and stays centered at the image plane located at $y_{\text{IM}} = 3.3a_0$ above the surface layer [18]. In the region close to the surface (within $\sim 4\text{--}5a_0$ from the surface layer) screening charge and projectile are not spatially separated so that a different description of the electronic stopping process is required.

In the surface region the electron density is quite inhomogeneous and decays from n_0 to almost zero within an interval of about $5\text{--}6a_0$ [14,18]. Electronic stopping in such an inhomogeneous electron gas has not been treated so far by using the density functional theory (DFT) in combination with a scattering approach, which appears to be the most accurate method currently available for the calculation of the electronic stopping of slow protons in metals [19]. Note that in the surface region the stopping problem is considerably complicated by the loss of spherical symmetry.

We will apply here the conceptually simpler scheme of the so-called “uniform density approximation” (UDA) which has been successfully used to calculate chemisorption energy and distance of single H atoms on jellium metal surfaces [20,21]. The basic idea of UDA, when adopted to the present problem, is: The position-dependent stopping power is calculated by considering the stopping inside a homogeneous electron gas with an effective electron density equal to the local electron density $n(y)$ of the unperturbed surface at position y . This approximation is plausible since the scattering of individual surface elec-

trons at the screened proton is a *local* process. Introducing the electron density profile $\rho(y) \equiv n(y)/n_0$ the electron density parameter (“one-electron radius”) is given by

$$r_s(y) = r_s/\rho(y)^{1/3}, \quad (3)$$

with $r_s = (3/4\pi n_0)^{1/3}$. Then the position and velocity dependent stopping power within the sea of surface electrons can be calculated according to

$$S_{\text{EL}}(v_{\parallel}, y) = S_{\text{B}}(v = v_{\parallel}, r_s = r_s(y)), \quad (4)$$

where S_{B} denotes the bulk stopping power for a projectile moving with velocity v inside a homogeneous electron gas with density parameter r_s . For the bulk of Al we take $r_s = 2.075$ and $\rho(y)$ from the work of Lang and Kohn [14] for a semi-infinite jellium metal with $r_s = 2$ (see also Ref. [18]). The UDA is a method to *extrapolate* from bulk properties to the corresponding properties in the near-surface region. Based on chemisorption studies [20,21] we assume that the UDA is applicable up to about $y = 4-5a_0$. S_{B} has been calculated as a function of v for $2 \leq r_s \leq 15$.

The problem of electronic stopping of protons moving with velocities up to about $v_F = 1.9192/r_s$ within a uniform electron gas of metallic density can not be treated adequately by use of the dielectric linear response formalism (i.e., linear screening of the perturbing charge and first-order treatment of the ion-induced electron-gas excitation) [19]. The screening turns out to be nonlinear, that is, the screening potential around the proton depends on the projectile charge and the electron-gas parameters in a mixed manner. The screened scattering potential is a property of the composite proton–electron gas system. A model potential, which accounts reasonably well for the screening of a proton within an electron gas of metallic density, has been proposed by Nagy et al. [22].

We consider a screened proton moving with velocity v in a homogeneous gas of free (i.e. non-interacting) electrons. Since the proton mass M is large compared to the electron mass m , we approximate the center-of-mass frame by the proton’s frame of reference. In the latter the conduction electrons are elastically scattered by the screened proton from occupied states to unoccupied states. In the static case such an elastic scattering is inhibited by the Pauli principle. However, at finite velocities it becomes possible due to the Galilean transformation between the reference frames of metal surface and moving proton, respectively. We assume that this type of electron-gas excitation is the predominant source of stopping here, whereas the excitation of bulk plasmons is expected to be negligible [23].

The total energy-loss rate for a proton moving within a homogeneous free-electron gas is found to be [24]

$$\begin{aligned} \frac{dE}{dt} = & -2 \times 2\pi \sum_{\mathbf{k}} \sum_{\mathbf{k}'} f(\mathbf{k} + \mathbf{v})(1 - f(\mathbf{k}' + \mathbf{v})) \\ & \times v(\mathbf{k}' - \mathbf{k}), |\langle \mathbf{k}' | V | \mathbf{k} + \mathbf{v} \rangle|^2 \delta(E(\mathbf{k}') - E(\mathbf{k})). \end{aligned} \quad (5)$$

$f(\mathbf{k} + \mathbf{v})$ represents the distribution of occupied metal states in the reference frame of the projectile. The matrix element for the electron transition $\mathbf{k} \rightarrow \mathbf{k}'$ depends on the spherically symmetric screened scattering potential $V(r)$ and the scattering state $|\mathbf{k} + \mathbf{v}\rangle$, which tends asymptotically towards a plane wave state $|\mathbf{k}\rangle$ plus an outgoing spherical wave. The energy transfer to a conduction electron in a single binary collision is $v(\mathbf{k}' - \mathbf{k}) > 0$ in the laboratory frame of reference. In the rest frame of the moving proton the electron energy is conserved, that is, $E(\mathbf{k}') = E(\mathbf{k})$. The energy loss rate dE/dt can be converted via $dx = v dt$ into a stopping force $F = dE/dx$ opposite in direction to $\mathbf{v} = v\hat{\mathbf{x}}$. Details on our calculations will be given elsewhere [7]. In general, S_{B} depends on the proton velocity v and, via $V(r)$ and the Fermi energy $E_F = 1.8416/r_s^2$, on the electron-gas density parameter r_s : $S_{\text{B}} = S_{\text{B}}(v, r_s)$. For low velocities ($v < v_F$) a Taylor expansion of the Fermi–Dirac distribution in Eq. (5) yields:

$$S_{\text{B}} = \alpha(r_s)v - \beta(r_s)v^3 + O(v^5). \quad (6)$$

For a constant velocity and a simple trajectory $x(t) = v_{\parallel}t$, $y(t) = v_{\perp}|t|$ the integration of Eq. (1) results in

$$\Delta E = \alpha'E_0 - \beta'E_0^2 + O(E_0^3). \quad (7)$$

In case the energy loss is dominated by binary collisions with conduction electrons, the functional dependence of ΔE on E_0 should follow Eq. (7).

The model potential of Nagy et al. [22] binds two electrons in an atomic-type s-orbital with an energy slightly below the bottom of the conduction band. Slow protons appear as dressed “ H^- ions” within the electron gas in agreement with self-consistent DFT calculations [25]. Note that a transition of bound electrons to continuum states of the electron gas is restricted by the Pauli principle, though the binding energy is rather low. As a consequence efficient stripping of H^- is prevented up to velocities comparable to the average electron velocity in the electron gas, i.e. $\langle v \rangle \approx 0.6v_F$ [25].

At sufficiently large velocities, however, kinematic effects open up phase space for electron loss to the electron gas, e.g., by an Auger-type ionisation process. In fact, H^0 as well as H^+ appear beyond $v \approx 0.5v_0$ in an electron gas with $r_s = 2$ [25]. Each of these species is associated with its own scattering potential and thus its own stopping power function. Weighting these partial stopping power functions S^Q with the corresponding charge state fractions N^Q yields the effective stopping power

$$\langle S_{\text{B}} \rangle = S^- \left[N^- + \frac{S^0}{S^-} N^0 + \frac{S^+}{S^-} N^+ \right] = S^- K. \quad (8)$$

This has been calculated for an uniform electron gas ($r_s = 2$) by Peñalba et al. [25]. Instead of performing similar calculations for $r_s = 2$ to $r_s = 15$, we estimate the function K in a first step for $r_s = 2$ using the charge state distributions given in Ref. [25] and the stopping power

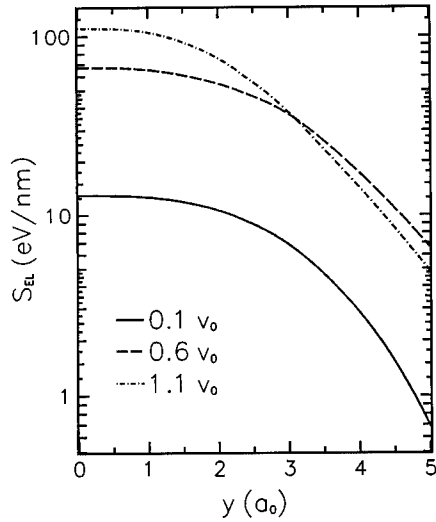


Fig. 4. Position dependent stopping power S_{EL} due to collisions of a proton with the conduction electrons of an Al(111)-surface in dependence on the distance from the topmost atomic layer ($y = 0$) for three projectile velocities.

ratios $S^0/S^- = 1.2$ and $S^+/S^- = 1.6$ from Refs. [3,4] and re-express the v -dependence in terms of the scaled velocity v/v_F , i.e. we assume the r_s -dependence of K enters predominantly via v_F .

This procedure reproduces the velocity dependence of bulk stopping powers for protons in metals up to $v \approx 1.2$ – $1.3 v_F$ quite well [7]. Inserting Eq. (8) into Eq. (4) yields the position-dependent stopping power S_{EL} in the very surface region (Fig. 4). We note that the position- and velocity-dependence of the stopping power does not factorize in general, contrary to what is assumed in Refs. [5,6].

3.3. Trajectory

According to Eq. (1) ΔE results from an integration of $S(v_{\parallel}, y)$ along the trajectory of the projectile. The trajectory of the projectiles is calculated for the planar surface potential and the dynamical image potential. In the numerical calculations we use the continuum surface potential as derived from the Thomas–Fermi–Molière potential

$$V(y) = 2\pi Z_1 Z_2 a_s N \sum_{i=1}^3 \frac{\alpha_i}{\beta_i} \exp\left(-\frac{\beta_i y}{a_s}\right), \quad (9)$$

where $\alpha_i = \{0.1, 0.55, 0.35\}$ and $\beta_i = \{6.0, 1.2, 0.3\}$. N is the planar density of surface atoms and Z_1, Z_2 are the atomic numbers of projectile and target, respectively. The screening parameter a_s is chosen as $0.76 a_{\text{FIRSOV}}$ ($a_{\text{FIRSOV}} = 0.8854 a_0 / (Z_1^{1/2} + Z_2^{1/2})^{2/3}$ is the Firsov screening length) [26]. By this choice of a_s , $V(y)$ becomes almost

identical to the universal potential of Ziegler et al. [27]. The dynamical image potential is calculated from [12,15]:

$$V_{\text{IM}}(y') = -Z^2 \int_0^\infty dQ \exp(-2Qy') \int_{Qv_{\parallel}}^\infty d\omega S(Q, \omega) \times \frac{1}{\sqrt{\omega^2 - (Qv_{\parallel})^2}}, \quad (10)$$

where Z is the charge state of the ion and $S(Q, \omega)$ is the surface loss function of Eq. (2).

The dynamical image force accelerates the ion towards the surface so that it penetrates deeper into the sea of conduction electrons at the surface. Below the image plane at y_{IM} , the charge of the ion is screened and V_{IM} saturates. Since the dynamical image potential affects only charged particles, one has to take into account charge transfer between metal and projectile (resonant tunneling and Auger transfer). Zimny et al. [28] have discussed charge exchange during grazing scattering of protons from an aluminum surface. According to that work the initial and final electron transfer (on the incoming and outgoing trajectory, respectively) takes place within a well-defined interval around an “effective distance” y^* , located about $7a_0$ in front of the topmost layer of target atoms. For distances smaller than y^* the projectiles cannot survive in a fixed charge state and the image interaction is (partially) screened.

At present, calculations of charge state distributions are available only for the bulk [25] and for $y \geq 5a_0$ [28]. For the intermediate region it is not known, how these substantially different distributions transform into each other. To incorporate screening of the image interaction into the calculation of the trajectory, we define a distance y_F ($y_{\text{IM}} \leq y_F \leq y^*$) and consider all particles as ions for $y \geq y_F$ whereas for $y < y_F$ the image force is neglected. The choice of $y_F = y^*$ means perfect screening of the ion in the interval $y_{\text{IM}} \leq y \leq y^*$, whereas for $y_F = y_{\text{IM}}$ neutralisation of the ion is neglected and the ion charge is assumed to be unscreened above the image plane.

In our model for the position-dependent stopping power we distinguish two regions: “vacuum” and “electron selvedge”. Close to the surface we use bulk-like stopping powers, which become y -dependent via the UDA, whereas in the vacuum region a dielectric approach is used. The UDA-concept breaks down about $5a_0$ above the topmost atomic layer, whereas the dielectric approach of Eq. (2) is valid only well above the image plane. The switching between the models thus has to be done in almost the same interval as the switching of the charge state in the calculation of the trajectory. It is then plausible to unite the two “switching distances”, especially since the stopping power of Eq. (2) affects only charged projectiles. The switching distance y_F is, within the bounds $y_{\text{IM}} \leq y_F \leq y^*$, the only adjustable parameter of our model.

4. Discussion

The good fit of the two data sets in Fig. 3 by a function as given in Eq. (7) indicates that protons are predominantly stopped by binary collisions with electrons in the near surface region. In our calculations we find indeed that about 90 to 95% of the total energy loss are due to binary collisions in the electron selvage between y_F and the topmost layer of surface atoms, whereas only 5–10% of ΔE originate from the vacuum region above y_F (cf. Fig. 3).

The results of our calculations are displayed in Figs. 2 and 3. The dependence of the calculated energy loss on y_F is small as can be seen in Fig. 2, where the energy loss of specularly reflected protons with an incident energy of 25.1 keV is displayed as function of the angle of incidence.

The decrease of ΔE with increasing angle of incidence is the result of two counteracting effects: a decrease of the distance of closest approach when Φ_{IN} is raised resulting in a deeper penetration of the proton into the sea of surface electrons (larger stopping) and a decrease of the length of the trajectory (smaller stopping). Here the effect of the shorter trajectory is stronger than the increase of ΔE due to a closer approach to the surface. This compensation, however, depends on the details of trajectory and stopping power function. As an example we show the results of calculations for $y_F = 7a_0$ in Fig. 2. In this case the effect of image charge on the trajectory is small, and at small angles of incidence the increase of ΔE due to a closer approach to the surface plane is stronger than the effect of the shorter trajectory. Then a maximum in the dependence of ΔE on Φ_{IN} is found.

The shape of the dependence of ΔE on E_0 (Fig. 3) is also reproduced well by our model. We neglect here energy loss due to charge exchange which is expected to contribute less than 10% in the velocity range studied here [25].

In summary protons scattered with velocities $v \leq v_0$ from the topmost layer of an Al(111)-surface lose their energy predominantly via binary collisions with conduction electrons in the electron selvage of the surface. Consequently the majority of emitted electrons are excited by this interaction mechanism as well [29].

Acknowledgements

The assistance of H.W. Ortjohann in the preparation of the experiments is gratefully acknowledged. This work is

supported by the Sonderforschungsbereich 216 (Bielefeld/Münster).

References

- [1] K. Kimura, M. Hasegawa and M. Mannami, *Phys. Rev. B* 36 (1987) 7.
- [2] H. Winter, J. Remillieux and J.C. Poizat, *Nucl. Instr. and Meth. B* 48 (1990) 382.
- [3] A. Nürmann, H. Franke, K. Schmidt, A. Arnau and W. Heiland, *Nucl. Instr. and Meth. B* 69 (1992) 158.
- [4] A. Nürmann, K. Schmidt, C. Höfner, W. Heiland and A. Arnau, *Nucl. Instr. and Meth. B* 78 (1993) 72.
- [5] F. Stölzle and R. Pfandzelter, *Europhys. Lett.* 20 (1992) 369.
- [6] R. Pfandzelter and F. Stölzle, *Nucl. Instr. and Meth. B* 72 (1992) 163.
- [7] R. Zimny, M. Wilke and H. Winter, to be published.
- [8] Y.H. Ohtsuki, K. Koyama and Y. Yamamura, *Phys. Rev. B* 20 (1979) 5044.
- [9] F. Stölzle and R. Pfandzelter, *Phys. Lett. A* 150 (1990) 315; *Surf. Sci.* 251/2 (1991) 383.
- [10] H. Winter and M. Sommer, *Phys. Lett. A* 168 (1992) 409.
- [11] H. Winter, *Phys. Rev. A* 46 (1992) R13; *Europhys. Lett.* 18 (1992) 207.
- [12] F. Flores and F. Garcia-Moliner, *J. Phys. C* 12 (1979) 907.
- [13] R. Núñez, P.M. Echenique and R.H. Ritchie, *J. Phys. C* 13 (1980) 4229.
- [14] N.D. Lang and W. Kohn, *Phys. Rev. B* 12 (1970) 4555.
- [15] Z. Penzar and M. Sunjić, *Phys. Scripta* 30 (1984) 431.
- [16] R. Zimny, *Nucl. Instr. and Meth. B* 78 (1993) 153.
- [17] B. Gumhalter, *J. Phys. (Paris)* 38 (1977) 1117.
- [18] P.A. Serena, J.M. Soler and N. Garcia, *Phys. Rev. B* 37 (1988) 8701.
- [19] P.M. Echenique, F. Flores and R.H. Ritchie, *Solid State Phys.* 43 (1990) 229.
- [20] J.K. Nørskov and N.D. Lang, *Phys. Rev. B* 21 (1980) 2131.
- [21] M.J. Stott and E. Zaremba, *Phys. Rev. B* 22 (1980) 1564.
- [22] I. Nagy, A. Arnau, P.M. Echenique and K. Ladányi, *Phys. Rev. A* 43 (1991) 6038; K. Ladányi, I. Nagy and B. Apagyi, *Phys. Rev. A* 45 (1992) 2989.
- [23] J.C. Ashley, *Nucl. Instr. and Meth.* 170 (1980) 197.
- [24] L. Bönig and K. Schönhammer, *Phys. Rev. B* 39 (1989) 7413.
- [25] M. Peñalba, A. Arnau, P.M. Echenique, F. Flores and R.H. Ritchie, *Europhys. Lett.* 19 (1992) 45.
- [26] D.J. O'Connor and J.P. Biersack, *Nucl. Instr. and Meth. B* 15 (1986) 14.
- [27] J.F. Ziegler, J.P. Biersack and U. Littmark, *The Stopping and Range of Ions in Solids*, (Pergamon, New York, 1985).
- [28] R. Zimny, Z.L. Mišćović, N.N. Nedeljković and L.D. Nedeljković, *Surf. Sci.* 255 (1991) 135.
- [29] A. Hegmann, R. Zimny, H.W. Ortjohann, H. Winter and Z.L. Mišćović, *Europhys. Lett.* 26 (1994) 383.



ELSEVIER

Potential and kinetic electron emission from clean gold induced by multicharged nitrogen ions

M. Vana, H. Kurz, HP. Winter, F. Aumayr *

Institut für Allgemeine Physik, Technische Universität Wien, Wiedner Hauptstraße 8–10 / 134, A-1040 Wien, Austria

Abstract

Total electron yields have been determined from electron emission statistics measured for impact of N^{4+} , N^{5+} and N^{6+} under normal incidence on clean polycrystalline gold. The projectile velocities were varied from 2×10^4 m/s, where potential emission (PE) is the exclusive electron emitting mechanism, over the threshold for kinetic emission (KE) at about $(2-3) \times 10^5$ m/s, up to 10^6 m/s, where KE has become the dominant contribution. Separation of the respective PE- and KE contributions led to two remarkable results. (i) Comparison with measurements for inclined ion incidence from Hughes et al. (Phys. Rev. Lett. 71 (1993) 291) suggests that the resulting PE yields not only depend on the given “vertical impact velocity”, presumably due to different conditions for the subsurface part of PE. (ii) The KE yields increase the stronger with impact velocity the lower the primary ion charge, which is explained from a similar projectile charge dependence of the leading electron production mechanism for the KE process.

1. Introduction

The bombardment of solid surfaces, in particular of a clean metal, by multiply charged ions (MCI) causes electron emission due to transfer of (i) potential energy (potential emission/PE), and of (ii) kinetic energy (kinetic emission/KE) from the projectile onto target electrons. PE becomes most important at the lowest possible impact velocities v which, however, cannot become zero because of projectile self-acceleration into the metal target [1–4]. KE can only become significant above a certain impact velocity threshold, which for clean metal surfaces is between 2 and 3×10^5 m/s [5,6]. In recent years, PE induced by slow ($v \ll 1$ a.u.) MCI impact on clean metal surfaces has attracted considerable interest, since the resulting total electron yields γ become quite significant for higher ion charge states (for a recent review cf. Ref. [7]). Two different approaches have been chosen for imposing such low MCI velocities, that studies in the region of exclusive PE may be conducted, i.e. either normal incidence of actually rather slow (≥ 1 eV/amu) MCI (e.g. Refs. [3,4,8–14]), or inclined/grazing incidence of much faster MCI (e.g. Refs. [1,2,15–18]) under the assumption that only the velocity component normal to the target surface (“vertical velocity” v_{\perp}) is of importance for PE. However, this should only be the case if the involved PE processes have already ended before the MCI hit the

surface, since only then the PE yield γ_{PE} clearly depends on the elapsed interaction time and thus of v_{\perp} . From recent work – both theoretical [19,20] and experimental [15,16,21,22] – it has become apparent that a significant fraction of the electrons contributing to PE is being emitted only upon or after surface impact. The second experimental approach has originated from a practical need for sufficiently high MCI currents to conduct the measurements of interest, and calls for monocrystalline samples with rather flat surfaces, whereas for the first approach polycrystalline surfaces are appropriate, as well. With fast, grazing incident MCI the also produced KE has to be subtracted from the measured total electron yields for finding the respective PE yields.

We have compared the total electron yields measured by Hughes et al. [17] for grazing incidence of N^{5+} and N^{6+} ions on a clean Au(011) surface with our corresponding data derived from electron emission statistics (ES) measured for impact of N^{4+} , N^{5+} and N^{6+} ions under normal incidence on a clean polycrystalline gold surface. In these latter measurements, the MCI impact velocities have been varied from 2×10^4 m/s up to 1×10^6 m/s, to cover the exclusive PE regime, the KE threshold region and the range for already dominant KE, respectively.

2. Experimental method and evaluation and presentation of data

Our measurements have been performed with multicharged N^{q+} ions obtained either from a recoil ion source

* Corresponding author, tel. +43 1 58801 5723, Fax +43 1 5864203, E-mail: aumayr@eapv38.tuwien.ac.at

at the GSI UNILAC (projectile velocities $v \leq 2 \times 10^5$ m/s [13]) or from a 5 GHz ECR ion source [23] ($v \leq 10^6$ m/s). After magnetic q/m separation, the selected MCI were shot under normal incidence on the surface of an atomically clean, polycrystalline gold target. The MCI could be decelerated just in front of the target to impact energies as low as $(2 \pm 1)q$ eV. Electrons emitted from the target surface were extracted and accelerated by 25 kV into a surface barrier detector behind the target. The whole experimental setup and the data evaluation procedures applied for determination of the electron emission statistics (ES) – i.e. the probabilities W_n that one projectile causes emission of a number of n electrons – and of the related total electron yields γ as the mean values of these ES have been described in detail elsewhere [4,13,14,24,25]. Fig. 1 shows, for N^{5+} and N^{6+} ions of selected kinetic energies, the resulting ES distributions, from which the corresponding total electron yields γ have been derived by the relations

$$\gamma = \sum_{n=0}^{\infty} n W_n; \quad \sum_{n=0}^{\infty} W_n = 1. \quad (1)$$

Since the probability W_0 for emission of no electron is not directly available from our measurements, one must

either assure that it is negligibly small (in which case Eq. (1) is directly applicable for evaluation of the total electron yield γ), or W_0 can be obtained either from independent measurements of γ [24,25] or by fitting an appropriate statistical distribution to the measured relative emission probabilities for $n \geq 1$. We have applied a linear least squares fit of Polya distributions to our measured relative probabilities with the fitting parameters \bar{n} and b , as given in Eq. (2).

$$W_n(\bar{n}, b) = \frac{\bar{n}^n}{n!} (1 + b\bar{n})^{-\frac{1}{b}} \prod_{i=1}^n (1 + (i-1)b). \quad (2)$$

For $b = 0$, the Polya distribution degenerates into a Poisson distribution (Eq. (2a))

$$W_n(\bar{n}) = \frac{\bar{n}^n}{n!} e^{-\bar{n}}. \quad (2a)$$

The use of Polya distributions to reproduce experimentally obtained ion induced electron emission statistics in the KE region has extensively been discussed, e.g. by Dietz and Sheffield [26]. In Fig. 1 we have shown both the Polya distributions (dashed curves) obtained from fitting to our relative emission probabilities, and the resulting normalized values of the latter (solid barrows), from which

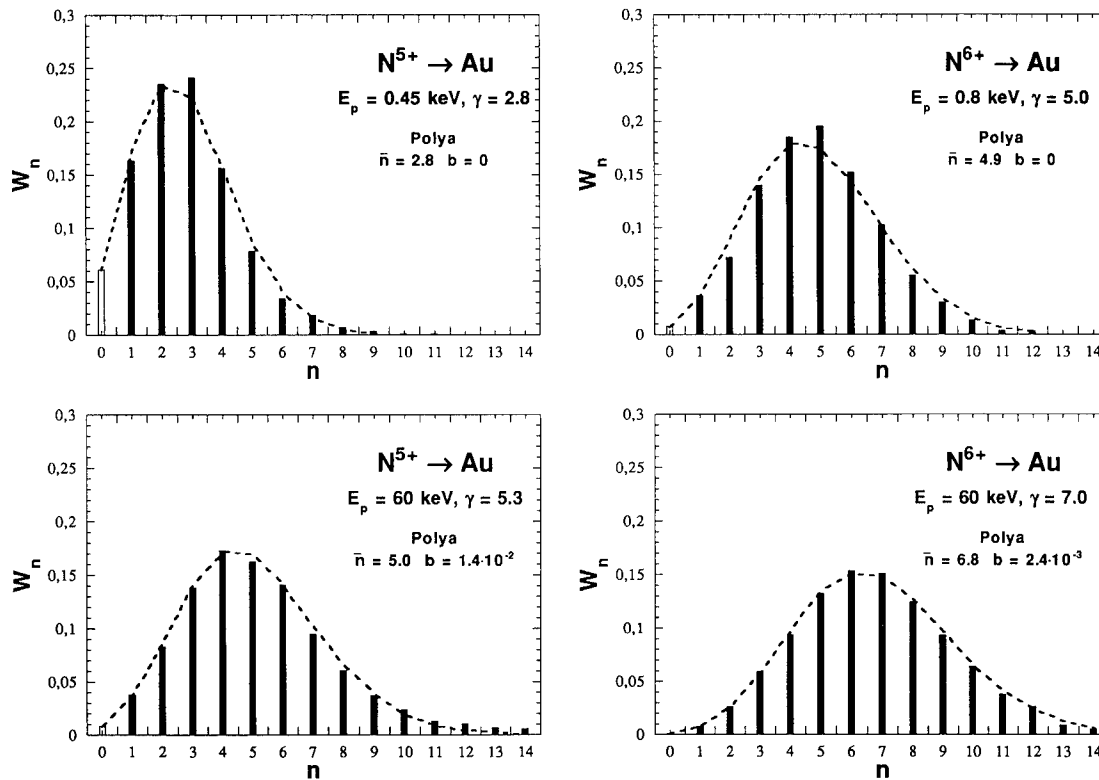


Fig. 1. Electron emission probability distributions for normal incidence of N^{5+} and N^{6+} ions on clean polycrystalline gold at low and high impact velocities, respectively. Dashed curves show Polya distributions fitted to the measured ES with free parameters \bar{n} and b used to obtain the appropriate W_0 data.

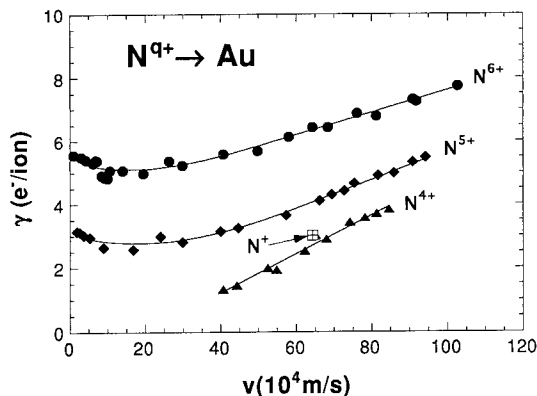


Fig. 2. Total electron yields γ versus projectile velocity ν for normal incidence of N^{4+} (triangles), N^{5+} (diamonds) and N^{6+} (circles) on clean polycrystalline gold (data for $\nu \leq 2 \times 10^5$ m/s agree with measurements of Ref. [13]). The single data point labelled " N^+ " is from Ref. [5].

the actual γ values to be discussed further have been evaluated. We note that in the low impact energy regime the ES are rather closely resembled by Poissonians, whereas at high impact energies the Polya character of the corresponding ES becomes clearly apparent. These results are in full agreement with the arguments put forward in Ref. [26]. We further remark that for high impact energies the fits of our measured relative emission probabilities to the respective Polya distributions become almost perfect.

For cases where the probability W_0 for emission of no electrons is negligibly small, total electron yields γ can be directly evaluated via Eq. (1) from the measured ES, and in such cases are accurate within typically $\pm 4\%$ [4,13]. If, however, W_0 has to be obtained by a fitting process as described above, the resulting γ values will be less accurate, with the involved errors to be estimated from a comparison of the mean value \bar{n} of the respective Polya fit with the actual value of γ as determined from the normalized ES.

In Fig. 2 total electron yields γ for impact of N^{4+} (triangles), N^{5+} (diamonds) and N^{6+} (circles) have been plotted as a function of the projectile velocity ν . For N^{4+} at low impact velocity ($\nu \leq 4 \times 10^5$ m/s) the total yield γ was found to be much smaller ($\gamma \approx 0.8$) than measured for impact on clean W by Fehring et al. [11], whereas for N^{5+} as well as N^{6+} the total yields are of comparable size for both target species. Since in the case of N^{4+} the probability W_0 is significant, our determination of γ from the measured ES was subject to a rather large uncertainty, and the respective results should be reconfirmed by other, independent measurements. However, from our measurements and simulations [4,13] we are quite safe to assume that towards higher impact velocities ($\nu > 3 \times 10^5$ m/s) γ_{PE} remains practically constant.

The single data point labelled by " N^+ " was taken

from Ref. [5], and applies – as in our case – to normal incidence on clean polycrystalline gold. Earlier comparisons of absolute γ data measured by means of our statistical technique with similar data from Baragiola's group showed generally full agreement within the combined experimental errors (cf. Refs. [27,28]). The obtained velocity dependence of γ can be reproduced rather well by a sum (solid lines) of two mutually independent functions γ_{PE} and γ_{KE} , ascribed to two contributions to the total yield by PE (first two terms, cf. Refs. [4,13]) and KE (last term, formulated by assuming a linear dependence of γ_{KE} on MCI impact velocity ν , and a stepfunction Θ starting at the KE threshold velocity ν_{th}), respectively.

$$\gamma(\nu) = \gamma_{PE} + \gamma_{KE} = \frac{c_1}{\sqrt{\nu}} + \gamma_\infty + k(\nu - \nu_{th})\Theta(\nu - \nu_{th}). \quad (3)$$

ν_{th} should be of the order of the "classical" KE threshold velocity as obtained by Baragiola et al. [5] for kinetic energy transfer from the projectile ions onto free electrons in the solid ($\nu_{th} \approx 2.5 \times 10^5$ m/s \triangleq 315 eV/amu for Au). However, Alonso et al. [28] have shown that KE can extend well below this classical threshold velocity, which was also found by Lakits et al. [27] and explained by (generally small) contributions from quasimolecular autoionization due to electron promotion ("Pauli excitation") in close encounters between the projectiles and the target ion cores. Anyhow, subtraction of γ_{PE} as evaluated from a fit according to Eq. (3) to the γ data shown in the low impact energy region of Fig. 2, delivered the KE contributions γ_{KE} to the total electron yields, which then have been plotted versus projectile velocity in Fig. 3.

The " N^+ " value from Ref. [5] has been added without change, taking into account the comparably small recombination energy of 14.5 eV for N^+ . Accordingly, the possibly involved PE yield cannot become larger than a few

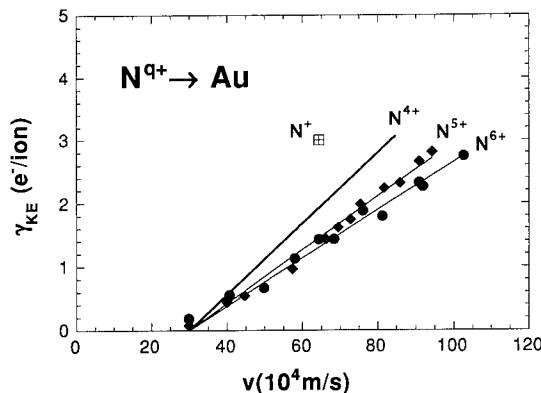


Fig. 3. γ_{KE} , the contributions by kinetic emission to the total electron yields γ , as derived from data in Fig. 2 by procedures described in text.

percent [27] and thus remains negligible. The solid lines in Fig. 3 are linear least-squares fits to the data points; their intersection with the abscissa corresponds rather well with the above given “classical” KE threshold velocity. Fig. 3 reveals at once the interesting observation, that KE induced by fast N^{q+} ions of given impact velocity becomes less efficient with higher charge state q . This remarkable result will be shortly discussed later on, with a more detailed treatment of its implications to be given elsewhere.

3. Discussion

For comparison of our data presented in Fig. 2 with measurements performed by Hughes et al. [17] for N^{5+} and N^{6+} ions impinging under $\phi = 20^\circ$ (i.e. 70° from the surface normal) on a clean Au(011) surface, in the latter case one first has to consider the involved KE, which is significantly increased due to the small incidence angle applied. Hughes et al. [17] have actually assumed that for impact of N^{5+} and N^{6+} at the same impact geometry and velocity, the respective KE yields are the same, and therefore the difference of the respective total yields is exclusively caused by different values for γ_{PE} . According to Hasselkamp ([6] and references therein), ion induced KE yields are roughly proportional to the length of the projectile's trajectory in closer vicinity to the surface than the escape depth of the low energy electrons produced inside the solid, i.e. $\gamma_{KE}(\phi) \approx \gamma_{KE}(90^\circ)/\sin \phi$. Note that Hughes et al. [17] chose an azimuthal angle of 6° to the (100) direction, to avoid possible effects from projectile channelling. Therefore, their results remain comparable to the measurements presented in this work, where a polycrystalline surface was used. Assuming that γ_{PE} , the PE related contribution to the total yield, depends only on the normal component v_\perp of the projectile's total velocity v , one can use Eq. (3) to estimate the total electron yields for inclined ion incidence, if the parameters c_1 , γ_∞ , v_{th} and k have already been determined for normal incidence. We simply insert the perpendicular velocity $v_\perp = v \sin \phi$ into the expression for γ_{PE} , multiply γ_{KE} by $1/\sin \phi$, and obtain

$$\gamma(v, \phi) = \gamma_{PE}(v \sin \phi) + \gamma_{KE}(v)/\sin \phi. \quad (4)$$

A prediction for impact of N^{5+} and N^{6+} at $\phi = 20^\circ$ as extrapolated according to Eq. (4) from our data for normal incidence, has been shown in Fig. 4 (strong lines), together with the total electron yields actually measured by Hughes et al. [17] (full symbols). Both sets of data have been plotted as a function of the respective perpendicular projectile velocity v_\perp . As can be seen clearly, the yields measured for 20° incidence are by about a factor of 1.5 larger than the ones estimated by means of Eq. (4) from our measurements under 90° incidence.

From the apparent discrepancy between the measurements by Hughes et al. [17] and the extrapolations from

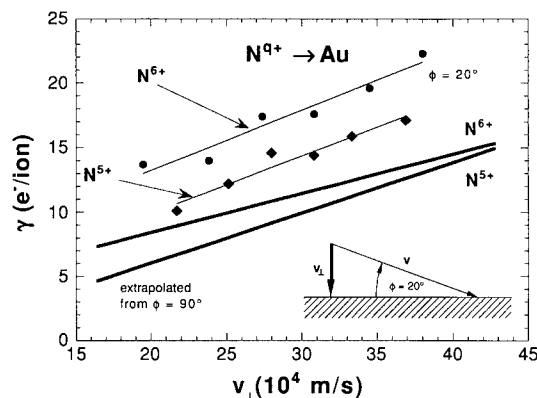


Fig. 4. Total electron yields γ versus “vertical projectile velocity” v_\perp as measured by Hughes et al. [17] for impact of N^{5+} (diamonds) and N^{6+} (circles) on clean Au(011) under an ion incidence angle of 20° . Strong full lines give extrapolations for corresponding yields as derived according to Eq. (4) from data of this work which have been measured under normal incidence at equal “vertical impact velocities”.

our measurements (strong lines in Fig. 4) to their experimental geometry, we are led to the conclusion that at least one of our assumptions underlying the extrapolation, namely:

(i) $\gamma_{KE} \propto 1/\sin \phi$, and

(ii) γ_{PE} only dependent on the impact velocity component normal to the surface,

has to be inappropriate. Because the angular dependence of γ_{KE} is well established from many experimental studies [6], it is probably the first term in Eq. (4) connected with our assumption on γ_{PE} , that has to be adapted.

If one takes into account that a non-negligible fraction of the PE related electron emission takes place below the surface [17], a similar argument as for the increase of γ_{KE} with decreasing angle of incidence should also apply for the below-surface fraction of γ_{PE} . Even if we assume, that about one half of γ_{PE} actually originates below the surface and thus becomes subject to an angular dependence similar as for γ_{KE} , we end up with extrapolated values still deviating considerably from the data of Hughes et al. [17]. The discrepancy between the impact velocity dependences of our extrapolated γ versus v_\perp characteristics and the (parallel) course of the γ data for N^{6+} and N^{5+} from Ref. [17] can probably be explained by an ion charge state dependence of γ_{KE} , which thus has been demonstrated for the first time in the present work. Such a q -dependence has to result from the electron production processes responsible for KE inside the target bulk, and thus points to an important contribution to KE by the promotion mechanism as already described in Section 2, since only this process can become less efficient for electron production with higher initial projectile charge state q .

4. Conclusion

Accurate measurements of multicharged ion induced electron emission from a clean Au surface over a wide range of impact velocities, and the here applied procedure to separate the respective contributions of PE and KE according to their genuine impact velocity dependences, for the first time permitted an isolation of exclusive KE yields in the presence of PE yields of comparable size. With this important achievement, a direct comparison between measurements carried out for ion beams incident under different angles to the target surface has become feasible. Apparent discrepancies among different sets of data may partially result from the fact that collision systems involving different angles of incidence but equal “vertical impact velocities” are actually not identical with respect to the conditions given for PE. Rather, we found clear evidence that one has not only to correct for the dependence of KE on the angle of incidence, when comparing measurements carried out in different impact geometries. Since a significant fraction of the PE is only produced after the projectile has penetrated the surface, we have discarded the (often implicitly assumed) concept that the PE related part of MCI induced electron emission is only dependent on the projectile’s velocity component normal to the surface. To compare results from studies of PE processes induced by highly charged ions on solid surfaces under different angles of incidence, it is obviously not sufficient to regard the perpendicular component of the projectile velocity, but one also has to take into account the details of MCI neutralization dynamics resulting in electron production below the surface. On the other hand, accurate studies of electron emission with projectiles of given perpendicular impact velocity, but different absolute velocities promise further insight into the electron emission processes involved, as to the ratio of above/below surface PE and to the region below the surface where the corresponding PE processes actually takes place.

Finally, the present work has provided evidence that kinetic electron emission yields induced by impact of multicharged nitrogen ions on clean gold, at a given impact velocity and geometry, also depend on the initial ion charge state q , i.e. the KE yields decrease with increasing q . This very interesting result can be explained by assuming that an important fraction of the KE is produced in close collisions between projectiles and target ion cores via the so-called Pauli excitation mechanism.

Acknowledgements

The authors thank Mr. C.O. Lemell who has performed helpful simulations of ion–surface interactions and electron transport in solids. This work has been supported by Austrian Fonds zur Förderung der wissenschaftlichen Forschung and by Kommission zur Koordination der Kernsionsforschung at the Austrian Academy of Sciences.

References

- [1] H. Winter, *Europhys. Lett.* 18 (1992) 207.
- [2] H. Winter, C. Auth, R. Schuch and E. Beebe, *Phys. Rev. Lett.* 71 (1993) 1939.
- [3] F. Aumayr, H. Kurz, D. Schneider, M.A. Briere, J.W. McDonald, C.E. Cunningham and HP. Winter, *Phys. Rev. Lett.* 71 (1993) 1943.
- [4] H. Kurz, F. Aumayr, D. Schneider, M.A. Briere, J.W. McDonald and HP. Winter, *Phys. Rev. A* 49 (1994) 4693.
- [5] R.A. Baragiola, E.V. Alonso, J. Ferrón and A. Oliva-Florio, *Surf.Sci.* 90 (1979) 240.
- [6] D. Hasselkamp, in: *Particle Induced Electron Emission II*, G. Höhler, ed. (Springer, Heidelberg, 1992) p. 1.
- [7] F. Aumayr, and HP. Winter, *Comm. At. Mol. Phys.* 29 (1994) 275.
- [8] H.D. Hagstrum, *Phys. Rev.* 96 (1954) 325.
- [9] U.A. Arifov, L.M. Kishinevskii, E.S. Mukhamadiev and E.S. Parilis, *Sov. Phys. Tech. Phys.* 18 (1973) 118.
- [10] M. Delaunay, M. Fehring, R. Geller, D. Hitz, P. Varga and HP. Winter, *Phys. Rev. B* 35 (1987) 4232.
- [11] M. Fehring, M. Delaunay, R. Geller, P. Varga and HP. Winter, *Nucl. Instr. and Meth. B* 23 (1987) 245.
- [12] H. Kurz, K. Töglhofer, HP. Winter, F. Aumayr and R. Mann, *Phys. Rev. Lett.* 69 (1992) 1140.
- [13] H. Kurz, F. Aumayr, C. Lemell, K. Töglhofer and HP. Winter, *Phys. Rev. A* 48 (1993) 2182.
- [14] H. Kurz, F. Aumayr, C. Lemell, K. Töglhofer, and HP. Winter, *Phys. Rev. A* 48 (1993) 2192.
- [15] F.W. Meyer, S.H. Overbury, C.C. Havener, P.A. Zeijlmans van Emmichoven, J. Burgdörfer and D.M. Zehner, *Phys. Rev. A* 44 (1991) 7214.
- [16] P.A. Zeijlmans van Emmichoven, C.C. Havener and F.W. Meyer, *Phys. Rev. A* 43 (1991) 1405.
- [17] I.G. Hughes, J. Burgdörfer, L. Folkerts, C.C. Havener, S.H. Overbury, M.T. Robinson, D.M. Zehner, P.A. Zeijlmans van Emmichoven and F.W. Meyer, *Phys. Rev. Lett.* 71 (1993) 291.
- [18] R. Morgenstern and J. Das, *Physica Scripta* T46 (1993) 231.
- [19] J. Burgdörfer, P. Lerner and F.W. Meyer, *Phys. Rev. A* 44 (1991) 5674.
- [20] J. Burgdörfer, in: *Fundamental Processes and Applications of Atoms and Ions*, ed. C.D. Lin (World Scientific, 1993).
- [21] J. Das, L. Folkerts and R. Morgenstern, *Phys. Rev. A* 45 (1993) 4669.
- [22] S. Schippers, S. Hustedt, W. Heiland, R. Köhrbrück, J. Bleck-Neuhaus, J. Kemmler, D. Lecler and N. Stolterfoht, *Nucl. Instr. and Meth. B* 78 (1993) 106.
- [23] M. Leitner, D. Wutte, J. Brandstötter, F. Aumayr and HP. Winter, *Rev. Sci. Instr.* 65 (1994) 1091.
- [24] G. Lakits, F. Aumayr and HP. Winter, *Rev. Sci. Instr.* 60 (1989) 3151.
- [25] F. Aumayr, G. Lakits and HP. Winter, *Appl. Surf. Sci.* 47 (1991) 139.
- [26] L.A. Dietz and J.C. Sheffield, *J. Appl. Phys.* 46 (1975) 4361.
- [27] G. Lakits, F. Aumayr, M. Heim and HP. Winter, *Phys. Rev. A* 42 (1990) 5780.
- [28] E.V. Alonso, M.A. Alurralde and R.A. Baragiola, *Surf. Sci.* 166 (1986) L155.



ELSEVIER

TPD and ESD of hydrogen from disilane covered Si(100)

J. Lozano, J.H. Craig Jr. *, J.H. Campbell, M.V. Ascherl

Department of Physics, University of Texas at El Paso, 500 W. University Ave., El Paso, TX 79968-0515, USA

Abstract

Disilane covered Si(100) was investigated using temperature programmed desorption (TPD) and electron stimulated desorption (ESD) for various disilane exposures. At low coverages, only monohydride species are observed on the surface as seen by TPD. At high coverages, dihydride species appear. Kinetic energy distributions (KEDs) for H^+ and H^- were also obtained from Si(100) covered with varying amounts of disilane. Both H^+ and H^- KEDs exhibited two peaks each, suggesting that there are at least two types of hydrogen bound states on the surface. ESD decay curves were also obtained and exhibited double exponential decay behavior. ESD total cross sections were calculated using H^+ and H^- signal decays and compared with related data from the literature.

1. Introduction

The adsorption of disilane on silicon has recently generated considerable interest since this system constitutes one possible route to attainment of atomic layer epitaxy on silicon [1–3]. In addition to an appropriate choice of a molecular precursor, it is also necessary to employ a low thermal budget during processing. Selective desorption of ligands by low energy electrons is one possible route to remove hydrogen during wafer processing. The results presented below constitute an initial attempt to study the electron desorption characteristics of hydrogen from a disilane ad-layer on silicon.

2. Experimental

The UHV system used in these studies had a base pressure of 5×10^{-10} Torr. The chamber was equipped with a single pass cylindrical mirror analyzer for Auger electron spectroscopy (AES); a Kimball Physics low energy electron gun and a Bessel box energy analyzer [4] for electron stimulated desorption (ESD); an Argon ion gun for secondary ion mass spectroscopy (SIMS); a quadrupole mass spectrometer for residual gas analysis and temperature programmed desorption (TPD); and a gas dosing tube.

Boron p-doped Si(100) wafers, 3 cm \times 1 cm, were obtained from the Science and Technology Center at University of Texas at Austin. The samples were mounted on a sample holder described elsewhere [5]. The samples were

resistively heated at a typical rate of 3 K/s for TPD and cooled by contact with a liquid nitrogen reservoir. A base temperature of 130 K was achieved. A chromel–alumel (type K) thermocouple was pressed against the back of the sample to monitor the temperature. The thermal desorption temperatures of hydrogen published by Yates et al. [6] were used as a standard to calibrate the TPD spectra presented below. Each sample was originally annealed to 1100 K for 5 min to remove the native protective oxide layer and residual carbon. Cleanliness was confirmed by AES. During dosing, the samples were placed in front of the dosing tube, about 1 cm away from the tube aperture. For purposes of reproducibility, the sample dose is reported in terms of Langmuir, although the actual dose is estimated to be a factor of 25 larger than the indicated value. Based on the area under the TPD curves, saturation of the surface occurs at approximately 0.21 L.

To calculate total cross sections from ESD decay curves, a Faraday cup was used to obtain an electron beam profile. The measured electron beam had a Gaussian profile given by

$$J(r) = J_0 e^{-r^2/a^2}, \quad (1)$$

where $J_0 = 6.03 \times 10^{-5}$ A/cm² for H^- and $J_0 = 3.82 \times 10^{-5}$ A/cm² for H^+ at 150 eV and $a = 0.72$ cm.

3. Results and discussion

Fig. 1 shows the H_2 TPD spectra for various exposures of Si(100) to disilane. At low exposures (< 0.026 L), a single peak (β_1) appears at 800 K, and saturates at 0.21 L. At 0.026 L, a second peak (β_2) develops at 700 K and saturates at 0.42 L. In studies of desorption of hydrogen

* Corresponding author, tel. +1 915 747 5715, fax +1 915 747 5447.

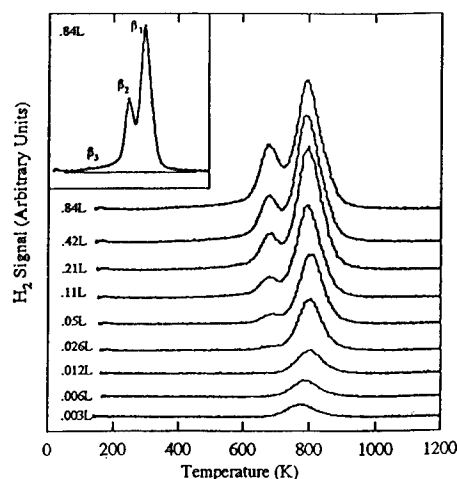


Fig. 1. H_2 TPD spectra from Si(100) for varying exposures of disilane. The monohydride peak (β_1), dihydride peak (β_2), and the trihydride peak (β_3) are shown in the inset. The dosing temperature was 130 K.

from Si(100), several authors [6,7] have associated the β_1 and β_2 peaks with the mono- and di-hydride species, respectively. The presence of monohydride (β_1) and dihydride (β_2) species on the surface is confirmed by the presence of peaks at 29 and 30 amu in the SIMS spectrum shown in Fig. 2. The SIMS spectrum also shows a small signal at mass 31 that may correspond to a trihydride species. This species is only observed in the TPD spectra at the highest coverages as a low temperature shoulder on the β_2 peak, as shown in the inset in Fig. 1. This result agrees well with the previously reported experiments for hydrogen on Si(100) by Yates and Cheng [7].

H^- and H^+ ESD kinetic energy distributions (KEDs) were obtained from disilane covered Si(100) at 130 K. The

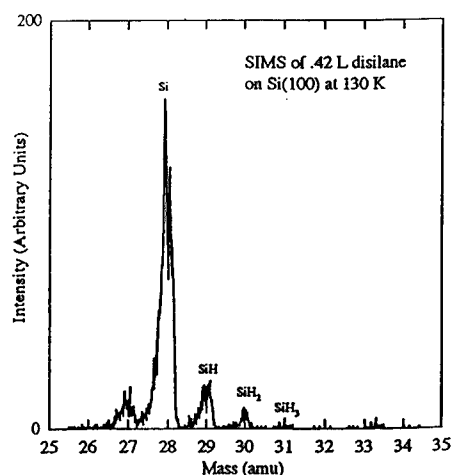


Fig. 2. SIMS spectrum of 0.42 L disilane on Si(100) showing the presence of monohydride (SiH), dihydride (SiH_2), and trihydride (SiH_3) species on the surface. The spectrum was taken at 130 K.

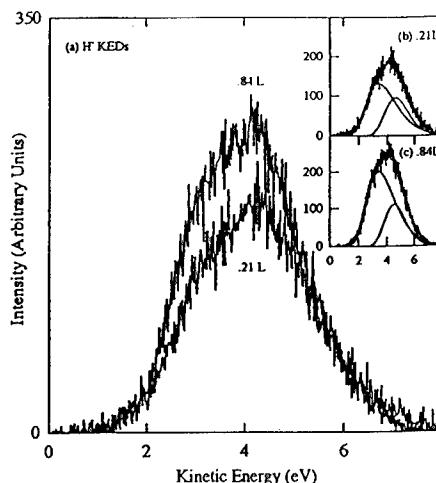


Fig. 3. H^- ESD kinetic energy distributions for (a) 0.21 and 0.84 L disilane doses on Si(100). Plots (b) and (c) show the component peaks necessary to fit the kinetic energy distributions for the two curves in (a). The low energy peak increases more rapidly than the high energy peak as a function of exposure.

distributions were least squares fit, using the model proposed by Nishijima and Propst [8], in order to study the KED behavior at different hydrogen exposures. A similar analysis has been carried out by Ascherl et al. [9] and Campbell et al. [5] for trimethylsilane on Si(100). Fig. 3 shows H^- ESD KEDs for exposures of 0.21 L and 0.84 L. Both KEDs were best fit with two curves, one centered at 3.3 ± 0.2 eV and the other one at 4.5 ± 0.2 eV, as shown in Figs. 3b and 3c. The intensity of the low energy peak increases relative to the high energy peak with increasing exposure. H^+ ESD KEDs are shown in Fig. 4. These KEDs are also bimodal, with the computed curves centered at 2.7 ± 0.2 eV and 4.3 ± 0.2 eV, as shown in Figs. 4b and 4c. Again, we observe that the low energy peak increases relative to the high energy peak as the exposure is increased. Comparison of the ESD KEDs with our TPDs lead us to propose that the high energy KED peaks correspond to the monohydride species, since this species saturates at 0.21 L. Similarly, the increase in the low energy KED peaks from 0.21 L to 0.84 L indicate that these ESD peaks correspond to dihydride species. Similar bimodal behavior has been observed previously [10–12] for ESD KEDs from hydrogen terminated Si(100) surfaces.

In order to measure the total cross section for hydrogen removal, H^- and H^+ decay curves were obtained for exposures of 0.21 L and 0.84 L. Since the measured quantity in this case is the ion current, the equation to model the data had the form

$$I_{\text{ion}} = I_{\text{background}} + \alpha \left[\frac{1 - e^{-\beta t}}{\beta t} \right]. \quad (2)$$

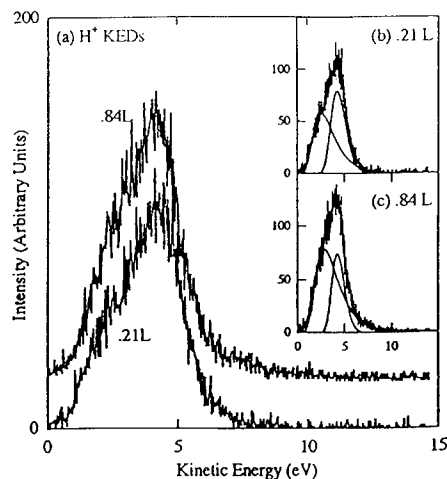


Fig. 4. H⁺ ESD kinetic energy distributions for (a) 0.21 and 0.84 L disilane doses on Si(100). Plots (b) and (c) show the component peaks necessary to fit the kinetic energy distributions for the two curves in (a). The low energy peak increases more rapidly than the high energy peak as a function of exposure.

This equation was derived taking into account the measured Gaussian electron beam profile [13,14] and assuming first order desorption kinetics. The total cross section was assumed to be independent of coverage.

The fitted data for H⁻ and H⁺ ESD decays are shown in Fig. 5. In both cases, the fit required two exponentials.

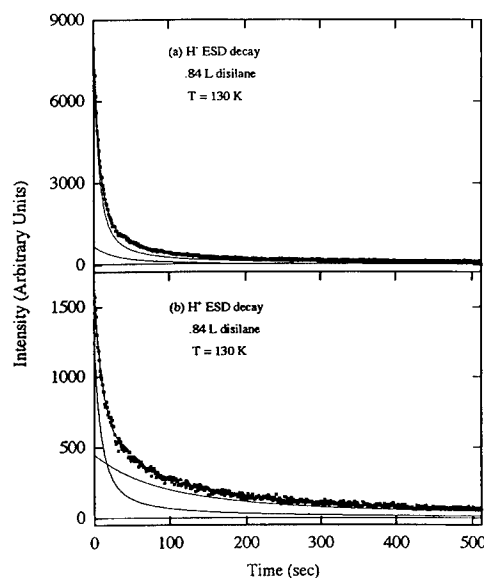


Fig. 5. ESD decay curves for (a) H⁻ and (b) H⁺ for 0.84 L disilane dose on Si(100) at 130 K. Each decay curve required a double exponential fit (Eq. (2)). The decay constants are respectively for H⁻, 0.059 s⁻¹ and 0.282 s⁻¹, and for H⁺, 0.019 s⁻¹ and 0.182 s⁻¹.

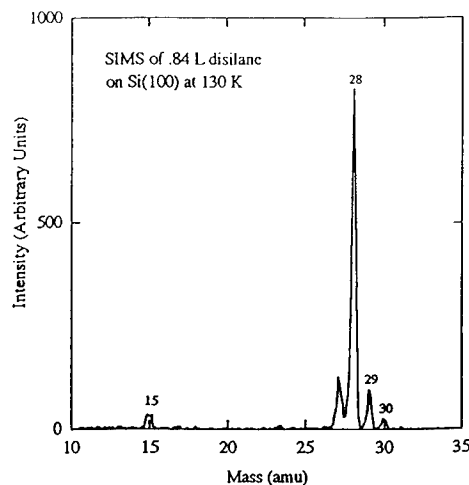


Fig. 6. SIMS spectrum for 0.84 L disilane dose on Si(100) at 130 K for a carbon contaminated sample.

The rates of decay were obtained from these curves. The rate of decay is related to the total cross section by

$$Q = \beta \frac{e}{J_0}, \quad (3)$$

where J_0 is the maximum electron beam current density in A/cm². Using the measured current density, the total cross sections can be readily calculated:

$$Q = (2.65 \times 10^{-15}) \beta, \quad \text{for H}^-, \quad (4)$$

$$Q = (4.18 \times 10^{-15}) \beta, \quad \text{for H}^+. \quad (5)$$

The total cross sections for both the H⁻ and H⁺ ESD decay curves were $(1.5 \pm 0.3) \times 10^{-16}$ cm² and $(7.5 \pm$

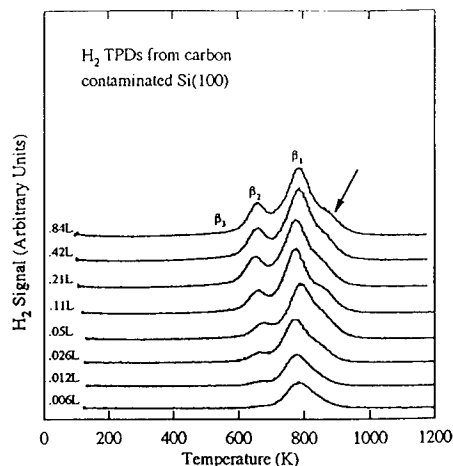


Fig. 7. H₂ TPD for various disilane doses on carbon contaminated Si(100). The adsorption temperature was 130 K. The arrow indicates the new feature which develops as a result of carbon contamination.

$0.3) \times 10^{-16} \text{ cm}^2$. As the coverage increased, the higher cross section component contribution increases more rapidly than the lower cross section component. Thus, the high cross section component appears to be associated with the low energy H^- and H^+ KED peaks. Making this association suggests that the total cross section for desorption of the dihydride species is considerably larger than that for the monohydride species.

It was observed that electron beam processing leads to the deposition of small amounts of carbon on the silicon surface, possibly from the dissociation of residual CO deposited on the surface. A SIMS scan shows the presence of methyl groups at 15 amu (Fig. 6). Surface carbon concentration for the same sample as measured from Auger spectra is estimated at 7%. TPD spectra from a carbon contaminated surface exhibit development of a shoulder on the high temperature side of the monohydride peak, as shown in Fig. 7. The onset of development of this shoulder is at 0.26 L, while saturation occurs at 0.42 L. The strong correlation between the presence of carbon on the silicon surface and the development of a new feature in the TPD spectra strongly suggests the presence of a new hydrogen state, which is apparently associated with a C–H bond.

4. Summary

Our TPD and SIMS data show the presence of monohydride, dihydride, and trihydride species on the disilane dosed Si(100) surface. The ESD KEDs showed bimodal behavior for both the H^- and the H^+ ions. We propose that the low energy ESD KED peaks correspond to the dihydride species, while the high energy ESD KED peaks correspond to the monohydride species. Similarly, both the H^- and H^+ ESD decay curves were best fit with two exponential curves from which the total cross sections were obtained. Our results show that the total cross section for the dihydride species is approximately a factor of 5 higher than that of the monohydride species. It was observed that carbon contamination on the surface was re-

sponsible for the development of a shoulder on the high temperature side of the monohydride peak.

Acknowledgements

This work was supported in part by the Science and Technology Center Program of the National Science Foundation, Grant no. CHE8920120. The authors wish also to acknowledge the support received from the Materials Research Center of Excellence at U.T. El Paso.

References

- [1] S. Asami, N.M. Russell, A. Mahajan, P.A. Steiner IV, D.J. Bonser, J. Fretwell, S. Banerjee, A. Tasch, J.M. White and J.G. Ekerdt, 3rd. Int. Symp. on Atomic Layer Epitaxy and Related Surface Processes, Sendai, Japan, 1994, to be published in *Appl. Surf. Sci.*
- [2] Y. Suda, D. Lubben, T. Motooka and J.E. Greene, *J. Vac. Sci. Techn. B* 7 (1989) 1171.
- [3] D. Lubben, R. Tsu, T.R. Bramblett and J.E. Greene, *J. Vac. Sci. Techn. A* 9 (1991) 3003.
- [4] J.H. Craig Jr. and W.G. Durrer, *J. Vac. Sci. Techn. A* 7 (1989) 3337.
- [5] J.H. Campbell, M.V. Ascherl, and J.H. Craig Jr., *J. Vac. Sci. Techn. A* 12 (1994) 2128.
- [6] K. Sinniah, M.G. Sherman, L.B. Lewis, W.H. Weinberg, J.T. Yates Jr. and K.C. Janda, *J. Chem. Phys.* 92 (1990) 5700.
- [7] C.C. Cheng and J.T. Yates Jr., *Phys. Rev. B* 43 (1991) 4041.
- [8] M. Nishijima and F.M. Propst, *Phys. Rev. B* 2 (1970) 2368.
- [9] M.V. Ascherl, J.H. Campbell, and J.H. Craig Jr., *Appl. Surf. Sci.* 74 (1994) 121.
- [10] J.H. Craig Jr., C. Cariss and M.J. Craig, *J. Vac. Sci. Techn. A* 11 (1993) 554.
- [11] K. Ueda, S. Kodama and A. Takano, *Appl. Surf. Sci.* 60/61 (1992) 178.
- [12] K. Ueda, S. Kodama and A. Takano, *Appl. Surf. Sci.* 283 (1993) 195.
- [13] J.C. Lin and R. Gomer, *Surf. Sci.* 172 (1986) 183.
- [14] B. Xia and S.C. Fain Jr., *Phys. Rev. B* 50 (1994) 14565.



ELSEVIER

Growth of ultrathin alumina films on W(110)

J. Günster, M. Brause, Th. Mayer, A. Hitzke, V. Kempter *

Physikalisches Institut der Technischen Universität Clausthal, Leibnizstr. 4, D-38 678 Clausthal-Zellerfeld, Germany

Abstract

The interaction of oxygen with Al(111) and Al adlayers (< 2.5 adlayers thickness) on W(110) is studied using metastable impact electron spectroscopy (MIES) and photoelectron spectroscopy (UPS). The coadsorption of Al and oxygen at a hot (725 K) W(110) surface is studied with the same techniques. Information on the electronic properties of the surfaces obtained in this way is linked to their structural properties via LEED measurements. It is concluded that alumina layers with excellent thermal and chemical properties can be produced by a coadsorption while the surface produced by oxygen sorption on the Al/W(110) surface requires an additional heat treatment to become transformed into alumina.

1. Introduction

Thin film forms of aluminium oxides have found widespread application due to their superior mechanical, chemical and electrical properties. For example,

- Alumina thin film coatings are used for wear and corrosion resistance, in particular at high temperatures,
- Planar alumina thin films are used as support for metal particles in model catalyst studies,
- Solid-state catalysis by oxide materials is performed with oxide materials whose structural and electronic properties are affected by the substrate used to support the oxide layer.

As pointed out in Ref. [1] fundamental questions, in particular concerning the nucleation, the growth and the epitaxy of alumina (as well as of other oxides such as MgO) remain. The structural properties of ultrathin alumina layers grown on Ta(110) were studied in detail by LEED [1]. But no correlation to the electronic structure of the produced layers could be made. The present paper is a continuation of our earlier work dealing with the oxygenation and the preparation of ultrathin alumina layers on W(110) [2]; by combining the techniques of MIES and UPS with LEED we are able to link the structural and the electronic properties of the adlayers.

Metastable impact electron spectroscopy (MIES), i.e. the analysis of the electron energy spectra induced by the interaction of thermal metastable He^* atoms with surfaces, combined with photoelectron spectroscopy (UPS), has become a powerful tool for the study of the electronic structure of adsorbates, in particular oxygen on surfaces

[3,4,6,7]. It is now also possible to simulate the MIES spectra once the electronic structure of the surface top layer can be modeled [5,8].

The same interaction processes form the basis of ion impact electron spectroscopy (IIES) (see Ref. [8] for a review) where the electron emission is induced by slow grazing ion collisions with surfaces. We have shown however [9–11] that MIES is superior to IIES for studying insulating adlayers because

- the existence of a band gap prevents the tunneling of the 2s electron of the metastable He^* into the solid. In consequence, Auger de-excitation of the projectile will occur in front of the surface producing narrow structures in the electron energy spectra, similar to those seen in UPS (but with absolute surface sensitivity). On the other hand, approaching ions, as used in IIES, will suffer Auger capture which leads to broad structures which are more difficult to interpret.
- MIES is a “softer” technique because at thermal projectile energies there is no penetration of the projectile into the surface nor is there any kinetic electron emission (induced by the motion of the projectile).

In this study we apply MIES combined with UPS, supplemented by the standard techniques XPS and LEED, to the study of the epitaxial growth of alumina on W(110). The focus of this paper is on the change of the electronic structure during layer growth and on the electronic structure of the alumina adlayer.

2. Experimental details

The apparatus has been described previously [10–13]. Briefly, a cold cathode He gas discharge serves both as source for an intense He metastable beam (for MIES) and as HeI photon source (for UPS). The incidence angle of

* Corresponding author, tel. +49 5323 72 2363, Fax +49 5323 72 3600, E-mail: kempter@physik.tu-clausthal.de.

metastables and photons is 45° with respect to the surface. The ejected electron energy spectra are recorded normal to the surface. The time required to collect a complete spectrum is 1 min for MIES, and 2 min for UPS. The energy scales in the figures are adjusted in such a way that

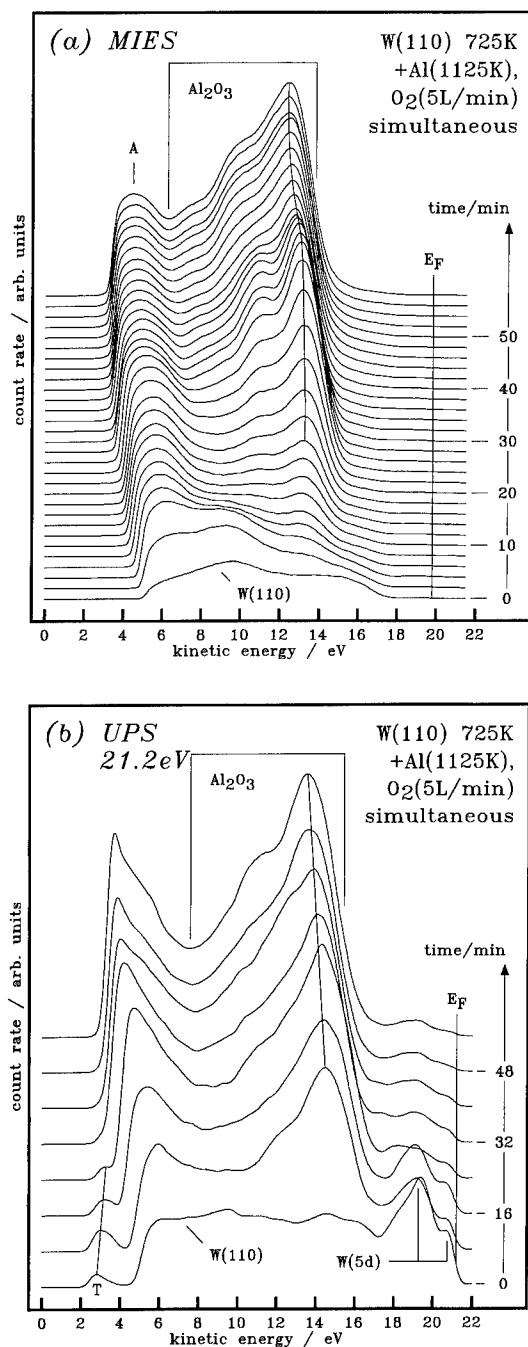


Fig. 1. MIES (a) and UPS (b) spectra during the coadsorption of Al (evaporation temperature: 1150 K) and oxygen (5 L/min) onto W(110) held at 750 K.

electrons emitted from the Fermi level, i.e. the electrons with the maximum kinetic energy, occur at 21.2 eV in UPS and at 19.8 eV in the MIES spectra (because of the 1.4 eV smaller excitation energy of the He metastables (19.8 eV for He(2^3S)). The energy at which electrons originating from the Fermi level appear in the photoemission or Auger de-excitation spectra (in MIES) is denoted by E_F . The low energy cutoffs in the spectra give directly the change of the work function of the W(110) crystal (5.2 eV for clean tungsten) as a function of the Al coverage or its variation with oxygen exposure irrespective of the actual interaction process which leads to the production of electrons.

In addition there are facilities for AES and LEED. The apparatus is furthermore equipped with a twin anode (Mg, Al) XPS source.

As in Ref. [14] Al metal was evaporated from an MBE – cell with a crucible made from pyrolytic boronnitride (model KCH 10 from VSW company). The crucible was carefully outgassed until a base pressure below 2×10^{-10} Torr is reached when operating the Al filled crucible at 1175 K with the shutter of the cell closed [14]. LEED measurements were made at various Al coverages, and were correlated with the work function results in order to determine the film thickness [2]. The Al–oxygen interaction was studied for Al layers of about 2.5 adlayers thickness. The Al(111) surface was prepared by repeated cycles of heating (to about 900 K) and sputtering (with 2 keV $2.5 \mu\text{A}/\text{cm}^2 \text{Ar}^+$) [15].

Two different strategies were followed to produce alumina adlayers:

(1) Aluminium oxide layers are grown by coadsorbing Al and oxygen to a W(110) surface kept at 725 K during the deposition procedure (Figs. 1a and 1b). This temperature was chosen primarily in order to avoid a contribution to the electron spectra from thermal emission. MIES and UPS spectra are recorded continuously during the growth period. The variation in work function is small throughout the adsorption procedure.

(2) Oxygen is offered to Al(111) and to Al adlayers on W(110) at a slow rate (5 Langmuirs (L) per minute typically) at room temperature, and MIES or UPS spectra (Figs. 2, 3a and 3b) are recorded continuously during the oxygen exposure. The changes in work function remain small (below 0.5 eV for 100 L exposure).

3. Results and discussion

3.1. Structural and electronic properties of the Al surfaces

The oxygen treatment was applied to Al films having a thickness of about 2.5 adlayers; we have throughoutly characterized [2] the electronic and structural properties of these Al films by combining work function, LEED, MIES and UPS measurements. In particular, in simulating the

MIES results (with the method described in Refs. [5,8]) and employing available information on the density of states of Al(111), we could compare the electronic structure of the adlayer with that of the single crystal [2]. We can now directly compare the MIES and UPS spectra with

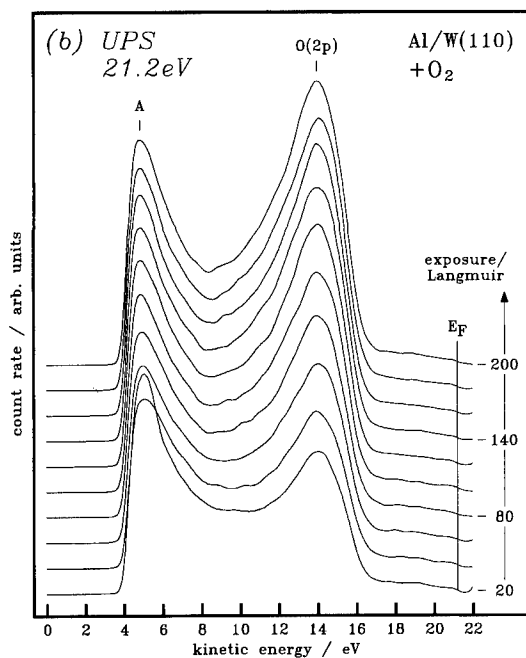
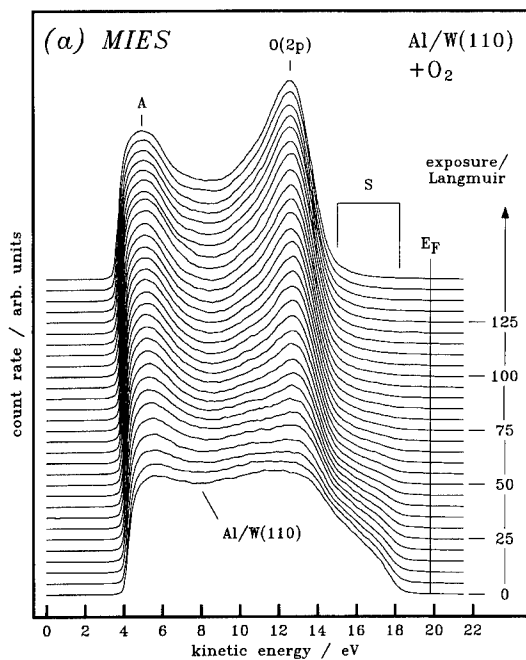


Fig. 2. MIES (a) and UPS (b) spectra during the exposure of Al(2.5 adlayers)/W(110) to oxygen at room temperature.

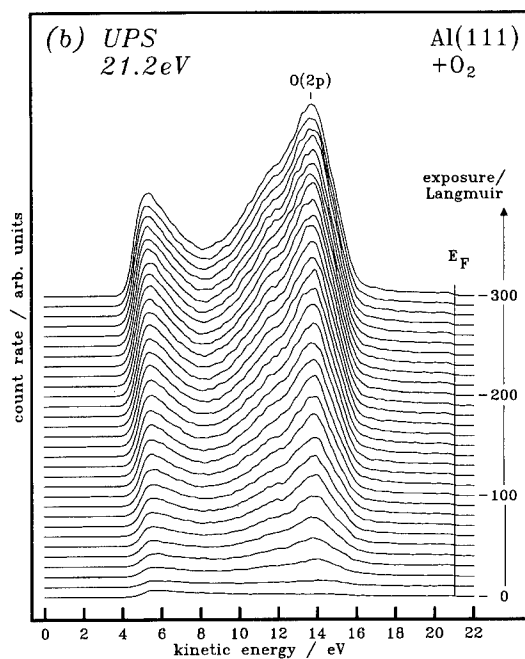
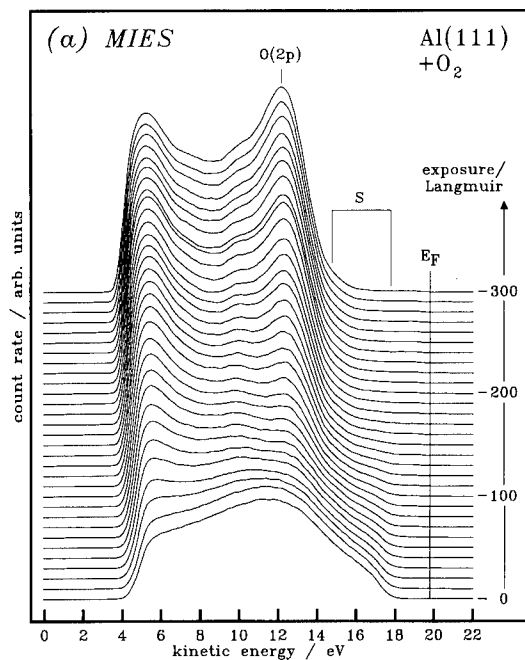


Fig. 3. MIES (a) and UPS (b) spectra during the exposure of Al(111) to oxygen at room temperature.

those obtained from Al(111) (see Figs. 3a and 3b). The shoulder "S" seen in the lower curves of the set of MIES spectra in Fig. 2 is indeed characteristic for surface states of the metallic Al-adlayer and the Al(111) surface. The presence of this shoulder "S" is in fact a sensitive indica-

tor to decide whether the surface still displays regions with metallic character. From the combination of the MIES/UPS results, the LEED patterns, and the simulations it follows that the Al film (2.5 adlayers thick) is essentially an Al(111) surface in Kurdjumov–Sachs orientation.

3.2. Coadsorption of Al and oxygen on W(110)

The adlayers produced by simultaneous application of Al and oxygen at 725 K quickly develop characteristics typical for alumina films:

(1) The spectra typical of clean W(110) (induced by Auger capture in Fig. 1a, and dominated by W 5d emission in Fig. 1b) turn into those characteristic for alumina: both the MIES and UPS spectra display a 7.5 eV wide structure whose maximum is located between $E_B = 6.5$ and 7.5 eV depending on the exposure time. From the general similarity of the MIES and UPS spectra we conclude that in MIES this structure (Fig. 1a) is caused by the Auger de-excitation process involving states from the selvedge of the adlayer. There is very little emission between E_F and about 15 eV; this is compatible with the formation of an insulator surface having a bandgap of about 8.5 eV width (estimated under the assumption that E_F is located in the middle of the bandgap). There is in particular no indication for metallic Al in the toplayer (see also the AES results): this would lead to emission near E_F in the MIES spectra similar to what is observed for the Al adlayers and for the initial stage of oxygen sorption (Figs. 1 and 2a).

(2) The UPS spectra of these films look rather similar to those characteristic for bulk alumina [16,17]. Upon further application of Al and oxygen they remain essentially unchanged except for a further reduction of the substrate induced emission.

(3) AES [18] shows essentially only the Al^{3+} line (at 54 eV) which is slightly asymmetrical on the high-energy side. The asymmetry could very well be caused by electron stimulated desorption during the AES analysis. From this we conclude that metallic Al is absent in the layer obtained with this preparation procedure. When coadsorbing Al and oxygen on W(110) kept at room temperature both the metallic Al (at 68 eV) and the Al^{3+} line (at 54 eV) are present [18].

(4) Under the chosen growth conditions the oxygen exposed Al layer exhibits a characteristic LEED pattern indicative of an oxygen induced two-dimensional structure. It is identical to that reported in Fig. 2 of Ref. [1] for alumina layers on Ta(110). As for Ta(110) [1] the results suggest the existence of a pseudo-hexagonal epitaxial overlayer on the W(110) substrate.

We conclude that the coadsorption of Al and oxygen on W(110) at elevated temperatures indeed leads to the formation of Al oxide layers. Although studies were performed at 725 K only, the only requirement appears to be the establishment of the correct stoichiometry between Al and

oxygen. Thus, the substrate temperature must be sufficiently high to remove excess Al atoms. Temperatures of the substrate during coadsorption can probably be chosen anywhere below 900 K.

Based on the amount of Al offered to the surface during the coadsorption procedure and the suppression of the W(110)-substrate signal in UPS the thickness of the alumina adlayer amounts to about 13 Å.

We have corroborated this conclusion by simulating MIES spectra (see Ref. [2] for details of the procedure and results). In the simulations we assumed that:

(1) the He projectile interacts with the surface adlayer via the Auger de-excitation process only: in order for the Auger capture process to take place, the 2s He electron must be transferred resonantly to an unoccupied state in the surface. Because of the presence of the band gap there are no empty states into which a resonant transfer of electrons could take place, and

(2) the energy band structure is similar to that for the ideal $\alpha-Al_2O_3$ (0001) surface as displayed in Fig. 7 of Ref. [19]. It must be pointed out that the SDOS of Ref. [19] was calculated under the assumption that Al atoms constitute the toplayer and that all oxygen atoms are located in the second layer which is certainly not the case under our conditions. However, the SDOS is qualitatively very similar to the bulk density of states in Fig. 7 of Ref. [19] (apart from the appearance of surface states) [19]. For the simulations the Fermi level was placed in the middle of the bandgap.

The simulation [2] reproduces very well the position and general shape of the asymmetric structure centered at about $E_B = 7$ eV. Besides the main maximum the structured shoulder towards larger binding energies is also reproduced. It is shown in Ref. [19] that the states accessible to MIES display a large fraction of O(2p) character. The inspection of the density of states calculated in Ref. [19] indicates that the MIES emission between about 10 and 15 eV is mainly caused by the O(2p) orbital density while that observed between 10 eV and structure (A) lies in the (O(2p)–Al(3p)) hybridization region. The strong signal caused by the O(2p) orbital density in MIES indicates that a large fraction of the oxygen atoms occupies locations within the toplayer (in a manner that they can interact with the He^* probe efficiently). Obviously, the O(2p) orbital does protrude sufficiently far into the vacuum.

The structure “A” observed close to the low-energy cutoff of the MIES and UPS spectra is attributed by us to the emission of secondary electrons. These come from primary electrons that are emitted toward the surface by the He^* probe (or in the photoemission process). The kinetic energy of the secondaries is limited to

$$E_{kin} = E^* - 2BG,$$

where E^* is the initial potential energy of the probe (about 19.8 eV for He^* and 21.2 eV for HeI photons) [20].

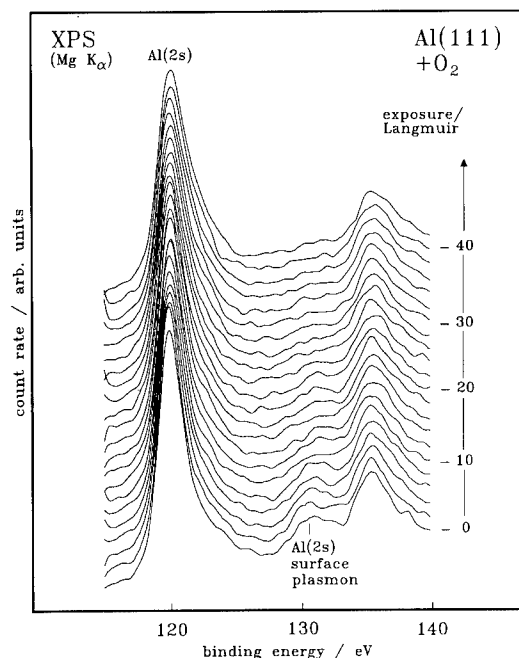


Fig. 4. XPS spectra during the exposure of Al(111) to oxygen. Shown is the Al(2s) signal together with the surface (-11 eV) and bulk (-15 eV) plasmon losses (numbers are with respect to the adiabatic line).

BG (about 9 eV) is the width of the alumina bandgap. Thus in the MIES spectra the emission of secondary electrons will be confined to about 2 eV from the low-energy cutoff of the spectra.

In conclusion, we observe heteroepitaxial growth of thin Al_2O_3 layers on W(110) when coadsorbing Al and oxygen at elevated temperatures (725 K). Also, the alumina adlayer shows excellent adhesion to the tungsten substrate. We find it thermally stable up to about 1200 K.

3.3. Al/W(110) and Al(111) + O_2

The shoulder “S” seen with MIES for Al(111) and Al/W decreases in intensity quickly with exposure and is barely visible beyond 50 L. This behavior correlates with the disappearance of the Al surface plasmon upon oxygen exposure as seen with EELS [21] and with XPS (see Fig. 4). We conclude that not only the surface states have disappeared at 50 L, but that the surface has practically lost its metallic character at this point.

Upon oxygen exposure of Al($\theta = 2.5$ ML)/W(110) and Al(111) at room temperature an O(2p) derived structure appears both in the MIES and in the UPS spectra of Figs. 2 and 3 at $E_B = 7$ eV. Its location and width is qualitatively similar to that developing during the coadsorption procedure in the previous section although some details in the oxygen induced feature are different: as compared to Fig. 1 the fine structure at the low-energy side

is less pronounced. In particular, for oxygen exposure of Al/W(110) only an asymmetry of the feature is seen. The comparison with Fig. 1 indicates that both Al surfaces develop oxide features during the oxygen exposure beyond 100 L (Al(111)) and 50 L (Al/W(110)), namely a strong decrease of the emission intensity below E_F indicating the formation of a band gap, and the emergence of the O(2p) induced emission with its maximum around $E_B = 6.5$ eV. These characteristics correlate with the degradation of the shoulder “S” indicating that the loss of metallic character of the surface goes together with oxide formation at the surface of the adlayers, and that the chemisorption regime is confined to below 50 L for Al/W(110) and 100 L for Al(111).

We have made an attempt [2] to simulate the topmost MIES spectrum in Fig. 3a on the basis of a SDOS for $p(1 \times 1)$ O/Al(111) [22] obtained from LAPW-calculations. No satisfactory fit was possible, but reasonable agreement with experiment could be obtained by assuming that the SDOS is essentially given by the oxygen derived density of states as given in Ref. [22], i.e. we conclude that the oxygenation procedure produces a surface whose density of states is mainly determined by the O(2p) wavefunctions protruding into the vacuum (see Section 3.2).

The adlayer produced during the oxygen sorption onto the Al film can be transformed into a surface which shows the same MIES/UPS spectra as those discussed in Section 3.2: by annealing the Al/oxygen layers shown as the top curves of Figs. 1a and 1b for 5 min at 1000 K and in addition for 5 min at 1225 K the MIES and UPS spectra turned into those obtained at 725 K surface temperature for the Al/oxygen coadsorption under saturation conditions.

The oxygen sorption on Al(111) obviously results in the growth of an amorphous oxide layer: extra spots, characteristic of alumina (see next section), appear only after an extended exposure to oxygen (10^7 L) [23].

4. Summary

The interaction of oxygen with Al adlayers on W(110) and with Al(111) surfaces was studied using metastable impact electron spectroscopy (MIES) and photo-electron spectroscopy (UPS). The information on the electronic properties of the surface layers obtained with these techniques was linked to their structural properties by LEED, XPS, and workfunction measurements. The thickness of the Al-adlayers before subjected to oxygen sorption was determined by combining LEED and work function measurements. Simulated MIE spectra could be generated for O/Al and oxide layers since information on the surface density of states is available in these cases. On the basis of the experimental results and those obtained from the simulations we conclude:

(1) Thin epitaxial alumina layers can be grown by coadsorbing Al and O_2 on W(110) kept at 725 K. They

show remarkable thermal stability. The elevated temperature appears to be necessary to remove excess Al atoms from the surface and establish the correct stoichiometry between Al and oxygen.

(2) For the oxygen adsorption on an Al layer on W(110) (2.5 adlayers) (at room temperature) the surface is practically covered by oxygen and has lost its metallic character at about 50 Langmuir oxygen exposure. Its electronic structure, although still different from alumina at this stage, can be transformed into that characteristic of the oxide by a simple annealing procedure.

(3) The exposure of Al(111) to oxygen gives results similar to those obtained with thin Al films. The LEED results suggest that the oxide film grown on Al(111) is amorphous (at least up to exposures of 200 L).

Acknowledgements

Financial support of this work by the Bundesminister für Forschung und Technologie (BMFT) under contract number 13N5676 and by the Deutsche Forschungsgemeinschaft (SFB 180) is gratefully acknowledged.

References

- [1] P.J. Chen, D.W. Goodman, *Surf. Sci.* 312 (1994) L767.
- [2] A. Hitzke, J. Günster, J. Kolaczkiwics, V. Kempter, *Surf. Sci.* 139 (1994) 318.
- [3] G. Ertl, J. Küppers, *Low Energy Electrons and Surface Chemistry* (VCH, Weinheim, 1985).
- [4] J. Küppers, *Physics and Chemistry of Alkali Metal Adsorption* (Elsevier, Amsterdam, 1989).
- [5] A. Niehaus, in: *Ionization of Solids by Heavy Particles*, R. Baragiola, ed. (Plenum, 1993).
- [6] W. Maus-Friedrichs, S. Dieckhoff, M. Wehrhahn, S. Pülm, V. Kempter, *Surf. Sci.* 271 (1992) 113.
- [7] W. Maus-Friedrichs, S. Dieckhoff, V. Kempter, *Surf. Sci.* 273 (1992) 311.
- [8] H. Müller, R. Hausmann, H. Brenten, V. Kempter, *Nucl. Instr. and Meth. B* 78 (1993) 239.
- [9] S. Pülm, A. Hitzke, J. Günster, H. Müller, V. Kempter, *Radiat. Eff. Def. Solids* 128 (1994) 151.
- [10] S. Dieckhoff, H. Müller, W. Maus-Friedrichs, H. Brenten, V. Kempter, *Surf. Sci.* 279 (1992) 233.
- [11] A. Hitzke, S. Pülm, H. Müller, R. Hausmann, J. Günster, S. Dieckhoff, W. Maus-Friedrichs, V. Kempter, *Surf. Sci.* 291 (1993) 67.
- [12] W. Maus-Friedrichs, S. Dieckhoff, V. Kempter, *Surf. Sci.* 237 (1990) 257.
- [13] W. Maus-Friedrichs, S. Dieckhoff, V. Kempter, *Surf. Sci.* 253 (1991) 137.
- [14] M. Vermeersch, R. Sporken, Ph. Lambin, R. Caudano, *Surf. Sci.* 235 (1990) 5.
- [15] K. Horn, J. Somers, T. Lindner, A.M. Bradshaw, in: *Physics and Chemistry of Alkali Metal Adsorption* (Elsevier, Amsterdam, 1989).
- [16] I.P. Batra, L. Kleinman, *J. El. Spectr. Relat. Phenom.* 33 (1984) 175.
- [17] D.W. Bullett, *Surf. Sci.* 93 (1980) 213.
- [18] A. Hitzke, Diploma Thesis TU Clausthal (1993), unpublished.
- [19] S. Ciraci, I.P. Batra, *Phys. Rev. B* 28 (1983) 982.
- [20] T. Munakata, T. Hirooka, K. Kuchitsu, *J. El. Spectr. Rel. Phenom.* 18 (1980) 51.
- [21] A.M. Bradshaw, W. Domcke, L. Cederbaum, *Phys. Rev. B* 16 (1977) 1480.
- [22] D.S. Wang, A.J. Freeman, H. Krakauer, *Phys. Rev. B* 24 (1981) 3092 and 3104.
- [23] A. Jimenez-González, D. Schmeisser, *Surf. Sci.* 250 (1991) 59.

H⁻ formation in proton (Ba)/Ag(111) collisions: effects of the surface structure

W.R. Koppers^{a,*}, B. Berenbak^a, D. Vlachos^b, U. Van Slooten^{a,1}, A.W. Kleyn^a

^a FOM-Institute for Atomic and Molecular Physics, Kruislaan 407, 1098 SJ Amsterdam, Netherlands

^b Dept. of Physics, University of Ioannina, GR-451 10 Ioannina, Greece

Abstract

Effects of the surface structure on H⁻ scattering from clean and Ba covered Ag(111) are reported. The collision energy in this study is around 750 eV. The H-atoms are scattered from the surface as well as from deeper layers of the crystal. This is clearly seen in the angular distributions of the back scattered ions. The Ba atoms sit at lattice positions of the Ag(111) substrate. The adsorbate layer contains vacancies to accommodate the large Ba atoms on the substrate.

1. Introduction

Formation of H⁻ in collisions of protons at low work-function (alkali or barium covered) surfaces has been observed already in the seventies and early eighties by several groups, see e.g. the recent papers by Van Os et al., Shi et al., Müller et al. and Van Slooten et al. [1–4]. In most experiments the differential conversion efficiency η is determined, where $\eta = I(\text{H}^-)/[I(\text{H}^-) + I(\text{H}^0)]$. I is the intensity for ions or neutrals measured with the same detection efficiency. At a given incident energy E and angle of incidence θ_i , η is measured as a function of the final scattering angle θ_f . Scattering angles are measured from the surface normal. Such experiments have been carried out very recently by Van Slooten et al. for a Ba covered Ag(111) surface [4]. Good agreement between the experimental results for η and theoretical models has been obtained. The topic has been reviewed earlier by Los and Geerlings [5].

All of the studies mentioned above have been carried out at incident energies around 1 keV and at low work-function surfaces. The number of studies on clean metal surfaces is very small. In the group of Winter the effect of a high parallel velocity v_{\parallel} has been explored extensively for H⁻ formation at a clean Al(111) surface ($\Phi = 4.24$ eV) [6]. For such a workfunction the affinity level of the H-atom does not decrease sufficiently due to the image potential to obtain a charge transfer rate exceeding a few

percent. However, by increasing v_{\parallel} considerably, the shifted affinity level can be brought into resonance with the metal electrons. Parallel velocities of 0.5 atomic units $\approx 10^6$ m/s are needed. The corresponding energies used in the experiments are from 1 to 30 keV.

The angular distributions of the scattered neutrals or ions have not been studied in detail. This is because the shape of the angular distributions is not relevant in the simple models used in the description of the negative ion formation. Van Wunnik et al. measured the angular distributions of the scattered particles (H⁰ + H⁻) [7]. It was found that the FWHM of the distributions was about 20° at $E = 400$ eV, $\theta_i = 75^\circ$. In addition, the energy spectrum of the scattered H⁻ ions showed two peaks. These peaks have been attributed to H-atoms reflected at the Cs atoms and H-atoms reflected at the W-atoms under the Cs layer. The latter H-atoms are decelerated by electronic stopping (≈ 3 eV/Å). Van Slooten et al. have studied the angular and energy distributions of H⁻ scattered at a Ba covered Ag(111) surface in great detail [4]. For $\theta_i = 80^\circ$ and $E = 500$ eV an angular distribution peaked in the specular direction is found, which is reminiscent of earlier results on Cs/W(110) [7]. Changing θ_i to smaller values shows a drastic change in the scattering pattern. At $\theta_i = 40^\circ$ a double peak structure is observed, which will be discussed later.

Van Slooten et al. performed measurements of the H⁻-intensity as a function of the azimuthal orientation of the Ag(111) crystal while keeping θ_i , θ_f and final energy E_f fixed. A very pronounced dependence on the azimuthal orientation was observed. All structures observed are due to structure scattering of the H-atoms at the Ba overlayer and Ag crystal. Here structure scattering is contrasted to so-called thermal scattering in which the surface is consid-

* Corresponding author. Tel. +31 20 6081234, fax +31 20 6684106, e-mail Koppers@amolf.nl.

¹ Present address: Philips Natuurkundig Laboratorium, Prof. Holstlaan, 5656 AA Eindhoven, Netherlands.

ered flat and structureless, see e.g. Ref. [8]. In structure scattering the surface appears corrugated leading to for example rainbow scattering, see e.g. Ref. [9]. Scattering of low energy ions (typically 1 keV) has been studied extensively, see e.g. Ref. [10], but the scattering process has received only very limited attention in the case of H^- formation at surfaces. Therefore, we have studied the scattering dynamics in great detail and will present an experimental study on negative ion formation in scattering of a proton beam from a clean and Ba covered Ag(111) crystal.

The Ba overlayer has been previously characterised using Auger electron spectroscopy (AES), X-ray photoelectron spectroscopy (XPS), workfunction measurements (WF) and medium energy ion scattering (MEIS) [11,12]. It was found that the density of the first Ba layer is less than that of the Ag substrate and was completed before the next layer starts to grow. For subsequent layers a random Poissonian growth was observed. More than about two full layers could not be grown. The structure of both first and subsequent layers was not determined. In view of the different size of the Ag-atoms in the lattice and Ba atoms, epitaxial growth seemed unlikely. However, from their H^- formation data Van Slooten et al. conclude that the Ba overlayer has the same structure as the underlying Ag(111) bulk [11].

In this contribution we will present results on scattering of H^+ leading to H^- on clean Ag(111) and Ba covered Ag(111). Studies at the clean surface are performed because here the surface structure is well known, as shown in Fig. 1. We will demonstrate: the presence of structure scattering, that scattering from deeper layers is important, a large increase in negative ion yield with increasing Ba

coverage, and the absence of structural changes in the scattered signal upon Ba adsorption, suggesting a kind of epitaxial growth of the Ba overlayer.

2. Experimental

The apparatus used consists of two UHV chambers. In one the crystal can be cleaned, characterised by several surface analytical techniques (AES, XPS, work function measurements) and Ba layers can be grown. Crystals prepared in this chamber can be transferred under UHV to a two axis goniometer in the second chamber. In this chamber a differentially pumped electron impact H^+ ion source is mounted. The ion energies E_i range from 250 to 3000 eV. The beam is purified using a Wien filter. The particles scattered from the crystal can be monitored using an electrostatic energy analyser with an energy resolution $\Delta E/E = 0.08$ and a channeltron, yielding angle and energy resolved intensities of the scattered ions. In addition, a detector capable of measuring the fraction of negative ions in the total scattered flux is available. The experimental arrangement has been described in more detail by Van Slooten et al. [4].

3. Results and discussion

The fraction of negative ions has been measured previously by Van Slooten et al. for a Ba bi-layer on Ag(111) [4]. The yield is about 20% for scattering angles $\theta_f < 60^\circ$ and decreases for larger θ_f . Here θ_f is measured from the surface normal. The relative yield is not structured. Therefore, all structure observed in measured intensities of scattered ions has to be due to the scattering process and not to a change in probability of negative ion formation. At the clean Ag(111) surface the negative ion is much smaller ($< 1\%$) and its precise value is hard to measure.

However, the yield of negative ions at the clean Ag(111) surface is sufficient to measure angular and energy distributions of H^- formed. The final energy (E_f) distributions of the negative ions are very broad, as can be seen in Fig. 2. Here the intensity distributions for scattered H^- as a function of E_f and θ_f are shown for $\theta_i = 60^\circ$ and $\phi = 0^\circ$, the azimuthal orientation of the crystal, defined in Fig. 1. For near normal exit angles energy losses up to 400 eV are found for H^+ incident at $E_i = 750$ eV. Since the energy loss in a binary H–Ag collision is very small ($< 0.037E_i$), electronic stopping will be mainly responsible for the observed loss. The H-atoms must have travelled through many atomic layers to lose such a large amount of energy, as observed previously for proton scattering at Ni(001) [13]. The angular distribution at $E_f \approx E_i$ is clearly structured. Due to the limited energy resolution of the electrostatic energy analyzer ($\Delta E/E = 0.08$) also particles with energies higher than E_i are observed.

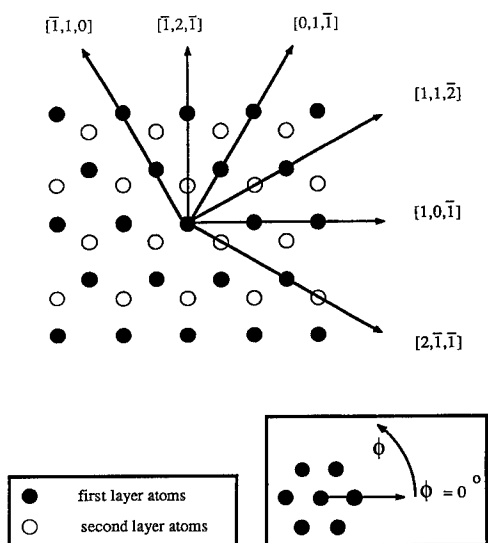


Fig. 1. Crystallographic drawing of the (111) face of a Ag crystal. The crystal directions and the definition of ϕ are indicated.

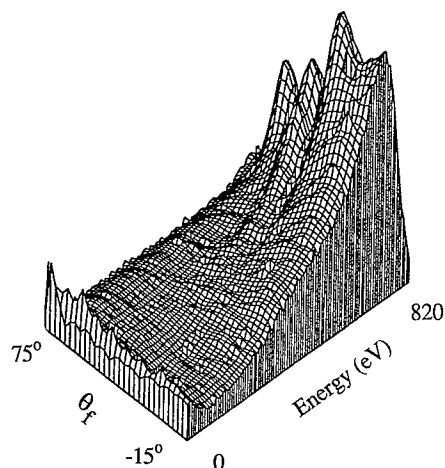


Fig. 2. Three-dimensional distribution $I(E_f, \theta_f)$ for negative ions formed in 750 eV H^+ scattering from Ag(111) at $\theta_i = 60^\circ$. The scattering plane is along the $[1, 0, -1]$ azimuthal direction or $\phi = 0^\circ$. The intensity is plotted on a linear scale. No correction for the energy dependent transmission of the energy analyser has been applied.

Examples of measured angular distributions are shown in Fig. 3 and 4. Here the intensity of the scattered H^- ions is plotted as a function of θ_f for two different values of θ_i , the angle of incidence, also measured from the surface normal. The beam energy is 750 eV in all cases. The final energy E_f is also 750 eV. The positions of the structures observed in the figures are not strongly dependent on E_i nor E_f (> 600 eV). The azimuthal orientation ϕ is along the $[1, 1, -2]$ axis, $\phi = 30^\circ$, for the data of Fig. 3. The azimuthal orientation of the crystal for the data of Fig. 4 is $\phi = -30^\circ$, along the $[2, -1, -1]$ axis. Here, in contrast to $\phi = 30^\circ$, the second layer Ag atoms are especially for

$\theta_i = 40^\circ$ shadowed by surface atoms and invisible to the impinging particles. Van Slooten et al. have published an angular distribution for $\theta_i = 40^\circ$ [4]. They have attributed the absence of the scattering signal around $\theta_f = 40^\circ$ to blocking of H-atoms scattered from the second layer by atoms of the first layer. In the present case of a pure Ag crystal the same interpretation is valid, which has been verified by classical trajectory calculations. This effect of blocking can also be seen at $\theta_i = 80^\circ$. According to the classical trajectory calculations the dip around $\theta_f = 40^\circ$ is due to blocking of H-atoms scattered from the second layer by first layer atoms. In all spectra a clear peak is visible around $\theta_f = 17^\circ$. Because this peak is independent of the angle of incidence, it is attributed to scattering from deeper layers through a channel of the crystal. The same is true for the feature at $\theta_f = -5^\circ$. This is confirmed by classical trajectory calculations. It is remarkable that even for $\theta_i = 80^\circ$ features due to scattering from deeper layers are observed. Clearly penetration of the lattice by H-atoms occurs at all angles at these energies. This is due to the small size of the H-atoms, which is clear from an inspection of the interaction potential [14].

The scattering patterns in Fig. 4 for $\phi = -30^\circ$ are more complex. The large minimum around the specular scattering direction for $\theta_i = 40^\circ$ has disappeared. For $\theta_i = 80^\circ$ a dip at $\theta_f = 75^\circ$ is still observed. This is according to a classical trajectory analysis mainly due to surface rainbow scattering, leading to two closely spaced peaks in the forward direction, see e.g. Ref. [9]. In addition, several other peaks are visible which are again due to scattering through the channels of the lattice. It should be noted that these peaks are much more clearly visible than in previous studies. Van Slooten et al. did not observe such clear structures for Ba overlayers [4]. This can in part be due to disorder in these layers, as will be discussed later. In addition, the negative ion formation probability on Ag(111)

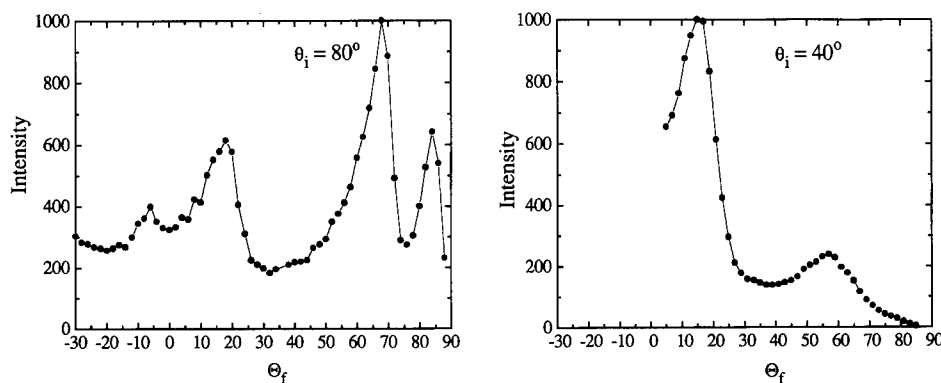


Fig. 3. Angular distributions for H^- production in collisions of H^+ and clean Ag(111). The incident energy $E_i = 750$ eV. The detector energy $E_f = 750$ eV. Results for two different angles of incidence, $\theta_i = 40^\circ$ and 80° are shown. The scattering plane is along the $[1, 1, -2]$ azimuthal direction or $\phi = 30^\circ$.

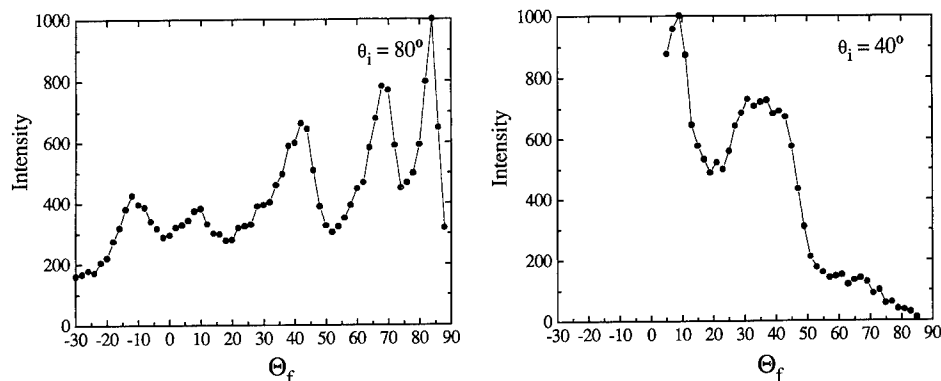


Fig. 4. Angular distributions for H^- production in collisions of H^+ and clean Ag(111). The incident energy $E_i = 750$ eV. The detector energy $E_f = 750$ eV. Results for two different angles of incidence, $\theta_i = 40^\circ$ and 80° are shown. The scattering plane is along the $[2, -1, -1]$ azimuthal direction or $\phi = -30^\circ$.

is such that it suppresses the H^- yield at grazing exit angles, thus relatively enhancing the structures at smaller θ_f . By probing positive ions, detection of deeper layers is very difficult because of the very efficient neutralisation of positive ions in the bulk [10].

There is another method to determine if penetration of the surface occurs. This can be measured by spinning the crystal around its axis, thus scanning the azimuthal orienta-

tion of the scattering plane. If only surface atoms are involved, such azimuthal scans should exhibit the 60° periodicity of the surface. If the second and/or deeper layers are involved, the azimuthal scans should exhibit a 120° symmetry. If the scattering process involves many layers and collisions, it may lead to complete randomisation of the exit azimuthal angle, and a flat distribution is expected. Results of such azimuthal scans for $\theta_i = 40^\circ$ are

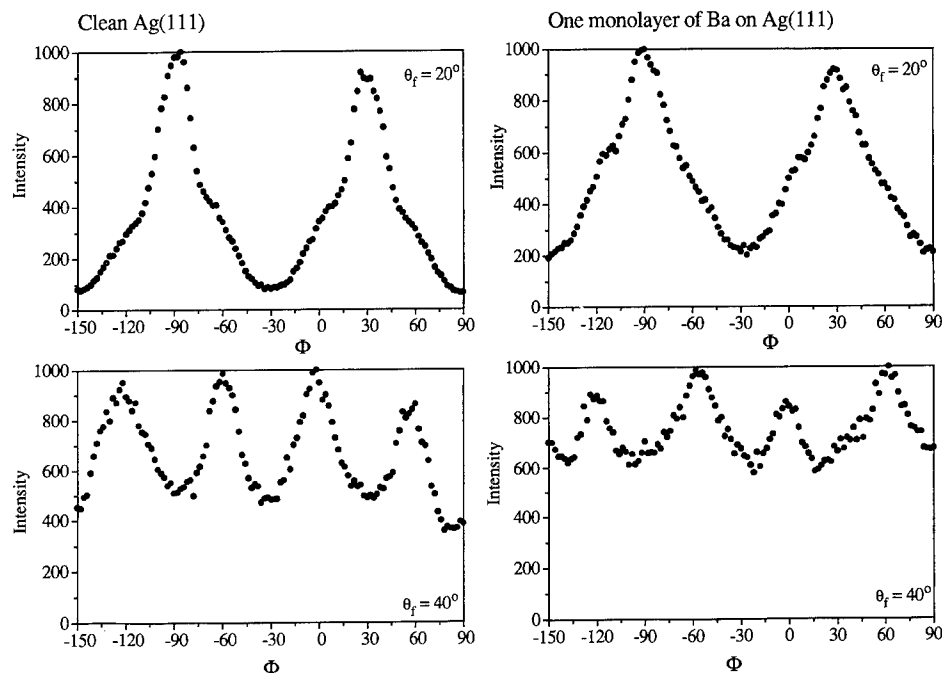


Fig. 5. Azimuthal or ϕ dependence of H^- production in collisions of H^+ and Ag(111) (left) and Ag(111) covered by a monolayer of Ba (right) at $\theta_i = 40^\circ$. The incident energy $E_i = 750$ eV. The detector energy $E_f = 750$ eV (left), $E_f = 710$ eV (right). Results for two different scattering angles θ_f (20° and 40°) are shown.

shown in Fig. 5 (left). At $\theta_i = 40^\circ$ a 60° periodicity is seen. Apparently the second and/or deeper layer atoms do not contribute to the structure observed in the scattering. This is consistent with our observations in Fig. 3 and 4. At $\theta_i = 40^\circ$ and $\phi = 30^\circ$ a dip in the signal around $\theta_f = 40^\circ$ is attributed to blocking of the scattered signal from the second layer [4,15]. Effectively this makes the second layer atoms invisible at this particular setting. At $\theta_i = 40^\circ$, $\theta_f = 40^\circ$ and $\phi = -30^\circ$ the second layer atoms are effectively shadowed by the first layer atoms, again resulting in no scattered signal from the second layer. Therefore, scattering observed for $\theta_i = 40^\circ$, $\theta_f = 40^\circ$ reflects the periodicity of the first layer. The periodic structure is superimposed on a uniform background of ions coming from deeper layers.

The azimuthal scans at $\theta_i = 40^\circ$, $\theta_f = 20^\circ$ exhibit a clear structure with a symmetry of 120° (peaking at $\phi = -90^\circ$ and $\phi = 30^\circ$) on which a structure with a 60° symmetry (due to scattering from the surface atoms) and a uniform background are superimposed. The origin of the maximum of this azimuthal scan can be seen in the angular distribution in Fig. 3. For $\theta_i = 40^\circ$ and $\phi = 30^\circ$ we observe in this figure a peak at $\theta_f = 20^\circ$, which is due to scattering from the second layer deflected by the first layer atom to yield an enhanced intensity at $\theta_f = 20^\circ$ and $\theta_f = 60^\circ$. This confirms that the feature showing a symmetry of 120° in the azimuthal scan is due to scattering from the second layer. In the angular distribution in Fig. 4 at $\phi = -30^\circ$ no enhanced intensity is seen at $\theta_i = 40^\circ$, $\theta_f = 20^\circ$. This is due to the blocking of the second layer by the first. Here only scattering from the first (and possibly random scattering) contribute. Indeed, the structure exhibiting the 120° periodicity in ϕ is due to the second layer.

If adsorption of Ba on to the Ag(111) crystal would lead to a modified structure of the overlayer with respect to the substrate, one would expect the peak positions in the angular and azimuthal scans to shift. This turns out not to be the case. The results for $\theta_i = 40^\circ$ in Fig. 3 resemble the results by Van Slooten et al. very closely [4]. New data on scattering from Ba covered surfaces confirms these observations. The relative intensity of the peaks is changed very much, especially for $\theta_f > 60^\circ$. This is due to a different angular dependence of the negative ion formation probability. Azimuthal scans of the H^- signal from a monolayer of Ba on Ag(111) are shown in Fig. 5 (right). It is clear that the structures observed are very similar. At $\theta_f = 40^\circ$ the 60° periodicity seems to be broken. At $\theta_f = 20^\circ$ the signal from the surface layer seems a bit stronger than that from the second layer. These and other results obtained suggest that the Ba atoms are located on lattice positions of the Ag(111) substrate.

Earlier work has indicated that first a monolayer of Ba was formed, after which a rather open overlayer is formed by Poisson growth [11,12]. The present work suggests that the Ba atoms sit at lattice positions of the substrate. However, in view of the larger size of the Ba atoms, the

density in the Ba layer is lower than in the substrate. This is consistent with the measurement of the density by Van Slooten et al. [11]. A precise determination of the structure cannot be made with the present ion scattering results, because they are not sensitive to the long range order of the Ba overlayer. The suggestion of a structure of the overlayer being epitaxial, but exhibiting vacancies to accommodate the large Ba atoms has been found for Cs adsorption on Ag(111) as well. Lamble and King determined the overlayer structure using EXAFS [16]. A very open structure in which all Cs atoms are sitting at the three-fold hollow sites was found. A structural determination using for instance LEED is necessary to shed more light in this problem.

4. Conclusions

We have shown that scattering from deeper layers for both Ag(111) and Ba/Ag(111) is observed. The H^- observed can have travelled many atomic layers deep. Polar and azimuthal scans indicate clearly that both the surface layer and deeper layers contribute to the H^- yield. The peak positions in the angular distributions of scattered H^- from Ba/Ag(111) coincide with those observed for the clean Ag(111) surface. The azimuthal scans are very similar for clean and Ba covered surfaces. This indicates that the Ba overlayer is epitaxially grown; i.e. all Ba atoms sit in the three-fold hollow sites of the Ag(111) lattice. Due to the size of the Ba atoms, this layer is incomplete and contains vacancies.

Acknowledgements

This work is part of the research programme of FOM and is supported financially by NWO.

References

- [1] C.F.A. Van Os, P.W. Van Amersfoort and J. Los, *J. Appl. Phys.* 64 (1988) 3863.
- [2] M. Shi, J.W. Rabalais and V.A. Esaulov, *Rad. Eff. Def. Sol.* 109 (1989) 81.
- [3] H. Müller, R. Hausmann, H. Breiten and V. Kemper, *Surf. Sci.* 284 (1993) 129.
- [4] U. Van Slooten, O.M.N.D. Teodoro, A.W. Kleyn, J. Los, D. Teillet-Billy and J.P. Gauyacq, *Chem. Phys.* 179 (1994) 227.
- [5] J. Los and J.J.C. Geerlings, *Phys. Rep.* 190 (1990) 133.
- [6] F. Wypuuta, R. Zimny and H. Winter, *Nucl. Instr. and Meth. B* 58 (1991) 379.
- [7] J.N.M. Van Wunnik, J.J.C. Geerlings, E.H.A. Granneman and J. Los, *Surf. Sci.* 131 (1983) 17.
- [8] J.A. Barker and D.J. Auerbach, *Surf. Sci. Rep.* 4 (1984) 1.
- [9] A.W. Kleyn and T.C.M. Horn, *Phys. Rep.* 199 (1991) 191.

- [10] H. Niehus, W. Heiland and E. Taglauer, *Surf. Sci. Rep.* 17 (1993) 213.
- [11] U. Van Slooten, W.R. Koppers, A. Bot, H.M. Van Pinxteren, A.M.C. Moutinho, J.W.M. Frenken and A.W. Kleyn, *J. Phys. Condens. Matter* 5 (1993) 5411.
- [12] A. Bot, U. Van Slooten, W.R. Koppers and A.W. Kleyn, *Surf. Sci.* 287 (1993) 901.
- [13] R.J. MacDonald, D.J. O'Connor, B.V. King, Y. Shen and G. Xu, *Nucl. Inst. and Meth. B* 78 (1993) 56.
- [14] U. Van Slooten, E.J.J. Kirchner and A.W. Kleyn, *Surf. Sci.* 283 (1993) 27.
- [15] J.F. Van Der Veen, *Surf. Sci. Rep.* 5 (1985) 199.
- [16] G.M. Lamble and D.A. King, private communication, 1994.



ELSEVIER

Inelastic collisions as the source of circumlunar sodium

M. Marconi *

Atmospheric and Environmental Research, 840 Memorial Dr., Cambridge, MA 02139, USA

Abstract

In 1988 Potter and Morgan [Science 241 (1988) 675] detected a sodium atmosphere above the limb of the sunlit lunar surface. There are three possible mechanisms which could generate a circumlunar sodium atmosphere. These are solar wind ion sputtering of the lunar surface by ~ 1 keV protons and 4 keV alpha particles, micrometeoroid bombardment of the lunar surface, and photostimulated release of sodium by solar photons. Models of the lunar sodium atmosphere are presented and compared to the spatially extended sodium brightness observations of Mendillo et al. [Geophys. Res. Lett. 18 (1991) 2097]. The comparison strongly suggests that sodium from micrometeoroid bombardment or directly from ion sputtering cannot account for the observations. Instead the sort of sodium velocity distributions which are deduced from the observations appear to be most compatible with either a photostimulated desorption process or ion sputtered sodium which suffers some collisions within the porous surface of the moon before entering the atmosphere. Laboratory studies of the interaction of solar photons and solar wind ions with lunar type surfaces are required to verify this.

1. Introduction

In 1988 Potter and Morgan [7] discovered bright emissions at 5890 Å and 7699 Å above the limb of the sunlit atmosphere of the Moon. These were easily identified by Potter and Morgan as being due to the resonant scattering of solar radiation by a tenuous atmosphere composed of sodium and potassium atoms. Since the initial detection a number of other viewings of the sodium atmosphere have been reported [2,4,5,7,8,10,11]. The result of these observations is a collection of sodium brightness data extending from an altitude above the lunar surface of a few tens of kilometers to 5 lunar radii (1 lunar radius = 1738 km) on the sunlit side and to 15–20 lunar radii on the antisunward side of the Moon.

There are three possible sources for the observed sodium atmosphere: sputtering from the lunar surface by bombardment from solar wind 1 keV protons and 4 keV alpha particles; micrometeoroid bombardment vaporization of surface material; and photostimulated release by solar photons. The sodium generated from these quite dissimilar processes displays a velocity distribution which is highly characteristic. As a result it may be anticipated that since the sodium atmosphere is everywhere collisionless, it will strongly reflect the nature of its source. Consequently, it is possible through the use of models of the lunar atmosphere in conjunction with observations to discriminate between

these mechanisms for sodium production. The aim of this paper is to utilize comparisons of models with observations of the sodium lunar atmosphere to show that photostimulated release and/or ion sputtering followed by a few collisions in the porous lunar surface are likely the predominant sources of sodium.

Below we first discuss the theory of the lunar atmosphere, then we briefly describe the model, next we compare model and data, and lastly we discuss the implications of the comparison. A more thorough discussion of the theory and model can be found in Ref. [9].

2. Theory

The above processes give rise to a flux of sodium atoms with a particular initial velocity distribution. Since atom-atom collisions are rare in the very tenuous lunar atmosphere, the sodium atom with some initial velocity will, after exiting the surface, move only under the combined influence of solar radiation pressure and gravity. Depending on the initial velocity, a sodium atom may either escape or return to the surface. A small fraction of the sodium atoms may also be photoionized. The sodium atoms which return to the surface may or may not stick to the surface. Those that stick will be available for relaunching by the above processes or thermal desorption. Those that do not stick will exchange some energy with the surface and emerge almost instantly with a new velocity whose magnitude should be somewhere between the initial speed and a thermal speed characteristic of the surface

* Corresponding author. Tel. +1 617 547 6207, fax +1 617 661 6479, e-mail max@aer.com.

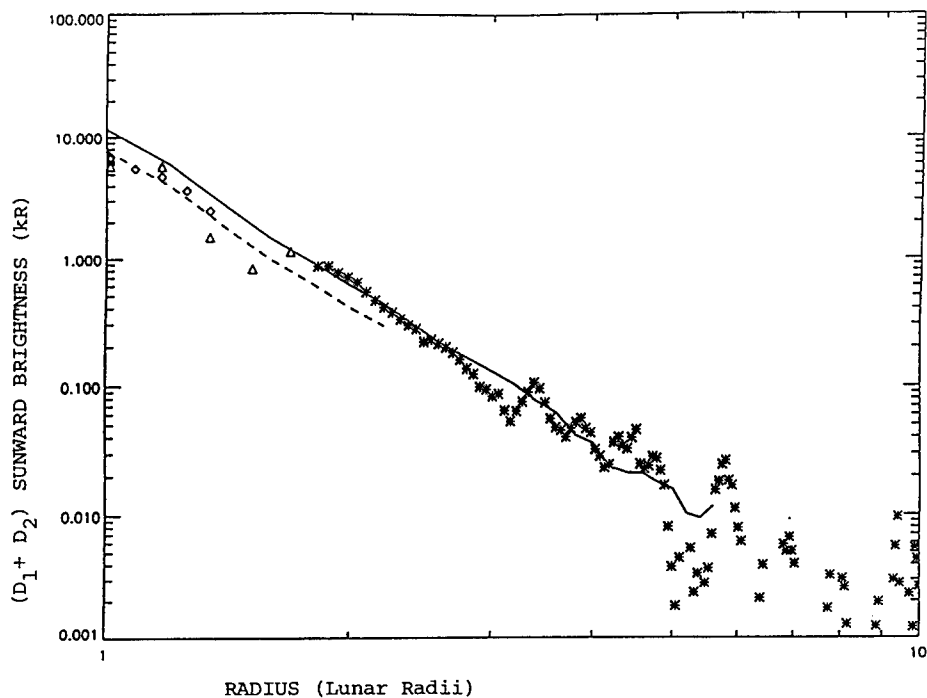


Fig. 1. The (D₁ + D₂) sodium brightness observations of Morgan and Potter (diamonds and triangles) and Mendillo et al. (asterisks) are compared to a model run with a 1000 K Maxwellian velocity distribution, hemispherical source, and 100% sticking (solid line).

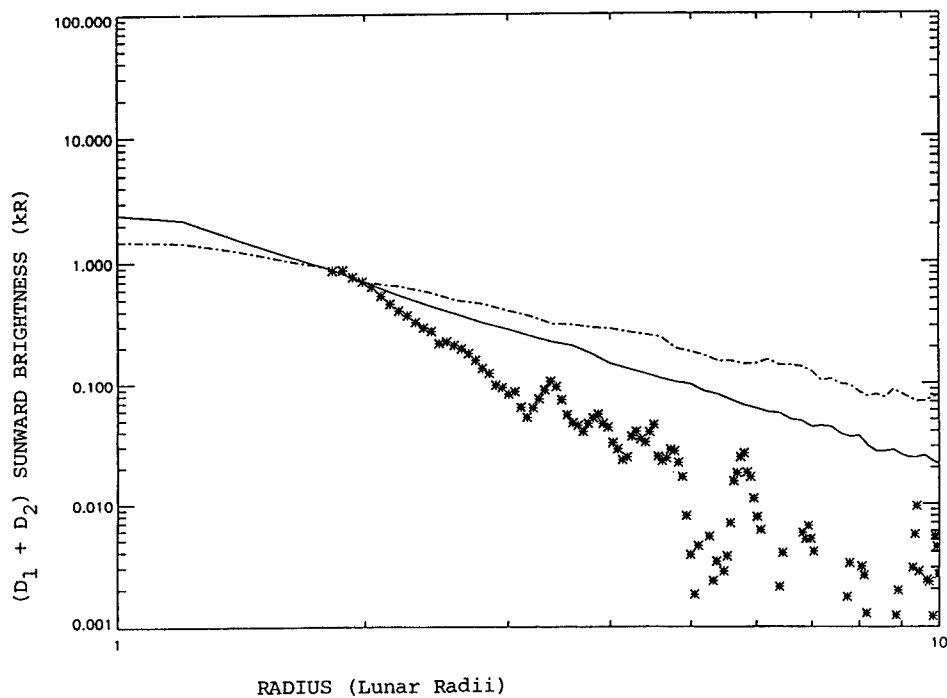


Fig. 2. The (D₁ + D₂) sodium brightness observations of Mendillo et al. (asterisks) are compared to model runs with a 2000 K Maxwellian velocity distribution (solid line) and a Sigmund-Thompson velocity distribution (dot dash line) with binding energy of 0.75. Both models are for a hemispherical source and 100% sticking.

temperature. In this case, the atom will be even less able to escape so that it will bounce around until it sticks or is photoionized. The collection of sodium atoms with orbits determined in this manner constitute the lunar atmosphere.

3. Model

We have developed a model of the lunar atmosphere based on the preceding scenario. A collection of sodium atoms with whatever distribution of velocities and initial positions on the surface of the Moon is deemed appropriate is launched. The atom orbits, determined by gravity of the Moon and the Earth and radiation pressure of the sun, are calculated. If an atom hits the surface, the new velocity of the particle is determined by an energy accommodation coefficient which assigns the new velocity a value between the initial velocity and a thermal velocity characteristic of the surface temperature (< 400 K). In addition, a sticking coefficient determines what fraction of the atoms will return to the atmosphere after striking the surface. Although there is a notion that sodium should stick $\sim 20\%$ of the time and accommodate almost all of the time on a lunar surface with a temperature under 400 K, in reality the outcome of a sodium surface collision is unknown so that sticking and accommodation are parameters that must be varied to determine their effect on the model atmospheres. By spatially sampling the collection of orbits which constitute the model atmosphere and computing the number of solar photons at the sodium D line wavelengths (in the rest frame of the atom) scattered by the atoms, a model spatial brightness distribution that may be compared to the observed brightness is obtained.

4. Results

All the figures are profiles of the sunward sodium D1 + D2 brightness in kiloRayleighs vs. distance from the center of the Moon in lunar radii. Fig. 1 displays the brightness profiles of Mendillo et al. [5], (asterisks), derived from measurements extending from ~ 1.8 to ~ 5.0 lunar radii taken on Feb. 20, 1990 and also the measurements of Potter and Morgan [8] extending from near the limb to 0.7 lunar radii taken on Oct. 2 (diamonds) and Oct. 3 (triangles) 1988. The solid line and broken lines are identical model runs except that they were normalized to Mendillo's and Potter and Morgan's data respectively. The model was generated with a 1000 K Maxwell–Boltzmann velocity distribution, a uniform hemispherical spatial source which only emits sodium atoms on the sunlit side of the Moon, and 100% sticking. In Fig. 2 we see the effects of changing the velocity distribution. The asterisks represent Mendillo's brightness profile as before. The solid line is a model with a 2000 K Maxwell–Boltzmann velocity distribution and the dot dash line corresponds to a Sigmund–

Thompson sputtering distribution for a binding energy of 0.75 eV. It is quite clear from Figs. 1 and 2 that only the 1000 K Maxwellian fits the data.

5. Discussion

The 2000 K Maxwellian, which should be regarded as a lower bound to the temperature of vapor from micrometeoroid bombardment (Morgan and Shemansky [6], estimate 3000–6000 K for the temperature), clearly has a much shallower slope than the data indicating an excess of material at large distances due to an excess of high velocity particles. The same may be said of the sputtering (Sigmund–Thompson) distribution for a binding energy of 0.75 eV which may be roughly typical of surface binding energies and a cutoff at 27 eV which was chosen to be about 25% of the maximum energy that a sodium atom could have as a result of colliding with a 1 keV solar wind proton.

Of course, this demonstration of the effect of the velocity distribution raises the question of what would happen if the various parameters such as sticking coefficient, accommodation coefficient, and binding energy for the sputtering distribution, for example, were varied. A more thorough study is presented in Ref. [9] which treats a broader array of distributions and surface parameters with the same conclusion. It appears that quite generally neither a sputtering velocity distribution nor the type of distribution from micrometeoroid generated vapor is able to fit the observations. This apparently leaves photostimulated desorption of sodium as the remaining possibility.

The type of velocity distribution that leads to agreement with data requires a tail similar to that of a 1000 K Maxwellian. The low velocity region of the distribution is not well determined and depends on the assumed surface properties of the Moon, i.e., accommodation and sticking. Interestingly, it seems that thermal Maxwellian velocity distributions (see for example Refs. [3,12]) have been observed for alkali atoms released as a consequence of photostimulated processes occurring near the surface of alkali halide crystals. However, the lunar sodium is non-thermal at $2.5 \times$ the maximum surface temperature. A non-thermal 1880 K Maxwellian has been detected in the Zn from photon irradiated ZnS [1]. It therefore appears that photostimulated desorption of sodium is a candidate as the major supplier of sodium atoms to the lunar atmosphere. In order to be sure of this, laboratory studies of photostimulated processes taking place at the surface of Moon-like materials must be conducted.

As discussed in Ref. [9], however, there is also a plausible mechanism by which sputtered particles may attain a velocity distribution of the type discussed above. In summary, most of the incident ions will sputter in the cavities of the porous lunar surface, leading to the possibility of the initially Sigmund–Thompson distributed sput-

tered sodiums colliding with the interior of a cavity and quasi-thermalizing before leaving the surface. This way the Sigmund–Thompson velocity distribution of the freshly sputtered sodiums may be converted to a more thermal distribution which could fit the observations. Here too laboratory studies are required to determine the validity of this mechanism. Studies which explore this mechanism and also the photostimulated release of sodium are planned at the Center for Atomic and Molecular Physics at Surfaces at Vanderbilt University.

6. Conclusions

Direct sputtering and micrometeoroid bombardment cannot account for the sodium lunar atmosphere. The best candidates appear to be some type of solar photostimulated release of non-thermal sodium from the lunar surface or solar wind sputtering followed by partial collisional thermalization in the cavities of the porous lunar surface. Laboratory experiments which study the effect of solar photons and solar wind ions on the surface of lunar material are essential to clarify the source of sodium atoms of the lunar atmosphere. Other studies which explore the fate of a low energy sodium atom incident on the surface of lunar material are also required to fully understand the

velocity distribution of sodium atoms in the lunar atmosphere.

References

- [1] H.F. Arlinghaus, W.F. Calaway, C.E. Young, M.J. Pellin and D.M. Gruen, *J. Vac. Sci. Technol.*, a 7 (1989) 1766.
- [2] B. Flynn and M. Mendillo, *Science* 261 (1993) 184.
- [3] R.F. Haglund and N.H. Tolk, *Proc. SPIE* 690 (1986) 9.
- [4] R.W.H. Kozlowski, A.L. Sprague and D.M. Hunten, *Geophys. Res. Lett.* 17 (1990) 2253.
- [5] M. Mendillo, J. Baumgardner and B. Flynn, *Geophys. Res. Lett.* 18 (1991) 2097.
- [6] T.H. Morgan and D.E. Shemansky, *J. Geophys. Res.* 96 (1991) 1351.
- [7] A.E. Potter and T.H. Morgan, *Science* 241 (1988) 675.
- [8] A.E. Potter and T.H. Morgan, *Geophys. Res. Lett.* 15 (1988) 1515.
- [9] W.H. Smyth and M.L. Marconi, *Astrophys. J.* (1995), in press.
- [10] A.L. Sprague, R.W.H. Kozlowski, D.M. Hunten, W.K. Wells and F.A. Grosse, *Icarus* 96 (1992) 27.
- [11] A.L. Tyler, R.W.H. Kozlowski and D.M. Hunten, *Geophys. Res. Lett.* 15 (1988) 141.
- [12] P.C. Townsend, in: *Sputtering by Particle Bombardment*, ed. R. Berisch (Springer, Berlin, 1983) p. 147.



ELSEVIER

Wavelength-selective laser ablation of diamond using hydrogen-impurity vibration modes

A. Ueda ^a, R.G. Albridge ^a, A.V. Barnes ^a, A. Burger ^c, W.E. Collins ^c, J.L. Davidson ^b,
M.A. George ^c, Z. Hu ^c, M.L. Languell ^b, J.T. McKinley ^{a,*}, J. Tribble ^a, N.H. Tolk ^a

^a Department of Physics and Astronomy, Vanderbilt University, Nashville, TN 37235, USA

^b Department of Electrical Engineering, Vanderbilt University, Nashville, TN 37235, USA

^c Department of Physics, Fisk University, Nashville, TN 37208, USA

Abstract

We have observed wavelength-dependent laser ablation of diamond films demonstrating the C–H bond-stretching mode at 3.5 μm , which is important in the early stages of photodamage. In particular, there is a sharp drop in the ablation threshold near 3.5 μm . The measurements were made with the Vanderbilt Free-Electron Laser (FEL). We also observed the onset of morphological changes by using an atomic force microscope (AFM).

1. Introduction

Hydrogen incorporated during chemical vapor deposition (CVD) of diamond films produces a wavelength-specific damage mechanism. It has been reported that (100) and (111) surfaces of natural diamond are normally hydrogen-terminated. Below 1300 K the surface reconstructs to a simple truncated-bulk (1×1), while above 1300 K hydrogen atoms desorb, resulting in a (2×1) reconstruction [1]. High-resolution electron energy loss spectroscopy (HREELS) of the (100) and (111) surfaces of natural diamond reveal that the vibrational spectrum is hydrogen-related with surface phonon bands and C–H vibrational modes in the region of 2800–3100 cm^{-1} ; IR absorption bands exist near 2900 cm^{-1} [2,3].

The present experiment involves the irradiating CVD diamond films with intense ($1\text{--}100 \text{ GW/cm}^2$) pulsed radiation in the 3–4 μm region and investigates the wavelength-dependence of the resulting damage with scanning electron microscopy (SEM) and atomic force microscopy (AFM). Most studies have focused on the intensity and pulse duration dependency, while few studies exist until now for the wavelength dependency. Other known factors influencing the photodamage threshold include: polarization, surface roughness, and the ratio of film thickness-to-wavelength [4]. The photodamage intensity threshold typically increases with decreasing pulse duration [5] so that pulsed-photodamage studies require a very high power laser. IR transmission of CVD diamond films indicates that

the C–H stretch mode at 2900 cm^{-1} is correlating strongly with hydrogen concentration [6,7].

Near the C–H stretch mode ($\sim 3.5 \mu\text{m}$), we identified a definite relationship between the C–H single photon bond-stretching mode in CVD diamond films and the ablation threshold. Clearly, the C–H stretch mode plays an important role in the initial phases of energy ingestion by the CVD diamond. A sharply wavelength-dependent ablation threshold mitigates against the common view that all stages of ablation may be viewed as strictly thermal processes.

2. Experimental

The polycrystalline diamond films were grown by microwave plasma-assisted chemical vapor deposition [8,9]. The quality of the film is good as indicated by the narrowness ($\text{FWHM} = 3.7 \text{ cm}^{-1}$) of the Raman sp^3 diamond bond peak at 1332 cm^{-1} [10,11]; around 1575 cm^{-1} there is a small feature due to graphite and also a weak broad amorphous carbon feature from 1200 through 1650 cm^{-1} . All diamond films used in this study came from a single sheet of diamond film so that the synthesis conditions of each of the samples used were identical [7]. We took FTIR infrared absorption measurements using p-polarized incident light at Brewster's angle to avoid interference effects [12]. The index of refraction is 2.4 for diamond so that Brewster's angle is 67.38°. Spectra were recorded with 2 cm^{-1} resolution.

The Vanderbilt FEL is an upgraded version of the Stanford University Mk III [13] and is tunable over 2–10

* Corresponding author. Tel +1 615 343 0514, fax +1 615 343 7263, e-mail mckimbey@macpost.vanderbilt.edu.

μm wavelengths. It produces “macropulses” consisting of a 5 μs train of ~ 1 ps micropulses at a repetition rate of 2.856 GHz. Macropulses with 360 mJ energy at a repetition rate 20 Hz have been reliably demonstrated. The beam cross-section is Gaussian, $I = I_p \exp(-2r^2/w^2)$. The focal spot diameter is $2f\lambda/\pi w$ and is defined as the region having micropulse intensity greater than $I_p e^{-2}$. We used an $f = 12$ cm focusing lens, $\lambda \sim 3.5$ μm is the wavelength, I_p of ~ 8 MW, and a w -parameter prior to focusing of 0.47 cm. This produces a ~ 56 μm spot diameter with a peak micropulse intensity at the beam center of ~ 650 GW/cm². Beam intensity was controlled by a cross-polarizer. The total power of the beam was measured by a disc calorimeter (Scientech 36-0201). We studied the ablation produced by a single FEL macropulse on a free-standing 10 μm thick CVD diamond film held in a 10^{-9} Torr vacuum.

3. Results and discussion

Using p-polarized light at Brewster's angle to eliminate the interference pattern produces the FTIR transmission spectrum shown in Fig. 1. Even though we use the Brewster angle configuration, it is difficult to avoid the scattering from crystal facets or grain boundaries. This is the

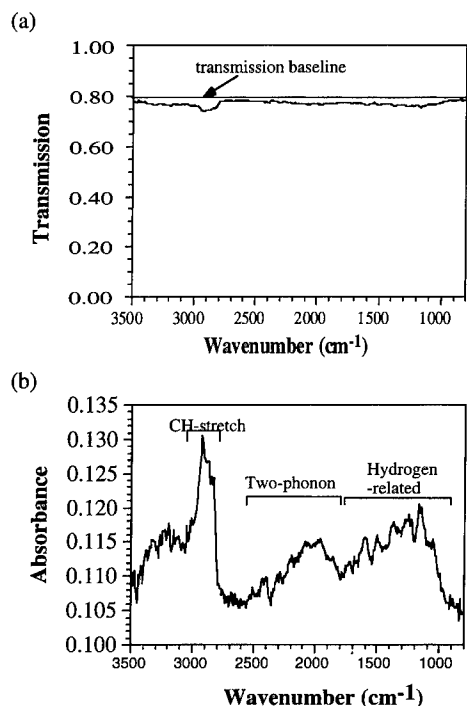


Fig. 1. Transmission and absorbance of a CVD diamond film. (a) Transmission spectrum in the range of 800–3500 cm^{-1} . (b) Absorbance in the same range, covering C–H stretch peak, two-phonon band, and hydrogen related absorption band.

reason why the average transmission baseline is only $\sim 79\%$. If the surface was perfectly flat, reflection would not be expected. However, since the diamond grain size is close to the wavelength of the light source for the FTIR transmission measurement and crystal facets are randomly oriented, the actual reflecting surfaces are distributed around Brewster's angle with respect to the incident light. Even though the spectrum has low signal-to-noise ratio because of the film thickness of 10 μm , the C–H stretch peak at 2900 cm^{-1} can be easily observed. Two-phonon and hydrogen-related bands are also distinguishable, and have been previously identified [6].

According to Lee and Apai [2], there are several C–H stretch modes in the region of 2800–3100 cm^{-1} ; the peak positions for (100) surfaces are at 3070, 3010, 2915, and 2820 cm^{-1} , while for (111) surfaces peaks are found at 3070, 3000, 2930, and 2850 cm^{-1} . The first two peaks in each group are for olefinic C–H (sp^2 hybridized) and the last two in each group are for aliphatic C–H (sp^3 hybridized). Trombetta et al. showed that this 3.5 μm feature consists of two sharp peaks at 2918 and 2834 cm^{-1} which they attribute to CH_2 groups involving sp^3 -bonded carbon [6]. Dischler et al. reported that differently prepared polycrystalline diamond films exhibited considerable differences in shape of the C–H stretch absorption band [3]. They resolved the convoluted C–H stretch band into 10 distinguishable subbands.

In our spectrum, assuming four Lorentzian peaks in this region, curve fitting showed the maximum position is at 2922 cm^{-1} with three smaller peaks at 2831, 2870 and 3002 cm^{-1} . Our samples have olefinic C–H bonds (sp^2) on the grain boundaries and defects as well as aliphatic C–H bonds (sp^3) on the flat facets. Thus the polycrystalline CVD diamond films used in this study may provide a variety of slightly varying bonding conditions, which accounts for the C–H peak shape in our measurements.

Holes produced by FEL pulses with intensities far beyond the ablation threshold were typically 45 μm in diameter, in rough agreement with the estimated focal spot diameter. There are several stages of damage that occur prior to the creation of holes in the film as follows: As the incident photon beam intensity increases, the first experimentally determined indication of damage is a small white spot observed in a SEM micrograph indicating a diminished electrical conductivity. This typically occurs at intensities below 20 GW/cm² depending on wavelength. However, at this early stage of damage no indication of damage is observed with an optical microscope even with high magnification, which means that the FEL irradiation causes some change in the electrical properties but not in the morphology. Praver et al. reported that a slab of natural IIa type diamond first implanted by 2.8 MeV C^+ ions which was subsequently heated with Nd-glass laser irradiation (531 nm, 14 ns pulse length) with a suitable intensity could anneal the implanted layer without any disruption to the morphology [14]. In our case, it is possible that the

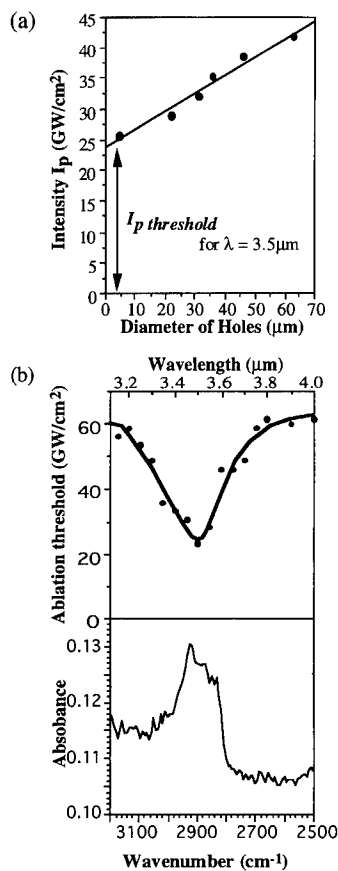


Fig. 2. (a) A plot of the micropulse beam-center intensity I_p versus the resulting hole diameter (for $\lambda = 3.5 \mu\text{m}$). The ablation threshold was defined as I_p extrapolated to zero hole diameter. (b) Top: The wavelength dependence of the ablation threshold. Bottom: The measured IR absorption spectrum in the range of 2500–3200 cm^{-1} .

irradiated area of the polycrystalline diamond was originally conducting due to defects at the grain boundaries, and then laser irradiation annealed the area to change it into a relatively more insulating material than before irradiation. For slightly higher intensities, a black spot appears at the center of white spot, which is probably due to early graphitization arising from the increased temperature.

For higher pulse intensities (20–30 GW/cm^2), plasma-affected areas (dark regions with a diameter of $\sim 500 \mu\text{m}$ each as seen in SEM micrographs) are observed in the region surrounding the irradiated spots [7]. It is probable that these plasma-affected areas become graphite, which is a conducting material. At the same time, a crater is observed at the center of the irradiated spot. The material from the crater obviously contributes to the plasma. The onset of crater formation is the physical manifestation of the ablation threshold which we define below.

By further increasing the intensity ($> 30 \text{ GW}/\text{cm}^2$), the craters evolve into holes that penetrate the entire thickness of the film. The annular region surrounding the hole in some cases became relatively higher than the original film surface level. We determined the massive ablation threshold by irradiating a series of different spots with a single macropulse each and subsequently measuring the hole diameter with a SEM. Fig. 2a shows a plot of the micropulse beam-center intensity I_p versus the resulting hole diameter for the case of $\lambda = 3.5 \mu\text{m}$. The ablation threshold was defined as I_p extrapolated to zero hole diameter. Some error is introduced into this determination because the micropulse intensity within a single macropulse varies slowly by 10–20% over 1 μs time scales. Thus, near the ablation threshold, some of the micropulses within a macropulse are below and some above the threshold. In Fig. 2b, the ablation threshold is shown to exhibit a sharp minimum (23 GW/cm^2 by $3.5 \mu\text{m}$). Fig. 2b emphasizes

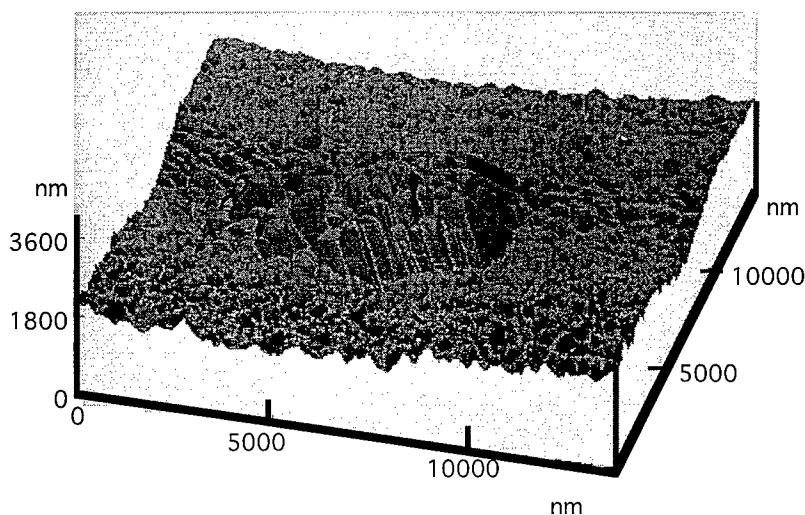


Fig. 3. AFM micrograph of an irradiated spot on a diamond film. The height of the raised region is higher than the original diamond surface level.

the similarity of the threshold curve to the C–H stretch infrared absorption band, which is centered at 3.5 μm and has a FWHM of $\sim 0.2 \mu\text{m}$. Note that the massive ablation threshold, as here defined, is much larger than the threshold for photodesorption ($\sim 3 \text{ GW}/\text{cm}^2$) [7].

Relatively low intensities ($< 30 \text{ GW}/\text{cm}^2$) produced morphological changes observable with the AFM. At the center of the irradiated spot a raised region with crystalline morphology appeared, (See the raised region in Fig. 3) and the area surrounding the raised region became lower than the original surface level. On the other hand, the elevation of the raised region is higher than the original level by about 1.5 μm , which indicates a rapid crystal growth under particular conditions. At slightly higher intensities ($\approx 30 \text{ GW}/\text{cm}^2$), a morphology change indicating graphitization appeared at the center surrounded by a crystalline phase. At even higher intensities craters were observed.

Although we do not know the ablation mechanism in detail, it is clear that the energy of the incident laser light is absorbed mainly by the C–H stretching vibrational mode, which clearly is a multiphoton process. Then the volume surrounding this C–H bond is excited sufficiently to break both C–H and C–C bonds, causing desorption of species such as CH and C_2 , finally resulting in a crater or a hole at the irradiated spot.

Additional work must be done to clarify the mechanism by which the absorbed energy is transferred to the bulk lattice and also to distinguish the effects of localized absorption as in the case of hydrogen impurities as opposed to delocalized absorption by, for example, the two-phonon band.

Acknowledgments

This work was supported by the Office of Naval Research under Contract N00014-91-C-0109. We particularly

acknowledge the efforts of the staff of the Vanderbilt Free-Electron Laser Center and also gratefully acknowledge the staff of the Vanderbilt Microelectronics Laboratory for growing the CVD-diamond films.

References

- [1] A.V. Hamza, G.D. Kubiak, and R.H. Stulen, *Surf. Sci.* 206 (1988) L833; A.V. Hamza, G.D. Kubiak, and R.H. Stulen, *Surf. Sci.* 237 (1990) 35.
- [2] S.-Tong Lee and G. Apai, *Phys. Rev. B* 48 (1993) 2684.
- [3] B. Dischler, C. Wild, W. Müller-Sebert and P. Koidl, *Physica B* 185 (1993) 217.
- [4] E.S. Bliss, *Opto-Electronics* 3 (1971) 99.
- [5] W.L. Smith, J.H. Bechtel, and N. Bloembergen, *Phys. Rev. B* 12 (1975) 706.
- [6] J.M. Trombetta, J.T. Hoggins, P. Klocek, and T.A. McKenna, *SPIE Proc.* 1534 (Diamond Optics IV) (1991) 77.
- [7] A. Ueda, J.T. McKinley, R.G. Albridge, A.V. Barnes, N.H. Tolk, J.L. Davidson and M.L. Languell, *Mat. Res. Soc. Symp. Proc.* 285 (1992) 215.
- [8] M. Kamo, Y. Sato, S. Matsumoto, and N. Setaka, *J. Cryst. Growth* 62 (1983) 1785.
- [9] W. Zhu, B.R. Stover, B.E. Williams, and J.T. Glass, *IEEE Proc.* 79.(5) (1991) 621.
- [10] R.J. Nemanich, J.T. Glass, G. Lucovsky, and R.E. Shroder, *J. Vac. Sci. Technol. A* 6 (1988) 1783.
- [11] J. Wagner, M. Ramsteiner, C. Wild, and P. Koidl, *Phys. Rev. B* 40 (1989) 1817.
- [12] H. Shirai, *J. Electrochem. Soc.* 139 (1992) 3272.
- [13] N.H. Tolk, C.A. Brau, G.S. Edwards, G. Margaritondo and J.T. McKinley, *Short-Wavelength Radiation Sources*, *SPIE* 1552 (1991) 7.
- [14] S. Praver, D.N. Jamieson, S.P. Dooley, P. Spizzirri, K.P. Ghiggino and R. Kalish, *Mat. Res. Soc. Symp. Proc.* 235 (1992) 431; S. Praver, D.N. Jamieson and R. Kalish, *Phys. Rev. Lett.* 69 (1992) 2991.



ELSEVIER

Statistical treatment of adsorbate effects on charge transfer in ion–surface collisions

Zoran L. Mišković^{*,1}, Sydney G. Davison², Frank O. Goodman²

Department of Applied Mathematics, University of Waterloo, Waterloo, Ontario N2L 3G1, Canada

Abstract

We present a theory which describes the effects of adatoms on the resonance charge transfer in ion–surface collisions, based on the statistical method similar to that used in evaluation of the spectral line shapes in plasmas. In front of a surface covered by a submonolayer of alkali atoms, the projectile valence energy level is randomly modulated by the laterally inhomogeneous electrostatic potential of the adlayer. Depending on the surface coverage and the arrangement of adatoms, we investigate the Poisson and Gaussian limits of this random process, and show that the resulting average shift and broadening of the projectile level may influence decisively the charge transfer. Based on the Anderson–Newns Hamiltonian, we study the effects of a random adlayer on the projectile charge state in both near-normal and grazing ion–surface scattering.

1. Introduction

It has been shown, in many experiments over the past ten years [1–3], that the presence of adsorbed alkali atoms on metal surfaces, even at coverages less than about one tenth of a monolayer, may strongly influence the charge transfer between the surface and low-energy atomic projectiles. Since alkali atoms are largely ionized at low coverages [4], one can associate a dipole with an adatom, formed by its positive effective charge Q (say) and the induced screening charge on the surface. A dipole layer, thus formed, induces a lowering of the substrate effective work function (WF) ϕ , according to the Helmholtz formula,

$$\phi = \phi_0 - 2\pi\rho\mu, \quad (1)$$

where ϕ_0 is the WF of a clean surface, ρ is the number of adatoms per unit area of surface, and μ is the dipole moment per adatom. Neglecting the adlayer depolarization at low coverages [4], μ may be considered as being approximately constant, and the linear dependence on ρ in Eq. (1) may lower ϕ by as much as several eV.

It is natural then to expect significant changes in the resonance charge transfer (RCT) between the substrate and

valence levels of low-energy alkali projectiles, which have rather low ionization potentials I . However, Eq. (1) describes the effective WF at macroscopic distances from the surface (much larger than $1/\sqrt{\rho}$), while the RCT probes distances which are typically comparable or smaller than $1/\sqrt{\rho}$ [1,2], where the electrostatic potential of the adlayer is by no means homogeneous across the surface. This lateral inhomogeneity of the adlayer has been shown, both experimentally [1,2] and theoretically [5,6], to yield a more gradual ϕ -dependence of the ion-survival probability P in alkali ion–surface scattering than expected from a homogeneous surface. Theoretical studies describe the RCT by means of the time-dependent Anderson–Newns (TDAN) Hamiltonian [7], either in the spinless form [1,2,5], or in the form involving the intra-atomic correlation [6]. In these studies, the adlayer inhomogeneity has been treated in several ways, including computer simulations, which obtain P as a statistical average over an ensemble of projectile trajectories with respect to a given configuration of adatoms [1,2], or employing phenomenological parameters, such as elevated electron temperature [5] and the ϕ -dependent RCT rate Δ (see below) [6]. Recently, we have proposed [8] a stochastic, parameter-free, treatment of the adsorbate effect on RCT, which we further elaborate in this report.

Atomic units will be used, unless otherwise indicated.

2. Description of adlayer

The basic idea underlying the statistical treatment of the adlayer effects in ion–surface scattering, rests on the

* Corresponding author, tel. +1 519 885 1211, ext. 5463, fax +1 519 746 6530, E-mail: zmiskovic@math.uwaterloo.ca.

¹ On leave from the Institute for Nuclear Sciences, Belgrade, Serbia, Yugoslavia.

² Also with the Department of Physics, University of Waterloo, and the Guelph–Waterloo Program for Graduate Work in Physics.

assumption that the main effect of its inhomogeneous electrostatic potential on RCT is to modulate the projectile valence energy level ϵ_a . If the projectile position is defined by the vector \mathbf{R} , in the directions parallel to the surface, and the distance Z from the surface (referred to the image plane), one can write, within first-order perturbation theory, $\epsilon_a(\mathbf{R}, Z) = \epsilon_s(Z) + \epsilon_r(\mathbf{R}, Z)$. ϵ_s denotes the “smooth” part of ϵ_a , containing only Z -dependent shifts of the unperturbed level ϵ_a^∞ , such as the image shift in front of a “jellium” surface, with the classical limit $\epsilon_s(Z) = \epsilon_a^\infty + 1/(4Z)$ for $Zk_{\text{TF}} \gg 1$ (k_{TF} being the Thomas–Fermi wave number of the substrate quasi-free-electron gas). ϵ_r denotes the “random” part of ϵ_a , resulting from the adlayer potential

$$\epsilon_r(\mathbf{R}, Z) = - \sum_{n=1}^N V_d(\mathbf{R} - \mathbf{r}_n, Z), \quad (2)$$

where we assume that N stationary adatoms are located at positions $\mathbf{r}_1, \mathbf{r}_2, \dots, \mathbf{r}_N$ across a large surface area S , so that $\rho = N/S$, and $V_d(\mathbf{R}, Z)$ is the electrostatic potential produced by an adatom at a position $\{\mathbf{R}, Z\}$ away from it. There are different levels of sophistication in obtaining $V_d(\mathbf{R}, Z)$. Representing each adatom as a point charge Q at a distance d from the surface, one can use the linear-response approximation for the substrate screening, and obtain the 2-dimensional Fourier transform $\tilde{V}_d(\mathbf{q}, Z)$ of $V_d(\mathbf{R}, Z)$ directly in terms of the surface dielectric function (see, e.g., Ref. [9]). With the condition $(Z + d)k_{\text{TF}} \gg 1$, one recovers the classical expression for $V_d(\mathbf{R}, Z)$, describing a dipole of length $2d$, which is centered at the image plane. It should be noted that, in a more advanced treatment, using the local-density approximation [10], the adatom potential is much more screened in radial directions \mathbf{R} than indicated by classical dipole formula. Since we shall be interested mostly in large distances from the adatoms, the following approximation will be used occasionally: $V_d(\mathbf{R}, Z) = \mu Z(Z^2 + R^2)^{-3/2}$, corresponding to $\tilde{V}_d(\mathbf{q}, Z) = 2\pi\mu \exp(-qZ)$, with $\mu = 2(d + k_{\text{TF}}^{-1})Q$ [9].

We also need information about the arrangement of atoms in the adlayer. It has been shown experimentally, by using low-energy electron diffraction (LEED) [11], that adatoms are spread randomly at low coverages. The resulting diffuse, ring-shaped, LEED patterns [11] indicate that adatoms are dispersed over the surface, in such a way, as to maximize the distance between them, owing to the strong dipole–dipole repulsion, which is believed to dominate the adatom–adatom interaction at low coverages [4,9]. In addition, computer simulations, using a disordered adlayer structure [2], showed better agreement with the experimental data for the ϕ -dependence of P than those using an ordered structure. Let us assume that the adlayer is described by the N -particle distribution function $f_N(\mathbf{r}_1, \mathbf{r}_2, \dots, \mathbf{r}_N)$, which we take to be normalized to unity. In the following section, we shall need the reduced

one-particle, $f_1(\mathbf{r})$, and two-particle, $f_2(\mathbf{r}_1, \mathbf{r}_2)$, distribution functions (which are related to f_N in the usual manner, and are both normalized to unity), as well as the pair-correlation function of the adlayer, namely,

$$g_2(\mathbf{r}_1, \mathbf{r}_2) = S^2[f_2(\mathbf{r}_1, \mathbf{r}_2) - f_1(\mathbf{r}_1)f_1(\mathbf{r}_2)]. \quad (3)$$

For a homogeneous disordered adlayer, one normally has $f_1(\mathbf{r}) = 1/S$ and $f_2(\mathbf{r}_1, \mathbf{r}_2) = f_2(|\mathbf{r}_1 - \mathbf{r}_2|)$. The pair-correlation function may be related to the LEED pattern intensity, that is, to the corresponding interference function, defined by

$$S(q) = 1 + 2\pi\rho \int d\mathbf{r} r g(r) J_0(qr), \quad (4)$$

where $g(r) \equiv g_2(|\mathbf{r}|)$ and J_0 is a Bessel function of the first kind. We shall model $g(r)$ by -1 for $r \leq 1/\sqrt{\pi\rho}$ and by 0 for $r > 1/\sqrt{\pi\rho}$, in which case, the structure factor $S(q)$ of the adlayer corresponds to the ring-shaped LEED patterns, whose radii scale as $\sqrt{\rho}$ [11].

3. Description of charge transfer

In recent experiments [2,3], the charge state of scattered particles was dominated by, and determined from, the parts of the scattered energy spectra corresponding to direct projectile–substrate atom scattering. Describing the projectile motion by a classical trajectory, we note that the normal component of the projectile velocity v_\perp is sufficiently small (typically of order of 0.01) that loss of memory of the initial charge state may be expected [7]; i.e., only large distances Z on the outgoing part of the trajectory are important for the final charge-state formation. Thus, for low coverages, we assume that the projectile trajectory is unaffected by the presence of adatoms, and model it by a specular reflection, $Z(t) = v_\perp |t|$ and $\mathbf{R}(t) = \mathbf{v}_\parallel t$, where \mathbf{v}_\parallel is the projectile velocity component parallel to the surface.

Assuming that the adatom potential is sufficiently screened inside the surface, we take, in the TDAN Hamiltonian, the coupling term V_{ak} between the projectile and substrate electron orbitals to be unaffected by the presence of adatoms, and the momenta \mathbf{k} to describe quasi-free electron states of a jellium surface. However, on the vacuum side, the tunneling rate between the projectile and the surface is increased in a narrow cylindrical region above an adatom, due to the lowering of the potential barrier [10,12]. We believe that the neglect of this effect on V_{ak} may be justified at low coverages and low ion velocities, when the projectile trajectory mainly samples the surface regions with no adatoms. Without full multi-dimensional calculations of the tunneling rates, it is difficult to specify the areas of the cylindrical regions above the adatoms where increased tunneling occurs, but estimates show that they are of the order of atomic size [13,14], which is much smaller than the mean distance between the

adatoms, $1/\sqrt{\pi\rho}$, at low coverages. In addition, the effect of the increased tunneling rate on RCT is masked somewhat by the fact that the dipole potential of the adlayer, in the vicinity of an adatom, locally lowers the projectile's valence level below the Fermi level, thus promoting ion neutralization anyway [15]. Thus, by taking $V_{ak} = V_{ak}(Z)$, one can obtain, from the spinless form of the TDAN Hamiltonian, the expectation value (with respect to the substrate ground-state electron configuration) of the projectile orbital occupation number, after the completion of the scattering, in the form [7]

$$\begin{aligned} \langle n_a(\infty) \rangle &= \frac{1}{\pi} \int_{-\infty}^{\infty} d\epsilon f(\epsilon) \int_{-\infty}^{\infty} dt_1 \\ &\times \int_{-\infty}^{\infty} dt_2 \sqrt{\Delta(t_1)\Delta(t_2)} \\ &\times \exp \left\{ - \int_{t_1}^{\infty} d\tau \Delta(\tau) - \int_{t_2}^{\infty} d\tau \Delta(\tau) \right. \\ &\left. + i \int_{t_1}^{t_2} d\tau [\epsilon - \epsilon_a(\tau)] \right\}. \end{aligned} \quad (5)$$

Here, $\epsilon_a(t) = \epsilon_a(v_{\parallel}t, Z(t))$ in the trajectory approximation, and the RCT rate $\Delta(t) = \pi \sum_k |V_{ak}(Z(t))|^2 \delta(\epsilon_k - \epsilon_a(t))$ is unaffected by the variation of $\epsilon_a(t)$ in the wide-band approximation [7]. Modeling the rate by $\Delta(t) = \Delta_0 \exp(-\alpha Z(t))$, we can neglect the so-called memory term in Eq. (5), on the ground that $\alpha v_{\perp} \ll 4\Delta_0$ [7]. Note that the Fermi level ϵ_F remains constant, even with adatoms on the surface, and the Fermi–Dirac (FD) distribution $f(\epsilon)$ can be modified, in such a way, as to include the Doppler effect due to v_{\parallel} , by shifting the Fermi sphere in the momentum space, according to $\mathbf{k} \rightarrow \mathbf{k} + v_{\parallel}$ [7].

Note that the function $\epsilon_a(t)$ contains a random function of time $\epsilon_r(t) = \epsilon_r(v_{\parallel}t, Z(t))$, or a stochastic process, whose realization depends, via Eq. (2), on the configuration of the atoms in the adlayer [16]. A large number of ion trajectories over the surface provides the ergodicity of this process, which is equivalently described by an ensemble of all configurations f_N , seen from a particular trajectory. Since $\epsilon_r(t)$ appears in the phase of the time-integrals in Eq. (5), we have the so-called random phase modulation [16], which acts to destroy the quantum phase coherence in Eq. (5). To see why it is important to describe the adlayer statistically, let us consider a single adatom at a distance r away from the projectile turning point at $t = 0$. The projectile forgets its initial quantum phase, if the total phase change η , due to the single adatom (defined as the time-integral of $V_d(v_{\parallel}t - r, v_{\perp}|t|)$ between $-\infty$ and ∞), is greater than, say, π [17]. Using the classical dipole potential for V_d , and assuming normal incidence ($v_{\parallel} = 0$), this occurs for distances r smaller than the so-called Weiskopf radius $r_w = d \operatorname{cosech}(\pi v_{\perp}/4Q)$. Thus, whenever the coverage ρ exceeds, say, $\rho_w = (\pi r_w^2)^{-1}$, one has to take into account the collective action of the adatoms on

the quantum phase evolution. In experimental situations [1–4], one typically has $v_{\perp} \ll Q \leq 1$, so that, $\rho_w \approx (\pi/4)(v_{\perp}/\mu)^2$, which has a rather small value, because of the large dipole moments of the alkali adatoms (several a.u.) [4]. Thus, practically speaking, one has to treat the potential of the adlayer as a whole, at all coverages. Alternatively, for sufficiently large v_{\perp} , one can consider a localized interaction with the nearest adatom. Allowing for grazing conditions, where $v_{\perp} = v \cos \theta \ll v_{\parallel} = v \sin \theta \approx 1$ (v being the total projectile velocity, and θ the angle of incidence with respect to the surface normal), one can obtain $\bar{\eta}$ as the average over the azimuthal angles with respect to the adatom at a distance r . Then, the phase change may be large ($\bar{\eta} > \pi$), only when $\max(r/d, \tan \theta) < \operatorname{cosech}(\pi v/4Q)$, a condition which is typically not fulfilled in grazing scattering, again indicating that the interaction with the nearest adatom dominates the phase change in Eq. (5). The two limits of the collective and the nearest-adatom influence of the adlayer on the quantum phase in Eq. (5) will be seen below to correspond, respectively, to the cases of slow and fast modulations of the random function $\epsilon_r(t)$.

4. Stochastic analysis of adsorbate effects

Now, taking the expectation value, denoted by $\langle \cdots \rangle$, of Eq. (5), by means of the distribution function f_N , produces in the right-hand side the relaxation function

$$R(t_1, t_2) = \left\langle \exp \left[-i \int_{t_1}^{t_2} d\tau \epsilon_r(\tau) \right] \right\rangle, \quad (6)$$

which is nothing but the characteristic functional of the random function $\epsilon_r(\tau) = \epsilon_r(v_{\parallel}\tau, Z(\tau))$, defined by Eq. (2). Based on the standard theory of pressure broadening of spectral lines in plasmas [18], the expectation value in Eq. (6) may be expressed in terms of the increasing order of correlations in the adatom positions within the adlayer. At very low coverages and small distances from the adlayer, only few nearest adatoms contribute significantly to $\epsilon_r(t)$, which then represents a *Poisson process* [16]. In such a situation, it is usually sufficient to neglect the correlation between the adatom positions by taking $g(r) = 0$, or $S(q) = 1$, so that,

$$\begin{aligned} R_P(t_1, t_2) &= \exp \left\{ \rho \int d^2r \right. \\ &\times \left[\exp \left(i \int_{t_1}^{t_2} d\tau V_d(v_{\parallel}\tau - r, Z(\tau)) \right) - 1 \right] \right\}. \end{aligned} \quad (7)$$

As the coverage increases, and we move away from the surface, the random function $\epsilon_r(t)$ meets the conditions for a *Gaussian process*, containing a large number of weak

contributions to the potential of the adlayer. In this case, one can use the cumulant expansion for $R(t_1, t_2)$ [16] and retain the first two terms

$$R_G(t_1, t_2) = \exp \left\{ -i \int_{t_1}^{t_2} d\tau \langle \epsilon_r(\tau) \rangle - \frac{1}{2} \int_{t_1}^{t_2} d\tau_1 \int_{t_1}^{t_2} d\tau_2 \times C_r(|\tau_2 - \tau_1|; Z(\tau_1), Z(\tau_2)) \right\}, \quad (8)$$

where the mean value of $\epsilon_r(\tau)$ is a function of $Z(\tau)$, i.e., $\langle \epsilon_r(\tau) \rangle = -\rho \tilde{V}_d(0, Z(\tau))$, which simply represents a drop of the potential through a continuous dipole layer, with the value $\Delta\phi = \phi - \phi_0 = -2\pi\rho\mu$ outside the layer. Since the correlation between the adatom positions is important in the Gaussian limit, the autocorrelation function of $\epsilon_r(\tau)$, viz.,

$$\begin{aligned} C_r(|\tau_2 - \tau_1|; Z(\tau_1), Z(\tau_2)) \\ \equiv \langle \epsilon_r(\tau_1) \epsilon_r(\tau_2) \rangle - \langle \epsilon_r(\tau_1) \rangle \langle \epsilon_r(\tau_2) \rangle \\ = \frac{\rho}{2\pi} \int_0^\infty dq q S(q) J_0(qv_{\parallel}|\tau_2 - \tau_1|) \\ \times \tilde{V}_d(q, Z(\tau_1)) \tilde{V}_d(q, Z(\tau_2)), \end{aligned} \quad (9)$$

is expressed in terms of the structure factor $S(q)$ of the adlayer.

The main difficulty with the stochastic analysis of the random function $\epsilon_r(\tau)$ lies in the fact that it is not stationary, due to its dependence on $Z(\tau)$. However, it is locally stationary around the symmetric time $t = (t_1 + t_2)/2$, owing to the rather slow modulation by the low normal velocity v_{\perp} . Henceforth, we shall consider the Poisson limit, only for a non-grazing scattering ($v_{\parallel} \ll 1$). Thus, we obtain the relaxation function (7) in a stationary form, $R_p(t_1, t_2) \approx R_p(\bar{t}, Z)$, by writing the time-integral in Eq. (7) as $i\tilde{V}_d(\bar{r}, Z)$, where $\bar{t} = t_2 - t_1$ and $Z = Z(\bar{t})$; this corresponds to Holtmark's theory of static line broadening [17,18]. In the Gaussian limit, one can obtain the relaxation function (8) in a stationary form, $R_G(t_1, t_2) \approx R_G(\bar{t}, Z)$, by writing the second term of the cumulant expansion in Eq. (8) as $\int_0^{\bar{t}} d\tau (\bar{t} - \tau) C_r(|\tau|; Z)$ [16], where $C_r(|\tau|; Z)$ is given by Eq. (9) with $Z(\tau_1) = Z(\tau_2) = Z(\bar{t}) = Z$. This is valid, e.g., for non-grazing scattering outside the adlayer, under the condition

$$v_{\perp}^2 \frac{\partial^2}{\partial Z^2} C_r(0, Z) \ll 12 C_r^2(0, Z),$$

or $\rho_w \ll \rho \leq (\pi Z^2)^{-1}$, which is typically fulfilled in experiments [2] (see below). Note, however, that the random function $\epsilon_r(\tau)$ is stationary with respect to the motion parallel to the surface, and the speed of modulation is given by the local correlation time τ_c at $Z = Z(\bar{t})$, defined by means of the autocorrelation function $C_r(\tau; Z)$ [16],

with the order of magnitude outside the layer $\tau_c \approx 2Z/v_{\parallel}$ (see below). Obviously, at distances close to the adlayer and under grazing conditions, one may expect a fast modulation of $\epsilon_r(\tau)$, resulting from the contribution of the nearest adatoms [16]. In this case, one can again neglect the correlated contribution of the other adatoms by taking $S(q) = 1$ in Eq. (9). Conversely, in non-grazing scattering ($v_{\parallel} \ll 1$) well outside the adlayer ($Z \geq 1/\sqrt{\pi\rho}$), the correlation time is large, and many adatoms simultaneously contribute to $\epsilon_r(\tau)$, so that it is important to describe their correlated positions by the structure factor $S(q)$ in Eq. (9). Using the expression for V_d from Section 2, we shall study the Poisson and Gaussian limits in non-grazing scattering, as well as the effects of parallel velocity on the Gaussian limit in grazing scattering.

5. Discussion

With the representation of the relaxation function (6) in a local form $R(\bar{t}, Z)$, dependent on $\bar{t} = t_2 - t_1$ and $Z = Z((t_1 + t_2)/2)$, one can manipulate accordingly the time-integrals in Eq. (5). In doing so, one encounters a situation where the destruction of the quantum phase by the relaxation function is analogous to increasing the temperature in the FD distribution, or to its smearing by the Doppler effect in grazing scattering. This enables one to obtain from Eq. (5) a semiclassical result [7] for the "double" expectation value of the occupation number in the form

$$\begin{aligned} \langle \langle n_a(\infty) \rangle \rangle &= \frac{2}{v_{\perp}} \int_{Z_0}^{\infty} dZ F(\epsilon_s(Z), Z) \Delta(Z) \\ &\times \exp \left[-\frac{2}{v_{\perp}} \int_Z^{\infty} dZ' \Delta(Z') \right]. \end{aligned} \quad (10)$$

Here, $F(\epsilon, Z)$ is the convolution $F(\epsilon, Z) = \int d\epsilon' f(\epsilon + \epsilon') \tilde{R}(\epsilon', Z)$ of the FD distribution $f(\epsilon)$ with the Fourier transform $\tilde{R}(\epsilon, Z)$ of $R(\bar{t}, Z)$, which characterizes the spectral line shape in plasma broadening problems [17,18]. Note that the integrand in Eq. (10), apart from the factor $F(\epsilon_s(Z), Z)$, is a peaked function of Z at the so-called *freezing distance* $Z_f = \alpha^{-1} \log(2\Delta_0/\alpha v_{\perp})$, which strongly suppresses the contributions to the integral for $Z < Z_f$. Z_f is typically very large, e.g., for scattering of K^+ ions with a kinetic energy of 100 eV from a K-covered Cu(100) surface [2], it is estimated to be $Z_f \approx 10$ [8]. Then, related to the memory-loss effect, Z_0 in Eq. (10) may be any point in the surface region ($Z_0 \approx 1$) [7], and one can obtain from Eq. (10) the *freezing* solution $\langle \langle n_a(\infty) \rangle \rangle \approx F(\epsilon_s(Z_f), Z_f)$, provided F is a slow function of Z . More importantly, we only need a proper description of the relaxation function $R(\bar{t}, Z)$, or $\tilde{R}(\epsilon, Z)$, for fairly large distances $Z \geq Z_f$, so that the use of the approximate dipole potential V_d from Section 2 seems partly justified. It is also important to relate such distances Z to the corrugation of

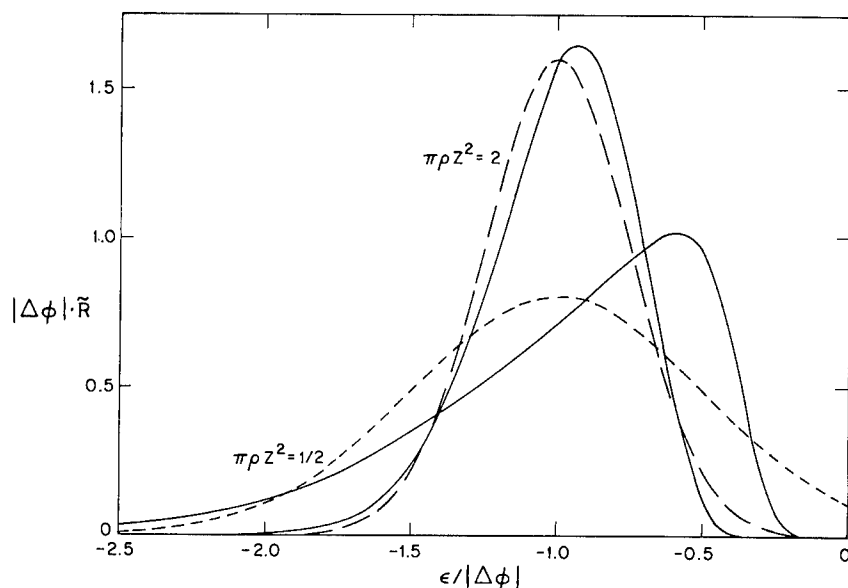


Fig. 1. The ϵ -dependence (in units of $|\Delta\phi| = 2\pi\rho\mu$) of the Fourier transform $\tilde{R}(\epsilon, Z)$ (in units of $|\Delta\phi|^{-1}$) of the Poisson (solid lines) and Gaussian (dashed lines) limits for the relaxation function $R(\epsilon, Z)$, for the two values of the parameter $\pi\rho Z^2$, $\frac{1}{2}$ and 2.

the adlayer, determined by the coverage ρ , which is usually expressed in terms of the relative coverage $\Theta = \rho/\rho_0$, where ρ_0 is the surface density of the substrate atoms ($\rho_0 = 0.0428$ for Cu(100)). Experiments [2] have been conducted for $\Theta < 0.1$, that is, with the mean distances between the adatoms $1/\sqrt{\pi\rho} > 10$ ($\sim Z_f$). As regards the Weisskopf radius, with the dipole moment $\mu \approx 5.28$ [2,8], we find $r_w \approx 10^2$, or $\Theta_w \approx 10^{-4}$. Obviously, the area of the adsorbed layer, influencing the projectile

valence level fluctuations is huge, owing to the long range of the dipole potential.

The first moment of $\tilde{R}(\epsilon, Z)$ is generally just $\langle \epsilon_f(Z) \rangle$, describing the average lowering of the projectile valence level ϵ_a due to the alkali adatoms, with the value $\Delta\phi$ outside the adlayer. The breadth $B(Z)$ of $\tilde{R}(\epsilon, Z)$ describes the dispersion of the valence level due to the inhomogeneity of the adlayer, and also facilitates the semiclassical approximation (10), provided $B(Z) \gg |\alpha v_\perp$

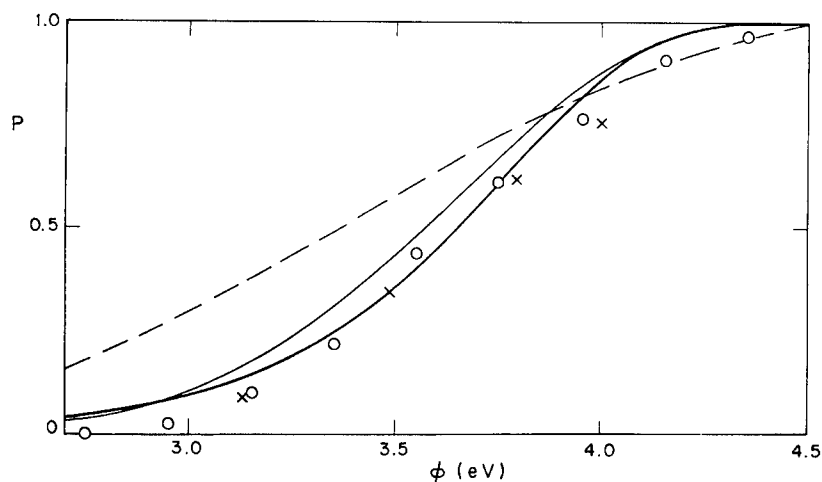


Fig. 2. The work function dependence of the ion-survival probability for 100 eV ions K^+ scattered from a K-covered Cu(100) surface. Freezing solutions, based on the Poisson (dashed line) and Gaussian (thin solid line) forms of the relaxation function, as well as the result of integration of Eq. (10) with the Gaussian form, are compared with the computer simulation (circles) and experimental data (crosses) of Ref. [2].

$-\Delta(Z)$ [7,19]. In the Gaussian limit, for non-grazing scattering ($v \ll 1$), the ϵ -dependence of $\tilde{R}_G(\epsilon, Z)$ is described by the Gaussian shape, peaked at $\Delta\phi$, with the breadth

$$B_{ng}(Z) = \sqrt{2C_r(0; Z)} \\ = \sqrt{\pi\rho} \frac{\mu}{Z} \left[1 - 8\pi\rho Z^2 \right. \\ \left. \times \left(1 - 2\sqrt{\pi\rho} Z / \sqrt{1 + 4\pi\rho Z^2} \right) \right]^{1/2}. \quad (11)$$

This same expression describes also the breadth in the Poisson limit for non-grazing scattering, but the ϵ -dependence of $\tilde{R}_p(\epsilon, Z)$ will be generally skewed with respect to the Gaussian shape. This is best seen in Fig. 1, where we compare the Poisson (solid lines) with the Gaussian (dashed lines) limits of $\tilde{R}(\epsilon, Z)$, with the neglect of the adatom pair-correlation function ($g(r) = 0$). From this figure, one concludes that the Gaussian limit may be expected to be a poorer approximation for $\tilde{R}(\epsilon, Z)$ than the Poisson limit, at the lowest coverages ($\pi\rho Z^2 < 1$). In Fig. 2, we have plotted the ϕ -dependence of the ion-survival probability $P = 1 - \langle \langle n_a(\infty) \rangle \rangle$, by using the freezing solution of Eq. (10), based on the Poisson (dashed line) and Gaussian (thin solid line) forms of $\tilde{R}(\epsilon, Z)$ for non-grazing scattering, as well as the result of the numerical integration of Eq. (10) with the Gaussian form (thick solid line). The parameters used correspond to the 100 eV potassium scattering from K/Cu(100) [2,8], while the crosses and the circles in Fig. 2 represent, respectively, the experimental and the computer simulation data [2]. Note that the Poisson limit gives a better agreement with the simulation data at high WF (the lowest coverages), but the Gaussian limit, involving the structure factor of the adlayer $S(q)$ in Eqs. (8) and (9), agrees better with the data at lower WF, indicating the importance of the adlayer structure at increased coverages. The agreement with the experimental data may be improved at higher coverages (lower WF) by taking into account the intra-atomic correlation effects in the TDAN, which should result in a reduction of P [6,19].

Considering the Gaussian limit for grazing scattering, the breadth $B_g(Z)$ of $\tilde{R}_G(\epsilon, Z)$ is reduced with respect to the value in Eq. (11) by the well-known effect of motional narrowing of the spectral shape [16], which accompanies a fast modulation of the random function $\epsilon_i(\tau)$, and $\tilde{R}_G(\epsilon, Z)$ no longer has a Gaussian shape. For sufficiently fast modulation ($B_{ng}\tau_c \ll 1$), one can estimate the breadth as [16]

$$B_g(Z) \approx C_r(0; Z)\tau_c \\ = \int_0^\infty d\tau C_r(\tau; Z) \\ = \pi\rho \frac{\mu^2}{v_\parallel Z} \left(\sqrt{1 + 4\pi\rho Z^2} - 2\sqrt{\pi\rho Z} \right)^2. \quad (12)$$

Actually, neglecting the pair-correlation function ($g(r) = 0$) of the adlayer in the limit $\rho < (4\pi Z^2)^{-1}$, one obtains

$$\tilde{R}_G(\epsilon, Z) = \frac{1}{\pi} \frac{ab e^{ab}}{\sqrt{(\epsilon - \Delta\phi)^2 + b^2}} \\ \times K_1 \left(a\sqrt{(\epsilon - \Delta\phi)^2 + b^2} \right), \quad (13)$$

where $a \equiv 2Z/v_\parallel \approx \tau_c$ and $b \equiv \pi\rho\mu^2/(v_\parallel Z) \approx B_g$, with K_1 being a modified Bessel function. The shape of this function nicely represents the transition from a Gaussian to a Lorentzian shape, as the parallel velocity increases from values $v_\parallel \ll \sqrt{\pi\rho}\mu$ to values $v_\parallel \gg \sqrt{\pi\rho}\mu$. Note that the narrowing of $\tilde{R}_G(\epsilon, Z)$ in grazing scattering is accompanied by a broadening of the FD distribution function itself by an amount $\sim v_F v_\parallel$, due to the Doppler effect [7] (where v_F is the Fermi velocity of electrons in the surface). The effects of the adlayer on the ion-survival probability in grazing scattering will be explored in more detail elsewhere.

Acknowledgements

The work of SGD and FOG was supported by the Natural Sciences and Engineering Research Council of Canada. ZLM thanks the Department of Applied Mathematics, University of Waterloo, for its kind support.

References

- [1] J.J.C. Geerlings and J. Los, Phys. Lett. A 102 (1984) 204; J.J.C. Geerlings, L.F.Tz. Kwakman and J. Los, Surf. Sci. 184 (1987) 305.
- [2] G.A. Kimmel, D.M. Goodstein, Z.H. Levine and B.H. Cooper, Phys. Rev. B 43 (1991) 9403.
- [3] L.Q. Jiang, Y.D. Li and B.E. Koel, Phys. Rev. Lett. 70 (1993) 2649; K.A.H. German, C.B. Weare, P.R. Varekamp, J.N. Andersen and J.A. Yarmoff, Phys. Rev. Lett. 70 (1993) 3510.
- [4] H.P. Bonzel, A.M. Bradshaw and G. Ertl, eds., Physics and Chemistry of Alkali Metal Adsorption (Elsevier, Amsterdam, 1989).
- [5] P. Nordlander and J.C. Tully, Surf. Sci. 211/212 (1989) 207.
- [6] L. Pan, Y. Wang, F. Huang, D. Fang, J. Tang and F. Yang, Nucl. Instr. and Meth. B 90 (1994) 49.
- [7] R. Brako and D.M. Newns, Rep. Prog. Phys. 52 (1989) 655; J. Los and J.J.C. Geerlings, Phys. Rep. 190 (1990) 133.
- [8] Z.L. Mišković, S.G. Davison and F.O. Goodman, Phys. Rev. Lett. 71 (1993) 4075.
- [9] O.M. Braun and V.K. Medvedev, Sov. Phys. Usp. 32 (1989) 328.
- [10] P. Nordlander and N.D. Lang, Phys. Rev. B 44 (1991) 13681.
- [11] R.L. Gerlach and T.N. Rhodin, Surf. Sci. 17 (1969) 32; T. Aruga, H. Tochihara and Y. Murata, Surf. Sci. 158 (1985) 490; 175 (1986) L725.

- [12] R.K. Janev and S.B. Vojvodić, *J. Phys. B* 13 (1980) 2481.
- [13] C.C. Hsu, A. Bousetta, J.W. Rabalais and P. Nordlander, *Phys. Rev. B* 47 (1993) 2369.
- [14] M. Sumetskii and A.A. Kornyshev, *Phys. Rev. B* 48 (1993) 17493.
- [15] I.F. Urazgil'din, *Phys. Rev. B* 47 (1993) 4139.
- [16] R. Kubo, in: *Fluctuation, Relaxation and Resonance in Magnetic Systems*, ed. D. Ter Haar (Oliver and Boyd, Edinburgh, 1961) p. 23.
- [17] V.S. Lisitsa, *Sov. Phys. Usp.* 20 (1977) 603.
- [18] G. Peach, *Adv. Phys.* 30 (1981) 367.
- [19] D.C. Langreth and P. Nordlander, *Phys. Rev. B* 43 (1991) 2541.



ELSEVIER

CN^{*} desorption from potassium-metal surfaces under electron bombardment

S. Vijayalakshmi^{*}, A.V. Barnes, R.G. Albridge, N.H. Tolk

*Center for Molecular and Atomic Studies at Surfaces, Department of Physics and Astronomy, Vanderbilt University,
Nashville, TN 37235, USA*

Abstract

First measurements of the energy-dependent desorption cross sections near threshold energy for electron-stimulated desorption of excited CN molecules from potassium-metal surfaces are presented. Threshold energies were observed to be different when the alkali metal surface was exposed to a CO₂ + N₂ mixture from that when exposed to H₂ gas, leading to the conclusion that two different chemical processes are involved. The rotational energy distribution was observed to be independent of incident electron energy. We postulate a desorption model similar to the Antoniewicz model.

1. Introduction

Desorption induced by electronic transitions (DIET) which includes electron- and photon-stimulated desorption [1] (ESD and PSD), provides information on the role of potential energy surfaces in adsorbate–surface interaction. Study of the desorption threshold behavior of ESD processes not only clarifies the basic excitation mechanism but also provides information about the sites and bonding states of the adsorbed species [2]. There are three leading models for the production of adsorbates on the surface by electrons and energetic photons: (a) the MGR (Menzel, Gomer, and Redhead) model [3], (b) the Knotek–Feibelman model [2], and (c) the Antoniewicz model [4].

In thermal molecular desorption experiments, the rotational distributions are observed to have a temperature-dependent Boltzmann-like character [5]. In surface molecule scattering experiments, rotational distributions are found to be distinctly non-Boltzmann [6], to vary only weakly with surface temperature and to depend strongly on the energy and the angle of the incident particle. Jun Xu and co-workers [7] have observed that the rotationally resolved spectrum of electronically stimulated CN desorption is independent of the substrate temperature and incident energy at energies much higher than the threshold energies.

In ESD, energy thresholds are difficult to determine as the energy transferred is not a definite quantity. However, the shape of the desorption cross section as a function of incident electron energy can be used to understand the

potential energy surfaces and the available final density of states for the electrons. Due to this deconvolution of the final density of states, no answers have yet been given to problems such as how many precursors participate in the desorption process, and whether the precursors in ESD and PSD are the same. In order to provide information on these problems, we have studied the desorption of excited CN due to electron bombardment near threshold energy. In this paper, we report the desorption yield of excited CN molecules from a potassium-rich surface as a function of incident-electron energy and the threshold-energy. In addition, the rotational distribution and ratio of various vibrational populations of the desorbing CN molecules near threshold energies are measured. The goal of these measurements is to understand the surface chemistry responsible for CN formation and the bond breaking that is responsible for the desorption of CN molecules in an excited state.

2. Experiment

The experimental procedure was similar to that described previously [8]. The experimental surface was prepared by evaporating a thick layer of potassium metal on a glass substrate under UHV conditions. Gases were introduced using two leak valves. A programmable electron gun, based on the design of Stoffel and Johnson [9] operating in the range of 4–700 eV was used for threshold measurements. Optical excitations arising due to electron irradiation were measured using a cooled photomultiplier tube attached to a McPherson 0.3 m monochromator. These optical excitations show sharp features correspond-

^{*} Corresponding author, tel. +1 615 322 6803, fax +1 615 343 7263, E-mail: vijayas@ctrvax.vanderbilt.edu.

ing to the $\text{CN}^* \text{B}^2\Sigma^+ (v=0)$ to $\text{X}^2\Sigma^+ (v=0)$ transition at 388 nm; another feature centered at 310 nm is due to OH^* . Some of the less prominent features at 357 nm and 420 nm are attributed to the $\text{CN} \text{B}^2\Sigma^+ (v=1)$ to $\text{X}^2\Sigma^+ (v=0)$ and $\text{B}^2\Sigma^+ (v=0)$ to $\text{X}^2\Sigma^+ (v=1)$ transitions respectively. Once the CN features were identified, energy dependent threshold measurements were taken using a peak counting rate program with linear background subtraction. The desorption yield at each energy value was normalized to electron current and the yield at beam energy 50 eV. This later normalization is necessary to

account for the dynamic changes during the measurements. For experiments with H_2 exposure, the CN signature was first observed after dosing with CO_2 and N_2 mixture and then H_2 gas was introduced using one of the leak valves.

The beam energy reported here was measured as the potential difference between the gun filament and the sample. The kinetic energy E_{kin} of the electrons is given by the potential difference between the vacuum levels of cathode and target [10]. However, measured energy U_{ct} which is the potential difference between cathode and target, lies between the two Fermi levels and hence the

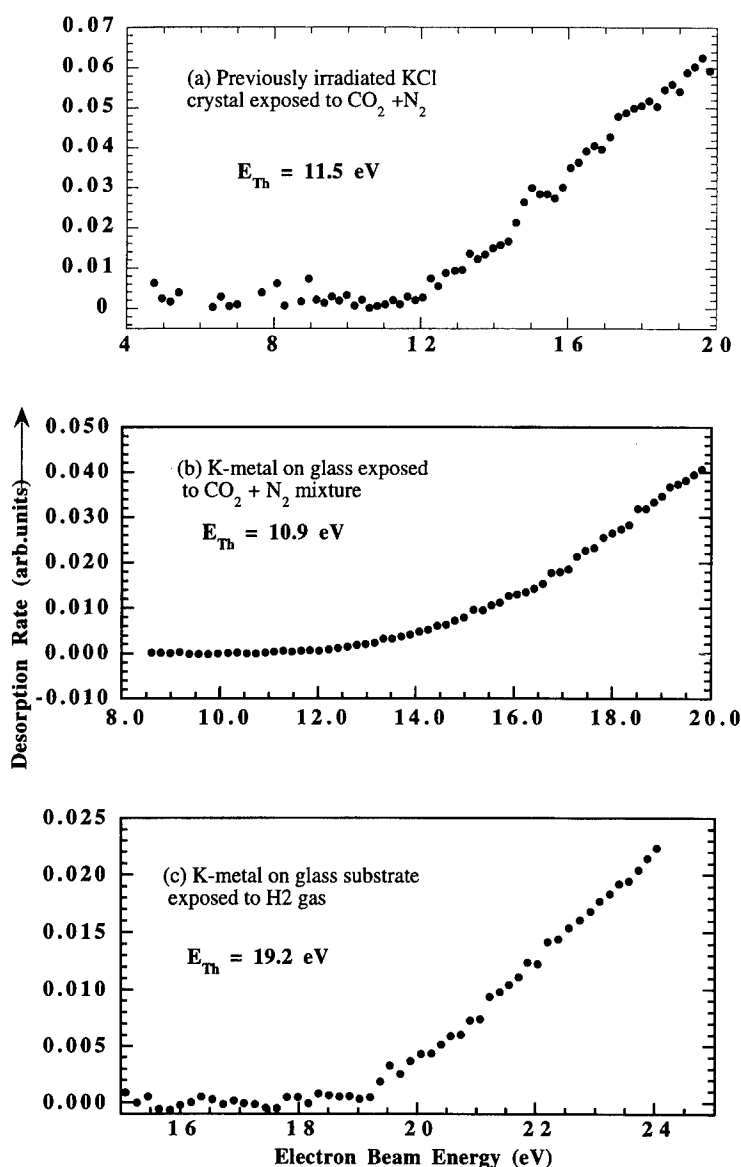


Fig. 1. CN desorption yield as a function of electron energy from (a) K-metal on glass substrate exposed to $\text{CO}_2 + \text{N}_2$ gases, (b) previously electron irradiated KCl exposed to $\text{CO}_2 + \text{N}_2$ gases, (c) surface prepared as in (a) exposed to H_2 gas.

work functions of cathode and target, Φ_c and Φ_t respectively, have to be accounted for as follows:

$$E_{\text{kin}} = eU_{\text{ct}} - \Phi_c + \Phi_t, \quad (1)$$

where e is the electron charge. The work function of the cathode is about 1.9 eV.

3. Results

Fig. 1a shows the CN^* desorption rate under electron irradiation from a previously electron-irradiated KCl crystal when exposed to CO_2 and N_2 gas mixture at a base pressure of 1.0×10^{-7} Torr. Fig. 1b shows the desorption rate for CN^* from K-metal deposited on a glass substrate when exposed to the same gas mixture. Fig. 1c shows the desorption rate when a previously CO_2 and N_2 exposed surface was exposed to H_2 gas at a partial pressure of 1.0×10^{-7} Torr. As can be seen in Fig. 1a, the desorption

rate from a previously electron irradiated KCl crystal is zero at low energies and exhibits a slow increase at higher energies. The threshold energy, which is estimated as the first point in energy at which the count rate is non zero, is 11.5 ± 0.2 eV for the desorption of CN^* molecules. The uncertainty in energy reported here is estimated from instrument uncertainty. Desorption rate shown in Fig. 1b has an intermediate curved shape before a clear linear shape is observed. Threshold energy in this case is estimated to be 10.9 ± 0.2 eV. From Fig. 1c, it can be seen that the desorption rate is zero at low energies and increases linearly above the threshold energy. The threshold is estimated as 19.2 ± 0.2 eV in this case.

Fig. 2a shows the envelope of the rotational distribution spectra, normalized to unity, of desorbing CN^* molecules from a potassium-rich surface under electron irradiation at various energies near threshold. These spectra were taken at medium resolution (~ 1.25 Å). As can be seen from this graph, the rotational distribution is independent of the

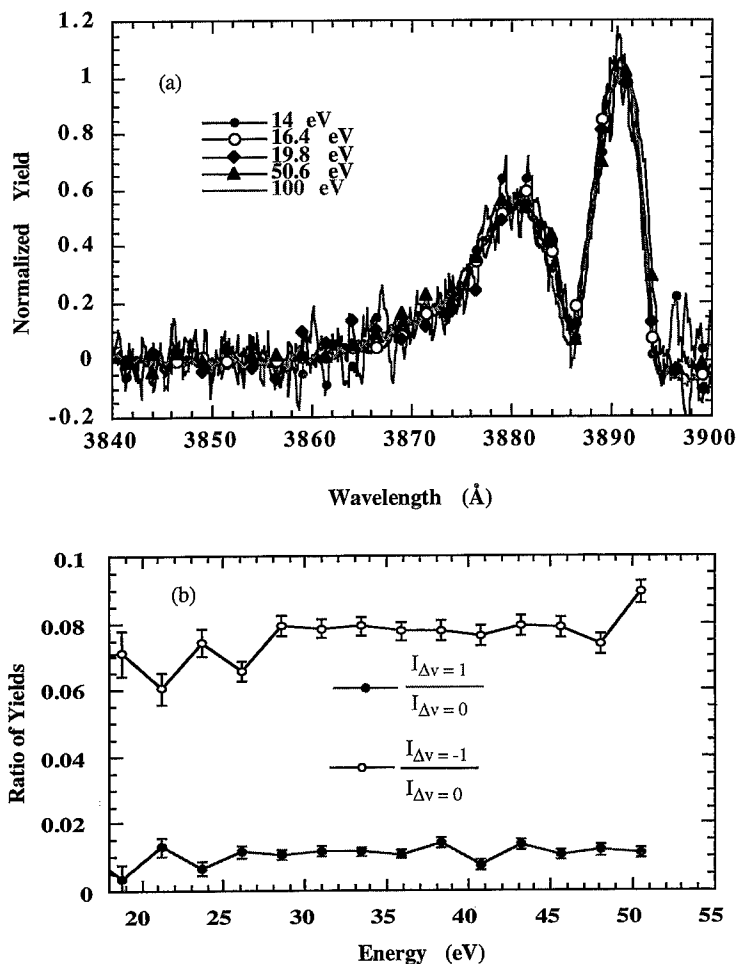


Fig. 2. (a) Rotational energy distribution of desorbing CN^* from potassium rich surface at various excitation energies normalized to unity. (b) Ratio of intensities of $\Delta v = +1$ and $\Delta v = -1$ transitions with $\Delta v = 0$ transition.

incident electron energy even near threshold energies. Shown in Fig. 2b are the vibrational transitions ($\Delta v = -1$ and $+1$) of the desorbing CN molecule. The data were obtained in a manner similar to the threshold measurements. The wavelengths corresponding to the transitions $\Delta v = -1, 0$, and $+1$ are centered at 357 nm, 388 nm, and 420 nm respectively. Peak rates were taken at wavelengths centered at these values and the corresponding peak width was used to subtract the linear background. The $v = 1 \rightarrow v = 0$ and $v = 0 \rightarrow v = 1$ yields were normalized to the yield of $v = 0 \rightarrow v = 0$ transition. The energy of the beam was moved to various values near and above threshold energies. As can be seen from Fig. 2b, the vibrational cross section is independent of incident electron energy. This shows that the relative excited state population in different vibrational states is independent of excitation energy.

4. Discussion

4.1. CN-surface bond

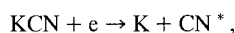
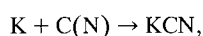
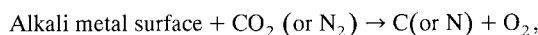
Rotational distribution studies show that the CN molecule is bound to the alkali component of the substrate [11]. Present studies further confirm this model since the threshold energies obtained from previously electron-irradiated KCl crystals and K-metal surface is 11.5 eV and 10.9 eV respectively (Fig. 1a and 1b). The difference in reported threshold energies may be attributed to different work functions of the prepared surfaces. The beam energy reported here is only the potential difference between the target and the filament and does not account for the differences in the work functions of the samples. Thus, within all these experimental uncertainties it can be concluded that the same CN-surface bond is broken under electron irradiation for the two surfaces reported here. In other words, it may be concluded that CN molecules are bound to the surface as alkali-CN.

A second interesting aspect of CN bonding with the surface can be seen from the threshold-energy measurements for CN* desorption from K-metal deposited on glass substrates exposed to H₂ gas (Fig. 1c). The threshold energy when the samples were exposed to CO₂ and N₂ mixture, was found to be 11.9 eV and 11.5 eV for K-metal on glass substrate and KCl respectively whereas for the case of H₂ exposure it was found to be 19.2 ± 0.2 eV. This difference is remarkable since ESD threshold energy for hydrogen desorption from KCl crystals using H_α desorption yield experiments was reported to be 18.5 eV [12]. This leads one to believe that the electron irradiation breaks an altogether different bond when the surface was exposed to H₂ gas.

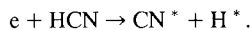
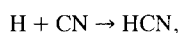
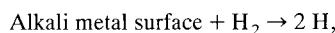
Rotational distribution of desorbing CN was reported to depend on the gases exposed [13]. It was also shown by the same authors [11] that the rotational distributions arise

from CN* desorbing from various alkali-halides depend only on the alkali component of the substrate and were independent of the halide component, surface temperature, and incident electron energy. Sensitivity of rotational distributions on adsorbate site was explained using a model of angle-hindered ground state potential [14] and anisotropic excited state potentials [15]. Present studies further confirm the model proposed by Jun Xu et al. in Ref. [13]. The different rotational structure was described using a model described by the following chemical reactions:

CO₂ + N₂ exposure:



H₂ exposure:



Present measurements of CN* desorption-threshold energies confirm the model proposed on the basis of rotational energy distribution experiments by Jun Xu et al. As stated earlier, desorption threshold energy for H_α desorption from KCl and KBr crystals were measured to be 18.50 eV, and 18.14 eV [12] respectively. Observed threshold energy for CN* desorption under H₂ exposure is 19.2 eV. This close agreement of threshold energies confirms that electron irradiation breaks HCN bond which results in H and CN desorption from the surface in excited states.

4.2. Desorption mechanism

In a model similar to the Antoniewicz model [4], we propose that the adsorbed CN can be excited to a higher electronic state resulting in a bound-bound transition under electron irradiation. Molecules in this highly excited state relax quickly to a lower repulsive state that is very close to this bound state. The threshold energy (10.88 ± 0.15 eV) then will be the energy difference between the two bound states. This is schematically shown in Fig. 3. $V_0(R)$ is the ground state potential for the KCN system while $V_1(R)$ and $V_2(R)$ are the excited bound and repulsive states respectively. R is the radial distance between potassium and CN center of mass. Upon electron irradiation, the system is first excited to $V_2(R)$ and relaxes to $V_1(R)$ resulting in desorption in an excited state.

As can be seen from the Fig. 2a, there is no change in the envelope of the rotational spectrum for various incident energies. It has been shown that these rotational energy distributions are independent of the substrate temperature and are non-Boltzmann [7]. The average rotational energy has been experimentally found for various alkali metals in the same paper. For potassium, $\langle E_r \rangle$ is given as 28 meV

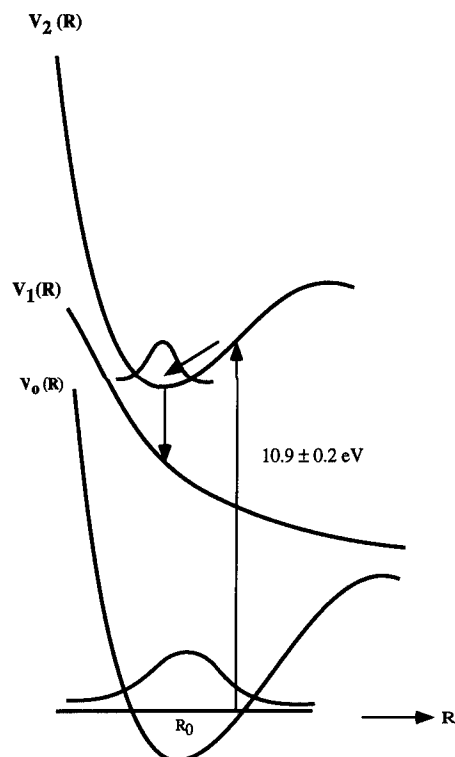


Fig. 3. Potential energy curves representing the Antoniewicz type model. $V_0(R)$ is the ground state potential, $V_2(R)$ is the excited bound state, while $V_1(R)$ is the repulsive potential energy curve. The system is first excited to $V_2(R)$ and then relaxes to $V_1(R)$ resulting in desorption. R is the distance between K and CN center of mass.

for a substrate temperature of 60 K. In the MGR type desorption process, the rotational-state populations of the molecules will depend on the initial bonding state, and the evolution of the molecule through an anti-bonding state to a free state. Some workers have explained rotational distributions arising from desorbed molecules due primarily to ground state potential surfaces [16], while others attribute the distribution to the repulsive-state potential surface [17]. Jun Xu et al. [11] have reported a quantum description of desorption and rotation in which the angular momentum may arise both from the initial wave function in the ground state and from the time evolution of the wave functions in the excited state as the molecule is ejected from the surface. Gadzuk and co-workers [18] explained rotational distributions based on a transition from a hindered rotor to a free rotor, where the angular distribution is unaffected by the time evolution in the repulsive state. In their model, a rigid dumbbell executes free rotations with small angular cone bounded by an infinitely repulsive wall. The wall is suddenly switched off by the electronic transition which results in a non-equilibrium population of free rotational states due to the conversion of zero point kinetic energy

into free rotational energy about the rotor center of mass. The rotational state distribution is given by the sum of rotational Frank–Condon factors between free-rotor wave function and hindered-rotor wave function. The angular momentum states, which gives rise to rotational distributions can be viewed as a direct measurement of ground state potential surface.

The potential-energy surface in the excited state determines the time evolution of the initial wave function. Hasselbrink [17] and Kremp [19] explained the final rotational distribution in terms of the potential-energy surface in the repulsive state. The anisotropy of the potential results in a net torque exerted on the molecule. This torque will influence the molecular rotation. For the case of rotational distribution arising from molecular scattering from surfaces, as studied by Barker et al. [20], the initial state is described by an incoming wave function. For the incoming wave function, there is no constraining potential or corresponding steady state solution to Schrödinger equation. The time evolution of the final state as the molecules leave the surface is the same for both the cases (scattering and DIET processes). Unlike the case of molecular scattering, where the rotational distribution depends on the incident energy and angle, the independence of the rotational distribution on incident electron energy only confirms the fact that the parent surface bond is the only key factor in DIET processes.

Using the Antoniewicz-type interpretation, the independence of rotational distribution with incident electron energy can be explained easily due to the intermediate bound state. Since the molecule is always excited to a certain upper bound state, the rotational motion of the molecule is entirely determined by the upper state potential energy curve $V_2(R)$. It may be concluded that on transition from $V_0(R)$ to $V_1(R)$, the molecule goes from one state of hindered rotor to another and the constraint imposed by the potential energy curve $V_2(R)$ is removed during the subsequent transition to $V_1(R)$ where it is a free rotor. Since this constraint imposed by $V_2(R)$ is independent of the excitation energy, the rotational distribution is unique for all incident electron energies. This will also explain the constancy of the relative populations of vibrational states.

5. Conclusions

In summary, we have measured the threshold energy for electron stimulated desorption of excited CN molecule from potassium surfaces to be different when exposed to various gases. The chemistry associated with the desorption is found to be different in the two cases. Independence of rotational distributions and the relative vibrational populations is used to interpret the data in the context of Antoniewicz model.

Acknowledgements

The authors thank J. Tellinghuesen, J. Xu, J. Tully, and J. W. Gadzuk for valuable discussions. This research was sponsored by the Office of Naval Research under the contract numbers N000014-91-0109 and N000014-91-J-4040.

References

- [1] N.H. Tolk, L.C. Feldman, J.S. Kraus, R.J. Morris, M.M. Traum and J.C. Tully, *Phys. Rev. Lett.* 49 (1982) 812.
- [2] P.J. Feibelman and M.L. Knotek, *Phys. Rev. Lett.* 40 (1978) 964.
- [3] P.A. Redhead, *Can. J. Phys.* 42 (1964) 886; D. Menzel and R. Gomer, *J. Chem. Phys.* 41 (1964) 3311.
- [4] P.R. Antoniewicz, *Phys. Rev. B* 21 (1980) 3811.
- [5] D.A. Mantell, R.R. Cavanaugh and D.S. King, *J. Chem. Phys.* 84 (1986) 1531; R.R. Cavanaugh and D.S. King, *Phys. Rev. Lett.* 47 (1981) 1829.
- [6] Greg O. Sitz, Andrew C. Kummel and Richard N. Zare, *J. Chem. Phys.* 89 (1989) 2558; B.H. Choi, Z.B. Guvenc and N.L. Liu, *Phys. Rev. B* 42 (1990) 3887; D. Weide, P. Audresen and H.J. Freund, *Chem. Phys. Lett.* 136 (1987) 106.
- [7] Jun Xu, Alan Barnes, Royal Albridge, Carl Ewig and Norman Tolk, *Phys. Rev. B* 48 (1993) 8222.
- [8] S. Vijayalakshmi, A.V. Barnes, R.G. Albridge and N.H. Tolk, to be published in *Phys. Rev. B*.
- [9] N.G. Stoffel and P.D. Johnson, *Nucl. Instr. and meth. A* 234 (1985) 230.
- [10] P. Wurz, J. Sarnthein, W. Husinsky, G. Betz, P. Nordlander and Y. Wang, *Phys. Rev. B* 43 (1991) 6729.
- [11] Jun Xu, L. Hullet Jr., A. Barnes, R. Albridge and N. Tolk, in: *Desorption Induced by Electronic Transitions, DIET V*, eds. A.R. Burns, E.B. Steechel and D.R. Jennison (Springer, Berlin, 1993) p. 313.
- [12] L. Hudson, Ph.D. Thesis, Vanderbilt University, Nashville, USA, 1989, pp. 62.
- [13] Jun Xu, Larry Hudson, Royal Albridge, Alan Barnes and Norman Tolk, *Surf. Sci. Lett.* 289 (1993) L622.
- [14] J.W. Gadzuk, U. Landman, E.J. Kuster, C.L. Cleveland and R.N. Barnett, *Phys. Rev. Lett.* 49 (1982) 426; *J. Electron Spectrosc. Relat. Phenom.* 30 (1983) 103; U. Landman, E.J. Kuster, C.L. Cleveland, R.N. Barnett and J.W. Gadzuk, *Phys. Rev. B* 29 (1984) 4313.
- [15] E. Hasselbrink, *Chem. Phys. Lett.* 170 (1990) 329.
- [16] A.R. Burns, E.B. Stechel and D.R. Jennison, *Phys. Rev. Lett.* 58 (1987) 250.
- [17] E. Hasselbrink, *Chem. Phys. Lett.* 170 (1990) 329.
- [18] J.W. Gadzuk, Uzi Landman, E.J. Kuster, C.L. Cleveland and R.N. Barnett, *Phys. Rev. Lett.* 49 (1982) 426; *J. Electron Spectrosc. Relat. Phenom.* 30 (1983) 103; Uzi Landman, E.J. Kuster, C.L. Cleveland, R.N. Barnett and J.W. Gadzuk, *Phys. Rev. B* 29 (1984) 4313.
- [19] Stefan Krempel, *Surf. Sci.* 259 (1991) 183.
- [20] J.A. Barker, A.W. Kleyn and D.J. Auerbach, *Chem. Phys. Lett.* 97 (1983) 9.

Loss of material from Ga–In liquid surface during bombardment by hyperthermal Ta, Pt and Au atoms

Martha Riherd Weller ^{a,*}, Robert A. Weller ^b

^a Middle Tennessee State University, P.O. Box 403, Murfreesboro TN 37132, USA

^b Vanderbilt University, Nashville, TN 37235, USA

Abstract

We have investigated the loss of incident atoms and of substrate atoms from the surface of the liquid Ga–In eutectic alloy during bombardment of the surface with hyperthermal Ta, Pt and Au atoms. Hyperthermal atoms were produced by sputtering solid metallic targets positioned directly above the liquid Ga–In surface. By analyzing material deposited on graphite collector surfaces which surrounded the liquid alloy during bombardment, angular distributions were determined for atoms leaving the liquid surface as a result of the bombardment. For all three species of incident atoms, we detected Ga and In as well as the primary sputtered species on the collectors. The angular distributions for the primary sputtered species were strongly peaked in a near-normal direction consistent with direct reflection from the liquid surface. In all cases, we observed angular distributions for the Ga which included a broad peak, centered near the surface normal, although not at the same angle as the maximum for the incident species. Such a broad distribution is consistent with secondary sputtering of the liquid surface by the incoming atoms. The distribution of indium atoms is also suggestive of sputtering. However, we observed significant asymmetry in the In distributions which may be correlated with the angular distributions for the incident species. Our results support previous data indicating that surface sputtering (or re-sputtering) and direct reflection of primary sputtered atoms are significant mechanisms for the loss of material from surfaces during hyperthermal processes such as sputter deposition.

1. Introduction

Sputter deposition of thin films has been of interest for many years from both a technical and a scientific viewpoint. Sputter-deposited films have a number of practical applications such as the fabrication of semiconductor devices [1], and have long been used as a method of investigating the sputtering process itself [2,3]. Understanding the mechanisms responsible for the loss of material from sputter-deposited films is important for all of these studies since the properties of the final film depend both on the deposition rate and on the loss rate. Re-sputtering by backscattered beam ions has long been recognized as a likely process [4], but other mechanisms [5,6], involving the interaction of sputtered atoms with the sputter-deposited surface, have also been proposed.

The dynamics of the interaction of an energetic atom with a surface are influenced by several parameters including the energy, E , of the incident atom as well as the masses of all the atoms involved. Atoms with very low

energies (< 1 eV) interact with the surface as a whole, or at least with several atoms simultaneously, while atoms with significantly higher energies (> 10 eV) interact through binary collisions involving only one target atom at a time. Sputtered atoms have an energy distribution of the form $E/(E + E_B)^3$ [7] where E_B is the surface binding energy, typically a few eV, for the sputtered material. Consequently these atoms have energies which span the transition region between whole surface interactions and binary collisions; the binding energy of the sputtered species determines the fraction of sputtered atoms with low energy relative to those with high energy.

The significance of the high energy portion of the sputtered particle spectrum is evident in studies [5] which show that resputtering of previously deposited atoms by these particles dominates resputtering by backscattered beam ions in some cases. However, resputtering has been ruled out as a loss mechanism for at least one system [8]. Although direct reflection of sputtered atoms from surfaces has been rejected as a loss mechanism based on the kinematics of binary collisions [5], low energy sputtered particles should interact with several atoms simultaneously so that reflection is feasible. In the absence of chemical effects, the relative importance of these two types of

* Corresponding author, tel. +1 615 898 2792, fax +1 615 898 5182, E-mail: mrw@physics.mtsu.edu.

interactions should vary systematically with the binding energy of the sputtered species in the original target.

We have measured angular distributions for material ejected or reflected from the liquid surface of the Ga–In eutectic alloy during exposure to the sputtered Ta, Pt and Au atoms. The three species selected for sputtering have similar masses (ranging from 181 u to 197 u), but substantially different binding energies (7.9 eV for Ta, 4.9 eV for Pt and 3.6 eV for Au) and thus different energy distributions. Our results suggest that both resputtering and direct reflection are mechanisms for the loss of material from surfaces exposed to sputtered atoms.

2. Experiment

Thick, high purity (> 99.99% for metal constituents in all cases) foils of Ta, Au and Pt were selected for sources of sputtered atoms in this experiment. The Ga–In eutectic alloy was chosen as the deposition surface because it is liquid at room temperature, an important property which eliminates consideration of surface structure or roughness in this experiment. This alloy has a bulk composition of 17 at.% In, 83 at.% Ga, but In segregates at the surface when the alloy is clean [3]. Thus, the alloy surface is nearly 100% indium. High-purity graphite foils were chosen for the secondary collector foils in this investigation because of the minimal interference this substrate presents during backscattering analysis of surface thin films.

The liquid alloy was loaded into a horizontal boat which was initially located in an auxiliary chamber, isolated from the target chamber. Immediately prior to the sputtering stage of the experiment, the surface of the alloy was sputter cleaned until Auger analysis showed no oxygen or carbon contamination of the alloy surface. After cleaning was completed, the liquid alloy was transferred in vacuo into the main target chamber.

Fig. 1 shows the geometry for the sputtering phase of the experiment. We mounted the sputter targets (Au, Pt, Ta) at an angle of 30° from the horizontal, facing downward. Narrow strips of graphite foil were clamped into place on a half-cylindrical holder which had an inner diameter of 2.54 cm. Each collector foil had a small circular hole at its center, directly below the center of the target foil, permitting sputtered atoms to impinge upon the liquid metal surface directly below the target. Ambient pressure in the target chamber was approximately 1×10^{-9} Torr.

Sputtering was performed using 150 keV Ar^+ ions. During the sputtering process, the beam passed through a 0.6 cm diameter hole and struck the target at an incidence angle of 60° . Sputtered atoms were ejected from the target in all directions. Atoms exiting through the small hole directly beneath the target impinged upon the surface of the liquid metal collector where they were either reflected from the surface or absorbed within the metal. During this

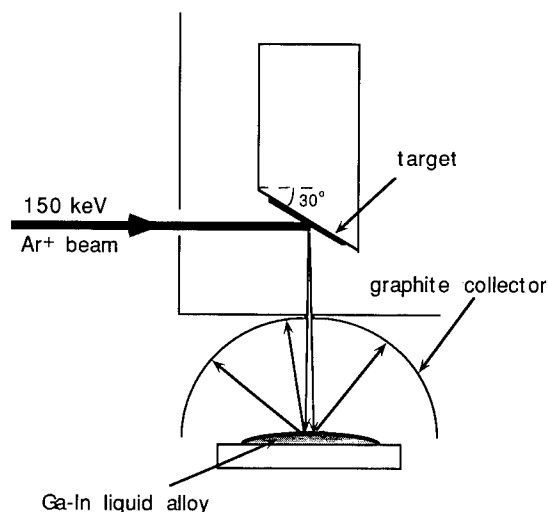


Fig. 1. Experimental geometry for collection of material lost from Ga–In alloy surface during sputter deposition onto liquid surface.

process, In and Ga atoms were also ejected from the liquid metal surface. Reflected sputtered atoms and ejected alloy atoms were collected on the graphite collector surrounding the liquid metal pool.

The metal targets were sputtered for Ar^+ doses ranging from 0.7 C for Ta to 1.0 C for Pt. The beam dose was determined by experimental operating conditions. Using the procedure of Matsunami et al. [9], we estimate total exposures for the liquid metal to the primary sputtered species of 1×10^{16} Ta atoms, 4×10^{16} Pt atoms, and 6×10^{16} Au atoms. In making these estimates, we have assumed an angular dependence of $\cos \theta$ for the primary sputtered particle yields where the ejection angle for sputtered atoms as measured from the surface normal is $\theta = 30^\circ$ for this geometry.

When sputtering was completed, the liquid metal alloy was immediately returned in vacuo to the auxiliary chamber and re-analyzed by Auger spectroscopy. This analysis revealed a very small level of oxygen contamination and no evidence of the primary sputtered species, indicating that these atoms did not remain on the alloy surface after incidence. Since the equivalent of several monolayers of each primary sputtered species was incident on the alloy surface, we would expect to observe the deposited atoms had they remained near the surface.

The final stage of the experiment consisted of analysis of the graphite collector foil by medium energy backscattering spectrometry [10]. 270 keV $^4\text{He}^+$ ions were used for the analysis. Compositions of the material collected on the surface of the graphite were determined at several positions on the collector, yielding angular distributions for the collected species. Data were taken at positions corresponding to approximately 5° intervals along the collectors.

3. Results and discussion

Figs. 2–4 show the angular distributions obtained for material deposited on the graphite collector surfaces during bombardment of the Ga–In liquid metal surfaces with Ta, Pt and Au sputtered atoms. Fig. 2 shows the distribution for the primary sputtered species. Fig. 3 consists of angular distributions for Ga atoms ejected from the liquid metal during bombardment while Fig. 4 shows the angular distributions for In in each case. For Figs. 3 and 4, each plot represents the actual accumulated counts during analysis normalized to correspond to equivalent analysis doses and equivalent sputter exposures. In addition, to facilitate direct comparisons of yields for the primary sputtered species, the plots in Fig. 2 have been scaled by the backscattering cross section for the species of interest relative to the cross section for gold (Lenz–Jensen for 270 keV He^+ scattered

at 150°). Except for Fig. 3, the solid lines should be regarded simply as lines to guide the eye.

There are a number of sources of experimental uncertainty associated with this experiment. Statistical uncertainties in the backscattering peak areas varied with location on the target. These ranged from above 10% in some cases to only 1% in others and are shown explicitly in the figures. There was also an uncertainty associated with the analysis position on the collector foil which was at most 2° . In comparing yields between different sets of data, there is a significant uncertainty in the estimate for the number of sputtered particles incident on the liquid metal in each case due to uncertainties in the estimated sputtering yield, the current integration during sputtering, and the position of the sputtered metal relative to the liquid metal surface. The detector efficiency is energy dependent, but the uncertainty in its value may be neglected when com-

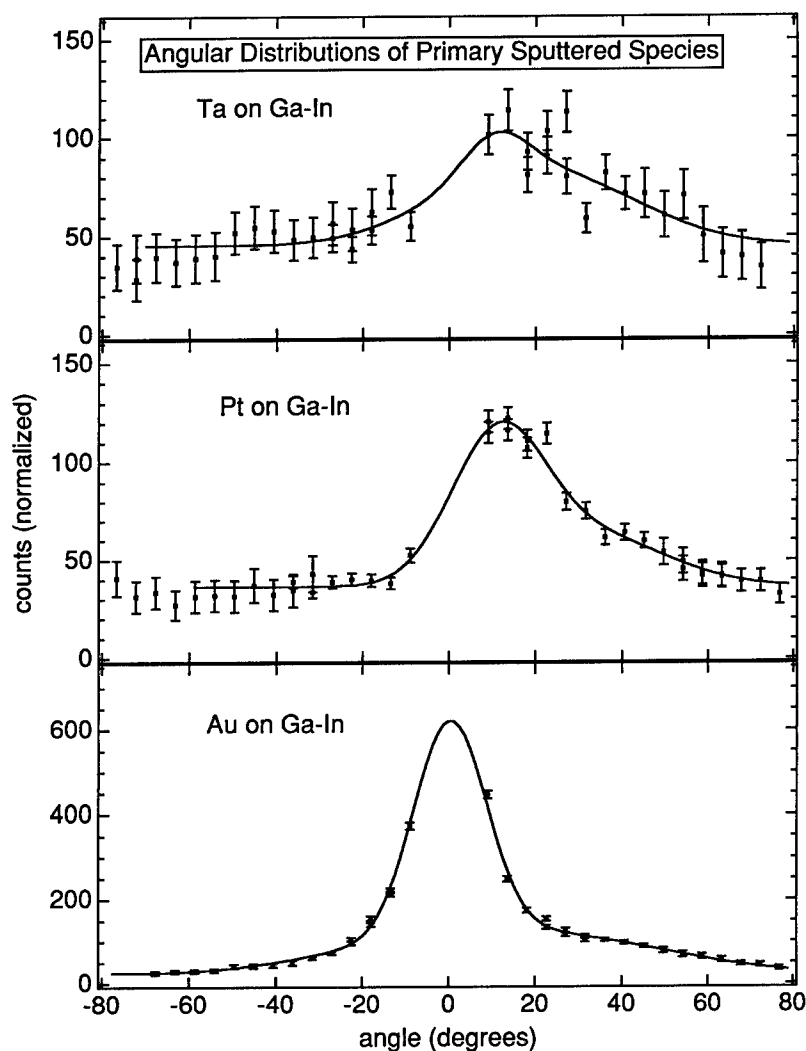


Fig. 2. Angular distribution on secondary collector foil for the primary sputtered species incident on Ga–In alloy surface.

paring backscattering yields from targets having similar masses. Thus, we expect to find essentially the same efficiencies for the data shown in Fig. 2 and can compare these results directly. Similarly, all the data in Fig. 3 correspond to the same detector efficiency (but different from Fig. 2) as do the data in Fig. 4. The solid angle of the detector is the same for all measurements and its uncertainty need not be considered for relative measurements.

Examining all the angular distributions, we note the lack of symmetry about 0° which may be attributed to several factors. The experimental apparatus itself is not symmetric. Even for a uniform, perfectly centered, but finite diameter, Ar^+ beam, backscattered beam particles and sputtered particles originating above the beam center strike the liquid metal at smaller incident angles (measured relative to the surface normal) and over a smaller surface area than do those originating below the beam center. This

leads to an asymmetric angular distribution for particles reflected from the liquid metal surface and could reasonably be expected to result in asymmetries in the distribution of atoms ejected from the liquid metal. Lack of uniformity in the beam or a small offset of the beam from the target center can either enhance or diminish the asymmetry, depending on the direction of the variation. In addition, an alloy surface which is slightly asymmetric about the center of the meniscus will result in asymmetric measured distributions for atoms ejected from the metal surface and for reflected atoms.

Looking more closely at the angular distributions for the primary sputtered species (Fig. 2), we note that, in every case, these distributions are more sharply peaked than the corresponding distributions for the alloy constituents. Since the primary sputtered species was not observed on the liquid metal surface after completion of

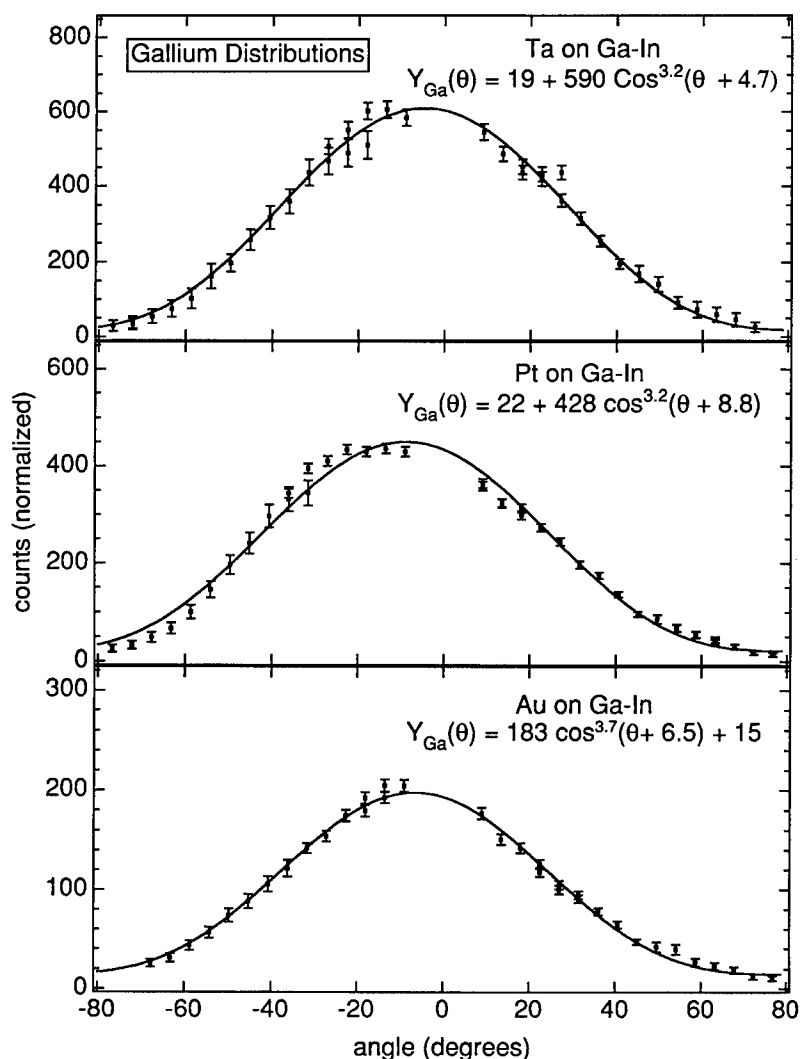


Fig. 3. Angular distribution on secondary collector foil for Ga removed from Ga-In alloy surface.

sputtering, these distributions are unlikely to result from resputtering of atoms deposited on the alloy surface. The relative yields for the three species are consistent, however, with direct reflection from the alloy surface. Low-energy atoms are more likely to be reflected from the surface since they interact simultaneously with several atoms rather than with a single atom. (Winters et al. [11] found that Xe and Ar atoms colliding with Pt behaved as if they had struck an effective mass of 1.5 Pt atoms for incident energies of 10 eV while, for incident energies below 1 eV, the effective mass was 5 Pt atoms.) Since the average energy of sputtered atoms scales with surface binding energy, we observe that Au atoms are reflected more efficiently than Pt atoms while Ta atoms bounce back less efficiently. This explanation is consistent with studies by Libbrecht et al. [8] showing that low energy sputtered

uranium atoms were more likely to be lost from collector surfaces than their higher energy counterparts. (This particular study also ruled out resputtering as a loss mechanism for sputter-deposited uranium atoms.)

The overall shapes of our angular distributions for the primary sputtered species are similar to angular distributions obtained by Rettner et al. [12] for scattering of low-energy Xe from Pt. (Although Xe is lighter than Pt, this comparison is reasonable since heavy atoms having energy below 10 eV scatter from an effective mass larger than that of a single substrate atom.) For non-normal incidence, the peak in the distribution occurs at an angle significantly beyond the specular result due to incomplete momentum reversal perpendicular to the surface. The extent to which this occurs determines the width of the peak with lower energies resulting in narrow peaks since the

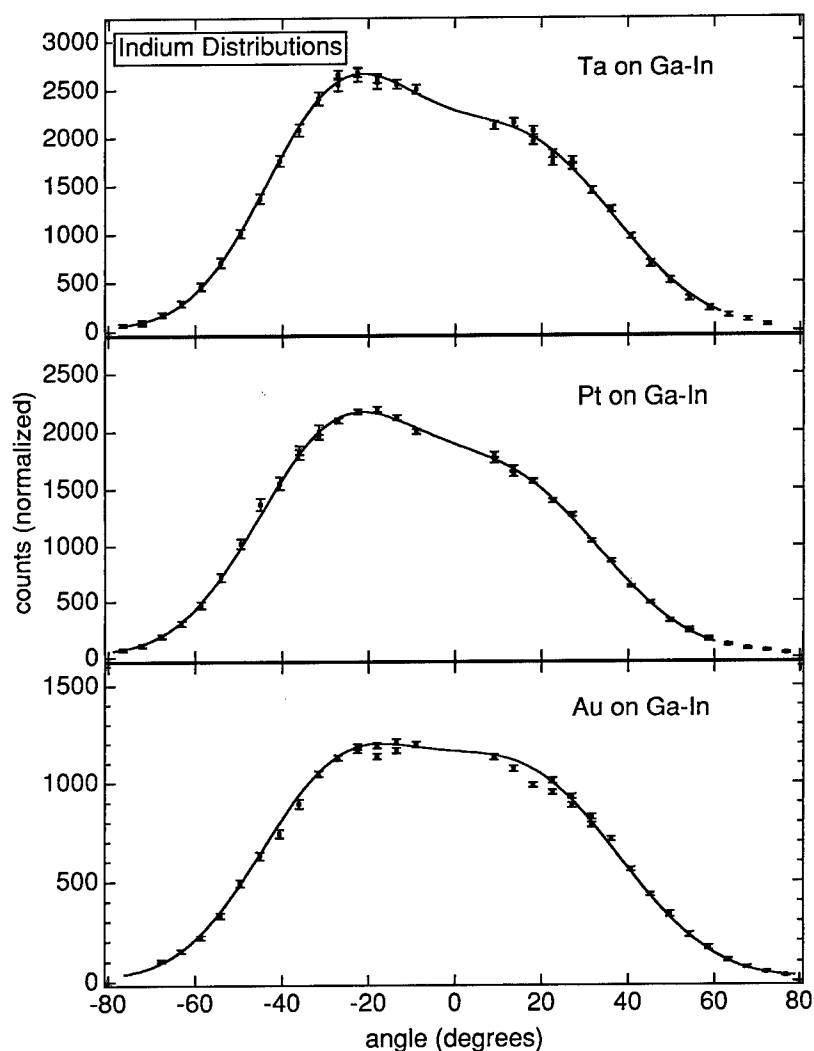


Fig. 4. Angular distribution on secondary collector foil for In removed from Ga-In alloy surface.

normal component of momentum is more effectively reversed. The long tails to the distributions presumably result from particles backscattered via multiple collisions.

The angular distributions for gallium atoms (Fig. 3) were broad and much more symmetric than those for any other species. Anticipating a sputtering-type distribution, we fit these data to the form

$$Y(\theta) = A_1 \cos^p(\theta - \theta_1) + B. \quad (1)$$

The solid lines in Fig. 3 indicate excellent fits for tantalum and gold incoming atoms. These distributions are similar to the sputtered Ga distributions obtained by both Dumke et al. [3] and Hubbard et al. [13] under more typical sputtering conditions. For incoming particle energies between 3 and 50 keV, they found that the exponent p in Eq. (1) ranged between 2.0 and 4.9, with most values between 3 and 4. While we are not inclined to give any significance to this particular functional form for the Ga distributions, the close resemblance of our data to sputtering distributions obtained for the same material indicates that sputtering of Ga occurs in our system as well. This sputtering may be caused by primary sputtered atoms or by backscattered beam ions.

The angular distributions for indium atoms (Fig. 4) were all relatively broad, qualitatively similar to those found by other groups during sputtering of the Ga–In alloy. Both Dumke et al. [3] and Hubbard et al. [13] obtained symmetric angular distributions for sputtered In which were relatively flat within 30° of the normal direction, falling off sharply at larger angles. For all three indium distributions, we observed a similar rapid decrease in indium concentrations at large angles. For Au incidence, the distribution is symmetric and approximately flat in the central region. For Ta and Pt incidence, we observed asymmetric central distributions with inflections which occurred at the same angles as inflections in the Au spectrum. Comparing the indium angular distributions to those for the corresponding incident species, there appears to be a correlation between the asymmetries in the two sets of angular distributions. We attribute the angular distributions for indium to sputtering by both backscattered beam ions and primary sputtered atoms. We suspect that the asymmetries in the In angular distributions result from asymmetries in the direction and location of impact for the primary sputtered atoms.

4. Conclusions

Measured angular distributions of material lost from a liquid Ga–In alloy during exposure to primary sputtered particles indicate that both Ga and In atoms are sputtered

from the alloy, probably by both the primary sputtered species (Ta, Pt, or Au) and backscattered Ar⁺ beam ions. In addition, angular distributions of the incident sputtered species demonstrate that some of incoming sputtered atoms are reflected from the surface. In a typical sputter deposition on a solid substrate, the relative importance of these processes will be determined both by chemistry and kinematics. Atoms with low binding energies in their original targets will be more easily reflected from the substrate surface, but reflection may also be the dominant loss process for materials such as uranium which are not easily resputtered.

Acknowledgements

We gratefully acknowledge the assistance of Mr. Jeff Ward, Mr. Mark Moser, Mr. David King and Mr. James Arps who assisted with data taking for this project. This project was supported by a Schering–Plough Grant of the Research Corporation. Additional support was provided by the United States Army Research Office under contract DAAL-03092-G-0037.

References

- [1] R. Bruce, S. Eicher and W.D. Westwood, *J. Vac. Sci. Tech.* A 6 (1988) 1642.
- [2] H.H. Andersen and H.L. Bay, in: *Sputtering by Particle Bombardment I: Topics in Appl. Phys.*, vol. 47, ed. R. Behrisch (Springer, Berlin, 1981) 145.
- [3] M.F. Dumke, T.A. Tombrello, R.A. Weller, R.M. Housley and E.H. Cirlin, *Surf. Sci.* 124 (1983) 407.
- [4] W. Krüger, K. Rödelberger and A. Scharmann, *Z. Phys.* 262 (1973) 315.
- [5] R. Buckard, D. Hasselkamp, A. Scharmann, K.-H. Scharfner and H.-W. Seibel, *Radiat. Eff.* 109 (1989) 301.
- [6] M.R. Weller, M.H. Mendenhall and R.A. Weller, *Nucl. Instr. and Meth. B* 59/60 (1991) 102.
- [7] M.W. Thompson, *Philos. Mag.* 18 (1968) 377.
- [8] K.G. Libbrecht, J.E. Griffith, R.A. Weller and T.A. Tombrello, *Radiat. Eff.* 49 (1980) 195.
- [9] N. Matsunami, Y. Yamamura, Y. Itikawa, N. Itoh, Y. Kazumata, S. Miyagawa, K. Morita, R. Shimizu and H. Tawara, *At. Data Nucl. Data Tables* 31 (1984) 1.
- [10] M.H. Mendenhall and R.A. Weller, *Nucl. Instr. and Meth. B* 47 (1990) 193.
- [11] H.F. Winters, H. Coufal, C.T. Rettner and D.S. Bethune, *Phys. Rev. B* 41 (1990) 6240.
- [12] C.T. Rettner, J.A. Barker and D.S. Bethune, *Phys. Rev. Lett.* 67 (1991) 2183.
- [13] K.M. Hubbard, R.A. Weller, D.L. Weathers and T.A. Tombrello, *Nucl. Instr. and Meth. B* 40/41 (1989) 278.

INSTRUCTIONS TO AUTHORS

Contributions to *Section B of Nuclear Instruments and Methods in Physics Research* must be in English and should have an abstract. The manuscript and copies of figures should be submitted in duplicate, together with one set of good quality figure material (for production of the printed figures), to one of the Editors, Prof. H.H. Andersen or Dr. L.E. Rehn. Together with the manuscript an exactly identical electronic version on diskette can be submitted. Upon acceptance of the article for publication, both the manuscript and the diskette will be sent by the Editor to the Publisher. Note that revisions in proofs of accepted papers are not possible. It is the authors' responsibility that the accepted paper is correct in every respect. It is suggested that manuscripts originating from Europe, India, The Middle East and Africa be sent to Copenhagen and manuscripts from The Americas, The Far East and Australasia, to Argonne.

Prof. H.H. Andersen
The Niels Bohr Institute, Ørsted Laboratory
Universitetsparken 5, DK-2100 Copenhagen Ø
Denmark
Tel. +45 35320482 FAX: +45 35320460
e-mail: nimb@meyer.fys.ku.dk

Dr. L.E. Rehn
Materials Science Division, Bldg. 223, RM S231
Argonne National Laboratory, 9700 South Cass Ave
Argonne IL 60439, USA
Tel. +1 708 2529297 FAX: +1 708 2523308
e-mail: lynn_rehn@qmgate.anl.gov

Short contributions of less than 1500 words and not subdivided into sections may be published as Letters to the Editor in a shorter time than regular articles as the proofs will normally be corrected by the Publisher.

Preparation of manuscripts

Manuscripts should be typed throughout with double line spacing and wide margins on numbered pages.

The *title page(s)* should contain, in addition to the article title, author(s) names and affiliations, the text of related footnotes and the text of the abstract. The author to whom proofs should be sent must be indicated with his/her full postal address, fax number, telephone number and/or e-mail address.

Tables should be typed on separate sheets at the end of the manuscript. In addition to its serial number, each table should have a sufficiently detailed heading or caption to explain the data displayed in it.

Figures should be numbered and their captions listed together at the end of the manuscript.

References in the text to other publications should be numbered consecutively within square brackets, for example: "Using a similar technique [1]..." or "As outlined in ref. [2]..." and listed together at the end of the text, for example:

[1] G.A. Smith, K.-H. Park, G.-C. Wang, T.-M. Lu and W.M. Gibson, *Surf. Sci.* 233 (1990) 115.

[2] T.Y. Tan, in: *Defects in Semiconductors*, eds. J. Narayan and T.Y. Tan (North-Holland, Amsterdam, 1981) p. 163.

In the case of multiple authorship all authors should be listed in the references provided they number less than ten. Only in case of more than ten authors is the first author et al. acceptable.

Formulae in the manuscript should be clearly written or typed with particular consideration given to characters that may be misinterpreted. If necessary, unusual symbols should be explained in pencil in the margin.

Preparation of figures

The Publisher requires a set of good quality drawings and photographs to produce the printed figures.

Line figures are preferably reduced to single-column width (~7.6 cm). Submitted drawings should be 1.5–3 times larger than the printed size; the height of letters and numbers should, after reduction, fall within the range 1.2–2.4 mm. Do not use too narrow pen widths for machine-plotted graphs. Shaded areas should be shown by means of cross-hatching or a matrix of dots, rather than a continuous grey wash.

Photographs should be already be screened (overprinted with the point matrix used by printers). The top side of a photograph should be marked if necessary.

Colour figures can be printed in colour when this is essential to the presentation. Authors will be charged for colour reproduction. Further information can be obtained from the publisher, or can be found in the second issue of volume 95, p. 284.

Electronic manuscripts

The Publisher invites the submission of electronic manuscripts for NIM-B. LaTeX articles and articles prepared with any of the well-known wordprocessors can be handled by the Publisher. It is the authors' responsibility that the electronic version exactly matches the paper manuscript. Further information can be obtained from the Publisher.

Correspondence with the Publisher

After acceptance of an article, any correspondence should be addressed to: NIM-B, Elsevier Science B.V., Physics and Materials Science Dept., P.O. Box 103, 1000 AC Amsterdam, The Netherlands. Telephone: (+31-20) 4852500, Fax: (+31-20) 4852775, e-mail: nimb-j@elsevier.nl.

Reprint order forms will be sent out with the proofs directly to the author. Fifty reprints are provided free. When page proofs of the accepted manuscript are made and sent out to authors, this is in order to check that no undetected errors have arisen in the typesetting or file conversion process. At the proof stage only printer's errors may be corrected. No changes in, or additions to, the edited manuscript will be accepted.

Nuclear Instruments & Methods in Physics Research

Section B

Beam Interactions with Materials and Atoms

Abstracted/Indexed in: Current Contents: Engineering, Technology and Applied Sciences; EI Compendex Plus; Engineered Materials Abstracts; Engineering Index; INSPEC; Metals Abstracts; Physics Briefs

VOLUME 100, NOS. 2,3, JUNE (I) 1995

CONTENTS

Proceedings of the Tenth International Workshop on
Inelastic Ion-Surface Collisions (IISC-10)
Grand Targhee Resort, Wyoming, USA, August 8-12, 1994

Edited by A.V. Barnes, P. Nordlander and N.H. Tolk



0168-583X(199506)100:2/3;1-Q